International Natural Science, Engineering and Material Technologies Conference
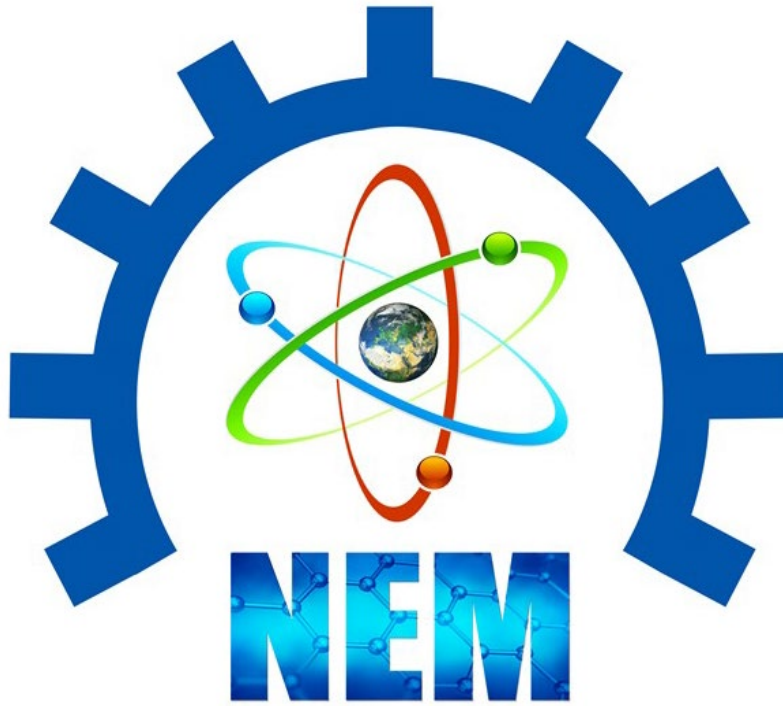**Sep 9-10, 2019 - İstanbul / TURKEY**

NEM 2019

FULL TEXT BOOK

International Natural Science, Engineering and Material Technologies Conference

(NEM 2019)

Sep 9-10, 2019 - İstanbul / TURKEY

FOREWORD

It is a pleasure for us to offer you this Full Text Book for the International Natural Science, Engineering and Material Technologies Conference (NEM2019). Our goal was to create a platform that introduces the newest results on internationally recognized experts to local students and colleagues and simultaneously displays relevant Turkish achievements to the world. The positive feedback of the community encouraged us to proceed and transform a single event into a conference series. Now, NEM 2019 is honoured by the presence of over 152 colleagues from various countries. We stayed true to the original NEM 2019 concept and accepted contributions from all fields of materials science and technology to promote multidisciplinary discussions. The focal points of the conference emerged spontaneously from the submitted abstracts: energy applications, advanced materials, electronic and optoelectronic devices, organic electronic materials, chemistry, physics, environmental science, applied and engineering science, computer simulation of organic structures, biomedical applications and advanced characterization techniques of nanostructured materials. Further fields of interest include e.g. new advanced and functional materials, advanced-functional composites, biomaterials, smart materials, dielectric materials, optical materials, magnetic materials, organic semiconductors, inorganic semiconductors, electronic materials, graphene, and more.

Therefore, we hope that getting first-hand access to so many new results, establishing new connections and enjoying the İstanbul / TURKEY ambience will make you feel that your resources were spent well in NEM 2019.

Our warmest thanks go to all invited speakers, authors, and contributors of NEM 2019 for accepting our invitation, visiting İstanbul and using NEM 2019 as a medium for communicating your research results.

We hope that you will enjoy the conference and look forward to meeting you again in one of the forthcoming NEM 2020 event.

Best regards,
Chairmen's of Conference

Asst. Prof. Burhan COŞKUN   **Prof. Dr. Fahrettin YAKUPHANOĞLU**

International **N**atural Science, **E**ngineering and **M**aterial Technologies Conference
Sep 9-10, 2019 - İstanbul / TURKEY

Full Text Book of the International Natural Science, Engineering and Material Technologies Conference

(NEM 2019)

Sep 9-10, 2019 - İstanbul / TURKEY

Editor:

Dr. Burhan COŞKUN

Published, September-2019

nem2019.klu.edu.tr

nem2019@klu.edu.tr

International Natural Science, Engineering and Material Technologies Conference
Sep 9-10, 2019 - İstanbul / TURKEY

HONORARY PRESIDENT
Prof. Dr. Bülent ŞENGÖRÜR (Rector of Kırklareli University)

CONFERENCE PRESIDENT
Prof. Dr. Fahrettin YAKUPHANOĞLU (Fırat University)

Asst. Prof. Burhan COŞKUN (Kırklareli University)

CO-CHAIRMEN
Berna AKGENÇ (Kırklareli University)

H. Hale KARAYER (Kırklareli University)

Mümin Mehmet KOÇ (Kırklareli University)

ORGANIZING COMMITTEE
Alper BİDECİ (Düzce University)

Macide CANTÜRK RODOP (Yıldız Technical University)

Meryem ÇAMUR (Kırklareli University)

Mustafa KURBAN (Ahi Evran University)

Ömer Suat TAŞKIN (İstanbul University)

Sermet KOYUNCU (Çanakkale Onsekiz Mart University)

Serpil AKÖZCAN (Kırklareli University)

Taner DAŞTAN (Cumhuriyet University)

SCIENTIFIC COMMITTEE
Abdel Salam Hamdy MAKHLOUF (University of Texas / UNITED STATES)

Adem TATAROĞLU (Gazi University / TURKEY)

Mustafa ERKOVAN (INESC-Microsistemas e Nanotecnologias/ PORTUGUAL)

Ahmed A. ALGHAMDI (King Abdulaziz University / SAUDI ARABIA)

Aicha BOUHAFSOUN (University of Science and Technology / ALGERIA)

Asa H. BARBER (London South Bank University/ UNITED KINGDOM)

Burç MISIRLIOĞLU (Sabancı University / TURKEY)

Cemile ÖZCAN (Kırklareli University / TURKEY)

Chung GWIY-SANG (Ulsan University / KOREA)

Denis NIKA (Moldova University / MOLDOVA)

Elias STATHATOS (Tecnological-Educational Institute of Patras / GREECE)

Elizabeth BLACKBURN (University of Birmingham / UNITED KINGDOM)

Evren ÇAĞLAER (Kırklareli University / TURKEY)

Harun UYAN (Kırklareli University / TURKEY)

Huriye İCİL (Eastern Mediterranean University / KKTC)

İsmail KILIÇ (Kırklareli University / TURKEY)

Mujdat ÇAĞLAR (Eskişehir Anadolu University / TURKEY)

Murat SOYLU (Bingöl University / TURKEY)

Mustafa ERKOVAN (Sakarya University / TURKEY)

Niyazi ÖZDEMİR (Fırat University / TURKEY)

Numan AKDOĞAN (Gebze Technical University / TURKEY)

Nuray ÇAĞLAR (İstanbul University / TURKEY)

Ram K. GUPTA (Pittsburg State University / UNITED STATES)

Raşit TURAN (Middle East Technical University / TURKEY)

S. MANSOURI (University of Gabès / TUNUSIA)

Sencer Süreyya KARABEYOĞLU (Kırklareli University / TURKEY)

Serap ŞENTÜRK DALGIÇ (Trakya University / TURKEY)

Serdar SARIÇİFTÇİ (Johannes Kepler Linz University / AUSTRIA)

W. Aslam FAROOQ (King Saud University / SAUDI ARABIA)

Yashar Azizian KALANDARAGH (University of Mohaghegh Ardabili / IRAN)

Yasin ÜNLÜTÜRK (Kırklareli University / TURKEY)

FULL TEXT PRESENTATION

Fahrettin Yakuphanoğlu	SYNTHESIS OF NANOMATERIALS FOR QUANTUM ELECTRONIC APPLICATIONS	636
Fatih Mehmet Coşkun	TEMPERATURE DEPENDENT CAPACITANCE AND OTHER ELECTRICAL PROPERTIES OF THE DEVICES WITH A STRUCTURE OF Al/YMn$_{0.95}$Os$_{0.05}$O$_3$/p-Si/Al	393
H. Hale Karayer	ANALYTICAL SOLUTION FOR DOUBLE CONFLUENT FORM OF HEUN EQUATION	616
H. İrem Özgündüz	BIOMASS OBTAINING HIGH ENERGY EFFICIENCY BIOFUEL VIA TORREFACTION PROCESS	129
Hilmican Caliskan	ANTIBACTERIAL AND ANTIFUNGAL ACTIVITIES OF THREE EXTRACTS FROM *CIRSIUM ITALICUM* (SAVI) DC	135
Israfil Kucuk	THE EFFECT OF PEG-40S SURFACTANT CONCENTRATION ON THE STABILITY OF ALGINATE MICROBUBBLES PRODUCED BY T-SHAPED MICROFLUIDIC JUNCTION DEVICE METHOD	525
Işıl Bolova	EVALUATION OF ADHESION OF ALKOXY BASED SILICONE ON SURFACE TREATED POLY(PROPYLENE) EXTERIOR TRIMS OF VEHICLES BEFORE AND AFTER AGEING TESTS	52
İlbilge Dökme	DEVIATIONS FROM THERMIONIC EMISSION IN CURRENT-VOLTAGE (*I-V*) CHARACTERISTICS OF SCHOTTKY STRUCTURES	104
İlbilge Dökme	THE INVESTIGATION OF EFFECTS OF (NANOCARBON DOPED-PVP) POLYMER INTERFACIAL LAYER ON THE MAIN ELECTRICAL PARAMETERS AND CONDUCTIVITY	112
Jovan Setrajcic	A METHOD FOR SOLVING OF DIFFERENCE EQUATIONS FROM ANALYSIS OF CRYSTALS WITH BROKEN TRANSLATIONAL SYMMETRY	15
Jovan Setrajcic	APPEARANCE OF DISCRETE ABSORPTION IN ULTRATHIN MOLECULAR NANOFILMS	24
Jovan Setrajcic	INFLUENCE OF CHARGE CARRIER AND PHONON SCATTERINGS TO ELECTRIC AND HEAT TRANSPORTS IN GRAPHENE	32
M. Talat Sarıaydın	QUASI ADJOINT CURVES AND THEIR CHARACTERIZATIONS IN 3-DIMENSIONAL SPACE	359
M. Talat Sarıaydın	ON QUASI PEDAL CURVES AND QUASI PEDAL SURFACES IN 3-DIMENSIONAL EUCLIDEAN SPACE	364
Macide Cantürk Rodop	INVESTIGATION OF ANNEALING OF SURFACES OF ITO and PEDOT:PSS FOR PERFORMANCE OF ORGANIC SOLAR CELLS	445
Mehmet Arınç Demirtaş	MEASUREMENT OF THERMAL STRAIN ON A PRINTED CIRCUIT BOARD	296

Merve Özer	ANTIBACTERIAL AND ANTIFUNGAL ACTIVITIES OF THREE EXTRACTS FROM *CIRSIUM CRETICUM SUBSP. CRETICUM*	140
Mine Celiker	ELECTROCHEMICAL CORROSION BEHAVIOR OF YTTRIA STABILIZED ZIRCONIA THERMAL BARRIER COATINGS (TBCs)	412
Murat Üçüncü	EVALUATION OF TECHNOLOGY TRENDS AND PROPOSAL FOR TECHNOLOGY INVESTMENT WAY AHEAD	86
Mustafa Kurban	ASSESSMENT OF LONG-RANGE CORRECTED (LC) PARAMETERS FOR PREDICTION OF ELECTRONIC STRUCTURE OF CARBAZOLE	484
Mustafa Kurban	BAND ENGINEERING AND PHOTOPHYSICAL PROPERTIES OF C-DOPED F8T2 ORGANIC COMPOUND	491
Mustafa Kurban	SIZE DEPENDENT ELECTRONIC STRUCTURE AND STRUCTURAL PROPERTIES OF CUPRIC OXIDE (CuO) NANOPARTICLES	497
Nazlı Turkten	THE EFFECT OF OPERATIONAL PARAMETERS ON THE PHOTOCATALYTIC DECOLORIZATION OF REACTIVE YELLOW 145	377
Oğuzhan Nogay	ANTIMICROBIAL ACTIVITIES OF VARIOUS PLANTS AGAINST FOODBORNE STAPHYLOCOCCUS AUREUS ATCC 6538 AND STAPHYLOCOCCUS AUREUS ATCC 29213 MIXTURE	167
Özgür Masalcı	MICELLIZATION AND THERMODYNAMIC PROPERTIES OFCATIONIC SURFACTANTCETYLTRIMETHYLAMMONIUM CHLORIDE(CTACl) IN AQUEOUS MIXTURE OF POLYVINYLPYRROLIDONE (PVP)	385
Özlem Özkan Önür	RESTORATION WORKS OF İBRAHİM PİLAVCI HOUSE BELONGING TO CIVIL ARCHITECTURE EXAMPLES IN TARAKLI	307
Pelin Ertürk Arı	HEALTH RISK ASSESMENT OF VOLATILE ORGANIC COMPOUNDS (VOCs) IN THE AMBIENT SEMI-URBAN LOCATION IN SUMMER AND WINTER SEASONS	74
Pelin Ertürk Arı	ORGANIC and ELEMENTAL CARBON CONCENTRATIONS on SIZE-SEGREGATED AMBIENT PARTICULATE MATTER in BOLU	80
Perihan Durmuş	^{60}Co GAMMA-RAY IRRADIATION EFFECTS ON THE MAIN ELECTRICAL PARAMETERS OF THE Au/(ZnO:Mn-PVA)/n-Si (MPS) STRUCTURES AT ROOM TEMPERATURE	1
Perihan Durmuş	CAPACITANCE-VOLTAGE (C-V) AND CONDUCTANCE-VOLTAGE (G/ω-V) CHARACTERISTICS BEFORE AND AFTER IRRADIATION IN Au/n-Si/Ag SCHOTTKY BARRIER DIODES (SBDs)	9

Rıdvan Cem Demirkol	ON THE DIFFERENTIAL GEOMETRY OF A SPACELIKE PARTICLE IN A HOMOGENEOUS ELECTROMAGNETIC FIELD IN DE-SITTER SPACE	232
Rıdvan Cem Demirkol	NORMAL FORCE MAGNETIC CURVES IN 3D RIEMANNIAN MANIFOLDS	240
Rıdvan Cem Demirkol	TIMELIKE SPHERICAL MAGNETIC CURVES IN THE DE-SITTER SPACE S_1^2	247
Selçuk Baş	INEXTENSIBLE FLOWS OF TIMELIKE CURVES WITH PARALLEL TRANSPORT FRAME IN MINKOWSKI SPACE-TIME	338
Selçuk Baş	INEXTENSIBLE FLOWS OF DUAL CURVES ACCORDING TO BISHOP FRAME IN DUAL EUCLIDEAN SPACE	346
Selçuk Baş	CONSTRUCTION OF B-FOCAL CURVES IN MINKOWSKI SPACE	353
Selda Güney	USING CONVOLUTIONAL NEURAL NETWORK AS A FEATURE SELECTION METHOD FOR MULTI-FINGERED ROBOT HAND PRESHAPING	588
Selda Güney	PREDICTION OF THE ISE100 INDEX USING PATTERN RECOGNITION ALGORITHMS	596
Semra Bilgiç	DETERMINATION METHODS FOR CORROSION RATE	423
Semra Bilgiç	PASSIVITY IN CORROSION	434
Servet Pirim	GENERAL STRUCTURES OF AUTOMOTIVE GLASSES AND REQUIREMENTS OF FILM COATING APPLICATIONS	158
Sıdıka Polat Çakır	THE ADDITION OF SELECTED ORGANOALUMINUM AND ORGANOZINC REAGENTS TO THE PROTECTED IMINO AND α-KETO PHOSPHONATES	119
Sibel Duman	COPPER(%1)@STARCH NANOPARTICLES: SYNTHESIS AND CATALYTIC ACTIVITY OF GREEN DEHYDROGENATION OF DIMETHYLAMINE BORANE	532
Sibel Duman	CATALYTIC ACTIVITY OF GREEN DEHYDROGENATION OF DIMETHYLAMINE BORANE BY CATALYZED RUTHENIUM(4%)@CELLULOSE NANOPARTICLES	542
Sunay Türkdoğan	GROWTH AND CHARACTERIZATION OF HYBRID STRUCTURES FOR HIGH EFFICIENCY SOLAR CELLS	553
Sunay Türkdoğan	NANOSHEET HETEROSTRUCTURE BASED CORRELATED COLOR TEMPERATURE (CCT) TUNABLE LIGHT EMITTERS	557
Şemsettin Altındal	ON THE FREQUENCY AND VOLTAGE DEPENDENCE OF COMPLEX DIELECTRIC, COMPLEX ELECTRIC MODULUS, AN AC ELECTRICAL CONDUCTIVITY IN AU/(ZNO2FE4-PVP)/N-SI (MPS) CAPACITORS	631

Talat Körpınar	A NEW CHARACTERIZATION OF SMARANDACHE TNB CURVES OF HELICES IN THE SOL SPACE Sol^3	186
Talat Körpınar	NEW APPROACH TO INEXTENSIBLE FLOWS OF Π_2 BISHOP SPHERICAL IMAGES ACCORDING TO TYPE-2 BISHOP FRAME IN E^3	193
Talat Körpınar	ON B-SURFACES OF BIHARMONIC CONSTANT Π_1-SLOPE CURVES ACCORDING TO TYPE-2 BISHOP FRAME IN THE SOL SPACE SOL^3	202
Taner Carkit	INVESTIGATION OF THE POSITIVE EFFECTS OF BATTERY ENERGY STORAGE SYSTEMS ON SOLAR ENERGY COMBINED INTERCONNECTED NATIONAL GRID	93
Taner Dastan	DETERMINATION OF VARIOUS ELEMENT LEVELS IN SOME HONEYS PRODUCED IN BINGOL PROVINCE	302
Tuba Çakıcı	BACTERIAL SYNTHESIS OF COMPLEX GO: Cu: In NANOPARTICLES AND THEIR USE AS THIN FILM IN Au / GO: Cu: In / p-Si STRUCTURE	507
Tuba Çakıcı	INVESTIGATION OF BACTERIAL SYNTHESIZED COMPLEX CuZnSe NANOPARTICLES AND FABRICATION OF CuZnSe THIN FILM	517
Tuğçe Açıkgöz	APPLICATION OF RADIO OVER FIBER MODULATION TECHNIQUES IN INTELLIGENT TRANSPORTATION SYSTEMS	477
Ufuk Akoğuz	FREQUENCY BEHAVIOUR ANALYSIS AND TEST OF PORTABLE MEASURING DEVICE: Cartesian Magnetic Flux Mapper Example	579
Y. Azizian-Kalandaragh	THE EFFECT OF THE ETCHING RATE ON THE MAIN ELECTRICAL PROPERTIES OF p-Si	606
Yasemin Kamaci	SYNTHESIS OF METAL OXIDE NANOPARTICLES BY AN EFFECTIVE COMBUSTION METHOD	417
Yasin Ünlütürk	INEXTENSIBLE FLOWS OF PSEUDO NULL CURVES DUE TO THE BISHOP FRAME IN MINKOWSKI 3-SPACE	254
Yasin Ünlütürk	SOME CHARACTERIZATIONS OF TYPE-3 NULL CARTAN SLANT HELICES DUE TO THE BISHOP FRAME IN MINKOWSKI SPACE TIME	266
Yasin Ünlütürk	ON DARBOUX HELICES DUE TO THE BISHOP FRAME	275
Yeliz Kara	ANNIHILATOR CONDITIONS ON RINGS	146
Yeliz Kara	MODULES WITH EXTENDING CONDITIONS	152
Zeliha Körpınar	ON SOLITON SOLUTION OF THE (3+1)-DIMENSIONAL NLSE WITH KERR LAW NONLINEARITY	209
Zeliha Körpınar	OPTICAL SOLITONS FOR MODIFIED UNSTABLE NONLINEAR SCHRÖDINGER'S EQUATION	215
Zeliha Körpınar	A NEW BIHARMONIC CURVES WITH EXTENDED DARBOUX FRAME	225

^{60}Co GAMMA-RAY IRRADIATION EFFECTS ON THE MAIN ELECTRICAL PARAMETERS OF THE Au/(ZnO:Mn-PVA)/n-Si (MPS) STRUCTURES AT ROOM TEMPERATURE

Perihan Durmuş[1], İlbilge Dökme[2]

[1] Department of Physics, Faculty of Science, Gazi University, TURKEY
[3]Science Education Department, School of Gazi Education, Gazi University, TURKEY

E-mail:pdurmus@gazi.edu.tr

Abstract

In this study, both the current-voltage (I-V) and capacitance-voltage-frequency (C-V) characteristics of the fabricated Au/(ZnO:Mn:PVA)/n-Si (MPS) structures have been investigated before and after 30 kGy ^{60}Co gamma-ray irradiation at room temperature. Experimental results show that ^{60}Co gamma-ray irradiation is very effects on the main electrical parameters such as ideality factor (n), barrier height (Φ_B), series and shunt resistances (R_s and R_{sh}), doping concentration atoms, and surface states (N_{ss})of the electrical characteristics especially in the reverse bias region due to the effect of high-external electric field in this region. ^{60}Co gamma-ray irradiation leads to degrade in the reverse leakage current. Both the value of C and G/ω at 500 kHz become increase under 30 kGy ^{60}Co gamma-ray irradiation due to the radiation induced electro-hole pairs.

Keywords: MPS structures, gamma-ray irradiation, electrical characteristics, surface states

1. INTRODUCTION

It is well known that metal-semiconductor (MS) type structures were studied by many researchers. Once it was found that their electrical characteristics are improved due to native or deposited insulating layer between metal and semiconductor, researchers have given their focus on characterization studies in which they use various insulating layer materials. When an insulating layer is grown between metal and semiconductor, the structure is referred as a metal-insulator-semiconductor (MIS) type structure. Additionally, depending on the nature of the material utilized, MS structures were referred as metal-polymer-semiconductor (MPS) or metal-ferroelectric-semiconductor (MFS) type structures. Polymers are utilized in various industries; renewable-energy, aerospace, medicine, irrigation, clothing, etc. Due to their organic nature, they also attain some features such as easy processing, low cost margin and high ratio of surface area to volume [1,2]. Moreover, their electrical and dielectric properties can be tailored by dispersing/doping agents in polymers [3-5]. Therefore, polymers are used in organic light emitting diodes, organic field effect transistors, organic solar cells and organic photodiodes which are basically comprised of MPS structure form. In the last decade, polyvinyl alcohol (PVA) has grasped considerable attention due to its conformity of being used in MPS devices and its suitability of being doped with agents [3-9]. Therefore, this study focuses on a MPS structure that has ZnO:Mn:PVA as polymeric interfacial layer

Characterizing Schottky devices such as MS, MIS, MFS or MPS structures under various conditions is of importance before they are used in any device form. Therefore these devices need to be tested for conditions such as low or high operating temperature, frequency and radiation. Effect of radiation on Schottky devices was explored by various authors [9-13]. In this study, Au/(ZnO:Mn:PVA)/n-Si (MPS) structures were fabricated and their electrical characteristics were explored before and after ^{60}Co gamma-ray irradiation in order to explore effect of radiation on the current-voltage (I-V), capacitance-voltage (C-V) and conductance-voltage (G/ω-V) characteristics of the device.

2. MATERIAL AND METHODS

Au/(ZnO:Mn:PVA)/n-Si (MPS) structures were fabricated using n-type (P-doped) single crystal silicon wafer with (110) surface orientation, 280 μm thickness, 3" diameter and 0.5 Ωcm resistivity. In order to prevent any impurities, grease and dirt on the wafer, it was cleaned ultrasonically using acetone and propanol and rinsed in deionized water after each step for about 10 min. Later, 3H2SO4:1H2O2 was utilized for cleaning the organic residues for 15 min. Then, the wafer was rinsed into 20% HF to get rid of the oxide layer occurred in the previous steps. After each cleaning step, the wafer was rinsed thoroughly in deionized

water of 18 MΩcm resistivity. Firstly, ohmic contact was formed on back side of wafer with 200 nm thick Al and the sample was annealed at 500 °C for 30 min., secondly ZnO:Mn:PVA was grown on front side of wafer, lastly rectifier contacts was formed on polymeric layer with 200 nm thick Au. Later the fabricated sample was mounted on cupper holder with silver paste for measurements. I-V measurements were taken between –5 V and 5 V using a Keithley 2400 sourcemeter. Admittance measurements were taken between –6 V and 6 V using a HP 4194A LF impedance analyzer. All measurements were held in dark and at room temperature.

3. RESULTS AND DISCUSSION

I-V characteristics of irradiated and unirradiated conditions of MPS structures are given in Figure 1. Both structures exhibit typical diode behaviour of rectification; rectification ratio of the MPS structures are approximately 270 and 200. In the forward bias region, sample with irradiated condition revealed current values that are very close to those of unirradiated case. However, there is prominent increase in current values in the reverse bias region after radiation exposure.

Figure 1. Semilogarithmic I-V plots of irradiated and unirradiated conditions of MPS structures.

According to thermionic emission (TE) theory, voltage dependence of current can be given as below for sufficiently high voltages (V>3kT/q) [1,3,7-9,13];

$$I = I_o \left[\exp\left(\frac{q(V - IR_s)}{nkT} \right) - 1 \right] \tag{1}$$

3

Here; q is electronic charge, V is applied forward bias voltage, n is ideality factor, k is Boltzmann constant, T is absolute temperature in Kelvin, the term IR_s is voltage drop across series resistance and I_o is reverse saturation current which is given as below [1,3,7-9,13];

$$I_o = AA^*T^2 \exp\left(-\frac{q\Phi_{Bo}}{kT}\right) \qquad (2)$$

where A is rectifier contact area, A* is effective Richardson constant (112 A/cm^2.K^2 for n-Si) and Φ_{Bo} is zero-bias barrier height.

Figure 2. lnI-V plots of irradiated and unirradiated conditions of MPS structures.

I-V data was also given as lnI-V plot in Figure 2 so that electrical parameters could be obtained from linear region of this plot. According to Equation 1, ideality factor could be obtained from the slope of this plot where y-axis intercept is utilized for obtaining I_o and later Φ_{Bo}. As seen in the figure, there is a linear region in the moderate forward bias region for each sample with linear fit function available in the figure. Using these functions and Equations 1 and 2, n and Φ_{Bo} values of unirradiated and irradiated conditions of MPS structures were calculated as 4.5 and 657 meV, and 6.0 and 664 meV, respectively. This indicates further deviation from ideality whereas the zero-bias barrier height remains almost same after radiation exposure.

4

I-V data was also utilized to obtain series resistance (R_s) and shunt resistance (R_{sh}) of the MPS structures. Using Ohm's law, resistance (R_i) values of the samples are calculated and given in Figure 3 in the form of semilogarithmic R_i-V plot. In this plot, R_{sh} values correspond to the resistance values in the high reverse bias limit whereas R_s values correspond to the resistance values in the high forward bias limit. It is seen that R_s values are very close to each other whereas radiation exposure caused increase in R_{sh} values in general.

Figure 3. R_i-V plots of irradiated and unirradiated conditions of MPS structures.

Moreover, C-V and G/ω-V plots are given in Figure 4 (a) and (b). Both unirradiated and irradiated conditions of MPS structures exhibit inversion, depletion and accumulation regions. In the figure, there appears slight increase in capacitance in inversion region whereas there is large increase for depletion region, however the trend changes in accumulation region. On the other hand, it is seen that exposure to radiation caused an increase in conductance similarly in depletion region particularly. Such increase in capacitance and conductance is associated with radiation induced electro-hole pairs.

Figure 4. (a) C-V and (b) G/ω-V plots of irradiated and unirradiated conditions of MPS structures.

Capacitance data was also given as C^{-2}-V plot for both irradiated and unirradiated conditions of MPS structures with linear fit lines.

Figure 5. C^{-2}-V plots of irradiated and unirradiated conditions of MPS structures.

Using data in Figure 5, some other electrical parameters could be extracted using the following equation [3,5,7,12];

$$C^{-2} = \frac{2}{q\varepsilon_s A^2 N_D}\left(V_o + V\right) \tag{3}$$

where ε_s, N_D and V_o are permittivity of semiconductor, carrier doping density of donors and the intercept of C^{-2} with voltage axis, respectively. Thus, experimental N_D values were extracted from linear

region of C^{-2}-V plot as 4.2×10^{15} cm^{-3} and 2.2×10^{15} cm^{-3} for unirradiated and irradiated conditions of MPS structures, respectively. Theoretical value of N_D was also calculated as 8.6×10^{15} cm^{-3} so that number of surface states (N_{ss}) can be obtained using c_2 parameter which is the ratio of experimental N_D to theoretical N_D. The relationship between c_2 and N_{ss} is given by following equation where δ and ε_i are thickness and permittivity of insulator layer [5,12];

$$c_2 = \frac{1}{1 + \dfrac{q\delta N_{ss}}{\varepsilon_i}} \qquad (4)$$

Thus N_{ss} values of unirradiated and irradiated conditions of MPS structures were calculated as 8.5×10^{11} eV^{-1}.cm^{-2} and 2.3×10^{12} eV^{-1}.cm^{-2}, respectively. It is clear that exposure to radiation caused restructuring and reordering of the traps in MPS structure and this led to an increase in surface states.

4. CONCLUSION

Au/(ZnO:Mn:PVA)/n-Si (MPS) structures were fabricated and their voltage dependent current and admittance characteristics were investigated before and after 30 kGy ^{60}Co gamma-ray irradiation at room temperature. Exposure to radiation decreased rectification ratio and increased ideality factor while keeping zero-bias barrier height almost unchanged. Gamma-ray irradiation also caused an increase in capacitance and conductance particularly in depletion region. These results are believed to be the outcome of lattice defects; such as vacancies, defect clusters, and dislocation loops due to gamma-ray irradiation. Using capacitance data, doping concentration of donor atoms was obtained and it was found lower after exposure to radiation. Thus, it was found that there occurs an increase in number of surface states after the exposure because of restructuring and reordering of traps.

REFERENCES

[1] Lim, L. W., Aziz, F., Muhammad, F. F., Supangat, A., Sulaiman, K., Electrical properties of Al/PTB7-Th/n-Si metal-polymer-semiconductor Schottky barrier diode, Synthetic Metals, 221, 169-175, 2016.

[2] Shahbazi, M., Bahari, A., Ghasemi, S., Structural and frequency-dependent dielectric properties of PVP-SiO2-TMSPM hybrid thin films, Organic Electronics, 32, 100-108, 2016.

[3] Sharma, M., Tripathi, S. K., Analysis of interface states and series resistance for Al/PVA: n-CdS nanocomposite metal–semiconductor and metal–insulator–semiconductor diode structures, Applied Physics A, 113(2), 491-499, 2013.

[4] Tunç, T., Gökçen, M., Uslu, I., Studies on frequency and gate voltage effects on the dielectric properties of Au/n-Si (110) structure with PVA–nickel acetate composite film interfacial layer, Applied Physics A, 109(3), 649-653, 2012.

[5] Nezhadesm-Kohardafchahi, S., Farjami-Shayesteh, S., Badali, Y., Altındal, Ş., Jamshidi-Ghozlu, M. A., Azizian-Kalandaragh, Y., Formation of ZnO nanopowders by the simple ultrasound-assisted method: Exploring the dielectric and electric properties of the Au/(ZnO-PVA)/n-Si structure, Materials Science in Semiconductor Processing, 86, 173-180, 2018.

[6] Sharma, M., Tripathi, S. K., Frequency and voltage dependence of admittance characteristics of Al/Al2O3/PVA: n-ZnSe Schottky barrier diodes, Materials Science in Semiconductor Processing, 41, 155-161, 2016.

[7] Yerişkin, S. A., Balbaşı, M., Orak, İ., The effects of (graphene doped-PVA) interlayer on the determinative electrical parameters of the Au/n-Si (MS) structures at room temperature, Journal of Materials Science: Materials in Electronics, 28(18), 14040-14048, 2017.

[8] Bilkan, Ç., Badali, Y., Fotouhi-Shablou, S., Azizian-Kalandaragh, Y., Altındal, Ş., On the temperature dependent current transport mechanisms and barrier inhomogeneity in Au/SnO 2–PVA/n-Si Schottky barrier diodes, Applied Physics A, 123(8), 560, 2017.

[9] Dökme, İ., Altındal, Ş., Uslu, İ., The effects of temperature, radiation, and illumination on current−voltage characteristics of Au/PVA (Co, Zn- doped)/n- Si Schottky diodes, Journal of Applied Polymer Science, 125(2), 1185-1192, 2012.

[10] Al-Dharob, M. H., Lapa, H. E., Kökce, A., Özdemir, A. F., Aldemir, D. A., Altındal, Ş., The investigation of current-conduction mechanisms (CCMs) in Au/(0.07 Zn-PVA)/n-4H-SiC (MPS) Schottky diodes (SDs) by using (IVT) measurements, Materials Science in Semiconductor Processing, 85, 98-105, 2018.

[11] Uslu, H., Yıldırım, M., Altındal, Ş., Durmuş, P., The effect of gamma irradiation on electrical and dielectric properties of organic-based Schottky barrier diodes (SBDs) at room temperature, Radiation Physics and Chemistry, 81(4), 362-369, 2012.

[12] Dökme, İ., Durmuş, P., Altındal, Ş., Effects of γ-ray irradiation on the C−V and G/ω−V characteristics of Al/SiO2/p-Si (MIS) structures, Nuclear Instruments and Methods in Physics Research Section B: Beam Interactions with Materials and Atoms, 266(5), 791-796, 2008.

[13] Tataroğlu, A., Altındal, Ş., Bülbül, M. M., 60Co γ irradiation effects on the current−voltage (I–V) characteristics of Al/SiO2/p-Si (MIS) Schottky diodes, Nuclear Instruments and Methods in Physics Research Section A: Accelerators, Spectrometers, Detectors and Associated Equipment, 568(2), 863-868, 2006.

CAPACITANCE-VOLTAGE (C-V) AND CONDUCTANCE-VOLTAGE (G/ω-V) CHARACTERISTICS BEFORE AND AFTER IRRADIATION IN Au/n-Si/Ag SCHOTTKY BARRIER DIODES (SBDs)

Perihan Durmuş[1], Ahmet Kaymaz[2], Şemsettin Altındal[1]

[1] Department of Physics, Faculty of Science, Gazi University, TURKEY
[2]Electric and Electronic Engineering Department, Engineering Faculty, Karabük University, TURKEY

E-mail: pdurmus@gazi.edu.tr

Abstract

It is important to evaluate the capacitance-voltage (C-V) and conductance-voltage (G/ω-V) characteristics of Schottky barrier diodes (SBDs) or such similar semiconductor-based structures in order to investigate the response of these structures after exposure them to the ^{60}Co-γ-irradiation. Therefore, in this study, the C-V and G/ω-V measurements of the Au/n-Si/Ag (MS) structure which have prepared is performed at enough high frequency (500 kHz) before and after 60 kGy irradiation. The frequency was selected as 500 kHz to eliminate the interface states caused by the fabrication stage, so that the effects of radiation can be accurately evaluated. For this aim, C-V and G/ω-V measurements were performed before and after 60 kGy irradiation at room temperature. Thus, the main diode parameters such as diffusion potential (V_D), doping concentration of donor atoms (N_D), Fermi energy level (E_F), maximum electric field (E_m), depletion layer width (W_D) and barrier height (Φ_B) were calculated from the intercept and slope of the reverse bias C^{-2}-V plots before and after 60 kGy irradiation. Experimental results show that all these parameters vary depending on radiation because of the radiation induces different life-time of surface states and also it causes to be restructured and reordered of them.

Keywords: Schottky barrier diodes (SBDs); C-V and G/ω-V characteristics; γ-irradiation

1. INTRODUCTION

Schottky barrier diodes (SBDs) and other semiconductor-based structures such as solar cells, metal-oxide/insulator/polymer-semiconductor (MOS/MIS or MPS) type structures and detectors are widely used in electronic components for space (satellite systems), nuclear industry, and medical applications. Although the importance of these structures in such electronics systems cannot be ignored it is well known that these structures are extremely sensitive to electromagnetic radiation such as β, x, γ rays and they lead to a considerably changes in the electrical characteristics of these structures [1]. In addition, the space environment consists of neutral species, charged particles, electric fields, magnetic fields, solar radiation, galactic radiation, space debris, etc. [2, 3]. On the other hand, biomedical materials are used intensively under radiation influence. Therefore, the investigation of ^{60}Co-γ-radiation effects on SBDs, especially analysis of C-V and G/ω-V characteristics of these structures after exposure them to the γ-rays is very important to determine the degree of hardness on the semiconductor based-devices. Some previous studies such as reference [4] have shown that the change in current-voltage (I-V) characteristics of semiconductor-based structures, especially at forward bias region when compared with reverse bias region, is lower than the C-V characteristics after exposure them to the γ-ray source due to the lower electric field. In addition, the C-V characteristics give us information about the barrier height (BH) changing of the MS and MIS type structures when viewed from the metal side, so that it can be obtained more detailed information about the reverse bias currents which affected a lot by irradiation [5-7].

In this study, C-V and G/ω-V characteristics of the Au/n-Si/Ag (MS) structure which have prepared is measured at 500 kHz frequency before and after 60 kGy irradiation. Due to the loss of the effects of the interfacial states (N_{ss}) caused by the fabrication stage at high frequency (f ≥ 500 kHz) [8, 9], the measurements have been performed in this frequency. Thus, influences of the radiation can be evaluated accurately. As a result of these measurements, they are extracted the basic diode parameters such as V_D, N_D, E_F, E_m, W_D, and Φ_B from the reverse bias C^{-2}-V characteristics and the calculations demonstrate that these parameters change after γ-irradiation due to radiation induces surface states and it also causes to be restructured and reordered of them under electric field.

2. EXPERIMENTAL DETAILS

Au/n-Si/Ag SBDs were fabricated on P-doped (n-Si) wafer with (100) orientation, 300 μm thickness and 0.4 Ω.cm resistivity. It was dipped in $5H_2SO_4+H_2O_2+H_2O$ solution at 1 min to remove oxide layer and organic impurities on surface, etched by H_2O+HCl solution, rinsed high-pure de-ionized water and then dried

with N_2 gas immediately. High-pure Au (99.999%) was thermally evaporated on the back side of the wafer at 10^{-6} Torr and then annealed at 500°C for 3 min bin the nitrogen ambient to get good ohmic contact. Finally, high purity Ag (99.999%) rectifier contacts with 0.00785 cm^2 areas were grown on the front surface of the n-Si wafer. More information for the fabrication processes can be also found in reference [10].

3. RESULTS AND DISCUSSION

The C-V and G/ω-V characteristics of Au/n-Si/Ag SBDs which are measured at 500 kHz in the wide voltage (± 6V) for before and after 60 kGy radiation are given in Fig. 1(a) and (b), respectively. It is clearly viewed in the C-V and G/ω-V characteristics three regions which are named accumulation, depletion and inversion region and ^{60}Co-γ-radiation are more effective on these plots especially in depletion and accumulation regions due to the effects of radiation induced of N_{ss} and series resistance (R_s), respectively. The depletion region shift towards the inversion region after 60 kGy radiation due to the enhancement of trapped charge densities [11]. On the other hand, it is seen apparent decrease in capacitance and conductance values after irradiation at accumulation region because of the increase of R_s under irradiation [12]. Detailed analysis to understand changes in these characteristics are given below.

Figure 1. The forward and reverse bias (a) C-V characteristics and (b) G/ω-V characteristics of the Au/n-Si/Ag structure

In SBDs, the depletion layer capacitance for reverse bias voltage can be written as Eq. (1) [9]

$$C^{-2} = \frac{2(V_D - \frac{kT}{q} - V}{q\varepsilon_S\varepsilon_0 N_D A^2} \tag{1}$$

In Eq. (1), ε_S and ε_0 are called the permittivity of semiconductor and vacuum while other parameters are well known in the literature. The diffusion potential value can be written V_D $(=V_0 + kT/q)$ while V_0 is referred to as intercept voltage. On the other hand, the values of $V_D, N_D, E_F, E_m, W_D,$ and Φ_B can be calculated using below equations [9].

$$E_F = \frac{kT}{q}\ln\left(\frac{N_C}{N_D}\right) \tag{2}$$

$$N_D = \frac{2}{q\varepsilon_S\varepsilon_0 A^2 \tan\theta} \tag{3}$$

$$E_m = \sqrt{\frac{2qN_D V_0}{\varepsilon_S\varepsilon_0}} \tag{4}$$

$$W_D = \sqrt{\frac{2\varepsilon_S\varepsilon_0 V_0}{qN_D}} \tag{5}$$

$$\Delta\phi_B = \sqrt{\frac{qE_m}{4\pi\varepsilon_S\varepsilon_0}} \tag{6}$$

$$\phi_{B(C-V)} = V_D + E_F - \Delta\phi_B = V_0 + \frac{kT}{q} + E_F - \Delta\phi_B \tag{7}$$

Here, N_C, $\Delta\phi_B$ and $\tan\theta$ are the effective density of states in the conductivity band (E_C), image force lowering of BH and the slope obtained from the linear region of the C^{-2}-V curves respectively. The obtained basic electric parameters of the Au/n-Si/Ag structure before and after radiation were tabulated in Table (1).

Table 1. Basic diode parameters for Au/n-Si/Ag (SBD)

	V_0 (eV)	V_D (eV)	N_D (cm^{-3})	EF (eV)	Em (V/cm)	W_D (cm)	$\Delta\Phi_B$ (eV)	Φ_B (eV)
BEFORE	0.823	0.849	5.52E+15	0.222	3.73E+04	4.48E-05	2.13E-02	1.049
60 KGY	0.628	0.654	6.46E+15	0.218	3.52E+04	3.64E-05	2.07E-02	0.851

Figure 2. Linear region of C^{-2}-V curves of the Au/n-Si/Ag structure

In Table (1), it is seen that V_0, V_D, E_F, E_m, W_D, ϕ_B values are decreased while N_D value is increased because of the reordering and restructuring of the N_{ss}. In other words, as a result of the decrease of the depletion layer width and barrier height, it is occurred increase of the reverse leakage current and decrease of the shunt resistance. It is concluded only with these situations that the diode characteristics is deteriorated after irradiation. Therefore, there are a lot of studies aimed rendering these structures resistant to the radiation effects [4-6, 13-15]. In fact, the increase in the doping concentration of donor atoms can be explained with the radiation induced interface states.

4. CONCLUSION

The forward and reverse bias C-V and G/ω-V measurements of Au/n-Si/Ag SBDs were recorded before and after ^{60}Co-γ-irradiation (60 kGy) in the wide range of bias voltage ($\mp 6V$). Experimental results show that the fabricated SBDs are very sensitive to the radiation. After irradiation, it was observed an increase at inversion and depletion regions and a decrease at accumulation region due to results of radiation induced N_{ss} and increase of R_s, respectively. On the other hand, it was seen shifts in depletion region toward the negative voltages after radiation. This behavior can be attributed to the enhancement of trapped charge densities and restructuring and reordering of them under electric field. Further, the increase of N_D leads to an increase or shirking of the W_D.

REFERENCES

[1] K. Ali, S. A. Khan, and M. Z. MatJafri, "^{60}Co γ-irradiation effects on electrical characteristics of monocrystalline silicon solar cell," *Int. J. Electrochem. Sci.*, 8 (6): 7831–7841 (2013).

[2] D. Binder, E. C. Smith, and A. B. Holman, "Satellite Anomalies From Galactic Cosmic Rays," *IEEE Trans. Nucl. Sci.*, 22 (6): 2675–2680 (1975).

[3] P. Laha, I. Banerjee, P. K. Barhai, A. K. Das, V. N. Bhoraskar, and S. K. Mahapatra, "Effects of 6 MeV electron irradiation on the electrical properties and device parameters of Al/Al$_2$O$_3$/TiO$_2$/n-Si MOS capacitors," *Nucl. Instruments Methods Phys. Res. Sect. B Beam Interact. with Mater. Atoms*, 283: 9–14 (2012).

[4] S. Kaya, E. Yilmaz, A. Kahraman, and H. Karacali, "Frequency dependent gamma-ray irradiation response of Sm$_2$O$_3$ MOS capacitors," *Nucl. Instruments Methods Phys. Res. Sect. B Beam Interact. with Mater. Atoms*, 358: 188–193 (2015).

[5] G. A. Umana-Membreno, J. M. Dell, G. Parish, B. D. Nener, L. Faraone, and U. K. Mishra, "^{60}Co Gamma Irradiation Effects on n-GaN Schottky Diodes," *IEEE Trans. Electron Devices*, 50 (12): 2326–2335 (2003).

[6] A. Teffahi *et al.*, "Effect of ^{60}Co γ-ray irradiation on electrical properties of Ti/Au/GaAs$_{1-x}$N$_x$ Schottky diodes," *Curr. Appl. Phys.*, 16 (8): 850–858 (2016).

[7] M. V. Kumar *et al.*, "Influence of High Dose Gamma Irradiation on Electrical Characteristics of Si Photo Detectors," *ECS J. Solid State Sci. Technol.*, 6 (10): Q132–Q135 (2017).

[8] A. B. Uluşan, S. A. Yerişkin, A. T. M. Balbaşı, and Y. A. Kalandaragh, "Electrical and impedance properties of MPS structure based on - (Cu$_2$O-CuO-PVA) interfacial layer," *J. Mater. Sci. Mater. Electron.*, 29 (10): 8234–8243 (2018).

[9] S. Nezhadesm-kohardafchahi, S. Farjami-shayesteh, Y. Badali, and Ş. Alt, "Materials Science in Semiconductor Processing Formation of ZnO nanopowders by the simple ultrasound-assisted method: Exploring the dielectric and electric properties of the Au/(ZnO-PVA)/ n-Si structure," 86: 173–180, (2018).

[10] Ç. Bilkan and Ş. Altındal, "Investigation of the C-V characteristics that provides linearity in a large reverse bias region and the effects of series resistance, surface states and interlayer in Au/n-Si/Ag diodes," *J. Alloys Compd.*, 708: 464–469 (2017).

[11] S. Kaya, A. Aktag, and E. Yilmaz, "Effects of gamma-ray irradiation on interface states and series-resistance characteristics of BiFeO$_3$ MOS capacitors," *Nucl. Instruments Methods Phys. Res. Sect. B Beam Interact. with Mater. Atoms*, 319: 44–47 (2014).

[12] V. Singh, N. Shashank, S. K. Sharma, R. S. Shekhawat, D. Kumar, and R. K. Nahar, "Frequency dependence studies on the interface trap density and series resistance of HfO$_2$ gate dielectric deposited on Si substrate: Before and after 50 MeV Li^{3+} ions irradiation," *Nucl. Instruments Methods Phys. Res. Sect. B Beam Interact. with Mater. Atoms*, 269 (23): 2765–2770 (2011).

[13] S. S. Barala, J. Singh, S. Ranwa, and M. Kumar, "Radiation Induced Response of Ba$_{0.5}$Sr$_{0.5}$TiO$_3$ Based Tunable Capacitors under Gamma Irradiation," *IEEE Trans. Nucl. Sci.*, 62 (4): 1873–1878 (2015).

[14] Ö. Güllü, M. Çankaya, M. Biber, and A. Türüt, "Gamma irradiation-induced changes at the electrical characteristics of organic-based Schottky structures," *J. Phys. D. Appl. Phys.*, 41 (13): (2008).

[15] S. Zeyrek, A. Turan, and M. M. Bülbül, "The C-V and G/ω-V electrical characteristics of ^{60}Co γ-Ray irradiated Al/Si$_3$N$_4$/p-Si (MIS) structures," *Chinese Phys. Lett.*, 30(7): (2013).

A METHOD FOR SOLVING OF DIFFERENCE EQUATIONS FROM ANALYSIS OF CRYSTALS WITH BROKEN TRANSLATIONAL SYMMETRY

J.P. Šetrajčić[1,2], S.M. Vučenović[3], S.K. Jaćimovski[4], I.J. Šetrajčić[2]

[1]*Academy of Sciences and Arts of the Republic of Srpska, Banja Luka, Republic of Srpska – BOSNIA AND HERZEGOVINA*
[2]*University "Union – Nikola Tesla", Faculty of Sport, New Belgrade, Vojvodina – SERBIA*
[3]*University of Banja Luka, Faculty of Sciences, Banja Luka, Republic of Srpska – BOSNIA AND HERZEGOVINA*
[4]*University of Criminal Investigation and Police Studies, Zemun, Vojvodina – SERBIA*

E-mail: jovan.setrajcic@gmail.com

Abstract

Analysis of the properties of condensed matter, especially of the nanostructured samples, is solved using the operator method and the second order non-linear difference equations. The general character of solution is verified through two concrete applications. Difficulties related with solving difference equations were analyzed in this work and discussed in detail. This method gives the compact solution if the variable coefficient is of exponential type and it can be applied to the problem of finding molecule displacements in crystalline chain with finite and very small length. It is shown that the molecule displacement can be represented as the specific superposition of harmonic functions depending on the space position phonon occurrence. Further, we considered the polymer molecular chain of the finite and ultra-short length with substitution impurities. In this particular case appear two types of exciton states: collective and localized ones.

Keywords: Operator method, Difference equation, Condensed matter, Molecule displacement, Polymer molecular chain

1. INTRODUCTION

In our previous work [1] we analyzed the application of specific expansion of hyperbolic type difference equations kernel into separable polynomials for the solving of the Schrödinger equation for particles and quasiparticles with zero rest mass. Presently we are focused at some nonlinear difference equations which play important roll in the condensed matter physics, especially for the problems related with crystal structures.[2-4] Probability amplitudes in one-particle wave function as well as Green's functions (GF) are the solutions of systems of precisely such difference equations. General type of difference equations defining mentioned quantities, are the following:

$$Y_{n+1} + Y_{n-1} + xY_n = 0, \tag{1}$$

where integer n denotes location of atom or molecule, while x is parameter related with physical characteristic of system. If crystal structure is transitionally invariant [5,6], parameter x does not depend on integer n (see, for example [7-10]). In the cases of broken symmetry (impurities, presence of boundaries etc), this parameter is dependent on molecule position. In the mentioned cases difference equation (1) goes over to equation with variable coefficient $x \equiv x_n$, i.e.

$$Y_{n+1} + Y_{n-1} + x_n Y_n = 0. \tag{2}$$

In the second section of this work the general procedure of solving the equation (2) will be presented. Based on this, two particular and very interesting examples will be solved too.

2. GENERAL OPERATOR SOLUTION

The homogeneous difference equation of second kind (2) will be solved using operator method. The application of this method requires introduction of translational operators $\hat{T}_l$ ($l \in \mathsf{N}$) obeying the following rules:

$$\hat{T}_l f_n = f_{n+l}; \quad \hat{T}_l = \left(\hat{T}_1\right)^l \equiv \hat{T}_1^l; \quad \hat{T}_l \cdot \hat{T}_k = \hat{T}_{l+k}; \quad \hat{T}_{-l} = \hat{T}_1^{-l}; \quad \hat{T}_0 = 1. \tag{3}$$

Taking this into account the equation (2) can be written in the form:

$$\left(\hat{T}_1 + \hat{T}_{-1} + x_n\right)Y_n = 0. \tag{4}$$

Operator solving requires that at least one of the left-hand side operators in (4) give zero when acting to the constant. It is easily seen that neither of operators, i.e. $\hat{T}_1 + \hat{T}_{-1}$ and x_n satisfies this requirement. Therefore we shall transform (4) in the following way:

$$\left[\left(\hat{T}_1 + \hat{T}_{-1}\right) - 2 + \left(x_n + 2\right)\right] Y_n = 0. \tag{5}$$

(It can be seen now that translational operator acting to constant gives zero.)

In order to make calculations more clear and compact, we shall introduce the following notations: $\hat{a} \equiv \hat{T}_1 + \hat{T}_{-1} - 2$ and $\hat{b}_n \equiv x_n + 2$. The equation (5) now has the form:

$$\left(\hat{a} + \hat{b}_n\right) Y_n = 0. \tag{6}$$

In this way the operator form in (5) is prepared for application of the operator method.

The operator method gives the solution of homogeneous difference equation expressed over two linearly independent solutions of the corresponding non-homogeneous equation:

$$\left(\hat{a} + \hat{b}_n\right) y_n = \Phi_n, \tag{7}$$

for a suitable function Φ_n. Precisely, if (7) has two linearly independent solutions $y_n^{(1)}$ and $y_n^{(2)}$, then the following is valid:

$$\left(\hat{a} + \hat{b}_n\right) y_n^{(1)} = \Phi_n; \qquad \left(\hat{a} + \hat{b}_n\right) y_n^{(2)} = \Phi_n.$$

Subtracting these equations and comparing this result with (6) we conclude:

$$\left(\hat{a} + \hat{b}_n\right)\left(y_n^{(1)} - y_n^{(2)}\right) = 0 \quad \Rightarrow \quad Y_n \equiv y_n^{(1)} - y_n^{(2)}. \tag{8}$$

The further question is how to find the functions $y_n^{(1)}$ and $y_n^{(2)}$? The formal solution of (7) is:

$$y_n = \left(\hat{a} + \hat{b}_n\right)^{-1} \Phi_n. \tag{9}$$

Now, it can be shown that there do exist two independent forms of the inverse operator:

$$\left(\hat{a} + \hat{b}_n\right)^{-1} = \begin{cases} \left[\hat{b}_n\left(1 + \hat{b}_n^{-1}\hat{a}\right)\right]^{-1} = \left(1 + \hat{b}_n^{-1}\hat{a}\right)^{-1} \hat{b}_n^{-1} = \sum_{k=0}^{\infty} (-1)^k \left(\hat{b}_n^{-1}\hat{a}\right)^k \hat{b}_n^{-1}, \\ \left[\hat{a}\left(1 + \hat{a}^{-1}\hat{b}_n\right)\right]^{-1} = \left(1 + \hat{a}^{-1}\hat{b}_n\right)^{-1} \hat{a}^{-1} = \sum_{k=0}^{\infty} (-1)^k \left(\hat{a}^{-1}\hat{b}_n\right)^k \hat{a}^{-1}. \end{cases} \tag{10}$$

Taking this into account we can write:

$$y_n^{(1)} = \left(1 - \hat{b}_n^{-1}\hat{a} + \hat{b}_n^{-1}\hat{a}\hat{b}_n^{-1}\hat{a} - \cdots\right) \hat{b}_n^{-1} \Phi_n, \qquad y_n^{(2)} = \left(1 - \hat{a}^{-1}\hat{b}_n + \hat{a}^{-1}\hat{b}_n \hat{a}^{-1}\hat{b}_n - \cdots\right) \hat{a}^{-1} \Phi_n. \tag{11}$$

Until now, Φ_n has been suitable. But, if we take that $\Phi_n \equiv \hat{b}_n$, then (11) gives:

$$y_n^{(1)} = 1, \qquad y_n^{(2)} = \hat{a}^{-1}\hat{b}_n - \hat{a}^{-1}\hat{b}_n \hat{a}^{-1}\hat{b}_n + \hat{a}^{-1}\hat{b}_n \hat{a}^{-1}\hat{b}_n \hat{a}^{-1}\hat{b}_n - \cdots \tag{12}$$

Taking into account formulas (10) and (12), we conclude that the solution of homogeneous equation (8) is

given as follows:

$$Y_n = \sum_{k=0}^{\infty} (-1)^k \left(\hat{a}^{-1} \hat{b}_n \right)^k. \tag{13}$$

We can find now the explicit form of the operator $\hat{a}^{-1} \equiv \left(\hat{T}_1 + \hat{T}_{-1} - 2 \right)^{-1}$:

$$\hat{a}^{-1} = \begin{cases} \left\{ -2 \left[1 - \dfrac{1}{2} \left(\hat{T}_1 + \hat{T}_{-1} \right) \right] \right\}^{-1} = -\displaystyle\sum_{k=0}^{\infty} 2^{-(k+1)} \left(\hat{T}_1 + \hat{T}_{-1} \right)^k, & \text{(a)} \\[4mm] \left\{ \left(\hat{T}_1 + \hat{T}_{-1} \right) \left[1 - 2 \left(\hat{T}_1 + \hat{T}_{-1} \right)^{-1} \right] \right\}^{-1} = \displaystyle\sum_{k=0}^{\infty} 2^k \left(\hat{T}_1 + \hat{T}_{-1} \right)^{-(k+1)}; & \text{(b)} \end{cases} \tag{14}$$

One can see that in the later expression figures power of the operator $\left(\hat{T}_1 + \hat{T}_{-1} \right)^{-1}$. This operator can be written in two ways:

$$\left(\hat{T}_1 + \hat{T}_{-1} \right)^{-1} = \begin{cases} \left[\hat{T}_1 \left(1 + \hat{T}_{-2} \right) \right]^{-1} = \displaystyle\sum_{k=0}^{\infty} (-1)^k \hat{T}_{-(2k+1)}, & \text{(a)} \\[4mm] \left[\hat{T}_{-1} \left(1 + \hat{T}_2 \right) \right]^{-1} = \displaystyle\sum_{k=0}^{\infty} (-1)^k \hat{T}_{2k+1}. & \text{(b)} \end{cases} \tag{15}$$

Now, all necessary elements for application of operator method are given.

3. APPLYING THE GENERAL SOLUTION

The method presented will be applied to the two particular examples: to the definition of specific phonons and the behaviour of non-homogenous exciton subsystem in the finite crystalline chains.

3.1. Phonons in crystalline chain

One dimensional propagation of mechanical waves in condensed matter physics is described, in the nearest neighbor approximation [5,6], by consideration of difference equation:

$$u_{n+1} + u_{n-1} + \rho u_n = 0 \tag{16}$$

valid for small displacements u_n of atom/molecule.[1] From its equilibrium site $n \in [0, N]$. For ultra-short ($L = Na$) crystalline chain [11-15], the quantity: $\rho \equiv \rho_n = 2(\cos n\xi - 1)$, $\xi \equiv \xi(\omega)$. The expression (16) is equivalent to (2) and we can apply the described operator method. It is seen from (5) and (6) that $b_n = e^{in\xi} + e^{-in\xi}$.

---

[1] Atom displacements $u_n \equiv u_n(\omega)$ are the Fourier's transform ($t \to \omega$) the space displacements $u_n(t)$.

At the beginning, we shall look for the function $\hat{a}^{-1}e^{in\xi}$ representing the operator $\hat{a}^{-1}$ by the formula (14a). Since

$$\left(\hat{T}_1 + \hat{T}_{+1}\right)^{-1}e^{in\xi} = 2e^{in\xi}\cos\xi,$$

it follows:

$$\hat{a}^{-1}e^{in\xi} = -\frac{1}{2}e^{in\xi} - \frac{1}{2^2}\left(\hat{T}_1 + \hat{T}_{-1}\right)^{+1}e^{in\xi} - \frac{1}{2^3}\left(\hat{T}_1 + \hat{T}_{-1}\right)^{+2}e^{in\xi} - \cdots =$$

$$= -\left(\frac{e^{in\xi}}{2} + \frac{e^{in\xi}}{2}\cos\xi + \frac{e^{in\xi}}{2}\cos^2\xi + \cdots\right) =$$

$$= -\frac{e^{in\xi}}{2}\sum_{k=0}^{\infty}\cos^k\xi = \frac{-e^{in\xi}}{2\left(1-\cos\xi\right)}.$$

Further we obtained:

$$\left(\hat{a}^{-1}e^{in\xi}\right)^2 = \hat{a}^{-1}e^{in\xi}\frac{-e^{in\xi}}{2\left(1-\cos\xi\right)} = \frac{e^{2in\xi}}{2^2(1-\cos\xi)(1-\cos2\xi)},$$

wherefrom it can be easily concluded

$$\left(\hat{a}^{-1}e^{in\xi}\right)^k = \frac{(-1)^k e^{kin\xi}}{2^k \prod_{q=1}^{k}(1-\cos q\xi)}; \quad k = 1,2,3,\ldots \tag{17}$$

On the basis of the general facts presented in Section 2, we must look for the solution $u_n(\xi)$ by (17), which satisfies the difference equation:

$$\left(\hat{a} + e^{in\xi}\right)u_n(\xi) = 0. \tag{18}$$

If we multiply this equation by $e^{-2in\xi}$ from left, and to the obtained equation add (18), we obtain:

$$\left(\hat{\alpha}_n + b_n\right)u_n(\xi) = 0, \tag{19}$$

where: $\hat{\alpha}_n \equiv \left(1 + e^{-2in\xi}\right)\hat{a}$ and $b_n \equiv 2\cos n\xi$. From (13), the solution of the upper equation is:

$$u_n(\xi) = \sum_{k=0}^{\infty}(-1)^k\left(\hat{\alpha}^{-1}b_n\right)^k. \tag{20}$$

It is easy to prove that $\hat{\alpha}^{-1}b_n \equiv \hat{a}^{-1}e^{in\xi}$, so − from (17) and (20), the wanted solution is:

$$u_n(\omega) \equiv u_n(\xi) = \sum_{k=0}^{\infty}\frac{e^{in\xi(\omega)}}{2^k\prod_{q=1}^{k}\left[1-\cos q\xi(\omega)\right]}. \tag{21}$$

As it is seen − the atom displacement represents the specific superposition of harmonic functions which

depend on space position. Physically, it is represented by the superposition of progressive plane and standing waves.

3.2. Excitons in polymer chain with impurities

Energy spectra of elementary excitations of ideal (bulk) molecular crystals (Frenkel excitons) can be analyzed in a comparatively simple manner [16] in the inverse lattice due to translational symmetry of the crystal lattice. The problem of the exciton energy spectrum of the massive (bulk) crystals with impurities is much more complicated due to the violation of translational invariance. In [17] is stressed that impurity presence can lead to the appearance of the localized states with discrete energies lying above or bellow exciton band. It is shown in [18] that these difficulties could be avoided by a suitable redefinition of the Hamiltonian, which allows to carry out the analysis in the inverse space. In [19] we proposed a method that allows the analysis in the direct space, and therefore we are able to analyze the chain of the finite length.

With respect to the analysis of the energy transport processes in the proteins, this means that we can analyze the processes in finite protein sequences, which is of great importance in the immunology, i.e. in the biophysical theory of immune-processes. We shall consider the polymer chain of the finite length $L = Na$, consisting of $N+1$ molecules at equal spacings a, having a single isotropic substitutional impurity at an arbitrary site $p \in [0, N]$. The Hamiltonian of the studied system in the direct space as well as in the nearest neighbors approximation has the form:

$$H = \sum_{n=0}^{N} \left(\Delta_n B_n^+ B_n + V_{n,n-1} B_n^+ B_{n-1} + V_{n,n+1} B_n^+ B_{n+1} \right) \tag{22}$$

The excitation energy of an isolated molecule Δ_n at the arbitrary chain site and the matrix elements of the dipole-dipole interaction of the impurity and host molecule will be written in the form:

$$\Delta_n = \Delta(1 + d\delta_{n,s}); \quad d \equiv \frac{\Delta_s - \Delta}{\Delta}; \quad V_{p,p\pm1} = V(1 + s), \tag{23}$$

where we have introduced a parameter s of the relative difference and V is host-host interaction.

Energy of elementary excitations of the system can be determined by GF method [12] in the following way:

$$G_{nm}(t) = \Theta(t) \left\langle \left[B_n(t), B_m^+(0) \right]_- \right\rangle; \quad n, m = 0, 1, 2, \ldots N;$$

$$i\hbar \frac{d}{dt} G_{nm}(t) = i\hbar \delta(t) \delta_{n,m} + \Theta(t) \left\langle \left[\left[B_n(t), H \right]_-, B_m^+(0) \right]_- \right\rangle. \tag{24}$$

After introducing the temporal Fourier transformations for GF only, and calculating the necessary

commutators, we obtain the following system of difference equations for $G_{n,m}(\omega)$:

$$D_{N+1}(\rho)\,G_m(\omega) = K_m, \tag{25}$$

where are:

$$G_m(\omega) = \begin{pmatrix} G_{0,m} \\ G_{1,m} \\ \vdots \\ G_{N,m} \end{pmatrix}; \quad K_m = K \begin{pmatrix} \delta_{0,m} \\ \delta_{1,m} \\ \vdots \\ \delta_{N,m} \end{pmatrix};$$

$$D_{N+1}(\rho) = (1+s)^2 \left(A_{s-2}A_{N-s-1} + A_{s-3}A_{N-s} - 2\rho A_{s-2}A_{N-s} \right) +$$
$$+ \rho\rho_s(\rho_s - 1)A_{s-3}A_{N-s} + \rho_s\left(\rho A_{s-2} - A_{s-3}\right)A_{N-s-1};$$

$$A_n(\rho) = \rho C_{n-1}(\rho) - C_{n-2}(\rho) \equiv C_n(\rho);$$

$$\rho = \frac{\hbar\omega - \Delta}{V}; \quad \rho_s = \rho - \frac{\Delta}{V}d; \quad K = \frac{i\hbar}{2\pi V} \tag{26}$$

and $C_n(\rho)$ are the Chebyshev polynomials of second type [20]. [2]

Solving the system of equations (25) we can obtain diagonal components of GF:

$$G_{n,n}(E) = K \sum_{v=1}^{N+1} \frac{g_{n,n}(\rho_v)}{E - E_v}; \quad E \equiv \frac{\hbar\omega}{V}, \tag{27}$$

whose spectral weights [5] has the form:

$$g_{n,n}(\rho_v) = \frac{\Delta_N(\rho_v)}{\left.\dfrac{d}{d\rho}D_{N+1}(\rho)\right|_{\rho=\rho_v}}; \quad \sum_{n=0}^{N} g_{n,n}(\rho_v) = 1, \quad \forall\, v = 1,2,\ldots,N+1. \tag{28}$$

The determinant $\Delta_N(\rho)$ is obtained by the standard procedure for solving the system of equations (4).

The spectral weights (28) representing the squared module of wave functions [5,12], enable us to separate localized excitations in the spectrum due to the important property: contrary to collective excitations present, at each site due to their "standing-wave" distribution along the chain, spectral weights for localized excitations show maximum at a given site and decrease sharply (i.e. exponentially) with the distance from the site. The attenuation parameter depends on the parameters describing impurities.

---

[2] The Chebyshev polynomials of second type satisfy the recurrent relation: $C_{n+1}(\rho) = \rho\, C_n - C_{n-1}(\rho); \; n = 0,1,2,\ldots$, with initial conditions: $C_{-1}(\rho) = 0$, $C_0(\rho) = 1$ and $C_1(\rho) = \rho$. This relation has same form as initial difference equation (1), i.e. (2), which solution must be given by exposed operator method.

4. CONCLUSION

This work contains two relatively different parts. The first part is rather of methodological character, demonstrating the method of operator solving of the basic solid-state difference equation with variable coefficient. In the second part of this analysis we demonstrated that the characteristic difference equation in translatory non-invariant crystalline structures theory could be of importance in some practical problems.

Because exposed general operator method gives the compact solution if the variable coefficient is of exponential type, it can be applied to the problem of finding molecular displacements in crystalline chain of finite length. It is shown that the atom displacement represents the specific superposition of plane and standing waves.

We considered the polymer chain of the finite length with substitution impurity. Due to the finite number of molecules in the chain, the spectrum of elementary excitations can be calculated immediately in the direct space. In this particular case there appear two types of excitations: collective and localized ones, which are discrete due to the spatial boundedness.

ACKNOWLEDGMENTS

REFERENCES

[1] Šetrajčić, J.P., Jaćimovski, S.K., Sajfert, V.D., Šetrajčić, I.J., Specific quantum mechanical solution of difference equation of hyperbolic type: application to exciton and phonon thin films, Commun. Nonlinear Sci. Numer. Simulat. 19/5, 1313-1328, 2014.

[2] Jerri, A.J., Linear Difference equations with discrete transforms method, Kluwer Ac. Publ., Dordrecht, 1996.

[3] Elaydi, S.N., Axler, S., Gehring, K.A., Ribet, F.W. An introduction to difference equations, Springer-Verlag, New York, 1999.

[4] Brand L,, Differential and difference equations, J.Wiley & Sons, New York, 1966.

[5] Mahan, G,. Many particle physics, Plenum Press, New York, 1990.

[6] Rickayzen, G., Green's functions and condensed matter, Academic Press, London, 1980.

[7] Davison, S.G., Steslicka, M., Basic theory of surface states, Clarendon, Oxford, 1996.

[8] Pruton, M., Introduction to surface physics, Clarendon, Oxford, 1995.

[9] Stojković, S.M., Mirjanić, D.Lj., Šetrajčić, J.P., Šijačić, D.D., Junger, I.K., Spectra and states of electrons in surface perturbed quantum wires, Surface Science 477, 235-242, 2001.

[10] Šetrajčić, J.P., Jaćimovski, S.K., Raković, Ilić, D.I., Phonon spectra in crystalline nanostructures, in: N.E. Mastorakis, V.V. Kluev, Dj. Koruga (Eds.), Electrical and computer engineering series: Advances in simulation, systems theory and systems engineering, ISBN 960-8052-70-X, WSEAS Press, Athens, 2003, pp. 146-151.

[11] Sajfert, V.D., Šetrajčić, J.P., Popov, D., Tošić, B.S. Difference equations in condensed matter physics and their applications to the exciton system in thin molecular film, Physica A 353, 217-234, 2005.

[12] Šetrajčić, J.P., Exact microtheoretical approach to calculation of optical properties of ultralow dimensional crystals, ArXiv 04, 1004.2387, 2010.

[13] Jaćimovski, S.K., Tošić, B.S., Šetrajčić, J.P., Zorić, V.M., Sajfert V.D. and Ilić, D.I., Thermodynamics of mechanical oscillations in crystalline superlattices, Int. J. Mod. Phys. B 21/6 (2007) 917-930.

[14] Jaćimovski, S.K., Raković, D.I., Šetrajčić, I.J., Armaković, S., Sajfert, V.D., Heat conductivity of some layered structures, Contemporary Materials 3/1, 81-85, 2012.

[15] Markoski, B., Šetrajčić, J.P., Petrevska, M. and Vućenović, S.M.,, Permittivity in perturbed molecular nanofilms, Int.J.Mod.Phys.B 26/15, 1250078-1-8, 2012.

[16] Agranovich, V.M., Theory of excitons, Nauka, Moskwa, 1968 – in Russian.

[17] Takeno, S., Vibrational properties of excitons in molecular crystals, J. Chem. Phys. 46, 2481-2496, 1967.

[18] Čabrić, Ristovski, Lj. and Davidović, G., Localized excitations in polymer chain with an istopically substituted host, Z. Phys. B 53, 79-82, 1983.

[19] Lazarev, S., Škrbić, Ž.M., Šetrajčić, J.P., Mirjanić D.Lj. and Ristovski, Lj., Analysis of the localized excitations in polymer chain with impurities, J. Phys. Chem. Sol. 58/5, 793-797, 1997.

[20] Gradshtein, I.S. and Ryzhik, I.M., Tables of integrals, sums, series and products, Fizmatgiz, Moskwa, 1962, p.1046 – in Russian.

APPEARANCE OF DISCRETE ABSORPTION IN ULTRATHIN MOLECULAR NANOFILMS

S.M. Vučenović[1], J.P. Šetrajčić[2,3], M. Vojnović [4], A.J. Šetrajčić-Tomić

[1]*University of Banja Luka, Faculty of Sciences, Banja Luka, Republic of Srpska – BOSNIA AND HERZEGOVINA*
[2]*Academy of Sciences and Arts of the Republic of Srpska, Banja Luka, Republic of Srpska – BOSNIA AND HERZEGOVINA*
[3]*University "Union – Nikola Tesla", Faculty of Sport, New Belgrade, Vojvodina – SERBIA*
[4]*University of Novi Sad, Faculty of Medicine, Novi Sad, Vojvodina – SERBIA*

E-mail: jovan.setrajcic@gmail.com

Abstract

We have supplemented already formulated microscopic theory of optical properties of ultrathin molecular films, i.e. quasi 2D systems parallel to XY planes bounded by two surfaces. Exposure of nanofilms to the external electromagnetic fields has result in creation of low concentration of Frenkel's excitons, but different than bulk ones in one direction perpendicular to surfaces. Analysis of the dielectric response of this exciton system show that optical properties of these crystalline nanosystems strongly depend on surface parameters and the thickness of the film. In addition, absorption and refraction indices show very narrow and discrete dependence of external electromagnetic field frequency, which is the consequence of confinement effects. Influences of boundary conditions on optical characteristics (through analyses of dynamical absorption and refraction indices) of these nanostructures were explored in details. Unlike the bulk structures which are total absorbers of near IR radiation, ultrathin perturbed films (with the very same crystallographic structure) manifest interesting possibility of appearance of discrete absorption peaks.

Keywords: Ultrathin molecular films, Frenkel's excitons, Optical properties, Dynamical absorption

1. INTRODUCTION

Using a specially adjusted method (Green's functions) for these very discrete crystalline structures (1) and supported by the research of changes of dynamic permittivity with pertubable ultrathin two-layered molecular crystalline films (2) we continued in this work with the research of optical properties of these structures. We determined the indices of absorption and refraction in layers and for the whole film, keeping up with the research from the previous work (3) in which we found out that the presence of boundaries and changes in boundary parameters will lead to the presence of discrete absorption and a possibility for a selective absorption of a single line of incoming electromagnetic radiation.

We carried out above mentioned research starting with the standard expression for effective exciton Hamiltonian [5], in Bose [6] and approximation of the closest neighbour along with the two boundary parameters: $d \in [-0,2; +0,2]$, $x \in [-0,99; +2,0]$ and for two-layer film $n_z = 0,1,2$. The method of Green's functions [7] has been used in the research, adjusted to structures with the interrupted symetry. By solving the system of non-homogeneous differential equations the Green's functions were determined: $G_{n_z}(\omega)$. On the basis of standard definition (linear response of system on external perturbation of electromagnetic field[5,8]) of relative permittivity with Green's functions we have found the expression for dependence of film relative permittivity on frequency of external electromagnetic field:

$$\varepsilon_{n_z} = \left\{ 1 + \frac{2\hbar S}{|X|} \sum_{\nu=1}^{N+1} g_{n_z}^{\nu} \frac{\frac{\Delta}{|X|} + F_{xy} - \rho_\nu}{\left(\frac{\hbar\omega}{|X|} \right) - \left(\frac{\Delta}{|X|} + F_{xy} - \rho_\nu \right)^2} \right\}^{-1} \tag{1}$$

All values in this expression have been defined in our previous paperwork [2].

2. DYNAMICAL OPTICAL PROPERTIES

The refraction (n) and absorption (κ) indices are usually defined in the literature [9] by permittivity term: $\sqrt{\varepsilon} = n + i\kappa$. Introducing the complex frequency: $\omega \to \omega + i\nu$ in expression for permittivity (1), we get complex permittivity: $\varepsilon = \varepsilon' + i\varepsilon''$, where: $\varepsilon' \equiv \varepsilon'(n_z) = \mathrm{Re}\{\varepsilon\}$ and $\varepsilon'' \equiv \varepsilon''(n_z) = \mathrm{Im}\{\varepsilon\}$. Based on this, we can find the expression for absorption and refraction indices in the following form:

$$\kappa_{n_z}(\omega) = \sqrt{\frac{\varepsilon'}{2} \left[\sqrt{1 + \left(\frac{\varepsilon''}{\varepsilon'} \right)^2} - 1 \right]}; \quad n_{n_z}(\omega) = \sqrt{\frac{\varepsilon'}{2} \left[\sqrt{1 + \left(\frac{\varepsilon''}{\varepsilon'} \right)^2} + 1 \right]} \tag{2}$$

From these expressions and expression (1) one can see that dynamical absorption and refraction indices as well as relative permittivity depends on position of film-layer (n_z) and on perturbation at and within ultrathin film.
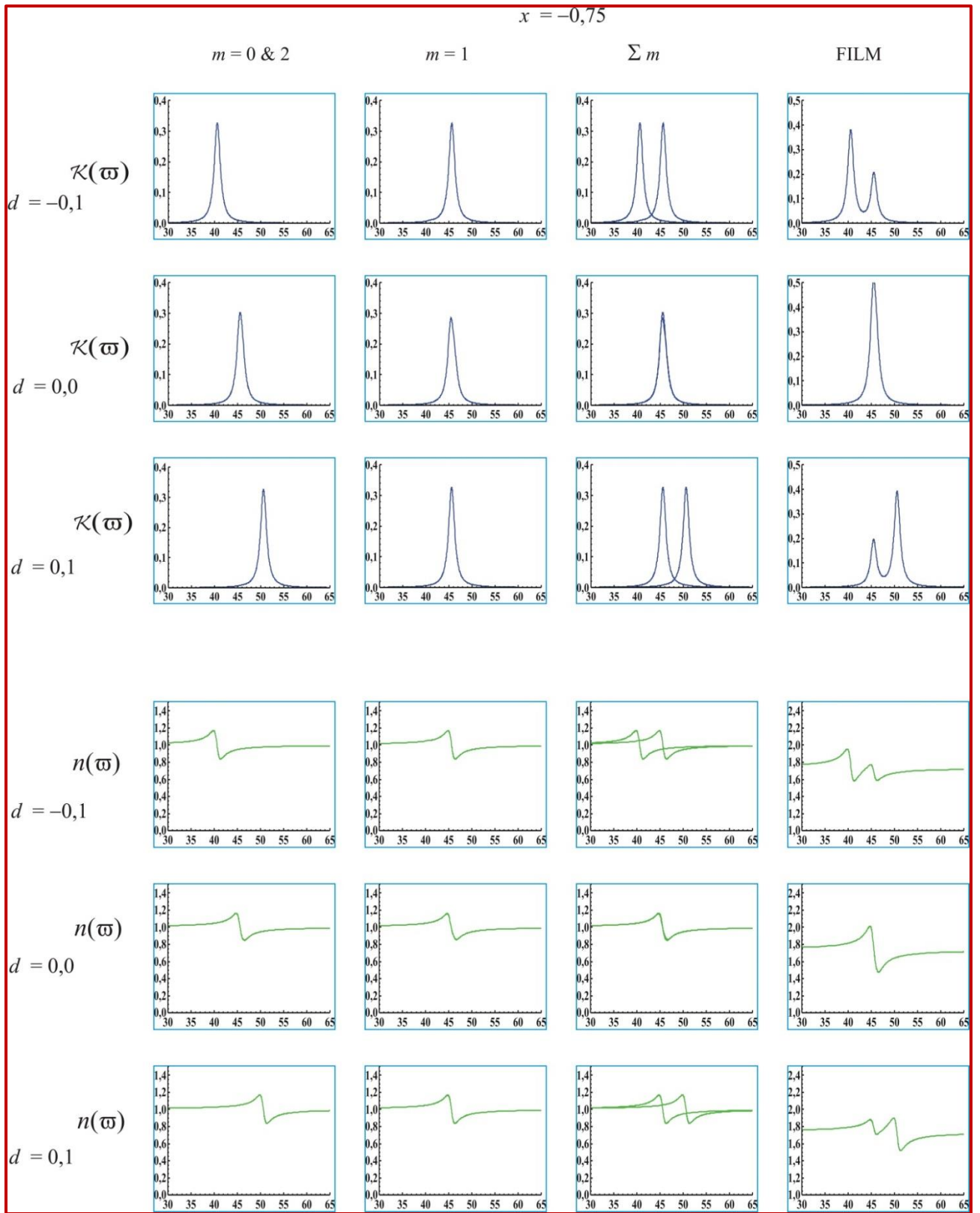
By numerical calculations, we have analyzed absorption index behavior on plane position and on values of boundary parameters, and calculated that. The number of resonant peaks directly depends on the film width, i.e. on the number of layers N. General rule is that the number of resonance peaks decreases inside layers of the film, although with influence of perturbation parameters d and x that rule can be broken and in that case number of peaks is $N + 1$, with possibility of some resonance peaks fading.
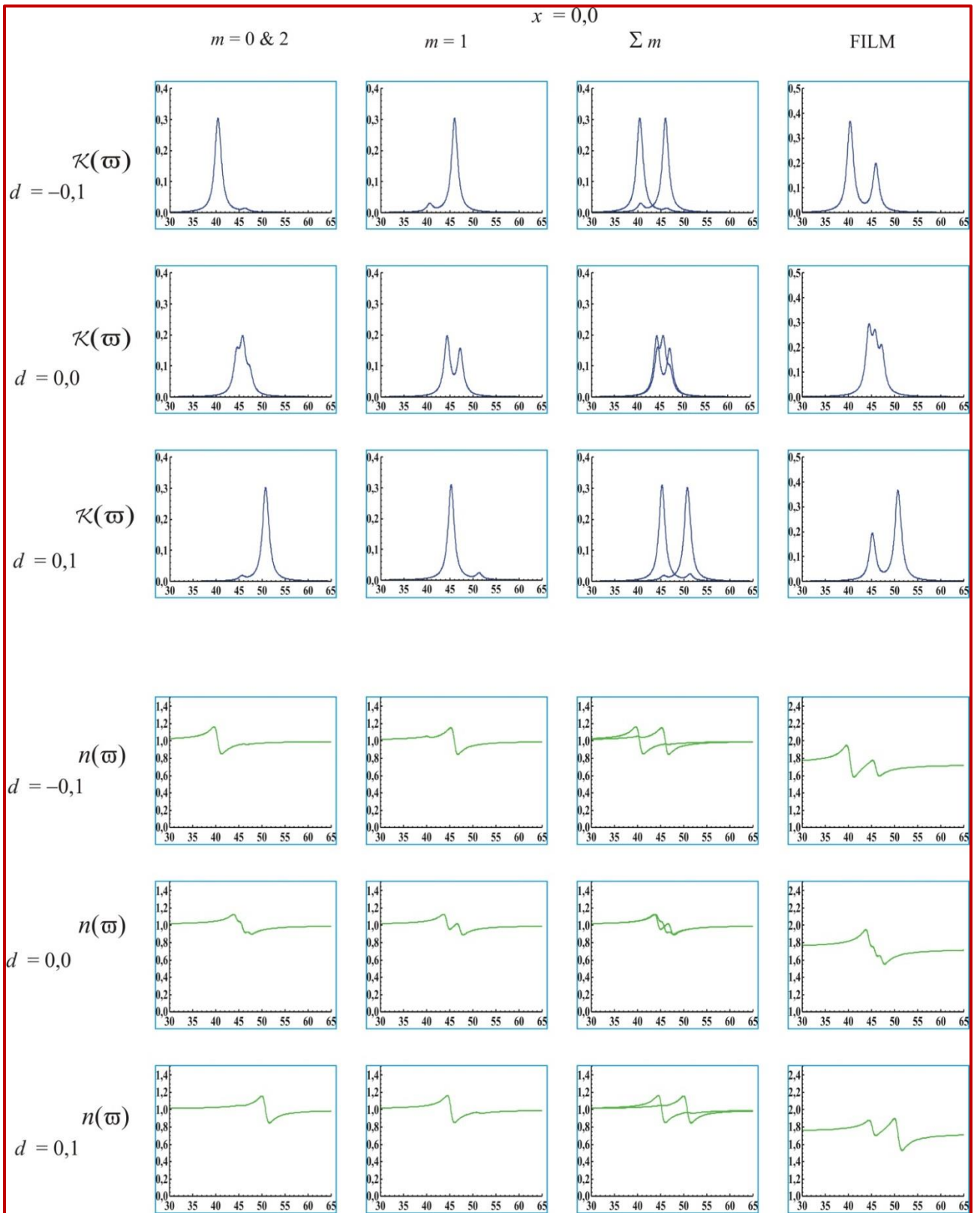
Subsequently we have carried on with the research of the same structures and investigated the influence of boundary parameters on refractive properties of these structures: $n_{n_z}(\omega)$ and showed results on Figure 1 a-c for different values of perturbation parameters: $x = -0,75; 0,0; +0,75$ and $d = -0,1; 0,0; +0,1$.

Since the emission and absorbtion spectra can be experimentally recorded but only for the whole film, we have determined these optical characteristics (indices of absorption and refraction) not only for the particular layers but for the whole film as well and in the normal direction on boundary surface of the film where the changes of these values occur in relation to their bulk values.

3. RESULTS AND DISCUSSION

Influence of change of parameter x is shown on all pictures: when the transfer of excitons in border layers is about half the value comparing to the bulk ($x = -0,75$), then when there is no change of transfer (ideal film: $x = 0,00$), than for the about two times higher border transfer ($x = +0,75$). On each of these three pictures influences of changes of value of parameter d are shown (ranging from the case when this parameter is lowered for 10% through the case when value of parameter d is unchanged comparing with bulk case, to the cases when this parameter is increased for 10% in the node of border area of film), while values of parameter x are fixed. Each picture has four columns with six graphs which show positions of absorption and refraction peaks on border plane of film, while right side next columns show positions of absorption and refraction peaks in internal plane of film. On each figure, ordinate has relative values of absorption index (comparing with bulk values), while abscise has non-dimensional values of frequencies of external electromagnetic field (defined in paper [3]). The last two columns show the sum of absorbtion and refraction spectra for the whole film.
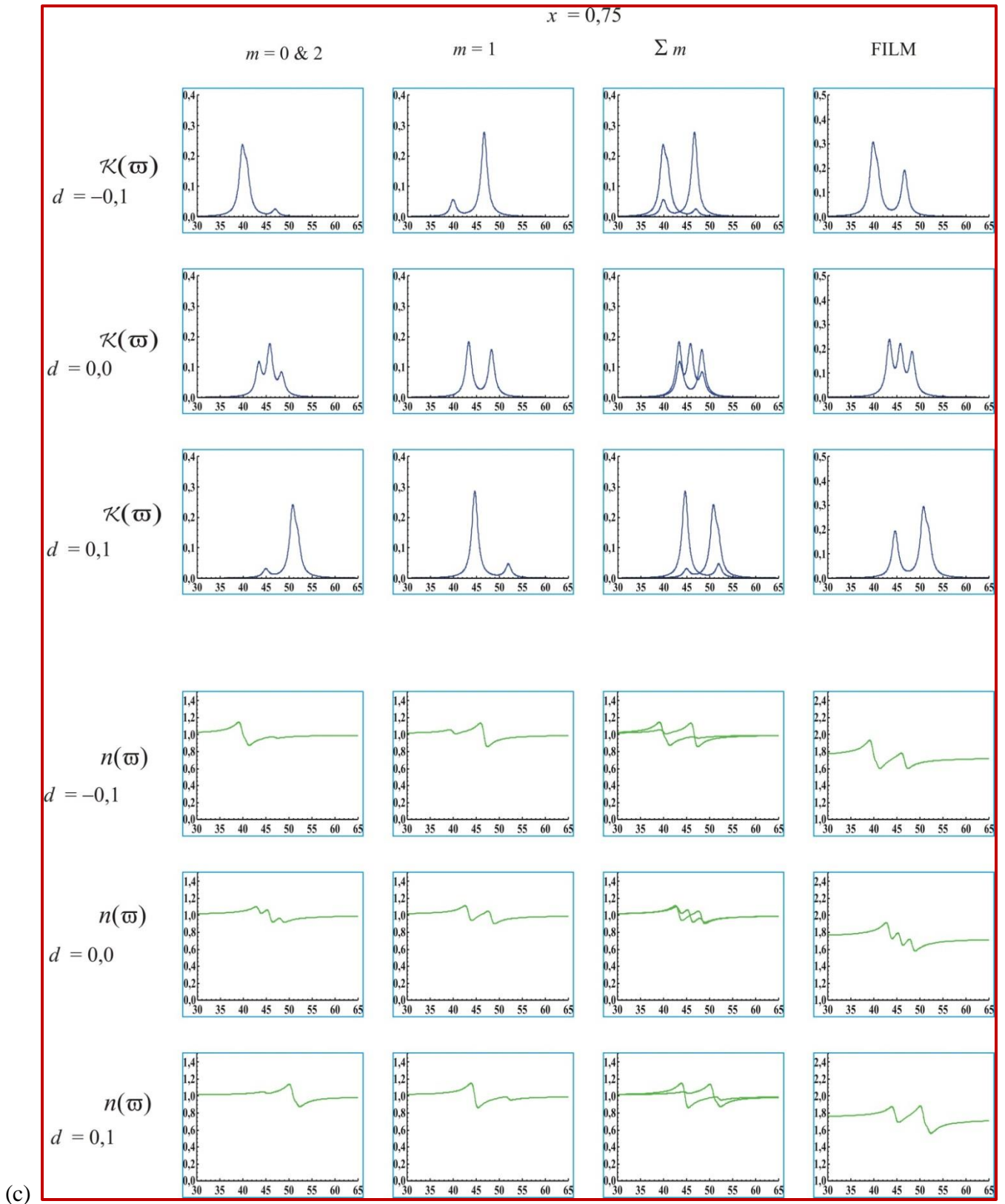
(b)

(c)

Figure 1: Dynamical absorption and refraction indices of perturbed symmetrical two-layered film

Comparing to resonant lines of permittivity, we can observe that there are less absorption peaks, i.e. that there are dominant frequencies which will be absorbed truly. Actually there is a dominant peak on boundary planes, but with the half of these cases that peak is narrow for lower values of parameter x, and in the other half its width is larger (x of a bit higher value).

For the whole film the absorption spectra possess one more expressive peak out of the three possible peaks in a narrow zone, except when $d = -d$, then we have two peaks symmetrical around central narrow zone. The place of peak and the zone depends on values d: when $d > 0$ then peak is on sides (on higher frequencies), but when $d < 0$ then it is the opposite way. The specific case is when $d=0$, then there appears only one (a little wider) absorption peak on certain frequency. In that case the position of zones and peaks in certain layers are congruous.

In the third colomn the dependancy of index of refraction on reduced frequency of external electromagnetic field is given. From all those given charts we can see that slight growth of refraction breaks at points of change of absorption characteristics. At the point where the index of absorption increases— the index of refraction decreases, at the point where the index of absorption alternates abruptly (increse/ decrease) there are the peaks of refraction index. This is in the accordance with the assumption of Kramer's theory, but there the effects only appear at the beginning and at the end of absorption zone, and here they are descreet and do not describe wider continual zone, but quantum and very selective narrow zone change.

In the area of frequency where absorption peaks and narrow absorption zone appear, there comes the decrease of refraction indices values. The interval of decreasing frequency of refraction index and the appearance of absorption peaks are identical. For certain layers the decrease is not monotonous function of frequency, but there appears certain number of extremes which is equal to number of absorption peaks.

4. CONCLUSION

These results may be better explained by experimental facts regarding resonating optical/ luminescence peaks in similar molecular layered nanostructures. In papers [10–12], this was evidenced in perylene chemical compounds and explained by resonating effects at specific unoccupied levels. These effects are manifested by narrow optic absorption and refraction in close infrared band. Very good agreement in resonating absorption may be attributed and explained by presence of boundary conditions and quantum size effects for nano-sized samples. Relative small differences in profile of absorption lines appear because we observed only electron line spectra in our work, disregarding oscillatory and rotational contributions.

ACKNOWLEDGMENTS

REFERENCES

[1] Šetrajčić, J.P., Ilić, D.I., Markoski, B., Šetrajčić, A.J., Vučenović, S.M., Mirjanić, D.Lj., Škipina, B., Pelemiš, S.S., Conformation and application of Green's functions method to optical properties of ultrathin molecular films searching, In: 15th Central european workshop on quantum optics, Belgrade, Serbia, 2008.

[2] Pelemiš, S.S., Šetrajčić, J.P., Markoski, B., Delić, N.V., Vučenović, S.M., Selective absorption in twolayered optic films, J. Comput. Theor. Nanosci. 6/7, 1474, 2009.

[3] Škipina, B., Mirjanić, D.Lj., Vučenović, S.M., Šetrajčić, J.P., Šetrajčić, I.J., Šetrajčić-Tomić, A.J., Pelemiš, S.S., Markoski, B., Selective ir absorption in molecular nanofilms, Optical Materials 33 1578, 2011.

[4] Šetrajčić, J.P., Pelemiš, S.S., Vučenović, S.M., Zorić, V.M., Armaković, S., Škipina, B., Šetrajčić, A.J., Absorption features of symmetric molecular nanofilms, Proceedings 27th MIEL, 1, 127–130, 2010.

[5] Agranovich, V.M., Ginzburg, V.L., Crystal optics with space dispersion – Theory of excitons, Nauka, Moskwa, 1979 (in Russian).

[6] Agranovich, V.M., Tosich, B.S., Collective properties of Frenkel excitons, ZhETF 53 149 1967.

[7] Šetrajčić, J.P., Exact microtheoretical approach to calculation of optical properties of ultralow dimensional crystals, arXiv:cond-mat/eprint:1004.2387, April 2010.

[8] Dzyaloshinski, I.E., Pitaevski, L.P., Van der Waals forces in an inhomogeneous dielectric, ZhETF 36, 1797, 1959.

[9] Ronda, C.R. (Ed.), Luminescence – From theory to applications, Ch. 1, Wiley, Weinheim, 2008.

[10] Vragović, I.D., Šetrajčić, J.P., Scholz, R., Quantum size effects in the optical properties of organic superlattices containing 3, 4, 9, 10 perylene tetracarboxylic dianhydride (PTCDA), Eur. Phys. J. B 66, 185, 2008.

[11] Galanin, M.D., Luminescence of molecules and crystals, p.116, Cambridge IPC, Cambridge 1996.

[12] Hippius, C., van Stokkum, I.H.M., Gsa1nger, M., Groeneveld, M.M., Williams, R.M., Würthner, F., Sequential FRET processes in calix[4]arene-linked orange-red-green perylene bisimide dye zigzag arrays, J. Phys. Chem. C 112, 2476, 2008.

INFLUENCE OF CHARGE CARRIER AND PHONON SCATTERINGS TO ELECTRIC AND HEAT TRANSPORTS IN GRAPHENE

S.K. Jaćimovski[1], J.P. Šetrajčić[2,3], S.M. Vučenović[4], N.R. Vojnović[5]

[1]*University of Criminal Investigation and Police Studies, Zemun, Vojvodina – SERBIA*
[2]*Academy of Sciences and Arts of the Republic of Srpska, Banja Luka, Republic of Srpska – BOSNIA AND HERZEGOVINA*
[3]*University "Union – Nikola Tesla", Faculty of Sport, New Belgrade, Vojvodina – SERBIA*
[4]*University of Banja Luka, Faculty of Sciences, Banja Luka, Republic of Srpska – BOSNIA AND HERZEGOVINA*
[5]*University of Novi Sad, Faculty of Technical Sciences, Novi Sad, Vojvodina – SERBIA*

E-mail: jovan.setrajcic@gmail.com

Abstract

The planar atom layer of carbon arranged in a two-dimensional hexagonal lattice is called graphene [1]. It possesses a range of interesting characteristics such as mechanical hardness of ≈ 1 Pa and high thermal conductivity $\approx 5 \cdot 10^3$ W·m^{-1}·K^{-1} and the highest electron mobility of all known materials $\approx 10^4$ cm·V^{-1}·s^{-1}. All this makes graphene the most perspective material for application. Temperature dependence on heat and electric conductivity, in the wider temperature interval of $3 - 5000$ K, has been analyzed in this work, by solving the Boltzmann transport equation in approximation of relaxation times, introduced phenomenologically. Thermal conductivity of graphene is essentially phonon-based. The coefficient of thermal conduction is proportional to T^2, and at high temperatures to T^{-1}. The electronic conductivity decreases with increasing temperature for $T > T_{BG}$ and increases for $T < T_{BG}$ in the event that we take into consideration the effect of all the relaxation mechanisms.

Keywords: Thermal conductivity, Electronic conductivity, Relaxation time, Boltzmann transport equation

1. INTRODUCTION

In order to fulfill the essential task of phonon engineering [1], to improve the electric and thermal transport properties of the given nanostructure, it is very important to get acquainted with its mechanisms of thermal conductivity. Since the contribution of phonon subsystems to thermodynamic analysis is the first step in research of nanostructure properties [2], special attention in this paper has been given to the study of phonon thermal conductivity of graphene.

Graphene is a single layer 2D structure whose surface is covered with regular hexagons of 0.142 nm side, with carbon atoms in hexagon vertices. It can be considered as a structural part of graphite, whose 3D structure is composed of graphene planes located at a distance of 3 nm [3]. Graphene has unique properties such as anomalous high electrical and thermal conductivity, extremely high mobility of charge carriers, and dependence of electric properties on the presence of admixtures on the surface, the ability to set the size of the band gap, quantum Hall effect and good electromechanical characteristics [4]. All of the above makes graphene a very promising material for nanoelectronic. The ideal pristine 2D structure cannot be obtained due to thermodynamic instability [5]. However, if this structure is strained or has defects, it can exist without contact with the wafer. It is experimentally established that there are free graphene sheets that constitute the complex wavy form [6]. Out of the mentioned properties the most striking is the anomalous high thermal conductivity. The measured thermal conductivity [7] is in the range from 3500 W/mK to 5500 W/mK, the largest among the all known materials so far.

The sheets of ideal graphene of infinite dimensions do not differ among each other. However, real samples differ not only in size but also in the structure of boundaries which modifies acoustic phonon properties such as phonon group velocity, polarization, density of states, and changes the way acoustic phonons interact with other phonons, defects and electrons [1], creating opportunities for engineering phonon spectrum in order to improve thermal properties [2]. A graphene of sufficiently large size cannot have an ideal structure, because the graphene surface contains structural defects depending on the synthesis and external conditions. These defects are: vacancies or adsorption of a functional group on the surface (which represent the most common type of defects), the Stone-Wales defect, isotopic defect, dislocations, etc. [3]. The existence of these defects and boundaries significantly affects the coefficient of thermal conductivity and other transport properties.

2. GRAPHENE THERMAL CONDUCTIVITY

Thermal properties of nanomaterial graphene (specific heat, thermal expansion coefficient, the coefficient of thermal conductivity) significantly depend on phonon characteristics. We have carried out considerable research to the phonon share in the thermodynamic properties of graphene as a 2D crystal

structure [8]. Since these results are required for the observation of the combined impacts (electrons and phonons), we will give a brief outline of the most important results and characteristics that we obtained in the cited papers.

Characteristics of phonon spectrum are determined by 2D structure of graphene. Graphene has a hexagonal structure with two carbon atoms in each cell. This causes the appearance of the six phonon branches in the dispersion spectrum: three acoustic (LA, TA and ZA) and three optical (LO, TO and ZO). The LA and TA modes correspond to longitudinal and transversal phonon oscillations in a graphene plane. The ZA mode corresponds to oscillations of phonons in the direction normal to the direction of oscillation modes LA and TA. The LA and TA modes have a linear dispersion law [9]: $\omega = \upsilon\, q$, with the velocities: $\upsilon_{LA} = 18.4\,\text{km/s}$ and $\upsilon_{TA} = 16.5\,\text{km/s}$. There is no agreement related to the dispersion law for the ZA mode. In our calculation we adopted the dispersion law given with $\omega_3 = \upsilon\, q^{3/2}$ and the velocity $\upsilon(ZA) = 9.2\,\text{km/s}$ [10].

The phonon thermal conductivity is determined from the Boltzmann transport equation [11]:

$$\kappa = \frac{1}{4\pi L_z k_B T^2} \sum_s \int_{\omega_{\min}}^{\omega_{\max}} (\hbar\omega_s)^2 e^{\frac{\hbar\omega_s}{k_B T}} \left(e^{\frac{\hbar\omega_s}{k_B T}} - 1 \right)^{-2} \frac{\upsilon}{u} (\tau_B^{-1} + \tau_U^{-1} + \tau_{pd}^{-1})^{-1} \omega_s \mathrm{d}\omega_s , \tag{1}$$

where $\vec{\upsilon}$ and $\vec{u}$ are group and phase velocity, respectively, L_z thickness of layer in z-direction and $\tau(\omega_s)$ are relaxation times. The main contribution to the thermal conductivity provides acoustic branches, while the contribution of optical branches is negligible.

The most common scattering processes are: scattering of phonons at boundaries, scattering of phonons at defects (isotopic admixtures, vacancies), and phonon-phonon scattering. Relaxation time for the appropriate type of scattering, considered below, is the estimated time.

Relaxation time for this case is defined in [12] as:

$$\frac{1}{\tau_B} = \frac{1-p}{1+p} \frac{\upsilon}{L_x} , \tag{2}$$

where p is a measure of surface roughness, and L_x is the smallest dimension of sheet.

In the case of elastic scattering on isotopes, the relaxation time is defined in [12] by expression:

$$\frac{1}{\tau_{pd}} = A_d \frac{2\pi\omega^3}{\omega_D^2} , \tag{3}$$

where $A_d = c_d \Delta M/M$. Here c_d is the concentration of defects and $\Delta M/M$ is the ratio of elementary cell atomic mass change and atomic mass of a cell; ω_D is the Debye frequency.
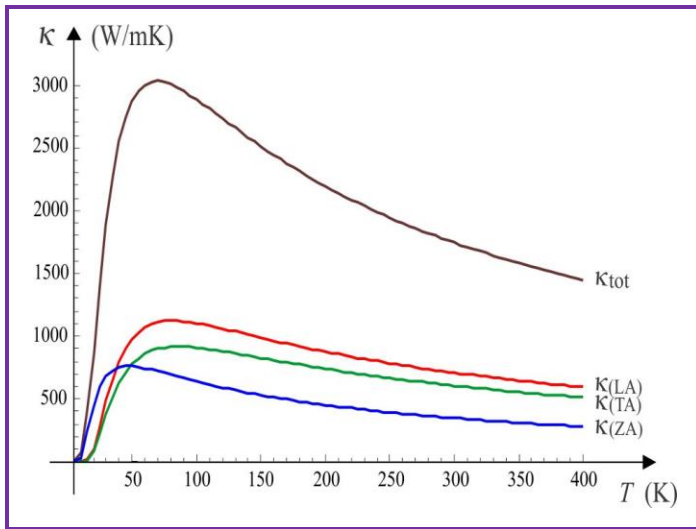
For U-processes the relaxation time is defined as [13]:

$$\frac{1}{\tau_u} = 2\gamma_s^2 \frac{k_B T}{Mv^2} \frac{\omega^2}{\omega_D} , \qquad (4)$$

where γ_s is the Grüneisen parameter. Therefore, lower limit of integral is not zero but a certain minimum value. Klemens gave a physical interpretation of the choice of this minimum value. He suggested the value ω_{min} to be determined from the assumption that average free path of phonon is not greater than the characteristic dimension L_x of graphene [13]:

$$l(\omega_s, T) = \frac{1}{2\gamma_s^2} \upsilon \frac{M\upsilon^2}{k_B T} \frac{\omega_D}{\omega_s^2} < L_x. \qquad (5)$$
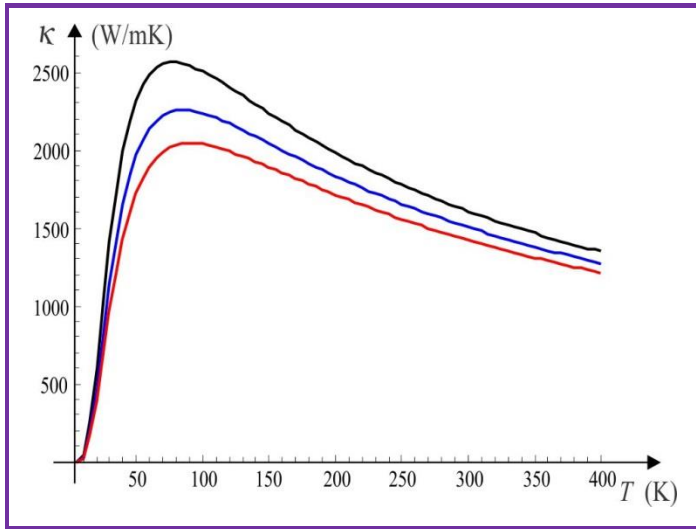

The result obtained by taking into account all the aspects of scattering (at the borders, phonon-phonon scattering and scattering at defects) is shown in Figure 1.

Figure 1*: Calculated thermal conductivity of graphene for different phonon branches and all mechanisms of relaxation: ZA –blue line, TA –green line, LA – red line, and total thermal conductivity – black line*

It can be seen from the Figure 1 that the total thermal conductivity for the adopted parameters is about 2.6 kW/(K·m), which is consistent with experimental data [14]. Also, in Figure 1 temperature dependences of individual phonon branches are given. The greatest contribution to the thermal conductivity is provided by the LA phonon branch, and the TA branch the TA branch provides only a slightly lower contribution. The smallest share of the thermal conductivity is provided by the ZA phonon branch, which is is about 20% of the total thermal conductivity. This is probably due to the small group velocity of the ZA mode and great value of the Grüneisen parameter. What is interesting is a low-temperature area in which the largest contribution to thermal conductivity is provided just by the ZA phonon branch.

It can also be noted from the Figure 2 that the thermal conductivity for the ZA branch drops to zero the fastest, i.e. it has the steepest decline. At a temperature T^*, slightly lower than 50 K, all three phonon branches give equal contribution to thermal conductivity of graphene. Up to this temperature, the contribution to the thermal conductivity of the TA phonon branch is larger than that of the LA branch, and for the values greater than T^* the contribution of these branches is inverse.

The influence of defects on the probability of scattering of phonons and the coefficient of thermal conductivity of real samples depends on the concentration of defects. The reduction of thermal conductivity coefficient of graphene with the increasing concentration of defects is experimentally measured [7−9]. In the case of graphene samples without defects the contribution of phonon branches of LA and TA is greater than in the case of samples with defects, which affects the growth of the total thermal conductivity, which now amounts to about 3.1 kW/(K·m). The contribution of the phonon branch ZA is approximately the same as in the case of the sample with defects.

Figure 2: The dependence of the coefficient of thermal conductivity for different concentrations of admixtures; $A_d = 4.5 \cdot 10^{-4}$ − black line, $A_d = 9 \cdot 10^{-4}$ − blue line, $A_d = 13.5 \cdot 10^{-4}$ − red line

When analyzing the effect of different concentrations of defects on the total thermal conductivity of graphene, it can be seen that the thermal conductivity decreases with increasing concentration of defects (Figure 3). In the case of up to 0.5% increase of admixtures concentration, for the values adopted in our example, the maximal thermal conductivity is reduced by about 12%, and the total thermal conductivity is reduced by 8.5%. For 1% increase of admixtures concentration, the maximal thermal conductivity is reduced by about 24% and the total thermal conductivity is reduced by 15%. In doing so, the maximum values of thermal conductivity move into the region of higher temperatures.

3. GRAPHENE ELECTRONIC CONDUCTIVITY

The dispersion law of is given as [14]:

$$E = \pm \hbar v_F \sqrt{1 + 4\cos^2 \pi k_y a + 4\cos \pi k_y a \cos \pi k_x a \sqrt{3}} . \tag{6}$$

Plus and minus signs are related to conductive and valence zone, respectively. Both zones are degenerated in the Dirac point. The Fermi level also passes through that point, which is why it can be said that graphene is a semiconductor without the energy gap or that it is semimetal. If we take into account only the area near the Dirac points K and K' dispersion relations can be significantly simplified. The relation then gets a linear form depending on the wave vector and is given by:

$$E = \hbar v_F k,$$ (7)

where v_F is the Fermi velocity (its experimentally determined value is $10^6 \, \text{m/s}$), k - modulus of the wave vector in two-dimensional space (with components (k_x, k_y)), calculated from K or K' Dirac point, $\hbar$ – the Dirac constant [14]. The zone has the form of a cone. A photon has a similar spectrum and therefore it is suggested that quasiparticles in graphene (electrons or cavities/holes) have zero effective mass. Since electrons and cavities are fermions their movement is described by the Dirac equation, or a zero-mass particles and antiparticles (similar to equation for massless neutrino) [15].

The linear dispersion law is the most important, if not unique, characteristic of quantum transport described by the Dirac equation. For positive energy (above the Dirac point) charge carriers are similar to electrons and they are negatively charged. For negative energy, if valence zone is not filled, quasiparticles behave as positively charged cavities, analog to positrons. The density state of quasi-particles in graphene is determined as a number of states per energy unit and area unit [16]:

$$D(\varepsilon) = 2 \frac{\varepsilon}{\pi \hbar^2 v_F^2}.$$ (8)

The basic limitation of charge carriers' mobility in graphene is generated by charged admixtures on a substrate of silica dioxide and phonon subsystem that always exists. Relaxation mechanisms that are found in in graphene, such as scattering of charge carriers on charged admixtures and phonons give the final value for the electronic conductivity of graphene. The final conductivity of graphene in the Dirac point is of particular interest. The electronic conductivity of graphene is analyzed semiclassically – by solving the Boltzmann transport equation in the relaxation time approximation [15]. The expression for the electrical conductivity of graphene is in a form of:

$$\sigma = \frac{e^2 v_F^2}{2} \int_0^\infty D(\varepsilon) \tau(\varepsilon) \left(-\frac{\partial f_0}{\partial \varepsilon} \right) d\varepsilon,$$ (9)

where $\tau(\omega)$ – relaxation time, e – charge of quasiparticles, and $f_0 = \left[\exp\left(\frac{\varepsilon - \mu}{k_B T} \right) + 1 \right]^{-1}$ – the Fermi-Dirac distribution function, μ – chemical potential of charged quasi-particles.

Scattering mechanisms and their relaxation time, analyzed in this paper are as follows [16]:

(a) Scattering of charge carriers in the neutral admixture with a short-range potential in the form of $U = V_0 \delta(\vec{r})$ provides relaxation time:

$$\frac{1}{\tau_1(x,T)} = \frac{n_i V_0^2}{4\hbar^3 v_F^2}(\mu + k_B Tx), \tag{10}$$

(b) Scattering at charged admixtures with a long-range Coulomb potential provides relaxation time:

$$\frac{1}{\tau_2(x,T)} = \frac{\pi^2 n_i}{\hbar}\frac{e^4}{(\varepsilon_0 \varepsilon_r)^2}\frac{1}{\mu + k_B Tx} \tag{11}$$

(c) Scattering of carriers on acoustic phonons has a relaxation time given by the expression

$$\frac{1}{\tau_3(x,T)} = \frac{D^2 k_B T}{8\hbar^3 v_F^2 \rho_m}(\frac{1}{v_L^2} + \frac{1}{v_T^2})(\mu + k_B Tx) \tag{12}$$

The scattering of phonons of the ZA branches is not taken into account. Scattering of phonons is analyzed for the case where $T \geq T_{BG}$ and $T < T_{BG}$ and where T_{BG} is the Bloch-Grüneisen temperature. Temperature T_{BG} is the temperature limit to which the phonon gas is degenerated, and over which it is not degenerated [14]. It is determined by the expression $T_{BG} = 2\hbar v_s k_F / k_B$.

(d) In the case when the scattering is realized on the particles with screen potential, relaxation time is given by the expression:

$$\frac{1}{\tau_4(x,T)} = \frac{1}{\tau_0}\frac{(\mu + k_B Tx)}{\varepsilon_F}[1 - a_1(\frac{(\mu + k_B Tx)}{\varepsilon_F} - 1) + a_2(\frac{(\mu + k_B Tx)}{\varepsilon_F} - 1)^2];$$

$$\frac{1}{\tau_0} = \frac{n_i}{2\pi\hbar}\left(\frac{2\pi e}{\varepsilon_0 \varepsilon_r}\right)^2 \frac{2I_0}{\varepsilon_F}; \quad a_1 = \frac{2I_1}{I_0}; \quad a_2 = \frac{3I_2}{I_0}; \quad I_n = \int_0^1 \frac{x^{2+n}\sqrt{1-x^2}}{(x + 2r_s)^{2+n}}; \quad r_s = \frac{e^2}{\varepsilon_0 \varepsilon_r \hbar v_F}. \tag{13}$$

Finally, relaxation time of charge carriers on vacancies is determined as:

$$\frac{1}{t_5(x,T)} = \frac{p^2 n_i \hbar v_F^2}{(m + k_B Tx)\ln^2\left\{\frac{(m + k_B Tx)R_0}{\hbar v_F}\right\}}. \tag{14}$$

For low temperature region (as in [16]), we transform equation (9):

$$\sigma = \frac{4\pi e^2}{h^2}\int_0^\infty dx\{k_B Tx + \varepsilon_F[1 - \frac{\pi^2}{6}(\frac{k_B T}{\varepsilon_F})^2]\}\tau(x)\frac{e^x}{(e^x + 1)^2}; \quad x = \frac{\varepsilon - \mu}{k_B T}; \quad \mu = \varepsilon_F - \frac{\pi^2}{6}\frac{(k_B T)^2}{\varepsilon_F}, \tag{15}$$

while for higher temperatures the equation is in the form of

$$\sigma = \frac{4\pi e^2}{h^2}\int_0^\infty dx\{k_B Tx + \frac{1}{4\ln 2}\frac{\varepsilon_F^2}{k_B T}\}\tau(x)\frac{e^x}{(e^x + 1)^2}; x = \frac{\varepsilon - \mu}{k_B T}; \mu = \frac{1}{4\ln 2}\frac{\varepsilon_F^2}{k_B T}. \tag{16}$$

Temperature dependence of the electrical conductivity for the temperatures $T < T_{BG}$ and in the case where all the relaxation mechanisms operate is given in Figure 3.

Figure 3: *Temperature-dependence of the electrical conductivity when all the relaxation mechanisms operate in case of T <T_{BG} (left) and when T > T_{BG} (right)*

As it can be seen, in the case where the charges interact only with the vacancies, electrical conductivity is negative and it increases with temperature reaching a corresponding saturation value. If the quasi-particles are influenced only by screen potential, then the dependence of the electrical conductivity of the temperatures has a distinctly oscillatory character. In cases where other relaxation mechanisms operate (short-range potential, long-range potential and phonons) electrical conductivity for $T > T_{BG}$ decreases with temperature. The same applies in case when $T > T_{BG}$ and all mechanisms of relaxation operate. However, for temperatures $T < T_{BG}$, which in our case is $T_{BG} = 59.27$ K, electrical conductivity increases with the increase of temperature. The paper which experimentally confirmed that the concentration of defects in graphene leads to an increase in electrical conductivity at lower temperatures was published in 2011. [10].

4. CONCLUSION

The study of graphene provides answers to fundamental issues related to the characteristics of the two-dimensional crystal structure. The very fact of the existence of graphene is contrary to the principle formulated seventy years ago on the thermodynamic instability of similar structures. The study of graphene is justified because of its exceptional characteristics and potential significant applications. The high thermal, mechanical and chemical stability associated with exceptional transport characteristics offer great opportunities for practical application of graphene. High value of coefficient of thermal conductivity is one of the important characteristics of graphene and has record levels of all known materials.

Thermal conductivity of graphene is essentially phonon-based. The analyzed grapheme samples' dimensions exceeded average free path of phonons (800 nm [3]). Otherwise, a so-called ballistic transport would appear, with phonons spreading through the sample without scattering. The obtained results have been achieved with a simplistic assumption that the Grüneisen parameters, group and phase velocity of phonons are constant values. These parameters generally depend on the phonon frequencies.

Different measurements of the coefficient of thermal conductivity of graphene, as well as different theoretical investigations, give different results. It is evident that at low temperatures, the coefficient of thermal conduction is proportional to T^2, and at high temperatures to T^{-1} which is in line with the general theory of the coefficient of thermal conductivity for 2D structures [9–11]. Also, the absolute value of the coefficient of thermal conductivity increases when graphene sheet dimensions increase, which is associated with an increase in the number of phonon modes that occur in the sample. However, it is obvious that there are several physical mechanisms that limit the increase of the coefficient of thermal conductivity with increasing dimensions. One such mechanism is the scattering of phonons on defects. Further research should provide the answer about other mechanisms. Also, one direction of research is changing the phonon spectra, density of states and group velocity of phonons which contribute to graphene thermal conductivity changes. Since experimental research of such miniature objects is difficult, numerical modeling should greatly provide information on important factors such as, for example, a form of potential interatomic interaction in graphene.

As for the electronic conductivity of graphene, the cases of operation of different relaxation mechanisms have been analyzed. The electronic conductivity decreases with increasing temperature for $T > T_{BG}$ and increases for $T < T_{BG}$ in the event that we take into consideration the effect of all the relaxation mechanisms.

Graphene is the first and significant representative of a new class of materials-two-dimensional crystals. It reveals a new paradigm – the "relativistic" physics of solid bodies. The uniqueness of its electronic properties is evident in the fact that the behavior of charge carriers is described by the Weyl-Dirac equation in a similar way as massless fermions rather than by the Schrödinger equation. It represents a serious candidate that could replace the silica in microelectronics. Only the first realized prototypes of the future devices based on graphene should be mentioned – field-effect transistors and ballistic transport at room temperature, gas sensors with extreme sensitivity, single electron transistor, liquid crystal displays and solar batteries in which a graphene is one electrode, spin transistor [15].

ACKNOWLEDGMENTS

REFERENCES

[1] A.A. Balandin, D.L. Nika, *Mater. Today* **15**/6, 266 (2012).

[2] J.P. Šetrajčić, S.K. Jaćimovski, V.D. Sajfert, *Mod. Phys. Lett. B* **29**/4, 1550008 (2015).

[3] A.V. Eletskii, I.M. Iskandarova, A.A. Knizhnik, D.N. Krasikov, *Physics-Uspekhi (Advances in Physical Sciences)* **54**/3, 233 (2011).

[4] S.K. Jaćimovski, V.D. Sajfert, J.P. Šetrajćić, D.I. Raković, *Quantum Matter* **4**, 1–4 (2015).

[5] S.K. Jaćimovski, M. Bukurov, J.P. Šetrajčić and D.I. Raković, *Superlattices and Microstr.* **88**, 330-337 (2015). doi:10.1016/j.spmi.2015.09.027.

[6] A. Alofi, G.P. Srivastava, *Phys. Rev. B* **87**, 115421 (2013).

[7] V. Adamyan, V. Zavalniuk, *J. Phys. Cond. Matt* **.24**, 415401 (2012).

[8] G.P. Srivastava, The Physics of Phonons, *Taylor & Francis*, New York 1990, pp.49-54.

[9] P.G. Klemens, D.F. Pedraza, *Carbon* **32**/4,735 (1994).

[10] S. Chen, A.L. Moore, W. Cai, J.W. Suk, J. An, C. Mishra, C. Amos. C.W. Magnuson, J. Kang, L. Shi, R.S. Ruff, *ACS Nano* **5**, 321 (2011).

[11] T. Stauber, N.M.R. Peres, F. Guinea, *Phys. Rev B* 76, 205423 (2007), pp.1-10. 12

[12] J. Radovanović, V. Milanović, Physical Electronics of Solid Body, *Faculty of Electrical Engineering,* Belgrade 2010, pp. 135-143 (in Serbian).

[13] E.H. Hwang, S. Das Sarma, *Physical Review B* 77, 115449 (2008), pp.1-6.

[14] S. Das Sarma, S. Adam, E.H. Hwang, E. Rosi, *arXiv*:1003.4731.v2, 5 Nov (2010).

[15] S.K. Jaćimovski, V.D. Sajfert, J.P. Šetrajčić and D.I. Raković, *Quantum Matter* **4**/6, 559-564 (2015).

[16] P. Wick, A.E. Louw-Gaume, M. Kucki, H.F. Krug, K.Kostarelos, B. Fadeel, K.A. Dawson, A. Salvati, E. Vazquez, L. Ballerini, M. Tretiach, F. Benfenati, E. Flahaut, L. Gauthier, M. Prato, A. Bianco, *Angew. Chem. Int. Ed*. **53**, 7714 (2014).

INVESTIGATION OF A HEATING SYSTEM UNDER ON-OFF CONTROL

B. Sandal[1], Y. Hacioglu [1], N. Yagiz [1]

[1]*Department of Mechanical Engineering, Faculty of Engineering, Istanbul University-Cerrahpasa, Istanbul, TURKEY*

E-mail: bsandal@istanbul.edu.tr

Abstract

The primary aim of this research is to study the dynamic behaviour of the on-off controller-controlled HVAC system in the heating and humidifying operation under the disturbance effect. Heat loss and humidity variation due to natural ventilation caused by the open window to the outdoor air has a disturbing effect on the system. The entire system's mathematical model is presented with mathematical models of HVAC system components. The model was divided into two sub-loops: temperature loop and humidity loop. Both the flow rates of hot water passing through the heating coil and the flow rate of water added by the humidifier into the air were controlled by an on-off controller to keep indoor air conditions within acceptable limits. The air temperature and relative humidity graphs of the zone were obtained from the simulations of the proposed model under winter climate conditions of Istanbul/Turkey. The results demonstrated that the designed on-off controller performed well.

Keywords: HVAC, Heating, Dynamic Model, Simulation, Disturbance, On-Off Controller

1. INTRODUCTION

HVAC systems modelling and simulation is extremely important in analysing system behaviour under different conditions, estimating energy requirements and efficiency, analysing newly designed circuit elements without expensive experiments and determining system preset values.
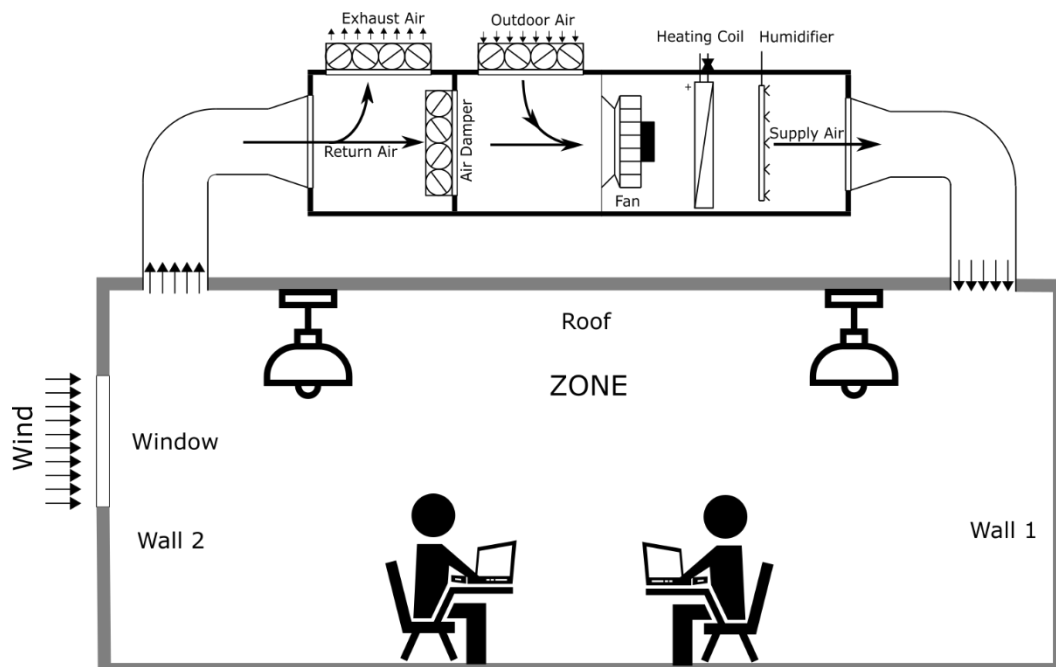
Alhashme and Ashgriz [1] placed the temperature gauge at the appropriate target point rather than placing it in a conventional location in the air-conditioned zone. They determined the temperature distribution in the zone by means of computational fluid dynamics (CFD) and controlled the HVAC system via the on-off controller using the temperature values of the target point. With this approach, more than 22% energy saving was achieved in simulations performed under different heat loss, air direction and air speed conditions. Cetin et al. [2] developed an on-off controller for the EnergyPlus software using a customized EYS (energy management system) for use in residential applications. Systems with and without the developed on-off controller are simulated in EnergyPlus and the results compared. The developed controller increased the accuracy of HVAC energy use results by around 19% and made the control signal more realistic in terms of the nature of DX coils. Soudari et al. [3] suggested a controller for HVAC systems to save energy by combining usage and weather data with predictive control. Based on the controller's pulse width modulation approach, the predictive controller switches the HVAC system on or off with optimal decisions. The proposed controller is simple and appropriate for residential and small commercial buildings where controller costs are crucial. Tyukov et al. [4] developed Supervisory on-off Weather Compensated Control (Sup-WCC) and Supervisory Model Predictive Control (Sup-MPC) algorithms to prevent overheating of office buildings and shopping malls. They have proposed that by supervisory control approach, energy saving will be achieved by depending on the weather conditions and approximate cost of installation. Nägele et al. [5] have divided the heating control approaches used in homes under 8 headings and evaluated each one in terms of energy consumption and comfort. In this evaluation, it was seen that the control approaches that automatically change the temperature setting value are superior to those that change over time. They observed higher energy saving and higher thermal comfort compared to the on-off control approach whose temperature set value did not change.

When HVAC system components, zone and weather conditions are combined, highly complex and often nonlinear system models are encountered. Thermal, fluid and structural coefficients used in these models change over time, especially depending on the temperature. Adding a disturbing effect of varying magnitude over time and expecting the control system to provide multiple expected values in the specific limits further

exacerbates the difficulty in model building. In this study, a time-varying thermal effect was added to the HVAC model working in the heating process and the on-off control method tried to keep the temperature and relative humidity in the specific limits. Firstly, the mathematical model based on the physical principles of the HVAC system and the zone was introduced, on-off controller was applied to the model, then the obtained system model was simulated and the results were discussed.

2. MATERIAL AND METHODS

This section provides a fully dynamic model of a single zone HVAC system. HVAC system components; zone, mixing box, recirculating air fan, heating coil, humidifier and air duct. As a disturbing effect, there is natural ventilation through a single opening on the wall. The temperature and relative humidity of the zone are controlled by the on-off control approach. Mathematical models of the whole system are given in detail. There are some assumptions in this study: the weather conditions are constant, the air in the zone is completely mixed, the density of the air is constant and friction losses are ignored. The HVAC system and zone used in this study are shown in Figure 1.

Figure 1. HVAC System Components and Zone

Effects of wall directions, roof, individuals and lights were considered during the modelling of the zone. Since it is assumed that the zone air is completely mixed, the temperature distribution within the zone is homogeneous. The heat and humidity generated by the individuals in the zone and caused by single sided ventilation are considered. Parallel direction walls (East&West and North&South) have the same effect on the energy balance of the zone. As shown in Figure 1, the East&West walls are referred to as Wall 1 and the North&South walls as Wall 2. The zone model is expressed by four temperatures (T_z, T_{w1}, T_{w2}, T_R) and a humidity variable (W_z). Equation (1) states the rate of change in the energy of the zone. Equations (2) – (4) state the rate of change in the energy through walls and roof. Equation (5) state the rate of change in the humidity content of the zone. Energy and mass balance equations of the zone are given below [6].

$$C_z \frac{dT_z}{dt} = \dot{V}_a \, \rho_a \, c_{p,a} \left(T_{d,o} - T_z \right) + 2 U_{w1} \, A_{w1} \left(T_{w1} - T_z \right) + U_R \, A_R \left(T_R - T_z \right) + 2 \, U_{w2} \, A_{w2} \left(T_{w2} - T_z \right) + q + \text{q}_{nv} \tag{1}$$

$$C_{w1} \frac{dT_{w1}}{dt} = U_{w1} \, A_{w1} \left(T_z - T_{w1} \right) + U_{w1} \, A_{w1} \left(T_{out} - T_{w1} \right) \tag{2}$$

$$C_{w2} \frac{dT_{w2}}{dt} = U_{w2} \, A_{w2} \left(T_z - T_{w2} \right) + U_{w2} \, A_{w2} \left(T_{out} - T_{w2} \right) \tag{3}$$

$$C_R \frac{dT_R}{dt} = U_R \, A_R \left(T_z - T_R \right) + U_R \, A_R \left(T_{out} - T_R \right) \tag{4}$$

$$V_z \frac{dW_z}{dt} = \dot{V}_a \left(W_{h,o} - W_z \right) + \frac{P}{\rho_a} + d_{nv} \tag{5}$$

Most HVAC systems are operated with mixing air to reduce energy expenses. The return air from the zone and the fresh air from the outdoor are mixed to a certain mixing ratio in the mixing box under constant and adiabatic conditions. Dampers can be used for adjusting the mixing ratio. The mixing ratio is constant in this study.

$$\dot{m}_{ret} \, c_{p,a} \, T_{ret} + \dot{m}_{out} \, c_{p,a} \, T_{out} = \dot{m}_{mix} \, c_{p,a} \, T_{mix,o} \tag{6}$$

$$\dot{m}_{ret} + \dot{m}_{out} = \dot{m}_{mix} \tag{7}$$

$$T_{mix,o} = \frac{\dot{m}_{ret} \, T_{ret} + \dot{m}_{out} \, T_{out}}{\dot{m}_{ret} + \dot{m}_{out}} \tag{8}$$

$$W_{mix,o} = \frac{\dot{m}_{ret} \, W_{ret} + \dot{m}_{out} \, W_{out}}{\dot{m}_{ret} + \dot{m}_{out}} \tag{9}$$

The energy required for air flow in the HVAC system is provided by the fan. Usually fans are driven by electric motors that lose some heat to their surroundings. If the fan motor is placed in the AHU, it is assumed that the heat energy they lose will increase the air temperature by about 1 °C.

$$T_{fan,o} = T_{mix,o} + 1 \tag{10}$$

Heating coils, which are simply water to air heat exchangers, are used to increase air temperature. They are created of metals with high thermal conductivity to enhance heat transfer through convection, so the thermal resistance can be neglected. Hot water is provided from the boiler to the heating coil at a constant temperature and the on-off controller regulates the flow of water through the coil.

$$C_{AHU} \frac{dT_{hc,o}}{dt} = \dot{V}_w \, \rho_w \, c_{p,w}\left(T_{hw,i} - T_{hw,o}\right) + UA_{AHU}\left(T_{out} - T_{hc,o}\right) + \dot{V}_a \, \rho_a \, c_{p,a}\left(T_{hc,i} - T_{hc,o}\right) \tag{11}$$

$$V_{AHU} \frac{dW_{hc,o}}{dt} = \dot{V}_a\left(W_{hc,i} - W_{hc,o}\right) \tag{12}$$

In the humidification process, the amount of water vapour in the air is increased to the desired value. Method of dispersing water into the air or method of adding water vapour to the air can be preferred. In our study, it was assumed that humidification process did not change the dry bulb temperature of the air.

$$C_h \frac{dT_{h,o}}{dt} = \dot{V}_a \, \rho_a \, c_{p,a}\left(T_{h,i} - T_{h,o}\right) + UA_h\left(T_{out} - T_{h,o}\right) \tag{13}$$

$$V_h \frac{dW_{h,o}}{dt} = \dot{V}_a\left(W_{h,i} - W_{h,o}\right) + \frac{h}{\rho_a} \tag{14}$$

Clark et al. [7] developed a transient model for duct unit.

$$\frac{dT_{d,o}}{dt} = \frac{(h_{d,i}+h_{d,o})\,\dot{m}_a\,c_{p,a}}{h_{d,i}\,m_d\,c_d}\left(T_{d,i} - T_{d,o}\right) \tag{15}$$

The relative humidity value is used to describe conditions of thermal comfort. The HVAC system aims to maintain the relative humidity within a certain range. In winter conditions, the minimum relative humidity should be 20%-25% and the maximum should be 80%. Relative humidity can be calculated using water vapour pressures using the following formulas [8].

$$\varphi = \frac{p_w}{p_{ws}} \tag{16}$$

$$W = \frac{M_w}{M_{da}} = 0.62198 \frac{p_w}{p - p_w} \tag{17}$$

$$p_w = \frac{W\,p}{0.62198 + W} \tag{18}$$

$$\ln p_{ws} = \frac{C_8}{T} + C_9 + C_{10}T + C_{11}T^2 + C_{12}T^3 + C_{13}\ln T \tag{19}$$

$$W_s = 0.62198 \frac{p_{ws}}{p - p_{ws}} \tag{20}$$

HVAC system is expected to maintain the air conditions of the zone around certain values and this is achieved after a period of operation. If the energy and mass balance of the zone changes after the steady state is reached, the control system is expected to meet this state. Leaving a window open to the outdoor for a certain period of time will create disturbing effect in terms of thermal and humidity due to the outdoor air entering the zone. The volumetric flow rate of the air flow caused by natural ventilation and the heat and humidity loads caused by this air flow can be calculated by the following equations. In the study, it was assumed that the wind speed changes according to a certain frequency [9].

$$\dot{V}_{nv} = 0.025 \, A_{wdo} \, V_{wind} \, f_{wind} \tag{21}$$

$$q_{nv} = \dot{V}_{nv} \, \rho_a \, c_{p,a}(T_{out} - T_z) \tag{22}$$

$$d_{nv} = \dot{V}_{nv} \, (W_{out} - W_z) \tag{23}$$

On-off control approach, also known as two-position control, is the simplest of feedback control approaches because of the two positions where the control response is open or closed. The controllers that use this approach are abundant because they are simple and cheap. During the control of the zone temperature in heating operation, a switch on signal is sent to the heating coil when the temperature falls below the set point called thermostat and a switch off signal is sent above the set point. If the cooling occurs shortly after the heater has been switched off, the controller will reactivate the heater quickly to switch on.

$$u_T = \begin{cases} 1.8 \, \dot{V}_w \rho_w & ; & T_{zref} - T_z > 0 \\ 0 & ; & T_{zref} - T_z < 0 \end{cases} \tag{24}$$

$$u_\phi = \begin{cases} 1.12 \, h & ; & \phi_{zref} - \phi_z > 0 \\ 0 & ; & \phi_{zref} - \phi_z < 0 \end{cases} \tag{25}$$

3. RESULTS AND DISCUSSION

The values of some of the desired, initial and system parameters used in the analysis are as follows:
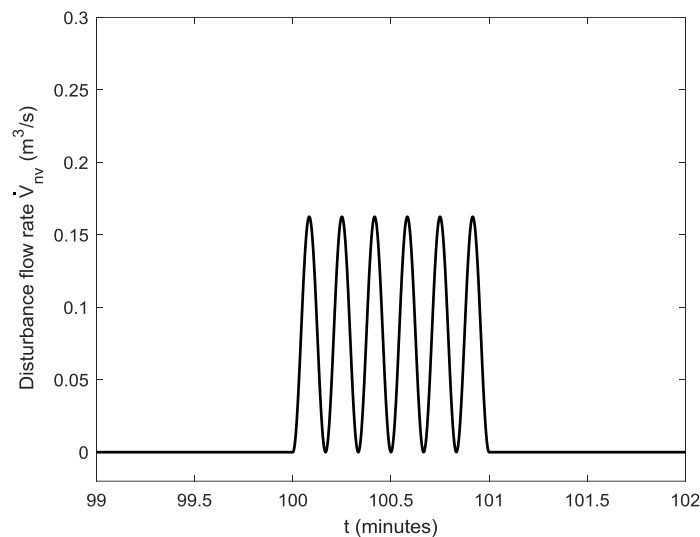
- Desired indoor conditions: T_z=22 °C, ϕ=50 %
- Outdoor conditions: T_{out}=5 °C, W_{out}=0.002 kg/kg (dry air)
- Wind conditions: V_{wind}=5 km/h, f_{wind}= 0,1 Hz
- The disturbance effect (opening of window) starts at 100th minute and lasts 1 minute.
- Volume flow rate of the supply air: $\dot{V}_a$ =0.192 m³/s
- The heat gains in the zone: 2 people each 0.15 kW, 2 lamps and 2 laptops total 1 kW
- The initial conditions of zone at t=0 are set to T_z (0) =7 °C and W_z (0) =W_{out}

Figure 2 displays the disturbance effect as the volumetric flow rate of air entering the zone due to natural ventilation by opening the window at 100th minute and keeping it open for 1 minute.

The temperature of the hot water supplied to the heating coil is constant in both controlled and uncontrolled systems analysis. Hot water flow rate was found in the uncontrolled model using the trial and error method to bring the zone temperature to the desired level. In the model with controller, on-off controller was designed. Initially, all temperatures in the system are 2 °C higher than the outdoor temperature. If the zone temperature is observed after the beginning of the heating process, the system without the controller reaches the desired temperature too late and the system with the on-off controller reaches within a few minutes. Shortly after reaching the steady state, the system is subjected to disturbing effect. During these moments, the uncontrolled system noted a sudden decrease in the zone temperature, while the on-off controller regulated the hot water mass flow rate and managed to maintain the temperature in the desired band (Figure 3). Figure 4 shows the control signal (hot water mass flow rate) for the designed on-off controller.
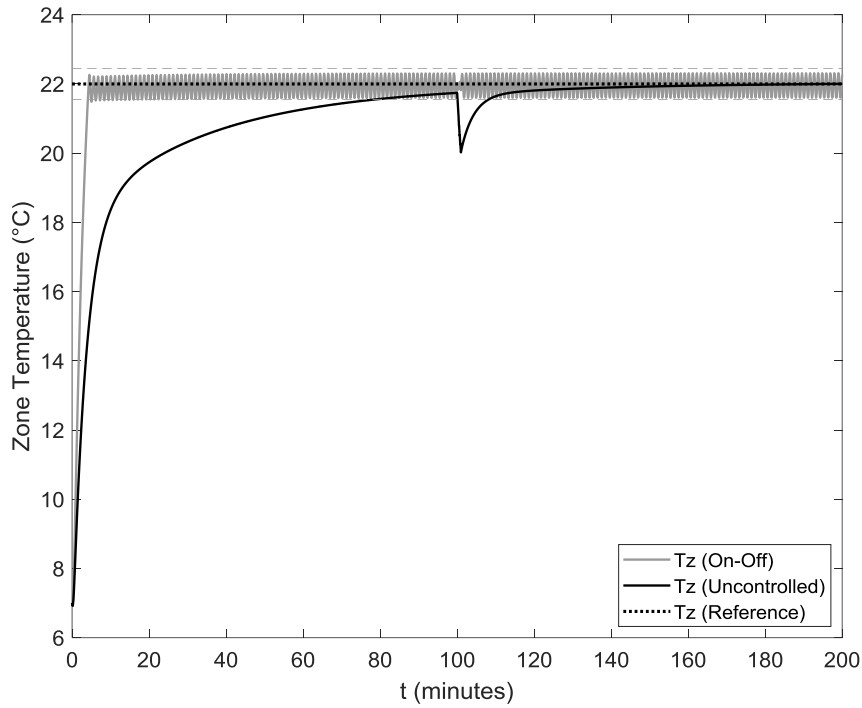

Figure 2. Volumetric Flow Rate of Naturel Ventilation to the Zone

Figure 5 presents the zone's relative humidity for controlled and uncontrolled systems. Relative humidity is the proportion of humidity in the air to the highest amount of humidity available at that temperature. Hence, its value relies on temperature and humidity. In the uncontrolled model, the mass flow rate of the humidity added to the air by the humidifier was determined using the trial and error method to bring the zone's relative humidity to the desired level. Initially, the humidity value at all points of the system is equal to the humidity of the outdoor air. In the uncontrolled model the relative humidity is high at the low zone temperatures observed at the start of the process because constant amount of humidity is continuously added from the humidifier to the air as soon as the heating process begins. However, it will return to its normal value with increasing zone temperature in the following minutes. With the opening of the window, a sudden

decrease in relative humidity is observed at 100th minute due to the drier air entering the zone, the value only improves with the elimination of the disturbing effect.

Figure 3. Zone Temperature for On-Off Controlled and Uncontrolled Systems

Figure 4. Mass Flow Rate of Hot Water Used by the On-Off Controlled System

Figure 5. Relative Humidity of Zone for On-Off Controlled and Uncontrolled Systems

Figure 6. Mass Flow Rate of Humidity Added to Air by the On-Off Controlled Humidifier

Figure 6 shows the control signal for the humidifying loop as the water mass flow rate added from the humidifier to the air.

4. CONCLUSION

In this study, a HVAC system is modelled with all its components, and the system is subject to short-term disturbance effect and the behaviour of humidity and temperature in the zone is examined for uncontrolled and on-off controlled cases. When the results are examined, it is noticed that the on-off controlled HVAC system worked very well even in the case of disturbing effects.

REFERENCES

[1] Alhashme, M., Ashgriz, N., A virtual thermostat for local temperature control, Energy and Buildings, 126, 323-339, 2016.

[2] Cetin, K.S., Fathollahzadeh, M.H., Kunwar, N., Do, H., Tabares-Velasco, P.C., Development and validation of an HVAC on/off controller in EnergyPlus for energy simulation of residential and small commercial buildings, Energy and Buildings, 183, 467-483, 2019.

[3] Soudari, M., Kaparin, V., Srinivasan, S., Seshadhri, S., Kotta Ü., Predictive smart thermostat controller for heating, ventilation, andair-conditioning systems, Proceedings of the Estonian Academy of Sciences,67(3), 291–299, 2018.

[4] Tyukov, A., Shcherbakov, M., Sokolov, A., Brebels, A., Al-Gunaid, M., Supervisory model predictive on/off control of HVAC systems, 8th International Conference on Information, Intelligence, Systems & Applications (IISA), Larnaca, 2017, 1-7, 2017.

[5] Nägele, F., Kasper, T., Girod, B., Turning up the heat on obsolete thermostats: A simulation-based comparison of intelligent control approaches for residential heating systems, Renewable and Sustainable Energy Reviews, 75, 1254-1268, 2017.

[6] Tashtoush, B., Molhim, M. Al-Rousan M., Dynamic model of an HVAC system for control analysis. Energy, 30 (10), 1729-1745, 2005.

[7] Clark, D.R., Hurley, C.W., Hill, C.R., Dynamic models for HVAC system components. ASHRAE Trans, 91(1), 737-751, 1985.

[8] Baird, J. (Ed.), ASHRAE 2001 HVAC Fundamentals Handbook. Atlanta, GA: American Society of Heating, Refrigerating, and Air-Conditioning Engineers, 2001.

[9] Edwards, R., Handbook of Domestic Ventilation, Elsevier Butterworth Heinemann, 2005.

EVALUATION OF ADHESION OF ALKOXY BASED SILICONE ON SURFACE TREATED POLY(PROPYLENE) EXTERIOR TRIMS OF VEHICLES BEFORE AND AFTER AGEING TESTS

I.Bolova

[1]*TOFAŞ, Türk Otomobil Fabrikası A.Ş., R&D Directorate, Material Engineering Administration, Bursa, TURKEY*
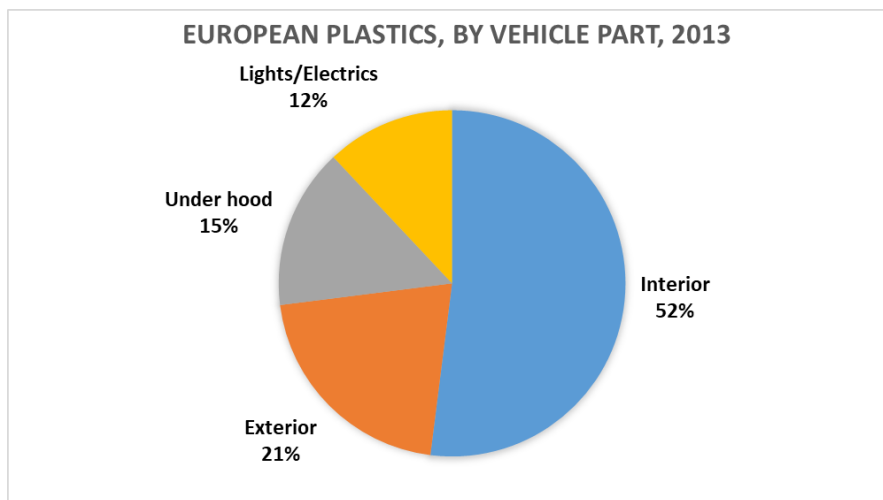
E-mail: isil.bolova40928@tofas.com.tr

Abstract

Silicone adhesives are used commonly for sealing and binding of exterior and engine trim parts, which have different thermal expansion values, in automotive industry due to their stable chemical structure under low and high temperature conditions, resistancy to ultraviolet (UV), moisture, oxygen, ozone and chemicals and their high gas permeability. In addition, silicones are very flexible materials even if it is exposed to very low temperature (-90°C and -115°C) and very high temperature (~300°C). In this regard, the aim of this study was evaluation of adhesion of alkoxy based silicones on mostly used plastic material poly(propylene) (PP) parts by bead peel tests at natural condition, after heat ageing and damp heat ageing. Before tests, plasma treatment was applied on poly(propylene) parts. Surface energy of untreated PP parts was measured as 28 dynes/mm. After plasma treatment, this value increased to 36 dynes/mm. Painted metal panels were used in order to simulate vehicle body. According to bead peel test results, silicone adhesive separation from PP samples was cohesive at natural conditions. After heat ageing, samples were conditioned for 2h and 24h at room temperature, silicone adhesive separation was cohesive. However after damp heat ageing test when samples were conditioned for 2h at room temperature, its separation was adhesive that silicone adhesive separated from sample surface completely there was no adhesive on PP parts. When they were conditioned for 24h at room temperature, silicone separation was cohesive and adhesion was evaluated as positive. The negativity of silicone separation from PP parts after conditioning 2h at room temperature depends on penetration of water into the cured silicone and occlusion of water there. Occlusion of water reduced the adhesion between PP and the alkoxy based silicone by playing a lubricant role between the polymer chains (plasticizer effect) and caused easily sliding of chains past each other. For damp heat aged samples, after 24h room temperature conditioning, samples dried and the cohesive characteristics of silicone from PP part surface occurred again. However performance was not on the original level.

Keywords: Alkoxy-based Silicone, Adhesion, Bead Peel, Polypropylene, Surface energy
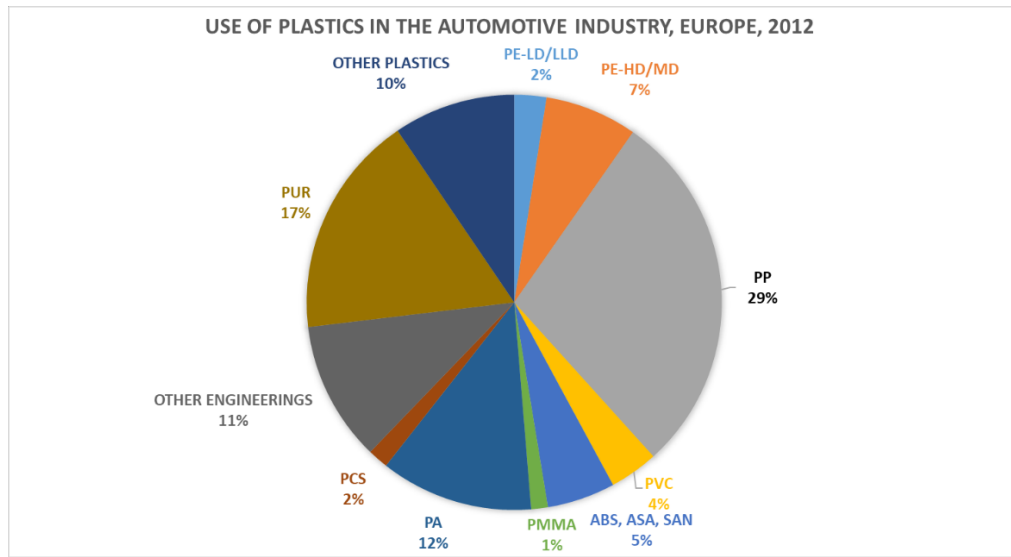
1. INTRODUCTION

In automotive industry, materials from metal to composite which have different thermal expansion values, are used. According to Plastics Europe, 16% of the total weight of a vehicle (about 115 kilograms) consists of plastics. Plastics are used interior (52,5%), exterior (21%), under hood (15%) and ligths and electrics (12%) (Figure 1). In 2020, plastics are expected to increase to 18% of the total vehicle weight, due to the increament of plastics usage in vehicle production [1].

Figure 1: Plastic usage in vehicle part [1]

In Europe, on average 29% of used plastics is poly(propylene) in 2012 (Figure 2) [1]. In the North America, poly(propylene) usage in automotive industry is %32 by 2017 (Figure 3) [2].

Polypropylene (PP) with talc additive is mostly used due to its good heat and electrical resistance, also chemical and fatigue resistance, being tough, having low density and higher rigidity. In automotive industry PP components are utilized some automotive parts, including heater cases; lamp housings, bumpers, instrument panels, rocker panels, interiors trims, interior pillar trims, scuff plates, cowl grills, boot liners, fans and shrouds, lighting, electrical housings, splash shields, fender liners, seating components, door trims and exterior trim [2, 3].

Figure 2: Plastic types usage in vehicle [1]

Figure 3: Plastic types usage in vehicle in North America, 2017 [4].

In order to bind plastic-metal; plastic-plastic and metal-metal material combinations, polyurethane, silicone, epoxy, modified silane, reactive or non-reactive hotmelts, pressure sensitive adhesives are generally applied in addition to screwing, riveting and welding technologies. Especially, silicone adhesives are preferable to adhere powertrain parts because of its sealing property and exterior trim plastics, such as poly(amide) (PA), poly(methyl methacrylate) (PMMA), poly(carbonate) (PC), poly(propylene) (PP) and

acrylonitrile-butadiene-styrene terpolymer (ABS) because of its versatile physical properties and cost advantages.

Silicone adhesives surface energy is very low ca. $21–22$ mNm^{-1}; cured silicone surface tension is 24 mNm^{-1} [5]. They can bind materials that have different thermal expansion values with its excellent elastomeric properties (high movement capability, high elastic recovery ($85–98\%$). Due to containing high energy Si-O bond and organo substituents in polymeric backbone, after curing it is chemically stable and this provides to have low creep, good fatigue resistance even if at low temperature, environmental resistance (including but not limited to ultraviolet- (UV), moisture-, oxygen- and ozone-resistance), high temperature resistance (up to $300°C$), fire resistant properties, high gas permeability, chemical resistance and effective sealing properties [6]. Besides, silicones have low toxicity and electrical properties ranging from high resistivity to high conductivity. All of these unique features allow us to use it; outside, under, engine, and inside of the vehicle. Its usage will increase with BEVs and become more widespread.

Silicones can be one component and two components and cured by relative humidity, heat, mixing of two components and ultraviolet light to form thermoset material. For one component silicones, curing systems and by products based on its functional groups and reaction was initiated by ambient relative humidity and cure proceeds from the outside into the interior of the material. During curing, condensation polymerization occurs and alcohols (Alkoxy- cross-linkers (methanol, ethanol etc.); ketoximes (Oxime- cross linkers), carboxylic acids (Acetoxysilane- crosslinkers (acetic acid)); amides (Amidosilane –cross linkers); hydroxylamines, amines (aminoxy- and aminosilane- cross linkers); and ketones release as by-products [6, 7]. Curing time of silicone beads depends on thickness, ambient temperature, relative humidity and functional groups.

In this study, adhesion of alkoxy- silicone adhesive was evaluated at room temperature, after ageing on polypropylene substrate with and without surface treatment by bead peel test.

2. MATERIAL AND METHODS

Poly(propylene) talc filled was used for testing that is commonly applied on exterior of vehicles. Stainless steel metal panels were painted with solvent-based paints according to FCA specifications in production line and it was used in order to simulate vehicle body. One component, room temperature vulcanized and Alkoxy- crosslinker containing silicone adhesive was used.

Table 1: Physical Properties of Alkoxy-Based Silicone

Material Properties	
Elongation at Break (%)	680
Specific Gravity (g/ml)	1.4
Application temperature	Room temp.
Tack free time (min)	2
Skin time (min)	15
Full curing (day)	7

All tests in this study were performed according to Fiat Chrysler Automobiles specifications. Test methods were described in details.

In order to measure surface energies of polypropylene materials surface energy inks (Arcotest) were used.

200mm x 25 mm dimensions PP samples were prepared according to FCA specifications. Materials' surfaces were cleaned with heptane towels and surface energy were measured and after cleaned samples, silicone adhesive was applied on the surface. Samples were conditioned at room temperature and they cured after 48h.

Other PP materials' surfaces were treated with plasma and adhesive was applied on the PP materials and they cured. Adhesion was evaluated by bead peel test according to DIN 54457. Bead peel test was performed after ageing tests.

150mm x 70 mm dimensions painted metal panels were prepared according to FCA specifications as plastic samples. Panels' surfaces were cleaned with heptane towels then silicone adhesive was applied on the surface. Samples were conditioned at room temperature until full curing occurred (48h).

Adhesion was evaluated visually by bead peel test. This test measures the fracture behavior of beads of elastic adhesive as silicones. It does not acquired the joint strength. In the test, adhesive bead is applied on

a material surface and it cures at room temperature (Figure 4). The bead peel test is generally performed together with ageing tests. In order to evaluate, changes of fracture patterns, the beads are peeled off the surface until fracture occurs. To give a meaningful result, a new starting cut made repeatedly at the contact point between the adhesive and substrate. This gives the bead a new opportunity to fracture. The fracture patterns can be compared before and after ageing that allows statements to be made about the relevant effects.

Figure 4: Example application of Silicone based adhesive and bead peel test.

Full cured samples were aged at 90°C in Thermoscientific Heratherm oven for different time intervals in order to investigate time effect. After ageing, samples firstly were conditioned at room temperature for 2h and 24h and then bead peel test was done.

Other cured samples were aged in Leibish damp heat ageing (at 40°C under saturated water vapor) cabinet for different time intervals to 500h in order to investigate time effect. After ageing, samples were conditioned at room temperature for 2h and 24h and then bead peel test was done.

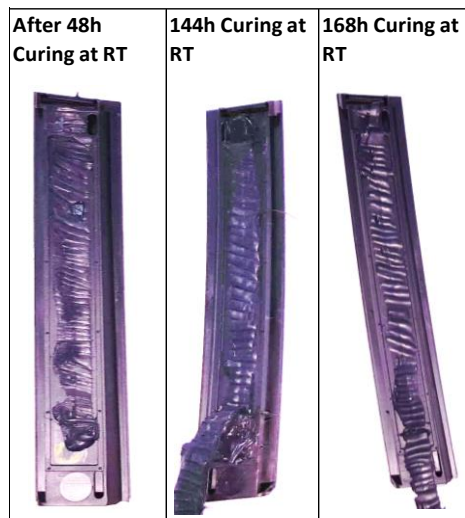## 3. RESULTS AND DISCUSSION

Surface energies of polypropylene materials were measured with and without plasma treatment by surface energy inks. Without plasma treatment, PP surface tension between 22 and 28 dyne/cm (Figure 5). Plasma equipment was established with respect to FCA specifications. After plasma, its surface energy increased to 38 dyne/cm.

Figure 5: Surface energy measurement by inks.

Silicone adhesive applied poly(propylene) and painted metal panel samples cured after 48h at room temperature and they were peeled by cutter. Figure 6 shows, after curing, adhesive separation from PP parts was cohesive at natural conditions. Adhesive separation from painted panel also was cohesive (Figure 7) at natural conditions.

Figure 6: Bead peeled samples at Natural Conditions before ageing tests.

Figure 7: Bead peeled samples at Natural Conditions before ageing tests.

Generally, heat affects positively in specific temperature values, except pressure sensitive tapes and hotmelts. Adhesive was peeled cohesively from plasma treated poly(propylene) surface and painted metal panels after even 500h heat ageing (Figure 8 and 9).

In order to investigate damp heat effect on 162h heat aged PP parts, it was put in to the damp heat cabinet for 24h. It was observed that damp heat did not influence adhesion negatively after heat ageing.

| 48h ageing+ 2h RT | 72h ageing+ 2h RT | 120h ageing+ 2h RT | 162h ageing +2h RT | 162h ageing +2h RT+24h DAMP HEAT | 288 h ageing +2h RT+24h RT | 306 h ageing +2h RT+24h RT | 386 h ageing +2h RT+24h RT | 485 h ageing +2h RT+24h RT | 500 h ageing +2h RT+24h RT |

Figure 8: Bead peeled PP samples after heat ageing at different time interval.

| 128h ageing +2h RT+24h RT | 500 h ageing +2h RT+24h RT |

Figure 9: Bead peeled painted metal samples after heat ageing.

Adhesion of silicone on PP parts were investigated by peeling after 72h, 96h, 120h and 148h damp heat ageing following 2h room temperature conditioning. According to results, silicone adhesive was peeled adhesively from plasma treated poly(propylene) parts. Adhesion was negative. However when damp heat aged parts were conditioned for 24h at room temperature after ageing, it was observed that adhesion of silicone on plasma treated PP was positive and adhesive separation was cohesive (Figure 10).

Figure 10: Bead peeled PP samples after damp heat ageing.

According to evaluation, silicone separation from painted panel was cohesive even after short time as 2h conditioning at room temperature (Figure 11).

Figure 11: Bead peeled painted metal samples after damp heat ageing.

4. CONCLUSION

As conclusion, adhesion of alkoxy-based silicone was evaluated on low surface energy poly(propylene) with plasma treatment and on painted panel which is simulated vehicle body.

Adhesion of silicone on PP parts with plasma treatment is positive that in order to use silicone for PP, surface energy of PP should be increased.

Heat has positive effect on silicone adhesion. But it may affect the elasticity of the adhesive. However after damp heat ageing, adhesion is negative until drying of parts. Because moisture penetrates through polymer chains and has a plasticizer effect on them. After drying, adhesion is positive again. In this study,

adhesion strength was not evaluated. This should be investigated to observe moisture effect on adhesion strength.

ACKNOWLEDGMENTS

REFERENCES

[1] Plastics Europe.org

[2] Stauber, R., Vollrath (Eds.), L., Plastics in Automotive Engineering Exterior Applications, Hanser Publishers, Munich, Cincinnati.

[3] Patil, A.; Patel A. and Purohit, R. An overview of Polymeric Materials for Automotive Applications Materials Today: Proceedings 4 (2017) 3807–3815.

[4] Gpca.org.ae/2019 (Article: Plastics in the automotive industry which materials will be winners and losers)

[5] White, C., Tan K., Advances in structural silicone adhesives, Chapter 4, National Institute of Standards and Technology, USA; A. Wolf, Dow Corning Corporation, Germany; and L. Carbary, Dow Corning Corporation, USA, 66-95, 2010.

[6] De Buyl, F. (2001), Silicone sealants and structural adhesives, International Journal of Adhesion and Adhesives, 21, 411–22.

[7] Dunn, D.J. (2003), Adhesives and Sealants – Technology, Applications and Markets, RAPRA Technology Limited, Shawbury, Shropshire, United Kingdom.

VOCs EMISSIONS FROM LASER PRINTERS AND HEALTH RISK ASSESMENT OF OFFICE EMPLOYEE

A.Arı[1], P. Ertürk Arı[1]

[1]Department of Environmental Engineering, Faculty of Engineering, Bolu Abant Izzet Baysal University, Bolu, TURKEY

E-mail: akifari@ibu.edu.tr

Photocopiers and laser printing devices have been used commonly in offices. These devices have emited potentially harmful pollutants such as toxic elements, carbon black, volatile organic compounds (VOCs) and polycyclic aromatic hydrocarbons (PAHs) which are used in toner as filling materials. Numerous studies have shown that both short- and long-term exposures to high concentrations of such as toxic compounds increases the health risks in indoor environment. Measurements of chemical pollutants released from printers in photocopy centers and office environments have been investigated in various studies. However, it is necessary to increase the number of health risk studies related to the risk of exposure to pollutant components in office environments where intensive printing and photocopying activities are performed. To this purpose current study, a general evaluation of indoor air quality in an office room with heavy printing activity was investigated. Indoor air quality was determined in a controlled staff room in an academic institution to idendify VOCs concentration behavior while printing periods of a laser printer operation. Besides, carcinogenic and non-carcinogenic health risks arose due to the exposure of indoor concentration of the VOCs were determined. As a result of the higher indoor concentration of the VOCs, a total hazard quotient (HQ) value was $9.9x10^{-2}$ and a total CR higher than $1.3x10^{-5}$ were estimated in the study atmosphere.

Keywords: Printer emissions; health risk assessment; VOCs; indoor air quality

INTRODUCTION

Indoor air quality has become a major public health concern due to the various emission sources of chemical contaminants, such as VOCs, gaseous inorganic contaminants primarily O_3 and nitrogen oxides (NO_x), and particulate matter (PM) from household electronic devices, furniture and several indoor activities [1, 2]. As people spend approximately 90% of their time at residents, offices, shopping malls, and similar environments; therefore the indoor air quality may significantly affect human health and concerned as a potential risk factor [2 - 4].

Photocopiers and laser printing devices have become common in homes, schools, offices and various other indoor environments. Such devices are known to emit potentially harmful pollutants, more clearly ultra-fine particles, increasing concern on toxic effects resulting from both short and long term exposures to such pollutants. Several studies have revealed that PM, VOCs, and O_3 are released during printing and copying operations, that induce significant indoor air quality degradation in offices [5 - 7].

In this study, the indoor air of a frequent laser printer used office room in an academic institution was inspected. Indoor air concentrations of VOCs were determined. A detailed inhalation health risk assessment was performed for office workers the exposure to the VOCs to conclude an integrated risk description.

MATERIALS and METHODS

Gaseous samples were collected from a test room described in Fig 1. Test room is located on the 2nd floor of the Engineering Faculty of Bolu Abant Izzet Baysal University, 10 km away from the city center and approximately 10 m high from the ground level. The test room includes a personal computer (PC), main office furnitures such as two desks and two seats, a bookshelf and a commercial brand laser printer with a printing speed of 30 pages per minute. The room is in regular use by the faculty staff as personnel working room. The inner volume of the test room was 60 m^3 (5m x 3m x 4m), and average temperature and humidity were 23±4°C and 35±6%, respectively while the samples were collected. Each test was performed for 9 hours, to represent the worker's daily shift time.

VOCs were sampled using stainless steel thermal desorption tubes packed with 160 mg of Tenax®TA 60/80 adsorbent (Perkin Elmer, USA). Tenax tubes were pre-conditioned at 335°C for 60 min under a flow of high-purity He (20 mL min^{-1}) to eliminate the initial impurities, then stored in sealed polypropylene tubes containing active charcoal and silica gel until sampling. Office air was passed through the 90 mm long and 5 mm internal diameter tubes for a sampling of VOCs for 9 hours with a flow rate of 200 mL min^{-1}. Indoor air PM and VOC measurements were carried out at 1.50 m above the office ground, 1 m distance from the printer

and at least 1.5 m from the closed window and door. Outdoor air around the building was sampled by the same approach to obtain outdoor concentrations, and also indoor to outdoor ratios of the VOCs. Collected samples were analyzed by using a thermal desorption-GC-MS system.

RESULTS and DISCUSSIONS

Measured indoor concentrations of the VOCs were shown in Table 1. Concentrations of 50 VOCs among 68 compounds were quantified in office samples. Highest concentrations were measured for namely n-hexane, toluene, benzaldehyde, benzothiazole, nonanal, isoprene, limonene, decanal, styrene, m+p-xylene, o-xylene, and benzene. One of the significant results of the study was the indoor median concentration of benzene was exceeded 5 μg m^{-3} limit value. The concentrations of these pollutants accounted for about 68.4% of the total VOC concentration measured in the office atmosphere. According to the relevant literature, benzaldehyde, benzene, ethylbenzene, nonanal, styrene, toluene, 1,1,1-trichloroethane, xylenes, and some inorganic gases such ozone and ammonia are the most specific emissions of the photo-imaging equipment [8, 9].

Probabilistic estimations of the carcinogenic and/or non-carcinogenic health risks due to the exposure of the air pollutants are explanatory tools on revealing the direct and indirect effects of the measured pollution levels on human health, and also on estimating the authorities expense budgets on public health cares. Inhalation health risk assessment of the employees in the printing office environment within this study was performed for VOCs. The perceivable nature of indoor air pollutants those causing an unpleasant working atmosphere, even in low concentrations they may be associated with chronic outcomes such as carcinogenic and non-carcinogenic effects. Hazard quotients and lifetime excess cancer risks indicating the potential chronic health effects of inhalation exposure to specific VOCs were evaluated in a controlled printing office environment by using USEPA's risk assessment method [10]. Average HQ and ILCR values with the standard deviations calculated for the exposure of the non-carcinogenic and carcinogenic VOCs were presented in Figures 2 and 3.
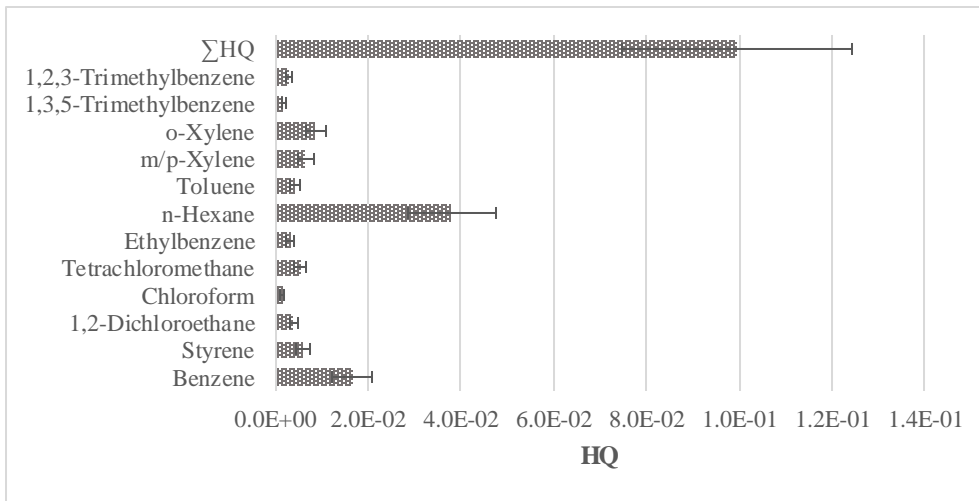
Table 1. Concentrations of the measured VOCs

VOC	Min-Max (µg m⁻³)	Median (µg m⁻³)	VOC	Min-Max (µg m⁻³)	Median (µg m⁻³)
Isoprene	5.9-20.8	6.70	3-Carene	-	Nd
Acrylonitrile	0.0-1.35	0.17	1,3,5-Trimethylbenzene	0.0-0.80	0.11
n-Hexane	19.9-55.1	26.9	Benzaldehyde	10.1-24.7	10.6
2-Methylfuran	0.0-0.67	0.28	1,4-Cineole	-	Nd
Chloroform	2.06-8.29	3.35	Limonene	4.23-9.05	6.59
1,1,1-Trichloroethane	0.0-1.18	0.20	m-Cymene	-	Nd
Tetrachloromethane	0.0-1.96	1.09	p-Cymene	0.0-0.63	0.25
Benzene	2.52-14.7	5.02	Ocimene	-	Nd
1,2-Dichloroethane	0.0-0.24	0.05	Eucalyptol	0.0-9.04	4.73
n-Heptane	0.0-0.63	0.30	1,2,3-Trimethylbenzene	0.0-2.78	0.15
Crotonaldehyde	-	Nd	4-Methylanisole	-	Nd
n-Octane	0.22-0.76	0.31	Gamma-Terpinene	-	Nd
Toluene	19.9-52.2	21.2	1,3-Diethylbenzene	0.28-1.36	0.86
Hexanal	6.33-29.1	5.18	1,4-Diethylbenzene	0.62-1.99	1.45
Chlorobenzene	-	Nd	Phenol	0.84-9.99	4.17
Ethylbenzene	2.68-6.23	3.45	1,2-Dichlorobenzene	0.0-5.88	0.88
m+p-Xylene	3.75-15.27	6.51	Terpinolene	-	Nd
o-Xylene	3.08-17.24	8.52	Dihydromyrcenol	0.0-15.4	4.68
Styrene	5.78-22.99	11.7	1-Octanol	0.0-5.78	3.54
1-Heptanal	0.0-3.96	1.83	Linalool	-	Nd
Alpha Pinene	3.41-7.42	4.15	Alloocimene	-	Nd
Isopropylbenzene	0.0-0.93	0.35	Nonanal	0.0-18.8	7.50
Camphene	-	Nd	Acetophenone	1.04-9.09	2.26
n-Propylbenzene	0.16-0.58	0.38	Alpha Terpinene	0.0-23.9	2.49
n-Nonane	0.0-0.35	0.18	L-Fenchone	-	Nd
n-Decane	-	Nd	n-Dodecane	0.0-23.5	4.76
m-Ethyltoluene	0.0-0.48	0.30	(+)-Camphor	-	Nd
p-Ethyltoluene	0.10-0.51	0.20	1-Terpinen-4-ol	-	Nd
Sabinene	0.0-1.52	0.55	Decanal	0.0-21.3	6.56
Beta Myrcene	0.0-5.10	1.86	Alpha Terpineol	-	Nd
1,2,4-Trimethylbenzene	0.0-0.47	0.11	Naphthalene	0.77-3.14	1.43
Beta Pinene	0.45-1.11	0.74	n-Tridecane	2.0-16.0	4.08
o-Ethyltoluene	0.0-0.34	0.11	Benzothiazole	4.57-25.0	8.08
Alpha Phellandrene	-	Nd	n-Tetradecane	2.79-15.8	4.87

Nd: Not detected

HQ was calculated for each compound individually using USEPA's risk assessment model. It was observed that the average values of HQ were in the range of 0.94 (isopropylbenzene) to 4.93 (toluene) for VOCs, exceeding the threshold of 1 by a total value of 21.5. Total risk arose from the 5 carcinogenic VOCs in this study was 1.41×10^{-5}, indicating a possible cancer risk by the categorizations of cancer risks.

Figure 2. HQ values due to VOC exposure

Figure 3. Calculated CR due to VOC inhalation

CONCLUSIONS

Indoor air quality measurements were performed for multiple VOCs in a frequent printer used staff room in an academic institution. Indoor concentrations of a wide variety of VOCs were measured to maintain the printer-related indoor concentrations. As it is cleared by the findings of the study, both carcinogenic and non-carcinogenic health risks arose mainly due to the inhalation of VOCs.

REFERENCES

[1] N. Kagi, S. Fujii, Y. Horiba, N. Namiki, Y. Ohtani, H. Emi, H. Tamura, Y.S. Kim, Indoor air quality for chemical and ultrafine particle contaminants from printers, Build. Environ. 42, 1949-1954 (2007).

[2] S.C. Lee, S. Lam, H.K. Fai, Characterization of VOCs, ozone and PM10 emissions from office equipment in an environmental chamber, Build. Environ. 36, 837-842 (2001).

[3] World Health Organisation (WHO), Selected Pollutants. WHO Indoor Air Quality Guidelines, WHO Regional Office for Europe, Copenhagen, 2010.

[4] D. Campagnolo, D.E. Saraga, A. Cattaneo, A. Spinazze, C. Mandin, R. Mabilia, E. Perreca, I. Sakellaris, N. Canha, V.G. Mihucz, T. Szigeti, G. Ventura, J. Madureira, E. de Oliveira Fernandes, Y. de Kluizenaar, E. Cornelissen, O. Hanninen, P. Carrer, P. Wolkoff, D.M. Cavallo, J.G. Bartzis, VOCs and aldehydes source identification in European office buildings – The OFFICAIR study, Build. Environ. 115, 18-24 (2017).

[5] USEPA, Building Air Quality: A Guide for Building Owners and Managers. EPA/400/1-91/033, Washington, DC, 1991.

[6] Z.M. Wang, J. Wagner, S. Wall, Characterization of laser printer nanoparticle and VOC emissions, formation mechanisms, and strategies to reduce airborne exposures, Aerosol Sci. Tech. 45, 1068-0-1068 (2011).

[7] J. Martin, D. Bello, K. Bunker, M. Shafer, D. Christiani, S. Woskie, P. Demokritou, Occupational exposure to nanoparticles at commercial photocopy centers, J. Hazard. Mater. 298, 351-360 (2015).

[8] C.W. Lee, D.J. Hsu, Measurements of fine and ultrafine particles formation in photocopy centers in Taiwan, Atmos. Environ. 41, 6598-6609 (2007).

[9] B.J. Mullins, D. Bertolatti, R. Mead-Hunter, Assessment of polyaromatic hydrocarbon emissions from laser printers, Atmos. Environ. 79, 428-432 (2013).

[10] K. Sexton, S.H. Linder, D. Marko, H. Bethel, P.J. Lupo, Comparative assessment of air pollution-derived health risks in Houston, Environ. Health Perspec. 115, 1388-1393 (2007).

HEALTH RISK ASSESMENT OF PAHs in SIZE SEGRAGATED PM SAMPLES COLLECTED FROM SEMI-URBAN LOCATION IN SUMMER AND WINTER SEASONS

A. Arı[1], P. Ertürk Arı[1], E.O. Gaga[2]

[1]Department of Environmental Engineering, Faculty of Engineering, Bolu Abant Izzet Baysal University, Bolu, TURKEY
[2]Department of Environmental Engineering, Faculty of Engineering, Eskisehir Technical University, Eskisehir, TURKEY

E-mail: pelinn.erturkk@gmail.com

Polycyclic aromatic hydrocarbons (PAHs) are important organic pollutants which are mainly released into atmosphere from anthropogenic sources as a result of incomplete combustion of fossil fuels and biomass. PAHs are increasing concern in urban and semi-urban atmosphere because of their toxic, carcinogenic and mutagenic effects. On the other hand, health effects of particulate matter mainy depend on the particle size distribution.

Size-segregated atmospheric particulate matter (PM) samples were collected from the Bolu Abant Izzet Baysal University campus for 30 days period of both summer and winter seasons. Size-segregated PM samples were collected using Sioutas Cascade Impactor (SCI) with 4 stages: >2.5, 2.5-1.0, 1.0-0.5, and 0.5-0.25 μm. To determinate PAHs concentrations, filters were sonicated with organic solvents and analysed with a gas chromatography coupled with a mass spectrometry (GC-MS) system. The most dominant PAH compounds in PM phase were Phe, Flt and Pyr both summer and winter samples. The highest concentrations of PM were obtained on the smallest PM size (PM<0.25 μm) both summer and winter seasons. Carcinogenic and non-carcinogenic health risks were determined for PAH compounds for two seasons. Lung cancer risk by the PAH exposure was founded higher in winter period than summer period.

Keywords: Size distribution, PAHs, carcinogenic potential

INTRODUCTION

Particulate matter (PM) is a mixture of many contaminating components. It is very important to determine the composition of the particulate matter resulting from various anthropogenic and natural activities. Prior to this, even knowing the mass of particulate matter is very important in determining the measures to be taken to protect the health of people living in a city.

PAHs are an important group of organic pollutants due to various sources and frequent occurence in urban atmospheres. PAHs are generated by incomplete combustion of organic materials and fossil fuels [1,2]. PAHs are semi-volatile organic compounds, so they can present on both gas and particle phases in atmosphere [5]. Particle size distribution of PAHs determine their environmental fate and health effects [3, 4].
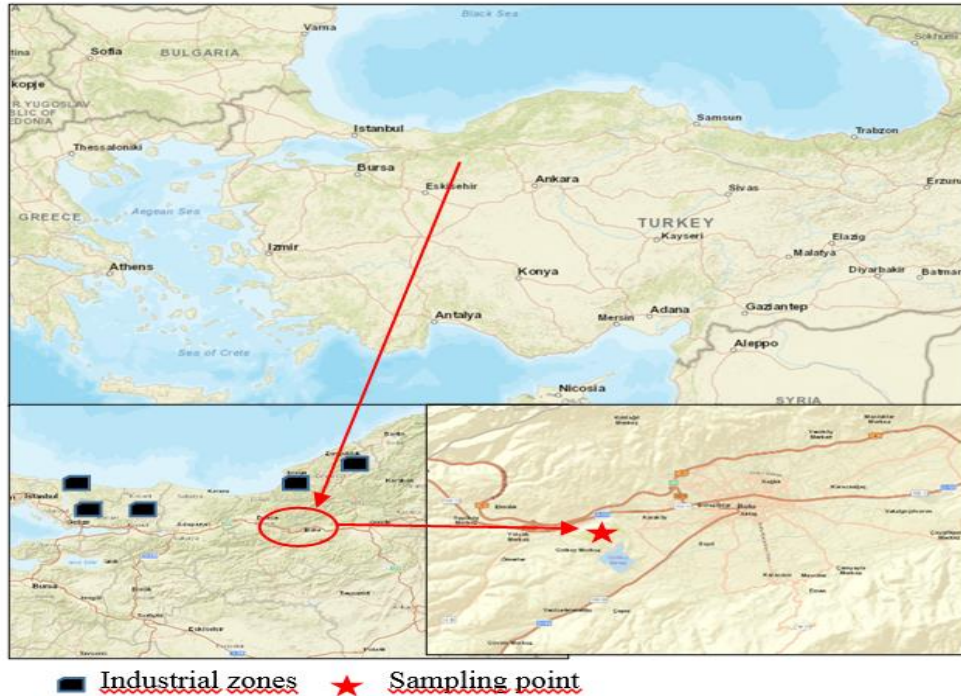
Many PAH compounds such as benzo(a)pyrene (BaP) and dibenzo(a,h)anthracene (DahA), have been identified as possible (Group 2B) or probable (Group 2A) human carcinogens. Some PAH or PAH derivative containing mixtures such as soot particles are considered as human carcinogens (Group 1) [7].

There have been many published studies in the literature on the health effects PAHs and the resulting cancer risk via exposure to PAHs [3, 6, 7]. Calculating the BAP equivalent (BaP$_{eq}$) toxic concentrations of individual PAHs by using toxic equivalency factors (TEFs) and assessing the inhalation unit risks are the most common techniques with the chronic daily intake (CDI) approach for estimation of the health risk of PAHs via inhalation [7].

In this study, size distribution of atmospheric particle-bound PAHs in winter and summer seasons were determined at a suburban location of Bolu, Turkey. Seasonal variations and inhalation health risk assessment was conducted by using BaP equivalent (BaP$_{eq}$) concentrations.

MATERIALS and METHODS

Ambient size-segregated samples were collected from a suburban location, Bolu Abant İzzet Baysal University (BAİBÜ) Campus, in the winter and summer seasons of 2019. 40 samples each were collected between 07 January and 15 February 2019 for winter, and 01 July- 09 August 2019 for the summer sampling campaigns.
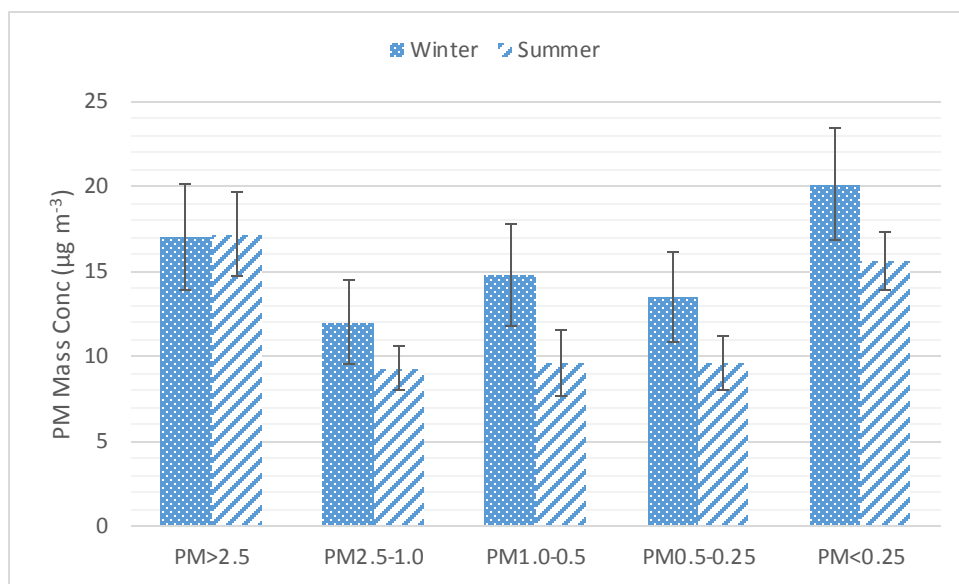
Figure 1. Sampling point

Size-segregated PM samples were collected using a Sioutas Cascade Impactor (SCI) in combination with a Leland Legacy Pump (SKC Inc., Pa, USA) with a 9 L min^{-1} flowrate. SCI was loaded with 25 mm quartz filters for first 4 stages and a back-up filter in 37 mm diameter (QFFs-Pall Life Sciences, USA). PM size fractions of >2.5; 2.5-1.0; 1.0-0.5; and 0.5-0.25 μm were collected on 25 mm filters; likewise, PM$_{<0.25}$ μm was gathered on 37 mm filters in the SCI. Quartz filters were burned at 600°C for 4 hours to eliminate initial carbon background, conditioned under controlled temperature and relative humidity (23°C ± 2°C and 30% ± 5%) and weighed before and after the sampling using a microbalance (Model 360 ES, Precisa Gravimetrics AG., Switzerland) to determine the mass concentration.

PAH concentration on size-segregated aerosol samples were determined by using a gas chromatography- mass spectrometry system (GC-MS: Agilent Technologies). PM samples were sonicated for 60 min in a 20 mL of mixture of ¼ dichloromethane/petroleum ether mixture. Sample volumes were decreased by a rotary evaporator, and then using a gentle stream of ultra pure N$_2$ gas. Evaporated samples were filtered through a column chromatography system for clean up, and then injected to GC-MS in 1 mL of n-hexane.

RESULTS and DISCUSSIONS

Average seasonal concentrations of the size-segregated PM and carbon species presented in Figure 2. Mass concentration of coarse PM (PM>2.5) is comparable in both winter and summer samples, whereas fine mode PM concentrations decreased significantly in summer period. The main reason of the higher winter PM concentrations is suspected to be the increasing emissions from space heating related coal and biomass combustion, and also the meteorological conditions such as decreasing atmospheric mixing layer height.

Figure 2. Average seasonal size-segregated PM mass concentrations

Size distribution of PAHs in winter and summer seasons were presented in Figure 3 and Figure 4. A sharp decrease in PAH concentrations were obtained in summer samples. Total concentration of atmospheric PAHs as the sum of 18 PAHs on 5 different size modes were 298.6 ± 182.5 ng m^{-3} in winter and 115.3 ± 72.9 ng m^{-3} in summer seasons. Besides the meteorological parameters such as atmospheric mixing layer height and ambient temperatures, the main sources of PAHs in urban atmosphere is fuel combustion. Increasing coal and biomass combustion especially in winter period for space heating is one of the most important reasons of higher concentrations in winter period.

Figure 3. Size distribution of PAHs in winter period

Figure 4. Size distribution of PAHs in summer period

Health risks occured due to the PAH exposure is estimated by using USEPA's risk assessment method [7]. BaP_{eq} concentrations of the PAHs were estimated by using toxic equivalency factors. Total BaP_{eq} concentrations were 65.3 ng m^{-3} and 25.5 ng m^{-3} in winter and summer, respectively. Cancer risk due to BaP inhalation was 2.8×10^{-5} in summer, but the risk value was 7.1×10^{-5} in winter season.

CONCLUSIONS

Size distributions, BaP equavalent concentrations and health risks of atmospheric polycyclic aromatic hydrocarbons were evaluated at a suburban location of a small town, Bolu, Turkey. Due to their high dependancy on combustion sources, a significant seasonality were observed. Ambient concentrations of PAHs were increased more than 3 times in winter period. As a result, cancer risk due to the inhalation of atmospheric PAHs were increased in winter period.

REFERENCES

[1] B.J. Finlayson-Pitts and J.N. Pitts, Chemistry of the upper and lower atmosphere: theory, experiments, and applications. Academic press (2000).

[2] A. Albinet, E. Leoz-Garziandia, H. Budzinski, E. Villenave, Polycyclic aromatic hydrocarbons (PAHs), nitrated PAHs and oxygenated PAHs in ambient air of the Marseilles area (South of France): concentrations and sources. Sci Total Environ 2002; 300, 213-28 (2002).

[3] J.S. Lighty, J.M. Veranth, A.F. Sarofim, Combustion aerosols: factors governing their size and combustion and implication to human health. J. Air Waste Manag. Assoc. 50, 1565-1619 (2000).

[4] X.H. Bi, G.Y. Sheng, P. Peng, Y.J. Chen, J.M. Fu, Size distribution of n-alkanes and polycyclic aromatic hydrocarbons (PAHs) in urban and rural atmospheres of Guangzhou, China, Atmos. Environ., 39, 477-487 (2005).

[5] C.A. Alves, A.M.P. Vicente, J. Gomes, T. Nunes, M. Duarte, B.A.M. Bandowe, Polycyclic aromatic hydrocarbons (PAHs) and their derivatives (oxygenated-PAHs, nitrated-PAHs and azaarenes) in size-fractionated particles emitted in an urban road tunnel, Atmos. Res., 180, 128-137 (2016).

[6] F. Aziz, J.H. Syed, R.N. Malik, A. Katsoyiannis, A. Mahmood, J. Li, G. Zhang, K.C. Jones, Occurence of polycyclic aromatic hydrocarbons in the Soan River, Pakistan: Insights into distribution, composition, sources and ecological risk assessment, Ecotox. Environ. Safe., 109, 77-84 (2014.)

[7] J.F. Collins, J.P. Brown, G.V. Alexeeff, A.G. Salmon, Potency equivalency factors for some polycyclic aromatic hydrocarbons and polycyclic aromatic hydrocarbon derivatives, Regul. Toxicol. Pharm., 28, 45-54 (1998).

HEALTH RISK ASSESMENT OF VOLATILE ORGANIC COMPOUNDS (VOCs) IN THE AMBIENT SEMI-URBAN LOCATION IN SUMMER AND WINTER SEASONS

A.Arı[1], P. Ertürk Arı[1], E.O. Gaga[2]

[1]Department of Environmental Engineering, Faculty of Engineering, Bolu Abant Izzet Baysal University, Bolu, TURKEY
[2]Department of Environmental Engineering, Faculty of Engineering, Eskisehir Technical University, Eskisehir, TURKEY

E-mail: pelinn.erturkk@gmail.com

ABSTRACT

Volatile organic compounds (VOCs) are emitted into the ambient from both anthropogenic (e.g., motor vehicles, petrochemical plants, refineries) natural (e.g., emissions from forests, wildfires) sources. VOCs are great concern due to their potential acute and chronic adverse effects to urban health. The concentrations of atmospheric VOC concentrations is varied from depending on sources, meteorological conditions and photochemical reactions. Ambient VOCs were collected from the Bolu Abant Izzet Baysal University campus for 30 days periods of both summer and winter seasons by using stainless steel tubes containing Tenax TA sorbent. Analyses of the samples were performed by a Thermal Desorber (Markes, Unity 2) connected to a Gas Chromatograph (GC) (Agilent, 6890) - Flame Ionization Detector (FID). In this study, inhalation cancer risk values were calculated for benzene by using data from USEPA's Integrated Risk Information System.

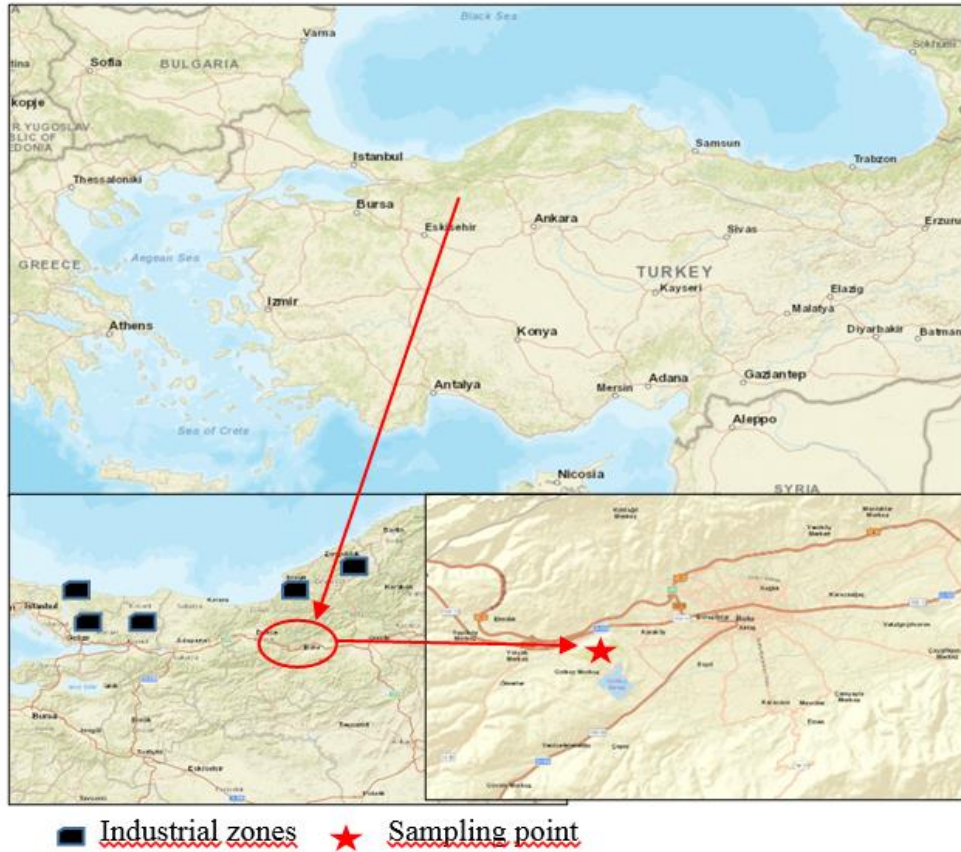**Keywords:** VOCs, health risk assesment, seasonal variations

INTRODUCTION

Volatile organic compounds (VOCs) are a widespread group of chemicals that can originate from natural and anthropogenic sources [1, 2, 4]. Natural sources include biogenic emissions from plants leaf surfaces and the metabolic activities of microorganisms while anthropogenic sources include fossil fuel combustion, traffic emissions, solvent use and industrial activities [5, 8, 9]. Some VOCs are suspected of causing cancer and some have been shown to cause cancer in humans. The health effects caused by VOCs depend on the concentration and length of exposure to the chemicals [3, 6, 7, 10].

VOCs are important precursors of secondary air pollutants such as ground level ozone (O_3), peroxyacetyl nitrate (PAN) and secondary organic aerosol (SOA) formation [6]. While the indoor air concentrations of many VOCs tend to be higher than the outdoor concentrations, due to their acute health effects, there is also ongoing interest in understanding their levels, sources and health risks in urban atmosphere. In view of the adverse health effects of VOCs on air quality and human health in Bolu atmosphere, this study have been aimed to characterize the seasonal ambient concentrations and associated human health risks of inhalation in a suburban location, in the winter and summer seasons, 2019.

MATERIALS and METHODS

Ambient VOC samples were collected from a suburban location, Bolu Abant İzzet Baysal University (BAİBÜ) Campus, in the winter and summer seasons of 2019. 40 samples each were collected between 07 January and 15 February 2019 for winter, and 01 July- 09 August 2019 for the summer sampling campaigns. Ambient VOCs were collected using stainless steel tubes (0.25 mm internal radius and 15 mm diffusion length) containing Tenax TA sorbent with 35–60 mesh particle size. Before sampling, the sampling tubes were conditioned using Markes TC-20 conditioning instrument by purging with nitrogen at 25 psi at 330 °C for 30 min. Ambient air was passed through the 90 mm long and 5 mm internal diameter tubes for a sampling of VOCs for 24 hours with a flow rate of 200 mL sec^{-1}.

Figure 1. Sampling point

After sampling, all the samplers were stored in a freezer (−18 °C) until they were analyzed. Analyses of the samples were performed by a Thermal Desorber (Markes, Unity 2) connected to a Gas Chromatograph (GC) (Agilent, 6890) - Flame Ionization Detector (FID). Analytes were thermally desorbed at 270 °C for 5 min, and then transferred to the cold trap (maintained at −10 °C), then heated rapidly to 270 °C and introduced to the GC. The GC is equipped with Deans' Switch System which allows transfer of sample in two columns having different polarities (Alumina Plot (HP-AL/S) (50 m, 0.32 mm i.d., 8 µm film thickness) and DB-1 (50 m, 0.25 mm i.d., 0,25 µm film thickness)) and connected to two FIDs.

Risk assessment studies focus on chronic exposure rather than acute exposure to chemicals that may or may not cause cancer. Inhalation cancer risk values were determined for benzene using the data from USEPA's Integrated Risk Information System. The lifetime cancer risk (LCR) and the hazard ratio (HR) were calculated to estimate the carcinogenic and non-carcinogenic influences using following Equations [11].

$$LCR = UR \times \frac{CA \times ET \times EF \times ED}{LT \times 365(days/year) \times 24(hours/day)}$$

$$HR = \frac{EC}{RfC}$$

$$EC = \frac{CA \times ET \times EF \times ED}{LT \times 365(days/year) \times 24(hours/day)}$$

where UR is the unit risk (m^3 μg^{-1}), CA is the VOC concentration, ET is the exposure time (24 h day^{-1}), EF is the exposure frequency (350 day $year^{-1}$, for a resident with 15 day $year^{-1}$ outside the study area), ED is the exposure duration (25 years; average assumed years lived in the study area), LT is life expectancy (75 years), EC is the exposure concentration (μg m^{-3}) and RfC is the inhalation reference concentration (μg m^{-3}) that is specific to each VOC compound.

RESULTS and DISCUSSION

Seasonal average concentrations of the measured VOCs were given in Table 1. In the winter period, toluene, 1-pentene, benzene, ethylbenzene, isopentane, n-pentene, n-hexane, and xylenes were the most abundant VOCs. In the summer season, the highest concentrations were measured for toluene, benzene, n-hexane, ethylbenzene and xylenes. Concentration of isoprene, an important biogenic VOC, was significantly increased in the summer period probably due to the emissions from the green plants. Total VOC concentration as the sum of the 45 measured compounds were 44.2 ± 14.3 μg m^{-3} in winter and 51.2 ± 14.3 μg m^{-3} in summer period.

Increasing rate of the vaporisation from asphalt surfaces and fugitive emissions from the automobile fuel tanks, increasing perpiration of the plant leaves are the main sources of the elevated summer concentrations of the VOCs. Hence, an elevated inhalation carcinogenic health risk of benzene was estimated in the summer period.

Hazard ratio (HR) which is an indicator of non-cancer health risks due to the exposure to the non-carcinogenic VOCs varied between 0.01 and 0.07 in winter and 0.02 to 0.1 in summer seasons. The values of the HR below 1.0 is accepted to be tolerable, so that concluded not a non-carcinogenic risk due to the VOC exposure in the study area. Cancer risk occured due to the ambient benzene inhalation was 5.1×10^{-6} in winter, and 1.1×10^{-5} in summer, and that was exceeding the suggested risk level of 1×10^{-6} by USEPA means that there was a significant risk of lung cancer due to benzene exposure and proper cautions should be taken to obtain safe levels.

Table 1. Ambient levels of VOCs measured at the sampling points for winter and summer season in $\mu g \ m^{-3}$.

VOCs	Winter season				Summer season			
	Avg	Std dev	Min	Max	Avg	Std dev	Min	Max
Isopentane	1.04	2.56	0.00	8.63	0.51	0.06	0.06	0.68
1-Pentene	3.04	4.08	1.17	15.16	2.46	0.33	0.33	3.03
n-Pentene	1.32	0.57	0.57	2.58	1.23	0.10	0.10	1.51
Isoprene	0.62	0.21	0.00	0.71	2.47	0.61	0.71	4.50
Trans-2-Pentene	1.31	0.14	0.14	1.67	0.88	0.01	0.01	0.90
Cis-2-Pentene	1.07	0.10	0.10	1.22	0.65	0.00	0.00	0.66
2,2-Dimethylbutane	0.14	0.25	0.00	0.64	0.00	0.00	0.00	0.00
Cyclohexane	0.14	0.25	0.00	0.76	0.17	0.02	0.02	0.20
Cyclopentane	1.05	0.12	0.12	1.38	0.87	0.02	0.02	0.91
2-Methylpentane	0.46	0.23	0.23	1.14	0.37	0.14	0.14	0.56
3-Methylpentane	0.64	0.17	0.17	1.01	0.54	0.07	0.07	0.64
n-Hexane	1.98	0.96	0.64	3.51	3.05	2.86	1.66	11.55
2,3-Dimethylbutane	1.19	0.41	0.00	1.52	1.72	0.08	0.08	1.85
Methylcyclopentane	0.79	0.08	0.08	0.96	0.48	0.04	0.04	0.53
2,4-Dimethylpentane	0.80	0.27	0.00	0.95	0.62	0.01	0.01	0.66
2-Methylhexane	0.26	0.35	0.00	0.81	0.52	0.01	0.01	0.54
2,3-Dimethylpentane	0.22	0.19	0.00	0.43	0.28	0.00	0.00	0.28
3-Methylhexane	0.09	0.10	0.00	0.24	0.16	0.01	0.01	0.18
Benzene	2.50	0.28	0.48	3.43	4.91	1.07	0.57	7.03
2,2,4-Trimethylpentane	0.00	0.00	0.00	0.00	0.00	0.00	0.00	0.00
n-Heptane	0.80	0.13	0.13	1.13	0.55	0.05	0.05	0.64
Methylcyclohexane	0.73	0.04	0.04	0.80	0.48	0.01	0.01	0.49
2,3,4-Trimethylpentane	1.11	0.40	0.00	1.59	0.79	0.04	0.04	0.88
Toluene	5.55	2.22	1.22	8.50	8.65	2.78	2.08	11.31
2-Methylheptane	0.79	0.05	0.05	0.93	0.51	0.01	0.01	0.54
3-Methylheptane	0.99	0.12	0.12	1.27	0.75	0.14	0.14	0.97
n-Octane	1.01	0.23	0.23	1.65	0.73	0.12	0.12	0.95
Ethylbenzene	1.45	0.53	0.33	4.49	2.35	0.71	0.81	6.38
m+p Xylene	1.70	0.55	0.15	5.55	2.29	0.62	0.92	5.46
Styrene	0.59	0.16	0.16	0.97	2.38	0.74	0.84	4.39
o-Xylene	1.90	0.56	0.29	3.32	2.29	0.62	0.82	5.35
n-Nonane	0.88	0.52	0.31	2.37	0.81	0.31	0.31	1.35
Isoprophylbenzene	0.28	0.01	0.01	0.30	0.17	0.01	0.01	0.18
n-Prophylbenzene	0.52	0.33	0.33	1.49	0.38	0.08	0.08	0.53
o-Ethyltoluene	0.57	0.17	0.17	0.99	0.42	0.04	0.04	0.48
p-Ethyltoluene	0.30	0.14	0.14	0.70	0.21	0.05	0.05	0.29
1,3,5-Trimethylbenzene	0.75	0.41	0.35	1.83	0.98	0.31	0.31	1.81
1,2,3-Trimethylbenzene	0.40	0.43	0.14	1.65	0.33	0.27	0.13	0.95
1,2,4-Trimethylbenzene	0.37	0.08	0.08	0.54	0.28	0.03	0.03	0.33
n-Decane	1.98	1.28	0.45	4.19	0.73	0.44	0.26	1.49
m-Ethyltoluene	1.93	0.72	0.72	3.61	1.34	0.53	0.53	2.17
m-Diethylbenzene	0.66	0.69	0.03	2.24	2.40	1.93	0.15	4.86
p-Diethylbenzene	0.46	0.10	0.10	0.74	0.31	0.05	0.05	0.41
n-Undecane	0.31	0.56	0.00	1.82	0.42	0.24	0.00	0.84
n-Dodecane	0.87	0.72	0.00	2.15	1.13	0.59	0.39	2.37

CONCLUSIONS

Ambient concentration levels of the VOCs in a suburban location of Bolu were monitored for 30 days periods in summer and winter, 2019. Elevated concentrations were observed in summer period due to the increased temperature. BTEX group compounds of benzene, toluene, ethylbenzene and xylenes were the most abundant compounds. Carcinogenic risks were doubled in summer period due to increasing ambient benzene

concentrations. Estimated risk levels were above the tolerable level of 1×10^{-6} suggested by the USEPA both in winter and summer seasons.

REFERENCES

[1] Y. Dumanoglu, M. Kara, H. Altiok, M. Odabasi, T. Elbir, A. Bayram, Spatial and seasonal variation and source apportionment of volatile organic compounds (VOCs) in a heavily industrialized region, Atmos. Environ. 98, 168–178 (2014).

[2] J. Zhang, Y. Sun, F.K. Wu, J. Sun, Y. Wang, The characteristics, seasonal variation and source apportionment of VOCs at Gongga Mountain, China, Atmos. Environ. 88, 297–305 (2014).

[3] S. Batterman, F.C. Su, S. Li, B. Mukherjee, C. Jia, Personal exposure to mixtures of volatile organic compounds: modeling and further analysis of the RIOPA Data, Res. Rep. Health Eff. Inst. 181, 3–63 (2014).

[4] I. Filella and J. Peñuelas, Daily, weekly and seasonal relationships among VOCs, NOx and O_3 in a semi-urban area near Barcelona, J. Atmos. Chem. 54, 189–201 (2006).

[5] G. Wang, S. Cheng, W. Wei, Y. Zhou, S. Yao, H. Zhang, Characteristics and source apportionment of VOCs in the suburban area of Beijing, China, Atmos. Pollut. Res. 7, 711-724 (2016).

[6] Y. Yang, D. Ji, J. Sun, Y. Wang, D. Yao, S. Zhao, X. Yu, L. Zeng, R. Zhang, H. Zhang, Y. Wang, Y. Wang, Ambient volatile organic compounds in a suburban site between Beijing and Tianjin: Concentration levels, source apportionment and health risk assessment, Sci. Total. Environ. 695, 133889 (2019).

[7] A. Bari, W.B. Kindzierski, Ambient volatile organic compounds (VOCs) in Calgary, Alberta: Sources and screening healht risk assessment, Sci. Total. Environ. 631-632, 627-640 (2018).

[8] X. Zhang, Z. Xue, H. Li, L. Yan, Y. Yang, Y. Wang, J. Duan, L. Li, F. Chai, M. Cheng, W. Zhang, Ambient volatile organic compounds pollution in China, J. Environ. Sci. 55, 69-75 (2017).

[9] A. Khanchi, C.A. Hebbern, J. Zhu, S. Çakmak, Exposure to volatile organic compounds and associated health risks in windsor, Canada, Atmos. Environ. 120, 152-159 (2015).

[10] E. Can, Ö. Özden Üzmez, T. Döğeroğlu, E.O. Gaga, Indoor air quality assessment in printmaking department of a fine arts faculty building, Atmos. Pollut. Res. 6, 1035-1045 (2015).

[11] EPA IRIS 2015. US Environmental Protection Agency, Integrated Risk Information System. http://www.epa.gov/iris/supdocs/0276index.html.

ORGANIC and ELEMENTAL CARBON CONCENTRATIONS on SIZE-SEGREGATED AMBIENT PARTICULATE MATTER in BOLU

A.Arı[1], P. Ertürk Arı[1]

[1]Department of Environmental Engineering, Faculty of Engineering, Bolu Abant Izzet Baysal University, Bolu, TURKEY

E-mail: pelinn.erturkk@gmail

ABSTRACT

It is well known that carbonaceous aerosol comprises a major fraction of atmospheric PM. Organic components constitute a significant percentage of atmospheric fine mode aerosol, as much as 50% or above by mass. This organic components of PM have been subjected to comprehensive research in recent years, due to their crucial impacts on many environmental aspects including the climate change, visibility reduction, source apportionment and also adverse human health effects.

Size-segregated PM samples were collected from a sub-urban location of Bolu in winter and summer periods of 2019 and OC/EC concentrations were determined. Percent OC and EC both increased by the decreasing PM size indicating that the anthropogenic emissions are the main sources of organic aerosol in ambient air together with the secondary organic aerosol formation. Contribution of the secondary organic aerosol to total PM mass was evaluated by using EC-Tracer approach. More than 50% of the fine and quasi-ultrafine mode aerosol were estimated to be secondary.

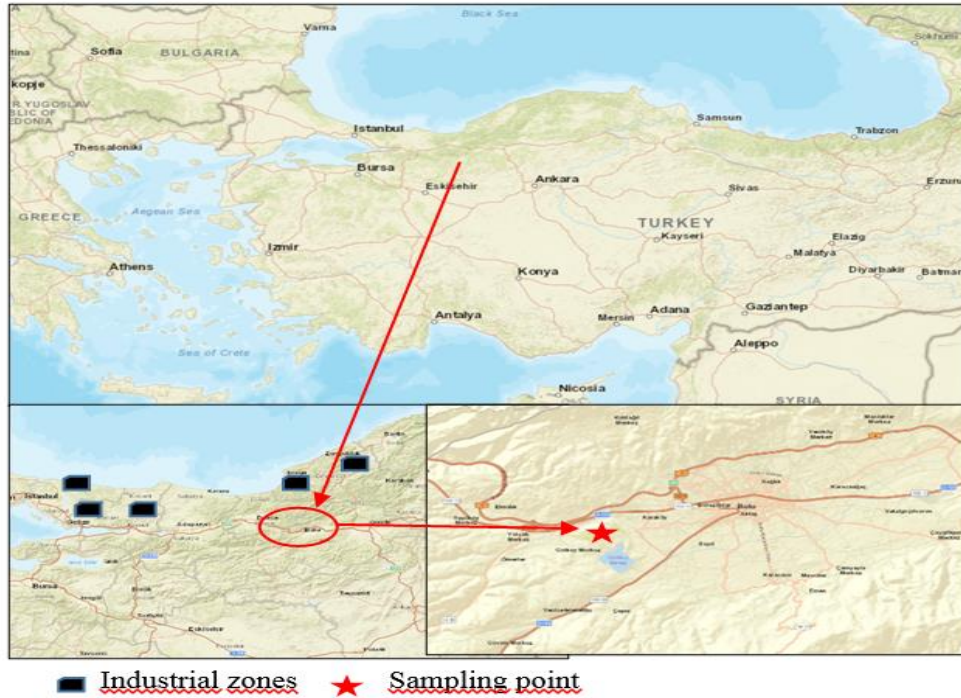**Keywords:** OC, EC, secondary organic aerosol, size-segregated PM

INTRODUCTION

Atmospheric aerosol is a complex mixture of solid and liquid particles suspended in the atmosphere. The main parameters determining the aerosol effects are particle sizes and chemical properties, which depend on source emissions and following transformations/reactions in atmosphere [1, 3, 5].

Carbon is one of the most abundant elements in atmospheric particulate matter (PM), which contains a complex mixture of organic carbon (OC) and elemental carbon (EC). Carbonaceous aerosols could have large health impacts and play a significant role in visibility and climate change through direct and indirect radiative forcing [10]. The two carbonaceous aerosol types are elemental carbon (EC), which is known to be an important contributor to radiative heating of the atmosphere, and organic carbon (OC), which is emitted along with EC, scatters radiation and has a cooling effect on the atmosphere [11].

The health effects of PM are closely related to chemical composition, size distribution and atmospheric concentrations. Identification of the size distribution and chemical composition of PM especially carbonaceous fraction is important to understand many atmospheric events such as secondary particle formation [1, 2, 4, 6]. Atmospheric carbonaceous aerosols have been sampled mostly using bulk samplers, which usually have an upper cutoff size point of 2.5 or 10 μm [10]. Information provided by these samplers is not sufficient when investigating the influence of carbonaceous aerosols on climate, visibility and human health since these influences depend strongly on the distribution of carbonaceous matter over the particle size.

MATERIALS and METHODS

Ambient size-segregated samples were collected from a suburban location, Bolu Abant İzzet Baysal University (BAİBÜ) Campus, in the winter and summer seasons of 2019. 40 samples each were collected between 07 January and 15 February 2019 for winter, and 01 July- 09 August 2019 for the summer sampling campaigns.

Figure 1. Sampling point

Size-segregated PM samples were collected using a Sioutas Cascade Impactor (SCI) in combination with a Leland Legacy Pump (SKC Inc., Pa, USA) with a 9 L min^{-1} flowrate. SCI was loaded with 25 mm quartz filters for first 4 stages and a back-up filter in 37 mm diameter (QFFs-Pall Life Sciences, USA). PM size fractions of >2.5; 2.5-1.0; 1.0-0.5; and 0.5-0.25 µm were collected on 25 mm filters; likewise, PM$_{<0.25}$ µm was gathered on 37 mm filters in the SCI. Quartz filters were burned at 600°C for 4 hours to eliminate initial carbon background, conditioned under controlled temperature and relative humidity (23°C ± 2°C and 30% ± 5%) and weighed before and after the sampling using a microbalance (Model 360 ES, Precisa Gravimetrics AG., Switzerland) to determine the mass concentration.

Following the gravimetric analysis, a rectangular part (with the area of 1 cm x 1.5 cm) of each QFF was analyzed for OC, EC and TC (OC+EC) by applying the NIOSH-5040 protocol based on Thermal Optical Transmittance (TOT) method [12] using a laboratory type OC/EC analyzer (Sunset Laboratory Inc., USA).
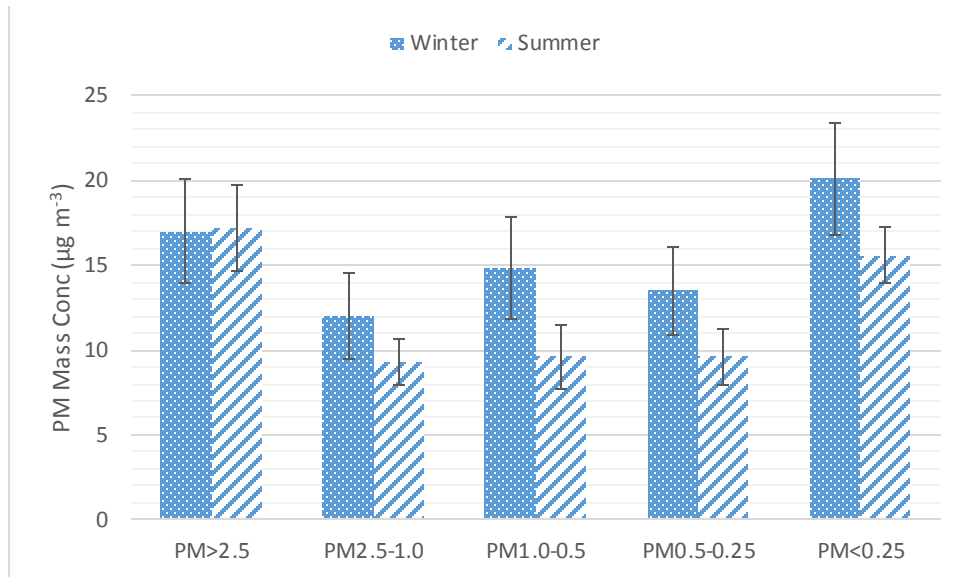
RESULTS and DISCUSSIONS

Average seasonal concentrations of the size-segregated PM and carbon species presented in Figure 2 and Table 1. Mass concentration of coarse PM (PM>2.5) is comparable in both winter and summer samples, whereas fine mode PM concentrations decreased significantly in summer period. The main reason of the

higher winter PM concentrations is suspected to be the increasing emissions from space heating related coal and biomass combustion, and also the meteorological conditions such as decreasing atmospheric mixing layer height.

Figure 2. Average seasonal size-segregated PM mass concentrations

Table 1 shows the seasonal average EC and OC concentrations, and average percent contributions of the measured species to PM mass. The concentrations of EC in PM varied from 0.7 to 3.1 µgC m^{-3}; approximately 15.2% of PM mass in winter and 4.9% in summer. The mass of total OC varied from 2.3 to 12.3 µgC m^{-3} (approximately 63% of fine PM mass in winter and 58% in summer). Total carbonaceous aerosols (TCA) accounted for ~55% of fine mode aerosols, annually. TCA was calculated as the sum of total organic matter (OM) and EC concentrations (TCA=OM+EC). The OM concentration was estimated by multiplying the OC concentration with a conversion factor of 1.6.

Table 1. Seasonal size-segregated OC and EC concentrations and secondary OC

		$PM_{>2.5}$	$PM_{2.5-1.0}$	$PM_{1.0-0.5}$	$PM_{0.5-0.25}$	$PM_{<0.25}$
Winter	OC	2.4±0.2	3.2±0.3	5.0±1.1	6.9±0.8	12.3±4.0
	EC	1.9±0.3	1.8±0.4	1.5±0.7	2.1±0.9	3.1±0.9
	OC/EC	1.3	1.8	1.5	2.1	3.1
	OCsec	1.1±0.8	1.4±0.3	1.9±1.1	2.1±1.3	2.6±1.2
Summer	OC	2.3±0.5	3.2±0.8	5.8±1.3	6.3±0.9	8.9±1.8
	EC	0.7±0.3	0.7±0.4	0.8±0.3	0.7±0.4	0.8±0.3
	OC/EC	3.3	4.6	7.3	9.0	11.1
	OCsec	1.2±0.6	1.8±0.8	3.6±1.2	4.1±1.1	6.3±1.5

Contribution of OC_{sec} to OC_{total} was calculated using EC tracer approach for the atmospheric PM samples both for summer and winter seasons. This approach uses EC as a tracer for the primary combustion sources, and fort hat, there should be a certain ratio at the combustion sources between OC and EC. This minimum ratio can be obtained by the measurements of no secondary OC is formed. The ratios exceeding the minimum ratio, the contribution to the OC is accepted as secondary [7-9].

Secondary OC was increased especially on smaller particles as a result of condensation and nucleation events on atmosphere. The contribution of secondary carbon to the total OC was significant especially in summer samples. Approximately 70% of PM<0.25μm particles, whereas the contribution of secondary in this size range was 25% in winter period.

CONCLUSIONS

By this study; OC and EC concentrations of size segregated PM samples were evaluated in a suburban location of a small city, Turkey. Higher concentrations of fine PM was measured with respect to many developed countries in the sampling point, as well as higher concentrations of OC and EC were observed. Ambient PM2.5 concentrations were exceed the EU limit values in 90% of the samples. Contribution of the secondary organic constituents to measured PM mass was estimated by an indirect (EC Tracer) approach to the evaluated data.

REFERENCES

[1] J. Zhang, L. Tong, Z. Huang, H. Zhang, M. He, X. Dai, J. Zheng, H. Xiao, Seasonal variation and size distributions of water-soluble inorganic ions and carbonaceous aerosols at a coastal site in Ningbo, China, Sci. Total. Environ. 639, 793-803 (2018).

[2] S. Tian, Y. Pan, Y. Wang, Ion balance and acidity of size-segregated particles during haze episodes in urban Beijing, Atmos. Res. 201, 159-167 (2018).

[3] G.P. Almeida, A.T. Bittencourt, M.S. Evangelista, M.S. Vieira-Filho, A. Fornaro, Characterization of aerosol chemical composition from urban pollution in Brazil and its possible impacts on the aerosol hygroscopicity and size distribution, Atmos. Environ. 202, 149-159 (2019).

[4] S. Frka, I. Grgic, J. Tursic, M.I. Gini, K. Eleftheriadis, Seasonal variability of carbon in humic-like matter of ambient size-segregated water soluble organic aerosols from urban background environment, Atmos. Environ. 173, 239-247 (2018).

[5] V. Bernardoni, M. Elser, G. Valli, S. Valentini, A. Bigi, P. Fermo, A. Piazzalunga, R. Vecchi, Size-segregated aerosol in a hot-spot pollution urban area: Chemical composition and three-way source apportionment, Environ. Pollut. 231, 601-611 (2017).

[6] X.X. Ding, L.D. Kong, C.T. Du, A. Zhanzakova, H.B. Fu, X.F. Tang, L. Wang, X. Yang, J.M. Chen, T.T. Cheng, Characteristics of size-resolved atmospheric inorganic and carbonaceous aerosols in urban Shanghai, Atmos. Environ. 167, 625-641 (2017).

[7] T. Gnauk, K. Müller, D. Van Pinxteren, L.Y. He, Y. Niu, M. Hu, H. Herrmann, Size-segregated particulate chemical composition in Xinken, Pearl River Delta, China: OC/EC and organic compounds, Atmos. Environ. 42, 6296-6309 (2008).

[8] C. Pio, M. Cerqueira, R.M. Harrison, T. Nunes, F. Mirante, C. Alves, C. Oliveira, A. Sanches de la Campa, B. Artinano, M. Matos, M., OC/EC ratio observed in Europe: re-thinking the approach for apportionment between primary and secondary organic carbon, Atmos. Environ. 45, 6121-6132 (2011).

[9] A. Saffari, S. Hasheminassab, M.M. Shafer, J.J. Schauer, T.A. Chatila, C. Sioutas, Nighttime aqueous-phase secondary organic aerosols in Los Angeles and its implication for fine particulate matter composition and oxidative potential, Atmos. Environ. 133, 112-122 (2016).

[10] S. Tian, Y. Pan, Z. Liu, T. Wen, Y. Wang, Reshaping the size distribution of aerosol elemental carbon by removal of coarse mode carbonates, Atmos. Environ, 214, 116852 (2019).

[11] L. Hong, G. Liu, L. Zhou, J. Li, H. Xu, D. Wu, Emission of organic carbon, elemental carbon and water-soluble ions from crop straw burning under flaming and smoldering conditions, Particuology, 31, 181-190 (2017).

[12] M. Birch, R. Cary, Elemental carbon-based method for monitoring occupational exposures to particulate diesel exhaust, Aerosol Sci. Tech. 25, 221–241 (1996).

EVALUATION OF TECHNOLOGY TRENDS AND PROPOSAL FOR TECHNOLOGY INVESTMENT WAY AHEAD

M.Üçüncü[1], B. Kazandır[2]

[1]Department of Electrical-Electronics Engineering Department, Faculty of Engineering , Başkent University, Ankara TURKEY
[2] The Former of the Head of Technology Management Department, Military Academy, Ankara,

E-mail: murat.ucuncu@yahoo.com.tr

It has become challenging to counteract against security threats recently. Therefore, the modernization planning in defense area and the procurement of necessary assets has become cumbersome since the way to handle these issues differs from planner to planner. The globalization, the developments in technology, never ending conflicts and problems are strongly related to the selection of the technology. The involvement of terrorist organization to the conflicts has forced the government bodies to change their approaches towards modernization. On the other hand, the convergence of civil and military technology has come close to each other. Therefore, it is a mutual benefit to use civil and military technology in a mixed way which is beneficial for the use of resources efficiently. Conflicts and wars experienced so far has demonstrated the importance of the technology for the result achieved at the end. In parallel to new technologies, it is certain that the strategy and tactics are also changing every day. Therefore, it is strictly necessary for the planners and capability developers to consider the developments very carefully in a systematic manner. This approach is not only confined to the development of military technology, but it also covers new and mixed type of threats, social changes etc. due to the developments in technology. To predict the emerging technologies and at the same time, understanding the threats are very helpful to technology developers. If defense and security planning experts fail to plan the necessary defense and security requirements and the associated supporting technology, it is a high probability that the defense against these new threats will not be enough. The main reason for USA to fall behind Russia in space program 1950's is stated to be the lack of predicting the future technology. In this study, a detailed survey of technology analysis conducted by several agencies has been reviewed and a technology way ahead is proposed for capability managers. We studied intensively several open source detailed reports on emerging technologies including NATO Science and Technology Organization and USA DARPA (Defense Advanced Research Advanced Program Agency). In our study, all these technologies has been categorized and a Technology Road Map for the next 20-years together with some considerations has been developed by utilizing well known scenarios. The aim of the study is to bring academician, industry and defense people to come together and develop technology capability for civil and defense sector. Thus, the study we believe will inform a guideline to all technology developers, and facilitate the technology investments planning. Finally, we propose 20 emerging technologies as a game changer.

1. INTRODUCTION

Throughout history, Science and Technology has been the driving force of progress and development in the world and has been seen as one of the most important factors affecting the destiny of countries. Although it is impossible to accurately predict the future, it is considered that which areas of development and progress in science and technology will be experienced and that the future clues of these developments will be examined and draw conclusions, and that it will play an important role in establishing and developing a sustainable and competitive defense technology base.

Today, innovation-based technological advances continue to become increasingly complex, especially in conjunction with Industry 4.0 and Digital Transformation leverages. In recent years, it has become very different to take measures against the global threats posed by technological developments and to develop talent and technology acquisition in every field of industry. The globalization of the world, technological developments, continuity of conflict and problem areas are very closely related to the choice of technology to be used. Convergence of industrial developments and technologies in the field of defense and security and taking advantage of each other's results have become a necessity in terms of cost efficiency and efficient use of scarce resources.

In this study, the new trends in science and technology of the strong organizations in the field of global technology evaluation and the activities of the two important institutions in the field of defense / security were analyzed by combining them in a single reference document and thus, it was aimed to reach two main objectives. One objective is to inform strategic technology leaders about future science and technology trends likely to impact business / everyday life and shape defense capabilities. The other objective is to contribute to the strategic studies related to science and technology investments that should be made in order to make technology-based superiority sustainable in the future activities of our national R & D system.

Within the scope of this study, the technology forecasts published by two leading companies in the sector (Frost & Sullivan, Deloitte) in 2018 regarding science and technology trends were analyzed by considering the country's capabilities. In addition, the defense-focused technology prediction report, which is expected to affect the next 20 years by the NATO Science and Technology Organization (STO), and the reports prepared by the Defense Advanced Research Program Agency (DARPA), which conducts research and development activities of the United States, are particularly examined.

2. MATERIAL AND METHODS

In order to synthesize the emerging technology trends, the data about 68 disruptive potentials project of the DARPA [1] with 300 technologies and identified in the above sources were evaluated together. It is possible to undergo quantitative analysis (Latent Semantic Analysis-LSA) and perform clustering once again (as done by the US Deputy Secretary of Land Forces Research and Technology). However, it is considered that this effort will not create added value in practice, and that the actual content of the science and technology trends (regardless of which group they belong to) should be examined qualitatively [2].

As it is known, there are some limitations of the studies for clustering. For example, the LSA cannot process multiple meaning words. Similarly, it has limited ability to combine synonyms and identify the deep structure based on contextual clues. Therefore, in the last step of the research, field experts' convictions are still necessary to ensure that these clusters make sense.

Therefore, in order to combine quantitative (LSA) and qualitative studies, and to reflect the emerging trends while supporting them with an objective analysis, in our study, in the light of the common values in the reports based on science and technology "mega trends" synthesized by DASA R&T; 20 Common Technology Trends identified with the potential to shape the future defense and security environment and the future work environment.

The basic approach used to predict global technology is based on a methodology including four steps. Step 1 includes to investigate around 300 technology by scanning the technology pool. The second step is to formulate priorities as IP activity, funding, market potential, megatrend impact, sectors of economic impact, technology disruptiveness. Step 3 is the evaluation phase in which Intensity of Impact, Period of Impact and Index of Disruption is utilized. The last step is the selection of Top Technologies by applying the Innovation Index Score [3].

3. RESULTS AND DISCUSSION

In order to understand the change and transformation of science and technology on a global scale, the research results of 4 important organizations which are Frost and Sullivan, Deloitte, NATO, DARPA are analyzed.

The review of the forecast study of Frost Sullivan [4], it can be stated that Science Fiction Becomes a Reality which implies that the Fiction part is getting disappeared. The Technology and Government relations becomes close as the influence of new technologies increases, the tax and similar legal sanctions of the state

elements increase. The Wide Spread of Technology to the Industry since the speed of technology changes spread across industries is increasing. The technology has become consumer driven technology since the most important common feature of new technologies is that they are customer oriented. The growth rate of the growing new technology is also increasing which is termed as "Big Tech Gets Bigger".

DELOITTE study [5] can be summarized to have three main results. The first one is the so called "Symphonic Enterprise" which is the thought of strategy and technology working together. The second one is the necessity of reengineering the technology When 2017's trend technologies are critical for IT only, trend technologies are cutting all the industries now. The third point is that of "Digitalization Reshape Everything "since Digitalization re-shapes everything using new products and technologies for innovation.

NATO's technology trends report [6] indicates mainly eight points. Every projection is supported by a Time Schedule which is a unique approach as compared the other organizations' study. The time schedule is defined as close term, medium term and long term effects. The digital transformation is considered to be inevitable and IT is believed not only in engineering departments, but everywhere. Layered Production is considered as an appropriate name to describe the technologies that build 3D objects by adding layer-upon-layer of material, whether the material is plastic, metal, concrete or one day human tissue. NATO thinks that, AI (Artificial Intelligence), is the only technology to sustain its impact in 20 years and beyond. Autonomous technology is found to be a class of technology that can respond to real world conditions without help. In addition to these Technologies Advanced Materials, Wearable Technologies and Robotic Technologies (Soldier Systems) and Electromagnetic Superiority and Supersonic Vehicles technologies are considered to be very important to shape the future of NATO.

As a national research organization of the USA, DARPA [7] is developing technology by establishing Technology Offices for persistent and sustainable technology management, Research Projects conducted by DARPA utilized all government laboratory and testing facilities. The importance of technology emphasized by DARPA is the so called "Seeds of Surprise" establishments which are the theoretical studies as Quantum physics, deep mathematic, new chemical processes, and new materials, "Counterterrorism" Technology Research, "Biology" Technology Research such as Nerve systems, epidemic disease, and synthetic biology. No effort is spend on Energy and Automotive by DARPA.

In June 2017, the US Accountability Office (GAO) issued a research report [8] to improve and better manage the US Department of Defense (DOD) technology and R & D investments. The report includes eight major and leading technology companies (Amazon, Dow Chemical, Honeywell, General Motors, IBM,

Qualcomm, Siemens, and AG Valvoline) to manage, prioritize and evaluate technology portfolios and identify the practices they use.

In order to organize the technology development activities of the technology companies in the scope of the study, a disciplined approach has been demonstrated by grouping their activities in two areas as gradual (incremental) and game changer (disruptive). Research in an Incremental Approach involves Integration of Low Risk projects outcome into short term products. Disruptive Research with High Risk potential may have major outcomes in the long run. Therefore, it is necessary to manage incremental and disruptive R & D projects and technology development activities with different planning and implementation methods. On the other hand, the definition and evaluation of technology projects as incremental and disruptive projects should be carried out separately.

Today, the development, growth, maturation of technologies with weak signals takes time [9]. Therefore, it constitutes a potentially early window of opportunity. In the final analysis, the ability to learn and act faster than our potential competitors will be our main competitive advantage in the future.

When approximately 300 technologies were analyzed in accordance with the methodology, 20 global technology recommendations were obtained. The Global Top Technologies are determined to be Collaborative Industrial Robots, Computer Integrated Manufacturing, Metal 3D Printing, Nano 3D Printing (producing miniaturized parts), Robotic Exoskeletons (bionic mechanical suits), Corrosion Mitigation, High-strength Lightweight Materials (reinforcing graphene and carbon fiber materials), Self-healing Materials, Smart Glass, Battery Energy Management (High Capacity Batteries), Distributed Energy Generation (energy storage and solar panel combination), 5G, Artificial Intelligence, Natural Language Interaction, Small Data, Holographic Display, Next Gen Data Storage, Wearables, Advanced Driver Assistance Systems (ADAS), Biosensors.

In the light of the information obtained from Frost and Sullivan, Deloitte, NATO and DARPA technology projections, considering the data of TUBITAK [10], SSB, STM Think Tech [11], Ministry of Industry, it is considered that the following 10 technologies will constitute a list of opportunities for our country. These are Intelligent Production, Artificial intelligence and Robotic, Big Data Analytics, Internet of Things, Enhanced Virtual Reality, Block Chain, Sensor Technologies, Nano and Bio Technologies, Intelligent Cities and Cyber security.

4. CONCLUSION

Throughout history, Science and Technology has been the driving force of progress and development in the world and has been seen as one of the most important factors affecting the destiny of countries. Although it is impossible to accurately predict the future, it is considered that which areas of development and progress in science and technology will be experienced and that the future clues of these developments will be examined and draw conclusions, and that it will play an important role in establishing and developing a sustainable and competitive defense technology base.

With this study, it has been tried to bring together the multi-faceted researches coming from academic, industrial and defense institutions and as a result contributing to the technological competencies and technological capabilities that will gain competitiveness both in civil and defense fields. Thus, it was aimed to provide reference information to all stakeholders in the field of science and technology, to inform strategic technology leaders, and to contribute to strategic studies related to the investments in science and technology.

It is believed that disruptive technology trends need to be taken into account in order to be ready for surprises at sectoral and country level and to have technologies that will surprise competitors if possible. It is considered that taking into account the analysis of global technology trends in the preparation of strategic plans, technology roadmaps and strategic technology programs is of utmost importance in terms of effective R & D and project investments [12].

As a result, when the technology predictions of the big organizations in the global and national sense are analyzed considering the industrial capacity of our country and the level of original technology levels, a very non-magical formula is obtained.

A three-component formula can be proposed to ensure that investment plans are aligned correctly with Technology Management principles and strategies. It is strongly believed the technology investment should include whether the technology is electrified, connected and autonomous (ECA).

REFERENCES

[1] http://www.technovelgy.com/ct/Technology-Article.asp?ArtNum=59, DARPA Project List (Defense Advanced Research Projects Agency), 2018

[2] Durgut, Metin., Göker, Aykut., Üçer, Ahmet Ş. Türkiye için Teknoloji Öngörü Çalışması Model Önerisi, 2001

[3] https://ww2.frost.com/about/best-practices-recognition/research-methodology/, Research Methodology

[4] Frost & Sullivan, The Top 50 Disruptive Technologies & Innovations Transforming Our World, 03 Apr, 2018

[5] Deloitte, Tech trends 2018 – The Symphonic Enterprice, 2017

[6] NATO Science & Technology Board, STO Tech Trends Report 2017, 8 August 2017

[7] Dormehl, Luke., 7 ambitious DARPA projects that could revolutionize the armed forces, September 27, 2018

[8] Accountability Office, DEFENSE SCIENCE AND TECHNOLOGY, Adopting Best Practices Can Improve Innovation Investments and Management, June 2017

[9] Tümer, Turgut., Teknolojide 2023'e Yolculuk, 2002

[10] Türkiye Bilimsel ve Teknik Araştırma Kurumu, Ulusal Bilim ve Teknoloji Politikaları 2003-2023 Strateji Belgesi, Kasım 2004

[11] STM ThinkTech, 2019 Teknoloji Öngörüleri, 02.2019 [8] United States Government

[12]https://www.nato.int/nato_static_fl2014/assets/pdf/pdf_2019_09/20190905_190905-STO-highlights2018.pdf , Science and Technology Organization, 2018 HIGHLIGHTS, Empowering the Alliance's Technological Edge, 2019

INVESTIGATION OF THE POSITIVE EFFECTS OF BATTERY ENERGY STORAGE SYSTEMS ON SOLAR ENERGY COMBINED INTERCONNECTED NATIONAL GRID

T. Carkit[1], M. Alci[2]

[1]*Department of Electrical and Electronics Engineering, Kırklareli University, Kırklareli, TURKEY*
[2]*Department of Electrical and Electronics Engineering,, [2]Erciyes University, Kayseri, TURKEY*

E-mail: tanercarkit@klu.edu.tr

Abstract

Energy has become an indispensable position into the development goals of today's countries. The need for energy is increasing in parallel with the development of the age and technology. To meet the energy demand; the use of alternative energy sources (AES) such as wind, solar, geothermal, hydroelectric, biomass, wave power, solar cell that support the conventional energy methods such as coal, oil, natural gas and nuclear is becoming widespread. To respond the increasing energy demand of the countries, various sources should work in the energy production and distribution systems coordinately. In such a system, energy management systems are planned in accordance with the determined policies. Following this planning, appropriate operational real time working strategies were carried out. As is known, the electrical energy production conditions of some plants may vary depending on atmospheric conditions. Energy storage systems (ESS) are used to eliminate the instability and the distrust that may occur in electricity generation facilities. Since energy constitutes the basic input of all industrial sectors, a small improvement in this direction will affect all industrial sectors with the butterfly effect and the parties will gain huge profits. Therefore, there is a need for optimization applications and functional algorithms on ESSs to increase the stability, reliability, sustainability and demand responsiveness of energy. ESSs reduce the domino effect of grid failures because they convert interconnected grid into a decentralized form. In this study, the solar energy data obtained through PVGIS (Photovoltaic Geographical Information System), GSA (Global Solar Atlas) and PVSYST programs are adapted to the operational strategic working algorithm which is created in Matlab program. The most suitable output data are obtained according to the changing situations with the support of the battery energy storage system. The established system that is aim to benefit the user, was interpreted in the presence of BESS and in the absence of BESS.

Keywords: Battery, battery energy storage system, solar energy, grid

1. INTRODUCTION

Energy demand in the world is increasing day by day. Therefore, to be able to meet the energy demand, interconnected grid distribution networks should be expanded and supported. The power generation of power plants that can operate in the interconnected grid network should be low cost, the source of energy generation should be reliable, stable and sustainable. Efficient production times of the solar power plant (SPP) should be determined in the power transmission network and the energy flow should be monitored in a controlled manner. Energy control and management systems are needed to control the EDSs and to meet the energy demand of the user continuously [1]. When efforts are made to overcome these challenges and available products emerge, the countries' energy reliability ratio will increase and the dependencies of nations to foreign nations will be reduced. However, the problems such as the establishment and operation costs of the alternative energy generation systems are higher than the energy capacities, the risk levels formed by the weather conditions which cannot be known clearly, and the choice of the suitable facility location cause many uncertainties. These uncertainties lead to inefficient use of the resources of the countries and cause inefficient spending of national wealth and create significant burdens on the economies of countries. The inefficient resources also affect the socio-economic structure of countries. Electrical energy obtained from AES changes continuously in minute, hourly, daily, weekly, monthly and yearly periods. The change in production causes instability; on the other hand, it does not exactly coincide with the demand for energy that has become a certain shape. In order to provide the amount of energy that users need, ESSs are a key [2]. ESS that is a flexible and adjustable power supply, provides new ideas for dealing with intermittent power integration [3]. Finding the right operational strategy to minimize the economic return time of an ESS is a very noteworthy area of research for many possible benefits. These strategies usually depend on future demand, production and price estimates [4]. In this study; with the programmatic simulation model developed in Matlab program, the most convenient and economic working strategy for the variable production and consumption situations of the designed system was determined and the results obtained were interpreted. Although the study data could be analyzed in minute and yearly periods, weekly data were used in this study.

2. USE OF BATTERY ENERGYS STORAGE SYSTEM (BESS) IN ELECTRICAL SYSTEMS

The balance between the interconnected grid system and the continuously changing energy demand-supply side should be created [5]. ESSs are the key system to be used to create this balance. ESSs use part of the power that they can store to meet their own needs. The fact that the ESS plant is not a clear electricity generator

or storage which is one of the significiant considerations. Therefore, diversified uses of ESSs in Figure-1 should be determined clearly [6-7].
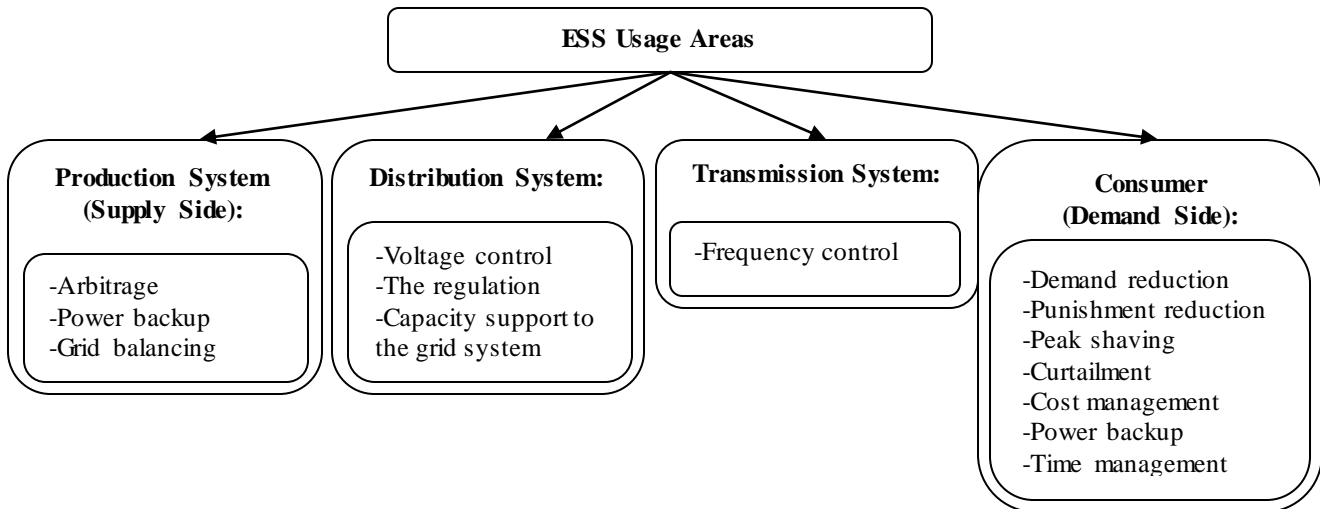

Figure-1: Usage areas of ESSs

There are many factors affecting the balance of power quality and stability in the interconnected electricity grid. Frequency and voltage are among the most critical of these factors [8]. The frequency value must be kept constant at certain intervals in order for a system to operate in a stable manner. The most considerable step in achieving this stability is the balance of power. The power balance is provided if the total production to which the losses are included is equal to the amount of consumption demanded by the user. If the amount of energy supply which is produced by the electric power generation plants which accepts a nominal frequency of 50 Hz, is more than the amount of energy demand of the consumer, the frequency value is higher than 50 Hz. If the energy demand is more than the energy supply, the nominal frequency drops to less than 50 Hz. When the downward or upward deviation from the nominal value appears in interconnected grid frequency, electricity production and consumption should be changed to solve this problem [9]. A BESS which can perform both functions, can serve as frequency holding units in the national electricity grid for the solution of network problems. The sudden voltage changes occurring in the grids can damage the electrical appliances used in the consumer side. It is noteworhy to check the voltage at the desired nominal range to prevent this damage. Generators, uninterruptible power supplies (UPS), power electronic equipment, transformers, compensation systems and BESSs can be used as voltage support control components in the reduction of the voltage drop effect. A clean voltage can be obtained at the output by eliminating changes in the defined voltage fluctuation tolerance range, thanks to DC/DC and AC/DC/AC converters in BESSs. A secure system forms the basis of a secure capacity in grids.

3. THE FORMING REAL TIME OPERATION ALGORITHM AND POSSIBLE STRATEGIC OPERATIONAL BEHAVIORS

Sustainability is one of the major features affecting the innovative value of world technologies. To ensure sustainability, the energy considered as the first input should be planned in an optimal way and then it should be able to be used at an adequate level. When the developments in the literature are examined; there are two substantial parameters of research and development studies; cycle life and investment cost [10-11]. In the area of investment cost, improvement works on the electricity market are frequently encountered for the balancing of electricity prices in time of different energy demand and for economic benefit [3]. In literature, it is also possible to encounter game theory load balancing models established to reduce the cost of electricity production and usage [12-13]. The implementation of load balancing procedures by using simulation models for many housing users is among the study topics in the literature [14-15]. Among the applications, improvement studies are carried out to determine the capacity and characteristics of the most suitable BESS for an existing electrical energy production facility [16]. The temporal changes in the production and consumption profile of electrical energy indicate the necessity of ESSs. As shown in Figure 2, the curve shown by the black line on the left shows the load [17]. As can be seen from the graph in the figure; energy demand, which has started to increase in the morning, reaches peak values in the evening hours. To meet the maximum demand, energy production plants increase the existing production capacity. On average, energy demand declines gradually after 20:00 pm. Decrease in supply, which does not overlap with demand, wasted in the form of an energy that cannot be used and can be classified as financial loss. This wasted amount of energy causes the production system not to be used efficiently [18-19]. When the production facilities provide energy output above the demand value during the low demand times, the excess energy produced can be stored by using BESS units. ESSs ensure the conservation of the stored electricity by putting them into use when there is insufficient electricity generation [20]. During the coordination of SPP and BESSs in the national interconnected grid, the realism parameter plays a role in the industrial applications. It is aimed to provide energy production-consumption balance in grids and to meet the demand of user electrical load [21]. In the system given in Figure-3, BESS plays a demand balancing role. BESS acts in such a way as to avoid overloading the national electricity grid network and to eliminate the lack of energy supply if the customer energy demand is not met by the SPP. This behavior of BESS supports supply stability and increases system reliability. Due to the fact that the electricity generation facilities are different from each other, system efficiency and availability in grid changes. Therefore, studies should be based on real-time algorithms and operational operational strategies. In this study; to meet the energy demand of an apartment with a daily

average energy demand of 65 kWh, solar energy generation data obtained from PVGIS program of 38.53 °N and 35.22 °E coordinates are accepted as P_{RPV} [22]. For SPP with a installed power of 22.5 kWh and planned as stationary land facility at the coordinates of 38.53 °N and 35.22 °E, the data prepared in the PVGIS and PVSYST computer programs were considered as the weekly average production value. The data obtained as a result of the program were controlled by the Global Solar Atlas program and all of the consistent data were accepted. Estimation data were obtained through the Matlab program by combining actual installed data and theoretical installed power. The variables given in the study are described in Table-1. The data of 48 weeks of P_D, P_{RPV}, P_{GPV}, S_{net} values in Figure-4 were accepted as input data.
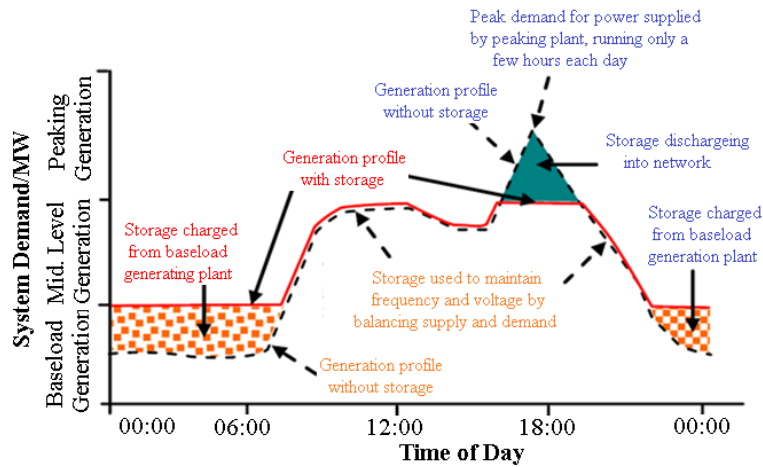

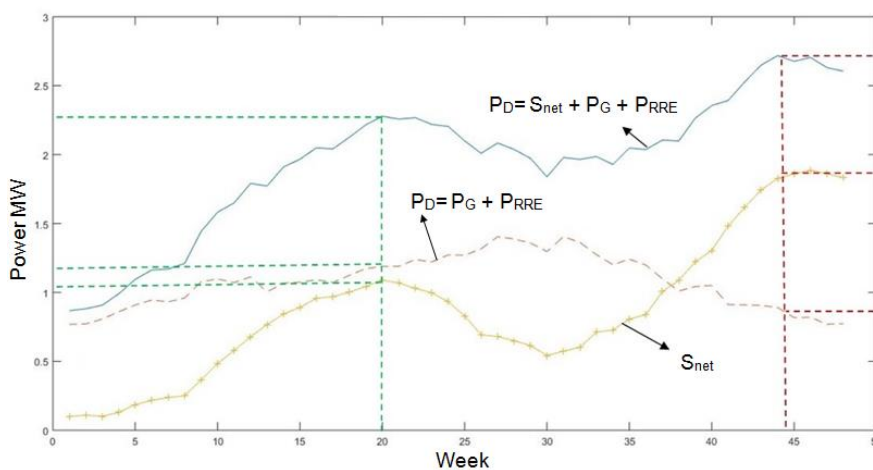Figure-2: The variation of typical electrical demand according to the time of day

Figure-3: Role of BESS on meeting customer energy demand

Table-1: Abbreviations used in real-time operational working strategy and algorithm for real conditions

Symbol/Abbreviation	Description
P_{PV}	Solar power generation
P_{BESS}	Output power of battery energy storage system (Positive for discharge, negative for charge)
$P_{PV+BESS}$	Output power of the inverter
P_{CL}	Customer load, energy demand
P_{IG}	Interconnected grid power
P_G	Power from grid
P_{RPV}	The real power of the solar power plant
P_D	The amount of power requested by the customer
P_{GPV}	Estimated average power of solar power plant
S_{net}	Clear power stored in the battery energy storage system
n_{de}	Discharge efficiency of battery energy storage system
n_{ce}	Charging efficiency of battery energy storage system

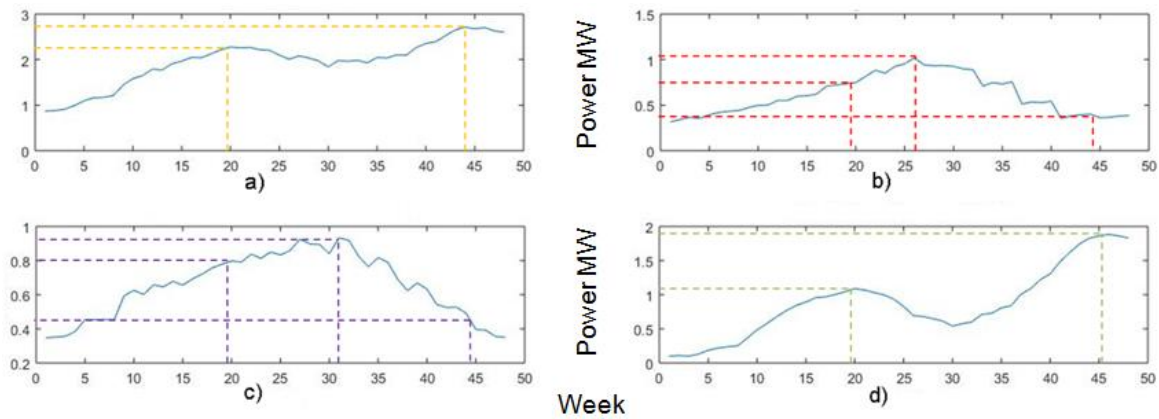

Figure-4: a) P_D, b) P_{GPV}, c) P_{RPV}, d) S_{net} input data for operational working algorithm

Charging time, discharging time and algorithm operation block diagram of BESS which is continuously in coordination with the generated algorithm is given in Figure-5. BESS is discharged when the energy supply in the SPP supported grid fails to meet the Demand. Where the energy supply is greater than the amount of energy demanded by the user, the excess energy generated by the SPP that is used to charge BESS for reuse. If there is no BESS and a useful functioning algorithm, the national electricity grid will be used predominantly to meet the user demand given in the graph in Figure-5. After that, unpredictable grid harmonics will emerge and the economic load on the user will increase. Although the grid usage seems to be high with the algorithm created, BESS + SPP + Grid usage works in a coordinated system in cases where demand increases. These data are adapted to the working block diagram of the BESS supported solar power generation system in the interconnected grid given in Figure 6. In the system shown in Figure-6, power obtained from photovoltaic (PV) panels is transferred to DC busbar by converting to DC/DC converters.
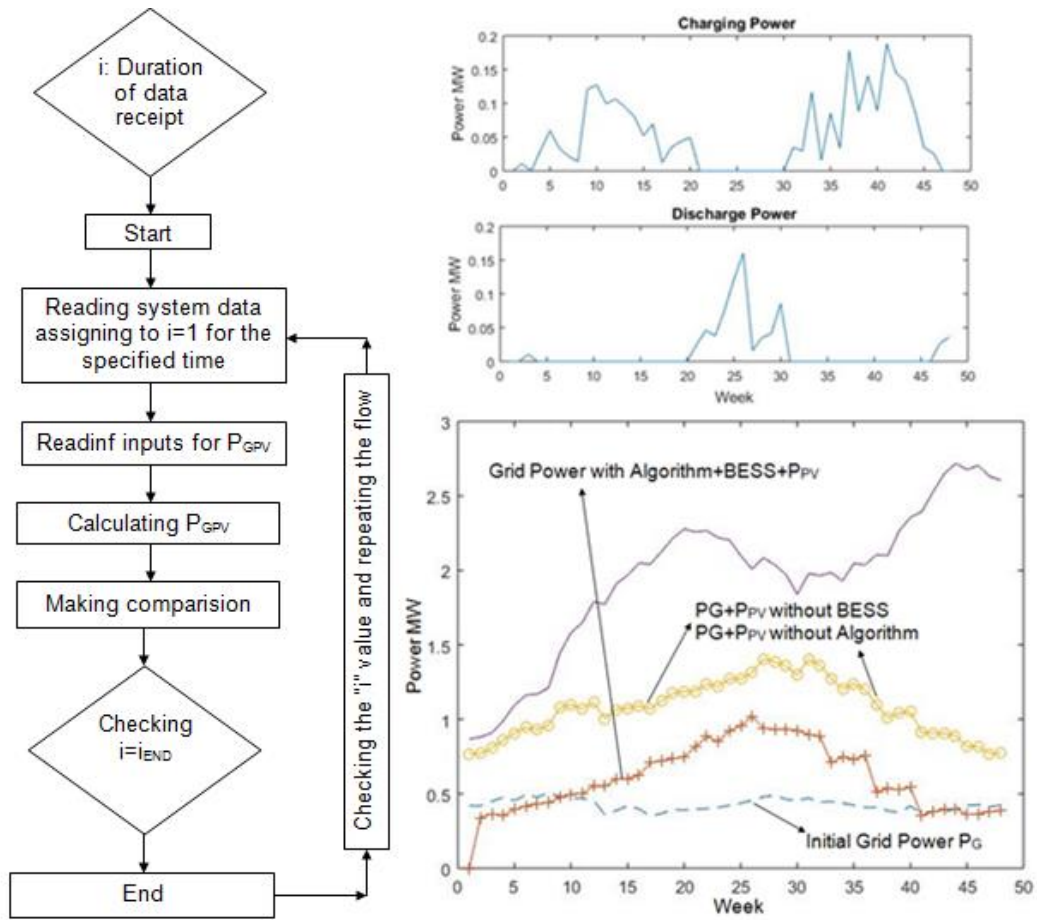
Figure-5: Output data for operational algorithm and flowchart of algorithm, the effect of algorithm and BESS on grid usage
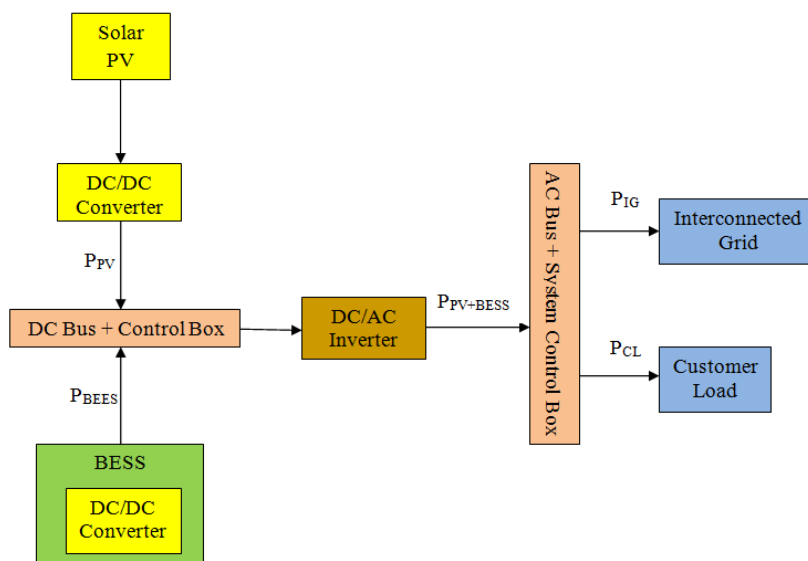

Figure-6: Block diagram of the real time operation of the SPP that is supported SPP in the interconnected grid system

The mechanism, which decides to store the generated photovoltaic energy or to transfer it to the interconnected grid, is the control system which is integrated into the DC bus. The output power of the BESS integrated photovoltaic power plant is converted to the appropriate format in the inverters and then this power is transferred to the AC busbar system. The output power from the AC busbar system is transmitted to the interconnected national grid or to private users. The formula in Eq.1 is used to obtain the net power whic is stored in the system. The overall power flow of the grid system is explained by the formula in Eq.2. The generated algorithm is used in the interconnected grid system where the BESS supported solar power generation system is in. BESSs are an alternative solution for energy surpluses in energy generation power plants to avoid problems in the national grid system. The process control and flow chart of this algorithm are shown in Figure-5. According to the result of running the Matlab program, output values according to different strategies were given in Figure-5 and the results are interpreted and explained. Once the most appropriate solution is obtained at the output according to the changing situation, the algorithm returns to the beginning. The hourly, weekly, monthly, seasonal and annual status of the data determines the repetition period of the algorithm. As a result of the strategic work algorithm and simulation, the amount of supply from the solar energy production system is compared with the demand of the user. Excess energy is stored by charging the BESS while the missing energy is met efficiently and effectively by discharging the BESS.

$$S_{net}(t) = \begin{cases} S_{net}(t-1) + [P_{RPV}(t)-P_{GPV}(t)]* n_{ce} & P_{GPV}(t)<P_{RPV}(t) \\ S_{net}(t-1) + [P_{RPV}(t)-P_{GPV}(t)]/n_{de} & P_{GPV}(t)>P_{RPV}(t) \end{cases} \tag{1}$$

$$P_{RPV}(t) + S_{net}(t) + P_G(t) = P_D(t) \tag{2}$$

When the output status in the graph which is shown in Figure-5 are analyzed, the normal deviation of the system shows that the status of the charge and discharge zones supports the data that is obtained. Grid usage in the designed system has been used as the last choice for cost reduction and economic gain. SPP and BESS took over duty of the grid. Frequency control is provided by power balance with this working strategy applied in interconnected systems. The usual deviation of the system has been kept at zero levels with the operational strategic working algorithm. As a result of the balance of power, improvement in system stability is considered. Supporting the national grid for supply and demand differences that are changing daily, is among the tasks of BESS. If there is no support, regulation costs and regulation works will increase in order to balance harmonics in the grid system. The harmonics in the grid will reduce the confidence to both BESS and the interconnected national grid.

4. CONCLUSION

Working strategies and algorithms can be analyzed in minute, hourly, daily, weekly, monthly and annual terms. The increase of the sample data constitutes a more accurate system due to the narrowing of the time interval. A battery energy storage system (BESS) which is designed according to the changing energy production profile of the solar energy production plant (SPP) is designed with the help of the algorithm that is created as a result of this study. As a result of the designed algorithm, energy consumption has been prevented and a strategic planning that can adapt to the changing situations, has been formed. In the strategic work created, energy stability is achieved by increasing the stability of the system by providing power balance and economic benefit is provided. The method and working algorithm of the working strategy to be designed should be in a direction to prevent voltage and frequency fluctuations, should exhibit behaviors in a way to reduce expenditures and provide economic advantage. Among the issues to be considered in design are; the surplus of the supply power provided by the energy production facility can be stored in storage systems and transferring of the stored energy to the grid in case of an increase in energy demand that the production facility cannot meet, is located. In the case of economically high costs, periodic leasing of energy storage systems takes place in alternative solutions. Periodically leased units pay off the rent and allow the production facility to gain profit in a short time. The operational strategies and simulation data which is obtained in this study, show that; if an intelligent grid is desired, an energy storage system must be used to tolerate the entry of unforeseen loads to the national grid. After this study; developing new approaches for increasing the efficiency of battery energy storage systems, solving the problems that is encountered in increasing the charging and discharging efficiency of BESS, designing the parameters used in battery management systems, among researches and studies planned are included.

REFERENCES

[1] Anayouchukwu, A., V., "Optimal Energy Management System for PV/Wind/Diesel-Battery Power Systems for Rural Health Clinic", Global Journal of Researches in Engineering: General Engineering, Vol. 14, Issue.1, pp: 26-34, 2014

[2] Çarkıt, T., Alçı, M., "Batarya Hücrelerindeki Elektrokimyasal Gürültülerin İncelenmesi", Kırklareli Universty Journal of Engineering and Science, Vol. 4, No. 2 , pp: 163-175, 2018

[3] Akhavan, H., Mohsenian, H., "Optimal Operation of Independent Storage Systems in Energy and Reserve Markets with High Wind Penetration", IEEE Transaction on Smart Grid, Vol. 5, pp: 1088-1097, 2014

[4] Abdulla, K., Hoog, J., D., Muenzel, V., Suits, F., Steer, K., Wirth, A., Halgamuge, S., "Optimal Operation of Energy Storage Systems Considering Forecasts and Battery Degration", IEEE Transaction on Smart Grid, Vol. 9, Issue. 3, pp: 2086-2096, 2017

[5] Holtinnen, H., Hirvonen, R., "Power System Requirements for Wind Power", Chapter 8 in Wind Power in Power Systems, pp: 144-167, 2005

[6] Sparacio, A. R., Reed, F., G., Kerestes, J., R., Grainger, M., B., Smith, T., Z., "Survey of Battery Energy Storage Systems and Modeling Techniques", IEEE Power ang Energy Society General Meeting, 2012

[7] Electric Power Research Institute (EPRI), "Electricity Energy Storage Technology Options A White Paper Primer on Applications, Costs and Benefits", 2010

[8] Werven, L., W., M., Beurskens, J., T., G., Pierik, "Integrating Wind Power in EU Electricity Systems, Economic and Technical Issues, One part of the Green Net Project Report", Energy Research Centre of The Netherlands (ECN), 2005

[9] Gardner, P., Snodin, H., Higgins, A., McGoldrick, S., "The Impacts of Increased Level of Wind Penetration on the Electricity Systems of the Republic of Ireland and Northern Ireland, Final Report", 2005

[10] Dunn, B., Kamath, H., Tarascon, J., M., "Electrical Energy Storage for the Grid: A Battery of Choices". Science, Vol. 334, Issue. 6058, pp: 928–934, 2011

[11] Muenzel, V., Hoog, J., D., Brazil, M., Vishwanath, A., Kalyanaraman, S., "A Multi-Factor Battery Cycle Life Prediction Methodology for Optimal Battery Management", 16th International Conference on Future Energy Systems, pp: 57-66, 2015

[12] Raj, B., N., Prakasa Rao, P., K., S., "A New Fuzzy Reasoning Approach for Load Balancing in Distribution System", IEEE Transactions on Power Systems, Vol. 10, No. 3, pp: 1426-1432, 1995

[13] Siti, M., W., Jimoh, A., A., Nicolae, D., V., "Phase Load Balancing in the Secondary Distribution Network Using Fuzzy Logic", AFRICON 2007, p: 1-7, 2007

[14] Duerr, S., Ababei, C., Ionel, D., M., "Load Balancing with Energy Storage Systems Based on Cosimulation of Multiple Smart Buildings and Distribution Networks", IEEE 6th International Conference on Renewable Energy Research and Applications (ICRERA), pp. 175-180, 2017

[15] Rajasekharan, J., Koivunen, V., "Cooperative Game-Theoretic Approach to Load Balancing in Smart Grids with Community Energy Storage", 23rd European Signal Processing Conference (EUSIPCO), pp: 1955-1959, 2015

[16] Jiang, X., Hao, G., Liu, H., Guo, Z., Zeng, Q., Jin, Y., "Optimization of Battery Energy Storage System Capacity for Wind Farm with Considering Auxiliary Services Compensation", Applied Sciences, Vol. 8, pp: 1-17, 2018

[17] Whittingham, S., "History, Evolution and Future Status of Energy Storage", IEEE, Vol. 100, pp: 1518-1534, 2012

[18] Turan, D., Yönetken, A., "Enerji Depolama Sistemlerinin Araştırılması ve Analizi", AKU Journal Of Science And Engineering, Special Issue, pp:113-121, 2016

[19] Koç, İ., M., Erhan, K., Aktaş, A., Özdemir, E., Özdemir, Ş., "Akıllı Şebeke Standartlarında Enerji Depolama Uygulamalarının İncelenmesi", VI. Enerji Verimliliği Kalitesi Sempozyumu (EVK), 2015

[20] Zhang, L., Gari, N., Hmurcik, L., W., "Energy Management in a Microgrid with Distributed Energy Resources", Energy Conversion and Management, Vol. 78, pp: 297-305, 2014

[21] Baran, B., Mamiş, S., M., Alagöz, B., B., "Management Simulation of Multi-Source Renewable Energy Microgrids", 2016 National Conference on Electrical, Electronics and Biomedical Engineering (ELECO), 2016

[22] The European Commission's Science And Knowledge Service, 2018
(https://ec.europa.eu/jrc/en/knowledge)

DEVIATIONS FROM THERMIONIC EMISSION IN CURRENT-VOLTAGE (*I-V*) CHARACTERISTICS OF SCHOTTKY STRUCTURES

İlbilge Dökme[1], Perihan Durmuş[2]

[1]Science Education Department, School of Gazi Education, Gazi University, TURKEY
[2]Physics Department, Science Faculty, Gazi University, TURKEY

E-mail: ilbilgedokme@gmail.com

Abstract

The temperature dependence of current-voltage characteristics permits us to know various aspects of current transport mechanisms of Schottky structures. Over the years, many studies have shown that the forward bias current-voltage characteristics of Schottky Structures deviate from the ideal Thermionic Emission Theory. It was often observed that the ideality factor *n* was found to increase, while the zero-bias barrier height of Schottky structures Φ_{Bo} decreases with decreasing temperature. Especially at low temperatures the changes are more remarkable. At low temperatures the standard Thermionic Emission Theory can fail to for explaining experimental results. In this study, the experimental forward bias current-voltage characteristics of Al/SiO$_2$/p-Si Schottky diodes with an insulator layer are reported low temperature ranges. The barrier height, ideality factor and series resistance were extracted from forward bias current-voltage measurements. The zero-bias barrier height decreases practically linearly with decreasing temperature to relatively low values. The series resistance R_s estimated from Cheung's method was strongly temperature dependent and abnormally decreased with decreasing temperature. This behavior as could be expected for semiconductors in the temperature region where there is no carrier freezing out which is non-negligible at low temperatures.

Keywords: Thermionic Emission Theory, Schottky Structures, current-voltage characteristics

1. INTRODUCTION

There are currently a vast number of reports on both experimentally and theoretically studies of Schottky structures because of the nature of barrier heights between metal and semiconductor. [1-7]. The current-voltage analysis of the Schottky structures only at room temperature does not give detailed information about their current transport mechanisms or the nature of barrier formation at interface . However, the temperature dependence of current-voltage characteristics permits us to know various aspects of current transport mechanisms of Schottky structures[4]. Over the years, many studies have shown that the forward bias current-voltage characteristics of Schottky Structures deviate from the ideal Thermionic Emission Theory. [3-6]. It was often observed that the ideality factor n was found to increase, while the zero-bias barrier height of Schottky structures Φ_{Bo} decreases with decreasing temperature[4]. Especially at low temperatures the changes are more remarkable. At low temperatures the standard Thermionic Emission Theory can fail to for explaining experimental results. At low temperatures, the lower barrier patches carry a larger fraction of the current because of the lower temperature dependence of the current through these patches[4].

The decrease in the barrier heght at low temperatures leads to non-linearity in the conventional Richardson plot[4]. Lately, the nature of origin of the decrease in the barrier height and increase in ideality factor with a decrease in temperature in some studies [2-5] have been successfully explained on the basis of a Thermionic Emission mechanism with Gaussian distribution of the Schottky barrier height [4]. The other parameter that exhibited in some cases abnormally behaviour is the R_s. Chand and Kumar studied its temperature dependence in Pd_2 Sip-Si (111) Schottky diodes [4,8]. They attributed the sharp increase of the series resistance below 110 K to the lack of free charge carries in semiconductor at low temperatures.

In this study, the experimental forward bias current-voltage characteristics of $Al/SiO_2/p$-Si Schottky diodes with an insulator layer are reported low temperature ranges. The barrier height, ideality factor and series resistance were extracted from forward bias current-voltage measurements. The zero-bias barrier height decreases practically linearly with decreasing temperature to relatively low values. The series resistance R_s estimated from Cheung's method was strongly temperature dependent and abnormally decreased with decreasing temperature. This behavior as could be expected for semiconductors in the temperature region where there is no carrier freezing out which is non-negligible at low temperatures[4].

2. MATERIAL AND METHODS

The Al/SiO$_2$/p-Si (MIS) structure was fabricated on a quarter of 2 diameter float zone <100> p-type (boron doped) single crystal silicon (Si) wafer having thickness of 350 μm with 0.8 Ω-cm resistivity. For the fabrication process the Si wafer was degreased in organic solutions of CHClCCl$_2$, CH$_3$COCH$_3$ and CH$_3$OH, then etched in a sequence of H$_2$SO$_4$ an H$_2$O$_2$ 20% HF, a solution of 6HNO$_3$: 1HF :35H$_2$O, 20% HF and finally quenched in de-ionized water for a prolonged time. Preceding each step, the wafer was rinsed thoroughly in de-ionized water of resistivity of 18 MΩ-cm. The high purity aluminum (Al) with a thickness of ≈ 2000 Å was thermally evaporated from tungsten filament onto the whole back side on the p-Si wafer at a pressure of ≈1 x 10^{-6} Torr in liquid nitrogen trapped oil-free ultra high vacuum pump system. The ohmic contact was formed by sintering the evaporated Al back contact at 700 ºC for 45 min. in a flowing dry oxygen ambient at rate of 1 lt/min. This process served both to sinter the Al and to form the required thin interfacial oxide layer (SiO$_2$) on the upper surface of the p-Si wafer. After oxidation, circular dots of 1 mm diameter and 2000 Å thick Al contacts were deposited onto the oxidized surface of the wafer through a metal shadow mask in liquid nitrogen trapped vacuum system in a vacuum of ≈1 x 10^{-6} Torr. This material is the same as the material of Reference [4]. But the different dot in the same wafer measured for this study.

The interfacial layer thickness was estimated to be about 36 Å from high frequency (1MHz) measurement of the oxide capacitance in the strong accumulation. Current-voltage measurements were performed by the use of a Keithley 220 current source, a Keithley 614 electrometer. The sample temperature was always monitored by using a copper-constantant thermocouple and a Lakeshore 321 auto-tuning temperature controller with sensitivity better than ± 0.1 K. All measurements were carried out with the help of a microcomputer through an IEEE-488 ac/dc converter card.

3. RESULTS AND DISCUSSION

Figure 1 shows the forward bias semi-logarithmic current-voltage measurements as a function temperature performed in this study for Al/SiO$_2$/p-Si structure.

As shown in Fig. 1, the forward bias current-voltage characteristics are linear on a semi-logarithmic scale at low forward bias voltages but deviate considerably from linearity due to the effect of the interfacial insulator layer, and the interface states when the applied voltage is sufficiently large [4]. An interesting feature of the forward bias semi-logarithmic current curves is the almost common intersection point of all the curves at certain bias voltage and for this voltage point the current through the diode is temperature independent. Chand reported that this crossing of forward

bias Ln*I-V* curves for a homogeneous Schotkky diode can only be realized in curves with zero series resistance [4, 8]. However, for ours sample, the interface states are shown to plays a crucial role in effecting forward bias current curves of barrier height and show the intersection behavior of the forward bias current curves[4]. This behavior of the crossing of *I-V* curves appears as an abnormality when seen with respect to the conventional behavior of Schottky structures[4]
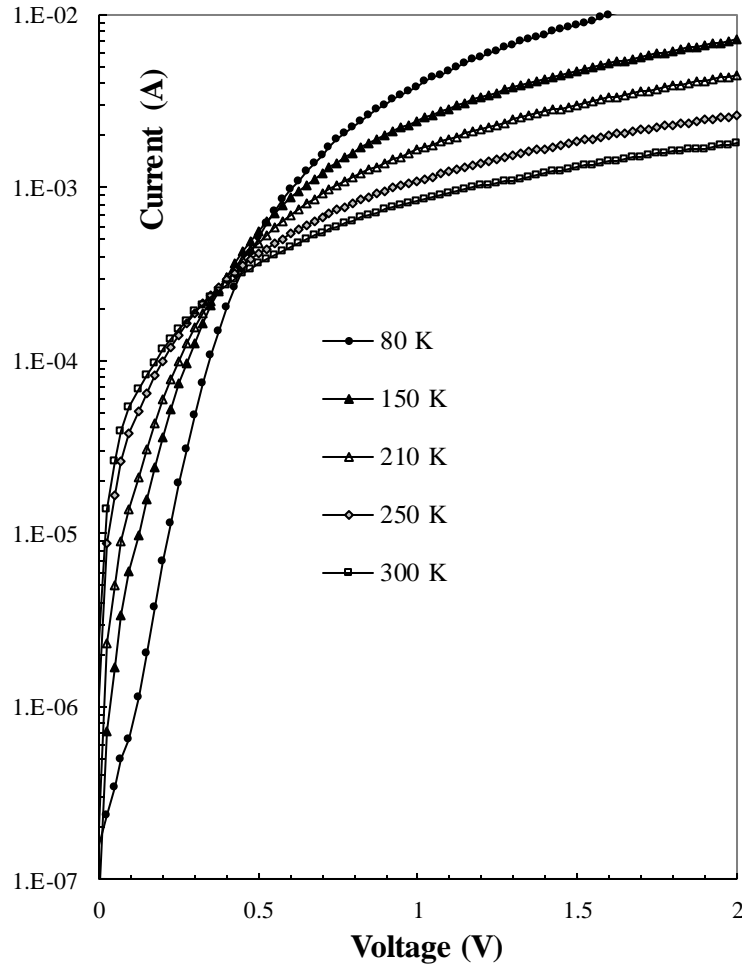
According to TE theory the forward bias current-voltage relationship for Schottky structures is given as follows [1-10]:

$$I = I_o \left[\exp(-\frac{qV_D}{kT}) - 1 \right] \tag{1}$$

where V_D *is* the voltage across onto the Schottky structure and described as $V_D = V\text{-}IR_s$, where *V* is the definite forward bias voltage, IR_s term is the voltage drop across series resistance of the device, *n* is the ideality factor, *k* is the Boltzmann constant and *T* is temperature in Kelvin. I_o is the reverse saturation current and expressed as

$$I_o = A^* A \, T^2 \exp(-q\Phi_{Bo} / kT) \tag{2}$$

where the quantities A^*, A, Φ_{Bo} are the effective Richardson constant and equals to 32 A/cm^{2}K^2 for p-type Si, the diode area and, the zero-bias barrier height, respectively.

Figure 1. The forward current-voltage characteristics of the Al/SiO$_2$/p-Si Schottky structure.

The saturation current I_o was obtained by extrapolating the linear portion of the Ln I-V curve to the intercept point with current axis at zero bias at each temperature and the zero bias barrier height Φ_{Bo} values were calculated from Eq. (2). The ideality factor was calculated from the slope of linear region of ln I-V plots at forward bias. The change in n and Φ_{Bo} with temperature is seen in Table 1. As shown in Table 1, the Φ_{Bo} and n determined from semi-log forward current-voltage plots were found to be a strong function of temperature. The values of ideality factor n were found increase, while the values of Φ_{Bo} decrease with decreasing temperature. As explained in [1-10], since current transport across the metal-semiconductor interface is a temperature- activated process; electrons at a low temperatures are able to surmount the lower barrier and therefore the current transport will be dominated by current flowing through the patches of lower Schottky barrier height and a larger ideality factor[4].

108

Table 1. Temperature dependent values of ideality factor and barrier height determined from forward bias current-voltage measurements of the studied Al/SiO₂/ p-Si Schottky structures.

T (K)	n (I-V)	Φ_{Bo} (I-V) (eV)
80	5.40	0.195
150	4.53	0.375
210	4.36	0.462
250	4.10	0.616
300	3.72	0.726

The density distribution curves of the interface state N_{ss} in equilibrium with the semiconductor can be determined from the forward bias current-voltage characteristics at each temperature [4]. The effective barrier height Φ_e is assumed to be bias-dependent due to the presence of an interfacial insulator layer and interface states located between interfacial layer and semiconductor interface, and is given by [4,5]

$$\Phi_e = \Phi_{BO} + \left(1 - \frac{1}{n(V)}\right)V \tag{7}$$

For Schottky structure having interface states N_{ss} in equilibrium with semiconductor, the ideality factor n becomes greater than unity and is given by
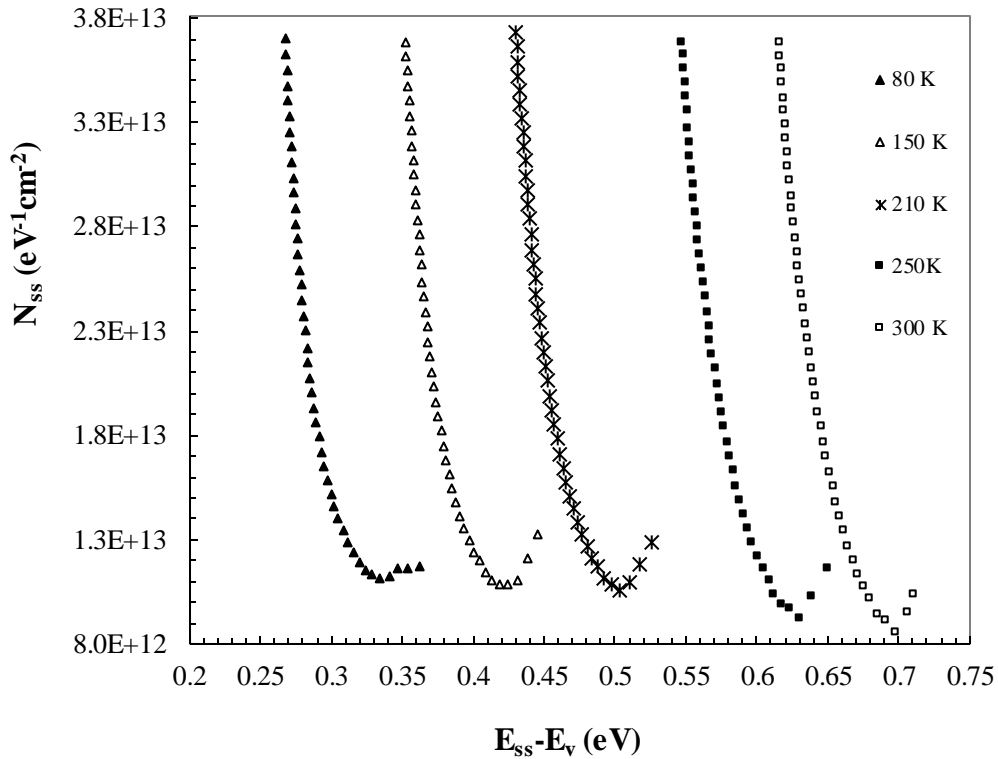
$$n(V) = 1 + \frac{\delta}{\varepsilon_i}\left[\frac{\varepsilon_s}{W_D} + qN_{ss}(V)\right] \tag{8a} \qquad \text{This expression}$$

is identical to Eq.(18) of Card and Rhoderick [5] and the expression for the interface state density as deduced by Card and Rhoderick [5] is reduced to

$$N_{ss}(V) = \frac{1}{q}\left[\frac{\varepsilon_i}{\delta}(n(V)-1) - \frac{\varepsilon_s}{W_D}\right] \tag{8b}$$

where δ is the thickness of interfacial insulator layer, W_D is the width of the space charge region, ε_i and ε_s are the permittivity of the interfacial insulator layer and the semiconductor, respectively. Furthermore, in p-type semiconductors, the energy of interface states N_{ss} with respect to the top of valance band E_v at the surface of the semiconductor is given [4] by

$$E_{ss} - E_v = q(\Phi_e - V) \tag{9}$$

Figure 2. Density of interface states N_{ss} as a function of E_{ss}-E_v from the current-voltage measurements at various temperature for the studied Al/SiO$_2$/ p-Si Schottky diode.

For each temperature, δ=54 Å, calculated from high-frequency (500 kHz) C-V characteristics using the equation $C_{ox}=\varepsilon_i\varepsilon_o A/\delta$, where C_{ox} is the capacitance of the interfacial layer, ε_i=7.2ε_o, ε_s=11.8ε_o [5] and ε_o are the permittivities of the interfacial layer, semiconductor and free space, respectively, the values of interface states N_{ss} were obtained as a function of (E_{ss}-E_v) and are given in Figure 2.

From Fig.2 for all temperature it is seen an exponential increase in the interface state density from midgap towards the top of valance band[4]. We have observed then that the values of N_{ss} increases with decreasing temperature[4].

4. CONCLUSION

The forward bias current-voltage characteristics of Al/SiO$_2$/p-Si Schottky structure were measured in the temperature range of 80-300 K. It has been founded that the experimental forward bias current-voltage results reveal an increase of the Φ_{Bo} and a decrease of the ideality factor with decreasing temperature; the changes are quite significant at low temperatures. The N_{ss} values as a function of E_{ss}-E_v decreased with

increasing temperature. It was seen to appear a minimum and shifting towards the valance band in the N_{ss} plots. The improvement obtained by the temperature effect is probably due to thermal restructuring and reordering of the Si/SiO$_2$ interface.

REFERENCES

[1] Rhoderick, E.H. and Williams R.H., "Metal-Semiconductor Contacts 2nd ed.", *Oxford University Press*, Oxford, 257 (1988).

[2] Cowley, A.M., Sze, S.M., "Surface State and Barrier Height of Metal Semiconductor Systems", *J. Appl. Phys.*, 36: 3212-3216 (1965).

[3] Fonash, S.J., "The role of the interfacial layer in Metal-Semiconductor Solar Cells", *J. Appl. Phys.*, 46: 1286-1289 (1975).

[4] Dökme, İ., Altındal, , Ş., "The distribution of the barrier height in Al–TiW–Pd2Si/n-Si Schottky diodes from *I–V–T* measurements", **Semiconductor Science and Technology**, 21, 035003(2006).

[5] Card, H.C., Rhoderick, E.H., "Studies of tunnel MOS diyotes I. Interface effects in silicon Schottky diodes", J. Phys. D: Appl. Phys., 4:1589-1601 (1971).

[6] Sze, S.M., "Physics of Semiconductor Devices 2nd ed.", *John Wiley & Sons*, New York, 245-390 (1981).

[7] Sing, A., Reinhard, K.C., Anderson, W.A., "Temperature dependence of the electrical characteristics of Yb/p-lnP tunnel metal-insulator-semiconductor junctions", *J. Appl. Phys.*, 68(7): 3475-3479 (1990).

[8] S. Chand and J. Kumar, "Current–voltage characteristics and barrier parameters of Pd2Si/p − Si(111) Schottky diodes in a wide temperature range," *Semicond. Sci. Technol.*, 10 (12) 1680–1688 (1995).

[9] Chattopadhyay, P., Daw, A.N., "On the current transport mechanism in a metal-insulator-semiconductor diode", *Solid State Electron.*, 29(5): 555-560 (1986).

[10] Türüt, A., Yalçın, N., Sağlam, M., "Parameter extraction from non-ideal C-V characteristics of a Schottky diode with and without interfacial layer", *Solid State Electron.*, 35: 835-841 (1992).

[11] Crowell, C.R. and Sze, S. M., "Surface states and barrier height of metal semiconductor Systems", *J. Appl. Phys.*, 36: 3212-3220 (1965).

THE INVESTIGATION OF EFFECTS OF (NANOCARBON DOPED-PVP) POLYMER INTERFACIAL LAYER ON THE MAIN ELECTRICAL PARAMETERS AND CONDUCTIVITY

İlbilge Dökme[1], Şemsettin Altındal[2]

[1]*Science Education Department, School of Gazi Education, Gazi University, TURKEY*
[2]*Physics Department, Science Faculty, Gazi University, TURKEY*

E-mail: ilbilgedokme@gmail.com

Abstract

In this study, both Al/p-Si (MS) and Al/(Nanocarbon-PVP)/p-Si (MPS) structures were fabricated on the same p-Si wafer in the same conditions to see the effects on the main electrical parameters and conductivity of them at room temperature. For this purpose, the forward and reverse bias current-voltage (I-V) measurements of them were performed in wide range of applied bias voltage ($\pm$ 3V) by 50 mV steps. Some main electrical parameters such as the reverse-saturation current (I_o), ideality factor (n), barrier height (Φ_B(I-V)), series (R_s) and shunt (R_{sh}) resistances, and rectifying rate (RR=I_F/I_R) of them were extracted from the I-V data as 2.36×10^{-8}A, 6.23, 0.69 eV, 2.94 kΩ, 1.90 MΩ, 6.44×10^2 for MS type SBD and 4.27×10^{-9}A, 2.86, 0.73 eV, 1.25 kΩ, 6.33 MΩ, 5.06×10^3 for MPS type structure, respectively. All these experimental results were confirmed that the used (nanocarbon-PVP) interlayer between Al and p-Si semiconductor leads to a decrease in the leakage current and Rs and increase of BH and RR and hence improved the performance of MS type SBD [1]. It is mean that such a (nanocarbon-doped PVP) polymer interlayer can be successfully instead of conventional insulator or oxide layer in respect of easy grown methods, low cost, low weight, low energy requirement, and flexibility when compared with insulator materials[2,3].

Keywords: Schottky structures, current-voltage characteristics, Polivinil Prolidon interface

1. INTRODUCTION

Metal-Semiconductor (MS) and Metal-polymer-Semiconductor (MPS) type electronic devices consist of an interfacial oxide and polymer layer srespectively between metal and semiconductor and many defects or impurities may be occurred during the elaboration/fabrication of them. They are surface/interface states/traps and may be changed the performance of these devices. These states are usually originated from dangling bounds at surface of semiconductor and chemical composition of the interface [1-5]. The charges in these traps and dislocations may be stored or released under electric field [6-9]. Therefore, we can estimate the changes to measure series resistance (R_s) or shunt resistance (R_{sh}) and interface state density (N_{ss}) etc [5-10].

The existence a native/deposited interlayer such as insulator or polymer at junction, MS structure converts to the MIS or MPS structures. The thickness of interface state layer and dielectric constant are also calculable quantiles from raw data which are important for the performance of these devices as well as barrier inhomogeneity [6-8]. Therefore, the ideality factor (*n*) value from the slope of forward bias Ln(I)-V curve becomes much higher than unity because of the existence of native or deposited interlayer, N_{ss}, inhomogeneous of BH, and tunneling of charge carriers through BH [6-9,11-15]. The R_s and R_{sh} of MS and MPS devices are also more effective on the performance of them. In general, R_s can be estimated from the ohmic and Schottky contacts of the device because of the used probe wires to get contacts, the resistance of the bulk semiconductor, and inhomogeneity doping atoms [7,9]. But, the value of R_{sh} can be estimated from the physical defects, grain boundaries, and leakage current, and probe wires to the ground.

The main aim of this study is to compare the basic diode parameters of fabricated the Al/p-Si (MS) and Au/(Nanocarbon-PVP)/p-Si (MPS) structures by considering the effects of nanocarbon-PVP interfacial layer, series resistance and shunt resistance. For this aim, current-voltage measurements were performed in wide range of applied bias voltage ($\pm$ 3V) by 50 mV steps. The main diode parameters of these two structures such as I_o, n, BH and R_s were calculated to compare them. The results show that the nanocarbon-PVP interfacial lead to a considerably increase in rectifying rate (RR), R_{sh} and BH when compared with reference device (MS).

2. MATERIAL AND METHODS

In order to specify the effects of nanocarbon-PVP interlayer on the performance of the conventional MS structure, both the Al/p-Si (MS) structure with and without this organic interlayer were performed on the B-doped (p-Si) wafer having (100) float zone, 350 µm thickness, 2'' diameter, and ~1.38×10^{16} cm^{-3} dopant donor

concentration atoms in same conditions. Firstly p-Si wafer was dipped in ammonium-peroxide at 50 seconds to remove native-oxide layer and organic impurities on the two side of wafers and then wafers etched in the ($H_2SO_4:H_2O_2:H_2O=3:1:1$) solutions and ($HCl:H_2O=1:1$) for one minute, respectively. After that, wafer was rinsed in ultra-pure water and then N_2 gas used for drying. Subsequently, 150 nm thickness of high-pure Al (99.999%) was evaporated on to the whole back side of the p-Si wafers at $\sim 10^{-6}$ Torr in high-vacuum thermally evaporation system and immediately it was sintered at 450 ℃ for 5 min in a N_2 atmosphere to perform the low resistivity ohmic contact. Secondly, utilizing electrospinning method, the growth of the prepared (Nanocarbon- PVP) organic solution was realized on the front of second quarter p-Si wafer. The organic layer thickness was predicted as 22 nm from the interlayer capacitance (C_i). Immediately, high-pure Al (99.999%) circular dots with 1 mm diameter and 150 nm thickness were deposited on the organic layer at 10^{-6} Torr evaporation system. The schematic diagrams of the fabricated MS and MPS type SBDs were also given in Fig. 1. The I-V measurements were realized by Keithley-2400 source-meter.
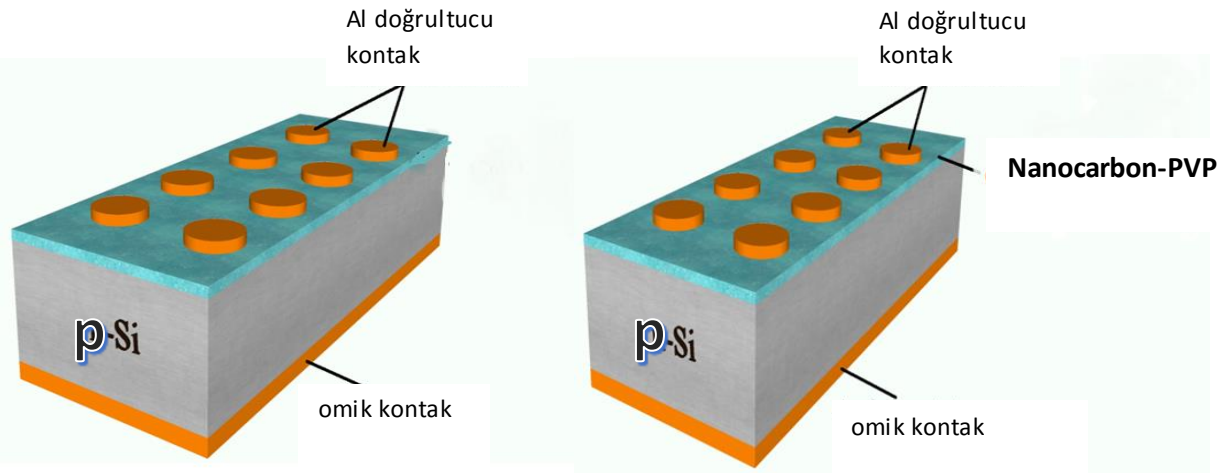

Fig.1. Schematic diagram of the Al/p-Si (MS) and Al/(nanocarbon- PVP)/p-Si (MPS) structures, respectively.

3. RESULTS AND DISCUSSION

Figure 2 shows the forward bias semi-logarithmic current-voltage measurements as a function temperature performed in this study for Al/p-Si (MS) and Al/(nanocarbon- PVP)/p-Si (MPS) structures. As seen in the Fig.2 clearly, the lnI-V curve for two structures exhibit typical diode behavior. lnI-V plots have liner part in the intermediate forward bias voltage up to $\sim$0.5 V and then deviate from linearity because of the Rs effects.
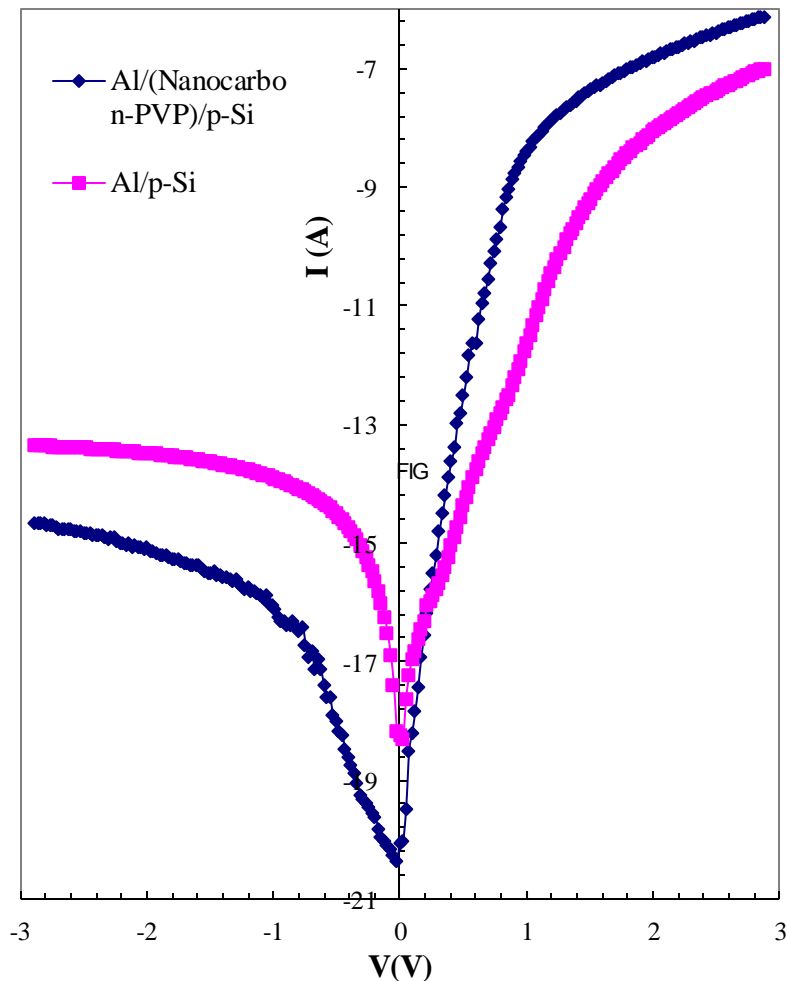
Because applied biases across the structure will be shared by R_s, interfacial layer and depletion layers. But R_s effect at low and moderate bias voltages can be neglected low.

Since electronic devices have both R_s and n is greater than unity, TE theory can also be used to determine electrical parameters and in this case the I-V relation (≥ 3 kT/q) is expressed as below [6-8].

$$I = AA^*T^2 \exp\left(-\frac{q}{kT}\Phi_{Bo}\right)\left[\exp\left(\frac{q(V-IR_s)}{nkT}\right)-1\right] = I_o\left[\exp\left(\frac{qV_D}{nkT}\right)-1\right] \qquad (1)$$

In Eq.(1) A^* is the effective Richardson constant (32 A/cm^{2}K^2 for n-Si), products of IR_s is the voltage drop across the R_s and the other quantities are most-known in the evaluable literature. Both I_o and n values can be extracted from the intercepts and slopes of lnI-V plot [Ln(I)=Ln(I$_o$) + (q/nkT)V] as following through the relation by using Eq.1, respectively [6-8]:

Fig. 2. The semi-logarithmic I-V plots of the MS and MPS structures.

115

$$n = \frac{q}{kT}\left(\frac{dV}{d(\ln I)}\right) \qquad (2)$$

Thus, Φ_{Bo} was extracted from Eq.1 by using the acquired I_o value and the diode area (A) for MS and MPS structures through the equation below [6-8].

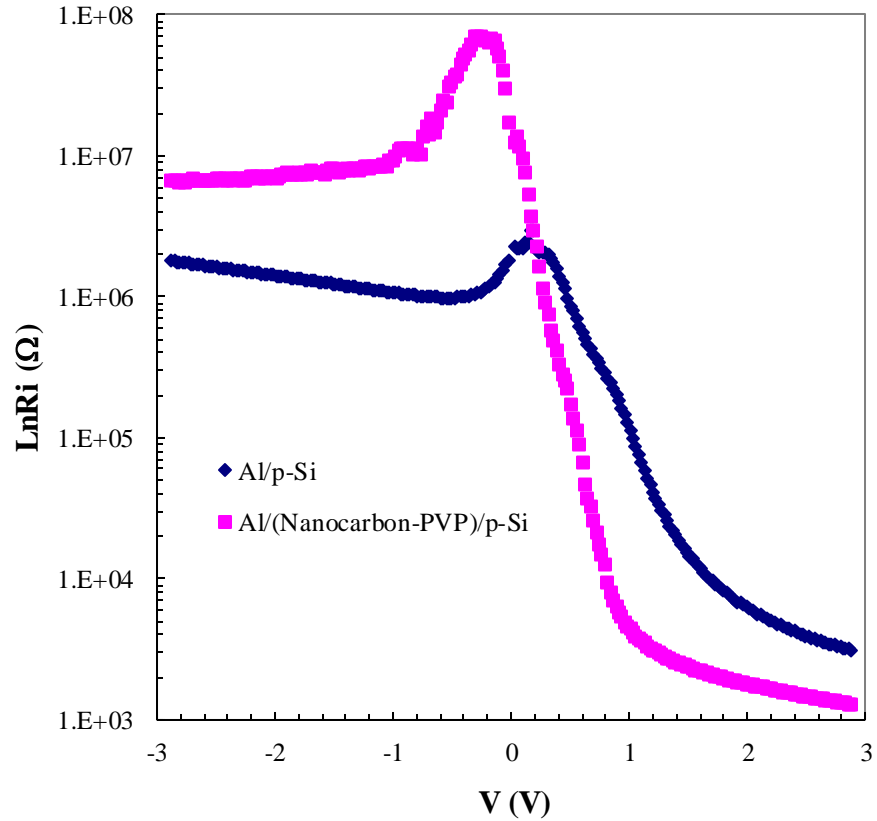$$\Phi_{Bo} = \frac{kT}{q} Ln\left(\frac{AA^*T^2}{I_0}\right) \qquad (3)$$

RR, I_o, n, Φ_{Bo}, and values were extracted from the Ln(I)-V plots and they are tabulated in Table 1, respectively.

Table 1. Diode parameters of the Al/p-Si (MS) and Au/(nanocarbon- PVP)/p-Si (MPS) structures.

Diyot Parametreleri	Al/p-Si	Al/(Nanocarbon-PVP)/p-Si
RR (=I_F/I_R)	6.44×10^2	5.06×10^3
I_o (A)	2.36×10^{-8}	4.27×10^{-9}
n	6.23	2.86
Φ_B (eV)	0.69	0.73
R_s (kΩ)	2.94	1.25
R_{sh} (MΩ)	1.90	6.33

It is clear that these values of n are higher than unity due to the lower BHs/patches at around mean barrier height, a spatial distribution of interface states densty at the interface. Many charge carriers (electron and holes) with low energies can easily pass across these patches and increase the n values. According to Saad and Kassis [11], the other reason of high value of n in these structures is the result of conduction dominated by interface recombination. The n value is a measure of TE theory and higher values of it deviates the structure from TE.

The voltage dependent resistance (R_i=V_i/I_i) of these structures can be extracted from the Ohm's law, but the real R_s value and R_{sh} of them corresponds to adequately high forward and reverse bias voltage [12]. Therefore, the values of R_s and R_{sh} were calculated as for MS and MPS at $\pm$ 3V in Table1 and Fig.3 respectively.

Fig 3. The LnR$_i$-V plots of the Al/p-Si (MS) and Au/(nanocarbon- PVP)/p-Si (MPS) structures.

4. CONCLUSION

In the present study, nanocarbon-PVP interlayered and without interlayer Al/p-Si structures were scrutinized at same conditions to determine the effects of nanocarbon-PVP interfacial layer on the I-V characteristics as well as performance of the MS structure at room temperature. For this purpose, the I-V measurements were performed at room temperature. In this way, the values of ideality factor, barrier height series and shunt resistance were obtained using the experimental measurement methods and also calculated methods namely TE theory. When these experimental results are compared for MS and MPS structures, the used nanocarbon-PVP interlayer at M/S interface leads to a quite decreases in R_s and n and an increase in rectifying rate (RR), R_{sh} and Φ_B. All these experimental results were confirmed that the used (nanocarbon-PVP) interlayer between Al and p-Si semiconductor leads to improved the performance of MS type diodes. It is mean that such a (nanocarbon-doped PVP) polymer interlayer can be successfully instead of conventional insulator or oxide

layer in respect of easy grown methods, low cost, low weight, low energy requirement, and flexibility when compared with insulator materials.

REFERENCES

[1] Rhoderick, E.H. and Williams R.H., "Metal-Semiconductor Contacts 2nd ed.", *Oxford University Press*, Oxford, 257 (1988).

[2] Cowley, A.M., Sze, S.M., "Surface State and Barrier Height of Metal Semiconductor Systems", *J. Appl. Phys.*, 36: 3212-3216 (1965).

[3] Fonash, S.J., "The role of the interfacial layer in Metal-Semiconductor Solar Cells", *J. Appl. Phys.*, 46: 1286-1289 (1975).

[4] Dökme, İ., Altındal, , Ş., "The distribution of the barrier height in Al–TiW–Pd2Si/n-Si Schottky diodes from *I–V–T* measurements", <u>**Semiconductor Science and Technology**</u>, 21, 035003(2006).

[5] Card, H.C., Rhoderick, E.H., "Studies of tunnel MOS diyotes I. Interface effects in silicon Schottky diodes", J. Phys. D: Appl. Phys., 4:1589-1601 (1971).

[6] Sze, S.M., "Physics of Semiconductor Devices 2nd ed.", *John Wiley & Sons*, New York, 245-390 (1981).

[7] Sing, A., Reinhard, K.C., Anderson, W.A., "Temperature dependence of the electrical characteristics of Yb/p-lnP tunnel metal-insulator-semiconductor junctions", *J. Appl. Phys.*, 68(7): 3475-3479 (1990).

[8] S. Chand and J. Kumar, "Current–voltage characteristics and barrier parameters of Pd2Si/p − Si(111) Schottky diodes in a wide temperature range," *Semicond. Sci. Technol.*, 10 (12) 1680–1688 (1995).

[9] Chattopadhyay, P., Daw, A.N., "On the current transport mechanism in a metal-insulator-semiconductor diode", *Solid State Electron.*, 29(5): 555-560 (1986).

[10] Türüt, A., Yalçın, N., Sağlam, M., "Parameter extraction from non-ideal C-V characteristics of a Schottky diode with and without interfacial layer", *Solid State Electron.*, 35: 835-841 (1992).

[11] M. Saad and A. Kassis, Analysis of illumination-intensity-dependent J–V characteristics of ZnO/CdS/CuGaSe$_2$ single crystal solar cells, Sol. Energ. Mat. Sol. C. 77 (2003) 415-422.

[12] Crowell, C.R. and Sze, S. M., "Surface states and barrier height of metal semiconductor Systems", *J. Appl. Phys.*, 36: 3212-3220 (1965).

THE ADDITION OF SELECTED ORGANOALUMINUM AND ORGANOZINC REAGENTS TO THE PROTECTED IMINO AND α-KETO PHOSPHONATES

S. Polat Çakır

Department of Chemical Engineering, Faculty of Engineering, Çanakkale Onsekiz Mart University, Çanakkale, TURKEY

E-mail: spcakir@comu.edu.tr

Abstract

Nucleophilic additions of Grignard and organolithium reagents to a compound having carbonyl functional group to form C-C bond are well known chemistry. Same addition chemistry is also performed for imine derivatives. The former reaction leads to formation of secondary alcohols and the latter addition reaction is used to prepare secondary amines. The syntheses of α-hydroxy phosphonates and α-amino phosphonates are very important in medicinal and synthetic organic chemistry because of close analogs of α-hydroxy phosphonic acids and α-amino phosphonic acids. Compounds containing this functional group in their structure are likely to exhibit a wide range of biological activities i.e. antibacterial, antitumor, antibiotic, enzyme inhibition. For that reason synthesis of phosphorous-containing α-hydroxy and α-amino compounds are crucial. Grignard and organolithium reagents are very reactive towards the aroyl phosphonates and imino phosphonates. With these reagents C-P bond breaks very easily. Herein, the investigation of direct addition of the selected organoaluminum and organozinc reagents to the protected imino and aroyl phosphonates will be presented at this conference.

Keywords: organoaluminum, organozinc, α-hydroxy phosphonates, α-amino phosphonates

1. INTRODUCTION

The syntheses of α-hydroxy phosphonates are very important in medicinal and synthetic organic chemistry due to close analogs of α-hydroxy carboxylic and phosphonic acids. They have also similar properties to important phosphate esters.[1] Compounds containing this functional group in their structure are likely to be an antibacterial and antiviral agent. Moreover, the syntheses of tertiary α-hydroxy phosphonates bearing three different substituents are even more important. α-Hydroxy phosphonates show wide range of activities such as enzyme inhibitors (farnesyl protein transferase, human rennin, human protein tyrosine phosphatase etc.) and anticancer activities (various humancancer cell lines and HIV). [2-9] Both α-hydroxy phosphonates and α-imino phosphonates [3] are attractive precursors in terms of their wide range applications in biological and pharmaceutical industries due to being potentially biologically active compounds. The traditional synthesis of α-hydroxy phosphonates is the nucleophilic additions of either Grignard or organolithium reagents to carbonyl functional group- aldeydes or ketones. [10] Similar 1,2 addition reactions to imino compounds are traditionally performed. Addition of organometallic reagents to both aroyl phosphonates and imino phosphonates is not preferred because these phosphonates containing functional groups are too reactive. These reagents let to cleavage of C-P bonds. The suitable and alternative organometallic reagents are organoaluminum and organozinc, which show similar reactivities like Grignard reagents. The use of latter reagents in the addition reaction led to the synthesis of enantioselective version of the biologically important compounds of α-hydroxy phosphonates and α-imino phosphonates. Herein, we report our efforts towards the alkyl addition of α-imino phosphonates to afford α-amino phosphonates derivatives using $AlMe_3$, $AlEt_3$, $ZnEt_2$ reagents. Aryl addition to α-keto phosphonates using $AlPh_3$/$ZnPh_2$ to synthesize tertiary α-hydroxy phosphonates is also reported.

2. MATERIALS AND METHOD

We have reported the addition of organoaluminum reagents ($AlMe_3$, $AlEt_3$, $Al(i\text{-but})_3$, $Al(CH\equiv CH)_3$, $Al(CH\equiv CCH_3)_3$, $Al(CH\equiv CPh)_3$ to α-keto phosphonates for the syntheses of α-hydroxy phosphonate derivatives in good yields. [11,12] Our interest in this α-keto phosphonate chemistry let us to investigate similar addition reactions to the protected imino phosphonates to provide a simple method for the synthesis of α-amino phosphonates. The required protected α-imino phosphonates were easily synthesized according to a procedure published in the literature. [13, 14]

In the investigation of the addition reactions of $AlPh_3$/$ZnPh_2$ the α- keto phosphonate derivatives used in this work were also synthesized following a literature procedure.[15] α-Keto phosphonates were prepared via Arbuzov reaction *i.e.* treating the parent chlorides with triethyl/trimetyhl phosphites.

Herein we use commercially available organoaluminum and organozinc reagents, which are easy to handle except diphenyl zinc reagents. Trialkyl aluminum and dialkyl zinc reagents are used as C-based nucleophiles i.e. alkyl donor. Arylation of α-keto phosphonate derivatives are carried out using diphenyl zinc (phenyl as a nucleophile).

3. RESULTS AND DISCUSSION

The addition of organoaluminum and organozinc reagents are investigated for substrates **1a**, **1b** and **1c** derivatives of iminophosphonates. Initially, the addition of commercially available $Al(CH_3)_3$ reagents to compound **1a** in DCM did not reacted at all. This could be due to the less electropositive C-atom in PMB-protected iminophosphonate **1a** and could be also due to the steric hindered around the C-atom. Then, we have used CF_3-iminophosphonate **1b** having more electropositive C-atom. Compound **1b** is reacted with $Al(CH_3)_3$ in different solvent systems i.e. DCM, toluene and acetonitrile. In all cases, the reactions were started at low temperature (-78ºC), then were increased slowly to find the best yield for the used solvent system (Table 1, entries 2-4). In Table 1 we summarize our optimized reaction conditions in each experiment. Compound **1b** was reacted with $Al(CH_3)_3$ and the desired product **2a** was isolated in 73% yield in DCM without the cleavage of C-P bond (Table 1, entry 2). However, compound **2b** in toluene was isolated in 56% yield, and compound **2b** in acetonitrile did not form at all (Table 1, entry 4). PMP protected CF_3 iminophosphonate **1c** in DCM gave the C-P bond cleaved product **3** in 52% yield (Table 1, entry 5). In toluene, we were able to isolate the desired addition compound **2c** in good yield (72%, Table 1, entry 6). The addition of $Al(CH_2CH_3)_3$ reagent was also investigated for both compounds **1b** and **1c** in DCM and toluene. The ethyl addition product **2d** in toluene was obtained in 61% isolated yield while compound **2d** was attained in low yield (48%, Table 1, entry 8) in DCM. In the case of compound **1c** the addition $Al(CH_2CH_3)_3$ was tested for both solvents (dichloromethane and toluene). The desired addition product was obtained in toluene at low temperature (Table 1, entry 10). However, compound **3e** in dichloromethane was isolated in 54% yield (entry 9).

Table 1.

$$ \underset{1}{\overset{\displaystyle R_1 \diagup \!\!\! \overset{N-R_2}{\underset{\parallel}{\overset{}{C}}} P(OR_3)_2} {}} \xrightarrow{\ Al(R_4)_3\ } \underset{2}{\overset{\displaystyle R_1 \underset{R_4}{\overset{HN-R_2}{|}} P(OR_3)_2}{}} + \underset{3}{\overset{\displaystyle R_1 \overset{N-R_2}{\diagdown\!\!\!\diagup} R_4}{}} $$

Entry	α-Imino phosphonates	Reaction Con.	Product	Yield(%)[a]
1	R_1= Ph, R_2= p-MeOPh, R_3=OEt, R_4=CH$_3$, **1a**	-78°C then RT	**2a**	NR[b]
2	R_1= CF$_3$, R_2= Ph, R_3= OMe, R_4= CH$_3$, **1b**	-78°C, DCM	**2b**	73
3	R_1= CF$_3$, R_2= Ph, R_3= OMe, R_4= CH$_3$, **1b**	0°C, toluene	**2b**	56
4	R_1= CF$_3$, R_2= Ph, R_3= OMe, R_4= CH$_3$, **1b**	-30°C, CH$_3$CN	**2b**	Decom.[c]
5	R_1=CF$_3$, R_2=p-MeOPh, R_3=OMe, R_4= CH$_3$, **1c**	0°C, DCM	**3c**	52
6	R_1= CF$_3$, R_2=p-MeOPh, R_3=OMe, R_4= CH$_3$, **1c**	-78°C, toluene	**2c**	72
7	R_1= CF$_3$, R_2=Ph, R_3=OMe, R_4=CH$_2$CH$_3$, **1b**	-78°C, DCM	**2d**	48
8	R_1= CF$_3$, R_2=Ph, R_3=OMe, R_4= CH$_2$CH$_3$, **1b**	0°C, toluene	**2d**	61
9	R_1= CF$_3$, R_2=p-MeOPh, R_3=OMe, R_4=CH$_2$CH$_3$, **1c**	0°C, DCM	**3e**	54
10	R_1= CF$_3$, R_2=p-MeOPh, R_3=OMe, R_4=CH$_2$CH$_3$, **1c**	-78°C, toluene	**2e**	68

[a]Yields refer to isolated yield. [b]NR: no reaction. [c]Decomposition

We have also investigated the addition of Zn(CH$_2$CH$_3$)$_2$ to compound **1b** and **1c** and our experimental results are listed in Table 2. The addition of Zn(CH$_2$CH$_3$)$_2$ to compound **1b** gave the desired product **2b** in good yields in DCM and toluene, 60% and 71% yields respectively (Table 2, entry 1-2). However the hydride addition product **4b** in acetonitrile was obtained solely, albeit in low yield (entry 3). When we reacted compound **1c** with Zn(CH$_2$CH$_3$)$_2$ at 0°C in DCM, the hydride addition product **4c** was isolated in 80% yield (entry 4). When the same reaction was repeated at low temperature, the desired ethyl addition compound **2c** was obtained in 62% yield (entry 5). However, the hydride addition compound **4c** was attained in 71% yield in toluene at 0°C. Compound **2c** was isolated albeit in low yield in acetonitrile (entry 8).

Table 2.

Entry	α-Imino phosphonate	Reaction Con.[a]	Product	Yield(%)[a]
1	R_1= Ph, **1b**	-30°C, DCM	**2b**	60
2	R_1= Ph, **1b**	0°C, toluene	**2b**	71
3	R_1= Ph, **1b**	-30°C, CH_3CN	**4b**	44
4	R_1= p-MeOPh, **1c**	0°C, DCM	**4c**	80
5	R_1= p-MeOPh, **1c**	-78°C, DCM	**2c**	62
6	R_1= p-MeOPh, **1c**	0°C, toluene	**4c**	71
7	R_1= p-MeOPh, **1c**	-30°C, CH_3CN	**2c**	36

[a]Yields refer to isolated yield.

Our plan is also to investigate the aryl addition to α-keto phosphonates derivatives using either triphenyl aluminum or diphenyl zinc reagents. We summarize our results in Table 3. Our first attempt was to use $AlPh_3$ reagents. This reagent was very reactive and in every attempts we could not isolate the desired 1,2-addition adduct **6a**. Then, we tested $ZnPh_2$ reagent for the C-arylation reaction of α-keto phosphonates. The additions of $ZnPh_2$ to compound **5a** both in toluene and DCM were tried. After the optimization of the reaction temperature, the best yield was obtained at -5°C in DCM (Table 3, entry 3). Compound **6c**, **6e** and **6f** were obtained in 38%, 56% and 73% yields, respectively (Table 3, entries 5, 7 and 8). In the case of electron rich benzoyl phosphonate **5d**, we could not isolate the addition product due to electron donating groups at the para position. The corresponding products were characterized by analyzing the proton and carbon NMR spectrum. The products displayed characteristic peaks for the quaternary carbon atom (C-P) in the carbon NMR having a large coupling constant. The quaternary C-atom resonances at around 78.0 ppm value as a doublet with a coupling constant value around 160-161 Hz (Table 2).

Table 3.

Entry	α-Keto phosphonate	Reaction Con.[a]	Yield(%)[a]
1	R^1= H, R^2=OEt, **5a**	$0°$C, toluene	**6a,** 58
2	R^1= H, R^2=OEt, **5a**	$-5°$C, toluene	**6a,** 62
3	R^1= H, R^2=OEt, **5a**	$-5°$C, DCM	**6a,** 87
4	R^1= H, R^2=OMe, **5b**	$0°$C, DCM	**6b,** 47
5	R^1= p-Me, R^2=OEt, **5c**	$0°$C, DCM	**6c,** 38
6	R^1= p-MeO, R^2=OEt, **5d**	$-5°$C, DCM	**6d,** Decom.[b]
7	R^1= p-F, R^2=OEt, **5e**	$-5°$C, DCM	**6e,** 56
8	R^1= p-Cl, R^2=OEt, **5f**	$-5°$C, DCM	**6f,** 73

[a]Yields refer to isolated chemical yields. [b] Decomposition

General Procedure for the AlMe$_3$/AlEt$_3$/ZnEt$_2$ addition to α-imino phosphonate: To a solution of α-imino phosphonate (1 equiv.) in toluene/DCM/CH$_3$CN (0.5 M) was added AlMe$_3$/AlEt$_3$/ZnEt$_2$ (3 equiv.) slowly at the specified temperature reported in Table 1 and 2. The resultant mixture was stirred at that temperature until the disappearance of α-imino phosphonate as indicated by TLC. The mixture was hydrolyzed by addition of water and was filtrated over Celite and then washed with EtOAc. Purification was carried out by using column chromatography.

Dimethyl 1,1,1-trifluoro-2-(phenylamino)propan-2-ylphosphonate **2b**: ^{1}H NMR (CDCl$_3$, 400 MHz): δ 1.5 (d, $J_{C\text{-}P}$ = 15.5 Hz, 3H, CH$_3$), 3.86 (d, J = 10.7 Hz, 3H, OCH$_3$), 3.89 (d, $J_{C\text{-}P}$ = 10.5 Hz, 3H, OCH$_3$), 4.13 (q, $J_{C\text{-}C}$ = 7.1 Hz, 1H, NH), 6.9 (d, $J_{C\text{-}P}$ = 7.4 Hz, 2H), 7.1 (t, $J_{C\text{-}P}$ = 6.3 Hz, 1H), 7.2 (d, $J_{C\text{-}P}$ = 7.5 Hz, 2H). ^{13}C NMR (CDCl$_3$, 100 MHz): δ 14.1 (d, $J_{C\text{-}F}$ = 2.8 Hz, CH$_3$), 52.9 (d, $J_{C\text{-}P}$ = 7.4 Hz, OCH$_3$), 53.7 (d, $J_{C\text{-}P}$ = 6.8 Hz, OCH$_3$), 61.3 (dq, $J_{C\text{-}F}$ = 27.2, $J_{C\text{-}P}$ = 158.0 Hz, quaternary C-atom), 122.4 (C), 122.9, 127.8, 128.7 (qd, $J_{C\text{-}P}$ = 11.6, $J_{C\text{-}F}$ = 286.6 Hz, CF$_3$).

Dimethyl 2-(4-methoxyphenylamino)-1,1,1-trifluoropropan-2-ylphosphonate **2c**: ^{1}H NMR (CDCl$_3$, 400 MHz): δ 1.48 (d, $J_{C\text{-}P}$ = 16.0 Hz, 3H, CH$_3$), 3.74 (s, NH), 3.78 (s, 3H, CH$_3$), 3.86 (d, $J_{C\text{-}P}$ = 10.7 Hz, 3H, POCH$_3$), 3.91 (d, $J_{C\text{-}P}$ = 10.5 Hz, 3H, POCH$_3$), 6.79 (d, $J_{C\text{-}P}$ = 8.9 Hz, 2H), 6.96 (d, $J_{C\text{-}P}$ = 8.9 Hz, 2H).

Dimethyl 1,1,1-trifluoro-2-(phenylamino)butan-2-ylphosphonate **2d**: ^{1}H NMR (CDCl₃, 400 MHz): δ 1.1. (t, J_{C-P} = 7.5 Hz, 3H), 2.1-2.2 (m, 2H), 3.8 (d, J_{C-P} = 2.6 Hz, 3H), 3.8 (d, J_{C-P} = 2.7 Hz, 3H), 4.2 (s, 1H), 6.9-7.0 (m, 3H), 7.2-7.3 (m, 2H). ^{13}C NMR (CDCl₃, 100 MHz): δ 8.30 (d, J_{C-P} = 3.8 Hz), 23.1, 54.1 (t, J_{C-P} = 7.6 Hz), 65.8 (dq, J_{C-P} = 152.6, J_{C-F} = 25.9 Hz), 122.4, 122.9, 128.8, 125.6 (qd, J_{C-F} = 287.6, J_{C-P} = 8.2 Hz), 142.9 (d, J_{C-P} = 8.9 Hz).

Dimethyl 2-(4-methoxyphenylamino)-1,1,1-trifluorobutan-2-ylphosphonate **2e**: ^{1}H NMR (CDCl₃, 400 MHz): δ 1.09 (t, J = 7.5 Hz, 3H, CH₃), 2.06-1.93 (m, 2H, CH₂CH₃), 3.77 (s, 3H, OCH₃), 3.84 (d, J_{C-P} = 1.3 Hz, 3H, POCH₃), 3.87 (d, J_{C-P} = 1.2 Hz, 3H, POCH₃), 3.96 (s, 1H, NH), 6.78 (d, J = 8.9 Hz, 2H), 7.00 (d, J = 8.8 Hz, 2H).

Dimethyl 2,2,2-trifluoro-1-(phenylamino)ethylphosphonate **4b**: ^{1}H NMR (CDCl₃, 400 MHz): δ 3.7 (d, J_{C-P} = 10.8 Hz, 3H), 3.8 (d, J_{C-P} = 11.1 Hz, 3H), 4.2-4.3 (m, 1H), 4.4 (t, J_{C-P} = 10.0 Hz, 1H), 6.7 (d, J_{C-P} = 7.9 Hz, 2H), 6.8 (t, J_{C-P} = 7.4 Hz, 1H), 7.1 (t, J_{C-P} = 7.4 Hz, 2H). ^{13}C NMR (CDCl₃, 100 MHz): δ 53.7 (d, J_{C-P} = 6.9 Hz), 54.2 (d, J_{C-P} = 6.6 Hz), 54.3 (dq, J_{C-P} = 154.5, J_{C-F} = 32.2 Hz), 113.5, 119.8, 126.6 (qd, J_{C-P} = 283.1, J_{C-F} = 11.2 Hz), 129.3, 145.2 (d, J_{C-P} = 6.5 Hz).

Dimethyl 1-(4-methoxyphenylamino)-2,2,2-trifluoroethylphosphonate **4c**: ^{1}H NMR (CDCl₃, 400 MHz): δ 3.65 (s, 3H, OCH₃), 3.70 (d, J_{C-P} = 10.8 Hz, 3H, POCH₃), 3.73 (d, J_{C-P} = 11.0 Hz, 3H, PCH₃), 4.27-4.08 (m, 1H, CH), 6.63 (d, J_{C-P} = 9.0 Hz, 2H), 6.71 (d, J_{C-P} = 9.0 Hz, 2H). ^{13}C NMR (CDCl₃, 100 MHz): δ 53.6 (d, J_{C-P} = 7.0 Hz, PCH₃), 55.1 (d, J_{C-P} = 6.5 Hz, POCH₃), 55.2 (dd, J = 153.1, 31.5 Hz), 55.4 (OCH₃), 114.8, 115.3, 126.8 (qd, J_{C-F} = 283.1, J_{C-P} = 11.8 Hz), 139.4, 153.5.

General Procedure for the ZnPh₂ addition to α-keto phosphonate: To a solution of α-keto phosphonate phosphonate (1 equiv.) in dry toluene/DCM (0.2 M) was added ZnPh₂ (1.1 equiv.) at -5°C. The mixture was stirred at this temperature until the disappearance of α-keto phosphonate as indicated by TLC. Then the mixture was quenched by addition of water (1 ml), and diluted with DCM. After extraction, the organic layer was separated, dried over MgSO4 and concentrated *in vacuo*. Crude compound was purified by silica gel chromatography.

Diethyl hydroxydiphenylmethylphosphonate **6a**: ^{1}H NMR (400 MHz, CDCl₃): δ 7.65-7.67 (m, 4H), 7.23-7.32 (m, 6H), 4.41 (broad -OH), 3.86-3.97 (m, 4H, POCH₂CH₃), 1.13 (t, J = 7.1 Hz, 6H, POCH₂CH₃). ^{13}C NMR (CDCl₃): δ 141.6 (d, J = 2.6 Hz), 127.8, 127.4 (d, J = 1.5 Hz), 127.2 (d, J = 5.5 Hz), 78.4 (d, J_{C-P} = 160.3 Hz, CP), 63.5 (d, J_{C-P} = 7.6 Hz, POCH₂CH₃), 16.1 (d, J_{C-P} = 5.5 Hz, POCH₂CH₃).

Dimethyl hydroxydiphenylmethylphosphonate 6b: ^{1}H NMR (400 MHz, CDCl$_3$): δ 7.65-7.63 (m, 4H), 7.24-7.33 (m, 6H), 3.57 (d, J = 10.3 Hz, 6H, POCH$_3$).

Dimethyl hydroxy(phenyl)(p-tolyl)methylphosphonate 6c: ^{1}H NMR (400 MHz, CDCl$_3$): δ 7.66 (d, J = 7.3 Hz, 1H), 7.54 (d, J = 8.0 Hz, 1H), 7.30 (t, J = 7.4 Hz, 2H), 7.27–7.21 (m, 1H), 7.12 (d, J = 7.9 Hz, 2H), 4.06–3.82 (m, 4H, POCH$_2$CH$_3$), 2.31 (s, J = 13.6 Hz, 3H, CH$_3$), 1.16 (q, J = 7.0 Hz, 3H, POCH$_2$CH$_3$). ^{13}C NMR (101 MHz, CDCl$_3$): δ 128.7 (d, J = 3.0 Hz), 127.9 (d, J = 4.0 Hz), 127.5 (d, J = 3.9 Hz), 127.1 (d, J = 4.5 Hz), 78.3 (d, J_{C-P} = 160.1 Hz, CP), 63.6 (d, J_{C-P} = 3.3 Hz, POCH$_2$CH$_3$), 63.5 (d, J_{C-P} = 3.6 Hz, POCH$_2$CH$_3$), 21.0 (s, CH$_3$), 16.3 (d, J_{C-P} = 5.5 Hz, POCH$_2$CH$_3$).

Dimethyl (4-fluorophenyl)(hydroxy)(phenyl)methylphosphonate 6e: ^{1}H NMR (400 MHz, CDCl$_3$) δ 7.65–7.58 (m, 4H), 7.34 –7.22 (m, 3H), 6.98 (t, J = 8.8 Hz, 2H), 4.60 (s, J = 2.6 Hz, 1H, OH), 3.97–3.85 (m, 4H, POCH$_2$CH$_3$), 1.14 (td, J = 7.1, 4.9 Hz, 6H, POCH$_2$CH$_3$). ^{13}C NMR (101 MHz, CDCl$_3$): δ 162.0 (d, J_{C-F} = 253.9 Hz), 141.6, 137.6, 129.2 (dd, J = 7.9, 5.5 Hz), 127.9, 127.6 (d, J = 1.4 Hz), 127.2 (d, J = 5.4 Hz), 114.6 (d, J = 21.4 Hz), 78.0 (d, J_{C-P} = 161.3 Hz, CP), 63.6 (t, J_{C-P} = 8.1 Hz, POCH$_2$CH$_3$), 16.2 (d, J_{C-P} = 5.6 Hz, POCH$_2$CH$_3$).

Dimethyl (4-chlorophenyl)(hydroxy)(phenyl)methylphosphonate 6f: ^{1}H NMR (400 MHz, CDCl$_3$) δ 7.54– 7.46 (m, 4H), 7.25 –7.15 (m, 5H), 4.92 (s, 1H, OH), 3.89–3.73 (m, 4H, POCH$_2$CH$_3$), 1.05 (q, J = 7.0 Hz, 6H, POCH$_2$CH$_3$). ^{13}C NMR (101 MHz, CDCl$_3$): δ 141.5, 140.5, 133.3, 128.8 (d, J = 5.3 Hz), 127.88, 127.87, 127.6 (d, J = 1.4 Hz), 127.2 (d, J = 5.5 Hz), 78.0 (d, J_{C-P} = 161.5 Hz, CP), 63.7 (d, J_{C-P} = 7.6 Hz, POCH$_2$CH$_3$), 63.6 (d, J_{C-P} = 7.6 Hz, POCH$_2$CH$_3$), 16.2 (d, J_{C-P} = 5.7 Hz, POCH$_2$CH$_3$).

4. CONCLUSION

A new synthetic route to tertiary α-hydroxy phosphonates having three different substituents from α-keto phosphonates is reported without the cleavage of the C-P bonds. Direct 1,2-addition of ZnPh$_2$ to α-keto phosphonate reactions proceeded in good to acceptable yields. Fairly electron poor substrates in the aroyl phosphonates gave good yields. However, low yields were obtained for the electron rich aroyl phosphonates. Electron donating ability of the substrate led to easy C-P bond breaking.

We have also showed that α-trifluoromethyl substituted α-amino phosphonates are easily prepared from the α-imino phosphonates via 1,2-addition of organoaluminum reagents. Trifluoromethyl containing α-amino phosphonates are potent biological activity compounds. The expected products were attained in good yields. Diethylzinc was also used as an alkyl donor in the 1,2 addition reactions of α-imino phosphonates.

ACKNOWLEDGMENTS

REFERENCES

[1] Naidu, K. R. M., Kumar, K. S., Arulselvan, P., Reddy, C. B., Lasekan, O., Synthesis of α-hydroxy phosphonates and their antioxidant properties, Archiv der Pharmazie Chemistry in Life Sciences, 345, 957-963, 2012.

[2] Dellaria, J. F., Maki, R. G., Stein, H. H., Cohen, J., Whittern, D., Marsh, K., Hoffman, D. J., Plattner, J. J., Perun, T. J., New inhibitors of renin that contain novel phosphostatine Leu-Val replacements, J. Med. Chem. 33, 534-542, 1990.

[3] Xu, Y., Yan, K., Song, B., Xu, G., Yang, S., Xue, W., Hu, D., Lu, P., Ouyang, G., Jin L., Chen, Z., Synthesis and antiviral bioactivities of α-aminophosphonates containing alkoxyethyl moieties, Molecules, 11, 666-676, 2006.

[4] Pompliano, D. L., Rands, E., Schaber, M. D., Mosser, S. D., Anthony, N. J., Gibbs, J. B., Steady-state kinetic mechanism of ras farnesyl: protein transferase, Biochemistry, 31, 3800-3807, 1992.

[5] Evitt, A. S., Cox, R. J., Molecular BioSystem, Synthesis and evaluation of conformationally restricted inhibitors of aspartate semialdehyde dehydrogenase, 7, 1564-1575, 2011.

[6] Kundarapu, M., Marchand, D., Dumbre, S. G., Herdewijn, P., Synthesis of new acyclic nucleoside phosphonates (ANPs) substituted on the1' and/or 2' positions, Tetrahedron Letters, 52, 6896-6898, 2011.

[7] Zalcharova, V. M., Serpi, M., Krylov, I. S., Peterson, L. W., Breitenbach, J. M., Borysko, K. Z., Drach, J. C., Collins, M., Hilfinger, J. M., Kashemirov, B. A., McKenna, C. E., Tyrosine-based 1-(S)-[3-hydroxy-2-(phosphonomethoxy)propyl]cytosine and -adenine ((S)-HPMPC and (S)-HPMPA) prodrugs: synthesis, stability, antiviral activity, and in vivo transport studies, Journal of Medicinal Chemistry, 54, 5680-5693, 2011.

[8] Ruiz, J., Beadle, J. R., Buller, R. M., Schreiwer, J., Prichard, M. N., Keith, K. A., Lewis, K. C., Hostetler, K. Y., Synthesis, metabolic stability and antiviral evaluation of various alkoxy alkyl esters of cidofovir and 9-(S)-[3-hydroxy-2-(phosphonomethoxy)- propyl]adenine, Bioorganic Medicinal Chemistry, 19, 2950-2958, 2011.

[9] Magee, W. C., Valiaeva, N., Beadle, J. R., Richman, D. D., Hostetler, K. Y., Evans, D. H., Inhibition of HIV-1 by octadecyloxyethyl esters of (S)-[3-hydroxy-2-(phosphonomethoxy)propyl] nucleosides and evaluation of their mechanism of action, Antimicrobial Agents Chemotherapy,55, 5063-5072, 2011.

[10] Liua, Y. L., Lina, X. T., Recent advances in catalytic asymmetric synthesis of tertiary alcohols via nucleophilic addition to ketones, Advanced Synthesis and Catalysis, 361, 876-918 , 2019.

[11] Seven, O., Polat-Cakir, S., Hossain, Md. S., Emrullahoglu, M., Demir, A. S., Reactions of acyl phosphonates with organoaluminum reagents: a new method for the synthesis of secondary and tertiary α-hydroxy phosphonates, Tetrahedron, 67, 3464-3469, 2011.

[12] Hossain, Md. S., Polat Çakır, S., Karaduman, A. B., Yamaç, M., Demir, A. S., Synthesis of tertiary propargylic phosphonates by addition of trialkynylaluminum reagents to acyl phosphonates and investigation of their antimicrobial activities, Turkish Journal of Chemistry, 38, 880-893, 2014.

[13] Goulioukina, N. S., Bondarenko, G. N., Lyubimov, S. E., Davankov, V. S., Gavrilov, K. N., Beletskaya, I. P., Catalytic hydrogenation of α- iminophosphonates as a method for the synthesis of racemic and optically active α- aminophosphonates, Advanced Synthesis and Catalysis, 350, 482-492,2008.

[14] Osipov, S. N., Artyushin, O. I., Kolomiets, A. F., New α-trifluoromethyl-substituted α-amino phosphonates, Mendeleev Communications, 10, 192, 2000.

[15] Berlin, K. D., Taylor, H. D., The reactions of aroyl halides with phosphites. Esters of aroylphosphonic acids1, Journal of the American Chemical Society, 86, 3862-3866, 1964.

BIOMASS OBTAINING HIGH ENERGY EFFICIENCY BIOFUEL VIA TORREFACTION PROCESS

H.İ. Özgündüz[1], N. Acaralı[1]

[1]*Department of Chemical Engineering, Faculty of Chemical-Metallurgical Engineering, Yildiz Technical University, İstanbul, TURKEY*

E-mail: iremozgunduz@gmail.com, nilbaran@gmail.com

Abstract

In this study, processed carob samples were used as organic additive to improve energy content. Verbascum plants were evaluated as biomass source. For torrefaction process, carob samples taken from molasses factory were subjected to torrefaction process at low heating rate (10°C/min) between 200-300°C and under inert nitrogen environment. In addition, in order to determine the effects of different torrefaction conditions on biomass yield, particle size (1000-5000 μm), process temperature (200-300°C) and process residence time (15-60 min) of the biomass were investigated in detail. The results were evaluated in terms of mass yields, energy densities and energy yield values.

Keywords: carob, biomass, torrefaction, Verbascum plant

1. INTRODUCTION

Biomass energy sources; wood and wood wastes, animal wastes, food production wastes, energy crops etc. were used for energy generation [1]. In recent years, the torrefaction process is applied to prevent the negative effects of biomass usage and to improve the physicochemical properties of biomass. In this way, the moisture content is reduced, the calorific value and energy density is increased, and also because of the breakage of the bonds between the lignocellulosic polymers, the products can be obtained with improved grindability [2].

During torrefaction, hemicellulose, cellulose and lignin polymers in the biomass structure are thermally degraded and depolymerized. As a result of the process, volatile gases and moisture in the biomass content move away from the structure, while degradation occurs in lignin, cellulose and hemicellulose structures [3,4].

Different organic wastes are used as additives to increase the energy potential of the endemic plants which are considered as an alternative to the traditional energy sources commonly used in our country.

2. MATERIALS AND METHOD

For the production of high energy biofuels, the torrefaction process was carried out by using Verbascum plant obtained from Afyonkarahisar as a biomass source and organic additive (carob), at low heating rate (10°C/min) and using an inert nitrogen environment. Samples after torrefaction process were given in Figure 1.

Design Expert program/central composite design method was used to optimize the energy potential of biofuel production and to evaluate the interaction of independent variables affecting the process with each other and response surfaces. In the design, which was entered as 4 independent variables, a total of 30 experiments with 6 replicates were created at the center.

Figure 1. Samples for different process conditions

3. RESULTS AND DISCUSSION

Efficient parameters were determined by Design Expert optimization method (Table 1). The results were showed in Figure 2.

When the experimental results were examined, the mass efficiency of the biofuel produced decreased and the mass loss increased with the increase in process temperature. This increase in mass loss is due to the difference in the degree of disintegration of hemicellulose, which is present in the biomass and has not very high thermal stability. It is known that the degree of degradation of hemicellulose, cellulose and lignin molecules in the biomass structure is greatly affected by the process conditions [5].

In addition, a decrease in the mass efficiency of biofuels was observed during torrefaction. This decrease may be due to thermal effects caused by depolymerization and moisture loss in the biomass cell wall. Because carbon monoxide, carbon dioxide, water and aromatic carbon in the structure are removed from the structure as a result of depolymerization of biomass. In addition, another reason for the decrease in mass efficiency is the removal of bound moisture and thermal decomposition and formation of volatile components such as H_2O, CO_2, CO, acetic acid and other organic compounds.

At a process temperature of 200°C, the majority of the mass loss occurs due to moisture loss, and mass losses at 260-300°C are mostly due to thermal degradation of hemicellulose in the biomass structure.

Torrefaction process decomposed the reactive hemicellulose fraction by the removal of oxygen from biomass with temperature and residence time. While the yield of biofuel decreased, energy density and the calorific value increased [6].

International Natural Science, Engineering and Materials Technology Conference

Sep 9-10, 2019, İstanbul / TURKEY

Table 1. The Results of Design Expert for Torrefaction Process

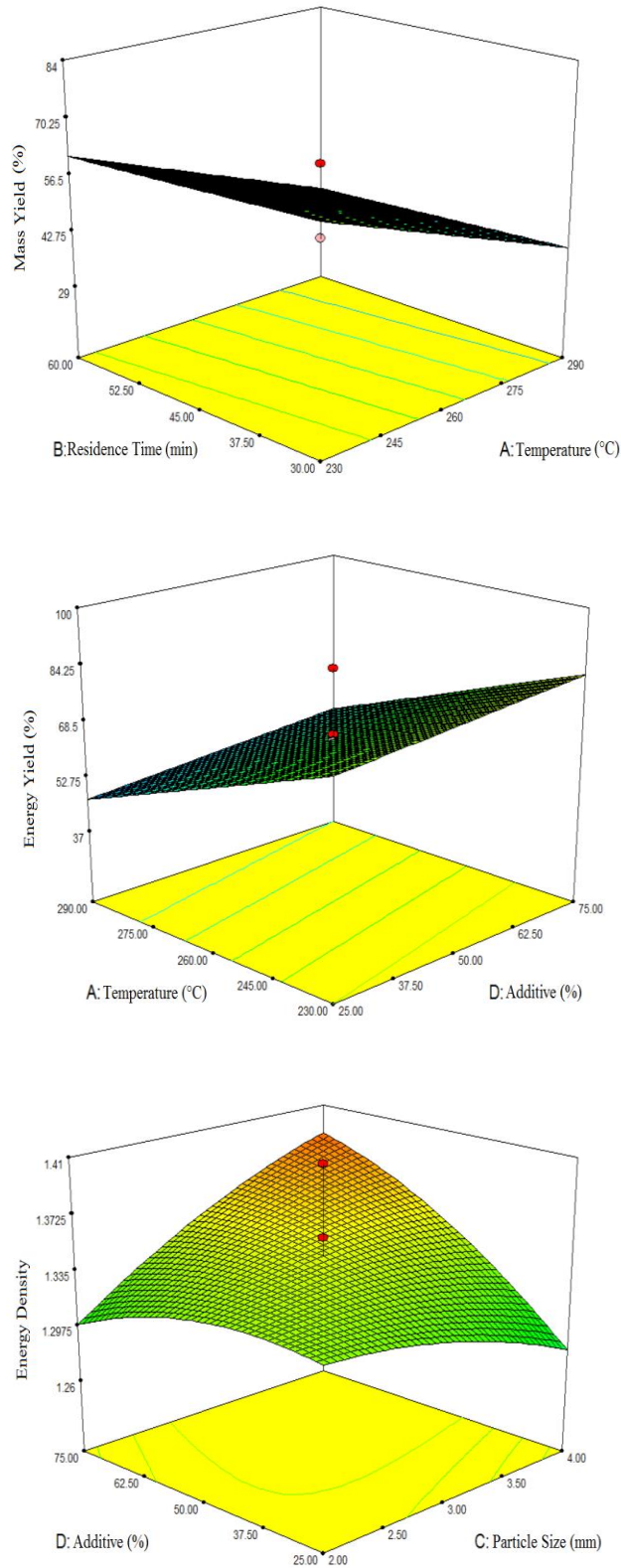| No	Temperature (°C)	Residence Time (min)	Particle Size (mm)	Carob (w/w, %)	Mass Yield (%)	Energy Yield (%)	Energy Density	Calorie (cal/g)
1	260	45	3	100	55,64633	78,18118	1,404966	5330,291824
2	230	60	4	75	57,27127	70,94604	1,238772	4807,392376
3	260	45	3	50	59,44805	83,56624	1,405702	5439,605852
4	260	45	3	50	41,18488	55,91910	1,357758	5254,079194
5	260	45	5	50	44,37624	59,98963	1,351841	5346,428029
6	290	60	2	75	34,35058	43,46150	1,265233	5143,731836
7	290	60	2	25	36,98434	47,13514	1,274462	5005,455536
8	290	60	4	75	37,48001	50,56660	1,349162	5235,791107
9	290	30	4	25	39,13442	49,12646	1,255326	5067,394277
10	260	75	3	50	45,66193	61,40126	1,344692	5203,518695
11	230	60	2	25	70,46360	85,23647	1,209653	4750,915656
12	230	60	4	25	58,10138	69,22542	1,191459	4809,580598
13	230	30	2	75	63,84613	76,89392	1,204363	4896,266436
14	230	30	4	25	58,82259	71,70059	1,218929	4920,470745
15	230	30	4	75	67,81468	84,79260	1,250358	4852,354173
16	200	45	3	50	83,56333	99,02562	1,185037	4585,704037
17	290	30	2	25	37,77618	48,14153	1,274388	5005,165971
18	260	45	3	50	47,22028	62,50364	1,323661	5122,133609
19	260	45	3	50	47,44605	63,34959	1,335192	5166,754949
20	260	45	3	0	40,06474	50,48689	1,260133	5023,354816
21	260	45	3	50	47,39852	63,02894	1,329766	5145,758788
22	230	60	2	75	62,47155	73,44993	1,175734	4779,877928
23	260	45	3	50	48,40809	65,01598	1,343081	5197,28293
24	290	30	2	75	45,96912	54,88303	1,193911	4853,774041
25	290	30	4	75	44,59036	63,03771	1,413707	5486,277081
26	320	45	3	50	29,67826	37,62243	1,267677	4905,492798
27	290	60	4	25	31,86954	38,77845	1,216787	4911,823513
28	260	45	1	50	47,81120	64,75342	1,354357	5343,532383
29	260	15	3	50	46,14106	61,86694	1,340822	5188,540748
30	230	30	2	25	69,77891	88,09624	1,262505	4958,494742

Figure 2. 3D graphs for interactions of process conditions

4. CONCLUSION

Torrefaction is an important pre-treatment convertional process in order to improve the biomass with a high quality properties such as grindability, energy density etc. A decrease in mass yield of biofuel was observed during torrefaction. This decrease may be due to thermal effects caused by depolymerization and moisture loss in the biomass. It can be seen that carbon ratio in structure increased due to losing oxygen and hydrogen. In this way, the net calorific value is affected and the biofuel becomes energy denser. In conclusion, as the energy density of torrefied product is significantly higher compared to untreated product, larger transportation distances can be allowed.

ACKNOWLEDGMENTS

REFERENCES

[1] N. Saraçoğlu, Modern energy forestry, biomass energy production and analyzes from forests, Meeting Report of General Directorate of Forestry, Ankara (2008).

[2] J. Poudel, T.I. Ohm and S.C. Oh, A study on torrefaction of food waste, Fuel, 140, 275–281 (2015).

[3] M. Phanphanich and A. Mani, Impact of torrefaction on the grindability and fuel characteristics of forest biomass, Bioresource Technology, 102, 1246-1253 (2011).

[4] A. Pimchuai, A. Dutta and P. Basu, Torrefaction of agriculture residue to enhance combustible properties, Energy Fuels, 24(9), 4638-4645 (2010).

[5] B. Arias, C. Pevida, J. Fermoso, M.G. Plaza, F. Rubiera and J.J. Pis, Influence of torrefaction on the grindability and reactivity of woody biomass, Fuel Processing Technology, 89, 169-175 (2008).

[6] M.J.C. van der Stelt, H. Gerhauser, J.H.A. Kiel and K.J. Ptasinski, Biomass upgrading by torrefaction for the production of biofuels: A review, Biomass and Bioenergy, 35, 3748-3762 (2011).

ANTIBACTERIAL AND ANTIFUNGAL ACTIVITIES OF THREE EXTRACTS FROM *CIRSIUM ITALICUM* (SAVI) DC.

H. Caliskan[1], D. Gulen[2], M. Ozer[1], T. Sabudak[1]

[1]*Department of Chemistry, Faculty of Science and Arts, Namik Kemal University, Tekirdag, TURKEY*
[2]*Department of Medical Microbiology School of Medicine, Namik Kemal University, Tekirdag, TURKEY*

E-mail: hlmcn.clskn@gmail.com

Abstract:

The objective of this study was to investigate the effect of antibacterial and antifungal activity on the raw extracts of *Cirsium italicum* (Savi) DC. Microdilution methods were used to investigations the antibacterial and antifungal effects of extracts obtained from the plant. Six micro-organisms were used for antimicrobial activity testing *Staphylococcus aureus*, *Bacillus subtilis*, *Escherichia coli*, *Pseudomonas aeruginosa*, *Proteus mirabilis*, *Salmonella typhimurium*. Six fungus were used for antifungal activity testing; *Candida albicans*, *Candida parapilosis*, *Candida glabrata*, *Candida krusei*, *Aspergillus funigatus*, *Penicillium chrysogenum*. The results showed that the antibacterial activity of *C. italicum* on *B. subtilis* was found with a MIC (Maximum Inhibition Concentration) level of 2.38 mg/ml and inhibition effects were determined higher than *C. italicum* ethyl acetate extract on the other bacterial strains. The highest inhibition effect of *C. italicum* ethyl acetate extract was found *C. parapilosis* with a MIC level of 1.98 mg/ml. The highest antibacterial and antifungal inhibition effect was determined in ethyl acetate extract of *C. italicum*. The present work is the first report on the antibacterial and antifungal activities of dichloromethane, ethyl acetate and n-butanol extracts of *C. italicum*.

Keywords: *Cirsium, C. italicum,* antibacterial activity, antifungal activity.

1. INTRODUCTION

Antibiotics are one of our most important weapons in fighting bacterial and fungal infections and have greatly benefited the health-related quality of human life since their introduction [1]. But, in recent years, many types of microorganisms have become resistant to antibiotics. The increase of multidrug resistant strains of fungus and bacteria caused reduced number of drugs are available. So it is necessary to discover new classes of antifungal and antibacterial compounds that inhibit these resistans mechanisms. This has led to a search for the therapeutic alternatives, particully among medicinal plants [2].

Cirsium italicum (Savi) DC. belongs to the Asteraceae family and is an annual herb plant natively grown mainly Turkey. In traditional medicine, some parts of *Cirsium* species, especially the roots or whole plants have been used for treatment some diseases such as hemorrhaging, inflammation of the liver and kidney, and a variety of abdominal and intestinal disorders [3]. It was reported that the extract from *C. italicum* prepared by boiling seeds can be effective for the treatment of haemorrhoid [4].

In our earlier communication, we have reported the antioxidant activity of new flavonoids and phenolic compounds from *C. italicum* and *C. creticum* subsp. *creticum* were determined, respectively [5, 6]. The antibacterial and antifungal activities of n-hexane extract of *C. italicum* have also been reported by Gulen et al. (2019) [7]. Here in, we wish to report the antibacterial and antifungal activities of the dichloromethane, ethyl acetate and n-butanol extracts of *C. italicum*. This is reported the first time from *C. italicum* three extracts in the literature.

2. MATERIAL AND METHODS

Plant material and extractions

C. italicum (NGBB 6807) which is wild plant species in Trakya region (Turkey), were collected in June 2017. The plants identified by Namik Kemal University, Faculty of Science and Arts, Department of Biology. The whole plant was ground and powder-homogenized after drying at room temperature. The extractions were carried out for 3 days each time, and a total of 4 times maceration was performed in 80% methanol. After evaporation of solvent in the evaporator, the crude extract was obtained. A small amount of water was added to the resulting crude extract, which was back-extracted with n-hexane, dichloromethane, ethyl acetate and n-butanol in polarity order. The solvents were evaporated to obtain each crude extracts.

Determination of antibacterial and antifungal activities

Microdilution methods were used to investigations the antibacterial and antifungal effects of extracts obtained from the plant. Antibacterial activitiy was carried out on two gram positive bacterial strains (*Staphylococcus aureus* (ATCC 43300), *Bacillus subtilis* (NRRL NRS-744)) and four gram negative bacterial strains (*Escherichia coli* (ATCC 35218), *Pseudomonas aeruginosa* (ATCC 27853), *Proteus mirabilis* (ATCC 12453), *Salmonella typhimurium* (ATCC 14028)) were grown in nutrient agar at 37°C for 18 hours. Antifungal activity test was carried out against six fungal strains; *Candida albicans* (ATCC 90028), *Candida glabrata* (ATCC 90030), *Candida parapsilosis* (ATCC 22019), *Candida krusei* (ATCC 6258), *Penicillium chrysogenum* (ATCC 48271) and *Aspergillus fumigatus* (ATCC 204305) were grown in Sabouraud dextrose agar (SDA) at 27°C. For both antimicrobial and antifungal testing, sterile microtiter plates with 96 "U" type wells were used. As bacterial growth medium Mueller hinton broth (Gibco®) was used.

For fungus growth RPMI 1640-L glutamin (Gibco®) was used as the medium and pH was adjusted to 7 by adding 34.53 gr/l MOPS as buffer. Prepared medium was sterilized by filtration and stored at +4°C until use. Bacterial inoculums prapared in Mueller hinton broth by using a Densitometer (Densimat; BioMèrieux). The McFarland bacterial suspension standart at a density of 0.5, approximately 108 CFU/ml. Fungus inoculums were prepared in RPMI 1640-L glutamin. By this process, stock yeast suspensions containing 1-5x10^6 cells/ml were obtained. Stock yeast suspension was diluted first with 1/50 and then 1/20, resulting in a final concentration of 1-5x10^3 cells/ml to be used in the test. The stock concentrations of extracts obtained from the plant for *C. italicum* was 1411 mg/ml. Serial dilutions to 12 wells are made. As antimicrobic control Penicillin G and Gentamicin was used as standart according to CLSI M-100 (2017) [8]. for determination of antibacterial activity. For antifugal control, Fluconazole as was used as standart for determination antifungal activity according to CLSI M27-A3 (2008) [9].

3. RESULTS AND DISCUSSION

The antibacterial and antifungal activity three extracts of *C. italicum* is summerized at Table 1 and Table 2. The antibacterial activity of *C. italicum* on *B. subtilis* was found with a MIC level of 2.38 mg/ml and inhibition effects were determined higher than *C. italicum* ethyl acetate extract the other bacterial strains (Table 1). The ethyl acetate exract showed higher antibacterial activity than n-butanol, dichloromethane and n-hexane. Gulen et al. (2019) [7] reported that results of antibacterial activity for n-hexane extract.

Table 1. Antibacterial activity of *Cirsium italicum* and references as MIC values.

Bacteria	Extracts (mg/ml)			Standart (mg/ml)
	Dichloromethane	Ethyl acetate	n-Butanol	Penicillin G[1] / Gentamicin
Staphylococcus aureus	-	9.5	94.5	0.125[1]
Bacillus subtilis	4.56	2.38	47.25	0.125
Escherichia coli	145.75	19	47.25	0.125
Pseudomonas aeruginosa	-	19	23.63	0.125
Proteus mirabilis	145.75	19	47.25	0.125
Salmonella typhimurium	-	19	47.25	0.125

[1] Penicillin was used only *Staphylococcus aureus*.

The highest inhibition effect of *C. italicum* ethyl acetate extract was found againts *C. parapilosis* with a MIC level of 1.98 mg/ml (Table 2). *C. italicum* ethyl acetate extract also showed higher inhibitory effect against *C. krusei* than other fungal strains. For n-butanol and dichloromethane extracts, the results established that the obtained extracts were unable to inhibit the grown of tested fungal strains. Gulen et al. (2019) [7] reported that results of antifungal activity for n-hexane extract.

Table 2. Antifungal activity of *Cirsium italicum* and references as MIC values.

Fungus	Extracts (mg/ml)			Standart (mg/ml)
	Dichloromethane	Ethyl acetate	n-Butanol	Fluconazole
Candida albicans	71.38	15.81	32.94	0.002
Candida parapilosis	8.92	1.98	4.12	0.032
Candida glabrata	142.75	31.63	32.94	0.002
Candida krusei	8.92	3.95	8.23	0.125
Aspergillus funigatus	35.69	15.81	16.47	0.256
Penicillium chrysogenum	17.84	31.63	32.94	0.256

4. CONCLUSION

The highest antibacterial inhibition effect of *C. italicum* obtained from ethyl acetate extract and against *Bacillus subtilis* (NRRL NRS-744) with a MIC level of 2.38 mg/ml. The highest antifungal inhibition effect was determined in ethyl acetate extract and against *Candida parapsilosis* (ATCC 22019) with a MIC level of

1.98 mg/ml. This present work, we can conclude *C. italicum* might have a possible uses as antibacterial, antifungal agent in medicinal uses.

ACKNOWLEDGMENTS

REFERENCES

[1] Janovska, D., Kubıkova, K., Kokoska, L., Screening for antimicrobial activity of some medicinal plants species of traditional Chinese medicine, Czech Journal of Food Sciences, 21(3), 107-110, 2003.

[2] Kirilmis, C., Ahmedzade, M., Servi, S., Koca, M., Kizilgil, A., Kazaz, C., Synthesis and antimicrobial activity of some novel derivatives of benzofuran: Part 2. The synthesis and antimicrobial activity of some novel 1-(1-benzofuran-2-yl)-2-mesitylethanone derivatives, European Journal of Medicinal Chemistry, 43(2), 300-308, 2008.

[3] Kim, J.G., Illustrated Natural Drugs Encyclopedia (Color Edition) Seoul, Nam San Dang, Seuol. 1, 37, 1997.

[4] Yesilada, E., Sezik, E., Honda, G., Takaishi, Y., Takeda, Y., Tanaka, T., Traditional medicine in Turkey, IX Folk medicine in North-west Anatolia, Journal of Ethnopharmacology, 64(3), 195-210, 1999.

[5] Sabudak, T., Caliskan, H., Orak, H.H., Ozer M., Biological activity of new flavonoids and phenolic compounds from *Cirsium italicum* (Savi) DC., Natural Product Research, Published online: 20 June 2019 doi.org/10.1080/14786419.2019.1630121.

[6] Sabudak, T., Ozer, M., Orak, H.H., Caliskan, H., Antioxidant Activity of Five New Phenolic Compounds from *Cirsium creticum* subsp. *creticum*, Phytochemistry Letters, 31, 181-186, 2019.

[7] Gulen, D., Sabudak, T., Orak, H.H., Caliskan, H., Ozer, M., Volatiles, Antibacterial and Antifungal Activities of *Cirsium creticum* and *Cirsium italicum,* Acta Scientiarum Polonorum Hostorum Cultus, 18(5) (Accepted), 2019.

[8] Clinical and Laboratory Standards Institute, *Performance Standards for Antimicrobial Susceptibility Testing Twenty-seventh Edition*, CLSI M-100, Clinical and Laboratory Standards Institute, Wayne, PA, 2017.

[9] Clinical and Laboratory Standards Institute, *Reference Method for Broth Dilution Antifungal Susceptibility Testing of Yeasts; Approved Standard Third Edition*, CLSI M27-A3, Clinical and Laboratory Standards Institute, Wayne, PA, 2008.

ANTIBACTERIAL AND ANTIFUNGAL ACTIVITIES OF THREE EXTRACTS FROM *CIRSIUM CRETICUM SUBSP. CRETICUM*

M. Ozer[1], D. Gulen[2], H. Caliskan[1], T. Sabudak[1]

[1] Department of Chemistry, Faculty of Science and Arts, Namik Kemal University, Tekirdag, TURKEY
[2] Department of Medical Microbiology School of Medicine, Namik Kemal University, Tekirdag, TURKEY

E-mail: merweozer92@gmail.com

Abstract

The objective of this study was to investigate the effect of antibacterial and antifungal activity on the raw extracts of *Cirsium creticum* subsp. *creticum* L. Microdilution methods were used to investigations the antibacterial and antifungal effects of extracts obtained from the plant. Six micro-organisms were used for antimicrobial activity testing; *Staphylococcus aureus, Bacillus subtilis, Escherichia coli, Pseudomonas aeruginosa, Proteus mirabilis, Salmonella typhimurium*. Six fungus were used for antifungal activity testing; *Candida albicans, Candida parapilosis, Candida glabrata, Candida krusei, Aspergillus funigatus, Penicillium chrysogenum*. The results showed that the antibacterial activity of *C. creticum* on *B. subtilis, E. coli, P. aeruginosa* and *P. mirabilis* was found similar with a MIC (Maximum Inhibition Concentration) level of 31.25 mg/ml and inhibition effects were determined higher than *C. creticum* methanol extract the other bacterial strains. The highest antifungal inhibition effect of *C. creticum* methanol extract was found againts *C. albicans, C. parapilosis* and *A. fumigatus* with a MIC level of 7.8125 mg/ml. *C. creticum* methanol extract also showed higher inhibitory effect against *C. glabrata and C. krusei* than other fungal strains. The highest antibacterial and antifungal inhibition effect of *C. creticum* obtained from methanol extract. The present work is the first report on the antibacterial and antifungal activities of methanol, diethyl ether and ethyl acetate extracts of *C. creticum*.

Keywords: *Cirsium, C. creticum*, antibacterial activity, antifungal activity.

1. INTRODUCTION

Plants have been classified as a principal source of medicinal agents for centuries and a great number of new drug components have been isolated from natural plant sources and it was used in traditional medicine. In recent years, natural products with antimicrobial effect gained importance in order to eliminate the use of synthetic antibiotics which cause the resistance of microorganisms and can exhibit side effects to human health. Natural products from plant may offer novel agents for antimicrobial use [1].

The Asteraceae family is one of the largest families of flowering plants (almost 1600 genera and over 23,000 species) [2] and *Cirsium* is one of its widespread species. *Cirsium* species have been defined to have a wide range of biological activities, including anticancer [3], antidiabetic [4], antimicrobial [5-10], antibacterial [11-13], antifungal [12], antiviral [12] and antioxidant activities [8,14-15]. Genc and Ozhatay [16] reported *C. creticum* are used as cure against mushroom poisoning. Also, it was explored that *C. creticum*'s stem can be eaten as raw vegetable or cooked in a meal after peeling its barks [17].

In our previous studies, antioxidant activity of new phenolic compounds and flavonoids from *C. creticum* subsp. *creticum* and *C. italicum* were determined, respectively [18,19]. Besides, antibacterial and antifungal activities of *n*-hexane extract of *C. creticum* have been detected [20]. The objective of this study was to investigate the effect of antibacterial and antifungal activities on the methanol, diethyl ether and ethyl acetate extracts of *C. creticum*. In the literature, there is no study on the antibacterial and antifungal activities of methanol, diethyl ether and ethyl acetate extracts of *C. creticum*.

2. MATERIAL AND METHODS

2.1. Plant material and preparation of extracts

The plant sample, which is a wild plant species from Trakya region, was collected in June 2016. It was classified by E. Cabi, Namik Kemal University, as *Cirsium creticum* subsp. *creticum* L. and a voucher specimen has been deposited in the Biology Department, Namik Kemal University (NGBB 7230). The whole plant were dried (583.74 g) and then cut into small pieces. Afterwards, they were macerated at room temperature with *n*-hexane, diethyl ether, ethyl acetate and methanol, respectively. The extracts were concentrated by using a rotary evaporator under vacuum.

2.2. Determination of antibacterial and antifungal activities

Microdilution methods were used to investigations the antibacterial and antifungal effects of extracts obtained from the plant. Antibacterial activity was carried out on two gram positive bacterial strains (*Staphylococcus aureus* (ATCC 43300), *Bacillus subtilis* (NRRL NRS-744)) and four grams negative bacterial strains (*Escherichia coli* (ATCC 35218), *Pseudomonas aeruginosa* (ATCC 27853), *Proteus mirabilis* (ATCC 12453), *Salmonella typhimurium* (ATCC 14028)) were grown in nutrient agar at 37 °C for 18 hours. Antifungal activity test was carried out against six fungal strains; *Candida albicans* (ATCC 90028)*, Candida glabrata* (ATCC 90030)*, Candida parapsilosis* (ATCC 22019), *Candida krusei* (ATCC 6258), *Penicillium chrysogenum* (ATCC 48271) and *Aspergillus fumigatus* (ATCC 204305) were grown in Sabouraud dextrose agar (SDA) at 27 °C. For both antimicrobial and antifungal testing, sterile microtiter plates with 96 "U" type wells were used. As bacterial growth medium Mueller hinton broth (Gibco®) was used.

For fungus growth RPMI 1640-L glutamin (Gibco®) was used as the medium and pH was adjusted to 7 by adding 34.53 gr/l MOPS as buffer. Prepared medium was sterilized by filtration method and stored at +4 °C until use. Bacterial inoculums prapared in Mueller hinton broth by using a Densitometer (Densimat; BioMèrieux). The McFarland bacterial suspension standart at a density of 0.5, approximately 10^8 CFU/ml. Fungus inoculums were prepared in RPMI 1640-L glutamin. By this process, stock yeast suspensions containing $1-5 \times 10^6$ cells/ml were obtained. Stock yeast suspension was diluted first with 1/50 and then 1/20, resulting in a final concentration of $1-5 \times 10^3$ cells/ml to be used in the test. The stock concentrations of extracts obtained from the plant was 1000 mg/ml for *C. creticum*. Serial dilutions to 12 wells are made. As antimicrobic control, Penicillin G and Gentamicin was used as standart according to CLSI M-100 [21] for determination of antimicrobial activity. For antifungal control, Fluconazole as was used as standart for determination antifungal activity according to CLSI M27-A3 [22].

3. RESULTS AND DISCUSSION

The antibacterial and antifungal activities of *C. creticum* extracts as summerized at Table 1. The antibacterial activity of *C. creticum* on *B. subtilis, E. coli*, *P. aeruginosa* and *P. mirabilis* was found similar with a MIC level of 31.25 mg/ml and inhibition effects were determined higher than *C. creticum* methanol extract the other bacterial strains. The methanol exract showed higher antibacterial activity than ethyl acetate, diethyl ether and *n*-hexane. Gulen et al. [20] reported that results of antifungal activity for *n*-hexane extract.

The highest inhibition effect of *C. creticum* methanol extract was found againts *C. albicans*, *C. parapilosis* and *A. fumigatus* with a MIC level of 7.8125 mg/ml. *C. creticum* methanol extract also showed higher inhibitory effect against *C. glabrata* and *C. krusei* than other fungal strains. For ethyl acetate and diethyl ether extracts, the results established that the obtained extracts was unable to inhibit the grown of tested fungal strains. Gulen et al. [20] reported that results of antifungal activity for *n*-hexane extract.

Table 1. Antibacterial and antifungal activities of raw extract from C. creticum.

Bacteria	Extracts (mg/ml)			Standart (mg/ml)
	Methanol	Ethyl acetate	Diethyl ether	Penicillin G[1] / Gentamycin
Staphylococcus aureus	125	125	125	0.125[1]
Bacillus subtilis	31.25	125	62.50	0.125
Escherichia coli	31.25	62.50	31.25	0.125
Pseudomonas aeruginosa	31.25	125	125	0.125
Proteus mirabilis	31.25	125	125	0.125
Salmonella typhimurium	31.25	125	125	0.125
Fungus				**Fluconazole**
Candida albicans	7.8125	-	-	0.002
Candida parapilosis	7.8125	-	-	0.032
Candida glabrata	15.625	250	-	0.002
Candida krusei	15.625	250	250	0.125
Aspergillus funigatus	7.8125	250	-	0.256
Penicillium chrysogenum	62.50	250	-	0.256

[1] Penicillin was used only *Staphylococcus aureus*.

4. CONCLUSION

The highest antibacterial inhibition effect of *C. creticum* obtained from ethyl acetate, diethyl ether extract and against *S. aureus, P. aeruginosa, P. mirabilis, S. typhimurium* with a MIC level of 125 mg/ml. The highest antifungal inhibition effect was determined in ethyl acetate extract and against *C. glabrata, C. krusei, A. Funigatus, P. chrysogenum* with a MIC level of 250 mg/ml. The obtained results in this study present the first report on the antibacterial and antifungal activities.

In conclusion, the results obtained confirm the folkoric anticipation of the antibacterial and antifungal influence and the therapeutic applications of the examined plants. The outcomes of these experiments showed that medicinal plants, *C. creticum* can to be a great alternative for synthetic preparations and that is the reason for an extensive assessment of their antibacterial and antifungal activities. This present work, we can finalize *C. creticum* might have a possible uses as antibacterial, antifungal agent in medicinal uses.

ACKNOWLEDGMENTS

REFERENCES

[1] Obeidat, M., Shatnawi, M., Al-alawi, M., Al-Zu'bi, E., Al-Dmoor, H., Al-Qudah, M., El-Qudah, J., Otri, I. Antimicrobial activity of crude extracts of some plant leaves, Research Journal of Microbiology, 7(1), 59-67, 2012.

[2] Bohm, B.A., Stuessy, T.F., Flavonoids of the sunflower family, Austria: Springer-Verlag/Wien, 2001.

[3] Liu, S., Zhang, J., Lı, D., Lıu, W., Luo, X., Zhang, R., Lı, L., Zhao, J., Anticancer activity and quantitative analysis of flavone of *Cirsium japonicum* DC., Natural Product Research, 21, 915–922, 2007.

[4] Perez, G.R., Ramirez, L.M., Vargas, S.R., Effect of *Cirsium pascuarens*e on blood glucose levels of normoglycaemic and alloxan- diabetic mice, Phytotherapy Research, 15, 552-554, 2001.

[5] Barbour, E.K., Al-Sharif, M., Sagherian, V.K., Habre, A.N., Talhouk, R.S., Talhouk, S.N., Screening of selected indigenous plants of Lebanon for antimicrobial activity, Journal of Ethnopharmacy, 93, 1-7, 2004.

[6] Loizzo, M.R., Statti, G.A., Tundis, R., Conforti, F., Ando, S., Menichini, F., Antimicrobial activity and cytotoxicity of *Cirsium tenoreanum*, Fitoterapia, 75, 577– 580, 2004.

[7] Nazaruk, J., Jakoniuk, P., Flavonoid composition and antimicrobial activity of *Cirsium rivulare* (Jacq.) All. Flowers, Journal Ethnopharmacology, 102, 208, 2005.

[8] Nazaruk, J., Czechowska, S.K., Markiewicz, R., Borawska, M.H., Polyphenolic compounds and in vitro antimicrobial and antioxidant activity of aqueous extracts from leaves of some *Cirsium species*, Natural Product Research, 22, 1583–1588, 2008.

[9] Kenny, O., Smyth, T.J., Walsh, D., Kelleher, C.T., Hewage, C.M., Brunton, N.P., Investigating the potential of under-utilised plants from the Asteraceae family as a source of natural antimicrobial and antioxidant extracts, Food Chemistry, 161, 79-86, 2014.

[10] Karasakal, A., Demirci, A.Ş., Demirok, N.T., Cabi, E., Antioxidant, antimicrobial activities and total flavonoid contents of *Cirsium bulgaricu*m *DC.* leaf extracts, Marmara Pharmaceutical Journal, 19, 43-51, 2015.

[11] Borawska, M.H., Czechowska, S.K., Markiewicz, R., Socha, K., Nazaruk, Pałka, J.J., Isidorov, V.A., Enhancement of antibacterial effects of extracts from *Cirsium* species using sodium picolinate and estimation of their toxicity, Natural Product Research, 24, 6, 554-561, 2010.

[12] Deliorman Orhan, D., Özçelik, B., Özgen, S., Ergun, F., Antibacterial, antifungal, and antiviral activities of some flavonoids, Microbiological Research, 165, 496-504, 2010.

[13] Kozyra, M., Biernasiuk, A., Malm, A., Chowaniec, M., Chemical compositions and antibacterial activity of extracts obtained from the inflorescences of *Cirsium canum* (L.) all., Natural Product Research, 29, 21, 2059-2063, 2015.

[14] Nazaruk, J., Antioxidant activity and total phenolic contents in *Cirsium* five species from north- east region of Poland, Fitoterapia, 79, 194, 2008.

[15] Yin, Y., Heo, S-II., Wang, M-H., Antioxidant and anticancer activities of methanol and water extracts from leaves of *Cirsium japonicum*, Journal of Applied Biological Chemistry, 51, 160-164, 2008.

[16] Genc, G.E., Ozhatay N., An ethnobotanical study in Çatalca (European Part of İstanbul) II., Turkish Journal Pharmaceutical Sciences, 3, 73-89, 2006.

[17] Kızılarslan, C., Ozhatay, N., An ethnobotanical study of the useful and edible plants of İzmit, Marmara Pharmaceutical Journal, 16, 134-40, 2012.

[18] Sabudak, T., Ozer, M., Orak, H.H., Caliskan, H., Antioxidant Activity of Five New Phenolic Compounds from *Cirsium creticum* subsp. *creticum*, Phytochemistry Letters, 31, 181-186, 2019.

[19] Sabudak, T., Caliskan, H., Orak, H.H., Ozer, M., Biological Activity of New Flavonoids and Phenolic Compounds from *Cirsium italicum* (Savi) DC., Natural Product Research, Published Online 20 June 2019. https://doi.org/10.1080/14786419.2019.1630121.

[20] Gulen, D., Sabudak, T., Orak, H.H., Caliskan, H., Ozer, M., Volatiles, Antibacterial and Antifungal Activities of *Cirsium creticum* and *Cirsium italicum,* Acta Sci Polo Hos Cultus (Accepted), 2019.

[21] Clinical and Laboratory Standards Institute, Reference Method for Broth Dilution Antifungal Susceptibility Testing of Yeasts; Approved Standard Third Edition, CLSI M27-A3. Clinical and Laboratory Standards Institute - Wayne – PA, 2008.

[22] Clinical and Laboratory Standards Institute, Performance Standards for Antimicrobial Susceptibility Testing Twenty-seventh Edition, CLSI M100, Clinical and Laboratory Standards Institute - Wayne – PA, 2017.

ANNIHILATOR CONDITIONS ON RINGS

Yeliz KARA

Department of Mathematics, Faculty of Arts and Sciences, Bursa Uludağ University, Bursa, TURKEY.

E-mail: yelizkara@uludag.edu.tr

Recall a ring R is *Baer* if the right annihilator of each nonempty set is generated by an idempotent. The concept of Baer rings has its roots in operator algebras and functional analysis. This class of rings has close links to C*-algebras and von Neumann algebras. A ring R is *quasi-Baer* if the right (left) annihilator of each ideal is generated by an idempotent element of R. Each of these conditions (Baer and quasi-Baer) have certain advantages over the other. In general, the Baer condition works well with one-sided ideals, whereas the quasi-Baer condition works well with two-sided ideals. Therefore, it is natural to investigate a class of rings which is strictly between the Baer and quasi-Baer classes. To this end, we investigate a new class of ring which satisfies the former condition. We present our results including some applications to polynomial rings and matrix rings.

Keywords: Baer rings, quasi-Baer rings, projection invariance.

1. INTRODUCTION

The concept of Baer rings dates back to the theory of von Neumann algebras. In 1936, Murray and von Neumann developed the notion of von Neumann algebras (also called *W*-algebras*) in an attempt to provide a rigorous mathematical model for quantum theory [9]. Their theory was based on rings of operators on a Hilbert space [7]. Rickart in 1946 studied C*-algebras which satisfy the condition that the right annihilator of every single element is generated by a projection (an idempotent e is called projection if $e = e*$). Rickart also showed that all von Neumann algebras satisfy this property [8]. Motivated by the work of Murray, von Neumann and Rickart, Kaplansky showed that von Neumann algebras, in fact, satisfied a stronger annihilator condition, namely, that these are rings with identity in which the right annihilator of any nonempty subset is generated by an idempotent [6]. He named a ring with this property a *Baer ring*. Kaplansky recognized that the notions of a Baer ring and a Baer *-ring provide a framework to study the algebraic properties of operator algebras. Clark called a ring *quasi-Baer* if the left annihilator of every ideal is generated by an idempotent [4]. Observe that all Baer rings and prime rings are quasi-Baer. In contrast to Baer rings, it was shown that the quasi-Baer ring property does transfer to several extensions, such as full and triangular matrix extensions as well as polynomial ring extensions of a quasi-Baer ring R.

Another weaker form of the Baer ring property has been defined recently. A ring R is called π-*Baer* provided that the right annihilator of each projection invariant left ideal Y (i.e., $eY \subseteq Y$ for all $e = e^2 \in R$) is generated by an idempotent element of R [3]. Observe that this class of rings is located strictly between the classes of Baer and quasi-Baer rings. It is proved that the π-Baer property is inherited by the full and triangular matrix rings extensions and certain polynomial extensions.

Throughout this paper, all rings are associative with unity and R denote such a ring. For a nonempty subset I of R, $I \leq R_R, I \unlhd R, I \unlhd_p R_R$, $Mat_n(R)$ and $T_n(R)$ denote I is a right ideal of R, I is an ideal of R, I is a projection invariant right ideal of R, the n-by-n full matrix ring over R, and the n-by-n upper triangular matrix ring over R, respectively. Let $\emptyset \neq X \subseteq R$. Then $r_R(X)$ and $l_R(X)$ stand by the right annihilator of X in R, and the left annihilator of X in R, respectively. Recall that a ring is *Abelian* if every idempotent elements are central. For other terminology and unknown definitions, we refer to [1], [2], and [5].

2. BASIC RESULTS

In this section, we present the definitions and relations between the classes of rings.

Definition 2.1. [5, 6] R is called a *Baer* ring if the right annihilator of every nonempty subset X of R is generated by an idempotent element.

Observe that any domain, the endomorphism ring of any vector space, the ring of all bounded linear operators on a Hilbert space, every von Neumann algebra and AW*-algebra are the examples of Baer rings.

It is investigated that how much the Baer property extends to the various its ring extensions such as matrix rings and polynomial extensions. In general, it is proved that Baer condition does not transfer from the base ring to the its extensions.

Example 2.2. Let $R = \begin{bmatrix} \mathbb{Z} & \mathbb{Z} \\ 0 & \mathbb{Z} \end{bmatrix} = \{\begin{bmatrix} a & b \\ 0 & c \end{bmatrix} : a, b, c \in \mathbb{Z}\}$, and $e_{ij} \in R$ be the matrix with 1 in the (i,j)-position and 0 elsewhere. Consider $\alpha = 2e_{11} + e_{12} \in R$ and $r_R(\alpha)$. Then $r_R(\alpha)$ is not generated by an idempotent of R. Therefore R is not a Baer ring, even though $\mathbb{Z}$ is a Baer ring.

The following result guarantees that when the Baer ring property transfers to the upper triangular matrix rings.

Proposition 2.3. [5] A is a division ring if and only if the upper triangular matrix ring over A, $T_n(A)$, is Baer for every positive integer n.

Example 2.4. Let $S = Mat_2(\mathbb{Z}[x])$. Then $\mathbb{Z}[x]$ is a Baer ring. Consider $\alpha = \begin{bmatrix} 2 & 0 \\ 0 & 0 \end{bmatrix} + \begin{bmatrix} 0 & 0 \\ 1 & 0 \end{bmatrix} x = \begin{bmatrix} 2 & 0 \\ x & 0 \end{bmatrix} \in S$. Note that $l_R(\alpha)$ is not generated by an idempotent of S. Thus S is not a Baer ring.

Example 2.4 shows that Baer ring property is not inherited by the full matrix rings and also the former property does not transfer to the polynomial rings. To this end, the next facts clarify that when Baer property works well with both full matrix ring and polynomial ring extensions.

Proposition 2.5. Let A be a commutative domain. Then A is a Prüfer domain if and only if $Mat_n(A)$ is a Baer ring for every $n > 1$.

Proposition 2.6. [1] Assume that R has no nonzero nilpotent elements. Then R is a Baer ring if and only if R[x], the polynomial ring over R, is a Baer ring.

Since the Baer property does not transfer to its various ring extensions without any additional conditions, classes of ring under somewhat weaker conditions are investigated.

Definition 2.7. [4] R is called a *quasi-Baer* ring if the right annihilator of every ideal X of R is generated by an idempotent element of R.

Notice that quasi-Baer ring property generalizes the Baer ring property. Thus, any Baer ring and any prime ring are examples of quasi-Baer rings. The following results explain that quasi-Baer ring property works better than Baer ring property in terms of its various ring extensions.

Proposition 2.8. R is a quasi-Baer ring if and only if $T_n(R)$, the n-by-n upper triangular matrix ring over R, is quasi-Baer for every $n > 1$.

Proposition 2.9. R is a quasi-Baer ring if and only if $Mat_n(R)$, the n-by-n full matrix ring over R, is quasi-Baer for every positive integer n.

Proposition 2.10. R is a quasi-Baer ring if and only if $R[x]$, the polynomial ring over R, is a quasi-Baer ring.

Observe that both Example 2.2 and Example 2.4 illustrate that the class of Baer rings is a proper subclass of the class of quasi-Baer rings.

3. A WEAKER VERSION OF BAER RING PROPERTY

Our motivation of this section is to investigate a weaker condition of Baer ring property which locates strictly between the Baer and the quasi-Baer conditions. Recall that a left ideal Y of R is called *projection invariant* in R if $Ye \subseteq Y$ for all $e = e^2 \in R$.

Definition 3.1. [3] A ring R is called *projection invariant Baer* (denoted, π-*Baer*) if for each projection invariant left ideal Y of R, there exists $c = c^2 \in R$ such that $r_R(Y) = cR$.

It is shown that π-Baer condition is left-right symmetric.

Proposition 3.2. R is Baer $\Rightarrow$ R is π-*Baer* $\Rightarrow$ R is quasi-Baer, but these implications are not reversible.
Proof. See the proof of [3, Theorem 2.1].

Proposition 3.3. (i) Assume that R is an Abelian ring. Then R is Baer if and only if R is π-Baer.

(*ii*) Let R be a ring such that R is generated by its idempotents. Then R is π-Baer if and only if R is quasi-Baer.

Proof. See the proof of [3, Corollary 2.2 and Lemma 2.3].

Corollary 3.4. If R is π-Baer, then $Mat_n(R)$, the n-by-n full matrix ring over R, is π-Baer.

Proof. Let R be π-Baer. Then $Mat_n(R)$ is quasi-Baer by Proposition 2.9 and Proposition 3.3. Note that $Mat_n(R)$ is generated by its all idempotent elements. Thus Proposition 3.3 (ii) yields the result.

Proposition 3.5. R is a π-Baer ring if and only if $T_n(R)$, the n-by-n upper triangular matrix ring over R, is π-Baer for every positive integer n.

Proposition 3.6. R is a π-Baer ring if and only if $R[x]$, the polynomial ring over R, is a π-Baer ring.

By using Propositions 3.5 and 3.6, it can be seen that Examples 2.2 and 2.4 are π-Baer rings which are not Baer. One might wonder whether the converse of Corollary 3.4 holds or not. The following example answer this situation in negative way.

Example 3.7. Consider a prime ring A which is not nonsingular. Hence A is quasi-Baer which is not π-Baer (see, [3, Theorem 2.1]). Let $R = Mat_n(A)$ for $n > 1$. Then R is quasi-Baer by Proposition 2.9. Moreover, R is π-Baer by Corollary 3.4.

Since π-Baer locates between the Baer and quasi-Baer properties, it is natural to notice that π-Baer property sometimes behaves like a Baer property, and it sometimes acts like a quasi-Baer property. For example, the ring extensions of a π-Baer ring is again a π-Baer (like the quasi-Baer property); whereas π-Baer property is not a Morita invariant property (like the Baer property).

REFERENCES

[1] Armendariz, E.P., A note on extensions of Baer and pp-rings. J.Austral.Math. Soc. 18, 470–473, 415, 1974.

[2] Birkenmeier, G.F., Park, J.K., Rizvi, S.T., Extensions of Rings and Modules, Birkhauser, Springer, New York, 2013.

[3] Birkenmeier, G.F., Kara, Y., Tercan, A., π-Baer rings, J. of Algebra and Appl., 17(2), Article ID 1850029, 19 pages, 2018.

[4] Clark, W.E., Twisted matrix units semigroup algebras, Duke Math. J., 34, 417-423, 1967.

[5] Kaplansky, I., Rings of Operators, Benjamin, New York, 1965.

[6] Kaplansky, I., Projections in Banach algebras, Ann. of Math., 53, 235-249, 1951.

[7] Murray, F. J., von Neumann, J., On rings of operators, Ann. Math., 37, 116-229, 1936.

[8] Rickart, C.E., Banach algebras with an adjoint operation, Ann. Math.,47, 528-550, 1946.

[9] von Neumann, J., Physical Applications of the Ergodic Hypothesis, Proc Natl Acad Sci, 18(3), 263–266, 1932.

MODULES WITH EXTENDING CONDITIONS

Yeliz KARA

Department of Mathematics, Faculty of Arts and Sciences, Bursa Uludağ University, Bursa, TURKEY.

E-mail: yelizkara@uludag.edu.tr

Abstract

Let M be a right R-module. Recall that M is called *extending (or CS)* if every submodule of M is essential in a direct summand of M. It is proved that extending property is closed under direct summands, however, it is not closed under direct sums, in general. Therefore, in order to avoid this unpleasant situation, it is natural to consider the extending property on suitable classes of submodules of M. To this end, it is investigated generalizations of extending modules including the following classes: (1) A module M is called *FI-extending (fully invariant-extending)* if every fully invariant submodule of M is essential in a direct summand of M. (2) A module M is called *π-extending (projection invariant-extending)* if every projection invariant submodule of M is essential in a direct summand of M. Not only module theoretic properties of the former classes are provided, but also the connections between these classes are presented. Furthermore, we attract our attention to the ring R as a right R-module which satisfies the above extending conditions.

Keywords: extending modules, projection invariant submodules, fully invariant submodules.

1. INTRODUCTION

All rings are associative with unity, and modules are unital right modules unless indicated otherwise. We use R to denote such a ring and M to denote such a module.

In this paper, we deal with the results which relate to extending conditions for modules. Recall from [4], [7] that a module M is called *extending* (or *CS*, or said to satisfy C_1) if every submodule of M is essential in a direct summand of M, or equivalently, every complement submodule of M is a direct summand of M. The origins of extending modules have two bases: (1) the work of von Neumann's' in continuous geometries and their relations as lattices of principal right ideals of regular rings, (2) the theory of injective modules. The class of extending modules contains the classes of injective modules, semisimple modules, and uniform modules.

Recall that extending property is inherited by direct summands (see, [7, Proposition 2.6]), but the former property is not closed under direct sums. For instance, let be the $\mathbb{Z}$-module such that $M = (\mathbb{Z}/\mathbb{Z}p) \oplus (\mathbb{Z}/\mathbb{Z}p^3)$ for any prime p; and let A be the $\mathbb{Z}$-module such that $A = (\mathbb{Z}/\mathbb{Z}p) \oplus \mathbb{Q}$. Then both M and A modules are not extending (see, [8]). To this end, it is investigated that when the extending property is closed under direct sums. Thus, the generalizations of extending modules with respect to various subsets of submodules are studied. These special subsets include projection invariant as well as fully invariant submodules. Recall from [5] that a submodule X of M is called *projection* (respectively, *fully*) *invariant* if $f(X) \subseteq X$ for all $f^2 = f \in End(M_R)$ (respectively, $f \in End(M_R)$). The set of projection (fully) invariant submodules includes many of the most significant submodules of a module (e.g., the Jacobson radical, the socle, the singular submodule of M). Motivating on these classes of submodules, a module M is called *projection invariant-extending*, π-*extending* [3], (resp., *fully invariant-extending*, *FI-extending* [1]) if every projection (resp., fully) invariant submodules are essential in a direct summand of M. Observe that extending implies π-extending, and π-extending implies FI-extending. However, it is shown that these three classes are different from each other (see, [3, Proposition 3.7]).

Module theoretic properties such as direct summands, and direct sums are provided for the classes of π-extending and *FI*-extending modules. In contrast to extending modules, the classes of both π-extending and *FI*-extending modules are closed under direct sums [3, Corollary 4.11]. However, it is shown that π-extending property is not inherited by direct summands (see, [3, Example 5.5] and [6, Theorem 2.4]). Therefore, it is natural to study on the conditions when the direct summands of π-extending modules are π-extending. On the other hand, it is still an open question whether the direct summand of FI-extending module is FI-extending or not (see, [1]).

Let X be a nonempty subset of M. Then $X \leq M, X \leq^{ess} M, X \leq^{\oplus} M, X \unlhd M, X \unlhd_p M$ denote X is the submodule of M, X is the essential submodule of M, X is the direct summand of M, X is the fully invariant submodule of M, X is the projection invariant submodule of M, respectively. Note that a ring R is *Abelian* if every idempotent of R is central. For unknown terminology and definitions, we refer to [2], [4], and [7].

2. BASIC RESULTS

In this section, preliminary results and basic definitions are provided. The connections between the classes of π-extending and FI-extending modules are presented.

Definition 2.1. Let N be a right R-submodule of M. N is called *projection* (resp., *fully*) *invariant* submodule of M if $f(N) \subseteq N$ for all $f = f^2 \in End(M_R)$ (resp., $f \in End(M_R)$).

Let R be a ring. Then a right ideal I of R is projection (resp., fully) invariant if and only if $eI \subseteq I$ for all $e = e^2 \in R$ (resp., $e \in R$). Observe that I is a two-sided ideal if and only if I is fully invariant in R. It is clear from Definition 2.1 that fully invariance implies projection invariance, but not vice versa. For example, let R be an Abelian ring. Consider a right ideal X of R which is not an ideal. Thus X is not fully invariant in R by the above observation. On the other hand, X is projection invariant by Proposition 2.3.

Definition 2.2. ([3], [1]) An R-module M is called right *π-extending* (resp., *FI-extending*) provided that every projection (resp., fully) invariant submodule of M is essential in a direct summand of M. A ring R is called right *π-extending* (resp., *FI-extending*) if R_R is π-extending (resp., FI-extending).

Proposition 2.3. Consider the following conditions:

(i) M is uniform.

(ii) M is extending.

(iii) M is π-extending.

(iv) *M is FI*-extending.

Then $(i) \Rightarrow (ii) \Rightarrow (iii) \Rightarrow (iv)$, but these implications are not reversible. Additionally, if M is an indecomposable module, $(i) \Leftrightarrow (ii) \Leftrightarrow (iii)$.

Proof. See the proof of [3, Proposition 3.7].

It is clear from Proposition 2.3 that if R is a domain, then uniform, extending, and π-extending properties coincide.

Proposition 2.4. *(i)* Let R be an Abelian ring. Then every one-sided ideal is projection invariant.

(ii) Assume that R is generated by its idempotent elements (e.g., $R = Mat_n(A)$ for $n \geq 2$). Then every projection invariant one-sided ideal is an ideal.

Proof. The proof is straightforward.

Proposition 2.5.*(i)* For an Abelian ring R, R is right extending if and only if R is right π-extending.

(ii) If R is generated by its idempotent elements, then R is right FI-extending if and only if R is right π-extending.

Proof. The proof follows from Proposition 2.2 and Proposition 2.3.

Corollary 2.6. Let $R = Mat_n(A)$ for $n \geq 2$. Then R is right FI-extending if and only if R is right π-extending.

Proof. It is a consequence of Proposition 2.5 (ii).

The following example shows that the submodule of π-extending (resp., FI-extending) modules need not to be π-extending (resp., FI-extending).

Example 2.7. *(i)* Let $R = \mathbb{Z} < x, y >$ be the free ring on two noncommuting indeterminates. Since R is a domain, R is indecomposable. Note that xR is not essential in R_R. Hence R is not uniform, so R is not π-extending by Proposition 2.3. Consider $E(R)$, the injective hull of R. Clearly, $E(R)$ is π-extending, but R is not.

(ii) Let D be a simple domain which is not a division ring, and consider $R = \begin{bmatrix} D & D \oplus D \\ 0 & D \end{bmatrix}$. It is clear from [1, Example 11] that R_R is not FI-extending. However, the injective hull of R_R is FI-extending.

The next result explains that when the π-extending (resp., FI-extending) property inherited by submodules.

Proposition 2.8. Let M be a π-extending (resp., FI-extending) module. Then every projection (resp., fully) invariant submodule of M is π-extending (resp., FI-extending).

Proof. Assume M is π-extending and $X \trianglelefteq_p M$. Let $A \trianglelefteq_p X$. Then $A \trianglelefteq_p M$ by [5, p.50]. Hence there exists a direct summand D of M such that $A \leq^{ess} D$. Observe that $M = D \oplus D'$ for some $D' \leq M$. Since $X \trianglelefteq_p M$, $X = (X \cap D) \oplus (X \cap D')$. Note that $A = X \cap A \leq^{ess} X \cap D$, where $X \cap D$ is a direct summand of X. Therefore X is π-extending. The proof of FI-extending case follows similarly.

3. DIRECT SUMS AND DIRECT SUMMANDS PROPERTIES

In this section, we deal with the direct sums and direct summands of π-extending (resp., FI-extending) modules. These classes behave differently than extending modules in terms of direct sums. Observe that the direct sums of extending modules are not extending, in general.

Proposition 3.1. ([3, Corollary 4.11]) The class of π-extending (resp., FI-extending) modules is closed under direct sums.

Recall from [7, Proposition 2.6] that extending property is inherited by direct summands. On the other hand, π-extending property behaves differently than extending modules with respect to direct summands.

Example 3.2. ([3, Example 5.5], or [6, Theorem 2.4]) Let R be the real field and n be any odd integer with n $\geq$ 3. Let S be the polynomial ring $R[x_1, x_2, \ldots, x_n]$ over R indeterminates $x_1, x_2, \ldots, x_n$. Let R be the ring S/Ss, where $s = x_1^2 + \ldots + x_{n-1}^2$. Then the free R-module, the countable direct sum $M = R^{(\mathbb{N})}$ of copies of R is π-extending contains a direct summand which is not π-extending.

We should mention that it is unknown whether the direct summand of FI-extending module is FI-extending or not. Now, we focus on the direct summand properties for both π-extending and FI-extending modules.

Proposition 3.3. *(i)* Assume that *M* has an Abelian endomorphism ring, and *X* is a direct summand of M. Then $X \unlhd_p M$. Moreover, $X \unlhd M$ if and only if $X \unlhd_p M$.

(ii) Let M be an π-extending (resp., FI-extending) with an Abelian endomorphism ring. Then every direct summand of M is π-extending (resp., FI-extending).

Proof. *(i)* Assume $S = End(M_R)$ and $X = eM$ for some $e = e^2 \in S$. Let $g = g^2 \in S$. Then $g(X) = g(eM) = e(gM) \subseteq eM = X$, so $X \unlhd_p M$. The remaining part is clear.

(ii) It follows from part *(i)* and Proposition 2.8.

Proposition 3.4. Let $M = M_1 \oplus M_2$ be a π-extending module such that M_2 is a projection invariant submodule of M and for every direct summand K of M with $K \cap M_2 = 0, K \oplus M_2$ is a direct summand of M. Then M_1 is π-extending.

Proof. See the proof of [6, Theorem 2.7].

Corollary 3.5. Let $M = M_1 \oplus M_2$ be a π-extending module with C_3 condition. If M_2 is a projection invariant submodule of M, M_1 and M_2 are π-extending.

Proof. Immediate from Proposition 2.8 and Theorem 2.7.

REFERENCES

[1] Birkenmeier, G.F., Muller, B.J., Rizvi, S.T., Modules in which every fully invariant submodule is essential in a direct summand, Communications in Algebra, 30(3), 1395-1415, 2000.

[2] Birkenmeier, G.F., Park, J.K., Rizvi, S.T., Extensions of Rings and Modules, Birkhauser, Springer, New York, 2013.

[3] Birkenmeier, G.F., Tercan, A., Yücel, C.C., The extending condition relative to sets of submodules, Communications in Algebra, 42(2), 764–778, 2014.

[4] Dung, N.V., Huynh, D.V., Smith, P.F., Wisbauer, R., Extending Modules, Longman, 1994.

[5] Fuchs, L., Infinite Abelian Groups I. New York, Academic Press, 1970.

[6] Kara,Y., Tercan, A,, Yaşar, R., PI-extending modules via nontrivial complex bundles and abelian endomorphism rings, Bulletin of the Iranian Mathematical Society, 43,121-129, 2017.

[7] Mohamed, S.H., Müller, B.J., Continuous and Discrete Modules, Cambridge University Press, Cambridge, 1990.

[8] Smith, P.F., Tercan, A., Generalizations of CS-modules, Comm. Algebra, 21, 1809-1847, 1993.

GENERAL STRUCTURES OF AUTOMOTIVE GLASSES AND REQUIREMENTS OF FILM COATING APPLICATIONS

S. Pirim

[1] *TOFAŞ R&D Department, İstanbul Cad. No: 574, 16110, Bursa, TURKEY*

E-mail: servet.pirim@tofas.com.tr

Abstract

Glass is suitable to use in different areas. It is a very important material for the automotive and construction industry. It offers a variety of products in different structures. Glass production is also a very difficult and fragile process. Especially in recent years, window film applications are in high demand by users. The main reason for this demand is the aesthetic concerns of the users. However, the place of window film applications in the automotive industry is not only to eliminate aesthetic concerns. with technological advances, many innovative solutions are offered to customers through the use of window film applications. Some requirements must be met for window film applications. In addition to the sun block function, window film applications have a significant contribution to increasing the level of safety in the vehicle. Glass, which is suitable for different production and application methods, is a component that goes far beyond a visual element with its film applications. In this article, besides the basic information about the glass used in the automotive sector, information about production processes, technological developments and window film applications are given.

Keywords: Glasses, Temper and Lamination Processes, Film Coating

1. INTRODUCTION

Glass is a solid material that is hard and brittle. It is also called a non-crystalline solid. It is an amorphous solid because its atomic structure is irregular. Glass does not have a definite melting point like other materials. It changes from liquid to solid, usually within a certain temperature range around 500 ° C. An important feature of glass is its high resistance to many chemicals, making it a very durable material. There are numerous types of glass with chemical and physical properties that vary depending on the area of use. The most common glass is soda-lime glass, also called soda-lime-silicate glass. Soda-lime glass as raw material; sand, soda ash and limestone; and small amounts of various additives. Especially for laminated glass, the mechanical properties of the sheets and the structural behaviour of the glass are very important.

Glass is a non-natural isotropic and brittle material at normal room temperature. It can be defined as a ductile material. Elastically deforms under stress and does not show plastic deformation before breaking. As a result, the behaviour of the glass is ideally considered elastic. The compressive strength is significantly higher than the tensile strength. Glass is susceptible to micro cracks and defects. Tensile strength is low. In case of stress loading; stress concentrations develop in micro cracks and defects. High stress concentration results from surface imperfections. Because glass does not exhibit plastic behaviour, there is no stress distribution to reduce local stress concentration, as is the case with other materials such as steel. Cracks or surface defects play an important role in mechanical strength. The practical value for mechanical strength is always low due to these defects. Theoretical tensile strength based on molecular forces is 32 GPa. The practical value is very low

2. FLAT GLASS PRODUCTION

Flat glass is the most widely used glass especially in laminated glass and is usually made of soda lime glass. Flat glass can be produced in different ways; however, flotation glasses also represent 90% of soda-lime glass production. In the buoyancy process invented by Pilkington in 1959, glass; produced by floatation in liquid tin bath when molten.

In this procedure, the glass forms a flat surface on both sides. The thickness of the flat glass can be adjusted by the rate at which the glass is withdrawn from the tin bath. Pine; entering the annealing furnace and tin bath is slowly cooled. The annealing process reduces the internal stresses in the material with controlled cooling process. Controlled and slow cooling is very important. Because irregular cooling can cause a decrease in mechanical strength. Another term for flat glass is tempered glass. The final process in glass production is

the examination and cutting of glass. However, float glass can be further processed to produce glass products such as heat-treated glass and laminated glass [1]. Figure 1 was prepared to show the flow chart of glass production operation.

Figure 1. Flow chart of glass production

3. HEAT TREATED GLASSES

Laminated glasses can be produced from annealed or heated glass. Besides; in view of the general definition, laminated glasses are a kind of tempered glass. Structural performance of laminated glass; it depends on the singular structure of the glass and the intermediate layer. The main advantage of heattreated glass is its improved mechanical strength. Due to the high strength, tempered glass is a good option when reinforced load bearing capacity is desired. A tempered glass can be chemically or tempered by means of a heat treatment[1].

Chemically tempering is carried out by an ion exchange process. Chemical annealing is rare in structural applications because this annealing is effective in thin glass which is not common in automotive. The mechanical strength of the annealed glass can be further improved by a heat treatment, as done in the annealing step. Heat treatment (annealing) is generally referred to as a process in which the float glass is heated to a glass transition temperature of from about 100 ° C to about 600 ° C. Unlike annealing in flotation, the glass is then quickly cooled by cold air jets. This process is called quenching. As a result of quenching, a structure is compacted and the tension is centered. There are two types of heat treated glass: fully tempered glass and heat-reinforced glass. Fully tempered glass is made by the process described above. Second, heat-

reinforced glass has a similar production methodology, but is produced with a lower cooling rate. Fully tempered glass is divided into small pieces in the face of impact and is thus considered as safety glass. Heat-reinforced glass is not considered safety glass because it is broken into larger pieces. The refraction pattern depends on the energy stored in the glass[1].

Due to the high residual tensile stress in the fully tempered glass, the material is divided into small pieces, unlike annealed glass which is divided into large pieces. Heat-reinforced glass can be said to be a material with properties between annealed glass and fully tempered glass. Mechanical strength is lower for heat-reinforced glass due to a low cooling rate. Fully tempered glass is four to five times stronger than annealed glass. About three times stronger than heat-reinforced glass.

Any work such as cutting, drilling or grinding on heat treated glass must be performed before tempering. Another disadvantage of heat-treated glass is the risk of spontaneous breakage; that is, the glass may break without apparent reason. Sudden fractures or bursts are caused by nickel-sulfide content, which is a small stone or crystal in the glass. There is always a risk for nickel-sulfide content during production. Although the probability is very low, it cannot be ruled out because of its serious consequences.

Annealed glass may also have a nickel-sulfur content, but that is a problem to be considered because it is present only in heat-treated glass. Due to the low cooling rate, nickel-sulfide particles are stable in tempered glass. When annealed glass is subjected to a heat treatment, the nickel-sulfite particles increase in volume. This causes spontaneous breakage, with high tensile stresses in the glass core. Self-breaking can occur days or even years after the production of heat-treated glass. Whether the glasses contain nickel sulphide is determined by heat treatment test. In the heat treatment test, the glass is heated slowly and the glass containing nickel-sulphite breakage is broken while maintaining the temperature at which the particles are transformed. Other unbreakable glasses can be sold. Heat treated glass is more expensive due to tempering and heat treatment testing.[2]. There is a comparison table between fully tempered and and heat strength glasses at Table 1.

Flat glasses exhibit very good optical properties and do not exhibit important deterioration, but visual degradation may occur with a heat treatment. Therefore, heat treated flat glasses may have low optical properties. Tempering reduces the time dependence of power. The greatest advantage obtained with tempered glass is that it is twice the high mechanical strength and is desirable.
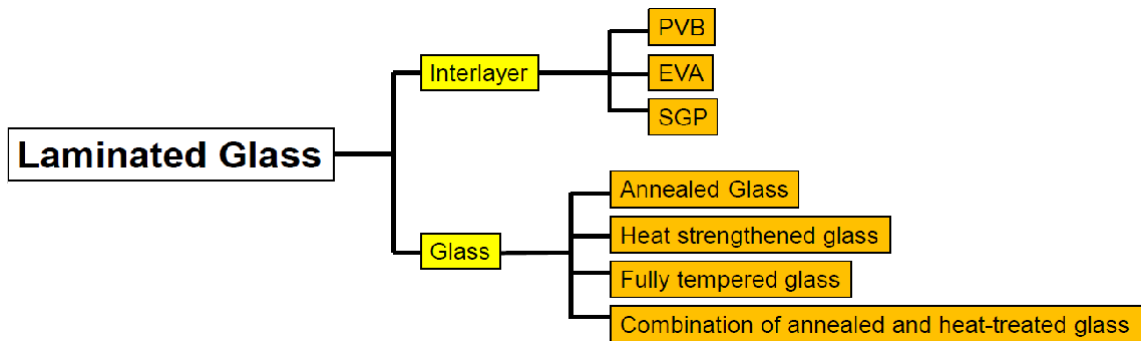
Table 1. Glass type, fracture pattern and mechanical strength comparison table

Type of glass	Fracture pattern	Mechanical strength
Fully tempered	Small, harmless pieces	4-5 times stronger
Heated strengthened	Larger pieces than fully tempered but smaller than annealed glass	2-3 times stronger

4. LAMINATED GLASS

Laminated glass was invented in 1909 by the French chemist Eduard Benedictus. Laminated glass is used in many different applications such as construction industry, aviation and automotive. Laminated glass was originally developed as a product with better load carrying capacity than tempered glass. In addition to its load-bearing capacity, it also has other desirable features such as improved safety, fire resistance and sound reduction. Resistance to impacts and explosion loads; Due to the plastic intermediate layer is very high for laminated glass. The laminated glass consists of two or more layers of glass interconnected by a plastic intermediate layer as previously mentioned. Laminated glasses of more than two layers of glass are called plural and are used, for example, in glass beams, columns, stair steps and descents. The adhesive contact between the glass and the intermediate layer is made with high pressure and heat around 140 ° C. This usually takes place in a container, autoclave. The purpose of the intermediate layer is to retain the parts after the breakage in the laminated glass, which eliminates the risk of injury from glass shards. Laminated glass can consist of different glass and intermediate layers [4].
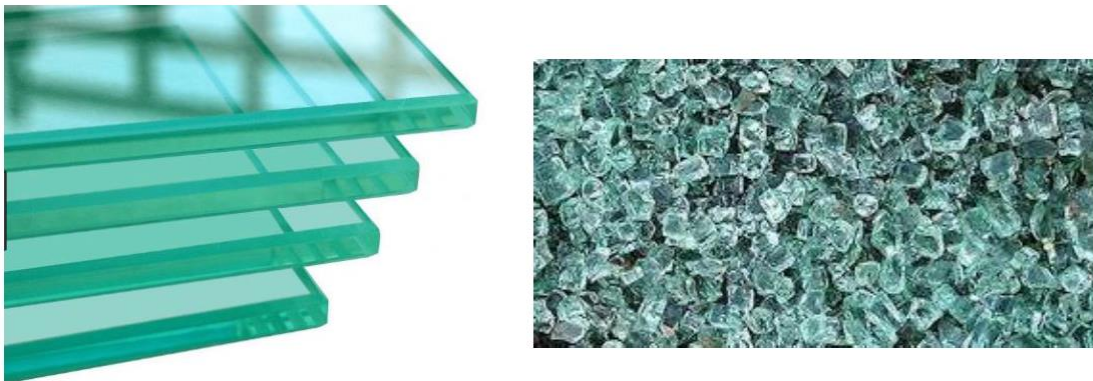
The thickness of the panels may be equal or different. The interlayer used in laminated glass is, for example, polyvinyl butyral (PVB), ethyl vinyl acetate (EVA) and SentryGlas® Plus (SGP) from DuPont (Figure 2). The laminated glass may also consist of a liquid resin instead of plastic-containing components. This production method is not very common. [1]

compress. Production glass is strong and weak in tension. Generally, the glass breaks in a bending mode when it is hit by an inside person or an external object. This causes compression of the impacted side and tension of the opposite side. With tempered glass, the tensile side is already compacted, and the bending must overcome the compressive stress before it enters the surface tensile state, while placing the side opposite the applied load tautly. Glass can be considered to be tempered when the surface compaction is 10,000 psi or higher. The automotive side and rear windows are usually tempered to a minimum of 20,000 psi [3].

6. FILM COATING APPLICATIONS

Automotive manufacturers have experienced that various environmental factors affect the quality of the vehicles after delivering their new vehicle to car owners. A large part of the automotive exterior consists of coatings and glass. In the early 1990s, Nitto Denko developed the world's first protective film for automotive coatings. Developed film can be suitable to conserve acid rain and other factors. After this result, protective films are widely used in automotive coatings, automotive glass repairs.

Damage to the windscreen can cause serious problems for drivers and passengers. Glass damage can occur not only during transport but also by the impact of small stones. Usually, when the car windows are damaged, they need to be replaced. Therefore, the cost of repair is proportional to the frequency of damage. Global warming is said to be caused by storm and hurricane sizes, causing damage to vehicle windows to occur in 10 to 15% of vehicles, causing a major economic problem. Although improving the performance of the tempered glass has alleviated the problem, it can only reduce the magnitude of the damage, not the frequency [5]. Figure 4 and 5 shown that the views during and after the film coating application at vehicle.

Figure 4. Film coating example at vehicle

The following elements are essential features for automotive glass protection film;

1. Good adhesion to the glass: The film should not be peeled off by water ingress. It should be easy to disassemble after film application.

2. Weather proofness: In case of outdoor exposure up to 6 months, there should be no deterioration.

3. Visibility: Adhesive film should provide minimum effect on the surface.

4. Notch protection: The film is protected against notch damage to the glass.

5. Preventing glass breakage: The film should prevent the glass from scattering when the glass breaks.

Figure 5. Film coated vehicle

7. CONCLUSION

In the automotive industry there are two different types of glass, laminated and tempered. Although the mechanical properties of these glasses are different, they are used in similar regions according to the expectations and requirements. The usage of laminated glass at windshields is a legal requirement. In addition, film coating applications have been developed as an alternative to privacy glasses. Design and application according to the desired performance level is important for window films applications. Especially because of the resistance wires used in the rear window, the application of window film may be dangerous. The resistance wires should not be damaged during the application of the window film to the vehicle.

REFERENCES

[1] Fors, C., Mechanical Properties of Interlayers In Laminated Glass Experimental and Numerical Evaluation, 3-21 , 2014.

[2] Rodloff, G., Breitenburger, G., Safety of Windshield Against Flying Stones, 3-5, 1967.

[3] Kramer, R.N., Loibl J.M., Morrison R.L., Saunby, S.S., A Comparative Study of Automotive Side Window Occupant Containment Characteristics for Tempered and Laminated Glass, 2-9 2006.

[4] Pyper, J., Use of PVB in Laminated Side Glass for Passenger Vehicle Interior Noise Reduction, 3-6, 2000.

[5] Satou, J., Shibata, K., Shinsuke, I., Kushioka, H., Newly Developed Automotive Glass Protection Film, 3-9, 2006.

ANTIMICROBIAL ACTIVITIES OF VARIOUS PLANTS AGAINST FOODBORNE STAPHYLOCOCCUS AUREUS ATCC 6538 AND STAPHYLOCOCCUS AUREUS ATCC 29213 MIXTURE

O. Nogay, B. Balkan

Vocational School of Technical Sciences, Kırklareli University, Kırklareli, Turkey

E-mail: oguzhannogay@klu.edu.tr

Abstract

In this study, antimicrobial activities of *Thymus longicaulis* C. Presl, *Sambucus ebulus* L., *Origanum vulgare* L. and *Clinopodium vulgare* L. aqueous extracts were determined against *Staphlococcus aureus* mixture obtained by using 1: 1 ratio of *Staphylococcus aureus* ATCC 6538 and *Staphylococcus aureus* ATCC 29213. In addition, the effects of temperature and pH stability on the antimicrobial activities of the extracts were investigated. We assessed bacterial cell viability in cheese and meat broth for 24 h at 7°C and 37°C. *S. ebulus* and *C. vulgare* aqueous extracts showed no inhibitory effect on the mixture of *S. aureus*. For *O. vulgare* and *T. longicaulis*, the minimum inhibitory concentrations (MIC) against the mixture of S. aureus were 1000 and 500 μ / mL, respectively. When the aqueous extracts of *O. vulgare* and *T. longicaulis* were heated at 100°C and 121°C for 15 minutes, an increase in antimicrobial activity against *S. aureus* mixture was determined. The inhibitory effect for *T. longicaulis* was better at pH 4.0 and 5.0. The *O. vulgare* and *T. longicaulis* (4MIC) reduced the viable counts of *S. aureus* mixture in cheese and meat broth over 24 h at 37°C. However, *O. vulgare* and *T. longicaulis* (4MIC) in the cheese and meat broth did not reduce the viable counts of *S. aureus* mixture for 24 h at 7°C. We can say that these findings strengthen the potential of *O. vulgare* and *T. longicaulis* as natural antimicrobials to control *S. aureus* mixture in cheese and meat.

Keywords: Antimicrobial activity, Meat broth, Cheese broth, *Staphylococcus aureus*, Plant extract

1. INTRODUCTION

Food safety is a general concern for both consumers and the food industry as the number of reported cases of foodborne infection continues to increase. Studies have reported that approximately one-third of foodborne infections are caused by bacterial agents and that *Staphylococcus aureus* is one of the leading factors [1]. *S. aureus* is a pathogen frequently associated with food outbreaks causing a typical intoxication through the ingestion of enterotoxins pre-formed in foods [2]. Cheeses and meats have been frequently involved in major outbreaks of staphylococcal intoxication worldwide [2,3]. *S. aureus* can be transmitted by infected animals from which food is obtained, people working in food processing, and utensils used in the preparation and distribution of food.

From the middle of the last century, synthetic compouds have been used as additives in foods to control the growth and survival of pathogens, such as *S. aureus*, and give them a long shelf life and safety [4]. However, concerns about the presence of chemical residues in food and the safety of certain chemical preservatives cause negative consumer reactions [5]. Therefore, interest in natural alternative food preservatives is increasing [6]. Increased foodborne disease rate combined with social and economic impacts means continuous efforts to produce safer food and develop new antimicrobial agents [7].

It has been suggested that the use of bacterial strain mixture could minimize the expected variation existent between different isolates of the same species, as well as the influence of the strain, obtaining an average tendency of strains behavior within species [8,9]. In this respect, in this study was evaluated antimicrobial activity against foodborne *Staphylococcus aureus* ATCC 6538 and *Staphylococcus aureus* ATCC 29213 mixture of aqueous extracts of Clinopodium *vulgare* L., *Thymus longicaulis* C. Presl, *Sambucus ebulus* L. ve *Origanum vulgare* L. Hirtum (Link) letsw and effects on viable cell counts in cheese and meat-based broth over time.

2. MATERIAL AND METHODS

Microorganisms

In this study, foodborne *Staphylococcus aureus* ATCC 6538 and *Staphylococcus aureus* ATCC 29213 bacterial species were obtained from Food Engineering culture collection, Yıldız Technical University, Turkey. The *S. aureus* mixture was obtained by preparing suspensions in sterile saline solution (0.85% NaCl) from overnight cultures grown in brain heart infusion agar at 37°C. The *S. aureus* mixture was obtained using a ratio of 1:1 of each strain (10^8 CFU/ml).

Plants materials and extract preparation

Plants from different locations were collected in Yıldız Mountains (Kırklareli, Turkey). Confirmation of the taxonomic identification of plants was done by Dr. Hüseyin ERSOY of Trakya University (Edirne, Turkey) (Table 1, Figure 1). Aqueous extracts were prepared in accordance with the method introduced by Khadri *et al.,* [10]. The obtained aqueous extracts were lyophilized and, then stored at -20°C until use.

Table 1: Plant locations

FAMILY	GENUS	SPECIES	SUBSP	PROVINCE	LOCALITIES
Lamiceae	*ORIGANUM L.*	*O. vulgare* L.	Hirtum (Link) letsw	Kırklareli	Between Yörükbayır and Armağan Village
Lamiceae	CLINIPODIUM L.	*C. vulgare* L.	vulgare	Kırklareli	Mahyatepe exit 8.5 km from the turnoff
Lamiaceae	THYMUS L.	*T. longicaulis* C. Presl	longicaulis	Kırklareli	Armagan Village Dam Area
Caprifoliaceae	SAMBUCUS L.	*S. ebulus L.*	-	Kırklareli	Dereköy exit

Figure 1: Plants

Origanum vulgare **L. hirtum (Link) letsw**

Thymus longicaulis **C. Presl longicaulis**

Clinopodium vulgare **L. vulgare**

Sambucus ebulus **L.**

Determination of the Minimum Inhibitory Concentration (MIC)

The MIC values of the aqueous extracts (1000 to 15.625 μg/ml) were determined according to the procedure of the Institute of Clinical and Laboratory Standards (Document M07-A9) [11]. Microdilution tests were carried out in triplicate in 96-well microplates.

Temperature and pH effect

To study the thermal stability of the extracts, the extracts were treated at 100 or 121°C for 15 min. It was then evaluated for antimicrobial activity. For pH stability tests, the extracts were adjusted to pH 4, 5 or 6 with 1N HCl and stored at 4°C for 24 hours. After 24 hours, the pH values were readjusted to their original values before use [12].

Effects on Viable Cell in Cheese and Meat Broth

To obtain cheese broth, the cheese (160 g) was cut into pieces of uniform sizes (1 cm × 1 cm × 1 cm), added to 1000 mL of sterile distilled water and hand-mixed with a sterile glass stem for 5 min to ensure even homogenization. Subsequently, the mixture was placed in a thermostatic water bath (42°C, for 50 min) and vacuum-filtered using Whatman no1 filter. The filtrate was sterilized in an autoclave for 15 min at 121°C [13]. For preparing meat-based broth, 500 g of beef lean meat type, trimmed of fat and whole external pieces of uniform size (3 cm × 3 cm × 3 cm) were boiled (90°C) in 1000 mL of distilled water for 30 min. Then, the liquid portion of the cooking material was separated from the solid material, vacuum filtered using Whatman no 1 filters and the filtrate was sterilized using autoclave for 15 min at 121°C. Broths were stored at −20°C in aliquots of 50 mL, and when required one aliquot was thawed under refrigeration (7 ± 1°C) and used for the assays.

The assays to verify the effects on the viable cell of *S. aureus* in cheese and meat broth over 24 h were carried out at various concentrations (4MIC) of *O. vulgare* and *T. longicaulis* aquaeus extracts. Plates inoculated with aliquots collected from cheese or meat broths containing *O. vulgare* and *T. longicaulis* aquaeus extracts were incubated for 24 h at 7°C and 37°C.

3. RESULTS AND DISCUSSION

The antimicrobial activities of the plant aqueous extracts tested are summarized in Table 2. The aqueous extract of *C. vulgare* and *S. ebulus* showed no inhibitory effect on *S. aureus* growth. *T. longicaulis* and *O. vulgare* showed an inhibitory effect on growth of *S. aureus* at a concentration of 500 and 1000 μg/ml, respectively. Plants abundantly have a broad range of bioactive secondary metabolites such as tannins, terpenoids, alkaloids, and flavonoids stated to possess in vitro antimicrobial properties. Moreover, a series of molecules that possess antimicrobial activity against different strains of bacteria have been found in plants. We can say that *T. longicaulis* and *O. vulgare* aqueous extracts have antimicrobial potential against *S. aureus* mixture.

Table 2. Antimicrobial activities of various plant aqueous extracts on *S. aureus* mixture

Plants	MIC (µg/mL)
Origanum vulgare	1000
Thymus longicaulis	500
Sambucus ebulus	ND
Clinopodium vulgare	ND

ND; No determined

In our previous study, the phenolic components of aqueous extracts of these plants were measured by HPLC analysis. (Table 3). Carvacrol has been reported to exhibit a broad spectrum of antimicrobial activity, particularly against *S. aureus*. It has been reported that carvacrol increases membrane fluidity, causes protons and potassium ions to leak, thus causing membrane potential to collapse and inhibition of ATP synthesis [14,15]. As seen in the table 3 carvacrol is not found in *C. vulgare* and is low in *S. ebulus*.

Table 3. Phenolic compounds and amounts of the plant aqueous extracts tested (mg/g) [16].

Plant Extracts	GA	PA	CLA	CA	V	PCA	FA	ER	CNA	LU	CF	AP	C
C. vulgare	0,10	0,17	0,54	0,52	0,17	0,17	*	*	0,30	0,91	0,33	0,42	*
O. vulgare	0,30	0,14	0,22	0,86	0,29	0,27	*	1,34	0,08	*	0,71	1,32	6,38
T. longicaulis	0,24	0,15	0,09	1,13	0,07	*	0,24	0,27	0,21	*	0,42	1,03	1,87
S. ebulus	*	0,27	2,40	0,30	0,22	0,05	0,08	*	*	0,13	0,09	0,37	0,06

*Unable to detect. GA; gallic acid, PA; procatechic acid, CLA; chlorogenic acid, CA; caffeic acid, V; vanillin, PCA; p-coumaric acid, FA; ferulic acid, ER; eriodikthiol, CNA; cinnamic acid, LU; luteolin, CA; kaemferol, AP; apigenin, C; carvacrol

Our study was continued with *O. vulgare* and *T. longicaulis* with antimicrobial potential against *S. aureus* mixture. In our country, *T. longicaulis* is known as "food thyme", which is used in meals. Turkey and Southern Europe shows spread. It is a perennial herbaceous plant with purplish flowers that can grow up to 10 cm. It blooms between April and August and grows in forest openings, rocky slopes and dry pastures. In Anatolia, the aromatic flowers and leaves of the plant are collected and dried, and then used to give flavor to the dishes. *O. vulgare* subsp. hirtum "Istanbul thyme" has a local name. In addition to being used as spices and tea, it is known to be good for headaches and stomach pains as a folk medicine.

Heat treatments commonly used in food processing are boiling (100°C) and autoclaving (121°C) [6]. After heating at 100 or 121°C for 15 minutes, the antimicrobial activity of the aqueous extracts of *T. longicaulis* and *O. vulgare* increased against *S. aureus* (Table 4). This may be due to the slight increase in antimicrobial agents by the effect of evaporation.

Table 4. Antimicrobial activity of *O. vulgare* and *T. longicaulis* aqueous extracts after various heat treatments (μg/ml)

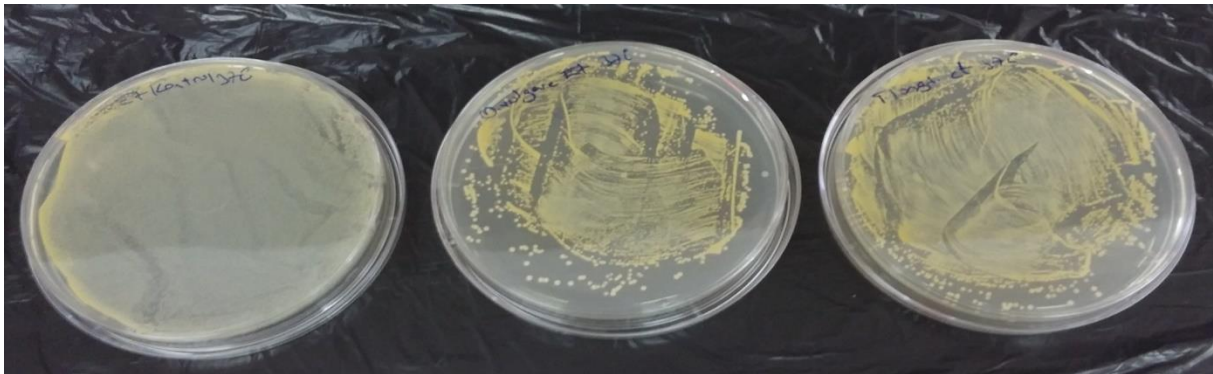| Plants	Control	100°C	121°C
Origanum vulgare	1000	250	125
Thymus longicaulis	500	250	125

The pH of processed foods usually varies between acid and neutral [5]. As shown in Table 5, *T. longicaulis* at pH 4 and 5 showed the best antimicrobial activity. It is reported that [17] easier dissolution of the target bacterium in the lipid of the cell membrane by the hydrophobicity of the antimicrobial activity of the extracts at low pH. According to the results, it can be predicted that *O. vulgare* and *T. longicaulis* aqueous extracts tested for thermal and pH stability can be applied to processed food products against *S. aureus*.

Table 5. Antimicrobial activity of *O. vulgare* and *T. longicaulis* aqueous extracts at various pH values (μg/ml)

Plants	Original pH*	pH 4	pH 5	pH 6
Origanum vulgare	1000	500	500	500
Thymus longicaulis	500	125	125	250

* *O. vulgare* pH 6.93, *T. longicaulis* pH 6.73

The antimicrobial activity of the extracts may vary according to the composition of the food, the temperature exposed and the time. The inhibitory effecs of *T. longicaulis* and *O. vulgare* aqueous extracts (4 MIC) on *S. aureus* pathogen were evaluated in food based media. Viable cell counts of *S. aureus* mixture when exposed to the different combinations (4 MIC) of *O. vulgare* and *T. longicaulis* in cheese and meat broths at 7°C and 37°C for 24 h are given in Figures 1, 2, 3 and 4. All assayed combinations of plant extracts caused similar decreases in counts of *S. aureus* mixture over 24 h in both cheese and meat broths. A sharp decrease in the number of *S. aureus* mixtures was observed in both cheese and broth at 7°C. The phospholipid composition of the cytoplasmic membrane of cells grown at 7°C has a higher degree of unsaturation than does that of cells grown at 35°C to maintain fluidity and function at low temperatures. The increased fluidity would enable the *O. vulgare* and *T. longicaulis* to dissolve more easily into the lipid bilayer of cells grown at 7°C than into that of cell grown at 35°C [17].
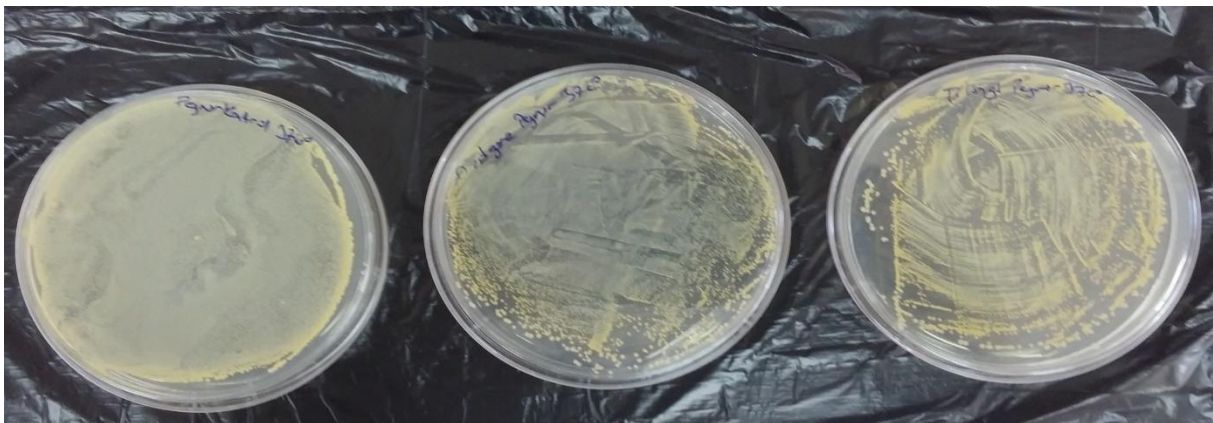
Control   *O. vulgare*   *T. longicaulis*

Figure 1. Effects on the viable cell of *S. aureus* mixture *O. vulgare* and *T. longicaulis* aqueous extracts in meat broth at 37 ᵒC.
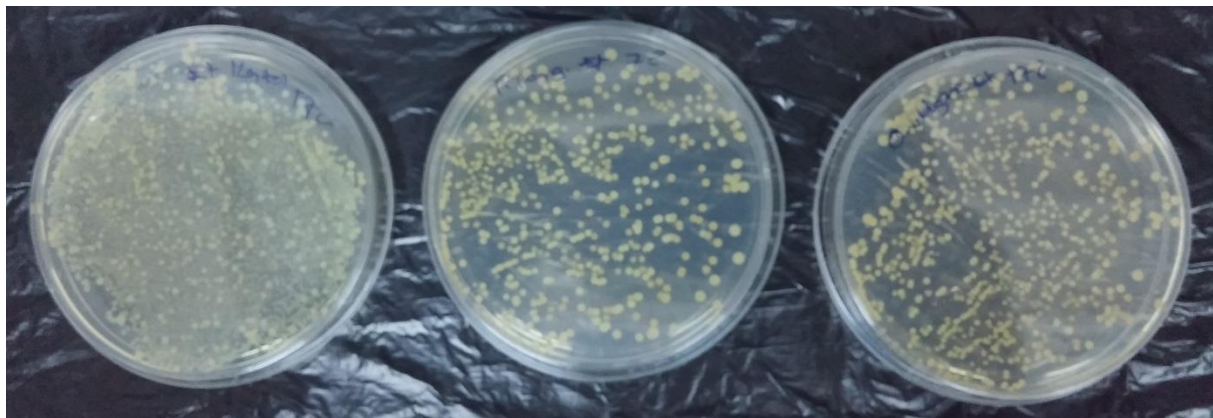

Control   *O. vulgare*   *T. longicaulis*

Figure 2. Effects on the viable cell of *S. aureus* mixture *O. vulgare* and *T. longicaulis* aqueous extracts in cheese broth at 37 ᵒC.

Control   *T. longicaulis*   *O. vulgare*

Figure 3. Effects on the viable cell of *S. aureus* mixture *O. vulgare* and *T. longicaulis* aqueous extracts in meat broth at 7 ℃.

Control   *O. vulgare*   *T. longicaulis*

Figure 4. Effects on the viable cell of *S. aureus* mixture *O. vulgare* and *T. longicaulis* aqueous extracts in cheese broth at 7 ℃.

As a result, application of *T. longicaulis* and *O. vulgare* aqueous extracts decreased the counts of *S. aureus* in cheese and meat broth stored at refrigerate temperature. These findings may enable the use of aqueous extracts of *O. vulgare* and *T. longicaulis* to control *S. aureus* at low temperatures, particularly in food products stored in cheese and meat.

REFERENCES

[1] Çakıcı, N., Demirel-Zorba, N.N. and Akçalı, A. 2015. Gıda endüstrisi çalışanları ve stafilokokal gıda zehirlenmeleri. Türk Hijyen ve Deneysel Biyoloji Dergisi. 72 (4): 337-350.

[2] Zeleny, R., Emteborg, H., Charoud-Got, J., Schimmel, H., Nia, Y., Mutel, I., et al. 2015. Development of a reference material for for Staphylococcus aureus enterotoxin A in cheese: feasibility study, processing, homogeneity and stability assessment. Food Chem. 168, 241–242.

[3] Wang, X., Tao, X., Xia, X., Yang, B., Xi, M., Meng, J., et al. 2013. Staphylococcus aureus and methicillin-resistant Staphylococcus aureus in retail raw chicken in China. Food Control 29, 103–106.

[4] Pesavento, G., Calonico, C., Bilia, A. R., Barnabei, M., Calesini, F., Addona, R., et al. 2015. Antibacterial activity of Oregano, Rosmarinus and Thymus essential oils against Staphylococcus aureus and Listeria monocytogenes in beef meatballs. Food Control 54, 188–199.

[5] Mau J.L., Chen C.P. and Hsieh P.C. 2001. Antimicribial effect of extracts from Chinese chivei cinnamon and corni fructus, J. Agric. Food Chem., 49:183-188.

[6] Hsieh P.C., Mau J.L. and Huang S.H., 2001. Antimicrobial effect of various combinations of plant extracts, Food Microbiology, 18:35-43.

[7] Smith-Palmer A., Stewart J. Ve Fyte L. The potential application of plant essential oils as natural food preservatives in soft cheese, Food Microbiology, 18:463-470.

[8] Gibson, A. M., Bratchell, N., and Roberts, T. A. (1987). The effect of sodium chloride and temperature on the rate and extent of growth of Clostridum botulinum type A in pasteurized pork slurry. J. Appl. Bacteriol. 62, 479–490.

[9] Romero, S. M., Pinto, V. F., Patriarca, A., and Vaamonde, G. (2010). Ochratoxin A production by a mixed inoculum of Aspergillus carbonarius at different conditions of water activity and temperature. Int. J. Food Microbiol. 140, 277–281.

[10] Khadri, A., M. Neffati, S. Smiti, P. Fale, A.R.L. Lino, M.L.M. Serralheiro and M.E.M. Araujo. 2010. Antioxidant, antiacetylcholin esterase and antimicrobial activities of *Cymbopogon schoenanthus* L. Spreng (lemon grass) from Tunisia. LWT-Food Sci. Technol., 43: 331-336.

[11] CLSI. 2012. Methods for dilution antimicrobial susceptibility tests for bacteria thar grow aerobically; approved standard-ninth edition, 32(2).

[12] Yu R.C. 1982. Antimicrobial activity of piper betle L. Master Thesis, National Taiwan Univercity, Taipei.

[13] Neviani, E., De Dea Lindner, J., Bernini, V., and Gatti, M. 2009. Recovery and differentiation of long ripened cheese microflora through a new cheese-based cultural medium. Food Microbiol. 26, 240–245.

[14] Fisher K. And Philips. 2009. The mechanism of action of a citrus oil blend against *E. Faecium* and *E. faecalis, faecalis,* Journal of Applied Microbiology, 106:1343-1349.

[15] Memar M.Y., Raei P., Alizadeh N., Aghdam M. And Kafil H.S. 2017. Carvacrol and thymol: strong antimicrobial agents against resistant isolates, Reviews in Medical Microbiology, 28:63-68.

[16] Balkan, B., S. Balkan, H. Aydoğdu, N. Güler, H. Ersoy and B. Aşkın. 2017. Evaluation of antioxidant activities and antifungal activity of different plants species against pink mold rot causing Trichothecium roseum. Arabian J. Sci. & Engin., 42: 2279-228.

[17] Cava R., Nowak E., Taboada A., Marın-Inıesta F.2007. Antimicrobial activity of clove and cinnamon essential oils against *L. Monocytogenes* in pasteurized milk, Journal of Food Protection, 70(12):2757-2763.

A CLOSE LOOK UP AT RECENT DEVELOPMENTS IN ROAD SIMULATORS

A.B. Tapan[1], M. Çakırca[1], Ö. Şengör[1], O. Yavuz[1]

[1]TOFAŞ R&D Department, İstanbul Cad. No: 574, 16369, Bursa, TURKEY

E-mail: ahmed.buraktapan@tofas.com.tr

Abstract

Nowadays, new product development process has become increasingly competitive. The automotive industry also needs technological innovations to develop and validate new vehicles in a short time. Durability road simulation tests, one of the validation activities, are increasingly important. However, duration of them is still considered to be long. There are still available durability road simulators which has single axis road load application capability. However, simulating one axis road load could not be sufficient to validate the vehicle life and may need several assumptions.

Accordingly, with the advances in testing technology, multi-axis road simulators become available in the markets which named 6 degrees of freedom. With this sophisticated test systems, durability road simulation tests could be performed reasonably in a short time. Also, they could give more realistic road simulation results in laboratory environment. 6 DOF test systems basically having a design to test complete vehicle or semi-cut vehicle. Therefore, they can be classified into two main groups as Full Vehicle and Half Vehicle road simulators which have their pros and cons with several parameters. This article discusses the basic technological features and test capabilities of these systems and gives information about their major selection criteria.

Keywords: Single axis road simulators, Multi-axis road simulators, Selection criteria of road simulators, Durability road simulation

1. INTRODUCTION

Technological developments have led to the transformation of new products into more complex structures. This effect transforms automobiles into electronic devices. Furthermore, just like a mobile phone, it has become usual expectation that a new vehicle should also be rapidly developed. Normally, this has led the process of new product development into a highly competitive environment in the automotive industry. To achieve this, necessity of the new technologies in the product development process has become a mandatory. One of the most prominent verification activities in the development phase of a vehicle is durability tests. The most important part of them is the road simulation tests performed in the laboratory environment. To perform road simulation tests in laboratory environment; a variety of sensors are placed on a specifically weighted test vehicle, it is driven on special test tracks to acquire road load data. These road loads are re-generated in the laboratory by using special road simulators and after necessary operational activities, they become ready to implement on the vehicle without any need for a real test track.

A wide variety of road simulators are available in markets today, to meet the above-mentioned product development and validation needs. There are companies working in this field in the world such as KNR, MTS, BIA, Moog, Instron [1-5]. These simulators could be monoaxial or single axis complete vehicle test systems or multi-axis systems which enable to perform complete or half vehicle tests.

In this article after brief information of single axis full vehicle road simulators, multi-axis full vehicle and half-vehicle simulators for vehicle durability testing are explained. It is better to explain that during the rest of this article, a half-vehicle is meant to testing any part or region of the vehicle, and for complete vehicle testing, is meant to testing a complete vehicle itself.

2. MATERIAL AND METHODS

The road simulators are divided into two according to the type of test vehicle installation;

- Tire coupled road simulator systems
- Spindle coupled road simulator systems

Basically, tire coupled road simulator systems are capable of applying road load in vertical Z axis through the tire of a vehicle, while spindle coupled road simulator systems generate multi-axis road load conditions through the spindle of a vehicle [6]. In this article, tire coupled road simulator is represented with single axis road simulator and spindle coupled road simulator is represented with multi-axis road simulator.

For the tire coupled system, vehicle could be freely moved to any location by its tires so, the test vehicle can be loaded on the test system without the need of any crane etc. equipment. However, since the vehicle is not movable, transport/lifting systems are needed for the spindle coupled systems. Furthermore, additional features such as precise x-y positioning system should be considered to ensure that the vehicle is loaded smoothly from the wheel center into the test system.

2.1. Single Axis Road Simulators

Single axis road simulators have one vertical input which allow to apply road load in Z-axis to each wheel simultaneously. Commercially these systems are also called Four Poster and is used in product development processes for durability tests [7]. As seen from Figure 1, these systems are used for different purposes in other areas such as vehicle durability test with climatic chamber, frequency response on the full vehicle and examination of vibration modes in the field of noise, vibration and harshness (NVH) with acoustic room. In the most basic way, Four Poster road simulators with single axis have a closed loop-controlled servo-hydraulic infrastructure with four actuators [8].

Figure 1. Different applications of single axis road simulators: (a) Tire coupled with climatic chamber, (b) Tire coupled with ambient temperature [7], (c) Tire coupled with acoustic room [9].

Recently, Four Poster road simulators with electrical infrastructure have been commercialized to meet not only NVH testing but also durability testing needs (MTS) [10]. The main parameter controlled here is the displacement of the piston shaft along the vertical axis for each actuator. As the actuators positioned in the vertical axis, these systems can only apply road loads to the vehicle in a single axis (z-axis) [7]. If the durability tests for the full vehicle are to be carried out using these systems, some assumptions are made because the road loads from other axes cannot be applied to the test vehicle. This situation requires increasing the tolerance range of the validation error predicted to perform the test.

On the other hand, as the tire of the vehicle is a flexible element, it can be seen some uncontrolled movement as a result of loading on the vertical axis z in the tire coupled systems. This may require additional convergence steps in the process of obtaining the road data on the vehicle. However, the vehicle already acts

similarly in actual use conditions. In spindle coupled systems, as there is no longer an elastic element between the test system and the vehicle, the loads in the vertical axis z can be transferred directly to the vehicle [9]. Thus, the obtaining of the road data can be completed with less convergence steps than the tire coupled systems. However, it should be noted that the entire duration of the convergence process depends on many parameters such as user competence, vehicle significance, placement of sensors in the vehicle, software and hardware capacity, calibration of the bench, appropriate hydraulic infrastructure, and so on.

2.2. Multi-axis Road Simulation Test Systems (6 DOF Test Systems)

The vehicle is not subjected to loads only on the z vertical axis under real road conditions. The structure of the road, obstacles on the road and driving maneuvers (lateral (y-axis), longitudinal (x-axis) and braking loads, and moments) reveals the loads in other axes and affect the vehicle. These multi-axis loads due to natural road conditions can be performed by using sophisticated test systems with newly developed 6 degrees of freedom (6 DOF).

Figure 2. General operation of the road simulation test process [8].

Figure 2 shows the general operation procedure of the road simulation. First step is obtaining of the data from test tracks which followed by data editing and creating desired data. When the same test vehicle is loaded on simulator, required drive file is generated with closed loop controller in laboratory environment. In this context, while one actuator control is provided for each axle in single degree of freedom systems such as Four Posters, 6 DOF systems have six actuator controls for each axle. 6 DOF road simulation test systems must have strong software and hardware in order to apply complex and nonlinear road loads to the complete

179

vehicle in any time period (t) [11]. Therefore, the control software and hardware of the system could be able to communicate properly with the sensors on the vehicle and the controller also should be able to run the system accordingly. It is necessary to take these features into consideration when selecting the appropriate 6 DOF systems on the market. When the multi-axis road loads are applied to the vehicle, the entire vehicle is vibrated on the multi-axis with respect to the loads given. Considering an average passenger vehicle, a load of around 300-400 kg per axle is required to be shaken in a certain way. In doing so, the test system itself is required to run smoothly without being affected by this vibration. So that, the stable operating frequency values of 6 DOF road simulation test systems appear as an important parameter during the test.

On the other hand, iterative methods for recovering the road data on the vehicle may be criteria such as RMS max / min, RMS error and damage for each road data. Considering that this process is performed with multi-axis road data, it is time-consuming to carry out these checks for each road data to continue until the target values are reached. In Table 1, the sensor parameters to be converged in single and multi-axis road simulator benches are given comparatively. As shown in the table, the number of channels to be converged in the iteration steps is higher in multi-axis road simulators. In order to complete the whole work in a short time the software's ability, clarity and user-friendly interface is one of the points to be considered.

Table 1. Used sensor parameters for different road simulators

Parameter	4 Poster Road Simulator	6 DOF Half Vehicle Road Simulator	6 DOF Full Vehicle Road Simulator
F_x		X	X
F_y		X	X
F_z		X	X
M_x		X	X
M_y		X	X
M_z		X	X
a_x		X	X
a_y		X	X
a_z	X	X	X
x_x		X	X
x_y		X	X
x_z	X	X	X
ε	X	X	X

As the 6 DOF systems have servo-hydraulic infrastructure and closed loop control system with feedback, they are the systems that works at high pressure (210-280 bars) to be able to perform desired

response and drive signal match in order to perform durability tests. So, there is a need for the use of high-quality oil in the hydraulic pumps, servo valves and other sub-components of the system. It is highly important for these systems to be used oil with proper cleaning level and to be performed regular maintenance & calibrations accurately. Otherwise, it has been reported to result in loss of system performance and subsequent malfunctions.

In road simulation activities to be performed in 6 DOF systems, road load data are used collected by means of appropriate sensors over vehicle body, suspension and identified critical parts. There are a wide range of sensors that can be used for this purpose. For each operation, the number of sensors, their position on the vehicle and the part are individually determined and can be completely different. The most common types of used sensors are given in the Table 2.

Table 2. Sensors and parameters used in multi-axis road simulators

Sensors	Parameters
Wheel Force Transducer	M_x, M_y, M_z, F_x, F_y, F_z
Strain Gauge	ε
Displacement Transducer	mm
Accelerometer	m/s^2, g
Thermocouple	$^\circ C$

Here, to read the force and torque parameters from the center of the wheel, three-axis wheel center force measurement sensor (Wheel Force Transducer-WFT) is used. Sensors such as string potentiometers can be used to measure the displacement movements of the suspension and related moving parts. By performing acceleration and strain measurements in critical or reference points and parts, it can be verified that road loads are properly transferred to the vehicle with more data. Multi-axis road simulators can be classified into two main groups: full vehicle and half vehicle road simulators. In the following sections, these two systems will be examined in order.

2.2.1. 6 DOF Full Vehicle Road Load Simulator

In this simulator systems, the entire vehicle is mounted to the test system from its center of the axles (Figure 3). Since each axle is mounted to the test system in such a way that it can move independently from

each other, the vehicle itself can move freely. For this reason, they can be called as free moving (floating body) road simulation test system [12]. At real conditions, the loads such as acceleration, displacement and force from the road, the vehicle's suspension and body are subjected to bending and torsion. These loading conditions that occur in the vehicle body stand out particularly in the complete body and suspension fatigue tests. The amount of torsion affects the amount of damage that will occur. The 6 DOF full vehicle test simulators allow the application of bending-torsional loads under real conditions to the vehicle in a meaningful manner. Thus, structural life-strength tests of body and suspension systems and parts of the vehicle can be performed by using these systems.

Collected road data on both the body and the suspension system are required to perform the 6 DOF full vehicle test, as it can be seen from Table 2. To work with 6dof road simulators, the need of using full vehicle having meaningful body and suspension system force company so that it should be compatible to product development overall planning.

Figure 3. 6 DOF full vehicle road simulation (a) view of the whole system [2], (b) view of the one corner [2], (c) 6 DOF with climatic chamber [5]

2.2.2. 6 DOF Half Vehicle Road Load Simulator

These are test simulators that simulates only the connection points and geometry on the vehicle or road simulators where suspension system tests can be performed using a half vehicle body instead of the full vehicle. In these systems, the test fixture to which the suspension is attached, or half vehicle body is located in a fixed manner. For that reason, these systems can be found as "fixed body"," fixed reacted" in literature [6].

The 6 DOF half-vehicle road simulator can perform the durability test of the front or rear complete suspension of the vehicle (Figure 4). Since the half vehicle body or fixture is fixed, the bending and torsion effects cannot be transmitted to the body via road signals. Therefore, the suspension system and body connections can be verified. To confirm the accuracy of the road simulation test, it is necessary to check that the convergence process made by collecting data with strain gauge on critical parts is at target values.

Figure 4. 6 DOF half vehicle road simulation (a) view of the whole system [13], (b) view of the one corner [12].

3. RESULTS AND DISCUSSION

Because of the requirements of competitiveness and environmentally friendly products, durability tests in automotive product development processes should be carried out in a shorter time and more realistic. While single-axis road simulators were developed and released in different versions, multi-axis road simulators were also developed. These systems have a wide variety of advantages and disadvantages, compared with each other and the place of use. Although these systems are essential in automotive product development processes, some constraints that may vary depending on their software & hardware and usage places play an important role in the selection of the simulators. These constraints are mentioned in below;

- User-friendly with software and hardware
- Remotely controllable and IoT (Internet of Things) compatible for efficient use
- The total investment, running and maintenance costs
- Designed to provide suitable environmental requirements
- Climatic chamber for body and chassis durability testing, acoustic room for NVH testing.
- Software and hardware infrastructures should be able to work with integrated systems; such as safety, alarm system according to CE (Conformity of European) etc.
- Product development strategy of the company

Since the users must comply with the legal environmental requirements, both for the single-axis and multi-axis, electrically-powered versions have started to be commercialized by the companies such as MTS, Moog and BIA. Electrical systems were initially intended for use in quality and NVH fields and became available in systems with increased capacity to perform new vehicle durability tests.

4. CONCLUSION

To move one step forward between the competitors, car manufacturers should consider the more realistic road simulation activities for their vehicle validation. Hence, 6 DOF multi-axis road simulators became a solution by providing more realistic simulation to meet durability testing and major advantages & disadvantages is given in Table 3:

Table 3. Advantage and Disadvantages of Multi-Axis Road Simulators.

Advantages	Disadvantages
• More realistic durability results	• High investment and maintenance cost
• To develop competitive products by eliminating over-engineering (cost & quality)	• May needs, more iteration time
• User friendly software structure	• Need more sensors
• Adaptable to safety precaution	• High experienced user is needed
• Hydraulic or electrical hardware alternatives	
• Compatible for NVH, body and chassis testing	
• Easy to adopt new technological requirements	

As seen from Table 3, for new technological road simulators, which can be said to be more complex, their software and hardware should be user-friendly and remotely controlled, and it is becoming more important that to be compatible with IoT for efficient using of these systems. On the other hands, ability of remotely access to the systems is important to track general trends or to report automatically for any problems to the related department staffs. This is also critical for the high cost of maintenance and the timely completion of the testing activities.

In addition, the total investment cost is expected to be high in the selection of such systems. Users maintenance costs, product development strategies and infrastructure facilities should also be taken into consideration. Moreover, systems must be designed to provide an environment that is suitable for occupational safety, and software infrastructures must be able to work integrated with such systems. Considering the speed of technology, in road simulation test systems, intelligent solutions that are easier to use and having compact structures expected to emerge. Moreover, it is expected that with the help of advanced engineering implementations, the need of physical test track usage will be dramatically decreased. Several studies have been already started on it [14,15].

REFERENCES

[1] KNR Systems INC., 4 Post Road Simulation System, http://www.knrsys.com/portfolio/simulation-testing-package-1/- (Date of access: 3.10.2019).

[2] MTS, Ground Vehicle Testing Solutions, http://www.mts.com/cs/groups/public/documents/library/dev_004670.pdf - (Date of access: 03.10.2019).

[3] BIA, 6 DOF Chassis Dynamometer, http://www.bia.fr/ - (Date of access: 03.10.2019).

[4] MOOG, Tire Coupled Simulation System, https://www.moog.com/content/dam/moog/literature/ICD/ Moog-Test-TireCoupledSimulationSystem-Overview-en.pdf - (Date of access: 03.10.2019).

[5] INSTRON, Structural Durability Solutions. https://www.instron.com.tr/tr-tr/products/testing-systems/ structural-durability/structural-durability-solutions - (Date of access: 03.10.2019).

[6] Xu, P., Wong, D., LeBlanc, P., Peticca, G., Road Test Simulation Technology in Light Vehicle Development and Durability Evaluation, SAE Technical Paper Series, 1, 854-865, 2005.

[7] MTS, Model 320 Tire-Coupled Road Simulators, http://www.mts.com/en/products/producttype/test-systems/simulation-systems/road-simulation/tire-coupled/index.htm - (Date of access: 03.10.2019)

[8] Chindamo, D., Gadola, M. and Marchesin, F.P., Reproduction of real-world road profiles on a four-poster rig for indoor vehicle chassis and suspension durability testing, Advanced in Mechanical Engineering, 9(8), 1-10, 2017.

[9] CFM-Schiller, Pit Covers-General Applications, http://www.cfm-schiller.de/en/test-rig-technology/ products/pit-covers/ - (Date of access: 03.10.2019).

[10] MTS, Model 320 ePost™ Tire-coupled Road Simulators, http://www.mts.com/cs/groups/public/ documents/library/mts_2010987.pdf - (Date of access: 03.10.2019).

[11] Colombet, F., Paillot, D., Merienne, F., Kemeny, A., Visual Scale Factor for Speed Perception, Journal of Computing and Information Science in Engineering, 11(4), 1-6, 2011.

[12] MTS, Model 329 Multiaxial Spindle-Coupled Road Simulators, http://www.mts.com/en/products/ producttype/ test-systems/simulation-systems/road-simulation/spindle-coupled/index.htm - (Date of access: 03.10.2019).

[13] The ARDC: FCA Canada/University of Windsor Labs., https://www.allpar.com/corporate/factories/ canada/labs.html - (Date of access: 03.10.2019).

[14] Fricke, D. and Frost, M., Development of a Full-Vehicle Hybrid-Simulation Test using Hybrid System Response Convergence (HSRC), SAE Int. J. Passenger Cars - Mechanical Systems, 5(2), 921-936, 2012.

[15] Fricke, D., Hybrid System Response Convergence (HSRC)-An Alternative Method for Durability Hybrid Simulation, Vehicle Dynamics Expo, 20-22 June 2010, Stuttgart, Germany.

A NEW CHARACTERIZATION OF SMARANDACHE TNB CURVES OF HELICES IN THE SOL SPACE Sol³

T. Körpınar[1], Y. Ünlütürk[2], S. Baş[3]

[1]*Department of Mathematics, Faculty of Arts and Sciences, Muş Alparslan University, Muş, TURKEY*
[2] *Department of Mathematics, Faculty of Arts and Sciences, Kırklareli University, Kırklareli, TURKEY*
[3] *Department of Mathematics, Faculty of Arts and Sciences, Muş Alparslan University, Muş, TURKEY*

E-mail: talatkorpinar@gmail.com

Abstract

In this paper, we characterize Smarandache **TNB** curves of helices in the Sol space Sol³. We characterize Smarandache **TNB** curves of helices in terms of their curvature and torsion. Finally, we find out their explicit parametric equations.

Keywords: General helix, Sol Space, Curvature, Torsion, Smarandache **TNB** curve.

1. INTRODUCTION

A fundamental advance in theory of curves was the advent of analytic geometry in the seventeenth century. This enabled a curve to be described using an equation rather than an elaborate geometrical construction. This not only allowed new curves to be defined and studied, but it enabled a formal distinction to be made between curves that can be defined using algebraic equations, algebraic curves. Some curves and surfaces have been also represented as motion by several authors [1-7].

The geometry of the Galilean Relativity works such as a bridge from Euclidean geometry to special Relativity. The geometry of curves in Euclidean space have been developed in the past [4]. In modern times, mathematicians have started to research curves and surfaces some different spaces [8-24].

Helices are among easy and simple styles that are located in the filamentary and molecular improvements of mechanics. A nearby physical elements of such components have a inclination to be made by way of a standard elastic potential energy dependent on bending and opinion, which is accurately what we call a pole version.

In this paper, we study Smarandache **TNB** curves of helices in the Sol^3. We characterize Smarandache **TNB** curves of helices in terms of their curvature and torsion. Finally, we find out their explicit parametric equations.

2. MATERIAL AND METHODS

Sol space, one of Thurston's eight 3-dimensional geometries, can be viewed as R^3 provided with Riemannian metric

$$g_{\mathsf{Sol}^3} = e^{2z}dx^2 + e^{-2z}dy^2 + dz^2,$$

where (x, y, z) are the standard coordinates in R^3.

Note that the Sol metric can also be written as [25]:

$$g_{\mathsf{Sol}^3} = \sum_{i=1}^{3} \boldsymbol{\omega}^i \otimes \boldsymbol{\omega}^i,$$

where

$$\boldsymbol{\omega}^1 = e^z dx, \ \boldsymbol{\omega}^2 = e^{-z} dy, \ \boldsymbol{\omega}^3 = dz,$$

and the orthonormal basis dual to the 1-forms is

$$\mathbf{e}_1 = e^{-z}\frac{\partial}{\partial x}, \ \mathbf{e}_2 = e^z\frac{\partial}{\partial y}, \ \mathbf{e}_3 = \frac{\partial}{\partial z}.$$

Assume that $\{\mathbf{T},\mathbf{N},\mathbf{B}\}$ be the Frenet frame field along γ. Then, the Frenet frame satisfies the following Frenet--Serret equations [26,27]:

$$
\begin{aligned}
\nabla_{\mathbf{T}}\mathbf{T} &= \kappa\mathbf{N}, \\
\nabla_{\mathbf{T}}\mathbf{N} &= -\kappa\mathbf{T} + \tau\mathbf{B}, \\
\nabla_{\mathbf{T}}\mathbf{B} &= -\tau\mathbf{N},
\end{aligned}
$$

where κ is the curvature of γ and τ its torsion and

$$
\begin{aligned}
g_{\mathrm{Sol}^3}(\mathbf{T},\mathbf{T}) &= 1, g_{\mathrm{Sol}^3}(\mathbf{N},\mathbf{N}) = 1, g_{\mathrm{Sol}^3}(\mathbf{B},\mathbf{B}) = 1, \\
g_{\mathrm{Sol}^3}(\mathbf{T},\mathbf{N}) &= g_{\mathrm{Sol}^3}(\mathbf{T},\mathbf{B}) = g_{\mathrm{Sol}^3}(\mathbf{N},\mathbf{B}) = 0.
\end{aligned}
$$

With respect to the orthonormal basis $\{\mathbf{e}_1,\mathbf{e}_2,\mathbf{e}_3\}$, we can write

$$
\begin{aligned}
\mathbf{T} &= T_1\mathbf{e}_1 + T_2\mathbf{e}_2 + T_3\mathbf{e}_3, \\
\mathbf{N} &= N_1\mathbf{e}_1 + N_2\mathbf{e}_2 + N_3\mathbf{e}_3, \\
\mathbf{B} &= \mathbf{T}\times\mathbf{N} = B_1\mathbf{e}_1 + B_2\mathbf{e}_2 + B_3\mathbf{e}_3.
\end{aligned}
$$

Theorem 2.1. ([28]) *Let* $\gamma : I \to \mathrm{Sol}^3$ *be a unit speed non-geodesic general helix. Then, the parametric equations of γ are*

$$
x(s) = \frac{\sin\mathrm{P}\, e^{-\cos\mathrm{P}s - C_3}}{C_1^2 + \cos^2\mathrm{P}}[-\cos\mathrm{P}\cos[C_1 s + C_2] + C_1\sin[C_1 s + C_2]] + C_4,
$$

$$
y(s) = \frac{\sin\mathrm{P}\, e^{\cos\mathrm{P}s + C_3}}{C_1^2 + \cos^2\mathrm{P}}[-C_1\cos[C_1 s + C_2] + \cos\mathrm{P}\sin[C_1 s + C_2]] + C_5,
$$

$$
z(s) = \cos\mathrm{P}s + C_3,
$$

where C_1, C_2, C_3, C_4, C_5 *are constants of integration.*

3. RESULTS AND DISCUSSION

Definition 3.1. *Let* $\gamma : I \to \mathsf{Sol}^3$ *be a unit speed helix in the Sol Space* Sol^3 *and* $\{\mathbf{T}, \mathbf{N}, \mathbf{B}\}$ *be its moving Frenet frame. Smarandache* **TNB** *curves are defined by*

$$\gamma_{\mathbf{TNB}} = \frac{1}{\sqrt{2\kappa^2 - 2\kappa\tau + 2\tau^2}}\left(\mathbf{T} + \mathbf{N} + \mathbf{B}\right).$$

Theorem 3.2. *Let* $\gamma : I \to \mathsf{Sol}^3$ *be a unit speed non-geodesic helix in the Sol Space* Sol^3. *Then, the equation of Smarandache* **TNB** *curve of a unit speed non-geodesic helix is given by*

$$
\begin{aligned}
\gamma_{\mathbf{TNB}} \quad = \quad & \mathsf{W}[\sin\mathsf{P}\cos[\mathsf{C}_1 s + \mathsf{C}_2] + \frac{1}{\kappa}[-\frac{1}{\mathsf{C}_1}\sin\mathsf{P}\sin[\mathsf{C}_1 s + \mathsf{C}_2] + \cos\mathsf{P}\sin\mathsf{P}\cos[\mathsf{C}_1 s + \mathsf{C}_2]] \\
& +[\frac{1}{\kappa}\sin\mathsf{P}\sin[\mathsf{C}_1 s + \mathsf{C}_2][\sin^2\mathsf{P}\sin^2[\mathsf{C}_1 s + \mathsf{C}_2] - \sin^2\mathsf{P}\cos^2[\mathsf{C}_1 s + \mathsf{C}_2] \\
& -\frac{1}{\kappa}\cos\mathsf{P}[\frac{1}{\mathsf{C}_1}\sin\mathsf{P}\cos[\mathsf{C}_1 s + \mathsf{C}_2] - \cos\mathsf{P}\sin\mathsf{P}\sin[\mathsf{C}_1 s + \mathsf{C}_2]]]\mathbf{e}_1 \\
& + \mathsf{W}[\sin\mathsf{P}\sin[\mathsf{C}_1 s + \mathsf{C}_2] + \frac{1}{\kappa}[\frac{1}{\mathsf{C}_1}\sin\mathsf{P}\cos[\mathsf{C}_1 s + \mathsf{C}_2] - \cos\mathsf{P}\sin\mathsf{P}\sin[\mathsf{C}_1 s + \mathsf{C}_2]] \\
& -[\frac{1}{\kappa}\sin\mathsf{P}\cos[\mathsf{C}_1 s + \mathsf{C}_2][\sin^2\mathsf{P}\sin^2[\mathsf{C}_1 s + \mathsf{C}_2] - \sin^2\mathsf{P}\cos^2[\mathsf{C}_1 s + \mathsf{C}_2] \\
& -\frac{1}{\kappa}\cos\mathsf{P}[-\frac{1}{\mathsf{C}_1}\sin\mathsf{P}\sin[\mathsf{C}_1 s + \mathsf{C}_2] + \cos\mathsf{P}\sin\mathsf{P}\cos[\mathsf{C}_1 s + \mathsf{C}_2]]]]\mathbf{e}_2 \\
& + \mathsf{W}[\cos\mathsf{P} + \frac{1}{\kappa}[\sin^2\mathsf{P}\sin^2[\mathsf{C}_1 s + \mathsf{C}_2] - \sin^2\mathsf{P}\cos^2[\mathsf{C}_1 s + \mathsf{C}_2]] \\
& +\frac{1}{\kappa}\sin\mathsf{P}\cos[\mathsf{C}_1 s + \mathsf{C}_2][\frac{1}{\mathsf{C}_1}\sin\mathsf{P}\cos[\mathsf{C}_1 s + \mathsf{C}_2] - \cos\mathsf{P}\sin\mathsf{P}\sin[\mathsf{C}_1 s + \mathsf{C}_2] \\
& -\frac{1}{\kappa}\sin\mathsf{P}\sin[\mathsf{C}_1 s + \mathsf{C}_2][-\frac{1}{\mathsf{C}_1}\sin\mathsf{P}\sin[\mathsf{C}_1 s + \mathsf{C}_2] + \cos\mathsf{P}\sin\mathsf{P}\cos[\mathsf{C}_1 s + \mathsf{C}_2]]]\mathbf{e}_3,
\end{aligned}
$$

where $\mathsf{C}_1, \mathsf{C}_2$ *are constants of integration and*

$$\mathsf{W} = \frac{1}{\sqrt{2\kappa^2 - 2\kappa\tau + 2\tau^2}}.$$

189

Corollary 3.3. *Let* $\gamma : I \to \mathsf{Sol}^3$ *be a unit speed non-geodesic helix in the Sol Space* Sol^3. *Then, the parametric equations of Smarandache* **TNB** *curves of a unit speed non-geodesic helix are given by*

$$
\begin{aligned}
x_{\mathbf{TNB}}(s) = \ & \exp[-W[\cos P + \frac{1}{\kappa}[\sin^2 P \sin^2[C_1 s + C_2] - \sin^2 P \cos^2[C_1 s + C_2] \\
& + \frac{1}{\kappa}\sin P \cos[C_1 s + C_2][\frac{1}{C_1}\sin P \cos[C_1 s + C_2] - \cos P \sin P \sin[C_1 s + C_2] \\
& - \frac{1}{\kappa}\sin P \sin[C_1 s + C_2][-\frac{1}{C_1}\sin P \sin[C_1 s + C_2] + \cos P \sin P \cos[C_1 s + C_2]]]] \\
& W[\sin P \cos[C_1 s + C_2] + \sin P \cos[C_1 s + C_2] + [\frac{1}{\kappa}\sin P \sin[C_1 s + C_2][\sin^2 P(1 - 2\cos^2[C_1 s + C_2]) \\
& - \frac{1}{\kappa}\cos P[\frac{1}{C_1}\sin P \cos[C_1 s + C_2] - \cos P \sin P \sin[C_1 s + C_2]]],
\end{aligned}
$$

$$
\begin{aligned}
y_{\mathbf{TNB}}(s) = \ & \exp[W[\cos P + \frac{1}{\kappa}[\sin^2 P \sin^2[C_1 s + C_2] - \sin^2 P \cos^2[C_1 s + C_2] \\
& + \frac{1}{\kappa}\sin P \cos[C_1 s + C_2][\frac{1}{C_1}\sin P \cos[C_1 s + C_2] - \cos P \sin P \sin[C_1 s + C_2] \\
& - \frac{1}{\kappa}\sin P \sin[C_1 s + C_2][-\frac{1}{C_1}\sin P \sin[C_1 s + C_2] + \cos P \sin P \cos[C_1 s + C_2]]]] \\
& W[\sin P \sin[C_1 s + C_2] + \sin P \sin[C_1 s + C_2] \\
& - [\frac{1}{\kappa}\sin P \cos[C_1 s + C_2][\sin^2 P(1 - 2\cos^2[C_1 s + C_2]) \\
& - \frac{1}{\kappa}\cos P[-\frac{1}{C_1}\sin P \sin[C_1 s + C_2] + \cos P \sin P \cos[C_1 s + C_2]]]],
\end{aligned}
$$

$$
\begin{aligned}
z_{\mathbf{TNB}}(s) = \ & W[\cos P + \frac{1}{\kappa}[\sin^2 P \sin^2[C_1 s + C_2] - \sin^2 P \cos^2[C_1 s + C_2] \\
& + \frac{1}{\kappa}\sin P \cos[C_1 s + C_2][\frac{1}{C_1}\sin P \cos[C_1 s + C_2] - \cos P \sin P \sin[C_1 s + C_2] \\
& - \frac{1}{\kappa}\sin P \sin[C_1 s + C_2][-\frac{1}{C_1}\sin P \sin[C_1 s + C_2] + \cos P \sin P \cos[C_1 s + C_2]]],
\end{aligned}
$$

where C_1, C_2 *are constants of integration and*

$$
W = \frac{1}{\sqrt{2\kappa^2 - 2\kappa\tau + 2\tau^2}}.
$$

REFERENCES

[1] V. Asil, T. Körpinar, S. Baş, Inextensible flows of timelike curves with Sabban frame in S_1^2, Siauliai Math. Semin. 7 (15) (2012), 5-12.

[2] MT Sariaydin, T Körpinar, New approach to Bäcklund transformations for a curve and its pedal curve, Afrika Matematika 30 (1-2) (2019), 209-216

[3] S. Baş, T Korpinar, Modified Roller Coaster Surface in Space, Mathematics 7 (2) (2019), 195

[4] M. Ergüt, S. Yilmaz, Y. Ünlütürk, Isotropic Smarandache curves in the complex 4-space, Honam Math. J. 40(1) (2018), 47-59.

[5] A. Mağden, S. Yilmaz, Y. Ünlütürk, Characterizations of special time-like curves in Lorentzian plane L2, Int. J. Geom. Methods Mod. Phys. 14(10) (2017), 1750140, 10 pp.

[5] Y. Ünlütürk, M. Dede, Ü.Z. Savci, C. Ekici, On curves of constant breadth in G13, TWMS J. Appl. Eng. Math. 6(1) (2016), 64-69.

[6] R.A. Abdel-Baky, Y. Ünlütürk, On the curvatures of spacelike circular surfaces. Kuwait J. Sci. 43(3) (2016), 50-58.

[7] L. R. Bishop: There is More Than One Way to Frame a Curve, Amer. Math. Monthly 82 (3) (1975) 246-251.

[8] M. Dede, C. Ekici, W. Goemans, Y. Ünlütürk, Twisted surfaces with vanishing curvature in Galilean 3-space. Int. J. Geom. Methods Mod. Phys. 15(1) (2018), 1850001, 13 pp.

[9] MT Sariaydin, T Korpinar, On d-pencil surface by using darboux frame in minkowski 3 space, Journal of Science and Arts 19 (2) (2019), 281-294

[10] T Korpinar, RC Demirkol, V Asil, A new approach to bending energy of elastica for space curves in De-Sitter space, Journal of Science and Arts 19 (2) (2019), 325-338

[11] T. Körpinar, R.C. Demirkol, Energy on a timelike particle in dynamical and electrodynamical force fields in De-Sitter space. Revista Mexicana de Fisica. 63, (2017), 560-568.

[12] Z.S. Körpinar, M. Tuz, T. Körpinar, New Electromagnetic Fluids Inextensible Flows of Spacelike Particles and some Wave Solutions in Minkowski Space-time, Int J Theor Phys 55 (1) (2016), 8-16

[13] T. Körpinar, A new version of energy for slant helix with bending energy in the Lie groups. Journal of Science and Arts 17(4) (2017), 721-730.

[14] T. Korpinar, E. Turhan, Time Evolution Equations for Surfaces Generated via Binormal Spherical Image in Terms of Inextensible Flows in E^3, J. Dyn. Syst. Geom. Theor. 12 (2) (2014), 145-157.

[15] M. Gage, R.S. Hamilton, The heat equation shrinking convex plane curves, J. Differential Geom. 23 (1986), 69-96.

[16] Y. Ünlütürk, S. Yilmaz, C. Ekici, The relations between null geodesic curves and timelike ruled surfaces in dual Lorentzian space $D^3 1$, Honam Math. J. 41(1) (2019), 185-195.

[17] T. Körpinar, E. Turhan, New solution of differential equation for dual curvatures of dual spacelike biharmonic curves with timelike principal normal according to dual Bishop frames in the dual Lorentzian space, Acta Universitatis Apulensis 30 (2012), 77-86.

[18] T. Korpinar, E. Turhan, New Approach for Binormal Spherical Image in Terms of Inextensible Flow in E^3, Prespacetime Journal 4 (4) (2013), 342-355.

[19] T. Körpinar, On the Fermi-Walker Derivative for Inextensible Flows, Zeitschrift für Naturforschung A. 70 (7) (2015), 477-482

[20] T Körpinar, S. Bas, A new approach to inextensible flows of curves with blaschke frame, Journal of Science and Arts 19 (1), 15-22

[21] T. Körpinar, New Characterization for Minimizing Energy of Biharmonic Particles in Heisenberg Spacetime, Int J Phys.53 (2014) 3208-3218

[22] T. Körpinar, Bianchi Type-I Cosmological Models for Inextensible Flows of Biharmonic Particles by Using Curvature Tensor Field in Spacetime, Int J Theor Phys 54 (2015), 1762-1770

[23] T Körpinar, RC Demirkol, Z Körp nar, Soliton propagation of electromagnetic field vectors of polarized light ray traveling in a coiled optical fiber in Minkowski space with Bishop equations, The European Physical Journal D 73 (9), 203

[24] T Korpinar, RC Demirkol, V Asil, A new approach to bending energy of elastica for space curves in De-Sitter space, Journal of Science and Arts 19 (2), 325-338

[25] Y. Ou and Z. Wang, Linear Biharmonic Maps into Sol, Nil and Heisenberg Spaces, Mediterr. j. math. 5 (2008), 379-394

[26] M. do Carmo, Differential Geometry of Curves and Surfaces, Prentice-Hall, Englewood Cliffs, 1976.

[27] D. J. Struik, Lectures on Classical Differential Geometry, Dover, New-York, 1988.

[28] T. Körpinar and E. Turhan, Integral Equations of Biharmonic Constant Π_1 – Slope Curves according to New Type-2 Bishop Frame in Sol Space SOL^3, Bol. Soc. Paran. Mat., 31 2 (2013), 205-212.

[24] E. Turhan and T. Körpinar, Parametric equations of general helices in the sol space, Bol. Soc. Paran. Mat., 31 (1) (2013), 99--104.

[25] D.J. Unger, Developable surfaces in elastoplastic fracture mechanics, Int. J. Fract. 50 (1991) 33-38.

[26] S. Yilmaz and M. Turgut, A new version of Bishop frame and an application to spherical images, J. Math. Anal. Appl., 371 (2010), 764-776.

NEW APPROACH TO INEXTENSIBLE FLOWS OF Π_2 BISHOP SPHERICAL IMAGES ACCORDING TO TYPE-2 BISHOP FRAME IN E³

T. Körpınar[1], Y. Ünlütürk[2], M.T. Sarıaydın[3]

[1]*Department of Mathematics, Faculty of Arts and Sciences, Muş Alparslan University, Muş, TURKEY*
[2] *Department of Mathematics, Faculty of Arts and Sciences, Kırklareli University, Kırklareli, TURKEY*
[3] *Department of Mathematics, Faculty of Arts and Sciences, Selçuk University, Konya, TURKEY*

E-mail: talatkorpinar@gmail.com

Abstract

In this paper, we study Π_2 Bishop spherical images in Euclidean space E³. Using the type-2 Bishop frame of the given curve, we present partial differential equations. We give some characterizations for curvatures of a curve in Euclidean space E³.

Keywords: Type-2 Bishop frame, Sol Space, Curvatures, Flows.

1. INTRODUCTION

Construction of fluid flows constitutes an active research field with a high industrial impact. Corresponding real-world measurements in concrete scenarios complement numerical results from direct simulations of the Navier-Stokes equation, particularly in the case of turbulent flows, and for the understanding of the complex spatio-temporal evolution of instationary flow phenomena. More and more advanced imaging devices (lasers, highspeed cameras, control logic, etc.) are currently developed that allow to record fully timeresolved image sequences of fluid flows at high resolutions. As a consequence, there is a need for advanced algorithms for the analysis of such data, to provide the basis for a subsequent pattern analysis, and with abundant applications across various areas, [1-12].

Physically, inextensible surface area and curve flows bring about motions where zero strain energy is normally induced. The swinging movement of a cord of set length, for instance, could be referred to by inextensible surface area and curve flows. Such motions occur quite normally in an array of physical applications, [13-29].

In this paper, we study Π_2 Bishop spherical images in Euclidean space E^3. Using the type-2 Bishop frame of the given curve, we present partial differential equations. We give some characterizations for curvatures of a curve in Euclidean space E^3.

2. MATERIAL AND METHODS

Let us express a relatively parallel adapted frame:

$$
\begin{aligned}
\nabla_{\mathbf{T}} \Pi_1 &= -\varepsilon_1 \mathbf{B}, \\
\nabla_{\mathbf{T}} \Pi_2 &= -\varepsilon_2 \mathbf{B}, \\
\nabla_{\mathbf{T}} \mathbf{B} &= \varepsilon_1 \Pi_1 + \varepsilon_2 \Pi_2,
\end{aligned}
$$

where

$$
\begin{aligned}
g(\mathbf{B},\mathbf{B}) &= 1, g(\Pi_1,\Pi_1)=1, g(\Pi_2,\Pi_2)=1, \\
g(\mathbf{B},\Pi_1) &= g(\mathbf{B},\Pi_2)=g(\Pi_1,\Pi_2)=0.
\end{aligned}
$$

We shall call this frame as Type-2 Bishop Frame, [30-32].

Definition 2.1. Let α be a regular curve in E^3. If we translate of the second vector field of type-2 Bishop frame to the center O of the unit sphere S^2, we obtain a spherical image ϕ. This curve is called Π_2 Bishop spherical image or indicatrix of the curve α [33].

3. RESULTS AND DISCUSSION

Let $\alpha(u,t)$ is a one parameter family of smooth curves in E^3.

Any flow of α can be represented as $\{\mathbf{\Pi}_1, \mathbf{\Pi}_2, \mathbf{B}\}$

$$\frac{\partial \alpha}{\partial t} = \mathsf{b}_1 \mathbf{\Pi}_1 + \mathsf{b}_2 \mathbf{\Pi}_2 + \mathsf{b}_3 \mathbf{B},$$

where $\mathsf{b}_1, \mathsf{b}_2, \mathsf{b}_3 \in C^\infty(\mathsf{E}^3)$.

Definition 3.1. *The flow $\dfrac{\partial \alpha}{\partial t}$ in E^3 are said to be inextensible if*

$$\frac{\partial}{\partial t}\left|\frac{\partial \alpha}{\partial u}\right| = 0.$$

Lemma 3.2. *Let $\dfrac{\partial \alpha}{\partial t}$ be a smooth flow of the curve α according to new type-2 Bishop frame. The flow is inextensible if and only if*

$$(\frac{\partial \mathsf{b}_1}{\partial u} + \mathsf{b}_3 v \varepsilon_1)\sin \mathsf{A} = (\frac{\partial \mathsf{b}_2}{\partial u} + \mathsf{b}_3 v \varepsilon_2)\cos \mathsf{A},$$

where $\mathsf{b}_1, \mathsf{b}_2, \mathsf{b}_3 \in C^\infty(\mathsf{E}^3)$.

Theorem 3.3.

$$\frac{\partial \mathbf{\Pi}_1}{\partial t} = [\mathsf{p}_1 - \cos \mathsf{A}(\frac{\partial \mathsf{b}_1}{\partial s} + \mathsf{b}_3 \varepsilon_1 + \frac{\partial \mathsf{A}}{\partial s}\cos \mathsf{A})]\mathbf{\Pi}_2 + \mathsf{p}_2 \mathbf{B},$$

$$\frac{\partial \mathbf{\Pi}_2}{\partial t} = [\mathsf{p}_3 + (\frac{\partial \mathsf{b}_2}{\partial s} + \mathsf{b}_3 \varepsilon_2 - \frac{\partial \mathsf{A}}{\partial s}\sin \mathsf{A})\sin \mathsf{A}]\mathbf{\Pi}_1 + \mathsf{p}_4 \mathbf{B},$$

$$\frac{\partial \mathbf{B}}{\partial t} = [\mathsf{p}_5 + (\frac{\partial \mathsf{b}_3}{\partial s} - \mathsf{b}_1 \varepsilon_1 - \mathsf{b}_2 \varepsilon_2)\sin \mathsf{A}]\mathbf{\Pi}_1 + [\mathsf{p}_6 - (\frac{\partial \mathsf{b}_3}{\partial s} - \mathsf{b}_1 \varepsilon_1 - \mathsf{b}_2 \varepsilon_2)\cos \mathsf{A}]\mathbf{\Pi}_2,$$

where $\mathsf{p}_1, \mathsf{p}_2, \mathsf{p}_3, \mathsf{p}_4, \mathsf{p}_5, \mathsf{p}_6 \in C^\infty(\mathsf{E}^3)$.

Theorem 3.4.

$$\frac{\partial \mathbf{T}^{\beta}}{\partial t} = [\mathsf{p}_5 + (\frac{\partial \mathsf{b}_3}{\partial s} - \mathsf{b}_1 \varepsilon_1 - \mathsf{b}_2 \varepsilon_2) \sin A] \mathbf{\Pi}_1$$

$$+ [\mathsf{p}_6 - (\frac{\partial \mathsf{b}_3}{\partial s} - \mathsf{b}_1 \varepsilon_1 - \mathsf{b}_2 \varepsilon_2) \cos A] \mathbf{\Pi}_2,$$

$$\frac{\partial \mathbf{N}^{\beta}}{\partial t} = [-\frac{\partial}{\partial t}(\frac{\varepsilon_1}{\varepsilon_2 \kappa^{\beta}}) - \frac{1}{\kappa^{\beta}}[\mathsf{p}_3 + (\frac{\partial \mathsf{b}_2}{\partial s} + \mathsf{b}_3 \varepsilon_2 - \frac{\partial A}{\partial s} \sin A) \sin A]] \mathbf{\Pi}_1$$

$$+ [-\frac{\partial}{\partial t}(\frac{1}{\kappa^{\beta}}) - \frac{\varepsilon_1}{\varepsilon_2 \kappa^{\beta}}[\mathsf{p}_1 - \cos A(\frac{\partial \mathsf{b}_1}{\partial s} + \mathsf{b}_3 \varepsilon_1 + \frac{\partial A}{\partial s} \cos A)]] \mathbf{\Pi}_2$$

$$- [\frac{\varepsilon_1}{\varepsilon_2 \kappa^{\beta}} \mathsf{p}_2 + \frac{1}{\kappa^{\beta}} \mathsf{p}_4] \mathbf{B},$$

$$\frac{\partial \mathbf{B}^{\beta}}{\partial t} = [\frac{\partial}{\partial t}(\frac{1}{\kappa^{\beta}}) - \frac{\varepsilon_1}{\varepsilon_2 \kappa^{\beta}}[\mathsf{p}_3 + (\frac{\partial \mathsf{b}_2}{\partial s} + \mathsf{b}_3 \varepsilon_2 - \frac{\partial A}{\partial s} \sin A) \sin A]] \mathbf{\Pi}_1$$

$$+ [\frac{1}{\kappa^{\beta}}[\mathsf{p}_1 - \cos A(\frac{\partial \mathsf{b}_1}{\partial s} + \mathsf{b}_3 \varepsilon_1 + \frac{\partial A}{\partial s} \cos A)] - \frac{\partial}{\partial t}(\frac{\varepsilon_1}{\varepsilon_2 \kappa^{\beta}})] \mathbf{\Pi}_2$$

$$+ [\frac{1}{\kappa^{\beta}} \mathsf{p}_2 - \frac{\varepsilon_1}{\varepsilon_2 \kappa^{\beta}} \mathsf{p}_4] \mathbf{B},$$

where $\mathsf{p}_1, \mathsf{p}_2, \mathsf{p}_3, \mathsf{p}_4, \mathsf{p}_5, \mathsf{p}_6, \mathsf{b}_1, \mathsf{b}_2, \mathsf{b}_3$ *are smooth functions of time and arc length.*

Theorem 3.5. *Let* $\frac{\partial \alpha}{\partial t}$ *be inextensible according to new type-2 Bishop frame. If* β *is spherical image of* α, *then,*

$$\varepsilon_1[\mathsf{p}_5 + (\frac{\partial \mathsf{b}_3}{\partial s} - \mathsf{b}_1 \varepsilon_1 - \mathsf{b}_2 \varepsilon_2) \sin A] + \varepsilon_2[\mathsf{p}_6 - (\frac{\partial \mathsf{b}_3}{\partial s}$$

$$- \mathsf{b}_1 \varepsilon_1 - \mathsf{b}_2 \varepsilon_2) \cos A]] = \varepsilon_2[\frac{\varepsilon_1}{\varepsilon_2 \kappa^{\beta}} \mathsf{p}_2 + \frac{1}{\kappa^{\beta}} \mathsf{p}_4],$$

where $\mathsf{p}_1, \mathsf{b}_1, \mathsf{b}_2, \mathsf{b}_3$ *are smooth functions of time and arc length.*

Corollary 3.6.

$$\frac{\partial}{\partial s}[\mathsf{p}_5 + (\frac{\partial \mathsf{b}_3}{\partial s} - \mathsf{b}_1 \varepsilon_1 - \mathsf{b}_2 \varepsilon_2) \sin A] = [\varepsilon_2[-\frac{\partial}{\partial t}(\frac{\varepsilon_1}{\varepsilon_2 \kappa^{\beta}})$$

$$- \frac{1}{\kappa^{\beta}}[\mathsf{p}_3 + (\frac{\partial \mathsf{b}_2}{\partial s} + \mathsf{b}_3 \varepsilon_2 - \frac{\partial A}{\partial s} \sin A) \sin A]] - \frac{\partial}{\partial t} \varepsilon_2 \frac{\varepsilon_1}{\varepsilon_2 \kappa^{\beta}}],$$

where $\mathsf{p}_i, \mathsf{b}_i$ *are smooth functions of time and arc length.*

Corollary 3.7.

$$\varepsilon_2[-\frac{\partial}{\partial t}(\frac{1}{\kappa^\beta}) - \frac{\varepsilon_1}{\varepsilon_2\kappa^\beta}[\mathsf{p}_1 - \cos A(\frac{\partial \mathsf{b}_1}{\partial s} + \mathsf{b}_3\varepsilon_1 + \frac{\partial A}{\partial s}\cos A)]]$$

$$-\frac{\partial}{\partial t}\varepsilon_2\frac{1}{\kappa^\beta}] = \frac{\partial}{\partial s}[\mathsf{p}_6 - (\frac{\partial \mathsf{b}_3}{\partial s} - \mathsf{b}_1\varepsilon_1 - \mathsf{b}_2\varepsilon_2)\cos A],$$

where $\mathsf{p}_i, \mathsf{b}_i$ are smooth functions of time and arc length.

Theorem 3.8. *Let $\frac{\partial \alpha}{\partial t}$ be inextensible according to new type-2 Bishop frame. If β is spherical image of α, then,*

$$-[\frac{\partial}{\partial s}[\frac{\varepsilon_1}{\varepsilon_2\kappa^\beta}\mathsf{p}_2 + \frac{1}{\kappa^\beta}\mathsf{p}_4] + \varepsilon_1[-\frac{\partial}{\partial t}(\frac{\varepsilon_1}{\varepsilon_2\kappa^\beta}) - \frac{1}{\kappa^\beta}[\mathsf{p}_3 + (\frac{\partial \mathsf{b}_2}{\partial s} + \mathsf{b}_3\varepsilon_2$$

$$-\frac{\partial A}{\partial s}\sin A)\sin A]] + \varepsilon_2[-\frac{\partial}{\partial t}(\frac{1}{\kappa^\beta}) - \frac{\varepsilon_1}{\varepsilon_2\kappa^\beta}[\mathsf{p}_1 - \cos A(\frac{\partial \mathsf{b}_1}{\partial s} + \mathsf{b}_3\varepsilon_1$$

$$+\frac{\partial A}{\partial s}\cos A)]]] = [(\tau^\beta\varepsilon_2)[\frac{1}{\kappa^\beta}\mathsf{p}_2 - \frac{\varepsilon_1}{\varepsilon_2\kappa^\beta}\mathsf{p}_4] - \frac{\partial}{\partial t}(\kappa^\beta\varepsilon_2)],$$

where $\mathsf{p}_1, \mathsf{p}_2, \mathsf{p}_3, \mathsf{p}_4, \mathsf{p}_5, \mathsf{p}_6, \mathsf{b}_1, \mathsf{b}_2, \mathsf{b}_3$ are smooth functions of time and arc length.

Corollary 3.9.

$$\frac{1}{\kappa^\beta}\frac{\partial}{\partial t}(\tau^\beta\varepsilon_2) - (\kappa^\beta\varepsilon_2)[\mathsf{p}_5 + (\frac{\partial \mathsf{b}_3}{\partial s} - \mathsf{b}_1\varepsilon_1 - \mathsf{b}_2\varepsilon_2)\sin A] + (\tau^\beta\varepsilon_2)[\frac{\partial}{\partial t}(\frac{1}{\kappa^\beta})$$

$$-\frac{\varepsilon_1}{\varepsilon_2\kappa^\beta}[\mathsf{p}_3 + (\frac{\partial \mathsf{b}_2}{\partial s} + \mathsf{b}_3\varepsilon_2 - \frac{\partial A}{\partial s}\sin A)\sin A]]] = [\frac{\partial}{\partial s}[-\frac{\partial}{\partial t}(\frac{\varepsilon_1}{\varepsilon_2\kappa^\beta})$$

$$-\frac{1}{\kappa^\beta}[\mathsf{p}_3 + (\frac{\partial \mathsf{b}_2}{\partial s} + \mathsf{b}_3\varepsilon_2 - \frac{\partial A}{\partial s}\sin A)\sin A]] - \varepsilon_1[\frac{\varepsilon_1}{\varepsilon_2\kappa^\beta}\mathsf{p}_2 + \frac{1}{\kappa^\beta}\mathsf{p}_4]],$$

where $\mathsf{p}_1, \mathsf{p}_2, \mathsf{p}_3, \mathsf{p}_4, \mathsf{p}_5, \mathsf{p}_6, \mathsf{b}_1, \mathsf{b}_2, \mathsf{b}_3$ are smooth functions of time and arc length.

Corollary 3.10.

$$\frac{\partial}{\partial s}[-\frac{\partial}{\partial t}(\frac{1}{\kappa^\beta}) - \frac{\varepsilon_1}{\varepsilon_2\kappa^\beta}[\mathsf{p}_1 - \cos A(\frac{\partial \mathsf{b}_1}{\partial s} + \mathsf{b}_3\varepsilon_1 + \frac{\partial A}{\partial s}\cos A)]]$$

$$-\varepsilon_2[\frac{\varepsilon_1}{\varepsilon_2\kappa^\beta}\mathsf{p}_2 + \frac{1}{\kappa^\beta}\mathsf{p}_4]] = [(\tau^\beta\varepsilon_2)[\frac{1}{\kappa^\beta}[\mathsf{p}_1 - \cos A(\frac{\partial \mathsf{b}_1}{\partial s} + \mathsf{b}_3\varepsilon_1 + \frac{\partial A}{\partial s}\cos A)]$$

$$-\frac{\partial}{\partial t}(\frac{\varepsilon_1}{\varepsilon_2\kappa^\beta})] - \frac{\varepsilon_1}{\varepsilon_2\kappa^\beta}\frac{\partial}{\partial t}(\tau^\beta\varepsilon_2) - (\kappa^\beta\varepsilon_2)[\mathsf{p}_6 - (\frac{\partial \mathsf{b}_3}{\partial s} - \mathsf{b}_1\varepsilon_1 - \mathsf{b}_2\varepsilon_2)\cos A]],$$

where $\mathsf{p}_1, \mathsf{p}_2, \mathsf{p}_3, \mathsf{p}_4, \mathsf{p}_5, \mathsf{p}_6, \mathsf{b}_1, \mathsf{b}_2, \mathsf{b}_3$ are smooth functions of time and arc length.

197

Theorem 3.11. *Let* $\dfrac{\partial \alpha}{\partial t}$ *be inextensible according to new type-2 Bishop frame. If* β *is spherical image of* α, *then,*

$$(\tau^\beta \varepsilon_2)[\frac{\varepsilon_1}{\varepsilon_2 \kappa^\beta}\mathsf{p}_2 + \frac{1}{\kappa^\beta}\mathsf{p}_4] = [\frac{\partial}{\partial s}[\frac{1}{\kappa^\beta}\mathsf{p}_2 - \frac{\varepsilon_1}{\varepsilon_2 \kappa^\beta}\mathsf{p}_4]$$

$$-\varepsilon_1[\frac{\partial}{\partial t}(\frac{1}{\kappa^\beta}) - \frac{\varepsilon_1}{\varepsilon_2 \kappa^\beta}[\mathsf{p}_3 + (\frac{\partial \mathsf{b}_2}{\partial s} + \mathsf{b}_3 \varepsilon_2 - \frac{\partial A}{\partial s}\sin A)\sin A]]$$

$$-\varepsilon_2[\frac{1}{\kappa^\beta}[\mathsf{p}_1 - \cos A(\frac{\partial \mathsf{b}_1}{\partial s} + \mathsf{b}_3 \varepsilon_1 + \frac{\partial A}{\partial s}\cos A)] - \frac{\partial}{\partial t}(\frac{\varepsilon_1}{\varepsilon_2 \kappa^\beta})]],$$

where $\mathsf{p}_1, \mathsf{p}_2, \mathsf{p}_3, \mathsf{p}_4, \mathsf{p}_5, \mathsf{p}_6, \mathsf{b}_1, \mathsf{b}_2, \mathsf{b}_3$ *are smooth functions of time and arc length.*

$$\frac{\partial}{\partial s}\frac{\partial \mathbf{B}^\beta}{\partial t} = [\frac{\partial}{\partial s}[\frac{\partial}{\partial t}(\frac{1}{\kappa^\beta}) - \frac{\varepsilon_1}{\varepsilon_2 \kappa^\beta}[\mathsf{p}_3 + (\frac{\partial \mathsf{b}_2}{\partial s} + \mathsf{b}_3 \varepsilon_2$$

$$-\frac{\partial A}{\partial s}\sin A)\sin A]] + \varepsilon_1[\frac{1}{\kappa^\beta}\mathsf{p}_2 - \frac{\varepsilon_1}{\varepsilon_2 \kappa^\beta}\mathsf{p}_4]]\mathbf{\Pi}_1$$

$$+[\frac{\partial}{\partial s}[\frac{1}{\kappa^\beta}[\mathsf{p}_1 - \cos A(\frac{\partial \mathsf{b}_1}{\partial s} + \mathsf{b}_3 \varepsilon_1 + \frac{\partial A}{\partial s}\cos A)]$$

$$-\frac{\partial}{\partial t}(\frac{\varepsilon_1}{\varepsilon_2 \kappa^\beta})] + \varepsilon_2[\frac{1}{\kappa^\beta}\mathsf{p}_2 - \frac{\varepsilon_1}{\varepsilon_2 \kappa^\beta}\mathsf{p}_4]]\mathbf{\Pi}_2$$

$$+[\frac{\partial}{\partial s}[\frac{1}{\kappa^\beta}\mathsf{p}_2 - \frac{\varepsilon_1}{\varepsilon_2 \kappa^\beta}\mathsf{p}_4] - \varepsilon_1[\frac{\partial}{\partial t}(\frac{1}{\kappa^\beta})$$

$$-\frac{\varepsilon_1}{\varepsilon_2 \kappa^\beta}[\mathsf{p}_3 + (\frac{\partial \mathsf{b}_2}{\partial s} + \mathsf{b}_3 \varepsilon_2 - \frac{\partial A}{\partial s}\sin A)\sin A]]$$

$$-\varepsilon_2[\frac{1}{\kappa^\beta}[\mathsf{p}_1 - \cos A(\frac{\partial \mathsf{b}_1}{\partial s} + \mathsf{b}_3 \varepsilon_1 + \frac{\partial A}{\partial s}\cos A)] - \frac{\partial}{\partial t}(\frac{\varepsilon_1}{\varepsilon_2 \kappa^\beta})]]\mathbf{B}$$

or, equivalently

$$\frac{\partial}{\partial t}\frac{\partial \mathbf{B}^\beta}{\partial s} = [\frac{\partial}{\partial t}(\tau^\beta \varepsilon_2)\frac{\varepsilon_1}{\varepsilon_2 \kappa^\beta} - (\tau^\beta \varepsilon_2)[-\frac{\partial}{\partial t}(\frac{\varepsilon_1}{\varepsilon_2 \kappa^\beta})$$

$$-\frac{1}{\kappa^\beta}[\mathsf{p}_3 + (\frac{\partial \mathsf{b}_2}{\partial s} + \mathsf{b}_3 \varepsilon_2 - \frac{\partial A}{\partial s}\sin A)\sin A]]]\mathbf{\Pi}_1$$

$$+[\frac{1}{\kappa^\beta}\frac{\partial}{\partial t}(\tau^\beta \varepsilon_2) - (\tau^\beta \varepsilon_2)[-\frac{\partial}{\partial t}(\frac{1}{\kappa^\beta}) - \frac{\varepsilon_1}{\varepsilon_2 \kappa^\beta}[\mathsf{p}_1$$

$$-\cos A(\frac{\partial \mathsf{b}_1}{\partial s} + \mathsf{b}_3 \varepsilon_1 + \frac{\partial A}{\partial s}\cos A)]]]\mathbf{\Pi}_2$$

$$+(\tau^\beta \varepsilon_2)[\frac{\varepsilon_1}{\varepsilon_2 \kappa^\beta}\mathsf{p}_2 + \frac{1}{\kappa^\beta}\mathsf{p}_4]\mathbf{B}$$

Thus, we obtain the theorem.

198

4. CONCLUSION

Corollary 4.1.

$$\frac{\partial}{\partial t}(\tau^{\beta}\varepsilon_2)\frac{\varepsilon_1}{\varepsilon_2\kappa^{\beta}} - (\tau^{\beta}\varepsilon_2)[-\frac{\partial}{\partial t}(\frac{\varepsilon_1}{\varepsilon_2\kappa^{\beta}}) - \frac{1}{\kappa^{\beta}}[\mathsf{p}_3 + (\frac{\partial \mathsf{b}_2}{\partial s}$$

$$+ \mathsf{b}_3\varepsilon_2 - \frac{\partial A}{\partial s}\sin A)\sin A]]] = [\frac{\partial}{\partial s}[\frac{\partial}{\partial t}(\frac{1}{\kappa^{\beta}}) - \frac{\varepsilon_1}{\varepsilon_2\kappa^{\beta}}[\mathsf{p}_3 + (\frac{\partial \mathsf{b}_2}{\partial s}$$

$$+ \mathsf{b}_3\varepsilon_2 - \frac{\partial A}{\partial s}\sin A)\sin A]] + \varepsilon_1[\frac{1}{\kappa^{\beta}}\mathsf{p}_2 - \frac{\varepsilon_1}{\varepsilon_2\kappa^{\beta}}\mathsf{p}_4]]$$

where $\mathsf{p}_1,\mathsf{p}_2,\mathsf{p}_3,\mathsf{p}_4,\mathsf{p}_5,\mathsf{p}_6,\mathsf{b}_1,\mathsf{b}_2,\mathsf{b}_3$ *are smooth functions of time and arc length.*

Corollary 4.2.

$$\frac{1}{\kappa^{\beta}}\frac{\partial}{\partial t}(\tau^{\beta}\varepsilon_2) - (\tau^{\beta}\varepsilon_2)[-\frac{\partial}{\partial t}(\frac{1}{\kappa^{\beta}}) - \frac{\varepsilon_1}{\varepsilon_2\kappa^{\beta}}[\mathsf{p}_1 - \cos A(\frac{\partial \mathsf{b}_1}{\partial s}$$

$$+ \mathsf{b}_3\varepsilon_1 + \frac{\partial A}{\partial s}\cos A)]]] = [\frac{\partial}{\partial s}[\frac{1}{\kappa^{\beta}}[\mathsf{p}_1 - \cos A(\frac{\partial \mathsf{b}_1}{\partial s} + \mathsf{b}_3\varepsilon_1$$

$$+ \frac{\partial A}{\partial s}\cos A)] - \frac{\partial}{\partial t}(\frac{\varepsilon_1}{\varepsilon_2\kappa^{\beta}})] + \varepsilon_2[\frac{1}{\kappa^{\beta}}\mathsf{p}_2 - \frac{\varepsilon_1}{\varepsilon_2\kappa^{\beta}}\mathsf{p}_4]]$$

where $\mathsf{p}_1,\mathsf{p}_2,\mathsf{p}_3,\mathsf{p}_4,\mathsf{p}_5,\mathsf{p}_6,\mathsf{b}_1,\mathsf{b}_2,\mathsf{b}_3$ *are smooth functions of time and arc length.*

REFERENCES

[1] J. Eells and L. Lemaire, A report on harmonic maps, Bull. London Math. Soc. 10 (1978), 1-68.

[2] J. Eells and J. H. Sampson, Harmonic mappings of Riemannian manifolds, Amer. J. Math. 86 (1964), 109-160.

[3] M. Gage, R.S. Hamilton, The heat equation shrinking convex plane curves, J. Differential Geom. 23 (1986), 69-96.

[4] M. Grayson, The heat equation shrinks embedded plane curves to round points, J. Differential Geom. 26 (1987), 285-314.

[5] T. Körpinar, Y. Ünlütürk, New Bianchi type-I cosmological models for biharmonic particles using string cosmology with exponential law, Gen. Relativity Gravitation 47(11) (2015), Art. 138, 12 pp.

[6] M. Dede, C. Ekici, Y. Ünlütürk, On motion of robot end-effector using the curvature theory of timelike ruled surfaces with timelike directrix, Malays. J. Math. Sci. 8(2) (2014), 189-204.

[7] Y. Ünlütürk, C. Ekici, On parallel surfaces of ruled surfaces with null ruling in Minkowski 3-space, Int. Math. Forum 7 (2012), no. 13-16, 727-736.

[8] C. Ekici, Y. Ünlütürk, C. Ekici, B.S. Ryuh, On motion of robot end-effector using the curvature theory of timelike ruled surfaces with timelike rulings, Math. Probl. Eng. 2008, Art. ID 362783, 19 pp.

[9] R.A. Abdel-Baky, Y. Ünlütürk, A study on classification of translation surfaces in pseudo-Galilean 3-space, J. Coupled Syst. Multi. Dyn. 6(3) (2018), 233-240.

[10] M. Çimdiker, Y. Ünlütürk, The construction of the space-like surface of constant breadth, Int. J. Geom. Methods Mod. Phys. 16(4) (2019), 1950060, 16 pp.

[11] V. Asil, T. Körpinar, S. Baş, Inextensible flows of timelike curves with Sabban frame in S_1^2, Siauliai Math. Semin. 7 (15) (2012), 5-12.

[12] L. R. Bishop, There is More Than One Way to Frame a Curve, Amer. Math. Monthly 82 (3) (1975) 246-251.

[13] T. Korpinar, E. Turhan, New Approach for Binormal Spherical Image in Terms of Inextensible Flow in E^3, Prespacetime Journal 4 (4) (2013), 342-355.

[14] T. Körpinar, On the Fermi-Walker Derivative for Inextensible Flows, Zeitschrift für Naturforschung A. 70 (7) (2015), 477--482

[15] T. Körpinar, R.C. Demirkol, Energy on a timelike particle in dynamical and electrodynamical force fields in De-Sitter space. Revista Mexicana de Fisica. 63, (2017), 560-568.

[16] Z.S. Körpinar, M. Tuz, T. Körpinar, New Electromagnetic Fluids Inextensible Flows of Spacelike Particles and some Wave Solutions in Minkowski Space-time, Int J Theor Phys 55 (1) (2016), 8--16

[17] T. Körpinar, A New Method for Inextensible Flows of Timelike Curves in Minkowski Space-Time E_1^4, International Journal of Partial Differential Equations, Volume 2014, Article ID 517070, 7 pages

[18] T. Körpinar, B-tubular surfaces in Lorentzian Heisenberg Group H_3, Acta Scientiarum. Technology 37(1) (2015), 63--69

[19] T. Körpinar, New characterization of b-m_2 developable surfaces, Acta Scientiarum. Technology 37(2) (2015), 245--250

[20] T. Körpinar, E. Turhan, A New Version of Inextensible Flows of Spacelike Curves with Timelike B_2 in Minkowski Space-Time E_1^4, Differ. Equ. Dyn. Syst., 21 (3) (2013), 281--290.

[21] T. Körpinar, A new version of energy for slant helix with bending energy in the Lie groups. Journal of Science and Arts 17(4) (2017), 721-730.

[22] T. Korpinar, E. Turhan, Time Evolution Equations for Surfaces Generated via Binormal Spherical Image in Terms of Inextensible Flows in E^3, J. Dyn. Syst. Geom. Theor. 12 (2) (2014), 145--157.

[23] T. Körpinar, New Characterization for Minimizing Energy of Biharmonic Particles in Heisenberg Spacetime, Int J Phys.53 (2014) 3208-3218

[24] T. Körpinar, Bianchi Type-I Cosmological Models for Inextensible Flows of Biharmonic Particles by Using Curvature Tensor Field in Spacetime, Int J Theor Phys 54 (2015), 1762-1770

[25] T Körpinar, RC Demirkol, Z Körp nar, Soliton propagation of electromagnetic field vectors of polarized light ray traveling in a coiled optical fiber in Minkowski space with Bishop equations, The European Physical Journal D 73 (9), 203

[26] T Körpinar, S. Ba s , A new approach to inextensible flows of curves with blaschke frame, Journal of Science and Arts 19 (1), 15-22

[27] T Korpinar, RC Demirkol, V Asil, A new approach to bending energy of elastica for space curves in De-Sitter space, Journal of Science and Arts 19 (2), 325-338

[28] D. Y. Kwon, F.C. Park, Evolution of inelastic plane curves, Appl. Math. Lett. 12 (1999), 115-119.

[29] DY. Kwon, FC. Park, DP Chi, Inextensible flows of curves and developable surfaces, Appl. Math. Lett. 18 (2005), 1156-1162.

[30] M. do Carmo, Differential Geometry of Curves and Surfaces, Prentice-Hall, Englewood Cliffs, 1976.

[31] D. J. Struik, Lectures on Classical Differential Geometry, Dover, New-York, 1988.

[32] D.J. Unger, Developable surfaces in elastoplastic fracture mechanics, Int. J. Fract. 50 (1991) 33-38.

[33] S. Yilmaz and M. Turgut, A new version of Bishop frame and an application to spherical images, J. Math. Anal. Appl., 371 (2010), 764-776.

ON B-SURFACES OF BIHARMONIC CONSTANT Π_1-SLOPE CURVES ACCORDING TO TYPE-2 BISHOP FRAME IN THE SOL SPACE SOL³

T. Körpınar[1], Y. Ünlütürk[2], R.C. Demirkol[3]

[1]*Department of Mathematics, Faculty of Arts and Sciences, Muş Alparslan University, Muş, TURKEY*
[2] *Department of Mathematics, Faculty of Arts and Sciences, Kırklareli University, Kırklareli, TURKEY*
[3] *Department of Mathematics, Faculty of Arts and Sciences, Muş Alparslan University, Muş, TURKEY*

E-mail: talatkorpinar@gmail.com

Abstract

In this paper, we study **B-** surfaces of biharmonic constant Π_1-slope curves according to type-2 Bishop in the SOL³. We characterize the **B-** surfaces of biharmonic constant Π_1-slope curves in terms of their Bishop curvatures. Finally, we find out their explicit parametric equations in the SOL³.

Keywords: Sol Space, Curvature, Torsion, **B-** surfaces.

1. INTRODUCTION

Design and style applying some type developable surfaces performs a great significant part on developing differential geometry. Presently virtually all industrial devices may certainly assist transforming free type surfaces inside estimate some new surfaces. Immediate style apply some new surfaces by means of illustrative curves [1-11].

Differentiable function $\phi : N \to M$ is labeled biharmonic if ϕ is a critical point of bienergy functional

$$E_2(\phi) = \int_N \frac{1}{2} |\mathsf{T}(\phi)|^2 dv_h.$$

Here $\mathsf{T}(\phi) := \mathrm{tr}\nabla^\phi d\phi$ is tension, [12,13]. Also, bitension field of ϕ is described by means of

$$\mathsf{T}_2(\phi) = -\Delta_\phi \mathsf{T}(\phi) + \mathrm{tr}R(\mathsf{T}(\phi), d\phi)d\phi.$$

Biharmonic curve also play important roles in geometry. Also, a large number of experts have analyzed geometric biharmonic curve and surface conditions. On the other hand, energy concept have been obtained with some characterizations, [14-20].

In this paper, we study $\mathbf{B}$ – surfaces of biharmonic constant $\mathbf{\Pi}_1$ – slope curves according to type-2 Bishop in the SOL^3. We characterize the $\mathbf{B}$ – surfaces of biharmonic constant $\mathbf{\Pi}_1$ – slope curves in terms of their Bishop curvatures. Finally, we find out their explicit parametric equations in the SOL^3.

2. MATERIAL AND METHODS

Sol space, one of Thurston's eight 3-dimensional geometries with group structure

$$(x, y, z) \cdot (\tilde{x}, \tilde{y}, \tilde{z}) = \left(x + e^z\tilde{x}, y + e^{-z}\tilde{y}, z + \tilde{z} \right)$$

and left invariant metric

$$g_{\mathsf{SOL}^3} = e^{2z}dx^2 + e^{-2z}dy^2 + dz^2,$$

where (x, y, z) are the standard coordinates in R^3.

The space Sol is realized as the following solvable matrix Lie group, [21-24]:

$$\mathsf{SOL}^3 = \left\{ \begin{pmatrix} 1 & 0 & 0 & z \\ 0 & e^z & 0 & x \\ 0 & 0 & e^{-z} & y \\ 0 & 0 & 0 & 1 \end{pmatrix} : x, y, z \in \mathsf{R} \right\}.$$

3. RESULTS AND DISCUSSION

Assume that $\{\mathbf{T},\mathbf{N},\mathbf{B}\}$ be the Frenet frame field along γ. Then, the Frenet frame satisfies the following Frenet-Serret equations:

$$\begin{aligned}
\nabla_{\mathbf{T}}\mathbf{T} &= \kappa\mathbf{N}, \\
\nabla_{\mathbf{T}}\mathbf{N} &= -\kappa\mathbf{T} + \tau\mathbf{B}, \\
\nabla_{\mathbf{T}}\mathbf{B} &= -\tau\mathbf{N},
\end{aligned}$$

where κ is the curvature of γ and τ its torsion, [25].

The Bishop frame or parallel transport frame is an alternative approach to defining a moving frame that is well defined even when the curve has vanishing second derivative, [26,27]. The Bishop frame is expressed as

$$\begin{aligned}
\nabla_{\mathbf{T}}\mathbf{T} &= k_1\mathbf{M}_1 + k_2\mathbf{M}_2, \\
\nabla_{\mathbf{T}}\mathbf{M}_1 &= -k_1\mathbf{T}, \\
\nabla_{\mathbf{T}}\mathbf{M}_2 &= -k_2\mathbf{T}.
\end{aligned}$$

Let γ be a unit speed regular curve in $\mathbf{SOL}^3$ and above equations be its Frenet--Serret frame. Let us express a relatively parallel adapted frame:

$$\begin{aligned}
\nabla_{\mathbf{T}}\Pi_1 &= -\varepsilon_1\mathbf{B}, \\
\nabla_{\mathbf{T}}\Pi_2 &= -\varepsilon_2\mathbf{B}, \\
\nabla_{\mathbf{T}}\mathbf{B} &= \varepsilon_1\Pi_1 + \varepsilon_2\Pi_2.
\end{aligned}$$

We shall call this frame as Type-2 Bishop Frame, [28].

With respect to the orthonormal basis $\{\mathbf{e}_1,\mathbf{e}_2,\mathbf{e}_3\}$, we can write

$$\begin{aligned}
\Pi_1 &= \pi_1^1\mathbf{e}_1 + \pi_1^2\mathbf{e}_2 + \pi_1^3\mathbf{e}_3, \\
\Pi_2 &= \pi_2^1\mathbf{e}_1 + \pi_2^2\mathbf{e}_2 + \pi_2^3\mathbf{e}_3. \\
\mathbf{B} &= B^1\mathbf{e}_1 + B^2\mathbf{e}_2 + B^3\mathbf{e}_3.
\end{aligned}$$

Theorem 3.1. *Let* $\gamma : I \to \mathsf{SOL}^3$ *be a unit speed non-geodesic biharmonic constant* $\mathbf{\Pi}_1 - slope\ curves$ *according to type-2 Bishop frame in the* SOL^3. *Then, the parametric equations of* γ *are*

$$
\begin{aligned}
\mathbf{x}(s) &= e^{\frac{1}{\kappa}\cos[\kappa s]\cos\mathsf{E}-\frac{1}{\kappa}\sin[\kappa s]\sin\mathsf{E}-\mathsf{R}_3}[\sin[\kappa s]\sin\mathsf{E}\cos[\mathsf{R}_1 s+\mathsf{R}_2] \\
&\quad -\cos[\kappa s]\cos\mathsf{E}\cos[\mathsf{R}_1 s+\mathsf{R}_2]]ds, \\
\mathbf{y}(s) &= \int e^{-\frac{1}{\kappa}\cos[\kappa s]\cos\mathsf{E}+\frac{1}{\kappa}\sin[\kappa s]\sin\mathsf{E}+\mathsf{R}_3}[\sin[\kappa s]\sin\mathsf{E}\sin[\mathsf{R}_1 s+\mathsf{R}_2] \\
&\quad -\cos[\kappa s]\cos\mathsf{E}\sin[\mathsf{R}_1 s+\mathsf{R}_2]]ds, \\
\mathbf{z}(s) &= -\frac{1}{\kappa}\cos[\kappa s]\cos\mathsf{E}+\frac{1}{\kappa}\sin[\kappa s]\sin\mathsf{E}+\mathsf{R}_3,
\end{aligned}
$$

where $\mathsf{R}_1, \mathsf{R}_2, \mathsf{R}_3$ *are constants of integration, [29] .*

4. CONCLUSION

The purpose of this section is to study $\mathbf{B}-$ surfaces of biharmonic constant $\mathbf{\Pi}_1 -$ slope curves according to new type-2 Bishop frame in Sol space SOL^3

The $\mathbf{B}-$ surface of γ is a ruled surface

$$\mathsf{E}(s,u) = \gamma(s) + u\mathbf{B}.$$

Theorem 4.1. *Let* $\gamma : I \to \mathsf{SOL}^3$ *be a unit speed non-geodesic biharmonic constant* $\mathbf{\Pi}_1 - slope\ curve$ *according to type-2 Bishop frame and* E *its* $\mathbf{B}-$ *surface in the* SOL^3. *Then, the equation of* E *is*

$$
\begin{aligned}
\mathsf{E}(s,u) &= [e^{-\frac{1}{\kappa}\cos[\kappa s]\cos\mathsf{E}+\frac{1}{\kappa}\sin[\kappa s]\sin\mathsf{E}+\mathsf{R}_3}\, e^{\frac{1}{\kappa}\cos[\kappa s]\cos\mathsf{E}-\frac{1}{\kappa}\sin[\kappa s]\sin\mathsf{E}-\mathsf{R}_3} \\
&\quad [\sin[\kappa s]\sin\mathsf{E}\cos[\mathsf{R}_1 s+\mathsf{R}_2]-\cos[\kappa s]\cos\mathsf{E}\cos[\mathsf{R}_1 s+\mathsf{R}_2]]ds \\
&\quad -u\sin[\mathsf{R}_1 s+\mathsf{R}_2]]\mathbf{e}_1 \\
&\quad +[e^{\frac{1}{\kappa}\cos[\kappa s]\cos\mathsf{E}-\frac{1}{\kappa}\sin[\kappa s]\sin\mathsf{E}-\mathsf{R}_3}\int e^{-\frac{1}{\kappa}\cos[\kappa s]\cos\mathsf{E}+\frac{1}{\kappa}\sin[\kappa s]\sin\mathsf{E}+\mathsf{R}_3} \\
&\quad [\sin[\kappa s]\sin\mathsf{E}\sin[\mathsf{R}_1 s+\mathsf{R}_2]-\cos[\kappa s]\cos\mathsf{E}\sin[\mathsf{R}_1 s+\mathsf{R}_2]]ds \\
&\quad +u\cos[\mathsf{R}_1 s+\mathsf{R}_2]]\mathbf{e}_2 \\
&\quad +[-\frac{1}{\kappa}\cos[\kappa s]\cos\mathsf{E}+\frac{1}{\kappa}\sin[\kappa s]\sin\mathsf{E}+\mathsf{R}_3]\mathbf{e}_3,
\end{aligned}
$$

where $\mathsf{R}_1, \mathsf{R}_2, \mathsf{R}_3$ *are constants of integration.*

Proof. We assume that γ is a unit speed biharmonic constant slope curve according to type-2 Bishop frame and in the SOL^3.

The vector $\mathbf{B}$ is a unit vector, we have the following equation

$$\mathbf{B} = -\sin[\mathsf{R}_1 s + \mathsf{R}_2]\mathbf{e}_1 + \cos[\mathsf{R}_1 s + \mathsf{R}_2]\mathbf{e}_2,$$

where $\mathsf{R}_1, \mathsf{R}_2 \in \mathsf{R}$. Thus, the proof is completed.

We can prove the following interesting main result.

Corollary 4.2. *Let* $\gamma : I \to \mathsf{SOL}^3$ *be a unit speed non-geodesic biharmonic constant* $\mathbf{\Pi}_1 - slope\ curve$ *according to type-2 Bishop frame and* E *its* $\mathbf{B} - surface\ in\ the$ SOL^3. *Then, the parametric equations of* E *are*

$$
\begin{aligned}
\mathbf{x}_\mathsf{E}(s,u) &= e^{-[-\frac{1}{\kappa}\cos[\kappa s]\cos\mathsf{E}+\frac{1}{\kappa}\sin[\kappa s]\sin\mathsf{E}+\mathsf{R}_3]}[e^{-\frac{1}{\kappa}\cos[\kappa s]\cos\mathsf{E}+\frac{1}{\kappa}\sin[\kappa s]\sin\mathsf{E}+\mathsf{R}_3} \\
&\quad e^{\frac{1}{\kappa}\cos[\kappa s]\cos\mathsf{E}-\frac{1}{\kappa}\sin[\kappa s]\sin\mathsf{E}-\mathsf{R}_3}[\sin[\kappa s]\sin\mathsf{E}\cos[\mathsf{R}_1 s+\mathsf{R}_2] \\
&\quad -\cos[\kappa s]\cos\mathsf{E}\cos[\mathsf{R}_1 s+\mathsf{R}_2]]ds - u\sin[\mathsf{R}_1 s+\mathsf{R}_2]], \\
\mathbf{y}_\mathsf{E}(s,u) &= e^{[-\frac{1}{\kappa}\cos[\kappa s]\cos\mathsf{E}+\frac{1}{\kappa}\sin[\kappa s]\sin\mathsf{E}+\mathsf{R}_3]}[e^{\frac{1}{\kappa}\cos[\kappa s]\cos\mathsf{E}-\frac{1}{\kappa}\sin[\kappa s]\sin\mathsf{E}-\mathsf{R}_3} \\
&\quad \int e^{-\frac{1}{\kappa}\cos[\kappa s]\cos\mathsf{E}+\frac{1}{\kappa}\sin[\kappa s]\sin\mathsf{E}+\mathsf{R}_3}[\sin[\kappa s]\sin\mathsf{E}\sin[\mathsf{R}_1 s+\mathsf{R}_2] \\
&\quad -\cos[\kappa s]\cos\mathsf{E}\sin[\mathsf{R}_1 s+\mathsf{R}_2]]ds + u\cos[\mathsf{R}_1 s+\mathsf{R}_2]], \\
\mathbf{z}_\mathsf{E}(s,u) &= -\frac{1}{\kappa}\cos[\kappa s]\cos\mathsf{E} + \frac{1}{\kappa}\sin[\kappa s]\sin\mathsf{E} + \mathsf{R}_3,
\end{aligned}
$$

where $\mathsf{R}_1, \mathsf{R}_2, \mathsf{R}_3$ *are constants of integration.*

REFERENCES

[1] V. Asil, T. Körpinar, Construction of Inextensible Flows of Dual Normal Surfaces in the Dual Space D^3, Bol. Soc. Paran. Mat., 31(2)) (2013), 31-37.

[2] V. Asil, T. Körpinar, S. Bas, Inextensible flows of timelike curves with Sabban frame in S_1^2, Siauliai Math. Semin. 7 (15) (2012), 5-12.

[3] M. Ergüt, T. Körpinar, E. Turhan, One Parameter Family of b-m_1 Developable Surfaces of Biharmonic New Type b-Slant Helices according to Bishop Frame in the Sol Space Sol^3, Bol. Soc. Paran. Mat., 31 (2) (2013), 121-128.

[4] T. Körpinar and E. Turhan, On characterization of B-canal surfaces in terms of biharmonic B-slant helices according to Bishop frame in Heisenberg group Heis ^{3}, J. Math. Anal. Appl. 382 (2011), 57-65.

[5] R.A. Abdel-Baky, Y. Ünlütürk, A study on classification of translation surfaces in pseudo-Galilean 3-space, J. Coupled Syst. Multi. Dyn. 6(3) (2018), 233-240.

[6] M. Çimdiker, Y. Ünlütürk, The construction of the space-like surface of constant breadth, Int. J. Geom. Methods Mod. Phys. 16(4) (2019), 1950060, 16 pp.

[7] R.A. Abdel-Baky, Y. Ünlütürk, On the curvatures of spacelike circular surfaces. Kuwait J. Sci. 43(3) (2016), 50-58.

[8] S. Yilmaz, Y. Ünlütürk, Contributions to differential geometry of isotropic curves in the complex space C3-II, J. Math. Anal. Appl. 440(2) (2016), 561-577.

[9] T. Körpinar, E. Turhan, Tubular Surfaces Around Timelike Biharmonic Curves in Lorentzian Heisenberg Group Heis ^{3}, An. St. Univ. Ovidius Constanta, 20 (1) (2012), 431-446.

[10] T. Körpinar, E. Turhan, Inextensible flows of S-surfaces of biharmonic S -curves according to Sabban frame in Heisenberg Group Heis ^{3}, Lat. Am. J. Phys. Educ. 6 (2) (2012), 250-255.

[11] T. Körpinar, E. Turhan, Tchebyshef net on B-Tangent Developable Surfaces of Spacelike Biharmonic New Type B-Slant Helices in H $_3$, Advanced Modeling and Optimization, 14 (2) (2012), 351-357.

[12] J. Eells and L. Lemaire, A report on harmonic maps, Bull. London Math. Soc. 10 (1978), 1-68.

[13] G. Y.Jiang: 2-harmonic isometric immersions between Riemannian manifolds, Chinese Ann. Math. Ser. A 7(2) (1986), 130-144.

[14] T. Körpinar, E. Turhan, On characterization of timelike biharmonic D-helices according to Darboux frame on non-degenerate timelike surfaces in the Lorentzian Heisenberg group H, Annals of Fuzzy Mathematics and Informatics, 4 (2) (2012), 393-400.

[15] E. Turhan and T. Körpinar, On Characterization Of Timelike Horizontal Biharmonic Curves In The Lorentzian Heisenberg Group Heis ^{3}, Zeitschrift für Naturforschung A- A Journal of Physical Sciences 65a (2010), 641-648.

[16] E. Turhan, T. Körpinar, Null Biminimal General Helices in the Lorentzian Heisenberg Group, Thai Journal of Mathematics, 9 (1) (2011), 127-137.

[17] E. Turhan and T. Körpinar, Parametric equations of general helices in the sol space, Bol. Soc. Paran. Mat. 31 (1) (2013), 99-104.

[18] T. Körpinar, Y. Ünlütürk, New Bianchi type-I cosmological models for biharmonic particles using string cosmology with exponential law, Gen. Relativity Gravitation 47(11) (2015), Art. 138, 12 pp.

[19] T. Körpinar, E. Turhan, V. Asil, Involute Curves Of Timelike Biharmonic Reeb Curves (LCS) $_3$ -Manifolds, Electronic Journal of Theoretical Physics, 9 (26) (2012), 183 - 190.

[20] Y. Ünlütürk, M. Dede, Ü.Z. Savci , C. Ekici, On curves of constant breadth in G13, TWMS J. Appl. Eng. Math. 6(1) (2016), 64-69.

[21] J. Inoguchi, Minimal surfaces in 3-dimensional solvable Lie groups II, Bull. Austral. Math. Soc. 73 (2006) 365-374.

[22] T. Körpinar, E. Turhan, Inextensible Flows of b-Tangent Developable Surfaces of Biharmonic New Type b-Slant Helices According to Bishop Frame in the Sol Space Sol^3, Journal of Science and Arts, 12 (2) (2012), 149-156.

[23] Y. Ou and Z. Wang, Linear Biharmonic Maps into Sol, Nil and Heisenberg Spaces, Mediterr. j. math. 5 (2008), 379-394

[24] M. Ergüt, E. Turhan, T. Körpinar, Characterization of Ricci tensor in the Lorentzian Heisenberg group $Heis^3$, Advanced Modeling and Optimization, 14 (2) (2012), 395-398.

[25] D. J. Struik, Lectures on Classical Differential Geometry, Dover, New-York, 1988.

[26] L. R. Bishop, There is More Than One Way to Frame a Curve, Amer. Math. Monthly 82 (3) (1975) 246-251.

[27] B. Bükcü, M.K. Karacan, Special Bishop motion and Bishop Darboux rotation axis of the space curve, J. Dyn. Syst. Geom. Theor. 6 (1) (2008) 27-34.

[28] S. Yilmaz and M. Turgut, A new version of Bishop frame and an application to spherical images, J. Math. Anal. Appl., 371 (2010), 764-776.

[29] T. Körpinar and E. Turhan, Biharmonic Constant Π_1 – Slope Curves according to New Type-2 Bishop Frame in Sol Space SOL^3, Bol. Soc. Paran. Mat. 32(2) (2014), 73-82.

ON SOLITON SOLUTION OF THE (3+1)-DIMENSIONAL NLSE WITH KERR LAW NONLINEARITY

Z. Körpınar[1], M. İnç[2]

[1]*Department of Administration, Faculty of Economic and Administrative Sciences, Muş Alparslan University, Muş, TURKEY*
[2] *Department of Mathematics, Faculty of Sciences, Fırat University, Elazığ, TURKEY*

E-mail: zelihakorpinar@gmail.com

Abstract

In this paper, the (3+1)-dimensional nonlinear Shrödinger equation with kerr law nonlinearity is analysed. An exact 1-soliton solution is obtained in closed form using the solitary wave ansatz. Then the conserved quantities are investigated via this soliton solution.

Keywords: Optical solitons, Nonlinear Shrödinger equation, Kerr law nonlinearity, Conserved quantity.

1. INTRODUCTION

In the past few decades, a lot of study on optical solitons has been doing [1-10]. The nonlinear wave process can be viewed in several scientific fields, such as optical fiber, quantum theory, plasma physics, fluid dynamics [11-14], etc. In the main, solitons are one pulse forms which are created due to the proportion between nonlinearity and wave stage speed dispersal impacts in the system. In addition to, solitons are the consequence of an attentive adjust between dispersal and nonlinearity. The envelope soliton which holds both fast and slow vibrations performs for nonlinearity proportions with the wave group dispersal impacts in the physical systems. The envelope soliton is controlled to a small field adjusted wave package whose dynamicals is controlled via the nonlinear Schrödinger equation (NSE) [1-14]. The analytical solutions of these NPDEs performs a significant part in the analyse of nonlinear phenomenal. Numerous methods were developed to obtain exact solutions of NPDEs as the inverse scattering method [15], Exp-Function method [16], Homotopy perturbation method [17], Hirota's bilinear method [18], homogeneous balance method [19], Bäcklund transformations [20] and Jacobi and Weierstrass elliptic function method [21], etc, in the past decades.

The (3+1)-dimensional dependent NLSE is given by:

$$iq_t + \nabla^2 q + \lambda F(|q|^2)q = 0. \tag{1.1}$$

Symmetry reductions for the (3 + 1)-dimensional NLSE are analysed in [10-14,22,23].

For kerr law nonlinearity, Eq. (1.1) is converted to

$$iq_t + \nabla^2 q + \lambda |q|^2 q = 0, t > 0. \tag{1.2}$$

In (1.2), the first expression describes the evolution condition, the second expressions, describe the dispersal in x, y and z directions while the third expression describes nonlinearity.

In this work, we analyse (3+1)-dimensional nonlinear Shrödinger's equation to obtain 1-soliton solution with the aid of the solitary wave transformation in closed form [23].

2. MATERIAL AND METHODS

(3 + 1)-dimensional NLSE by kerr law nonlinearity is as follows,

$$iq_t + (q_{xx} + q_{yy} + q_{zz}) + \lambda |q|^2 q = 0, t > 0. \tag{2.1}$$

Solitons are the product of a delicate adjust between dispersion and nonlinearity. In this work, we will use solitary wave transformation to obtain 1-soliton solution of Eq. (2.1). This solution isas follows [22, 24]

$$q(x, y, z, t) = \frac{A}{\cosh^r(\alpha_1 x + \alpha_2 y + \alpha_3 z - \beta t)} e^{i(-\varepsilon_1 x - \varepsilon_2 y - \varepsilon_3 z + \omega t + \psi)} \tag{2.2}$$

where, A is the amplitude of the soliton, α_1, α_2 and α_3 is the inverse width in the $x-, y-,\ z-$ directions respectively and β defines the velocity of the soliton. Also $\varepsilon_1, \varepsilon_2$ and ε_3 defines the soliton frequency in the $x-, y-$ and $z-$ directions respectively. ω is the solitary wave number and finally ψ is the phase constant of the soliton.

In Eq.(2.2), r will be decided while the exact soliton solution found.

Now, substituting Eq. (2.2) into Eq. (2.1), and equating the real and imaginary sections, gives the following pair of relations,

$$Ar\beta + 2A\varepsilon_2 r\alpha_2 + 2A\varepsilon_1 r\alpha_1 + 2A\varepsilon_3 r\alpha_3 = 0, \tag{2.3}$$

$$A^3 \lambda \cosh^{-3r}(\alpha_1 x + \alpha_2 y + \alpha_3 z - \beta t) + (-A(\varepsilon_1^2 + \varepsilon_2^2 + \varepsilon_3^2 + \omega)$$
$$+ \frac{1}{2} Ar^2(\alpha_1^2 + \alpha_2^2 + \alpha_3^2)) \cosh^{-r}(\alpha_1 x + \alpha_2 y + \alpha_3 z - \beta t) + (-Ar(\alpha_1^2 + \alpha_2^2 + \alpha_3^2)$$

$$- \frac{1}{2} Ar^2(\alpha_1^2 + \alpha_2^2 + \alpha_3^2)) \cosh^{-2-r}(\alpha_1 x + \alpha_2 y + \alpha_3 z - \beta t)) = 0 \tag{2.4}$$

From (2.3), it can be seen that

$$\beta = -2(\varepsilon_2 \alpha_2 + \varepsilon_1 \alpha_1 + \varepsilon_3 \alpha_3) \tag{2.5}$$

Now, from (2.4) equating the exponents $-3r$ and $-r-2$ gives

$$r = 1 \tag{2.6}$$

Then, Eq.(2.4) gives,

$$A = \sqrt{\frac{3}{2\lambda}(\alpha_1^2 + \alpha_2^2 + \alpha_3^2)} \tag{2.7}$$

and

$$\omega = \frac{1}{2}(\alpha_1^2 + \alpha_2^2 + \alpha_3^2) - (\varepsilon_1^2 + \varepsilon_2^2 + \varepsilon_3^2) \tag{2.8}$$

Thus, by using eqs.(2.5), (2.7) and (2.8), the 1-soliton solution of the NLSE in 3+1 dimensions by Kerr law nonlinearity is as follows

$$q(x, y, z, t) = \frac{A}{\cosh(\alpha_1 x + \alpha_2 y + \alpha_3 z - \beta t)} e^{i(-\varepsilon_1 x - \varepsilon_2 y - \varepsilon_3 z + \omega t + \psi)} \qquad (2.9)$$

3. RESULTS AND DISCUSSION

The surface graphic of the obtained solution were drawn below by using Mathematica. In Figs.1, we represent numerical models for $q(x, y, z, t)$ when $-10 \leq x \leq 10$ and $-10 \leq t \leq 10$.

Fig 1. a) The surface graphic of the $|q(x, y, z, t)|^2$, **b)** Contour plot for the $|q(x, y, z, t)|^2$

The above graphics were drawn for $\alpha_1 = \alpha_2 = \alpha_3 = 1, \varepsilon_1 = \varepsilon_2 = \varepsilon_3 = 2, \lambda = 1, \psi = 0$.

We obtained the 1-soliton solution found for the presented the (3+1)-dimensional NLSE with kerr law nonlinearities.

4. CONCLUSION

In this paper, exact 1-soliton solution of the (3+1)-dimensional NLSE with kerr law nonlinearities is obtained by using the solitary wave transformation. The obtained soliton solution is considerable for scientists for the agreement the physical effect of this equation. By choosing suitable values of parameters, the behaviors of $q(x, y, z, t)$ have been showed by using 3D and 2D graphic. These figures are also presented in $Fig.1$. We express that the applied method is convenient to investigate the many problems located in science and engineering.

REFERENCES

[1] H. Triki et al., Chirped singular solitons for Chen-Lee-Liu equation in optical fibers and PCF, Optik 157 (2018) 156-160.

[2] M.Inc, Z.S.Korpinar, M.M. Al Qurashi, D. Baleanu, A new method for approximate solution of some nonlinear equations: Residual power series method, Advances in Mechanical Engineering,8(4) (2016),1-7.

[3] A.H. Bhrawy, M.A. Abdelkawy, S. Kumar, S. Johnson, A. Biswas, Solitons and other solutions to quantum Zakharov--Kuznetsov equation in quantum magneto-plasmas, Indian J. Phys. 87 (2013) 455-463.

[4] S. Jana, S. Konar, A new family of Thirring type optical spatial solitons via electromagnetic induced transparency, Phys. Lett. A 362 (2007) 435-438.

[5] A.H. Bhrawy, M.A. Abdelkawy, Computational study of some nonlinear shallow water equations, Cent. Eur. J. Phys. 11 (2013) 518-525.

[6] A.H. Bhrawy, M.A. Abdelkawy, Integrable system modeling shallow water waves: Kaup--Boussinesq shallow water system, Indian J. Phys. 87 (2013) 665-671.

[7] A. Biswas and D. Milovic, Optical solitons in 1+2 dimensions with non-Kerr law nonlinearity, Eur. Phys. J. Special Topics 173, 81-86 (2009)

[8] T Körpinar, RC Demirkol, Z Körpinar, Soliton propagation of electromagnetic field vectors of polarized light ray traveling in a coiled optical fiber in Minkowski space with Bishop equations, The European Physical Journal D 73 (9) (2019), 203

[9] T Körpinar, RC Demirkol, Z Körpinar, Soliton propagation of electromagnetic field vectors of polarized light ray traveling in a coiled optical fiber in the ordinary space, International Journal of Geometric Methods in Modern Physics, 16(8) (2019), 1950117

[10] Z.S. Körpinar, M. Tuz, T. Körpinar, *New Electromagnetic Fluids Inextensible Flows of Spacelike Particles and some Wave Solutions in Minkowski Space-time,* Int J Theor Phys 55 (1) (2016), 8-16

[11] A.H. Bhrawy, M.A. Abdelkawy, A. Biswas, Optical solitons in (1+1) and (2+1) dimensions, Optik 125 (2014) 1537-1549.

[12] L. Gagnont, B. Grammaticos, A. Ramanil, P. Winternitz, Lie symmetries of a generalised non-linear Schrodinger equation: III. Reductions to third-order ordinary differential equations, J. Phys. A Math. Gen. 22 (1989) 499-509.

[13] L. Gagnon, C. Par, Nonlinear radiation modes connected to parabolic graded-index profiles by the lens transformation, Opt. Soc. Am. 8 (1991) 601-607.

[14] L. Gagnon, P. Winternitz, Lie symmetries of a generalised nonlinear Shrödinger equation III.reductions to third order ordinary differential equations, J.Phys. A 22 (1989) 469-509.

[15] S. Ghosh, S. Nandy, Inverse scattering method and vector higher order non-linear Schrödinger equation, Nucl. Phys. B 561 (3) (1999) 451-466.

[16] A.H. Bhrawy, A. Biswas, M. Javidi, W.X. Ma, Z. Pinar, A. Yildirim, New solutions for (1 + 1)-dimensional and (2 + 1)-dimensional Kaup-Kupershmidt equations, Result. Math. 63 (2013) 675-686.

[17] R. Sakthivel, C. Chun, A-A. Bae, A general approach to hyperbolic partial differential equations by homotopy perturbation method, Int. J. Comput. Math. 87 (2010) 2601-2606.

[18] A.M. Wazwaz, The Hirota's bilinear method and the tanh--coth method for multiple-soliton solutions of the Sawada-Kotera-Kadomtsev-Petvishvili equation, Appl. Math. Comput. 200 (1) (2008) 160-166.

[19] M.L. Wang, Y.B. Zhou, Z.B. Li, Application of a homogeneous balance method to exact solutions of nonlinear equations in mathematical physics, Phys. Lett. A 216 (1996) 67-75.

[20] A.H. Khater, D.K. Callebaut, A.H. Bhrawy, M.A. Abdelkawy, Nonlinear periodic solutions for isothermal magnetostatic atmospheres, J. Comput. Appl. Math. 242 (2013) 28-40.

[21] S.K. Liu, Z.T. Fu, S.D. Liu, Jacobi elliptic function expansion method and periodic wave solutions of nonlinear wave equations, Phys. Lett. A 289 (2001) 69-74.

[22] Ablowitz, M.J., Segur, H.: Solitons and the Inverse Scattering Transform. SIAM, Philadelphia (1981).

[23] A. Biswas, 1-Soliton Solution of 1+2 Dimensional Nonlinear Schrödinger's Equation in Kerr Law Media, Int J Theor Phys 48 (2009), 689-692.

[24] Biswas, A., Aceves, A.: Dynamics of solitons in optical fibers. J. Mod Opt. 48(7) (2001), 1135-1150.

OPTICAL SOLITONS FOR MODIFIED UNSTABLE NONLINEAR SCHRÖDINGER'S EQUATION

Z. Körpınar[1], M. İnç[2]

[1]*Department of Administration, Faculty of Economic and Administrative Sciences, Muş Alparslan University, Muş, TURKEY*
[2] *Department of Mathematics, Faculty of Sciences, Fırat University, Elazığ, TURKEY*

E-mail: zelihakorpinar@gmail.com

Abstract

In this article, the extended direct algebraic method (EDAM) is applied to obtain the optical solitons in modified unstable nonlinear Schrödinger's equation. First of all, this equation is changed into the ordinary differential equation by applying the wave variables transformation. Then new several forms of optical solitons are obtained by using EDAM.

Keywords: Optical solitons, Modified unstable nonlinear Schrödinger's equation, Extended direct algebraic method.

1. INTRODUCTION

Recently, many scientists studied several methods to form optical solutions in the field of nonlinear optics because of optical solitons shape the fundamental component to transport data from side to side the earth for very wide distances. Some of these methods are the functional variable method, the kudryashov method, the trial solution method, the Jacobi elliptic function expansion method, the Exp-function method, the sine-cosine method, residual power series method and others [1-8]. There is a countless of style that effectively define this movement of soliton construction [9--20].

In this work, we analyse a modification of the unstable nonlinear Schrödinger's equation (UNLSE) [9,10] to form optical solitons using the extended direct algebraic method (EDAM) [11,12]. The found solutions are identified bright optical soliton, dark soliton, singular soliton, combo soliton solution and periodic solutions.

The UNLSE is a kind of NLS equation with time and space variables. This kind of movement presents for the lossless symmetric two-stream plasma instability [13] and the two-layer baroclinic instability [14]. The UNLSE as follow

$$iq_t + q_{xx} + 2|q|^2 q - 2\gamma q = 0. \tag{1.1}$$

In [9] studied as a modification of UNLSE a similar Hamiltonian complex amplitude equation

$$iq_t + q_{xx} + 2\gamma|q|^2 q - \varepsilon q_{xt} = 0. \tag{1.2}$$

that definites standart instabilities of modulated wave-trains [10].

In this work we find exact solutions for a complex NLSE by using the EDAM. In [15-18], we showed the some studies that the solutions of NLSE obtained by using many other methods.

2. MATERIAL AND METHODS

Suppose that the general nonlinear partial differential equation,

$$A(q, q_t, q_x, q_{xx}, q_{tt}, ...) = 0. \tag{2.1}$$

where q is an unknown function depending on x and t, A is a polynomial in $q = q(x,t)$ and the sub-indices give the partial derivatives.

• Assume the traveling wave variable:

$$q(x,t) = u(\phi), \qquad \phi = x + Qt, \tag{2.2}$$

From Eq. (2.2), is obtained an ordinary differential equation for $u(\phi)$,

$$B(u, u_\phi, u_{\phi\phi}, u_{\phi\phi\phi}, ...) = 0. \tag{2.3}$$

where the sub-indices give the ordinary derivatives with respect to ϕ.

- Assume the solution of Eq. (2.3),

$$u(\phi) = \sum_{i=0}^{N} \alpha_i G^i(\phi), \tag{2.4}$$

where $\alpha_n \neq 0$ and $G(\phi)$ can be satisfied as follows:

$$G'(\phi) = \ln(A)(fG^2(\phi) + gG(\phi) + h), \quad A \neq 0,1, \tag{2.5}$$

where $f, g.h$ are arbitrary constants.

- N is found by balancing between the nonlinear terms and the highest order derivatives in Eq.(2.3).

- Replacing Eq. (2.4) together with Eq. (2.5) into the Eq. (2.3), then equating each coefficient of the polynomials to zero, give a set of algebraic equations for α_i $(i = 1,2,...,N)$, f, g, h and Q.

- Solving the obtained system, we find α_i $(i = 1,2,...,N)$ and Q. Thus, solutions of Eq. (2.3) are obtained. Where a few specific solutions of Eq. (2.3) are given by;

1) When $g^2 - 4hf < 0$ and $f \neq 0$,

$$G_1(\phi) = -\frac{g}{2f} + \frac{\sqrt{-(g^2 - 4hf)}}{2f} \tan_A \left(\frac{\sqrt{-(g^2 - 4hf)}}{2} \phi \right),$$

$$G_2(\phi) = -\frac{g}{2f} + \frac{\sqrt{-(g^2 - 4hf)}}{2f} \left(-\cot_A \left(\sqrt{-(g^2 - 4hf)} \phi \right) \pm \sqrt{\Delta\Omega} \csc_A \left(\sqrt{-(g^2 - 4hf)} \phi \right) \right).$$

2) When $g^2 - 4hf > 0$ and $f \neq 0$,

$$G_3(\phi) = -\frac{g}{2f} - \frac{\sqrt{g^2 - 4hf}}{2f} \tanh_A \left(\frac{\sqrt{g^2 - 4hf}}{2} \phi \right),$$

$$G_4(\phi) = -\frac{g}{2f} + \frac{\sqrt{g^2 - 4hf}}{4f} \left(\tanh_A \left(\frac{\sqrt{g^2 - 4hf}}{4} \phi \right) + \coth_A \left(\frac{\sqrt{g^2 - 4hf}}{4} \phi \right) \right).$$

3) When $hf > 0$ and $g = 0$,

$$G_5(\phi) = -\sqrt{\frac{h}{f}} \cot_A \left(\sqrt{hf} \phi \right),$$

$$G_6(\phi) = \sqrt{\frac{h}{f}} \left(\tan_A \left(2\sqrt{hf} \phi \right) \pm \sqrt{\Delta\Omega} \sec_A \left(2\sqrt{hf} \phi \right) \right).$$

4) When $hf < 0$ and $g = 0$,

$$G_7(\phi) = -\frac{1}{2}\sqrt{-\frac{h}{f}}(\tanh_A(\frac{\sqrt{-hf}}{2}\phi) + \coth_A(\frac{\sqrt{-hf}}{2}\phi)).$$

5) When $h = f$ and $g = 0$,

$$
\begin{aligned}
G_8(\phi) &= -\cot_A(2h\phi) \pm \sqrt{\Delta\Omega}\csc_A(2h\phi)), \\
G_9(\phi) &= \frac{1}{2}(\tan_A(\frac{h}{2}\phi) - \cot_A(\frac{h}{2}\phi)).
\end{aligned}
$$

6) When $h = -f$ and $g = 0$,

$$G_{10}(\phi) = -\frac{1}{2}(\tanh_A(\frac{h}{2}\phi) + \coth_A(\frac{h}{2}\phi)).$$

Remark. The generalized trigonometric and hyperbolic functions are defined as [19];

$$
\begin{aligned}
\sin_A(\phi) &= \frac{\Delta A^{i\phi} - \Omega A^{-i\phi}}{2i}, \cos_A(\phi) = \frac{\Delta A^{i\phi} + \Omega A^{-i\phi}}{2}, \\
\tan_A(\phi) &= -i\frac{\Delta A^{i\phi} - \Omega A^{-i\phi}}{\Delta A^{i\phi} + \Omega A^{-i\phi}}, \cot_A(\phi) = i\frac{\Delta A^{i\phi} + \Omega A^{-i\phi}}{\Delta A^{i\phi} - \Omega A^{-i\phi}}, \\
\sec_A(\phi) &= \frac{2}{\Delta A^{i\phi} + \Omega A^{-i\phi}}, \csc_A(\phi) = \frac{2i}{\Delta A^{i\phi} - \Omega A^{-i\phi}} \\
\sinh_A(\phi) &= \frac{\Delta A^{\phi} - \Omega A^{-\phi}}{2}, \cosh_A(\phi) = \frac{\Delta A^{\phi} + \Omega A^{-\phi}}{2}, \\
\tanh_A(\phi) &= \frac{\Delta A^{\phi} - \Omega A^{-\phi}}{\Delta A^{\phi} + \Omega A^{-\phi}}, \coth_A(\phi) = \frac{\Delta A^{\phi} + \Omega A^{-\phi}}{\Delta A^{\phi} - \Omega A^{-\phi}}, \\
\sec h_A(\phi) &= \frac{2}{\Delta A^{\phi} + \Omega A^{-\phi}}, \csc h_A(\phi) = \frac{2}{\Delta A^{\phi} - \Omega A^{-\phi}}.
\end{aligned}
$$

where $\Delta > 0$ and $\Omega > 0$ are deformation parameters and ϕ is an independent variable.

3. RESULTS AND DISCUSSION

Suppose the traveling wave variable as follows [6-8]

$$q(x,t) = u(\phi)e^{i(-\kappa x + wt)}, \qquad \phi = x + Qt, \tag{3.1}$$

where κ, w and Q, respectively, define the frequency, wave number and the speed of the wave.

By placing Eq. (3.1) into Eq. (1.2), are obtained real and imaginary sections.

The real sections are as follows;

$$(\kappa^2 - \kappa Q\varepsilon)u'' + 2\gamma u^3 + (-w - \kappa^2 + w\varepsilon\kappa)u = 0, \tag{3.2}$$

and the imaginary sections gives:

$$Q = \frac{-\kappa w \varepsilon - 2\kappa^2}{1 - \varepsilon \kappa},\qquad (3.3)$$

Consider the solution of Eq.(3.2) is expressed as a finite series as follows:

$$u(\phi) = \sum_{j=0}^{N} \alpha_j G^j(\phi) \qquad (3.4)$$

where $G(\phi)$ satisfies Eq.(2.5), $\phi = x + Qt$ and α_j for $j = \overline{1, N}$ are values to be definited.

By balancing u'' with u^3 in Eq. (3.2), is obtained $N = 1$.

The solution of Eq. (3.2) is given by:

$$u(\phi) = \alpha_0 + \alpha_1 G(\phi), \qquad (3.5)$$

where $G(\phi)$ satisfied Eq.(2.5).

Substituting (3.2) and (2.5) into (3.2), collecting the coefficients of $G(\phi)$, and solving the obtaining system, the following groups of some solutions are obtained:

One of the four groups of values is as follows

$$
\begin{aligned}
\alpha_0 &= \frac{ig\kappa\sqrt{-\frac{1}{2} + \kappa^2 \varepsilon^2}\,\ln(A)}{\sqrt{-\gamma(2(-1 + \kappa\varepsilon)^2 + (g^2 - 4fh)\kappa^2 \varepsilon^2 \ln(A)^2)}}, \\[2mm]
\alpha_1 &= \frac{if\kappa\sqrt{-2 + 4\kappa^2 \varepsilon^2}\,\ln(A)}{\sqrt{-\gamma(2(-1 + \kappa\varepsilon)^2 + (g^2 - 4fh)\kappa^2 \varepsilon^2 \ln(A)^2)}}, \\[2mm]
w &= -\frac{\kappa^2(2 - 2\kappa\varepsilon + (g^2 - 4fh)(1 + k\varepsilon)\ln(A)^2)}{2(-1 + \kappa\varepsilon)^2 + (g^2 - 4fh)\kappa^2 \varepsilon^2 \ln(A)^2}.
\end{aligned}
\qquad (3.6)
$$

The solutions of Eq.(1.2) are obtained as follows;

1) When $g^2 - 4hf < 0$ and $f \neq 0$, the singular periodic solutions are as below

$$
\begin{aligned}
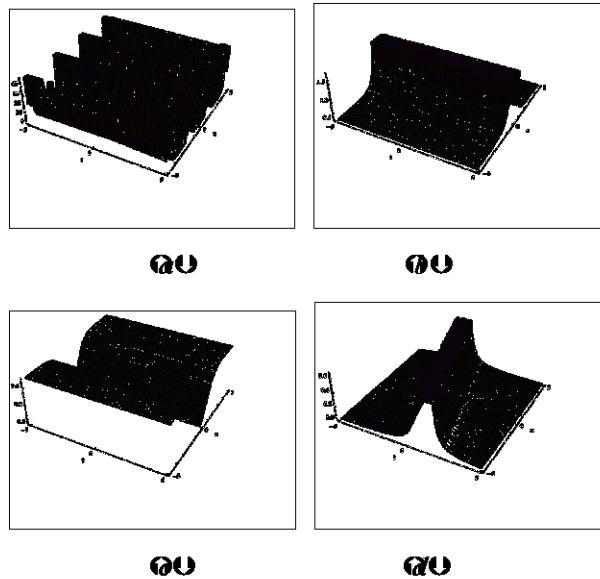q_1(x,t) =\ & e^{i(-\kappa x + wt)}\Big(\frac{ig\kappa\sqrt{-\frac{1}{2} + \kappa^2 \varepsilon^2}\,\ln(A)}{\sqrt{-\gamma(2(-1 + \kappa\varepsilon)^2 + (g^2 - 4fh)\kappa^2 \varepsilon^2 \ln(A)^2)}} \\[2mm]
& + \frac{if\kappa\sqrt{-2 + 4\kappa^2 \varepsilon^2}\,\ln(A)}{\sqrt{-\gamma(2(-1 + \kappa\varepsilon)^2 + (g^2 - 4fh)\kappa^2 \varepsilon^2 \ln(A)^2)}} \\[2mm]
& \left(-\frac{g}{2f} + \frac{\sqrt{-(g^2 - 4hf)}}{2f}\tan_A\left(\frac{\sqrt{-(g^2 - 4hf)}}{2}\left(x + \frac{-\kappa w\varepsilon - 2\kappa^2}{1 - \varepsilon\kappa}t\right)\right)\right)\Big),
\end{aligned}
$$

$$q_2(x,t) = e^{i(-\kappa x + wt)}\left(\frac{ig\kappa\sqrt{-\frac{1}{2}+\kappa^2\varepsilon^2}\ln(A)}{\sqrt{-\gamma(2(-1+\kappa\varepsilon)^2+(g^2-4fh)\kappa^2\varepsilon^2\ln(A)^2)}}\right.$$

$$+\frac{if\kappa\sqrt{-2+4\kappa^2\varepsilon^2}\ln(A)}{\sqrt{-\gamma(2(-1+\kappa\varepsilon)^2+(g^2-4fh)\kappa^2\varepsilon^2\ln(A)^2)}}$$

$$\left(-\frac{g}{2f}+\frac{\sqrt{-(g^2-4hf)}}{2f}\left(-\cot_A(\sqrt{-(g^2-4hf)}(x+\frac{-\kappa w\varepsilon-2\kappa^2}{1-\varepsilon\kappa}t))\right.\right.$$

$$\left.\left.\left.\pm\sqrt{\Delta\Omega}\csc_A(\sqrt{-(g^2-4hf)}(x+\frac{-\kappa w\varepsilon-2\kappa^2}{1-\varepsilon\kappa}t))\right)\right)\right).$$

2) When $g^2-4hf>0$ and $f\neq0$, thus the dark and the singular soliton solutions are as below

$$q_3(x,t) = e^{i(-\kappa x + wt)}\left(\frac{ig\kappa\sqrt{-\frac{1}{2}+\kappa^2\varepsilon^2}\ln(A)}{\sqrt{-\gamma(2(-1+\kappa\varepsilon)^2+(g^2-4fh)\kappa^2\varepsilon^2\ln(A)^2)}}\right.$$

$$+\frac{if\kappa\sqrt{-2+4\kappa^2\varepsilon^2}\ln(A)}{\sqrt{-\gamma(2(-1+\kappa\varepsilon)^2+(g^2-4fh)\kappa^2\varepsilon^2\ln(A)^2)}}$$

$$\left.\left(-\frac{g}{2f}-\frac{\sqrt{g^2-4hf}}{2f}\tanh_A(\frac{\sqrt{g^2-4hf}}{2}(x+\frac{-\kappa w\varepsilon-2\kappa^2}{1-\varepsilon\kappa}t))\right)\right),$$

$$q_4(x,t) = e^{i(-\kappa x + wt)}\left(\frac{ig\kappa\sqrt{-\frac{1}{2}+\kappa^2\varepsilon^2}\ln(A)}{\sqrt{-\gamma(2(-1+\kappa\varepsilon)^2+(g^2-4fh)\kappa^2\varepsilon^2\ln(A)^2)}}\right.$$

$$+\frac{if\kappa\sqrt{-2+4\kappa^2\varepsilon^2}\ln(A)}{\sqrt{-\gamma(2(-1+\kappa\varepsilon)^2+(g^2-4fh)\kappa^2\varepsilon^2\ln(A)^2)}}\left(-\frac{g}{2f}+\frac{\sqrt{g^2-4hf}}{4f}\right.$$

$$\left.\left.(\tanh_A(\frac{\sqrt{g^2-4hf}}{4}(x+\frac{-\kappa w\varepsilon-2\kappa^2}{1-\varepsilon\kappa}t))+\coth_A(\frac{\sqrt{g^2-4hf}}{4}(x+\frac{-\kappa w\varepsilon-2\kappa^2}{1-\varepsilon\kappa}t)))\right)\right),$$

3) When $hf>0$ and $g=0$, thus the singular periodic solutions are as below

$$q_5(x,t) = e^{i(-\kappa x + wt)}\left(\frac{ig\kappa\sqrt{-\frac{1}{2}+\kappa^2\varepsilon^2}\ln(A)}{\sqrt{-\gamma(2(-1+\kappa\varepsilon)^2+(g^2-4fh)\kappa^2\varepsilon^2\ln(A)^2)}}\right.$$

$$+\frac{if\kappa\sqrt{-2+4\kappa^2\varepsilon^2}\ln(A)}{\sqrt{-\gamma(2(-1+\kappa\varepsilon)^2+(g^2-4fh)\kappa^2\varepsilon^2\ln(A)^2)}}$$

$$\left.(-\sqrt{\frac{h}{f}}\cot_A(\sqrt{hf}(x+\frac{-\kappa w\varepsilon-2\kappa^2}{1-\varepsilon\kappa}t))))\right),$$

$$q_6(x,t) = e^{i(-\kappa x + wt)}\left(\frac{ig\kappa\sqrt{-\frac{1}{2}+\kappa^2\varepsilon^2}\ln(A)}{\sqrt{-\gamma(2(-1+\kappa\varepsilon)^2+(g^2-4fh)\kappa^2\varepsilon^2\ln(A)^2)}}\right.$$

$$+\frac{if\kappa\sqrt{-2+4\kappa^2\varepsilon^2}\ln(A)}{\sqrt{-\gamma(2(-1+\kappa\varepsilon)^2+(g^2-4fh)\kappa^2\varepsilon^2\ln(A)^2)}}\sqrt{\frac{h}{f}}(\tan_A(2\sqrt{hf}(x+\frac{-\kappa w\varepsilon-2\kappa^2}{1-\varepsilon\kappa}t))$$

$$\left.\pm\sqrt{\Delta\Omega}\sec_A(2\sqrt{hf}(x+\frac{-\kappa w\varepsilon-2\kappa^2}{1-\varepsilon\kappa}t))))\right).$$

4) When $hf < 0$ and $g = 0$, thus the dark, bright and singular soliton solutions are as below

$$q_7(x,t) = e^{i(-\kappa x + wt)}\left(\frac{ig\kappa\sqrt{-\frac{1}{2}+\kappa^2\varepsilon^2}\ln(A)}{\sqrt{-\gamma(2(-1+\kappa\varepsilon)^2+(g^2-4fh)\kappa^2\varepsilon^2\ln(A)^2)}}\right.$$

$$+\frac{if\kappa\sqrt{-2+4\kappa^2\varepsilon^2}\ln(A)}{\sqrt{-\gamma(2(-1+\kappa\varepsilon)^2+(g^2-4fh)\kappa^2\varepsilon^2\ln(A)^2)}}(-\frac{1}{2}\sqrt{-\frac{h}{f}}(\tanh_A(\frac{\sqrt{-hf}}{2}(x+\frac{-\kappa w\varepsilon-2\kappa^2}{1-\varepsilon\kappa}t))$$

$$\left.+\coth_A(\frac{\sqrt{-hf}}{2}(x+\frac{-\kappa w\varepsilon-2\kappa^2}{1-\varepsilon\kappa}t)))))\right),$$

5) When $h = f$ and $g = 0$, thus the singular periodic solutions are as below

$$q_8(x,t) = e^{i(-\kappa x + wt)}(\frac{ig\kappa\sqrt{-\frac{1}{2}+\kappa^2\varepsilon^2}\ln(A)}{\sqrt{-\gamma(2(-1+\kappa\varepsilon)^2+(g^2-4fh)\kappa^2\varepsilon^2\ln(A)^2)}}$$

$$+\frac{if\kappa\sqrt{-2+4\kappa^2\varepsilon^2}\ln(A)}{\sqrt{-\gamma(2(-1+\kappa\varepsilon)^2+(g^2-4fh)\kappa^2\varepsilon^2\ln(A)^2)}}(-\cot_A(2h(x+\frac{-\kappa w\varepsilon-2\kappa^2}{1-\varepsilon\kappa}t))$$

$$\pm\sqrt{\Delta\Omega}\csc_A(2h(x+\frac{-\kappa w\varepsilon-2\kappa^2}{1-\varepsilon\kappa}t))))),$$

$$q_9(x,t) = e^{i(-\kappa x + wt)}(\frac{ig\kappa\sqrt{-\frac{1}{2}+\kappa^2\varepsilon^2}\ln(A)}{\sqrt{-\gamma(2(-1+\kappa\varepsilon)^2+(g^2-4fh)\kappa^2\varepsilon^2\ln(A)^2)}}$$

$$+\frac{if\kappa\sqrt{-2+4\kappa^2\varepsilon^2}\ln(A)}{\sqrt{-\gamma(2(-1+\kappa\varepsilon)^2+(g^2-4fh)\kappa^2\varepsilon^2\ln(A)^2)}}\frac{1}{2}(\tan_A(\frac{h}{2}(x+\frac{-\kappa w\varepsilon-2\kappa^2}{1-\varepsilon\kappa}t))$$

$$-\cot_A(\frac{h}{2}(x+\frac{-\kappa w\varepsilon-2\kappa^2}{1-\varepsilon\kappa}t)))),$$

6) When $h=-f$ and $g=0$, thus the dark, bright and singular soliton solutions are as below

$$q_{10}(x,t) = e^{i(-\kappa x + wt)}(\frac{ig\kappa\sqrt{-\frac{1}{2}+\kappa^2\varepsilon^2}\ln(A)}{\sqrt{-\gamma(2(-1+\kappa\varepsilon)^2+(g^2-4fh)\kappa^2\varepsilon^2\ln(A)^2)}}$$

$$+\frac{if\kappa\sqrt{-2+4\kappa^2\varepsilon^2}\ln(A)}{\sqrt{-\gamma(2(-1+\kappa\varepsilon)^2+(g^2-4fh)\kappa^2\varepsilon^2\ln(A)^2)}}(-\frac{1}{2}(\tanh_A(\frac{h}{2}(x+\frac{-\kappa w\varepsilon-2\kappa^2}{1-\varepsilon\kappa}t))$$

$$+\coth_A(\frac{h}{2}(x+\frac{-\kappa w\varepsilon-2\kappa^2}{1-\varepsilon\kappa}t))))),$$

Graphical representation of the solutions

The graphical representations of the solutions are showed below in the figures by using Mathematica.

The graphics below were drawn for $\gamma=\varepsilon=2, \kappa=1, A=2.7, \Omega=\Delta=1$. We wrote the some of solutions found for Modified UNLSE. In addition to we drawn 3D graphics for some of solutions in Fig 1.

Fig 1. The 3D graphics for the $|q(x,t)|^2$ analitical solution of the Modified UNLSE obtained with EDAM.

(a) $q_1(x,t)$ $(f=1, g=h=2)$, (b) $q_5(x,t)$ $(f=1, g=0, h=1)$, (c) $q_8(x,t)$ $(f=1, g=0, h=1)$, (d) $q_{10}(x,t)$ $(f=1, g=2, h=1)$.

4. CONCLUSION

In this paper, the EDAM is used to find new soliton solutions of the modified unstable nonlinear Schrödinger's equation. These solutions consist of twelve different cases. The existences of solutions derived from these functions are all guaranteed through constraint conditions that are also listed beside the solutions. The obtained soliton solutions are important for scientists about the agreement the physical event of this equation. By selecting appropriate values of parameters, the behaviors of some solutions have been viewed with the help 3D graphics. We say that the presented method is suitable to examine the many problems located in science and engineering.

REFERENCES

[1] T Körpinar, RC Demirkol, Z Körpinar, Soliton propagation of electromagnetic field vectors of polarized light ray traveling in a coiled optical fiber in Minkowski space with Bishop equations, The European Physical Journal D 73 (9) (2019), 203

[2] T Körpinar, RC Demirkol, Z Körpinar, Soliton propagation of electromagnetic field vectors of polarized light ray traveling in a coiled optical fiber in the ordinary space, International Journal of Geometric Methods in Modern Physics, 16(8) (2019), 1950117

[3] Z.S. Körpinar, M. Tuz, T. Körpinar, *New Electromagnetic Fluids Inextensible Flows of Spacelike Particles and some Wave Solutions in Minkowski Space-time,* Int J Theor Phys 55 (1) (2016), 8-16

[4] F.Tchier, M.Inc, Z.S.Korpinar, D. Baleanu, Solution of the time fractional reaction-diffusion equations with residual power series method, Advances in Mechanical Engineering,8(10) (2016),1-10.

[5] M.Inc, Z.S.Korpinar, M.M. Al Qurashi, D. Baleanu, Anew method for approximate solution of some nonlinear equations: Residual power series method, Advances in Mechanical Engineering,8(4) (2016),1-7.

[6] M. Inc, ZS. Korpinar, On Approximate Solutions of Bright Optical Soliton for Schrödinger Equation of Power Law Nonlinearity, Journal of Advanced Physics 6(4) (2017) 534-539.

[7] MM. Al Qurashi, ZS. Korpinar, M. Inc, Approximate solutions of bright and dark optical solitons in birefrigent fibers, Optik 140(2017) 45-61.

[8] E. Mehmet, S. Abdullah, Optical solitons with Biswas-Arshed equation by extended trial function method, Optik 177 (2019) 13-20.

[9] M.M. Wadati, H. Segur, M.J. Ablowitz, A new Hamiltonian amplitude equation governing modulated wave instabilities, J. Phys. Soc. Jpn. 61 (1992) 1187-1193.

[10] H. Beuß , On unstable nonlinear Schrödinger equations, Nonlinear Anal. Theory Methods Appl. 26 (5) (1996) 903-914.

[11] H. Rezazadeh, New solitons solutions of the complex Ginzburg-Landau equation with Kerr law nonlinearity, Optik 167 (2018) 218-227.

[12] E.V. Krishnan, M. Al Ghabshi, Q. Zhou, K.R. Khan, M.F. Mahmood, Y. Xu, A. Biswas, M. Belic, Solitons in optical metamaterials by mapping method, J. Optoelectron. Adv. Mater. 17 (3-4) (2015) 511-516.

[13] M. Pawlik, G. Rowlands, The propagation of solitary waves in piezoelectric semiconductors, J. Phys. C 8 (1975) 1189-1204.

[14] V.E. Pedlosky, Finite-amplitude baroclinic waves, J. Atmos. Sci. 27 (1970) 15-30.

[15] Z. S. Korpinar, M. Inc, Numerical simulations for fractional variation of (1+ 1)-dimensional Biswas-Milovic equation, Optik 166 (2018) 77-85.

[16] M. Ekici, M. Mirzazadeh, A. Sonmezoglu, M.Z. Ullah, M. Asma, Q. Zhou, S.P. Moshokoa, A. Biswas, M. Belic, Optical solitons with Schrödinger-Hirota equation by extended trial equation method, Optik 136 (2017) 451-461.

[17] M. Ekici, A. Sonmezoglu, Q. Zhou, A. Biswas, M.Z. Ullah, M. Asma, S.P. Moshokoa, M. Belic, Optical solitons in DWDM system by extended trial equation method, Optik 141 (2017) 157-167.

[18] S-D. Zhu, The generalizing Riccati equation mapping method in non-linear evolution equation: application to (2 + 1)-dimensional Boiti--Leon--Pempinelle equation, Chaos, Solitons and Fractals 37 (2008), 1335-1342.

[19] H. Rezazadeh et al., New exact solutions of nonlinear conformable time-fractional Phi-4 equation, Chinese Journal of Physics 56 (2018) 2805-2816.

A NEW BIHARMONIC CURVES WITH EXTENDED DARBOUX FRAME

Z. Körpınar[1], V.Asil [2], T. Körpınar[3]

[1]Department of Administration, Faculty of Economic and Administrative Sciences, Muş Alparslan University, Muş, TURKEY
[2] Department of Mathematics, Faculty of Sciences, Fırat University, Elazığ, TURKEY
[3] Department of Mathematics, Faculty of Arts and Sciences, Muş Alparslan University, Muş, TURKEY

E-mail: zelihakorpinar@ gmail.com

Abstract

In this study, we firstly characterize biharmonic curves and associated curvature tensor field by considering extended Darboux frame. Then, we obtain the relation of each quasi curvatures of curve. Finally, we give some new conditions with the normal curvature, the geodesic curvatures, and the geodesic torsions of the curve.

Keywords: Extended Darboux frame, biharmonic curve, curvatures.

1. INTRODUCTION

Let (M, g) and (N, h) be manifolds and $\phi : M \to N$ a smooth map. Denote by ∇^{ϕ} the connection of the vector bundle $\phi^* TN$ induced from the Levi-Civita connection ∇^h of (N, h). The *second fundamental form* $\nabla d\phi$ is defined by

$$(\nabla d\phi)(X, Y) = \nabla_X^{\phi} d\phi(Y) - d\phi(\nabla_X Y), \ X, Y \in \Gamma(TM).$$

Here ∇ is the Levi-Civita connection of (M, g). The *tension field* $\tau(\phi)$ is a section of $\phi^* TN$ defined by

$$\tau(\phi) = tr \nabla d\phi.$$

A smooth map ϕ is said to be *harmonic* if its tension field vanishes. It is well known that ϕ is harmonic if and only if ϕ is a critical point of the *energy [1]*:

$$E(\phi) = \frac{1}{2} \int h(d\phi, d\phi) dv_g$$

over every compact region of M. Now let $\phi : M \to N$ be a harmonic map. Then the Hessian H of E is given by

$$\mathsf{H}_{\phi}(V, W) = \int h(\mathsf{J}_{\phi}(V), W) dv_g, \ V, W \in \Gamma(\phi^* TN).$$

Here the *Jacobi operator* J_{ϕ} is defined by

$$\mathsf{J}_{\phi}(V) := \overline{\Delta}_{\phi} V - \mathsf{R}_{\phi}(V), V \in \Gamma(\phi^* TN),$$

$$\overline{\Delta}_{\phi} := \sum_{i=1}^{m} \left(\nabla_{e_i}^{\phi} \nabla_{e_i}^{\phi} - \nabla_{\nabla_{e_i} e_i}^{\phi} \right), \mathsf{R}_{\phi}(V) = \sum_{i=1}^{m} R^N(V, d\phi(e_i)) d\phi(e_i),$$

where R^N and $\{e_i\}$ are the Riemannian curvature of N, and a local orthonormal frame field of M, respectively [1].

Let $\phi : (M, g) \to (N, h)$ be a smooth map between two Lorentzian manifolds. The *bienergy* $E_2(\phi)$ of ϕ over compact domain $\Omega \subset M$ is defined by

$$E_2(\phi) = \int_{\Omega} h(\tau(\phi), \tau(\phi)) dv_g.$$

A smooth map $\phi:(M,g)\rightarrow(N,h)$ is said to be *biharmonic* if it is a critical point of the $E_2(\phi)$.

The section $\tau_2(\phi)$ is called the *bitension field* of ϕ and the Euler-Lagrange equation of E_2 is

$$\tau_2(\phi):=-\mathsf{J}_\phi(\tau(\phi))=0.$$

Any harmonic map is biharmonic. Additionally, there are many works related with curves [2-18].

In this paper, we firstly characterize biharmonic curves and associated curvature tensor field by considering extended Darboux frame. Then, we obtain the relation of each quasi curvatures of curve. Finally, we give some new conditions with the normal curvature, the geodesic curvatures, and the geodesic torsions of the curve.

2. MATERIAL AND METHODS

By way of design and style, this is model to kind of a moving frame with regards to a particle. In the quick stages of regular differential geometry, the Frenet-Serret frame was applied to create a curve in location. After that, Frenet-Serret frame is established by way of subsequent equations for a presented framework [19],

$$\begin{bmatrix}\nabla_t\mathbf{t}\\\nabla_t\mathbf{n}\\\nabla_t\mathbf{b}\end{bmatrix}=\begin{bmatrix}0&\kappa&0\\\kappa&0&\tau\\0&-\tau&0\end{bmatrix}\begin{bmatrix}\mathbf{t}\\\mathbf{n}\\\mathbf{b}\end{bmatrix},$$

where $\kappa=\|\mathbf{t}\|$ and τ are the curvature and torsion of γ, respectively.

Let M be an orientable hypersurface oriented by the unit normal vector field $\mathbf{N}$ in E^4 and β be a Frenet curve of class C^n ($n\geq4$) with arc-length parameter s lying on M. We denote the unit tangent vector field of the curve by T, and denote the hypersurface unit normal vector eld restricted to the curve by $\mathbf{N}$, i.e.

$$\mathbf{T}(s)=\beta'(s),\mathbf{N}(s)=\mathbf{N}(\beta(s)).$$

We can construct the extended Darboux frame field along the Frenet curve as follows [20]:

Case 1. If the set $\{\mathbf{N},\mathbf{T},\beta''\}$ is linearly independent, then using the GramSchmidt orthonormalization method gives the orthonormal set $\{\mathbf{N},\mathbf{T},\mathbf{E}\}$, where

$$E=\frac{\beta''-<\beta'',\mathbf{N}>\mathbf{N}}{\|\beta''-<\beta'',\mathbf{N}>\mathbf{N}\|}.$$

Case 2. If the set $\{\mathbf{N},\mathbf{T},\beta''\}$ is linearly dependent, i.e. if β'' is in the direction of the normal vector $\mathbf{N}$, applying the Gram-Schmidt orthonormalization method to $\{\mathbf{N},\mathbf{T},\beta''\}$ yields the orthonormal set $\{\mathbf{N},\mathbf{T},\mathbf{E}\}$, where

$$\mathbf{E} = \frac{\beta''' - <\beta''',\mathbf{N}>\mathbf{N} - <\beta''',\mathbf{T}>\mathbf{T}}{\left\| \beta''' - <\beta''',\mathbf{N}>\mathbf{N} - <\beta''',\mathbf{T}>\mathbf{T}\right\|}.$$

In each case, if we define $\mathbf{D} = \mathbf{N} \otimes \mathbf{T} \otimes \mathbf{E}$, we have four unit vector fields $\mathbf{T},\mathbf{E},\mathbf{D}$, and $\mathbf{N}$, which are mutually orthogonal at each point of β. Thus, we have a new orthonormal frame field $\mathbf{T},\mathbf{E},\mathbf{D},\mathbf{N}$ along the curve β instead of its Frenet frame field. It is obvious that $\mathbf{E}$ (s) and $\mathbf{D}$ (s) are also tangent to the hypersurface M for all s. Thus, the set $\mathbf{T},\mathbf{E},\mathbf{D}$ spans the tangent hyperplane of the hypersurface at the point β (s) . We call these new frame fields " extended Darboux frame field of first kind" or in short " ED-frame field of first kind" in case 1, and " extended Darboux frame field of second kind" or in short " ED-frame field of second kind" in case 2, respectively.

Therefore, we obtain the differential equations of ED-frame fields:

Case 1:

$$\begin{aligned}
\mathbf{T}' &= \kappa_g \mathbf{E} + \kappa_n \mathbf{N}\\
\mathbf{E}' &= -\kappa_g \mathbf{T} + \tilde{\kappa}_g \mathbf{D} + \tau_g \mathbf{N}\\
\mathbf{D}' &= -\tilde{\kappa}_g \mathbf{E} + \tilde{\tau}_g \mathbf{N}\\
\mathbf{N}' &= -\kappa_n \mathbf{T} - \tau_g \mathbf{E} - \tilde{\tau}_g \mathbf{D}.
\end{aligned}$$

Case 2:

$$\begin{aligned}
\mathbf{T}' &= \kappa_n \mathbf{N}\\
\mathbf{E}' &= \tilde{\kappa}_g \mathbf{D} + \tau_g \mathbf{N}\\
\mathbf{D}' &= -\tilde{\kappa}_g \mathbf{E}\\
\mathbf{N}' &= -\kappa_n \mathbf{T} - \tau_g \mathbf{E}.
\end{aligned}$$

3. RESULTS AND DISCUSSION

Biharmonic equation for the curve γ reduces to

$$\nabla_{\mathbf{T}}^3 \mathbf{T} - R(\mathbf{T}, \mathbf{T}')\mathbf{T} = 0,$$

that is, γ is called a biharmonic curve if it is a solution of the above equation.

Theorem 3.1. *Let γ be a non-geodesic curve with ED-frame field of first kind in the ordinary space. Then γ is a non-geodesic biharmonic curve if and only if*

$$(\kappa_g(\kappa_g' - \kappa_n\tau_g) + \kappa_n(\kappa_n' + \kappa_g\tau_g) + (\kappa_g^2 + \kappa_n^2)') = 0,$$

$$((\kappa_g' - \kappa_n\tau_g)' - \tau_g(\kappa_n' + \kappa_g\tau_g) - \tilde{\kappa}_g(\kappa_g\tilde{\kappa}_g - \kappa_n\tilde{\tau}_g) - (\kappa_g^2 + \kappa_n^2)\kappa_g) = 0,$$

$$(\tilde{\kappa}_g(\kappa_g' - \kappa_n\tau_g) - \tilde{\tau}_g(\kappa_n' + \kappa_g\tau_g) + (\kappa_g\tilde{\kappa}_g - \kappa_n\tilde{\tau}_g)') = 0$$

$$((\kappa_n' + \kappa_g\tau_g)' + \tau_g(\kappa_g' - \kappa_n\tau_g) - (\kappa_g^2 + \kappa_n^2)\kappa_n + \tilde{\tau}_g(\kappa_g\tilde{\kappa}_g - \kappa_n\tilde{\tau}_g)) = 0.$$

Proof. From Biharmonic equation, we obtain

$$\begin{aligned}
\nabla_{\mathbf{T}}^3 \mathbf{T} = {} & -(\kappa_g(\kappa_g' - \kappa_n\tau_g) + \kappa_n(\kappa_n' + \kappa_g\tau_g) + (\kappa_g^2 + \kappa_n^2)')\mathbf{T} \\
& + ((\kappa_g' - \kappa_n\tau_g)' - \tau_g(\kappa_n' + \kappa_g\tau_g) - \tilde{\kappa}_g(\kappa_g\tilde{\kappa}_g - \kappa_n\tilde{\tau}_g) - (\kappa_g^2 + \kappa_n^2)\kappa_g)\mathbf{E} \\
& + (\tilde{\kappa}_g(\kappa_g' - \kappa_n\tau_g) - \tilde{\tau}_g(\kappa_n' + \kappa_g\tau_g) + (\kappa_g\tilde{\kappa}_g - \kappa_n\tilde{\tau}_g)')\mathbf{D} \\
& + ((\kappa_n' + \kappa_g\tau_g)' + \tau_g(\kappa_g' - \kappa_n\tau_g) - (\kappa_g^2 + \kappa_n^2)\kappa_n + \tilde{\tau}_g(\kappa_g\tilde{\kappa}_g - \kappa_n\tilde{\tau}_g))\mathbf{N}.
\end{aligned}$$

A direct computation using flat space yields

$$R(\mathbf{T}, \mathbf{T}')\mathbf{T} = 0.$$

These, together with above equation, complete the proof of the theorem.

Theorem 3.2. *Let γ be a non-geodesic curve with ED-frame field of second kind in the ordinary space. Then γ is a non-geodesic biharmonic curve if and only if*

$$\kappa_n^{'}\kappa_n \;=\; 0,$$
$$\kappa_n^{''} - \kappa_n^3 - \kappa_n\tau_g^2 \;=\; 0,$$
$$2\kappa_n^{'}\tau_g + \kappa_n\tau_g^{'} \;=\; 0,$$
$$\kappa_n\tau_g\tilde{\kappa}_g \;=\; 0.$$

Proof. By using ED-frame field of second kind, we have

$$\nabla_{\mathbf{T}}^3\mathbf{T} \;=\; (\kappa_n^{''} - \kappa_n^3 - \kappa_n\tau_g^2)\mathbf{N} - 3\kappa_n^{'}\kappa_n\mathbf{T}$$
$$-(2\kappa_n^{'}\tau_g + \kappa_n\tau_g^{'})\mathbf{E} - \kappa_n\tau_g\tilde{\kappa}_g\mathbf{D}.$$

From biharmonic equation, we get

$$\kappa_n \;=\; const,$$
$$\kappa_n(\kappa_n^2 + \tau_g^2) \;=\; 0,$$
$$\kappa_n\tau_g^{'} \;=\; 0,$$
$$\kappa_n\tau_g\tilde{\kappa}_g \;=\; 0.$$

4. CONCLUSION

Biharmonic features are used in several physical circumstances, especially on smooth mechanics and flexibility complications. Virtually all essential uses of the basic principle of features of a complicated variable were acquired inside aircraft principles of flexibility and during the approximate principles of system subject matter to regular packing. Specifically, in circumstances once the alternatives are biharmonic maps. In sequential elasticity, in the event that equations are developed by way of displacements meant for two-dimensional conditions after that the release of a tension action contributes to a fourth-order equation of biharmonic design.

In this study, we firstly characterize biharmonic curves and associated curvature tensor field by considering extended Darboux frame. Then, we obtain the relation of each quasi curvatures of curve. Finally, we give some new conditions with the normal curvature, the geodesic curvatures, and the geodesic torsions of the curve.

REFERENCES

[1] G.Y. Jiang, 2-harmonic isometric immersions between Riemannian manifolds, Chinese Ann. Math. Ser. A 7 (1986), 130-144

[2] S. Baş, T Korpinar, Modified Roller Coaster Surface in Space, Mathematics 7 (2) (2019), 195

[3] S. Baş and T. Körpinar, A New Characterization of One Parameter Family of Surfaces by Inextensible Flows in De-Sitter 3-Space, Journal of Advanced Physics, 7 (2) (2018), 251-256.

[4] T. Körpinar, R.C. Demirkol, A New characterization on the energy of elastica with the energy of Bishop vector fields in Minkowski space. Journal of Advanced Physics. 6(4) (2017), 562-569.

[5] T. Körpinar, New type surfaces in terms of B-Smarandache Curves in Sol^3, Acta Scientiarum Technology, 37(2) (2015), 245-250.

[6] T. Körpinar, On Velocity Magnetic Curves in Terms of Inextensible Flows in Space. Journal of Advanced Physics. 7(2) (2018), 257-260.

[7] T. Körpinar, On the Fermi-Walker Derivative for Inextensible Flows of Normal Spherical Image. Journal of Advanced Physics. 7(2) (2018), 295-302.

[8] T. Körpinar, A Note on Fermi Walker Derivative with Constant Energy for Tangent Indicatrix of Slant Helix in the Lie Groups. Journal of Advanced Physics. 7(2) (2018), 230-234.

[9] T Körpinar, On New Fermi Walker Derivative of Biharmonic Particles In Heisenberg Spacetime, Honam Mathematical J. 41(1) (2019), 153-161

[10] T Körpinar, S. Baş, A new approach to inextensible flows of curves with blaschke frame, Journal of Science and Arts 19 (1), 15-22

[11] T Körpinar, RC Demirkol, Magnetic motion of spherical frictional charged particles on the unit sphere, Revista Mexicana de Fsica 65 (2019), 496-502

[12] T Körpinar, RC Demirkol, Z Körpinar, Soliton propagation of electromagnetic field vectors of polarized light ray traveling in a coiled optical fiber in Minkowski space with Bishop equations, The European Physical Journal D 73 (9) (2019), 203

[13] E. Turhan, T. Körpinar, Characterize on the Heisenberg Group with left invariant Lorentzian metric, Demonstratio Mathematica 42 (2) (2009), 423-428.

[14] E. Turhan, T. Körpinar, On Characterization Of Timelike Horizontal Biharmonic Curves In The Lorentzian Heisenberg Group *Heis*^{3}, Zeitschrift für Naturforschung A- A Journal of Physical Sciences 65a (2010), 641-648.

[15] E. Turhan and T. Körpinar, Parametric equations of general helices in the sol space Sol^3, Bol. Soc. Paran. Mat. 31 (1) (2013), 99--104.

[16] T. Körpinar, Y. Ünlütürk, New Bianchi type-I cosmological models for biharmonic particles using string cosmology with exponential law, Gen. Relativity Gravitation 47(11) (2015), Art. 138, 12 pp.

[17] Y. Ünlütürk, S. Yilmaz, C. Ekici, The relations between null geodesic curves and timelike ruled surfaces in dual Lorentzian space D^{3}1, Honam Math. J. 41(1) (2019), 185-195.

[18] M. Yeneroğlu, T. Körpinar, A New Construction of Fermi-Walker Derivative by Focal Curves According to Modified Frame, Journal of Advanced Physics. 7(2) (2018), 292-294.

[19] M.P. Carmo, Differential Geometry of Curves and Surfaces, Prentice-Hall, New Jersey 1976.

[20] M. Duldul, B.U. Duldul, N. Kuruoglu, E. Ozdamar, Extension of the Darboux frame into Euclidean 4-space and its invariants, Turk J Math 41 (2017), 1628-1639

ON THE DIFFERENTIAL GEOMETRY OF A SPACELIKE PARTICLE IN A HOMOGENEOUS ELECTROMAGNETIC FIELD IN DE-SITTER SPACE

R.C.Demirkol[1], Z.Körpınar[2], S.Baş[3]

[1]Department of Mathematics, Faculty of Arts and Sciences, Mus Alparslan University, Mus, TURKEY
[2]Department of Administration, Faculty of Economic and Administrative Sciences, Muş Alparslan University, Muş, TURKEY
[3]Department of Mathematics, Faculty of Arts and Sciences, Mus Alparslan University, Mus, TURKEY

E-mail: rcdemirkol@ gmail.com

Abstract

We discuss the geometric characterization of the spacelike trajectory of a moving relativistic charged particle, for the case of a homogeneous electromagnetic field, in De-Sitter space when the motion is governed by the Lorentz equation. We employ totally relativistic approach during the discussion and it is based on a systematic use of the four-dimensional Frenet-Serret formulae, which is adapted to the De-Sitter space to determine the worldline geometry of the electromagnetic field acting on the particle in De-Sitter space, and of the Faraday antisymmetric tensor properties.

Keywords: De-Sitter space, Homogeneous electromagnetic field, Faraday antisymmetric tensor, Frenet-Serret frame, Trajectory of a charged particle.

1. INTRODUCTION

Principal least action governs the dynamics of a mechanical system between the times a and b. It is defined by the following integral and it takes the least possible value.

$$Q = \int_a^b L dt,$$

where L is used to describe positions and velocities of the system. The action is defined, for a free relativistic particle, by

$$Q = -mc^2 \int_a^b \sqrt{1 - \frac{v^2}{c^2}} dt,$$

where m is a mass, v is a velocity, and c is the speed of light in a vacuum. The dynamics of the relativistic particle has been studied intensively in Minkowski spacetime for a long time. In Minkowski spacetime, an event is described by the point particle motion whose collection creates the worldline of the particle. The generalization of the action of the relativistic particle can be given by the curvatures $(e_1, e_2, ..., e_n)$ of the worldline of the particle in $(n+1)$ dimensional Minkowski spacetime in the following manner.

$$Q[X] = \int L(e_1, e_2, ..., e_n) d\tau.$$

Here X^γ is embedding function of the particle given by $X^\gamma = (ct, x, y, z), \gamma = 0,1,2,3$ such that

$$d\tau = \sqrt{-\theta},$$

where $\theta = \sqrt{\eta_{\gamma\alpha} \frac{DX^\gamma}{ds} \frac{DX^\alpha}{ds}}$ [1]. This approach has been effectively used to determine the dynamics of a system even though its internal form is not fully solved. For example, in the bosonic theory, the action and evolving of a supersymmetric particle can be understood via curvature dependent action of the relativistic particle [2]. It was proved by Polyakov in [3] that explicit solutions of the dynamics of a rigid body are divided into three types: tachyonic, massless, and massive depending on the value of the invariant of the particle. Kuznetsov and Plyushchay in [4,5,6,7] investigated the curvature and torsion dependent model of the action of the relativistic particle linearly. The relationship between the equation of the motion of the relativistic charged particle in the homogeneous electromagnetic field and the equation of the motion of the particle containing a linear term on the torsion of the trajectory are demonstrated by Plyushchay in [8]. It was proved by the authors in [9–17] that the correspondence between the dynamics of a relativistic charged particle and the geometry of a worldline described by the Frenet-Serret equations can be given by using the invariants of the electromagnetic field and the curvatures of the worldline. Also some curves and surfaces with motion studied in [18-32].

The main goal of the present study is to investigate the motion of a relativistic charged particle in a homogeneous (uniform and constant) electromagnetic field by emphasizing on the invariant geometric description of its spacelike trajectory in De-Sitter spacetime. We also aim to clarify the nature of the Frenet-

Serret equations on the basis of a given physical system. This is achieved through the use of the Lorentz equation together with the Frenet-Serret formalism. We also establish a connection between the intrinsic scalars of the spacelike worldline of the curve and field invariants of the electromagnetic field in De-Sitter space.

2. MATERIAL AND METHODS

The intrinsic geometric features of a moving particle in space is determined mostly by using the Frenet-Serret formulae. These formulations are obtained by the Frenet-Serret (FS) tetrad, which is constructed by the tangent vector of the worldline, normal and binormal vectors together with a number of associated curvatures of the curve depending on a dimension of a space. In this work, the particle is assumed to follow a spacelike worldline in De-Sitter spacetime. Thus, as a result of this motion, it is obtained a curve, which has a spacelike tangent vector and timelike normal or binormal vector. Here, the arc-length parameter is also described to compute the distance traveled by the particle along its spacelike worldline. When the main tetrad is stated initially and the associated curvatures are defined in terms of the functions of the arc-length parameter on the path, then the trajectory is found thanks to the FS relations. By the assumption, we restrict ourselves to a spacelike curve $\boldsymbol{\beta}^{\gamma} = \boldsymbol{\beta}^{\gamma}(s)$, which corresponds to a moving spacelike particle in special relativity. In this theory, the complete coordinate system for any event is defined by

$$(\boldsymbol{\beta}^{\gamma}) = (ct, x, y, z), \gamma = 0,1,2,3.$$

The distance between two distinct events is computed by

$$ds^2 = \pm dx^2 \pm dy^2 \pm dz^2 + c^2 dt^2,$$

where c is the velocity of light in the vacuum. Thus, for a spacelike curve, we have

$$\eta_{\gamma\alpha}(\frac{D\boldsymbol{\beta}^{\gamma}}{ds})(\frac{D\boldsymbol{\beta}^{\alpha}}{ds}) = 1,$$

where $\eta_{\gamma\alpha}$ is a metric tensor and s is the arc-length parameter. If we choose components of the unit speed spacelike tangent vector as

$$\mathbf{T}^{\gamma} = \frac{d\boldsymbol{\beta}^{\gamma}}{ds}, \eta_{bc}\mathbf{T}^{b}\mathbf{T}^{c} = \mathbf{T}_{\gamma}\mathbf{T}^{\gamma} = 1,$$

then we have normal and binormal vectors $\underset{\gamma=1,2}{\mathbf{E}}$ defined along the curve. So far it is described three orthogonal vectors along the worldline. However, De-Sitter spacetime is a four-dimensional space. Thus, there must be a fourth vector in addition to the tangent, normal, and binormal vectors for the complete framework construction. Therefore, it is considered that the curve $\boldsymbol{\beta}$ itself is a vector to establish FS equation system in De-Sitter spacetime. Finally, the main tetrad $(\mathbf{T}^{\gamma}, \underset{1}{\mathbf{E}^{\gamma}}, \underset{2}{\mathbf{E}^{\gamma}}, \underset{3}{\mathbf{E}^{\gamma}})$ is defined by FS frame in the following manner.

$$\mathbf{T}_{k}\underset{\gamma=1,2,3}{\mathbf{E}^{k}} = 0; \underset{\gamma}{\mathbf{E}}_{k}\underset{\gamma}{\mathbf{E}^{k}} = \pm 1, \gamma = 1,2; \underset{3}{\mathbf{E}}_{k}\underset{3}{\mathbf{E}^{k}} = 1.$$

It implies that there exist two different cases for the construction of the orthonormal frame structure in De-Sitter spacetime according to the choice of the normal and binormal vectors $\underset{\gamma=1,2}{\mathbf{E}}$ as being timelike or spacelike. Here we exchange the notation of the spacelike curve $\boldsymbol{\beta}$ with $\underset{3}{\mathbf{E}}^k$ for the simplicity purpose of the notation. This construction also obeys the following FS equation system.

Case 1. If $\underset{1}{\mathbf{E}}^\gamma$ is timelike then, we have following FS equations $[18]$.

$$
\begin{aligned}
\frac{D\mathbf{T}^\gamma}{ds} &= e_1 \underset{1}{\mathbf{E}}^\gamma - \underset{3}{\mathbf{E}}^\gamma, \\
\frac{D\underset{1}{\mathbf{E}}^\gamma}{ds} &= e_1 \mathbf{T}^\gamma + \rho e_2 \underset{2}{\mathbf{E}}_k, \\
\frac{D\underset{2}{\mathbf{E}}^\gamma}{ds} &= e_2 \underset{1}{\mathbf{E}}_k, \\
\frac{D\underset{3}{\mathbf{E}}^\gamma}{ds} &= \mathbf{T}^\gamma,
\end{aligned}
$$

where $\rho = \pm 1$, e_1 is the curvature and e_2 is the torsion of the spacelike worldline.

3. RESULTS AND DISCUSSION

Now, we adapt FS frame construction to the De-Sitter spacetime to investigate the motion of the accelerated charged particle within the context of general and special relativity. This leads us to determine intrinsic geometric features of the spacelike trajectory of the moving charged particle in the electromagnetic field, ultimately. The first step in that process is to observe the behavior of the F_{uv} in the main tetrad.

Case 1. In this case, we assume that the normal vector is timelike. Thus, we have

$$
\underset{1}{\mathbf{E}}_k \underset{1}{\mathbf{E}}^k = -1
$$

We firstly write F_{uv} in terms of its bases, which are the class of antisymmetric tensors at each point of the spacelike curve.

$$
\begin{aligned}
\underset{\gamma}{C}^{uv} &= \mathbf{T}^u \underset{\gamma}{\mathbf{E}}^v - \mathbf{T}^v \underset{\gamma}{\mathbf{E}}^u, \gamma = 1,2,3, \\
\underset{4}{C}^{uv} &= \underset{1}{\mathbf{E}}^u \underset{2}{\mathbf{E}}^v - \underset{1}{\mathbf{E}}^v \underset{2}{\mathbf{E}}^u, \\
\underset{5}{C}^{uv} &= \underset{1}{\mathbf{E}}^u \underset{3}{\mathbf{E}}^v - \underset{1}{\mathbf{E}}^v \underset{3}{\mathbf{E}}^u, \\
\underset{6}{C}^{uv} &= \underset{2}{\mathbf{E}}^u \underset{3}{\mathbf{E}}^v - \underset{2}{\mathbf{E}}^v \underset{3}{\mathbf{E}}^u.
\end{aligned}
$$

Thus, we have

$$F^{uv} = \sum_{\gamma=1}^{6} b_\gamma \underset{\gamma}{C^{uv}},$$

where b_γ are some smooth functions along the worldline of the spacelike curve. Using simple algebraic properties and FS frame construction given in above equations we reach following equalities.

$$\underset{\gamma}{C_{uv}} \underset{\gamma}{C^{uv}} = -2, \text{when} \gamma = 1,4,5,$$

$$\underset{\gamma}{C_{uv}} \underset{\gamma}{C^{uv}} = 2, \text{when} \gamma = 2,3,6,$$

$$\underset{\gamma}{C_{uv}} \underset{\alpha}{C^{uv}} = 0, \text{when} \gamma \neq \alpha.$$

Then we are allowed to write

$$F_{uv} F^{uv} = \sum_{\gamma=1}^{6} b_\gamma \underset{\gamma}{C_{uv}} \sum_{\gamma=1}^{6} b_\gamma \underset{\gamma}{C^{uv}}.$$

Then

$$\left(R^2 - S^2\right) = \left(-b_1^2 + b_2^2 + b_3^2 - b_4^2 - b_5^2 + b_6^2\right)$$

Also, we can define the dual of each $\underset{\gamma=1,\dots,6}{C_{uv}}$ in the following manner.

$$\underset{\gamma=1,\dots,6}{*C_{uv}} = \frac{1}{2} \sigma_{uvab} \underset{\gamma=1,\dots,6}{C^{ab}}.$$

Here we assume that the FS tetrad $(\mathbf{T}^\gamma, \underset{1}{\mathbf{E}^\gamma}, \underset{2}{\mathbf{E}^\gamma}, \underset{3}{\mathbf{E}^\gamma})$ is positively oriented when

$$\sigma_{uvab} \mathbf{T}^u \underset{1}{\mathbf{E}^v} \underset{2}{\mathbf{E}^a} \underset{3}{\mathbf{E}^b} = 1.$$

Hence, we obtain that

$$*F_{uv} F^{uv} = \sum_{\gamma=1}^{6} b_\gamma \underset{\gamma}{*C_{uv}} \sum_{\gamma=1}^{6} b_\gamma \underset{\gamma}{C^{uv}}.$$

To expand the above equation we first need to give the following equalities, which are obtained by

$$\underset{\gamma}{*C_{uv}} \underset{\gamma}{C^{uv}} = 0, \text{when} \gamma = 1,\dots 6,$$

$$\underset{1}{*C_{uv}} \underset{6}{C^{uv}} = -\underset{2}{*C_{uv}} \underset{5}{C^{uv}} = \underset{3}{*C_{uv}} \underset{4}{C^{uv}} = 2,$$

$$\underset{\gamma}{*C_{uv}} \underset{\alpha}{C^{uv}} = 0 \text{ for other cases.}$$

Now, have

$$(\mathbf{S}\cdot\mathbf{R}) = b_1 b_6 - b_2 b_5 + b_3 b_4.$$

As a consequence, above equations give the invariant of the electromagnetic field in terms of arbitrary functions defined along the worldline of the curve. To observe the behavior of the F^{uv} along the spacelike worldline we also need to compute

$$\frac{DF^{uv}}{ds} = \sum_{\gamma=1}^{6} \frac{D}{ds}(b_\gamma \, C^{uv}_{\gamma}).$$

Differential properties of the tensor $C^{uv}_{\gamma=1,\dots,6}$ is calculated as

$$\frac{D}{ds}C^{uv}_1 = \rho e_2 \, C^{uv}_2 + C^{uv}_5, \quad \frac{D}{ds}C^{uv}_2 = e_1 \, C^{uv}_4 + C^{uv}_6 + e_2 \, C^{uv}_1,$$

$$\frac{D}{ds}C^{uv}_3 = e_1 \, C^{uv}_5, \quad \frac{D}{ds}C^{uv}_4 = e_1 \, C^{uv}_2,$$

$$\frac{D}{ds}C^{uv}_5 = e_1 \, C^{uv}_3 + \rho e_2 \, C^{uv}_6 - C^{uv}_1, \quad \frac{D}{ds}C^{uv}_6 = e_2 \, C^{uv}_5 - C^{uv}_2.$$

Thus, the evolution of F^{uv} on the spacelike worldline is stated by

$$
\begin{aligned}
\frac{DF^{uv}}{ds} = & \; (\frac{Db_1}{ds} + b_2 e_2 - b_5) C^{uv}_1 + (\frac{Db_2}{ds} + \rho b_1 e_2 + b_4 e_1 - b_6) C^{uv}_2 \\
& + (\frac{Db_3}{ds} + b_5 e_1) C^{uv}_3 + (\frac{Db_4}{ds} + b_2 e_1) C^{uv}_4 \\
& + (\frac{Db_5}{ds} + b_1 + b_3 e_1 + b_6 e_2) C^{uv}_5 + (\frac{Db_6}{ds} + b_2 + \rho b_5 e_2) C^{uv}_6.
\end{aligned}
$$

4. CONCLUSION

In the present paper, we introduce a geometric approach to investigate the motion of a spacelike relativistic charged particle subjected to a homogeneous electromagnetic field in De-Sitter space. Aside from the geometric characterization of the spacelike wordline of the charged particle in De-Sitter space we also correlate the intrinsic scalars of the worldline of the charged particle and field invariants of the electromagnetic field in De-Sitter space.

This study will also lead up to further research on the investigation of the dynamics of the moving charged particles when they are experienced some well-known external forces beside the electromagnetic field i.e. the frictional force, the gravitational force, the normal force, and the resultant force in De-Sitter space. Consequently, we aim to obtain more applicable and widely acceptable results to comprehend the exact

movement of the charged particle in a given homogeneous electromagnetic field in De-Sitter space when the motion is governed by the Lorentz equation.

REFERENCES

[1] G. Arreaga-Garcia, and J.S. Morales, Equations of motion of a relativistic charged particle with curvature dependent actions, *Palestine Journal of Mathematics.* 3 (2014), 218.

[2] A.M. Polyakov, *Gauge Fields and Strings.* (New York: Harwood Academic, 1987).

[3] M.S. Plyushchay, Massive relativistic point particle with rigidity, *Int. J. Mod. Phys.* **4** (1989), 3851.

[4] M.S. Plyushchay, Massive particle with rigidity as a model for the description of bosons and fermions, *Phys. Lett. B.* **243** (1990), 383.

[5] Y.A. Kuznetsov and M.S. Plyushchay, The model of the relativistic particle with curvature and torsion, *Nuclear Phys. B.* **389** (1993), 181.

[6] M.S. Plyushchay, Comment on "The relativistic particle with curvature and torsion of world trajectory", *arXiv preprint hep-th/9810101* (1998).

[7] Y.A. Kuznetsov and M.S. Plyushchay, Tachyonless models of relativistic particles with curvature and torsion, *Physics Letters B.* **297**, (1992), 49.

[8] M.S. Plyushchay, Relativistic particle with torsion and charged particle in a constant electromagnetic field: Identity of evolution. *Mod. Phys. Lett. A.* **10** (1995), 1463.

[9] J.L. Lopez Bonilla and E. Pina-Garza, Particulas Clasicas Cargadas en Relatividad Especial, *Direccion de Publicaciones del IPN.* (1980).

[10] J.B. Fomiga and C. Romero, On the Differential Geometry of time-like Curves in Minkowski spacetime, *Am. J. Phys.* **74** (2006), 1012.

[11] E. Honig, E.L. Schucking and C.V. Vishveshwara, Motion of charged particles in homogeneous electromagnetic fields, *Journal of Math. Phys.* **15** (1974), 774.

[12] J.V. Narkliar, *Introduction to Cosmology.* (Cambridge UniversityPress, Cambridge, 1993).

[13] H.C. Ohanian and R. Ruffini, *Gravitation and Spacetime, 2nd Edition.* (Norton, New York, 1994)

[14] J.P. Gazeau and P. Wlodzimierz, Coherent state quantization of a particle in de Sitter space, *Journal of Physics A: Mathematical and General.* **37** (2004), 6977.

[15] M. Arzano and J. Kowalski-Glikman, Kinematics of a relativistic particle with de Sitter momentum space, *Classical and Quantum Gravity.* **28** (2011), 105009.

[16] W.R.E. Miguel and J.G. Pereira, Cosmological Constant and the Speed of Light, *International Journal of Modern Physics D.* **10** (2001), 41.

[17] O.V. Veko, N.D. Vlasii, Yu. A. Sitenko, E.M. Ovsiyuk and V.M. Red'kov, Electromagnetic Field in de Sitter Expanding Universe Majorana-Oppenheimer Formalism, Exact Solutions in non-Static Coordinates, *Nonlinear Phenom. Complex Syst.* **17** (2014), 17.

[18] T. Turhan, N. Ayyildiz, Some Results on the Differential Geometry of Spacelike Curves in De-Sitter Space, *Journal of Applied Mathematics and Phys.* **1** (2013), 55.

[19] H.S. Abdel Aziz, New Spherical Surfaces in de Sitter 3-Space, *Applied Mathematics and Information Sci.* **2** (2008), 345.

[20] M. Barros, and A. Fernandez, A conformal variational approach for helices in nature. *J. Math. Phys.* **50** (2009) 103529.

[21] T Körpinar, RC Demirkol, Magnetic motion of spherical frictional charged particles on the unit sphere, Revista Mexicana de Fsica 65 (2019), 496.

[22] T Körpinar, RC Demirkol, Z Körp nar, Soliton propagation of electromagnetic field vectors of polarized light ray traveling in a coiled optical fiber in Minkowski space with Bishop equations, The European Physical Journal D 73 (9) (2019), 203

[23] T Körpinar, RC Demirkol, On the uniform motion of a relativistic charged particle in a homogeneous electromagnetic field in Minkowski space E_2^4, Mathematical Methods in the Applied Sciences, 42 (9) (2019), 3069.

[24] T Körpinar, RC Demirkol, Electromagnetic curves of the linearly polarized light wave along an optical fiber in a 3D semi-Riemannian manifold, Journal of Modern Optics 66 (8) (2019), 857.

[25] T. Körpinar, On the Fermi--Walker Derivative for Inextensible Flows, Zeitschrift für Naturforschung A. 70 (7) (2015), 477.

[26] Z. S. Körpinar, M. Tuz, T. Körpinar, New Electromagnetic Fluids Inextensible Flows of Spacelike Particles and some Wave Solutions in Minkowski Space-time, Int J Theor Phys 55 (1) (2016), 8.

[27] T. Körpinar, Bianchi Type-I Cosmological Models for Inextensible Flows of Biharmonic Particles by Using Curvature Tensor Field in Spacetime, Int J Theor Phys 54 (2015), 1762.

[28] T. Körpinar, Y. Ünlütürk, New Bianchi type-I cosmological models for biharmonic particles using string cosmology with exponential law, Gen. Relativity Gravitation 47(11) (2015), 138.

[29] T. Körpinar, On T-Magnetic Biharmonic Particles with Energy and Angle in the Three Dimensional Heisenberg Group H, Adv. Appl. Clifford Algebras, 28 (1) (2018), 1.

[30] T. Körpinar, New Characterization for Minimizing Energy of Biharmonic Particles in Heisenberg Spacetime. Int J Phys. 53 (2014), 3208.

[31] T. Körpinar, R.C. Demirkol, A new approach on the curvature dependent energy for elastic curves in a Lie Group. Honam Mathematical J. 39(4) (2017), 637.

[32] T. Körpinar, R.C. Demirkol, A New characterization on the energy of elastica with the energy of Bishop vector fields in Minkowski space. Journal of Advanced Physics. 6(4) (2017), 562.

NORMAL FORCE MAGNETIC CURVES IN 3D RIEMANNIAN MANIFOLDS

R.C.Demirkol[1], S.Baş[2], T.Körpınar [3]

[1]*Department of Mathematics, Faculty of Arts and Sciences, Mus Alparslan University, Mus, TURKEY*
[2]*Department of Mathematics, Faculty of Arts and Sciences, Mus Alparslan University, Mus, TURKEY*
[3]*Department of Mathematics, Faculty of Arts and Sciences, Mus Alparslan University, Mus, TURKEY*

E-mail: rcdemirkol@ gmail.com

Abstract

In this study, we investigate the special type of magnetic trajectories associated with a magnetic field B defined on a 3D Riemannian manifold. Firstly, we consider a moving charged particle which is under the action of a normal force, N_{f}, in the magnetic field B. Then, we assume that trajectories of the particle associated with the magnetic field B correspond to normal magnetic curves (N_{f}-magnetic curves) of magnetic vector field B on the 3D Riemannian manifold. Thus, we are able to investigate some geometric features and physical consequences of the particle, which is assumed to be under the action of normal force in the magnetic field B on the 3D Riemannian manifold

Keywords: De-Sitter space**,** magnetic field, timelike magnetic curve, energy, magnetic force, uniform motion.

1. INTRODUCTION

Lorentz force law together with Maxwell equations constitutes the basis for electric circuits, classical optics, and classical electrodynamics. Gauss law for magnetism is known as the second equation of Maxwell, i.e. $\nabla \cdot \mathbf{B} = 0$. It implies that magnetic field $\mathbf{B}$ is a divergence-free vector field. This property of Maxwell equations allows us to determine the magnetic field $\mathbf{B}$ on a $n-$dimensional oriented Riemannian manifold. The trajectory of a moving charged particle on the manifold corresponds to a magnetic curve under the action of the magnetic field. Magnetic curves generalize geodesics, which have the form of second order non-linear Euler-Lagrange differential equation, [1-9].

In the literature, one of the major goals is to obtain magnetic curves associated with the magnetic field $\mathbf{B}$ on a $n-$dimensional Riemannian manifold, [10-15]. Thus, intrinsic geometric features of the $n-$dimensional Riemannian manifold can be used to determine the curvature of the magnetic curves. Consequently, magnetic curves can be figured out completely depending on the particular structure of the manifold [16-19]. For instance, [20-22] obtained explicit trajectories associated with a Kahler magnetic fields by assuming the ambient space is a complex form of space. Also, energy and biharmonicity concept have been obtained with some characterizations, [23-28].

2. MATERIAL AND METHODS

Let Γ be a particle moving in a space such that the precise location of the particle is specified by $\Gamma = \Gamma(t)$, where t is a time parameter. Changing time parameter describes the motion and trajectory of the particle, ultimately. In most cases, this trajectory corresponds to a particular curve in the space. It is convenient to remind that arc-length parameter s is used to compute the distance traveled by a particle along its trajectory and defined by

$$v = \frac{ds}{dt} = \|\mathbf{v}\|,$$

where $\mathbf{v} = \mathbf{v}(t) = \dfrac{d\zeta}{dt}$ is the velocity vector and $\dfrac{d\zeta}{dt} \neq 0$. In particle dynamics, the arc-length parameter s is also considered as a function of t. Thanks to the arc-length, it is also determined Serret-Frenet frame, which allows us to describe the characterization of the intrinsic geometric features of the regular curve. This coordinate system is constructed by three orthonormal vectors $\mathbf{e}_{(\alpha)}^{\mu}$, assuming the curve is sufficiently smooth at each point. The index within the parenthesis is the tetrad index that describes a particular member of the tetrad. In particular, $\mathbf{e}_{(0)}^{\mu}$ is the unit tangent vector, $\mathbf{e}_{(1)}^{\mu}$, $\mathbf{e}_{(2)}^{\mu}$ are unit normal and binormal vectors of the curve ζ, respectively. Orthonormality conditions are summarized by $\mathbf{e}_{(\alpha)}^{\mu}\mathbf{e}_{(\beta)}^{\mu} = \eta_{\alpha\beta}$, where $\eta_{\alpha\beta}$ is Euclidean metric such that: $\text{diag}(1,1,1)$. For non-negative coefficients κ, τ, and vectors $\mathbf{e}_{(i)}^{\mu}(i = 0,1,2)$ following equations and properties satisfy [29]:

$$\nabla_{\zeta'} \mathbf{e}_{(0)}^{\mu} = \kappa \mathbf{e}_{(1)}^{\mu},$$

$$\nabla_{\zeta'} \mathbf{e}_{(1)}^{\mu} = -\kappa \mathbf{e}_{(0)}^{\mu} + \tau \mathbf{e}_{(2)}^{\mu},$$

$$\nabla_{\zeta'} \mathbf{e}_{(2)}^{\mu} = -\tau \mathbf{e}_{(1)}^{\mu}.$$

Arc-length parameter s is also necessary for defining velocity and acceleration of the particle. Here, we get

$$\mathbf{v}(s) = \frac{d\zeta}{dt} = \frac{ds}{dt} \mathbf{e}_{(0)}^{\mu}$$

and

$$\mathbf{a}(s) = \frac{d\mathbf{v}}{dt} = \frac{d^2 s}{dt^2} \mathbf{e}_{(0)}^{\mu} + \kappa \left(\frac{ds}{dt} \right)^2 \mathbf{e}_{(1)}^{\mu}.$$

The motion of the particle or block on a curve is a well-known problem for circular and flat surfaces. Point particle that slides on a downward concave surface under the action of frictional force, normal force, and gravitational force can be determined by the Serret-Frenet frame.

It is shown that for any particle sliding down on a surface with a mass m, the normal force is

$$\mathbf{N_f} = \grave{u} N \mathbf{e}_{(1)}^{\mu},$$

where $N = \|\mathbf{N_f}\|$, $\grave{u} = \pm 1$; the gravitational force is

$$\mathbf{G} = m(g_0 \mathbf{e}_{(0)}^{\mu} + g_1 \mathbf{e}_{(1)}^{\mu}),$$

where $g_{i=0,1}$ are gravitational coefficient; the frictional force is

$$f = -\alpha N \mathbf{e}_{(0)}^{\mu},$$

where α is frictional coefficient $[30,31]$.

3. RESULTS AND DISCUSSION

Now, we assume that for a moving charged particle in any magnetic field B on (M^3, ρ), there exists a normal force acting on the particle. Then, trajectories of the particle of the magnetic field B on the 3D Riemannian surface give a new kind of magnetic curve.

Definition 3.1 *Let* ζ *be an arc-length parameterized magnetic curve in the 3D Riemannian manifold* (M^3, ρ) *and* B *be a magnetic field on* M^3. *We call the curve* ζ *as a* $\mathbf{N_f}$*-magnetic curve if the normal force field of the curve meets the following Lorentz force equation;*

$$\nabla_{\zeta'} \mathbf{N_f} = \phi(\mathbf{N_f}) = \mathsf{B} \times \mathbf{N_f}.$$

Proposition 3.2 *Let* ζ *be an arc-length parametrized* $\mathbf{N_f} - magnetic\ curve\ of$ B *with the Frenet frame elements* $\{\mathbf{e}_{(0)}^{\mu}, \mathbf{e}_{(1)}^{\mu}, \mathbf{e}_{(2)}^{\mu}, \kappa, \tau\}$. *Then, Lorentz force* ϕ *of a magnetic field* B *is written in the Frenet frame as the following;*

$$\phi(\mathbf{e}_{(0)}^{\mu}) = \omega_1 \mathbf{e}_{(0)}^{\mu} + \kappa \mathbf{e}_{(1)}^{\mu} + \omega_2 \mathbf{e}_{(2)}^{\mu},$$
$$\phi(\mathbf{e}_{(1)}^{\mu}) = \omega_3 \mathbf{e}_{(0)}^{\mu} + \omega_4 \mathbf{e}_{(2)}^{\mu},$$
$$\phi(\mathbf{e}_{(2)}^{\mu}) = \omega_5 \mathbf{e}_{(0)}^{\mu} - \tau \mathbf{e}_{(1)}^{\mu} + \omega_6 \mathbf{e}_{(2)}^{\mu},$$

where ω_i, $1 \le i \le 6$ *are smooth functions along the curve* ζ.

Proof *Let* ζ *be an arc-length parametrized* $\mathbf{N_f} - magnetic\ curve\ in$ (M^3, ρ) *together with the Frenet frame elements* $\{\mathbf{e}_{(0)}^{\mu}, \mathbf{e}_{(1)}^{\mu}, \mathbf{e}_{(2)}^{\mu}, \kappa, \tau\}$. Knowing the fact that $\phi(\mathbf{e}_{(0)}^{\mu}) \in span\{\mathbf{e}_{(0)}^{\mu}, \mathbf{e}_{(1)}^{\mu}, \mathbf{e}_{(2)}^{\mu}\}$ and

$$-\grave{u}N\kappa\mathbf{e}_{(0)}^{\mu} = \rho(\phi(\mathbf{N_f}), \mathbf{e}_{(0)}^{\mu}) = -\rho(\mathbf{N_f}, \phi(\mathbf{e}_{(0)}^{\mu})) = -\rho(\grave{u}N\mathbf{e}_{(1)}^{\mu}, \phi(\mathbf{e}_{(0)}^{\mu})),$$

we get $\phi(\mathbf{e}_{(0)}^{\mu}) = \omega_1 \mathbf{e}_{(0)}^{\mu} + \kappa \mathbf{e}_{(1)}^{\mu} + \omega_2 \mathbf{e}_{(2)}^{\mu}$; where ω_1 and ω_2 are some smooth functions along the curve ζ. Proof is completed by using similar procedure for $\phi(\mathbf{e}_{(1)}^{\mu})$ and $\phi(\mathbf{e}_{(2)}^{\mu})$.

Theorem 3.3 ζ *is a unit speed* $\mathbf{N_f} - magnetic\ curve\ of\ the\ magnetic\ field$ B *if and only if*

$$\mathsf{B} = \tau\mathbf{e}_{(0)}^{\mu} - (\tau\frac{\omega_1}{\omega_3} + \kappa\frac{\omega_5}{\omega_3})\mathbf{e}_{(1)}^{\mu} + \kappa\mathbf{e}_{(2)}^{\mu}, \quad \omega_3 \ne 0$$

or equivalently

$$\mathsf{B} = \tau\mathbf{e}_{(0)}^{\mu} - (\tau\frac{\omega_2}{\omega_4} + \kappa\frac{\omega_6}{\omega_4})\mathbf{e}_{(1)}^{\mu} + \kappa\mathbf{e}_{(2)}^{\mu}, \quad \omega_4 \ne 0$$

along the curve ζ.

Proof Let us choose $\mathbf{B} = a_0\mathbf{e}_{(0)}^\mu + a_1\mathbf{e}_{(1)}^\mu + a_2\mathbf{e}_{(2)}^\mu$, where a_i, $i = 0,1,2$ are some functions along ζ. We also suppose that $\mathbf{B}$ does not vanish along the curve. Now, from the definition of $\mathbf{N_f}$-magnetic curve we have

$$\nabla_{\zeta'}\mathbf{N_f} = (a_0\mathbf{e}_{(0)}^\mu + a_1\mathbf{e}_{(1)}^\mu + a_2\mathbf{e}_{(2)}^\mu) \times (\grave{u}N\mathbf{e}_{(1)}^\mu).$$

Here, we obtain $a_0 = \tau$ and $a_2 = \kappa$. Also, from the definition of Lorentz force ϕ, we get $\phi(\mathbf{B}) = \mathbf{B} \times \mathbf{B} = 0$. Thus, we have

$$0 = a_0\phi(\mathbf{e}_{(0)}^\mu) + a_1\phi(\mathbf{e}_{(1)}^\mu) + a_2\phi(\mathbf{e}_{(2)}^\mu),$$

which means $a_1 = -(\tau\dfrac{\omega_1}{\omega_3} + \kappa\dfrac{\omega_5}{\omega_3})$, $\omega_3 \neq 0$ or equivalently $a_1 = -(\tau\dfrac{\omega_2}{\omega_4} + \kappa\dfrac{\omega_6}{\omega_4})$, $\omega_4 \neq 0$.

Corollary 3.4 *Let* ω_i, $1 \leq i \leq 6$ *be arbitrary smooth functions given in Proposition 3.2. Then, we have the following relation*

$$\frac{\tau}{\kappa} = \frac{\omega_6\omega_3 - \omega_5\omega_4}{\omega_1\omega_4 - \omega_2\omega_3}, \ \omega_1\omega_4 - \omega_2\omega_3 \neq 0$$

Proof By definition we get $\phi(\mathbf{B}) = \mathbf{B} \times \mathbf{B} = 0$. Thus, we have

$$0 = \phi(\mathbf{B}) = \tau\phi(\mathbf{e}_{(0)}^\mu) - (\tau\frac{\omega_1}{\omega_3} + \kappa\frac{\omega_5}{\omega_3})\phi(\mathbf{e}_{(1)}^\mu) + \kappa\phi(\mathbf{e}_{(2)}^\mu).$$

If we also use above theorem, then the proof is completed.

REFERENCES

[1] A. Comtet, On the Landau Hall levels on the hyperbolic plane, *Annals of Phys.* **173** (1987), 185.

[2] D.I. Efimov, The magnetic geodesic flows on a homogeneous sympletic manifold, *Siberian Math. J.* **46** (2005), 83.

[3] T. Körpinar, R.C. Demirkol, Gravitational magnetic curves on 3D Riemannian manifolds, International Journal of Geometric Methods in Modern Physics. 15 (2018), 1850184.

[4] T. Körpinar and R.C. Demirkol, Frictional magnetic curves in 3D Riemannian manifolds, International Journal of Geometric Methods in Modern Physics. 15 (2018), 1850020.

[5] T. Körpinar, A New Version of Normal Magnetic Force Particles in 3D Heisenberg Space, Adv. Appl. Clifford Algebras, 28(4) (2018), 1.

[6] T. Körpinar, On T-Magnetic Biharmonic Particles with Energy and Angle in the Three Dimensional Heisenberg Group H, Adv. Appl. Clifford Algebras, 28 (1) (2018), 1.

[7] T. Körpinar, On velocity magnetic curves in terms of inextensible flows in space, Journal of Advanced Physics, 7 (2018), 257.

[8] M. Barros, J.L. Cabrerizo, M. Fernandez and A. Romero, Magnetic vortex filament flows, *Journal of Math. Phys.* **48** (2007).

[9] J.L. Cabrerizo, Magnetic fields in 2D and 3D sphere, *Journal of Nonlinear Math. Phys.* **20** (2013), 440.

[10] Z. Bozkurt, İ. Gök, Y. Yayl and F.N. Ekmekci, A new approach for magnetic curves in 3D Riemannian manifolds, *Journal of Math. Phys.* **55** (2014).

[11] T Körpinar, RC Demirkol, Z Körp nar, Soliton propagation of electromagnetic field vectors of polarized light ray traveling in a coiled optical fiber in Minkowski space with Bishop equations, The European Physical Journal D 73 (9) (2019), 203

[12] T Körpinar, RC Demirkol, On the uniform motion of a relativistic charged particle in a homogeneous electromagnetic field in Minkowski space E24, Mathematical Methods in the Applied Sciences, 42 (9) (2019), 3069-3087

[13] T Körpinar, RC Demirkol, Electromagnetic curves of the linearly polarized light wave along an optical fiber in a 3D semi-Riemannian manifold, Journal of Modern Optics 66 (8) (2019), 857-867

[14] T Körpinar, RC Demirkol, Magnetic motion of spherical frictional charged particles on the unit sphere, Revista Mexicana de Fsica 65 (2019), 496-502

[15] T. Sunada, Magnetic flows on a Riemann surface, *Proc. KAIST Math. Workshop.* (1993), 93.

[16] T. Adachi, Kahler magnetic flow for a manifold of constant holomorphic sectional curvature, *Tokyo J. Math.* **18** (1995), 473.

[17] T. Adachi, Kahler magnetic on a complex projective space, *Proc. Japan Acad. Ser. A: Math Sci.* **70** (1994), 12.

[18] J.L. Cabrerizo, M. Fernandez and J.S. Gomez, On the existence of almost contact structure and the contact magnetic field, *Acta Math. Hung.* **125** (2009), 191.

[19] S.P. Novikov, The Hamiltonian formalism and a many valued analogue of Morse theory, *Russian Math. Surveys* **37** (1982), 1.

[20] S.L. Druta-Romaniuc and M.I. Munteanu, Magnetic Curves corresponding to Killing magnetic fields in E^3, *J. Math. Phys.* **52** (2011), 1.

[21] S. L. Druta-Romaniuc and M.I. Munteanu, Killing magnetic curves in a Minkowski 3-space, *Nonlinear Anal.:Real Word Application.* **14** (2013), 383.

[22] M.I. Munteanu and A.I. Nistor, The classification of Killing magnetic curves in $S^2 \times R$, *J. Geom. Phys.* **62** (2012), 170.

[23] Z. S. Körpinar, M. Tuz, T. Körpinar, New Electromagnetic Fluids Inextensible Flows of Spacelike Particles and some Wave Solutions in Minkowski Space-time, Int J Theor Phys 55 (1) (2016), 8--16.

[24] T. Körpinar, Bianchi Type-I Cosmological Models for Inextensible Flows of Biharmonic Particles by Using Curvature Tensor Field in Spacetime, Int J Theor Phys 54 (2015), 1762--1770

[25] T. Körpinar, Y. Ünlütürk, New Bianchi type-I cosmological models for biharmonic particles using string cosmology with exponential law, Gen. Relativity Gravitation 47(11) (2015), Art. 138, 12 pp.

[26] T. Körpinar, New Characterization for Minimizing Energy of Biharmonic Particles in Heisenberg Spacetime. Int J Phys. 53 (2014), 3208-3218.

[27] T. Körpinar, R.C. Demirkol, A new approach on the curvature dependent energy for elastic curves in a Lie Group. Honam Mathematical J. 39(4) (2017), 637-647.

[28] T. Körpinar, R.C. Demirkol, A New characterization on the energy of elastica with the energy of Bishop vector fields in Minkowski space. Journal of Advanced Physics. 6(4) (2017), 562-569.

[29] E. Honig, E.L. Schucking, C.V. Vishveshwara, Motion of charged particles in homogeneous electromagnetic fields, *Journal of Math*. Phys. **15** (1974).

[30] A. Coronel-Escamilla, J.F. Gomez-Angular, E. Alvarado-Mendez, G.V. Guerrero-Ramirez and R.F. Escobar-Jimenez, Fractional Dynamics of charged particles in magnetic fields, *Int. Journal of Modern Phys. C*. **27** (2016).

[31] F. Gonzales-Catoldo, G. Gutierrez and J.M. Yanez, Sliding down an arbitrary curve in the presence of friction, *American Journal of Physics*. **85** (2017), 108.

TIMELIKE SPHERICAL MAGNETIC CURVES IN THE DE-SITTER SPACE S_1^2

R.C.Demirkol[1], T.Körpınar[2], S.Baş[3]

[1]*Department of Mathematics, Faculty of Arts and Sciences, Mus Alparslan University, Mus, TURKEY*
[2]*Department of Mathematics, Faculty of Arts and Sciences, Mus Alparslan University, Mus, TURKEY*
[3]*Department of Mathematics, Faculty of Arts and Sciences, Mus Alparslan University, Mus, TURKEY*

E-mail: rcdemirkol@gmail.com

Abstract

We take the De-Sitter space S_1^2 and the transformation $\delta : I \rightarrow S_1^2 \subset R_1^3$. Considering their definition in terms of spherical geometry in the Minkowski space, we investigate the magnetic curves of the spherical vector field. An entire characterization is developed for timelike spherical magnetic curves, denoting particularly the changes of their energy with respect to time, the influence of the magnetic force on them, and the existence condition for the uniformity of these curves.

Keywords: De-Sitter space**,** magnetic field, timelike magnetic curve, energy, magnetic force, uniform motion.

1. INTRODUCTION

A classical model of magnetic fields is easily developed if one multiplies a scalar p (generally known as magnitude or strength) to the area form on a Riemannian surface (R, h). For instance, on a hyperbolic plane H^2, magnetic trajectories are either open curves or closed curves, on the Euclidean plane magnetic trajectories are circles, and on the sphere, they are tiny circles having a particular radius $[1-3]$.

In this construction, one can observe some exclusive behaviors in the three-dimensional case due to the fact that the volume form dv_h and the Hodge star operator of the manifold identify a $(1-1)$ correspondence between divergence-free vector fields and closed 2-forms. In three-dimensional pseudo-Riemannian manifold, this leads to describe the special class of Killing magnetic curves and Killing magnetic fields $[4,5]$. Also some curves and surfaces with energy studied in [6-29].

In this manuscript, we take the De-Sitter space S_1^2 and the transformation $\delta: \mathsf{I} \to \mathsf{S}_1^2 \subset \mathsf{R}_1^3$. Even though the selection of the spherical frame is basically owing to its geometrical understanding, it may be seen that features of the worldline of the particle frequently emerge in physics. Considering the definition of S_1^2 and δ in terms of pseudo-orthonormal frame, we investigate the magnetic curves of spherical vector field. An entire characterization is determined for its timelike magnetic curves. Moreover, we also obtain some physical properties of timelike magnetic curves lying on the S_1^2. We also analyze the necessary and sufficient conditions of the uniformity of the timelike magnetic curves lying on the S_1^2.

2. MATERIAL AND METHODS

Magnetic Curves

The trajectories of a charged particle moving under the influence of a magnetic field on any manifold are represented by a magnetic curve. A magnetic field on a k-dimensional semi-Riemannian manifold (R, h) is any closed 2-form G. The Lorentz force of the magnetic field G is an antisymmetric one-to-one tensor field Ψ such that it is defined by

$$h(\Psi(\mathsf{A}), \mathsf{B}) = \mathsf{G}(\mathsf{A}, \mathsf{B}), \text{where} \forall \mathsf{A}, \mathsf{B} \in \mathsf{X}(\mathsf{R}).$$

The magnetic trajectories of the magnetic field G correspond to magnetic curves δ on R. These curves satisfy the following Lorentz formula

$$\nabla_{\delta'} \delta' = \Psi(\delta').$$

Evidently, magnetic curves generalize geodesics due to the following equation, which is satisfied by geodesics.

$$\nabla_{\delta'} \delta' = 0.$$

This formula obviously represents the Lorentz formula in the nonappearance of the magnetic field. Consequently, a geodesic corresponds to a trajectory of the moving charged particle when it is free from the magnetic field $(\mathsf{G} = 0)$.

A significant feature of magnetic curves is that they have a constant kinetic energy since their speed is a constant. This is an obvious result of the antisymmetric propertiy of the Lorentz force.

In the case of a $3D$ pseudo-Riemannian manifold (R, h), vector fields and 2-forms may be described thanks to the volume form dv_h and the Hodge star operator $\mathring{a}$ of the manifold. Hence, divergence free vector fields and magnetic fields are in $(1-1)$ correspondence. Therefore, Lorentz formula is given for any vector field S on the $3D$ pseudo-Riemannian manifold as follows.

$$\Psi(\mathsf{A}) = \mathsf{G} \times \mathsf{A},$$

where G is a magnetic field such that $\forall \mathsf{A} \in \mathsf{X}(\mathsf{R})$ with $div(\mathsf{G}) = 0$. As a consequence, the magnetic flow reduced by the Lorentz formula is written as the following form.

$$\nabla_{\delta^{'}} \delta^{'} = \mathsf{G} \times \delta^{'}.$$

The Geometry of the De-Sitter Space S_1^2

Let $\delta : I \to \mathsf{S}_1^2$ be a unit speed timelike regular spherical curve, that is it is an arc-length parametrized and sufficiently smooth. Then Sabban frame is defined along the curve δ as follows.

$$\begin{aligned} \nabla_{\delta^{'}} \delta &= \mathbf{T}, \\ \nabla_{\delta^{'}} \mathbf{T} &= \delta + \mu \mathbf{N}, \\ \nabla_{\delta^{'}} \mathbf{N} &= \mu \mathbf{T}, \end{aligned}$$

where ∇ is a Levi-Civita connection and $\mu = \det(\delta, \mathbf{T}, \mathbf{T}^{'})$ is the geodesic curvature of δ. The following identities including pseudo vector product also hold $[10]$.

$$\delta = \mathbf{T} \times \mathbf{N}, \quad \mathbf{T} = \delta \times \mathbf{N}, \quad \mathbf{N} = \delta \times \mathbf{T}.$$

3. RESULTS AND DISCUSSION

Definition 1. Let $\delta : I \to \mathsf{S}_1^2$ *be a unit speed regular timelike spherical curve on the De-Sitter 2-space and* G *be the magnetic field on* S_1^2. *Timelike spherical magnetic curves of* β *are defined via the Lorentz force formula given by Eqs.* $(1-3)$ *as follows.*

$$\nabla_{\delta} \delta = \Psi(\delta) = \mathsf{G} \times \delta,$$
$$\nabla_{\delta} \mathbf{T} = \Psi(\mathbf{T}) = \mathsf{G} \times \mathbf{T},$$
$$\nabla_{\delta} \mathbf{N} = \Psi(\mathbf{N}) = \mathsf{G} \times \mathbf{N}.$$

For further references, we call these timelike spherical magnetic curves as a $\mathbf{S}\delta-$ *magnetic curve,* $\mathbf{ST}-$ *magnetic curve, and* $\mathbf{SN}-$ *magnetic curve, respectively. In other words,* δ *is called as an* $\mathbf{S}\delta-$ *magnetic curve if the first equation holds;* δ *is called as an* $\mathbf{ST}-$ *magnetic curve if the second equation holds;* δ *is called as an* $\mathbf{SN}-$ *magnetic curve if the third equation holds.*

Proposition 2. *Let* δ *be an arc-length parametrized timelike spherical magnetic curve together with the Sabban frame elements* $\{\delta, \mathbf{T}, \mathbf{N}, \mu\}$ *on the* De-Sitter space S_1^2. *Then, Lorentz force* Ψ *of the magnetic field* G *is written in the Sabban frame as follows.*

♦ *In the case of an* $\mathbf{S}\delta-$ *magnetic curve,* Ψ *is defined by*

$$\Psi(\delta) = \mathbf{T},$$
$$\Psi(\mathbf{T}) = \delta + c_1 \mathbf{N},$$
$$\Psi(\mathbf{N}) = c_1 \mathbf{T},$$

where c_1 *is an arbitrary smooth function along with the magnetic curve such that it satisfies* $c_1 = h(\Psi(\mathbf{T}), \mathbf{N})$.

♦ *In the case of an* $\mathbf{ST}-$ *magnetic curve,* Ψ *is defined by*

$$\Psi(\mathbf{T}) = \delta + \mu \mathbf{N},$$
$$\Psi(\delta) = \mathbf{T} + c_2 \mathbf{N},$$
$$\Psi(\mathbf{N}) = -c_2 \delta + \mu \mathbf{T},$$

where c_2 *is an arbitrary smooth function along with the magnetic curve such that it satisfies* $c_2 = h(\Psi(\delta), \mathbf{N})$.

♦ *In the case of an* $\mathbf{SN}-$ *magnetic curve,* Ψ *is defined by*

$$\Psi(\mathbf{N}) = \mu \mathbf{T}$$
$$\Psi(\delta) = c_3 \mathbf{T},$$
$$\Psi(\mathbf{T}) = c_3 \delta + \mu \mathbf{N}.$$

where c_3 *is an arbitrary smooth function along with the magnetic curve such that it satisfies* $c_3 = h(\Psi(\mathbf{T}), \delta)$.

Proof. Let δ *be an arc-length parametrized* $\mathbf{S}\delta$ *- magnetic curve* on the De-Sitter 2-space S_1^2. It is evidently true from the definition of the Sabban frame and Lorentz equation given in Eqs. $(4,5)$ that $\Psi(\delta) = \mathbf{T}.$ It is also canonically true that

$$\Psi(\mathbf{T}) = \eta_1 \delta + \eta_2 \mathbf{T} + \eta_3 \mathbf{N},$$

since $\Psi(\mathbf{T}) \in span\{\delta, \mathbf{T}, \mathbf{N}\}$. If one uses the features of anti-symmetry of the Lorentz force and consider the metric defined on the $\mathbb{S}_1^2$, one reaches that

$$\eta_1 = 1, \eta_2 = 0, \eta_3 = c_1,$$

where c_1 is an arbitrary smooth function along with the magnetic curve such that it satisfies $c_1 = h(\Psi(\mathbf{T}), \mathbf{N})$. By using a similar argument it is also obtained that $\Psi(\mathbf{N}) = c_1 \mathbf{T}$. This finalizes the proof for the case of $\mathbf{S}\delta - magnetic\ curves$. The rest of the proof is completed if one follows similar steps for other cases.

Theorem 3. *Let δ be an arc-length parametrized timelike spherical magnetic curve on the* De-Sitter space $\mathbb{S}_1^2$.

♦ δ *is an* $\mathbf{S}\delta$ *- magnetic curve of the magnetic field* $\mathbf{G}$ *on the* $\mathbb{S}_1^2$ *if and only if*

$$\mathbf{G} = c_1 \delta - \mathbf{N}$$

where $c_1 = h(\Psi(\mathbf{T}), \mathbf{N})$ along with the curve.

♦ δ *is an* $\mathbf{ST}$*- magnetic curve of the magnetic field* $\mathbf{G}$ *on the* $\mathbb{S}_1^2$ *if and only if*

$$\mathbf{G} = \mu\delta - c_2 \mathbf{T} - \mathbf{N}$$

where $c_2 = h(\Psi(\delta), \mathbf{N})$ along with the curve.

♦ δ *is an* $\mathbf{SN}$*- magnetic curve of the magnetic field* $\mathbf{G}$ *on the* $\mathbb{S}_1^2$ *if and only if*

$$\mathbf{G} = \mu\delta - c_3 \mathbf{N}$$

where $c_3 = h(\Psi(\mathbf{T}), \delta)$ along with the curve.

Proof. Let δ be an $\mathbf{S}\delta$ *- magnetic curve* of the magnetic field $\mathbf{G}$ on the $\mathbb{S}_1^2$. Let us choose $\mathbf{G} = a_0\delta + a_1\mathbf{T} + a_2\mathbf{N}$, where a_i, $i = 0,1,2$ are some smooth functions along with the curve δ. We also suppose that $\mathbf{B}$ does not vanish along with the curve. Now, from the definition of the $\mathbf{S}\delta$ *- magnetic curve*, one has

$$\nabla_{\delta'}\delta = \mathbf{G} \times \delta = (a_0\delta + a_1\mathbf{T} + a_2\mathbf{N}) \times \delta.$$

We already computed that $\Psi(\delta) = \mathbf{T}$. Hence, we obtain that $a_1 = 0$ and $a_2 = -1$ by using the basic properties of the vector product and the given equality $\Psi(\delta) = \nabla_{\delta'}\delta$. Also, from the definition of the Lorentz force Ψ, one knows that $\Psi(\mathbf{G}) = \mathbf{G} \times \mathbf{G} = 0$. Thus, one should have

$$0 = a_0\Psi(\delta) + a_1\Psi(\mathbf{T}) + a_2\Psi(\mathbf{N}).$$

If one plugs each Lorentz force computed in the above equality, then it is computed that $a_0 = c_1$.

Conversely, if we suppose that $\mathbf{G} = c_1\delta - \mathbf{N}$ and $c_1 = h(\Psi(\mathbf{T}), \mathbf{N})$, then we can easily observe that $\mathbf{G} \times \delta = \Psi(\mathbf{G}) = \nabla_{\delta'}\delta$. This fact obviously implies that the curve δ is an $\mathbf{ST}$*- magnetic curve* of the magnetic field $\mathbf{G}$ on the $\mathbb{S}_1^2$. The rest of the proof is completed if one follows similar steps for other cases.

4. CONCLUSION

The De-Sitter space is a famous and proper model in mathematical physics, and it has been investigating under a comprehensive range of distinct perspective. In mathematical point of view, De-Sitter space is identified to be the semi-Riemannian sphere in Minkowski spacetime with a positive curvature.

In this work, we investigate the magnetic curves of the spherical vector field. An entire characterization is developed for timelike spherical magnetic curves, denoting particularly the changes of their energy with respect to time, the influence of the magnetic force on them, and the existence condition for the uniformity of these curves.

REFERENCES

[1] M. Barros, J. L. Cabrerizo, M. Fernandez and A. Romero, Magnetic vortex filament flows, J. Math. Phys. 48 (2007) 082904.

[2] T. Sunada, Magnetic flows on a Riemann surface. Proceedings of KAIST Mathematics Workshop, (1993) 93.

[3] A. Comtet, On the Landau Hall levels on the hyperbolic plane, Ann. Phys. 173 (1987) 185.

[4] SL. Druta-Romaniuc, M.I. Munteanu, Magnetic Curves corresponding to Killing magnetic fields in E^3, J. Math. Phys. 52 (2011) 1.

[5] SL. Druta-Romaniuc, M.I. Munteanu, Killing magnetic curves in a Minkowski 3-space, Nonlinear Anal.: Real Word Application 14 (2013) 383.

[6] T. Körpinar, R.C. Demirkol, V. Asil, The motion of a relativistic charged particle in a homogeneous electromagnetic field in De-Sitter space, Revista Mexicana de Fisica 64 (2018) 176.

[7] T. Körpinar, R.C. Demirkol, Energy on a timelike particle in dynamical and electrodynamical force fields in De-Sitter space Revista Mexicana de Fisica 63 (2017) 560.

[8] J.J. Koenderink, Solid shape. MIT Press, Cambridge (1990).

[9] S. Izumiya, T. Nagai, Generalized Sabban curves in the Euclidean n-sphere and spherical duality. Results in Mathematics 72 (2017) 401.

[10] V. Asil, T. Körpinar, S. Bas, Inextensible flows of timelike curves with Sabban frame in S_1^2, Siauliai Mathematical Seminar 7 (2012) 5.

[11] G. Calvaruso, I. Munteanu, Hopf magnetic curves in the anti-de Sitter space H_1^3, J. of Nonlinear Mathematical Physics 25 (2018) 462.

[12] C.M. Wood, On the Energy of a Unit Vector Field, Geom. Dedic. 64 (1997) 319.

[13] J. Guven, D.M. Valencia, J. Vazquez-Montejo, Environmental bias and elastic curves on surfaces, Phys. A: Math. Theory 47 (2014) 355201.

[14] W. Rindler, Lenght contraction paradox, Am. J. Phys. 24 (1961) 365.

[15] W. Rindler, Hyperbolic motion in curved space time, Phys. Rev. 119 (1961) 2082.

[16] Y. Friedman, T. Scarr, Making the relativistic dynamics equation covariant:explicit solutions for motion under a constant force, Phys. Scr. 86 (2012) 065008.

[17] Y. Friedman, T. Scarr, Uniform acceleration in general relativity, General Relativity and Gravitation 47 (2015) 121.

[18] D. de la Fuente, A. Romero, Uniformly accelerated motion in General Relativity: Completeness of inextensible trajectories, General Relativity and Gravitation. 47(4), (2015), 33.

[19] D. de la Fuente, A. Romero, P.J. Torres, Unchanged direction motion in general relativity: the problems of prescribing acceleration and the extensibility of trajectories, Journal of Math. Phys. (2015) 56, 112501.

[20] D. de la Fuente, A. Romero, P.J. Torres, Uniform circular motion in general relativity: existence and extendibility of the trajectories, Classical and Quantum Gravity. 34 (2017) 125016.

[21] R.K. Sachs, H. Wu, General Relativity for Mathematicians. Grad. Tets in Math., vol. 48. Springer, New York, (1977).

[22] T Körpinar, RC Demirkol, Magnetic motion of spherical frictional charged particles on the unit sphere, Revista Mexicana de Fsica 65 (2019), 496-502

[23] T Körpinar, RC Demirkol, Z Körpinar, Soliton propagation of electromagnetic field vectors of polarized light ray traveling in a coiled optical fiber in Minkowski space with Bishop equations, The European Physical Journal D 73 (9) (2019), 203

[24] T Körpinar, RC Demirkol, On the uniform motion of a relativistic charged particle in a homogeneous electromagnetic field in Minkowski space E_2^4, Mathematical Methods in the Applied Sciences, 42 (9) (2019), 3069-3087

[25] T Körpinar, RC Demirkol, Electromagnetic curves of the linearly polarized light wave along an optical fiber in a 3D semi-Riemannian manifold, Journal of Modern Optics 66 (8) (2019), 857-867

[26] T. Körpinar, On the Fermi-Walker Derivative for Inextensible Flows, Zeitschrift für Naturforschung A. 70 (7) (2015), 477-482

[27] Z. S. Körpinar, M. Tuz, T. Körpinar, New Electromagnetic Fluids Inextensible Flows of Spacelike Particles and some Wave Solutions in Minkowski Space-time, Int J Theor Phys 55 (1) (2016), 8-16.

[28] T. Körpinar, Y. Ünlütürk, New Bianchi type-I cosmological models for biharmonic particles using string cosmology with exponential law, Gen. Relativity Gravitation 47(11) (2015), 138

[29] M. Babaarslan, Y. Yayli, Timelike constant slope surfaces and spacelike Bertrand curves in Minkowski 3-space, Proceedingss of the National Academy of Sciencesi India Section A: Physical Sciences 84 (2014) 535.

INEXTENSIBLE FLOWS OF PSEUDO NULL CURVES DUE TO THE BISHOP FRAME IN MINKOWSKI 3-SPACE

Yasin Ünlütürk[1] , *Talat Körpınar*[2]

[1] *Department of Mathematics, Faculty of Art and Science, Kırklareli University, Kırklareli, TURKEY*
[2] *Department of Mathematics, Faculty of Art and Science, Muş Alparslan University, Muş, TURKEY*

E-mail: *yasinunluturk@klu.edu.tr, tkorpinar@alparslan.edu.tr*

 Abstract

In this work, we study inextensible flows of pseudo null curves according to the Bishop frame in Minkowski 3-space. We present some necessary and sufficient conditions as a partial differential equation involving the curvatures for inextensible flows of pseudo null curves according to the Bishop frame in E_1^3.

 AMS Subject Classification: 53A04.

 Keywords: Inextensible flow, Pseudo null curve, Bishop frame, Minkowski 3-space.

1. INTRODUCTION

Inextensible flows of curve and surface give rise to motions in which no strain energy is induced from the point of view of physics. The swinging motion of a cord of fixed length, for example, or of a piece of paper carried by the wind, can be described by inextensible curve and surface flows. Such motions arise quite naturally in a wide range of physical applications. For example, both Chirikjian and Burdick [4] and Mochiyama et al. [16] studied the shape control of hyper-redundant, or snake-like, robots. Inextensible curve and surface flows also arise in the context of many problems in computer vision [9] and [15] and computer animation [5], and even structural mechanics [19].

The time evolution of a curve or surface is generated by its corresponding flow in E^3. For this reason we shall also refer to curve and surface evolutions as flows throughout this article. Flow is said to be inextensible if, in the former case, its arclength is preserved, and in the latter case, if its intrinsic curvature is preserved.

Kwon et al. investigated inextensible flows of curves and developable surfaces in E^3 [14]. Necessary and sufficient conditions for an inextensible curve to be flow first were expressed as a partial differential equation involving the curvature and torsion [14]. Then, they derived the corresponding equations for the inextensible flow of a developable surface, and showed that it suffices to describe its evolution in terms of two inextensible curve flows [14]. Inextensible flows have been studied as handled intensively with many different aspects by Körp nar, (see, [10], [11], [12], [13]) In addition, many researchers have studied on inextensible flows such as [1], [2], [6], [8] and [21].

The behaviour of curves are generally studied by making use of Frenet-Serret frame. But there are some alternative frames to Frenet-Serret frame such as Bishop frame (parallel transport frame), Sabban frame, etc. In [3], Bishop defined an alternative over Frenet frame for a curve and called it Bishop frame. The advantage of Bishop frame is well-defined when the curve has a vanishing second derivative in 3-dimensional Euclidean space E^3 unlike Frenet frame. Also, Bishop frame is used in many applications such as engineering, computer aided design, DNA analysis etc. By means of this alternative frame, there are many studies about theory of curves and surfaces, for some of them, see ([7], [8]).

In this work, we study inextensible flows of pseudo null curves according to the Bishop frame in Minkowski 3-space . We present some necessary and sufficient conditions as a partial differential equation involving the curvatures for inextensible flows of pseudo null curves according to the Bishop frame in E_1^3.

2. PRELIMINARIES

The three dimensional Minkowski space E_1^3 is a real vector space R^3 endowed with the standard indefinite flat metric $\langle .,. \rangle$ defined by

$$\langle , \rangle = -x_1 y_1 + x_2 y_2 + x_3 y_3, \tag{2.1}$$

where $x = (x_1, x_2, x_3)$ and $y = (y_1, y_2, y_3)$ are any two vectors in E_1^3. Since this metric is an indefinite metric. an arbitrary vector $x \in E_1^3$ has one of three Lorentzian characters: it is a spacelike vector if $\langle x, x \rangle > 0$ or $x = 0$; timelike $\langle x, x \rangle < 0$ and null (lightlike) $\langle x, x \rangle = 0$ for $x \neq 0$. The pseudo-norm of an arbitrary vector $x \in E_1^3$ is given by $\|x\| = \sqrt{|\langle x, x \rangle|}$. Similarly, an arbitrary curve $\gamma = \gamma(s)$ in E_1^3 can locally be spacelike, timelike or null (lightlike) if its velocity vector γ' are, respectively, spacelike, timelike or null (lightlike), for every $s \in I \subset E$. The curve $\gamma = \gamma(s)$ is called a unit speed curve if its velocity vector γ' is unit one i.e., $\|\gamma'\| = 1$ [17].

A spacelike curve $\gamma : I \to E_1^3$ is called a pseudo null curve, if its principal normal vector field N and binormal vector field B are null vector fields satisfying the condition $\langle N, B \rangle = 1$. The Frenet formulae of a non-geodesic pseudo null curve $\gamma = \gamma(s)$ have the form

$$\begin{bmatrix} T' \\ N' \\ B' \end{bmatrix} = \begin{bmatrix} 0 & \kappa & 0 \\ 0 & \tau & 0 \\ -\kappa & 0 & -\tau \end{bmatrix} \begin{bmatrix} T \\ N \\ B \end{bmatrix}, \tag{2.2}$$

where the first Cartan curvature $\kappa(s) = 1$ and the second Cartan curvature (torsion) $\tau(s)$ is an arbitrary function of arclength parameter s of γ [20]. Also the vector fields of Frenet frame holds the following relations:

$$\langle T, T \rangle = 1, \langle N, N \rangle = \langle B, B \rangle = 0, \langle T, N \rangle = \langle T, B \rangle = 0, \langle N, B \rangle = 1,$$

and

$$T \times N = N, \quad N \times B = T, \quad B \times T = B.$$

The Cartan frame $\{T, N, B\}$ is positively oriented, if $\det(T, N, B) = [T, N, B] = 1$.

Definition 2.1. The Bishop frame $\{T_1, N_1, N_2\}$ of a pseudo null curve γ in E_1^3 is positively oriented pseudo-orthonormal frame consisting of the tangential vector field T_1 and two relatively parallel lightlike normal

vector fields N_1 and N_2 [7].

The vector fields of The Bishop frame of a pseudo null curve γ in E_1^3 satisfy the relations (see [7])

$$\langle T_1, T_1 \rangle = 1, \langle N_2, N_2 \rangle = \langle N_1, N_1 \rangle = 0, \langle T_1, N_1 \rangle = \langle T_1, N_2 \rangle = 0, \langle N_1, N_2 \rangle = 1, \tag{2.3}$$

and

$$T_1 \times N_1 = -T_1, \quad N_1 \times N_2 = -N_2, \quad N_2 \times T_1 = N_1. \tag{2.4}$$

Theorem 2.2. ([7]) Let γ be a pseudo null curve in E_1^3 parameterized by the arc-length s with the curvature $\kappa(s) = 1$ and the torsion $\tau(s)$:

(i) Then the Bishop frame $\{T_1, N_1, N_2\}$ and the Frenet frame $\{T, N, B\}$ of γ are related by:

$$\begin{bmatrix} T_1 \\ N_1 \\ N_2 \end{bmatrix} = \begin{bmatrix} 1 & 0 & 0 \\ 0 & \dfrac{1}{\kappa_2} & 0 \\ 0 & 0 & \kappa_2 \end{bmatrix} \begin{bmatrix} T \\ N \\ B \end{bmatrix}, \tag{2.5}$$

and the Frenet equations of γ according to the Bishop frame read

$$\begin{bmatrix} T_1' \\ N_1' \\ N_2' \end{bmatrix} = \begin{bmatrix} 0 & \kappa_2 & \kappa_1 \\ -\kappa_1 & 0 & 0 \\ -\kappa_2 & 0 & 0 \end{bmatrix} \begin{bmatrix} T_1 \\ N_1 \\ N_2 \end{bmatrix}, \tag{2.6}$$

where $\kappa_1(s) = 0$ and $\kappa_2(s) = c_0 e^{\int \tau(s)ds}, c_0 \in P_0^+$;

(ii) Then the Bishop frame $\{T_1, N_1, N_2\}$ and the Frenet frame $\{T, N, B\}$ of γ are related by:

$$\begin{bmatrix} T_1 \\ N_1 \\ N_2 \end{bmatrix} = \begin{bmatrix} -1 & 0 & 0 \\ 0 & 0 & -\kappa_1 \\ 0 & -\dfrac{1}{\kappa_1} & 0 \end{bmatrix} \begin{bmatrix} T \\ N \\ B \end{bmatrix}, \tag{2.7}$$

and the Frenet equations of γ according to the Bishop frame read

$$\begin{bmatrix} T_1' \\ N_1' \\ N_2' \end{bmatrix} = \begin{bmatrix} 0 & \kappa_2 & \kappa_1 \\ -\kappa_1 & 0 & 0 \\ -\kappa_2 & 0 & 0 \end{bmatrix} \begin{bmatrix} T_1 \\ N_1 \\ N_2 \end{bmatrix}, \tag{2.8}$$

where $\kappa_1(s) = c_0 e^{\int \tau(s)ds}, c_0 \in P_0^-$ and $\kappa_2(s) = 0$.

3. INEXTENSIBLE FLOWS OF PSEUDO NULL CURVES DUE TO THE BISHOP FRAME IN MINKOWSKI 3-SPACE E_1^3

Given that $\gamma : [0,l] \times 0, \omega] \rightarrow E_1^3$ is a one parameter family of smooth pseudo null curves due to the Bishop frame in Minkowski 3-space E_1^3, where l is arclength of the initial curve. Let u be the curve parametrization variable, $0 \le u \le 1$. The arclength of γ is given by $s(u) = \int_0^u \left\| \frac{\partial \gamma}{\partial t} \right\| du.$

The operator $\frac{\partial}{\partial s}$ is given in terms of u by $\frac{\partial}{\partial s} = \frac{1}{v} \frac{\partial}{\partial u}$, where $v = \left\| \frac{\partial \gamma}{\partial t} \right\|$. The arclength parameter is $ds = v \, du$.

Definition 3.1. Let γ be a pseudo null curve with the Bishop frame $\{T_1, N_1, N_2\}$ in Minkowski 3-space E_1^3. Any flow of the pseudo null curves can be given as follows

$$\frac{\partial \gamma}{\partial t} = \alpha_1 T_1 + \alpha_2 N_1 + \alpha_3 N_2, \tag{3.1}$$

where α_i $(1 \le i \le 3)$ is a smooth function.

Let the arclength parameter be $s(u,t) = \int_0^u v \, du$. Pseudo null curves are not subjected to any elongation or compression can be expressed by the condition $\frac{\partial}{\partial t} s(u,t) = \int_0^u \frac{\partial v}{\partial t} du = 0$, where $u \in [0,l]$.

Definition 3.2. Let γ be a pseudo null curve with the Bishop frame $\{T_1, N_1, N_2\}$ in Minkowski 3-space E_1^3. A pseudo null curve evolution $\gamma(u,t)$ and its flows $\frac{\partial \gamma}{\partial t}$ are said to be inextensible if

$$\frac{\partial}{\partial t} \left\| \frac{\partial \gamma}{\partial u} \right\| = 0. \tag{3.2}$$

3.1. INEXTENSIBLE FLOWS OF PSEUDO NULL CURVES WITH $\kappa_1(s) = 0$ DUE TO THE BISHOP FRAME

In this section, we study inextensible flows of pseudo null curves with $\kappa_1(s) = 0$ in E_1^3.

Lemma 3.3. Let $\frac{\partial \gamma}{\partial t} = \alpha_1 T_1 + \alpha_2 N_1 + \alpha_3 N_2$ be a smooth flow of a pseudo null curve with $\kappa_1(s) = 0$ in E_1^3. If the flow is inextensible, then

$$\frac{\partial v}{\partial t} = \frac{\partial \alpha_1}{\partial u} - \alpha_3 \kappa_2 v. \qquad (3.3)$$

Proof. Given that $\frac{\partial \gamma}{\partial t}$ is a smooth flow of pseudo null curve γ with $\kappa_1(s) = 0$ in E_1^3. By using the definition of γ, we have

$$v^2 = \left\langle \frac{\partial v}{\partial u}, \frac{\partial v}{\partial u} \right\rangle. \qquad (3.4)$$

Differentiating (3.4) with respect to t gives

$$v \frac{\partial v}{\partial t} = \left\langle \frac{\partial \gamma}{\partial u}, \frac{\partial}{\partial u}\left(\frac{\partial \gamma}{\partial t} \right) \right\rangle. \qquad (3.5)$$

Substituting (3.1) into (3.5), we obtain

$$v \frac{\partial v}{\partial t} = \left\langle \frac{\partial \gamma}{\partial u}, \frac{\partial}{\partial u}\left(\alpha_1 T_1 + \alpha_2 N_1 + \alpha_3 N_2 \right) \right\rangle \qquad (3.6)$$

which implies that

$$\frac{\partial v}{\partial t} = \left\langle T_1, \left(\frac{\partial \alpha_1}{\partial u} - \alpha_3 \kappa_2 v \right) T_1 + \left(\alpha_1 \kappa_2 v + \frac{\partial \alpha_2}{\partial u} \right) N_1 + \frac{\partial \alpha_3}{\partial u} N_2 \right\rangle. \qquad (3.7)$$

By (3.7), we have

$$\frac{\partial v}{\partial t} = \frac{\partial \alpha_1}{\partial u} - \alpha_3 \kappa_2 v \qquad (3.8)$$

which completes the proof.

Theorem 3.4. Let $\frac{\partial \gamma}{\partial t} = \alpha_1 T_1 + \alpha_2 N_1 + \alpha_3 N_2$ be a smooth flow of a pseudo null curve with $\kappa_1(s) = 0$ in E_1^3. Then the flow is inextensible if and only if

$$\frac{\partial \alpha_1}{\partial u} = \alpha_3 \kappa_2 v. \qquad (3.9)$$

Proof. Let $\frac{\partial \gamma}{\partial t}$ be inextensible. From (3.2), we have

$$\frac{\partial}{\partial t} s(u,t) = \int_0^u \frac{\partial v}{\partial t} du = 0.$$

Substituting (3.3) in (3.11), we find $\frac{\partial \alpha_1}{\partial u} = \alpha_3 \kappa_2 v.$

We now restrict ourselves to arc length parametrized curves. That is, $v = 1$ and the local coordinate u

corresponds to the curve arclength s. Then, we have the following lemma.

Lemma 3.5. Let $\dfrac{\partial \gamma}{\partial t} = \alpha_1 T_1 + \alpha_2 N_1 + \alpha_3 N_2$ be a smooth flow of a pseudo null curve with $\kappa_1(s) = 0$ in E_1^3.

Then we have the following

$$\frac{\partial T_1}{\partial t} = \left(\frac{\partial \alpha_1}{\partial s} - \alpha_3 \kappa_2 \right) T_1 + \left(\alpha_1 \kappa_2 + \frac{\partial \alpha_2}{\partial s} \right) N_1 + \frac{\partial \alpha_3}{\partial s} N_2,$$

$$\frac{\partial N_1}{\partial t} = -\frac{\partial \alpha_3}{\partial s} T_1 + \psi N_1,$$

$$\frac{\partial N_2}{\partial t} = \left(-\alpha_1 \kappa_2 - \frac{\partial \alpha_2}{\partial s} \right) T_1 - \psi N_2,$$

where $\psi = \left\langle \dfrac{\partial N_1}{\partial t}, N_2 \right\rangle$.

Proof. Let $\dfrac{\partial \gamma}{\partial t} = \alpha_1 T_1 + \alpha_2 N_1 + \alpha_3 N_2$ be a smooth flow of a pseudo null curve with $\kappa_1(s) = 0$ in E_1^3. Then

$$\frac{\partial T_1}{\partial t} = \frac{\partial}{\partial t} \frac{\partial \gamma}{\partial s} = \frac{\partial}{\partial s} \frac{\partial \gamma}{\partial t} = \frac{\partial}{\partial s} \left(\alpha_1 T_1 + \alpha_2 N_1 + \alpha_3 N_2 \right) \qquad (3.10)$$

which results

$$\frac{\partial T_1}{\partial t} = \left(\frac{\partial \alpha_1}{\partial s} - \alpha_3 \kappa_2 \right) T_1 + \left(\alpha_1 \kappa_2 + \frac{\partial \alpha_2}{\partial s} \right) N_1 + \frac{\partial \alpha_3}{\partial s} N_2. \qquad (3.11)$$

From (3.11), we obtain

$$0 = \frac{\partial}{\partial t} \langle T_1, N_1 \rangle = \left\langle \frac{\partial T_1}{\partial t}, N_1 \right\rangle + \left\langle T_1, \frac{\partial N_1}{\partial t} \right\rangle = \frac{\partial \alpha_3}{\partial s} + \left\langle T_1, \frac{\partial N_1}{\partial t} \right\rangle,$$

$$0 = \frac{\partial}{\partial t} \langle T_1, N_2 \rangle = \left\langle \frac{\partial T_1}{\partial t}, N_2 \right\rangle + \left\langle T_1, \frac{\partial N_2}{\partial t} \right\rangle = \alpha_1 \kappa_2 + \frac{\partial \alpha_2}{\partial s} + \left\langle T_1, \frac{\partial N_2}{\partial t} \right\rangle,$$

$$0 = \frac{\partial}{\partial t} \langle N_1, N_2 \rangle = \left\langle \frac{\partial N_1}{\partial t}, N_2 \right\rangle + \left\langle N_1, \frac{\partial N_2}{\partial t} \right\rangle = \psi + \left\langle N_1, \frac{\partial N_2}{\partial t} \right\rangle$$

which involves

$$\frac{\partial N_1}{\partial t} = -\frac{\partial \alpha_3}{\partial s} T_1 + \psi N_1,$$

$$\frac{\partial N_2}{\partial t} = \left(-\alpha_1 \kappa_2 - \frac{\partial \alpha_2}{\partial s}\right) T_1 - \psi N_2,$$

where $\psi = \left\langle \dfrac{\partial N_1}{\partial t}, N_2 \right\rangle$. This completes the proof.

Theorem 3.6. Let $\dfrac{\partial \gamma}{\partial t} = \alpha_1 T_1 + \alpha_2 N_1 + \alpha_3 N_2$ be a smooth flow of a pseudo null curve with $\kappa_1(s) = 0$ in E_1^3.

Then the following partial differential equations hold:

$$\frac{\partial \kappa_2}{\partial t} + \kappa_2 \psi = \kappa_2 \frac{\partial \alpha_1}{\partial s} - \alpha_3 \kappa_2^2 + \frac{\partial}{\partial s}(\alpha_1 \kappa_2) + \frac{\partial^2 \alpha_2}{\partial s^2},$$

$$\frac{\partial^2 \alpha_1}{\partial s^2} - \frac{\partial}{\partial s}(\alpha_3 \kappa_2) = 0, \tag{3.12}$$

$$\frac{\partial^2 \alpha_3}{\partial s^2} = 0.$$

Proof. From Lemma 3.5, we have

$$\frac{\partial}{\partial s}\frac{\partial T_1}{\partial t} = (\frac{\partial^2 \alpha_1}{\partial s^2} - \frac{\partial}{\partial s}(\alpha_3 \kappa_2) - \kappa_2 \frac{\partial \alpha_3}{\partial s})T_1 + (\kappa_2 \frac{\partial \alpha_1}{\partial s} - \alpha_3 \kappa_2^2 + \frac{\partial}{\partial s}(\alpha_1 \kappa_2) + \frac{\partial^2 \alpha_2}{\partial s^2})N_1 + \frac{\partial^2 \alpha_3}{\partial s^2} N_2.$$

On the other hand,

$$\frac{\partial}{\partial t}\frac{\partial T_1}{\partial s} = \frac{\partial}{\partial t}(\kappa_2 N_1) = \frac{\partial \kappa_2}{\partial t} N_1 + \kappa_2 \frac{\partial N_1}{\partial t} = -\kappa_2 \frac{\partial \alpha_3}{\partial s} T_1 + (\frac{\partial \kappa_2}{\partial t} + \kappa_2 \psi)N_1.$$

From the equality of the Bishop vector fields in above equations, we get the results in (3.12).

Theorem 3.7. Let $\dfrac{\partial \gamma}{\partial t} = \alpha_1 T_1 + \alpha_2 N_1 + \alpha_3 N_2$ be a smooth flow of a pseudo null curve with $\kappa_1(s) = 0$ in E_1^3.

Then the following partial differential equations hold:

$$\frac{\partial \psi}{\partial s} - \kappa_2 \frac{\partial \alpha_3}{\partial s} = 0,$$

$$\frac{\partial^2 \alpha_3}{\partial s^2} = 0. \tag{3.13}$$

Proof. From Lemma 3.5, we have

$$\frac{\partial}{\partial s}\frac{\partial N_1}{\partial t} = -\frac{\partial^2 \alpha_3}{\partial s^2}T_1 + (\frac{\partial \psi}{\partial s} - \kappa_2 \frac{\partial \alpha_3}{\partial s})N_1$$

On the other hand,

$$\frac{\partial}{\partial t}\frac{\partial N_1}{\partial s} = \frac{\partial}{\partial t}(0) = 0.$$

From the equality of the Bishop vector fields in above equations, we get the results in (3.13).

Theorem 3.8. Let $\frac{\partial \gamma}{\partial t} = \alpha_1 T_1 + \alpha_2 N_1 + \alpha_3 N_2$ be a smooth flow of a pseudo null curve with $\kappa_1(s) = 0$ in E_1^3.

Then the following partial differential equations hold:

$$\alpha_3 \kappa_2^2 - \frac{\partial \kappa_2}{\partial t} = \kappa_2 \psi - \frac{\partial^2 \alpha_2}{\partial s^2} - \alpha_1 \frac{\partial \kappa_2}{\partial s},$$

$$\kappa_2 \frac{\partial \alpha_3}{\partial t} = \frac{\partial \psi}{\partial t}.$$

(3.14)

Proof. From Lemma 3.5, we have

$$\frac{\partial}{\partial s}\frac{\partial N_2}{\partial t} = (\kappa_2 \psi - \frac{\partial^2 \alpha_2}{\partial s^2} - \frac{\partial}{\partial s}(\alpha_1 \kappa_2))T_1 + (-\alpha_1 \kappa_2^2 - \kappa_2 \frac{\partial \alpha_2}{\partial s})N_1 - \frac{\partial \psi}{\partial s}N_2.$$

On the other hand,

$$\frac{\partial}{\partial t}\frac{\partial N_2}{\partial s} = \frac{\partial}{\partial t}(\kappa_2 T_1) = -\frac{\partial \kappa_2}{\partial t}T_1 - \kappa_2 \frac{\partial T_1}{\partial t} = (\alpha_3 \kappa_2^2 - \kappa_2 \frac{\partial \alpha_1}{\partial s} - \frac{\partial \kappa_2}{\partial t})T_1 + (-\alpha_1 \kappa_2^2 - \kappa_2 \frac{\partial \alpha_2}{\partial s})N_1 - \kappa_2 \frac{\partial \alpha_3}{\partial t}N_2$$

From the equality of the Bishop vector fields in above equations, we get the results in (3.14).

3.2. INEXTENSIBLE FLOWS OF PSEUDO NULL CURVES WITH $\kappa_2(s) = 0$ DUE TO THE

BISHOP FRAME

In this section, we give the results about inextensible flows of pseudo null curves with $\kappa_2(s) = 0$ in E_1^3.

Lemma 3.9. Let $\frac{\partial \gamma}{\partial t} = \alpha_1 T_1 + \alpha_2 N_1 + \alpha_3 N_2$ be a smooth flow of a pseudo null curve with $\kappa_2(s) = 0$ in E_1^3. If

the flow is inextensible, then $\frac{\partial v}{\partial t} = \frac{\partial \alpha_1}{\partial u} - \alpha_2 \kappa_1 v$.

Theorem 3.10. Let $\frac{\partial \gamma}{\partial t} = \alpha_1 T_1 + \alpha_2 N_1 + \alpha_3 N_2$ be a smooth flow of a pseudo null curve with $\kappa_2(s) = 0$ in E_1^3.

Then the flow is inextensible if and only if $\dfrac{\partial \alpha_1}{\partial u} = \alpha_2 \kappa_1 v.$

Lemma 3.11. Let $\dfrac{\partial \gamma}{\partial t} = \alpha_1 T_1 + \alpha_2 N_1 + \alpha_3 N_2$ be a smooth flow of a pseudo null curve with $\kappa_2(s) = 0$ in E_1^3.

Then we have the following

$$\frac{\partial T_1}{\partial t} = \left(\frac{\partial \alpha_1}{\partial s} - \alpha_2 \kappa_2 \right) T_1 + \frac{\partial \alpha_2}{\partial s} N_1 + \left(\alpha_1 \kappa_1 + \frac{\partial \alpha_3}{\partial s} \right) N_2,$$

$$\frac{\partial N_1}{\partial t} = \left(-\alpha_1 \kappa_1 - \frac{\partial \alpha_3}{\partial s} \right) T_1 + \psi N_1,$$

$$\frac{\partial N_2}{\partial t} = -\frac{\partial \alpha_2}{\partial s} T_1 - \psi N_2,$$

where $\psi = \left\langle \dfrac{\partial N_1}{\partial t}, N_2 \right\rangle.$

Theorem 3.12. Let $\dfrac{\partial \gamma}{\partial t} = \alpha_1 T_1 + \alpha_2 N_1 + \alpha_3 N_2$ be a smooth flow of a pseudo null curve with $\kappa_2(s) = 0$ in E_1^3.

Then the following partial differential equations hold:

$$\frac{\partial \kappa_1}{\partial t} - \kappa_1 \psi = \kappa_1 \frac{\partial \alpha_1}{\partial s} - \alpha_2 \kappa_1^2 + \frac{\partial}{\partial s}(\alpha_1 \kappa_1) + \frac{\partial^2 \alpha_3}{\partial s^2},$$

$$\frac{\partial^2 \alpha_1}{\partial s^2} - \frac{\partial}{\partial s}(\alpha_2 \kappa_1) = 0,$$

$$\frac{\partial^2 \alpha_2}{\partial s^2} = 0.$$

Theorem 3.13. Let $\dfrac{\partial \gamma}{\partial t} = \alpha_1 T_1 + \alpha_2 N_1 + \alpha_3 N_2$ be a smooth flow of a pseudo null curve with $\kappa_2(s) = 0$ in E_1^3.

Then the following partial differential equations hold:

$$\frac{\partial \kappa_1}{\partial t} - \alpha_2 \kappa_1^2 = \frac{\partial \kappa_1}{\partial s} \alpha_1 + \kappa_1 \psi + \frac{\partial^2 \alpha_3}{\partial s^2},$$

$$\frac{\partial \psi}{\partial s} + \kappa_1 \frac{\partial \alpha_2}{\partial s} = 0.$$

Theorem 3.14. Let $\dfrac{\partial \gamma}{\partial t} = \alpha_1 T_1 + \alpha_2 N_1 + \alpha_3 N_2$ be a smooth flow of a pseudo null curve with $\kappa_2(s) = 0$ in E_1^3.

Then the following partial differential equations hold:

$$\kappa_1 \frac{\partial \alpha_2}{\partial s} + \frac{\partial \psi}{\partial s} = 0,$$

$$\frac{\partial^2 \alpha_2}{\partial s^2} = 0.$$

REFERENCES

[1] Baş, S., Körpınar, T., Turhan, E., New type of inextensible flows of timelike curves in Minkowski space-time E_1^4, Advanced Modeling and Optimization, 14, 2, 359—368, 2012.

[2] Baş, S., Körpınar, T., Inextensible flows of spacelike curves on spacelike surfaces according to Darboux frame in M_1^3, Boletim da Sociedade Paranaense de Matematica, 31, 2, 9-17, 2013.

[3] Bishop, R.L., There is more than one way to frame a curve, American Mathematical Monthly, 82, 3, 246-251, 1975.

[4] Chirikjian, G., Burdick, J., A modal approach to hyper-redundant manipulator kinematics, IEEE Transactions on Robotics and Automation, 10, 343-354, 1994.

[5] Desbrun, M., Cani-Gascuel, M.P., Active implicit surface for animation, in: Proc. Graphics Interface-Canadian Inf. Process. Soc. 143-15, 1998.

[6] Ergüt, M., Turhan, E., Körpınar, T., Characterization of inextensible flows of spacelike curves with Sabban frame in S_1^2, Boletim da Sociedade Paranaense de Matematica, 31, 2, 47-53, 2013.

[7] Grbovic, M., Nesovic, E., On the Bishop frames of pseudo null and null Cartan curves in Minkowski 3-space, Journal of Mathematical Analysis and Applications, 461, 219-233, 2018.

[8] Grbovic, M., Nesovic, E., On generalized Bishop frame of null Cartan curve in Minkowski3-space, Kragujevac Journal of Mathematics, 43, 4, 559-573, 2019.

[9] Kass, M., Witkin, A., Terzopoulos, D., Snakes: active contour models. in: Proc. 1st Int. Conference on Computer Vision, 259-268, 1987.

[10] Körpınar, T., Asil, V., Baş, S., On characterization inextensible flows of curves according to Bishop frame in E^3, Revista Notas de Matematica, 7, 37-45, 2011.

[11] Körpınar, T., Turhan, E., Time evolution equations for surfaces generated via binormal spherical image in terms of inextensible flows in E^3, Journal of Dynamical Systems and Geometric Theories, 12, 2, 145-157, 2014.

[12] Körpınar, T., Turhan, E., Approximation for inextensible flows of curves in E^3, Boletim da Sociedade

Paranaense de Matematica, 32, 2, 45-54, 2014.

[13] Körpınar, T., Turhan, E., A new version of inextensible flows of spacelike curves with timelike B2 in Minkowski space-time E_1^4. Differential Equations and Dynamical Systems, 21, 3, 281-290, 2013.

[14] Kwon, D.Y., Park, F.C., Chi, D.P., Inextensible flows of curves and developable surfaces, Applied Mathematics Letters, 18, 1156-1162, 2005.

[15] Lu, H.Q., Todhunter, J.S., Sze, T.W., Congruence conditions for nonplanar developable surfaces and their application to surface recognition CVGIP. Image Underst. 56, 265-285, 1993.

[16] Mochiyama, H., Shimemura, E., Kobayashi, H., Shape control of manipulators with hyper degrees of freedom, International Journal of Robotics Research, 18, 584-600, 1999.

[17] O'Neill, B., Semi-Riemannian geometry with applications to relativity, New York: Academic Press 1983.

[18] Uçum, A., Erdem, H.A., İlarslan, K., Inextensible flows of partially null and pseudo null curves in semi-Euclidean 4-space with index 2, Novi Sad Journal of Mathematics, 46, 1, 115-129, 2016.

[19] Unger, D.J., Developable surfaces in elastoplastic fracture mechanics, International Journal of Fracture, 50, 33-38, 1991.

[20] Walrave, J., Curves and Surfaces in Minkowski Space, Ph.D. thesis, Leuven University, 1995.

[21] Yüzbaşı, Z.K., Bektaş, M., A note on inextensible flows of partially & pseudo null curves in E_1^4, Prespacetime Journal, 7, 5, 818-827, 2016.

SOME CHARACTERIZATIONS OF TYPE-3 NULL CARTAN SLANT HELICES DUE TO THE BISHOP FRAME IN MINKOWSKI SPACE TIME

Yasin Ünlütürk[1] , *Talat Körpınar*[2]

[1] *Department of Mathematics, Faculty of Art and Science, Kırklareli University, Kırklareli, TURKEY*
[2] *Department of Mathematics, Faculty of Art and Science, Muş Alparslan University, Muş, TURKEY*

E-mail: yasinunluturk@klu.edu.tr, tkorpinar@alparslan.edu.tr

Abstract

In this work, we extend null Cartan slant helix by using Bishop frame to Minkowski space-time. We define type-1 and type-3 null Cartan slant helices due to the Bishop frame in Minkowski space-time . Moreover, we present some characterizations of such curves.

AMS Subject Classification: 53A04.

Keywords: Bishop frame, Null Cartan slant helix, Type-1 slant helix, Type-3 slant helix.

1. INTRODUCTION

A. Einstein's theory opened a door of use of new geometries at the begining of the twentieth century. One of them, Minkowski space-time, which is simultaneously the geometry of special relativity and the geometry induced on each fixed tangent space of an arbitrary Lorentzian manifold, was introduced by the researchers.

In the case of a differentiable curve, at each point a tetrad of mutually orthogonal unit vectors (called tangent, normal, binormal and trinormal) was defined and constructed, and the rates of change of these vectors along the curve define the curvatures of the curve in the space E_1^4 [19]. Helices (inclined curves) are a well-known concept in classical differential geometry, see ([4], [10]). The notion of a slant helix is due to Izumiya and Takeuchi [10]. They defined that a curve $\varphi = \varphi(s)$ with non-vanishing first curvature is called a slant helix in E^3 if the principal lines of φ make a constant angle with a fixed directon.

In recent years, the theory of degenerate submanifolds are treated by the researchers and some of classical differential geometry topics are extented to Lorentz manifolds, see ([12], [13], [14], [15], [16]). For instance, K.L. Duggal and D. H. Jin [4] studied null curves and hypersurfaces of semi-Riemannian manifolds. And also, A. Ferrandez et al. [6] study null generalized helices in Lorentz-Minkowski space. In the light of degenerate submanifold theory, in [11], the authors define null slant helix and write some characterizations in E_1^3 and also prove that there does not exist a null slant helix in E_1^4. Moreover, some characterizations of the Cartan framed null generalized helix and also null slant helix having non-null axis in Lorentz-Minkowski space are given in [5]. Also there is nowadays a common research field called as $k-$ type slant helices in different spaces [1, 17, 18, 20].

The Bishop frames of null Cartan curves and pseudo null curves have been obtained, and some characterizations of slant helices according to this frame have been given in Minkowski spaces [7, 8, 9].

In this paper, our motivation is based on the work of Turgut and Yılmaz [21]. We define a special slant helix whose *Bishop vector field* N_1 lines make a constant angle with a fixed direction and call such curves "type-1 slant helices" and similarly, whose *Bishop vector field* N_3 lines make a constant angle with a fixed direction and call such curves "type-3 slant helices". Additionally, we present some characterizations of mentioned curves according to the Bishop frame of null Cartan curves given by Ilarslan [9] in the space E_1^4.

2. PRELIMINARIES

Minkowski space-time E_1^4 is the real vector space R^4 provided with the standard indefinite flat metric $\langle .,. \rangle$ given by

$$\langle x, y \rangle = -x_1 y_1 + x_2 y_2 + x_3 y_3 + x_4 y_4, \qquad (2.1)$$

for any two vectors $x = (x_1, x_2, x_3, x_4)$ and $y = (y_1, y_2, y_3, y_4)$ in E_1^4 [19].

Since $\langle .,. \rangle$ is an indefinite metric, recall that a vector $v \in E_1^4$ can have one of the three causal characters;

(i) spacelike if $\langle v, v \rangle > 0$ or $v = 0$;

(ii) timelike if $\langle v, v \rangle < 0$;

(iii) null (lightlike) if $\langle v, v \rangle = 0$ and $v \neq 0$. Similary, an arbitrary curve $\alpha = \alpha(s)$ in E_1^4 can be locally spacelike, timelike or null (lightlike), if all of its velocity vectors $\alpha'(s)$ are respectively spacelike, timelike or null [19].

The norm of a vector v is given by

$$\|v\| = \sqrt{|\langle v, v \rangle|}.$$

Therefore, v is a unit vector if $\langle v, v \rangle = \pm 1$. Next, vectors v, w in E_1^4 are said to be orthogonal if $\langle v, w \rangle = 0$. The velocity of the curve $\alpha(s)$ is given by $\|\alpha'(s)\|$. Let a and b be two spacelike vectors in E_1^4, then there is a unique real number $0 \leq \delta \leq \pi$, called the angle between a and b, such that $\langle a, b \rangle = \|a\|.\|b\| \cos \delta$. Let $\psi = \psi(s)$ be a curve in E_1^4. If the tangent vector field of this curve forms a constant angle with a constant vector field U, then this curve is called a general helix or an inclined curve [19].

A curve $\psi : I \rightarrow E_1^4$ is called a null curve, if its tangent vector $\psi' = T$ is a null vector. A null curve ψ is called a null Cartan curve, if it is parameterized by the pseudo-arc function s defined, ([2]) by

$$s(t) = \int_0^t \sqrt{\|\psi''(u)\|} \, du. \qquad (2.2)$$

The moving frame $\{T(s), N(s), B(s), E(s)\}$ along a non-geodesic null Cartan curve $\psi(s)$ is called the Cartan frame in the space E_1^4. The vectors T, N, B, E are called, respectively, the tangent, the principal normal, the

binormal, and the trinormal vector fields. The Cartan frame equations of the curve $\psi = \psi(s)$ are given as follows:

$$\begin{bmatrix} T' \\ N' \\ B' \\ E' \end{bmatrix} = \begin{bmatrix} 0 & \kappa_1 & 0 & 0 \\ -\kappa_2 & 0 & \kappa_1 & 0 \\ 0 & -\kappa_2 & 0 & \kappa_3 \\ \kappa_3 & 0 & 0 & 0 \end{bmatrix} \begin{bmatrix} T \\ N \\ B \\ E \end{bmatrix}, \tag{2.3}$$

where the first Cartan curvature $\kappa_1(s) = 1$ and the second and the third Cartan curvatures $\kappa_2(s)$ and $\kappa_3(s)$ are arbitrary functions in pseudo-arc parameter s. If the second Cartan curvature $\kappa_2(s)$ vanishes, then the curve is said to be null Cartan cubic [4]. The Cartan's frame vectors satisfy the following relations:

$$\langle T,T \rangle = \langle B,B \rangle = 0, \langle N,N \rangle = \langle E,E \rangle = 1,$$

$$\langle T,N \rangle = \langle N,B \rangle = \langle T,E \rangle = \langle B,E \rangle = 0, \langle T,B \rangle = -1. \tag{2.4}$$

The Bishop frame of a null Cartan curve in E_1^4 parameterized by pseudo-arc s whose the third Cartan curvature $\kappa_3(s)$ is non-vanishing ([9]). The relation between the Bishop frame $\{T, N_1, N_2, N_3\}$ and the Cartan frame $\{T, N, B, E\}$ of the curve $\psi = \psi(s)$ is given by

$$\begin{bmatrix} T \\ N_1 \\ N_2 \\ N_3 \end{bmatrix} = \begin{bmatrix} 1 & 0 & 0 & 0 \\ -\sigma_1\sigma_2 - \sigma_3\sqrt{\sigma_1'^2 + \sigma_3'^2} & \sigma_1 & 0 & \sigma_3 \\ \dfrac{\sigma_2^2 + \sigma_1'^2 + \sigma_3'^2}{2} & -\sigma_2 & 1 & \sqrt{\sigma_1'^2 + \sigma_3'^2} \\ \sigma_2\sigma_3 - \sigma_3\sqrt{\sigma_1'^2 + \sigma_3'^2} & -\sigma_3 & 0 & \sigma_1 \end{bmatrix} \begin{bmatrix} T \\ N \\ B \\ E \end{bmatrix}, \tag{2.5}$$

and ([9]) the Cartan equations of ψ due to the Bishop frame are given as follows:

$$\begin{bmatrix} T' \\ N_1' \\ N_2' \\ N_3' \end{bmatrix} = \begin{bmatrix} \sigma_2 & \sigma_1 & 0 & -\sigma_3 \\ 0 & 0 & \sigma_1 & 0 \\ 0 & 0 & -\sigma_2 & 0 \\ 0 & 0 & -\sigma_3 & 0 \end{bmatrix} \begin{bmatrix} T \\ N_1 \\ N_2 \\ N_3 \end{bmatrix}, \tag{2.6}$$

where the first Bishop curvature

$$\sigma_1(s) = \sin\theta(s), \tag{2.7}$$

the second Bishop curvature $\sigma_2(s)$ satisfies the differential equation

269

$$\sigma_2(s) = \frac{\kappa_3(s) - \theta''(s)}{\theta'(s)}, \quad \theta'(s) \neq 0, \tag{2.8}$$

the third Bishop curvature

$$\sigma_3(s) = \cos\theta(s), \tag{2.9}$$

and the function $\theta(s)$ satisfies the differential equation

$$2\theta'(\theta''' - \kappa_3') + 2\theta''(\kappa_3 - \theta'') + \theta'^4 - (\kappa_3 - \theta'')^2 - 2\kappa_2\theta'^2 = 0, \tag{2.10}$$

where

$$\theta(s) \notin \{\frac{\pi}{2} + k\pi, k\pi\}, k \in \mathbb{Z}. \tag{2.11}$$

The Bishop frame vectors satisfy the following relations:

$$\begin{aligned}
&\langle T,T \rangle = \langle N_2, N_2 \rangle = 0, \langle N_1, N_1 \rangle = \langle N_3, N_3 \rangle = 1, \\
&\langle T, N_1 \rangle = \langle N_1, N_2 \rangle = \langle T, N_3 \rangle = \langle N_2, N_3 \rangle = 0, \langle T, N_2 \rangle = -1.
\end{aligned} \tag{2.12}$$

3. TYPE-1 AND TYPE-3 SLANT HELICES IN MINKOWSKI SPACE-TIME E_1^4

Definition 3.1. A null Cartan curve $\psi = \psi(s)$ is said to be

(i) a type-1 slant helix according to the Bishop frame if the lines of ψ spanned by the vector field N_1 make a constant angle with a fixed direction in E_1^4, and

(ii) a type-3 slant helix according to the Bishop frame if the lines of ψ spanned by the vector field N_3 make a constant angle with a fixed direction in E_1^4.

Theorem 3.2. Every null Cartan curve $\psi = \psi(s)$ with the third Cartan curvature $\kappa_3 \neq 0$ due to the Bishop frame in E_1^4 is a type-1 slant helix.

Proof. Assume that $\psi(s)$ is a type-3 slant helix. Hence there is a relation between the vector field N_1 and the non-zero fixed direction U such that

$$\langle N_1, U \rangle = C, \tag{3.1}$$

where C is a constant from definition of type-1 slant helix. Considering the Bishop frame, the axis U can be decomposed by

$$U = \alpha_1 T + C N_1 + \alpha_2 N_2 + \alpha_3 N_3, \tag{3.2}$$

where $\alpha_i = \alpha_i(s)(i=1,2,3)$ are analytic functions of pseudo arc length s. Differentiating (3.2) with respect to s, we get

$$(\alpha_1' + \sigma_2\alpha_1)T + (\sigma_1\alpha_1)N_1 + (\alpha_2' - \sigma_2\alpha_2 - \sigma_2\alpha_3 + C\sigma_1)N_2 + (\alpha_3' - \sigma_3\alpha_1)N_3 = 0, \qquad (3.3)$$

which suggests the following system of differential equations:

$$\begin{cases} \alpha_1' + \sigma_2\alpha_1 = 0, \\[2mm] \sigma_1\alpha_1 = 0, \\[2mm] \alpha_2' - \sigma_2\alpha_2 - \sigma_2\alpha_3 + C\sigma_1 = 0, \\[2mm] \alpha_3' - \sigma_3\alpha_1 = 0. \end{cases} \qquad (3.4)$$

From $(3.4)_2$, we have two cases such that either $\sigma_1 = 0$ or $\alpha_1 = 0$:

Case 1: If $\sigma_1 = 0$, then using the expression $\sin\theta(s) = 0$ in (2.7), it is seen that the first Bishop curvature σ_1 can not be vanishing. So we exclude this case.

Case 2: If $\alpha_1 = 0$, then we find the function α_3 as

$$\alpha_3 = C_1, \qquad (3.5)$$

where C_1 is a constant. By using (3.5) in $(3.4)_3$, we obtain the function α_2 as

$$\alpha_2 = e^{\int \sigma_2 ds}(C_1\sigma_3 - C\sigma_1)e^{-\int \sigma_2 ds} ds. \qquad (3.6)$$

The axis in (3.2) is formed as

$$U = CN_1 + e^{\int \sigma_2 ds}(C_1\sigma_3 - C\sigma_1)e^{-\int \sigma_2 ds} ds N_2 + C_1 N_3. \qquad (3.7)$$

Differentiating (3.13), we have $U' = 0$, that is, U is a constant vector field. Conversely, defining the axis as in (3.7), we see that null Cartan slant helix is a type-1 slant helix.

Corollary 3.3. Let $\psi = \psi(s)$ be a type-1 null Cartan slant helix due to the Bishop frame in E_1^4. Then the axis of type-1 null Cartan slant helix is obtained as

$$U = CN_1 + e^{\int \sigma_2 ds}(C_1\sigma_3 - C\sigma_1)e^{-\int \sigma_2 ds} ds N_2 + C_1 N_3, \qquad (3.8)$$

where C, C_1 are constants.

Proof. It has been obtained in the proof of Theorem 3.2.

Corollary 3.4. The causal character of the axis of a type-1 null Cartan slant helix due to the Bishop frame in E_1^4 is spacelike.

Proof. It is straightforwardly seen from $\langle U, U \rangle = C^2 + C_1^2 \geq 0$.

Theorem 3.5. Every null Cartan curve $\psi = \psi(s)$ with the third Cartan curvature $\kappa_3 \neq 0$ due to the Bishop frame in E_1^4 is a type-3 slant helix.

Proof. Assume that $\psi(s)$ is a type-3 slant helix. Hence there is a relation between the vector field N_3 and the non-zero fixed direction U such that

$$\langle N_3, U \rangle = C, \tag{3.9}$$

where C is a constant from definition of type-3 slant helix. Considering the Bishop frame, the axis U can be decomposed by

$$U = \alpha_1 T + \alpha_2 N_1 + \alpha_3 N_2 + C N_3, \tag{3.10}$$

where $\alpha_i = \alpha_i(s) (i = 1, 2, 3)$ are analytic functions of pseudo arc length s. Differentiating (3.10) with respect to s, we get

$$(\alpha_1' + \sigma_2 \alpha_1)T + (\alpha_2' + \sigma_1 \alpha_1)N_1 + (\alpha_3' + \sigma_1 \alpha_2 - \sigma_2 \alpha_3 - C\sigma_3)N_2 + (-\sigma_3 \alpha_1)N_3 = 0, \tag{3.11}$$

which suggests the following system of differential equations:

$$\begin{cases} \alpha_1' + \sigma_2 \alpha_1 = 0, \\ \\ \alpha_2' + \sigma_1 \alpha_1 = 0, \\ \\ \alpha_3' + \sigma_1 \alpha_2 - \sigma_2 \alpha_3 - C\sigma_3 = 0, \\ \\ \sigma_3 \alpha_1 = 0. \end{cases} \tag{3.12}$$

From $(3.12)_4$, we have two cases such that either $\sigma_3 = 0$ or $\alpha_1 = 0$:

Case 1: If $\sigma_3 = 0$, then using the expression $\cos\theta(s) = 0$ from (2.9), it is seen that the third Bishop curvature σ_3 can not be vanishing. So we exclude this case.

Case 2: If $\alpha_1 = 0$, then we find the function α_2 as

$$\alpha_2 = C_1, \tag{3.13}$$

where C_1 is a constant. By using (3.13) in $(3.12)_3$, we obtain the function α_3 as

$$\alpha_3 = e^{\int \sigma_2 ds}(C\sigma_3 - C_1\sigma_1)e^{-\int \sigma_2 ds}. \tag{3.14}$$

The axis in (3.10) is formed as

$$U = C_1 N_1 + e^{\int \sigma_2 ds}(C\sigma_3 - C_1\sigma_1)e^{-\int \sigma_2 ds}ds N_2 + CN_3. \tag{3.15}$$

Differentiating (3.15), we have $U' = 0$, that is, U is a constant vector field. Conversely, defining the axis as in (3.15), we see that null Cartan slant helix is a type-3 slant helix.

Corollary 3.6. Let $\psi = \psi(s)$ be a type-3 null Cartan slant helix due to the Bishop frame in E_1^4. Then the axis of type-3 null Cartan slant helix is obtained as

$$U = C_1 N_1 + e^{\int \sigma_2 ds}(C\sigma_3 - C_1\sigma_1)e^{-\int \sigma_2 ds}N_2 + CN_3, \tag{3.16}$$

where C, C_1 are constants.

Proof. It has been obtained in the proof of Theorem 3.5.

Corollary 3.7. The causal character of the axis of a type-3 null Cartan slant helix due to the Bishop frame in E_1^4 is spacelike.

Proof. It is straightforwardly seen from $\langle U, U \rangle = C_1^2 + C^2 \geq 0$.

We infer out the following result from Theorem 3.2 and Theorem 3.5:

Corollary 3.8. Type-3 null Cartan slant helices according to the Bishop frame is also type-1 slant helices.

REFERENCES

[1] A. Ali, R. Lopez, M. Turgut, $k-$type partially null and pseudo null slant helices in Minkowski 4-space, Math. Commun. 17(1) (2012) 93-103.

[2] W. B. Bonnor, Null curves in a Minkowski space-time, Tensor 20 (1969) 229–242.

[3] L. R. Bishop, There is more than one way to frame a curve, Amer. Math. Monthly, 82(3) (1975) 246-251.

[4] K. L. Duggal and D. H. Jin, Null Curves and Hypersurfaces of Semi-Riemannian Manifolds, World Scientific, Singapore, 2007.

[5] M. Erdogan and G. Yilmaz, Null generalized and slant helices in 4-dimensional Lorentz-Minkowski space, Int. J. Contemp. Math. Sci. 3(23) (2008), 1113-1120.

[6] A. Ferrandez, A. Gimenez and P. Lucas, Null generalized helices in Lorentz-Minkowski spaces, J. Phys. A: Math. Gen. 35 (2002), 8243-8251.

[7] M. Grbovic, E. Nešovic, On the Bishop frames of pseudo null and null Cartan curves in Minkowski 3-

space, J. Math. Anal. and Appl. 461(1) (2018) 219-233.

[8] M. Grbovic, E. Nešovic, On generalized Bishop frame of null Cartan curve in Minkowski 3-space, Kragujevac J. Math. 43(4) (2019) 559-573.

[9] K. Ilarslan and E. Nesovic, On Bishop frame of a null Cartan curve in Minkowski space-time, Int. J. Geom. Methods Mod. Phys. 15(8) (2018) 1850142 (16 pages).

[10] S. Izumiya, N. Takeuchi, New special curves and developable surfaces, Turk J. Math. 28(2) (2004) 153-163.

[11] H. B. Karadağ and M. Karadağ, Null generalized slant helices in 4-dimensional Lorentzian space, Differ. Geom. Dyn. Syst. 10 (2008) 178-185.

[12] T Körpınar, RC Demirkol, On the uniform motion of a relativistic charged particle in a homogeneous electromagnetic field in Minkowski space E24, Mathematical Methods in the Applied Sciences, 42 (9) (2019), 3069-3087.

[13] Z. S. Körpinar, M. Tuz, T. Körpinar, New Electromagnetic Fluids Inextensible Flows of Spacelike Particles and some Wave Solutions in Minkowski Space-time, Int J Theor Phys 55 (1) (2016), 8-16.

[14] T. Körpınar, Bianchi Type-I Cosmological Models for Inextensible Flows of Biharmonic Particles by Using Curvature Tensor Field in Spacetime, Int J Theor Phys 54 (2015), 1762-1770

[15] T. Körpınar, E. Turhan: A New Version of Inextensible Flows of Spacelike Curves with Timelike B_2 in Minkowski Space-Time E_1^4, Differ. Equ. Dyn. Syst., 21 (3) (2013), 281-290.

[16] T. Körpınar, R.C. Demirkol, A New characterization on the energy of elastica with the energy of Bishop vector fields in Minkowski space. Journal of Advanced Physics. 6(4) (2017), 562-569.

[17] E. Nešovic, E. B. Koç Öztürk, U. Öztürk, $k-$type null slant helices in Minkowski space-time, Math. Commun. 20(1) (2015) 83-95.

[18] E. Nešovic, E. B. Koç Öztürk, U. Öztürk, On $k-$type null Cartan slant helices in Minkowski 3-space, Math. Methods Appl. Sci. 41(17) (2018) 7583-7598.

[19] B. O'Neill, Semi-Riemannian Geometry with Applications to Relativity, Academic press Inc, London, 1983.

[20] J. Qian, Y. H. Kim, Null helix and $k-$type null slant helices in E_1^4, Rev. Un. Mat. Argentina 57(1) (2016) 71-83.

[21] M. Turgut and S. Yılmaz, Some characterizations of type-3 slant helices in Minkowski space-time, Involve 2(1) (2009) 115-120.

ON DARBOUX HELICES DUE TO THE BISHOP FRAME

Yasin Ünlütürk[1] *, Talat Körpınar*[2]

[1]*Department of Mathematics, Faculty of Art and Science, Kırklareli University, Kırklareli, TURKEY*
[2]*Department of Mathematics, Faculty of Art and Science, Muş Alparslan University, Muş, TURKEY*

E-mail: yasinunluturk@klu.edu.tr, tkorpinar@alparslan.edu.tr

Abstract

In this study, we give a characterization of Darboux helices in Euclidean 3-space E^3 by using Darboux vector of an curve according to the Bishop frame. We obtain the position vector of a non-zero fixed direction U. Then we present some characterizations of Darboux helices due to the Bishop frame in Euclidean 3-space E^3.

AMS Subject Classification: 53A04.

Keywords: Darboux helix, K-type slant helix, Darboux vector, Bishop frame.

1. INTRODUCTION

General helix is a curve whose tangent makes a constant angle with a non-zero constant vector field (the axis of the helix) in the local diferential geometry of space curves. Moreover, the necessary and sufficient condition for a curve to be a general helix is the ratio of the curvature and the torsion of that curve to be constant [6]. There are also different studies on curves from physical point of view, see ([10], [11], [13]).

A slant helix is defined as a curve whose principal normal vector makes a constant angle with a fixed direction by Izumiya and Takeuchi in E^3 [9]. Some characterizations of slant helices have been investigated in Euclidean 3-space E^3, see ([1], [14]). Ali and Turgut have generalized the notion of slant helix to Euclidean n-space E^n and given some properties of slant helices [2]. Öztürk et.al. have considered the focal representation and some properties of focal curves with their curvatures of k-slant helices in E^{m+1} [15].

The behaviour of curves are generally studied by making use of Frenet-Serret frame. But there are some alternative frames to Frenet-Serret frame such as Bishop frame (parallel transport frame), Sabban frame, etc. In [3], Bishop defined an alternative over Frenet frame for a curve and called it Bishop frame. The advantage of Bishop frame is well-defined when the curve has a vanishing second derivative in 3-dimensional Euclidean space E^3 unlike Frenet frame. Also, Bishop frame is used in many applications such as engineering, computer aided design, DNA analysis etc. By means of this alternative frame, there are many studies about theory of curves and surfaces, for some of them, see ([4], [5], [12]).

As a special case of helices, Darboux helices are formed by obtaining the relation between the Darboux vector of the curve and a non-zero fixed direction. Darboux helices were studied in both Euclidean and Minkowski 3-spaces by [8, 16, 18, 19].

In this study, using Darboux vector of an curve according to the Bishop frame, we give a characterization of Darboux helices in Euclidean 3-space E^3. We obtain the position vector of non zero fixed direction U. Then we present some characterizations of Darboux helices due to the Bishop frame in Euclidean 3-space E^3.

2. PRELIMINARIES

The standard flat metric in Euclidean 3-space E^3 is given by

$$\langle.,.\rangle = dx_1^2 + dx_2^2 + dx_3^2, \tag{2.1}$$

where (x_1, x_2, x_3) is a rectangular coordinate system of Euclidean 3-space E^3. The norm of an arbitrary vector $a \in E^3$ is given by $\|a\| = \sqrt{\langle a,a \rangle}$. The curve γ is called an unit speed curve if velocity vector v of γ satisfies

$\|v\| = 1$. For vectors $v, w \in E^3$ it is said to be orthogonal if and only if $\langle v, w \rangle = 0$. Let $\gamma = \gamma(s)$ be a regular curve in Euclidean 3-space E^3. If the tangent vector field of this curve forms a constant angle with a constant vector field U, then this curve is called a general helix or an inclined curve [6].

Denote by $\{T, N, B\}$ the moving Frenet-Serret frame along the curve γ in the space E^3. For an arbitrary curve α in Euclidean 3-space E^3, the following Frenet-Serret formulae is given with respect to the first curvature κ, the second curvature τ, ([7]), as

$$\begin{bmatrix} T' \\ N' \\ B' \end{bmatrix} = \begin{bmatrix} 0 & \kappa & 0 \\ -\kappa & 0 & \tau \\ 0 & -\tau & 0 \end{bmatrix} \begin{bmatrix} T \\ N \\ B \end{bmatrix}, \qquad (2.2)$$

where T, N, B are called the tangent, the principal normal, the binormal vectors of the curve α, respectively.

Bishop frame is also referred to as parallel transport that is an orthonormal frame formed by transporting in parallel each component of the frame. The parallel transport is formed with tangent vector and any convenient arbitrary basis for the remainder of the frame (for details, see [3, 4]). Then, the relations between Frenet-Serret frame and parallel transport frame for the curve $\gamma : I \subset R \to E^3$ are given as follows:

$$T(s) = T(s),$$

$$N(s) = \cos \theta(s) M_1 + \sin \theta(s) M_2, \qquad (2.3)$$

$$B(s) = -\sin \theta(s) M_1 + \cos \theta(s) M_2,$$

The parallel transport frame equations are expressed as [4]

$$\begin{bmatrix} T' \\ M_1' \\ M_2' \end{bmatrix} = \begin{bmatrix} 0 & k_1 & k_2 \\ -k_1 & 0 & 0 \\ -k_2 & 0 & 0 \end{bmatrix} \begin{bmatrix} T \\ M_1 \\ M_2 \end{bmatrix}, \qquad (2.4)$$

where

$$\kappa(s) = \sqrt{k_1^2 + k_2^2}, \quad \theta(s) = \arctan(\frac{k_2}{k_1}), \quad \tau(s) = -\frac{d\theta(s)}{ds}. \qquad (2.5)$$

The Bishop Darboux vector of the curve $\gamma(s)$ is, ([4]), as follows:

$$w = -k_2 M_1 + k_1 M_2.$$

$$(2.6)$$

ON DARBOUX HELICES DUE TO THE BISHOP FRAME

Definition 3.1. Let $\gamma(s)$ be a unit speed curve framed by the Bishop frame $\{T, M_1, M_2\}$ in E^3. If there exists a nonzero constant vector field $U \in E^3$ such that

- $\langle T, U \rangle$ is a constant, then it is said to be a $0-$type helix (general helix),

- $\langle M_k, U \rangle$ $(k = 1, 2,$ respectively) $k-$type helices, and U is called the axis of $\gamma(s)$.

Definition 3.2. A curve $\gamma : I \subset E \to E^3$ with the Darboux vector w is called Darboux helix, if there exists a non-zero fixed direction $U \in E^3$ such that

$$\langle w, U \rangle = C, \tag{3.1}$$

where C is a constant.

Theorem 3.3. Let $\gamma = \gamma(s)$ be a unit speed curve in E^3. $\gamma(s)$ is a Darboux helix if and only if the Bishop curvatures satisfy the condition

$$k_2 k_1'^2 (k_2 - k_2') = 0. \tag{3.2}$$

Proof. ($\Rightarrow$): Assume that $\gamma(s)$ is a Darboux helix. Hence there is a relation between the Darboux vector w and the non-zero fixed direction U such that

$$\langle w, U \rangle = C, \tag{3.3}$$

where C is a constant from definition of Darboux helix. Considering the Bishop frame, the axis U can be decomposed by

$$U = \alpha_1 T + \alpha_2 M_1 + \alpha_3 M_2, \tag{3.4}$$

where $\alpha_i = \alpha_i(s)(i = 1, 2, 3)$ are analytic functions of arc length s. Putting (2.6) and (3.4) into (3.3), we obtain

$$-k_2 \alpha_2 + k_1 \alpha_3 = C. \tag{3.5}$$

Differentiating (3.4) with respect to s, we get

$$(\alpha_1' - k_1 \alpha_2 - k_2 \alpha_3)T + (\alpha_2' + k_1 \alpha_1)M_1 + (\alpha_3' + k_2 \alpha_1)M_2 = 0, \tag{3.6}$$

which suggests the following system of differential equations:

$$\alpha_1' - k_1\alpha_2 - k_2\alpha_3 = 0,$$

$$\alpha_2' + k_1\alpha_1 = 0,$$

$$\alpha_3' + k_2\alpha_1 = 0. \tag{3.7}$$

Rewriting (3.5) gives

$$\alpha_2 = \frac{k_1}{k_2}\alpha_3 - \frac{1}{k_2}C. \tag{3.8}$$

Substituting (3.8) into (3.7)$_2$, we obtain

$$(\frac{k_1}{k_2}\alpha_3 - \frac{1}{k_2}C)' + k_1\alpha_1 = 0, \tag{3.9}$$

substituting (3.7)$_3$ into (3.9), we have

$$\alpha_3 = \frac{Ck_2'}{k_1k_2' - k_1'k_2}. \tag{3.10}$$

Using (3.8) in (3.6) gives

$$\alpha_2 = \frac{Ck_1'}{k_1k_2' - k_1'k_2}. \tag{3.11}$$

To find the fuction α_1, we put (3.10) and (3.11) into (3.7)$_1$, then we have

$$\alpha_1 = C\frac{k_1k_1' + k_2k_2'}{k_1k_2' - k_1'k_2}ds. \tag{3.12}$$

The axis in (3.4) is formed as

$$U = C\frac{k_1k_1' + k_2k_2'}{k_1k_2' - k_1'k_2}dsT + \frac{Ck_1'}{k_1k_2' - k_1'k_2}M_1 + \frac{Ck_2'}{k_1k_2' - k_1'k_2}M_2, \tag{3.13}$$

The vector U' to vanish, the following condition has to be satisfied:

$$k_2k_1'^2(k_2 - k_2') = 0. \tag{3.14}$$

($\Leftarrow$): Conversely, Assume that (3.1) holds. We define the vector field U as

$$U = C\frac{k_1k_1' + k_2k_2'}{k_1k_2' - k_1'k_2}dsT + \frac{Ck_1'}{k_1k_2' - k_1'k_2}M_1 + \frac{Ck_2'}{k_1k_2' - k_1'k_2}M_2, \tag{3.15}$$

where C is constant. Considering (3.1) in the differentiation of (3.15), we have $U' = 0$, that is, U is a constant vector field. Because $\langle w, U \rangle = C$ is a constant, so we arrive the result that $\gamma(s)$ is a Darboux helix.

Corollary 3.4. Let $\gamma = \gamma(s)$ be a Darboux helix due to the Bishop frame in E^3. Then the axis of Darboux helix is obtained as

$$U = C\frac{k_1 k_1' + k_2 k_2'}{k_1 k_2' - k_1' k_2} ds\, T + \frac{Ck_1'}{k_1 k_2' - k_1' k_2} M_1 + \frac{Ck_2'}{k_1 k_2' - k_1' k_2} M_2, \tag{3.16}$$

where C is constant.

Proof. It has been obtained in the proof of Theorem 3.2.

Corollary 3.5. Let $\gamma = \gamma(s)$ be a Darboux helix due to the Bishop frame in E^3. Then the following condition holds:

$$\frac{k_1 k_1' + k_2 k_2'}{k_1 k_2' - k_1' k_2} ds = \sqrt{C_0 - \frac{k_1'^2 + k_2'^2}{(k_1 k_2' - k_1' k_2)^2}}, \tag{3.17}$$

where C_0 is constant.

Proof. It is straightforwardly seen by using the feature of the axis to be constant, that is, $\langle U, U \rangle = C_0$.

Corollary 3.6. Let $\gamma = \gamma(s)$ be a Darboux helix due to the Bishop frame in E^3. Then Darboux helix is a curve of constant precession if and only if the Bishop curvatures satisfy the condition

$$k_1'^2 + k_2'^2 = C, \tag{3.18}$$

where C is a constant.

Proof. Scofield defined that curves of constant precession are curves whose Darboux vectors make a constant angle with a fixed direction and rotate about it with a constant speed [17]. Taking into account of Darboux helix γ with the Darboux vector w, If the speed of Darboux vector is constant, that is,

$$\|w'\|^2 = \|-k_2' M_1 + k_1' M_2\|^2 = k_1'^2 + k_2'^2 = C.$$

Theorem 3.7. Let $\gamma = \gamma(s)$ be a Darboux helix due to the Bishop frame in E^3. Then,

(i) $\gamma = \gamma(s)$ is a $0-$type slant helix if and only if the equation

$$C\frac{(k_1^2 + k_2^2)'}{(\frac{k_2}{k_1})' k_1^2} = 0 \tag{3.19}$$

holds. Here C is taken as nonzero constant.

(ii) $\gamma = \gamma(s)$ is a $1-$type slant helix if and only if the equation

$$Ck_1 \frac{k_1 k_1^{'} + k_2 k_2^{'}}{k_1 k_2^{'} - k_1^{'} k_2} \, ds = 0 \tag{3.20}$$

holds. Here C is taken as nonzero constant.

(iii) $\gamma = \gamma(s)$ is a $2-$type slant helix if and only if the equation

$$Ck_2 \frac{k_1 k_1^{'} + k_2 k_2^{'}}{k_1 k_2^{'} - k_1^{'} k_2} \, ds = 0 \tag{3.21}$$

holds. Here C is taken as nonzero constant.

Proof. (i) Let isotropic Darboux helix $\gamma = \gamma(s)$ be $0-$type slant helix in E^3. Then the relation

$$\langle T, U \rangle = \text{constant} \tag{3.22}$$

holds. Differentiating (3.22), we have

$$\langle T^{'}, U \rangle = \langle k_1 M_1 + k_2 M_2, U \rangle = 0. \tag{3.23}$$

From (3.23), we obtain the relation in (3.19).

Conversely, assume that the relation (3.19) holds. Then, since $\gamma = \gamma(s)$ is a Darboux helix, using the axis in (3.16) which is a non-zero fixed direction, we have the result

$$\langle T, U \rangle = C \frac{k_1 k_1^{'} + k_2 k_2^{'}}{k_1 k_2^{'} - k_1^{'} k_2} \, ds, \tag{3.24}$$

where C is a constant. Rewriting (3.24) by using (3.19) gives

$$\langle T, U \rangle = 0, \tag{3.25}$$

which means that Darboux helix $\gamma = \gamma(s)$ is a $0-$type slant helix, that is, general helix.

(ii) Let Darboux helix $\gamma = \gamma(s)$ be $1-$type slant helix in E^3. Then the relation

$$\langle M_1, U \rangle = \text{constant} \tag{3.26}$$

holds. Differentiating (3.26), we have

$$\langle M_1^{'}, U \rangle = \langle -k_1 T, U \rangle = 0. \tag{3.27}$$

From (3.27), we obtain the relation in (3.20).

Conversely, assume that the relation (3.20) holds. Then, since $\gamma = \gamma(s)$ is a Darboux helix, using the axis in (3.16), we have the result

$$\langle M_1, U \rangle = \frac{Ck_1^{'}}{k_1 k_2^{'} - k_1^{'} k_2}, \tag{3.28}$$

where C is a constant. Rewriting (3.28) by using (3.20) gives

$$\langle M_1, U \rangle = 0, \tag{3.29}$$

which means that Darboux helix $\gamma = \gamma(s)$ is a $1-$type slant helix.

(iii) Let Darboux helix $\gamma = \gamma(s)$ be $2-$type slant helix in E^3. Then the relation

$$\langle M_2, U \rangle = \text{constant} \tag{3.30}$$

holds. Differentiating (3.30), we have

$$\langle M_2', U \rangle = \langle -k_2 T, U \rangle = 0. \tag{3.31}$$

From (3.31), we obtain the relation in (3.21).

Conversely, assume that the relation (3.21) holds. Then, since $\gamma = \gamma(s)$ is a Darboux helix, using the axis in (3.16), we have the result

$$\langle M_2, U \rangle = \frac{Ck_2'}{k_1 k_2' - k_1' k_2}, \tag{3.32}$$

where C is a constant. Rewriting (3.32) by using (3.21) gives

$$\langle M_2, U \rangle = 0, \tag{3.33}$$

which means that Darboux helix $\gamma = \gamma(s)$ is a $2-$type slant helix.

REFERENCES

[1] A. T. Ali, Position vectors of slant helices in Euclidean 3-space, J. Egyptian Math. Soc. 20(1) (2012) 1-6.

[2] A. T. Ali, and M. Turgut, Some characterizations of slant helices in the Euclidean space E^n, Hacettepe J. Math. Stat. 39(3) (2010) 327-336.

[3] L. R. Bishop, There's more than one way to frame a curve, Amer. Math. Monthly 82(3) (1975) 246–251.

[4] B. Bükçü, M.K. Karacan, Special Bishop motion and Bishop Darboux rotation axis of the space curve, J. Dyn. Syst. Geom. Theor., 6(1) (2008) 27-34.

[5] B. Bükçü, M.K. Karacan, The slant helices according to Bishop frame, World Acad. Sci. Eng. Technol. 59 (2009) 1039-1042.

[6] M. P. Do Carmo, Differential Geometry of Curves and Surfaces, Prentice Hall, Englewood Cliffs, New Jersey, 1976

[7] H. H. Hacisalihoğlu, Differential Geometry I, Ankara University Faculty of Science Press, Ankara, 2000.

[8] K. Ilarslan, M, Yildirim, On Darboux helices in Euclidean 4-space, Math. Meth. Appl. Sci. (2018) 1–6. https://doi.org/10.1002/mma.5260

[9] S. Izumiya, N. Takeuchi, New special curves and developable surfaces, Turk. J. Math. 28(2) (2004) 531–537.

[10] T. Körpınar, On the Fermi-Walker Derivative for Inextensible Flows, Zeitschrift für Naturforschung A. 70 (7) (2015), 477—482

[11] T. Körpınar, A new version of energy for slant helix with bending energy in the Lie groups. Journal of Science and Arts 17(4) (2017), 721-730.

[12] T. Körpınar, R.C. Demirkol, A New characterization on the energy of elastica with the energy of Bishop vector fields in Minkowski space. Journal of Advanced Physics. 6(4) (2017), 562-569.

[13] T Körpınar, S. Baş, A new approach to inextensible flows of curves with blaschke frame, Journal of Science and Arts 19 (1) (2019), 15-22

[14] L. Kula, N. Ekmekçi, Y. Yayl , and K. İlarslan, Characterizations of slant helices in Euclidean 3-space, Turkish J. Math. 34 (2010) 261-273.

[15] G. Öztürk, B. Bulca, B. Bayram, and K. Arslan, Focal representation of k-slant helices in E^{m+1}, Acta Univ. Sapientiae Mathematica 7(2) (2015) 200-209.

[16] U. Öztürk, E. Nešovic, On pseudo null and null Cartan Darboux helices in Minkowski 3-space, Kuwait J. Sci. 43(2) (2016) 64–82.

[17] P. D. Scofield, Curves of constant precession, Amer. Math. Monthly 102 (1995) 531-537.

[18] A. Şenol, E. Zıplar, Y. Yayli, and R. Ghadami, Darboux helices in Minkowski space, Life Science Journal 9(4) (2012) 5905-5910.

[19] E. Zıplar, A. Şenol, Y. Yaylı, On Daboux helices in Euclidean 3-space, Global J. Sci. Front. Res. Mathem. Decision Sci. 12(13) (2012) 73-80.

EFFECT OF SiC AND NANO-FeB ON MICROSTRUCTURE AND CORROSION RESISTANCE OF ALUMINUM

Canser GÜL, Hülya DURMUŞ, Nilay ÇÖMEZ

Manisa Celal Bayar University, Dept. of Metallurgical and Materials Engineering, Manisa, TURKIYE.

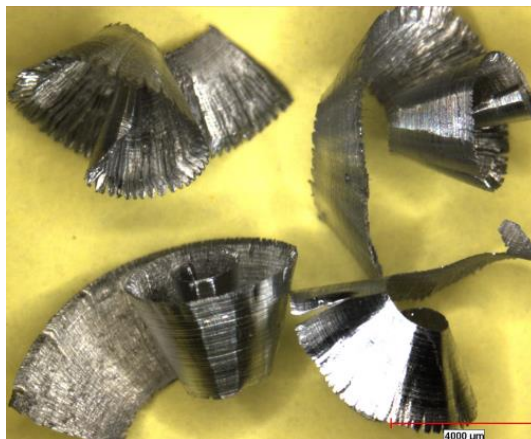E-mail: canser.gul@cbu.edu.tr

Abstract

Aluminum is one of the most important metallic material that has a combination of various features such as high specific strength, corrosion resistance against harsh environments and lightness. In order to improve properties of aluminum such as corrosion or wear resistance, toughness or hardness, hard particles are being used currently. This study concerned with the corrosion behavior of Al and Al/SiC/nano-FeB metal matrix composite samples. These composites which include various weight contents of SiC and nano-FeB (0%, 10%) are produced by powder metallurgy-hot pressing method. Optical microscopy was used to study the effect of SiC and nano-FeB on microstructure. Then the samples were exposed to corrosion in 3.5 % NaCl solution. From the results of the electrochemical potentiodynamic test SiC and nano-FeB reinforced composite was exhibited higher corrosion resistance compared to pure Al.

Keywords: Aluminum, SiC, FeB, Metal matrix composites (MMCs), Corrosion

1. INTRODUCTION

Aluminum composites are used in many fields such as automotive and aerospace industry, because of high of great strength, elastic modulus, toughness and impact resistance, low sensitivity-to changes in temperature or thermal shock, high surface durability, low sensitivity to surface flaws, high electrical and thermal conductivity, superior wear resistance when compared to unreinforced materials [1] Metals are reinforced with hard particles such as SiC, B_4C, TiC, and Al_2O_3 to enhance mechanical properties to produce composite [2]. The recent studies in metal matrix nanocomposites are getting more and more attractive in the field of automotive and aerospace industries [3]. Metal-ceramic nano composites are particularly interesting as they offer a combination of high ductility of metallic parts and the strength and stiffness of ceramic parts. [4]. Owing to their excellent mechanical properties SiC particulates were among the most preferred reinforcements especially that the addition of such a material was not found to significantly affect the density of the final composite [5]. Ferro-boron (Fe-B) is a binary alloy of iron with boron content between 10 % and 20 % and is the lowest cost boron additive [6]. So, micro SiC and nano-FeB reinforcements have used as reinforcing elements in this study.

The present work is the first attempt to produce an Al/SiC/nanoFeB hybrid composite. The main objective is developing a high strength SiC and nano FeB reinforced-aluminum-matrix-composite with uniform spreading of reinforcements. The microstructure mechanical and corrosion properties of manufactured composites are studied. The paper is organized as follows: the experimental procedure is presented in section 2, microstructural observations, mechanical properties, and characterization are illustrated in section 3. Conclusion remarks are finally presented in section 4.

2. MATERIAL AND METHODS

Pure aluminum powder was used as a matrix material. Nano-FeB particles have an average size of 600 nm and SiC particles were used as reinforcements. Aluminum powders and reinforcements were hot-pressed for 1 hour at 500 ºC and 300 MPa. The produced samples were cut into 16x16x6 mm^3 pieces.

Densities of the composite samples were determined by using the Archimedes principle. Microstructural investigations were fulfilled by Nikon Eclipse LV 150 optical microscope using Clemex Software. Hardness measurements were carried out by using Duravision 2000 EMCO Test Brinell hardness tester under 6.25 kg load.

A corrosion cell with three electrodes (shown in **Fig 1.**) was used for corrosion tests. Saturated calomel electrode was used as a reference electrode, graphite electrode was used as a contrary electrode and, a sample used as a working electrode. Corrosion tests were performed in 3.5% NaCl solution in room temperature. The open-circuit potential was measured for 30 minutes before the Tafel measurement began, and measurements were started after this value was fixed. The -0.25 anodic and 0.25 cathodic potential ranges were scanned at a scanning rate of 1 mV/s and then the corrosion rates were calculated by Tafel extrapolation using the instrument software.

Figure 1. Corrosion cell with three electrodes

3. RESULTS AND DISCUSSION

The density of samples was calculated as theoretical and the actual densities were measured by practical. The density-porosity values shown in **Table 1.** The true density values achieved were slightly below the theoretical values in both samples. Moreover, it was above the expected level and very close to the theoretical density in the nFeB-SiC sample. Although Al powders have approximately the same size and spherical in shape, SiC and nFeB particles have different shapes and are smaller in support of pressability. This increased the expected true densities and reduced the amount of porosity compared to the pure aluminum sample containing the same size particles.

Table 1. Density values of samples

Sample	Theoretical density (g/cm^3)	True density (g/cm^3)	Density value (%)	Porosity (%)
Al	2.70	2.66	98.5	1.5
Al + nFeB/SiC	2.85	2.83	99.3	0.7

When the studies in the literature were examined, it was seen that the amount of porosity increases during compaction of particles of the same size and the porosity amount of pure materials containing mixed shaped particles is lower [7]. For composite samples in our study, it was thought that nFeB particles reduced the porosity both with their size and reticulated structures.

The microstructure images of the composite samples produced were shown in **Fig 2**. The grains were nearly equiaxial. SiC-nFeB particles showed an almost homogeneous distribution in the aluminum matrix. Some porosities also were observed in the microstructure. These porosities in microstructure are thought to be compatible with the porosity percent values in **Table 1**.

Figure 2. Microstructures of composites a) pure Aluminum, b) 10 wt.% SiC/nFeB reinforced aluminum composite

Figure 3. Brinell Hardnesses of samples

Reinforced SiC and nFeB particles were positively affected the Brinell hardness (**Fig 3**). Due to their hardnesses and physical properties, hard particles may contribute to Al matrix hardnesses. Not only the hardness but also they may encourage wear and mechanical properties of aluminum alloys [8].

Figure 4. Corrosion test results

When Tafel curves examined it was seen that the potential (V) value of reinforced composite shifts toward a more positive zone (shown in **Fig 4**). This roughly shows that pure aluminum is more corroded than nFeB and SiC reinforced samples. When the corrosion rates calculated by the Tafel extrapolation method are compared, we can easily see the same situation. The corrosion rate of aluminum is 0.07408 mm/year while the corrosion rate of the reinforced sample is 0.04106. When the results were examined, it was observed that the added supplements reduced the corrosion rate.

4. CONCLUSION

The aim of the study is to obtain a homogeneously distributed composite structure by adding reinforcements of various sizes. At the same time, this reinforced aluminum-matrix nano-composite structure should provide high strength and high corrosion resistance. In this study, the following results were obtained for these purposes.

-SiC particles showed an almost homogeneous distribution in the aluminum matrix.

-Porosities were found to be less in two samples from density tests and microstructure investigations.

-Reinforcements had a little positive effect on the hardness of the samples.

-With the addition of reinforcements, the corrosion potential toward shifted a more positive zone. The addition of nFeB and SiC increased the corrosion resistance 1.5 times.

References

[1] Kalkanlı, A., Yılmaz, S., Synthesis and characterization of aluminum alloy 7075 reinforced with silicon carbide particulates, Materials & Design, 29(4), 775-780, 2008.

[2] Durmuş, H., Gül, C., Çömez, N., Yurddaşkal, M., Investigación sobre el comportamiento al desgaste de los compuestos Alumix321/SiC envejecidos y fabricados por prensado en caliente. Revista de Metalurgia, 55(3), 148, 2019.

[3] Sachit, T. S., Mohan, N., Wear Behavior of Aluminum LM4 Reinforced with WC and Ta/NbC Hybrid Nano-Composites Fabricated Through Powder Metallurgy Technique. FME Transactions, 47(3), 535, 2019.

[4] Singh S., Chang, S., Kaira C.S., Baldwin,J.K., Mara, N., Chawla, N., Microstructure and mechanical properties of co-sputtered Al-SiC composites, Materials & Design, 168, 2019.

[5] Youssef, Y., El-Sayed, M., Effect of Reinforcement Particle Size and Weight Fraction on the Mechanical Properties of SiC Particle Reinforced Al Metal Matrix Composites, International Review of Mechanical Engineering, 10(4), 2016.

[6] Sarıyer, D., Küçer, R., Küçer, N., Neutron Shielding Properties of Concretes Containing Boron Carbide and Ferro – Boron, Procedia - Social and Behavioral Sciences, 195, 1752-1756,2015.

[7] Hassani A., Bagherpour E., Qods F., Influence of pores on workability of porous Al/SiC composites fabricated through powder metallurgy + mechanical alloying, 591, 132–142, 2014.

[8] Annigeri U., and Veeresh Kumar G., Effect of Reinforcement on Density, Hardness and Wear Behavior of Aluminum Metal Matrix Composites: A Review, Materials Today: Proceedings 5(5), 11233–11237, 2018.

HARDNESS AND MICROSTRUCTURAL PROPERTIES OF AA7075 SWARF/Al$_2$O$_3$ COMPOSITES DEPENDING ON DIRECTION

Canser GÜL, Nilay ÇÖMEZ, Hülya DURMUŞ

Manisa Celal Bayar University, Dept. of Metallurgical and Materials Engineering, Manisa, TURKIYE.

E-mail: canser.gul@cbu.edu.tr

Abstract

Aluminum is one of the most important metallic material that has a combination of various features such as high specific strength, corrosion resistance against harsh environments and lightness. In order to improve both the strength and toughness of the alloys, hard particles such as TiC, SiC and Al$_2$O$_3$ are being used currently. But today, recycling is needed to support environmentally friendly production techniques. In this study, Al$_2$O$_3$ reinforced composites were produced by the swarf of AA7075 aluminum alloy as matrix material. Samples were produced by hot pressing. Changes in the mechanical properties of the produced composites depending on pressing direction were investigated.

AA7075 swarf have 5-25 mm length and 3 mm width and Al$_2$O$_3$ powders were hot-pressed for 1 hour at 500 ºC and 300 MPa. Microstructural investigations were fulfilled by Nikon Eclipse LV 150 optical microscope using Clemex Software. Hardness measurements were carried out by using Duravision 2000 EMCO Test Brinell hardness tester under 6.25 kg load. The investigations were made both from parallel to the pressing direction and from the vertical surfaces. And the differences between the hardness values of these two surfaces were evaluated.

Microstructural images showed that the grains of AA7075 swarf are equiaxed. Samples have micro-sized pores within the matrix phase. This can be attributed to the low compressibility of the swarf matrix phase which resulted in the insufficient bond between the soft phase particles at this level of pressure. Hardness test results revealed that both the pressing direction and reinforcement amount affected the hardness of the composite. When the hardness test results were examined, it was increased by ≈ 27 % on the surface and by 29 % on the cross-section.

Keywords: Aluminum, 7075, Swarf, Metal matrix composites (MMCs), Recycling

1. INTRODUCTION

Aluminum is one of the most important metallic material that has a combination of various features such as high specific strength, corrosion resistance against harsh environments and lightness [1, 2].

2xxx, 5xxx, 6xxx and 7xxx Al alloy series have been widely used as matrix materials [3]. In order to improve both the strength and toughness of the matrix alloys, hard particles such as TiC, SiC and Al_2O_3 are being used currently [2]. But today, recycling is needed to support environmentally friendly production techniques [4, 5]. By using some methods such as powder metallurgy (PM), severe plastic deformation, equal channel angular pressing (ECAP), cyclic extrusion compression (CEC), friction stir extrusion (FSE), high pressure torsion (HPT) or spark plasma sintering (SPS) metal chips can be returned directly to bulk material. In addition, there is less energy loss and metal loss while recycling. The harmful gases emitted to the environment are also less [6-9].

In this study, Al_2O_3 reinforced composites were produced by the swarf of AA7075 aluminum alloy as matrix material. Samples were produced by hot pressing. Changes in the mechanical properties of the produced composites depending on pressing direction were investigated.

2. MATERIAL AND METHODS

AA7075 swarf shown in Fig.1, that have 5-25 mm length and 3 mm width were used as a matrix material. The chemical composition of AA7075 alloy is given in Table 1. Al_2O_3 particles have an average size of 1 μm. Hot pressing was applied for 1 hour at 500 ºC and 300 MPa. The produced composite was cut into 16x16x6 mm^3 pieces. Then the second sintering process was applied at 600 ºC for 1 hour.

Figure 1. AA7075 Swarf

Table 1. Chemical composition of AA7075

Element	Zn	Mg	Cu	Cr	Si	Fe	Mn	Zi+Ti	Other	Al
wt. %	5.1-6.1	2.1-2.9	1.2-2.0	0.18-0.28	0.4 max	0.5 max	0.3 max	0.25 max	0.15	Balance

Microstructural investigations were fulfilled by Nikon Eclipse LV 150 optical microscope using Clemex Software. Hardness measurements were carried out by using Duravision 2000 EMCO Test Brinell hardness tester under 6.25 kg load. The investigations were made both from parallel to the pressing direction and from the vertical surfaces. And the differences between the hardness values of these two surfaces were evaluated.

3. RESULTS AND DISCUSSION

Figure 2. Microstructures of composites from the surface, **a)** unreinforced, **b)** 5% **c)** 10% **d)** 15% reinforced with Al_2O_3 by weight

As a result of the microstructure studies, some porosity was observed between the grains and swarf at the microstructure (**Fig. 2**). These porosities observed between the grains are the porosities found in the bulk

aluminum itself, but the porosities at the swarf boundaries are caused by the low compressibility of the swarf. Some swarf was also distant from each other during sintering and this prevents the reduction of porosities. In addition, reinforcements that were thought to be Al_2O_3 in the middle parts of the grains could also be observed in the microstructure.

Figure 3. Microstructures of composites from the cross section **a)** unreinforced **b)** 5% **c)** 10% **d)** 15% reinforced with Al_2O_3 by weight

When the images taken from the cross-section were examined (**Fig. 3**), it was observed that the distance between the swarf increased with an increasing amount of Al_2O_3. However, when the SEM images were examined in **Fig. 4**, it was observed that the situation was much more striking. Considered as porosity in the microstructure was observed to be actually filled with swarf layer. Al_2O_3 reinforcements distributed homogeneously into the microstructure were clearly visible. Although some porosity was observed in SEM images, good results were obtained for a production with such large swarf using the powder metallurgy method.

Figure 4. SEM images of **a)** 5 wt.% Al$_2$O$_3$ reinforced composite surface, **b)** 10 wt.% Al$_2$O$_3$ reinforced composite cross section, **c)** 15 wt.% Al$_2$O$_3$ reinforced composite

Figure 5. Brinell Hardness test results taken from surface and cross section

When the hardness values of the samples taken from the surface and cross-section were examined (**Fig. 5**), it was observed that the Brinell hardness of the samples increased with the increase of reinforcement up to 10% reinforcement ratio. Both surface and section hardness were higher than all other samples in 10 wt. % Al$_2$O$_3$ reinforced sample. However, a decrease in hardness was observed by increasing the amount of reinforcement to 15%. This may be related to the compressibility of the hard particles. With the increasing amount of reinforcements, the reinforcements were filled between the swarf and increased the hardness. However, excess amounts of reinforcement filled the areas between the swarf to be pressed and sintered. This is thought to cause a decrease in the mechanical properties of these parts.

4. CONCLUSION

Microstructural images showed that the grains of AA7075 swarf were equiaxed. Samples have micro-sized pores within the matrix phase. This can be attributed to the low compressibility of the swarf matrix phase which resulted in the insufficient bond between the soft phase particles at this level of pressure.

Hardness test results revealed that both the pressing direction and reinforcement amount affected the hardness of the composite. When the hardness test results were examined, it was increased by $\approx 27\%$ on the surface and by 29 % on the cross-section up to 10% reinforced sample. However, excess amounts of reinforcement filled the areas between the swarf to be pressed and sintered and caused a decrease in the mechanical properties.

REFERENCES

[1] Kowles, A.J., Jiang, X., Galano, M., Audebert, F., Microstructure and mechanical properties of 6061 Al alloy based composites with SiC nanoparticles, Journal of Alloys and Compounds 615, 401-405, 2014.

[2] Ramkumar, K.R., Sivasankara, S., Al-Mufadi, F., Siddharth, S., Raghu, R., Investigations on microstructure, mechanical, and tribological behaviour of AA 7075–x wt.% TiC composites for aerospace applications, Archives of Civil and Mechanical Engineering 19(2), 428-438, 2019.

[3] Reena Kumari, P.D., Nayak, J., Shetty A.N., Corrosion behavior of 6061/Al-15 vol. pct. SiC(p) composite and the base alloy in sodium hydroxide solution, Arabian Journal of Chemistry, 9(2), 1144-1154, 2016.

[4] Chiba R. and Yoshimura, M., Solid-state recycling of aluminium alloy swarf into c-channel by hot extrusion, Journal of Manufacturing Process 17, 1-8, 2015.

[5] Hu, M., Ji, Z., Chen, X., Wang, Q., Ding, W., Solid-state recycling of AZ91D magnesium alloy chips, Trans. Nonferrous Met. Soc. China, 22, 68-73, 2012.

[6] Wan, B., Chen, W., Lu, T., Liu, F., Jiang, Z., Review of solid state recycling of aluminum chips, Resources, Conservation & Recycling, 125, 37-47, 2017.

[7] Luo, P., McDonald, D.T., Xu, W., Palanisamy, S., Dargusch, M.S., Xia, K., A modified Hall–Petch relationship in ultrafine-grained titanium recycled from chips by equal channel angular pressing, Scr. Mater. 66, 785–788, 2012.

[8] Cui, J.R., Guo, W., Roven, H.J., Wang, Q.D., Chen, Y.J., Peng, T., Recycling of aluminum scrap by severe plastic deformation. Mater. Sci. Forum 667-669, 1177–1182, 2011.

[9] El Aal, M.I.A., Yoon, E.Y., Kim, H.S., Recycling of AlSi8Cu3 alloy chips via high pressure torsion. Mater. Sci. Eng. A 560, 121–128, 2013.

MEASUREMENT OF THERMAL STRAIN ON A PRINTED CIRCUIT BOARD

M. A. Demirtaş[1], A. Özsunar[1], B. Altıntaş[1]

[1] *Department of Mechanical Engineering, Graduate School of Natural and Applied Sciences, Gazi University, Ankara, TURKEY*

E-mail: arincd@gmail.com

Abstract

Contraction or expansion of printed circuit boards (PCB's) due to thermal effects can damage solder joints or directly cause failures due to deformations on the PCB itself. In this study, a PCB used in a missile being carried on an unmanned aerial vehicle (UAV) is being examined. Finite element analysis is conducted to determine the time for the PCB to reach the minimum temperature specification limit (-35°C) in UAV cruising altitudes. A specimen was cut-out from the PCB and subjected to cold test chamber using the temperature and time data. Strain data from the sample are gathered using a strain gauge and a data acquisition system. Obtained strain values are compared to industry standards to see if there is failure risk or not. Strain levels are found out to be fairly under acceptable standard limits. Moreover, thermal expansion values obtained during the tests can be used in applications using similar type of PCB's.

Keywords: Missile, Strain, Pcb, Cold, Contraction

Figure 1. Experiment plan.

A flat PCB part is cut out and a FRA-1-11 strain gauge is applied on the specimen. Thermocouple is applied on the opposite side of the PCB. Wheatstone bridge is established for fine reading of strain data. As there is only one strain gage in the experiment, quarter bridge method is used.

Figure 2. Wheatstone bridge and Quarter Bridge strain gage circuit respectively.

In Wheatstone bridge, if R1 = R2 = R3 = R4 or R1 x R3 = R2 x R4 is known, Output voltage is zero regardless of the input voltage. If one of the resistances changes, an output voltage occurs, which can be acquired and interpreted as strain in software. [7]

$$e = \frac{1}{4}\frac{\Delta R_1}{R_1}E \qquad (1)$$

As temperature changes during experiment, strain gage properties also differ. Strain gage material itself also expands and contracts under temperature changes and this causes misinterpretation of the output data. To overcome this problem, strain gage temperature correction polynomial that is provided in strain gage datasheet is implemented in software, therefore providing a pure result.

$$\varepsilon_{T/O} = A_0 + A_1T + A_2T^2 + A_3T^3 + A_4T^4 \qquad (2)$$

3. RESULTS AND DISCUSSION

Temperature data that is obtained from thermocouple is recorded as 28,3°C and changes to -34,8°C in along the experiment. As a tri -3axial strain gage is used, results are obtained in different directions. Directions are provided in Figure 3

Figure 3. Strain directions on PCB

Data is obtained in 100Hz and simplified to 1/10Hz. Results are plotted versus time.

Figure 4. Strain results in different directions

Maximum strain is measured as -350 μ in direction 3. After further examining the results, it is clearly seen that PCB does not behave isotropic, which is expected. Using this data, thermal expansion coefficient is also calculated. To determine thermal expansion coefficient with strain gages, a prior or simultaneous experiment should be conducted with a known material [8]. In this study, a prior strain gage calibration test results that is provided in datasheet will be used. Calibration was done on SS400 steel.

$$\alpha_S - \alpha_R = \frac{(\varepsilon_S - \varepsilon_R)}{\Delta T} \quad (3)$$

In equation 3, α_S is specimen thermal expansion factor, α_R is reference material thermal expansion factor and ε values are strain results. α_S can be found as 15,57x10-6 /°C in maximum strain direction and 13,37x10-6 /°C in mininum strain direction.

4. CONCLUSION

Strain results are compared to IPC standards for possible solder damages and mechanical deformations on board structure. -350 μ with low strain rates are below %10 of the specified limits [9]. Therefore it can be stated that PCB remains safe in mechanical terms after experiencing such temperature changes.

It should be noted that PCB properties can vary due to watermarks and components on pcb structre, therefore obtained cannot be valid for every section of the PCB. Also, PCB layers and material types can

change according to the application, therefore corresponding experiments should be conducted for that specific PCB beforehand.

ACKNOWLEDGMENTS

REFERENCES

1. Arwidson, J. (2013). Thermal Fatigue Life Prediction of Solder Joints in Avionics by Surrogate Modeling a Contribution to Physics of Failure in Reliability Prediction. Department of Science and Technology, Linköping University.

2. Šuba, O., Sýkorová, L., Šanda, Š., & Staněk, M. (2011). Modelling of thermal stresses in printed circuit boards. Recent Researches in Automatic Control - 13th WSEAS International Conference on Automatic Control, Modelling and Simulation, ACMOS'11, 173–176.

3. Hertl, M, Fayolle, R., Weidmann, D., Lecomte, J.-C., Hertl --, M., Fayolle -Diane, R., & Lecomte, W.-J.-C. (2006). Thermal Stress Failures: A New Experimental Approach For Prediction and Prevention. Proceedings from 12th International Workshop on Thermal Investigations of IC's, 169-174.

4. Hertl, Michael, & Weidmann, D. (2010). Advanced assessment of thermal stress related failure modes occurring during the assembly of high pin count BGAs on PCBs. Electronics System Integration Technology Conference, ESTC 2010 - Proceedings. https://doi.org/10.1109/ESTC.2010.5643010

5. Geczy, A., Fejos, M., Tersztyanszky, L., Kemler, A., & Szabo, A. (2014). Investigating Printed Circuit Board shrinkage during reflow soldering. Proceedings of the 2014 37th International Spring Seminar on Electronics Technology, ISSE 2014, 215–220.

6. Dash, P. K., Mary Thraza, M., & Babithakodavanla. (2018). Modelling and simulation of effect of component stiffness on dynamic behaviour of printed circuit board. International Journal of Mechanical and Production Engineering Research and Development, 8(2), 307–314.

7. Gayevoy, A. v, & Lissel, S. L. (2005). Strain reading correction for apparent strain and thermal expansion coefficient of masonry and brick. 10th Canadian Masonry Symposium, Banff, Alberta

8. Poore, M. W., & Kesterson, K. F. (1977). A strain-gage technique for measuring the thermal expansion of solids. Y-2065. Oak Ridge, Tenessee, Union Carbide

9. İnternet: IPC. URL: http://www.ipc.org/4.0_Knowledge/4.1_Standards/IPC-WP-011.pdf, Son Erişim Tarihi: 03.09.2019

DETERMINATION OF VARIOUS ELEMENT LEVELS IN SOME HONEYS PRODUCED IN BINGOL PROVINCE

T. Dastan[1]*, İ. Timur[2], S. DurnaDastan[2]

[1]Department Medical Services and Techniques, Yildizeli Vocational School, Sivas Cumhuriyet University, Sivas, TURKEY

[2]Department of Biology, Faculty of Science, Sivas Cumhuriyet University, Sivas, TURKEY

E-mail*: tdastan@cumhuriyet.edu.tr

Abstract

Honey is produced by honey bees (*Apis mellifera*) by using nectar secreted from the flowers or other living parts of the plants. It is a natural, sweet and functional food produced by collecting, changing the compositions, storing in the honeycomb cells and maturing the nectars by honey bees. The chemical composition of honey varies according to geographical and climatic conditions, environmental factors and plant diversity. Inorganic compounds known to be present in honey are potassium (K), calcium (Ca), magnesium (Mg), copper (Cu), manganese (Mn), iron (Fe), chloride (Cl), sulfur (S), phosphorus (P) and silicium (Si). However, the mineral content of honey varies according to the geographical characteristics of the region where it is produced. In this research, metal contents were monitored by flame atomic absorption spectrometer (FAAS) equipped with a D2 background correction. By using these calibration graphs, the quantities of the relevant metals in the honey samples were determined. The amounts of metal elements in honeys are as follows respectively with their maximum and minimum values: Zn (142.0-446.2 μg kg^{-1}), Pb (13.6- 301.2 μg kg^{-1}), Mn (10.4- 229.5 μg kg^{-1}), Co (28.4- 278.4 μg kg^{-1}), Cd (21.4- 275.9 μg kg^{-1}), Cu (39.9- 289.5 μg kg^{-1}), V (10.5- 274.7 μg kg^{-1}), Fe (128.5- 484.2 μg kg^{-1}). The mineral content and trace elements of honey can be used to determine the geographical origin of honey.

Keywords: Atomic absorption, metal element content, honey

1. INTRODUCTION

Nectar collected by bees from plant sources converts honey into metabolic biochemical process in a natural environment in the hive. There are approximately 10000 -40000 bees in each hive and each bee get out of the hive for 10-15 times a day, and for each exit, bees collects nectar and pollen from 80-100 flowers [1,2]. There are approximately more than 200 kinds of ingredients in honey contents. Honey is an important functional food with its nutritious and terapotic properties due to ingredients like vitamins, minerals, organic acids, flavonoids, phenolic acids, amino acids and enzymes [3,4]. The chemical composition of honey varies by geographical and botanical source. But basically honey is formed about 82% carbohydrate, 17% water, 0.7% mineral, 0.3% protein, vitamins, organic acids, phenolic compounds and free macro and micro components [3-7]. Also honey is very rich source of minerals with the potassium, phosphorus, iron, magnesium, sodium, manganese, chlorine, sulfur and iodine mineral composition. In some studies, honey samples have heavy metals inside, and therefore bee products can be one of the indicators of pollution and it is inexpensive and effective to determine and to follow up the environmental pollution with this method [1,2]. Today, environmental pollution from industry threatens bees and bee products. Metaller in the environment come mainly from industry and traffic and can contaminate bee colonies and bee products. Lead (Pb) and cadmium (Cd) are the most important heavy metal impurities for the bee products. Pb compounds on air comes mainly from traffic and directly contaminates nectar and bees but does not move from plants. Cd compound from industry and wastes is transported from soil to plants, which contaminates nectar, honey and the other bee products [2,8].

2. MATERIAL AND METHODS

In this study, it is aimed to determine the amount of some of the elements in honey samples collected from Bingol province and surrounding villages which is widely used in beekeeping activities in Turkey by using spectrophotometrical analysis. Honey samples included in the study were obtained from various bee breeders engaged in beekeeping activities in a total of 6 different regions of Bingol province and its vicinity. Metal contents were monitored by flame atomic absorption spectrometer (FAAS, Shimadzu AAS-6300 model) equipped with a D_2 background correction. Calibration graphs are prepared using the aqueous standards of each analyte. By using these calibration graphs, the quantities of the relevant metals in the honey samples were determined.

3. RESULTS AND DISCUSSION

In this study, the amounts of metal elements in honeys from different localities were obtained as follows respectively with their maximum and minimum values: Zn (142.0-446.2 µg kg-1), Pb (13.6- 301.2 µg kg-1), Mn (10.4- 229.5 µg kg-1), Co (28.4- 278.4 µg kg-1), Cd (21.4- 275.9 µg kg-1), Cu (39.9- 289.5 µg kg-1), V (10.5- 274.7 µg kg-1), Fe (128.5- 484.2 µg kg-1). The quantities of the different elements found in each honey sample are detailed in the Table 1. The mineral content and trace elements of honey can be used to determine the geographical origin of honey. It also gives an idea about the pollution in the environment where the bee feeds according to the amount of heavy metal in honey. Generally the quantities of Lead (Pb), Cadmium (Cd), Iron (Fe), Zinc (Zn), Aluminum (Al), Mercury (Hg) and Copper (Cu) were investigated in different honey brands and other bee products according to the literature [8-10]. Pb levels were found between 0.001-1.8 mg/kg in different honey samples and in different countries. In honey studies conducted in different countries, Cd levels were found to be different values in the range of 0.001 - 0.113 mg/kg [2,8,10]. In a study conducted in Turkey found some metal levels in a variety of honey brands were as follows, respectively: Cd (0.216-1.553 mg/kg), Pb (0.699- 12.3 mg/kg), Fe (13.45-97.3 mg/kg), Zn (3.82- 17.96 mg/kg), Al (0.038-4.57 mg/kg), Hg (0.25-0.852 mg/kg), Cu (0.011- 0.098 mg/kg) [8]. In this study, the amounts of different metal elements found in different honey samples were found to be quite low compared to the studies given in the literature in general. However, the amount of Cu metal in honey samples in our study was found to be higher than other studies in the literature (Table 1).

No standards have been established for the amount of metal contents that should be present in the honey samples. The greatest concern was in the past due to the amount of Pb. However, after the prohibition of leaded gasoline, this concern gradually disappears. Rather than honey samples, bees retain the Pb element more in their own bodies. Therefore, bees are considered as bioindicators for metal gathering for a 3 km radius around them. The element Pb is not a problem in honey, but due to its accumulation, it is necessary to pay attention to propolis and keep it away from contaminated areas with Pb. Also the levels of Ni, Hg and other undesirable metals likely to be present in honey are quite low [2,8].

…

Table 1. The metal amounts of the various honey samples from Bingol province.

Sample	Added (µg kg-1)	Zn(µg kg-1)		Pb(µg kg-1)		Mn(µg kg-1)		Co(µg kg-1)		Cd(µg kg-1)		Cu(µg kg-1)		V(µg kg-1)		Fe(µg kg-1)	
		Found	Recovery%	Found	Recovery%	Found	Recovery%	Found	Recovery%	Found	Recovery%	Found	Recovery%	Found%	Recovery%	Found	Recovery%
Bingol province-Genc district-Sancak village	-	167.4	-	13.6	-	10.4	-	88.2	-	44.6	-	68.2	-	10.5	-	229.4	-
	200	361.2	96.9	206.6	96.5	206.0	97.8	278.4	95.1	236.2	95.8	260.4	96.1	198.3	93.9	422.4	96.5
Diyarbakir province-Hani district	-	223.6	-	45.8	-	18.8	-	61.7	-	28.3	-	46.7	-	18.2	-	163.7	-
	200	408.0	92.2	233.6	93.9	215.5	98.4	254.3	96.3	218.5	95.1	240.5	96.9	207.6	94.7	355.9	96.1
Bingol province-Genc district-Servi village	-	175.7	-	66.2	-	29.4	-	39.1	-	79.4	-	102.1	-	26.8	-	188.4	-
	200	371.5	97.9	260.6	97.2	222.6	96.6	232.3	96.9	272.2	96.4	289.5	93.7	220.6	96.9	383.0	97.3
Bingol province-Genc district	-	255.4	-	56.9	-	31.3	-	28.4	-	82.7	-	77.1	-	35.9	-	294.2	-
	200	446.2	95.4	251.7	97.4	229.5	99.1	224.0	97.8	275.9	96.9	274.9	98.9	230.3	97.2	484.2	95.0
Bingol province-Solhan district	-	142.0	-	105.4	-	17.5	-	71.8	-	29.4	-	39.9	-	19.5	-	128.5	-
	200	338.6	98.3	301.2	97.9	214.1	98.3	264.4	96.3	224.4	97.5	232.5	96.3	210.5	95.5	325.9	98.7
Bingol province-Kigi district	-	178.5	-	27.2	-	26.9	-	30.9	-	21.4	-	78.4	-	77.9	-	225.4	-
	200	374.5	98.0	224.6	98.7	220.1	96.9	225.9	97.5	210.0	94.3	271.2	96.4	274.7	98.4	423.8	99.2

4. CONCLUSION

In our study, the examined metal elements in the honey samples were generally found lower than the metal ranges from the literature. Only Cu metal value was obtained slightly higher according to the literature knowledge. Honey has a very complex structure due to the differences in the substances it carries. It shows quite different structures according to various regions and times of acquisition.

REFERENCES

[1] Nisbet, C., Güler, A., Yarım, G.F., Cenesiz, S., Ardalı, Y., Çevre ve flora kaynaklarının arı ürünlerinin mineral madde içerikleriyle ilişkisi, Turkish Journal of Biochemistry, 38(4), 494-498, 2013.

[2] Mutlu, C., Erbaş, M., Arslan Tontul, S., Bal ve diğer arı ürünlerinin bazı özellikleri ve insan sağlığı üzerine etkileri, Akademik Gıda, 15(1): 75-83, 2017.

[3] Özmen, N., Alkın, E., Balın antimikrobiyal özellikleri ve insan sağlığı üzerine etkileri, Uludağ Arıcılık Dergisi, 4,155-160, 2006.

[4] Spiloti, E., Jaakkola, M., Tolonen, T., Lipponen, M., Virtanen, V., Chinou, I., Kassi, E., Moutsatsou, P., Phenolic acid composition, antiatherogenic and anticancer potential of honeys derived from various regions in Greece, PloS One, 9(4), 2014.

[5] Karabagias, I.K., Badeka, A.V., Kontakos, S., Karabournioti, S., Kontominas, M.G., Botanical discrimination of Greek unifloral honeys with physico-chemical and chemometric analyses, Food Chemistry, 165, 185-190, 2014.

[6] İslam, A., Khalil, I., Islam, N., Moniruzzaman, M., Mottalib, A., Sulaiman, S.A., Gan, S.H., Phsicochemical and antioxidant properties of Bangladeshi honeys stored for more than one year , BMC Complementary and Alternative Medicine, 12(1), 177, 2012.

[7] Moniruzzaman, M., Rodriguez, I., Ramil, M., Cela, R., Sulaiman, S., Gan, S., Assessment of gas chromatography time of flight accurate mass spectrometry for identification of volatile and semi volatile compounds in honey , Talant, 129, 505-515, 2014.

[8] Sireli U.T, Iplikcioglu-Cil G., Yurdakok-Dikmen B., Filazi, A., Ulker, H., Detection of metals in different honey brands, Kafkas Univ Vet Fak Derg, 21 (6), 915-918, 2015.

[9] Bogdanov, S., Contaminants of bee products, Apidologie, 38(1), 1-18, 2006.

[10] Bogdanov, S., Jurendic, T., Sieber, R., Gallmann, P., Honey for nutrition and health: A review. J Am Coll Nutr, 27, 677-689, 2008.

RESTORATION WORKS OF İBRAHİM PİLAVCI HOUSE BELONGING TO CIVIL ARCHITECTURE EXAMPLES IN TARAKLI

Ö. Özkan Önür[1], Ö. Yerli[2]

[1]*Department of Coll Interdisciplinary Composite Material Technologies, Institute of Science, Düzce University, Düzce, Turkey*
[2]*Department of landscape* architecture, *Düzce University, Düzce, Turkey*

E-mail: ozkanonurozlem@gmail.com

Abstract

Wood, which constitutes the original texture of Anatolian architecture, is an important building material that maintains its sustainability even today, transferring its existence to future generations throught history. It is useful in historical buildings due to its features such as processing, obtaining and easy transportation. Wooden structures are more common in forested areas. İbrahim Pilavcı House, which is one of the examples of civil architecture of Taraklı architecture, the interior layout, construction system, roof features and environmental compatibility with the original quality. Considering these characteristics, the damage status of the building was examined and information was obtained by interviewing the landlord. İbrahim Pilavcı House's rolove, restitution, restoration projects were prepared and their facade features, plan properties were supported with pictures and reports were prepared and documented with the approval of Kocaeli Regional Cultural Heritage Protection Board. After the architectural, structural and structural analysis of İbrahim Pilavcı House, the techniques applied during the application phase and the use of natural materials without deteriorating the originality of the structure were controlled under the supervision of the repair techniques and the works were completed.

Keywords: Wood, Taraklı, Restoration.

1. INTRODUCTION

Figure 1. General view from Taraklı [1].

Taraklı is one of the important settlements that shows the qualified examples of the traditional Ottoman settlement texture in Anatolia and can survive the majority of the tissue to date [2]. Taraklı, which is connected to Sakarya province, is one of the districts that exemplify the Western Black Sea architecture. The traditional architectural texture of Taraklı has survived to the present day with its necessary features [4].

In Taraklı architecture, pine tree species is generally used. Resin of these trees causes high strength. Taraklı architecture contains beautiful examples of wooden construction art.

Figure 2. Taraklı architecture [3].

Figure 3. Taraklı architecture [3].

İbrahim Pilavcı House, which is one of the examples of Taraklı's civil building, has been chosen as the subject of the study and its physical structure, historical and architectural values have been examined together with its environment for an effective restoration.

2. RESTORATION WORKS OF IBRAHIM PILAVCI HOUSE

2.1. Location and General Characteristics of the Building

İbrahim Pilavcı House; Adapazarı province Taraklı district, Ulu Mosque Quarter, Hamam is located on the street. The structure is made of wood carcass technique on a stone foundation in a sloping land and consists of ground and first floor. The exact date of the construction has not been reached. However, it is estimated that it was built in 1950 [5].

Figure 4. Plan example of İbrahim Pilavcı House [5].

2.2. Facade Features of the Building

2.2.1. Southern Facade

Figure 5. İbrahim Pilavcı House's view rolove of the southern facade.

The southern facade of İbrahim Pilavcı House is the most spectacular facade of the building. Entrance is provided from the ground floor. On the first floor there is a wooden balcony with a triangular pediment. There are a total of 10 windows on this facade of the building.

The balcony is made of wood with a triangular pediment. There are breaks on the balustrades of the balcony and decay in the wooden material.

Figure 6. İbrahim Pilavcı House of balcony view and detailing system.

2.2.2. Western Facade

Figure 7. İbrahim Pilavcı House's view rolove of the western facade.

2.2.3. Northern Facade

Figure 8. İbrahim Pilavcı House's view rolove of the northern facade.

2.2.3. Eastern Facade

Figure 9. İbrahim Pilavcı House's view rolove of the eastern facade.

2.3. Plan Features of the Building

All the ceilings of the ground floor and first floor spaces are wooden beamed flooring. Most ceilings have deformations.

Figure 10. İbrahim Pilavcı House's view rolove of ground floor and first floor ceiling plans.

Figure 11. Ceiling view of İbrahim Pilavcı House.

The ground floor rooms have wooden flooring, kitchen, warehouse, bathroom and hall flooring floors are in concrete. The floors of the spaces of the first floor are also wooden covering. There are breaks and decay on wooden flooring.

Figure 12. İbrahim Pilavcı House of floor and first floor flooring plans.

Figure 13. İbrahim Pilavcı House of flooring.

All the windows of the building are guillotine and rectangular wooden frame.

Figure 14. İbrahim Pilavcı House rolove of window detailing.

Figure 15. İbrahim Pilavcı House of window views.

The entrance to the structure is provided by two-leaf wooden doors. Above the door there are overhead window divided into 4 sections with wooden laths. The exterior of the door is painted. In time, cracks in the paints have been formed and degradation is possible due to atmospheric conditions.

Figure 16. İbrahim Pilavcı House of rolove entrance door detailing.

Figure 17. İbrahim Pilavcı House of entrance door from inside and outside views.

The interior doors of the building are made of wood. The exterior surfaces of some doors are painted.

Figure 18. İbrahim Pilavcı House of door views.

The walls of the building are mud plaster on mudbrick filling between wooden carcass. There are serious damage to the wall caused by atmospheric conditions.

Figure 19. İbrahim Pilavcı House of wall views.

2.3.1. Ground Floor Plan

Figure 20. İbrahim Pilavcı House of ground floor plan.

There is a wooden staircase leading from the ground floor to the top floor. There is also a worktop on stone foundation and a demolished stove in the kitchen.

Figure 21. İbrahim Pilavcı House of stairs and ve kitchen views.

2.3.2. First Floor Plan

Figure 22. Ibrahim Pilavci House of rolove first floor plan.

This floor has a plan with a central sofa. The main feature of the plan type with a central sofa is that surrounding by rooms. Room entrances are chamfer. The sofa and rooms have cedar.

Figure 23. İbrahim Pilavcı House of cedar and cupboard views.

Figure 24. Ibrahim Pilavci House of first floor interior views.

Figure 25. İbrahim Pilavcı House of first floor sofa view.

2.3.3. Roof Plan

Figure 26. İbrahim Pilavcı House of rolove roof plan.

The roof of the structure has a plan feature with a broken roof. Generally, this type of plan is encountered in the buildings with middle sofa. The roof material is alaturka tile and the construction elements are wooden.

Figure 27. İbrahim Pilavcı House of roof views.

2.3.4. Section Views of the Structure

Figure 28. İbrahim Pilavcı House of rolove A-A section and B-B section.

3. RESTORATION PROJECT

The house, which is architecturally and structurally problematic, has serious damages. Taking these damages into consideration, rolove, restitution and restoration projects were prepared.

Figure 29. İbrahim Pilavcı House of restoration ground floor and first floor plan.

Figure 30. İbrahim Pilavcı House's view restoration of ground floor and first floor ceiling plans.

Figure 31. İbrahim Pilavcı House of restoration roof plan and roof view.

Figure 32. İbrahim Pilavcı House of restoration A-A section and B-B section.

Figure 33. İbrahim Pilavcı House's view restoration of the southern facade and eastern facade.

Figure 34. İbrahim Pilavcı House's view rolove of the western facade and northern facade.

Figure 35. İbrahim Pilavcı House of restoration entrance door detailing.

Figure 36. İbrahim Pilavcı House of restoration wood window detailing.

4. RESTORATION PROPOSAL

First, roof tiles and damaged construction elements should be removed and replaced with new ones, It should be made in such a way that the original construction system and insulating material. Walls should be scrapped to see the state of the carrier system and should be replaced with appropriate material. Elements in good condition should also be cleaned and maintained on site if necessary. Deformed elements should be replaced with materials suitable for the original material. Wall fillings should be made with appropriate materials and techniques, interior walls should be plastered with Baghdadi plaster technique. Wooden windows should be repaired without deteriorating the originality, and windows in very bad condition should be replaced with new ones. Wooden doors and floors should be maintained and damaged ceilings caused by water intake from the roof should be repaired. Stair steps and railings should be rebuilt without deteriorating the originality. The cupboards and cedars in the rooms should be preserved and re-used with on-site repairs. In the facade coating, the ground floor and the first floor should be made as lime whitewash over the adobe.

The restoration of the Ibrahim Pilavci House, which was supported by the project and the pictures, was completed a few years after the preliminary preparations and the analysis studies were carried out and the application was completed under the supervision of the authorities.

Figure 37. İbrahim Pilavcı House of after restoration views [23].

5. CONCLUSION

The restoration works applied to restore the original appearance of the historical wooden structures, fittings and furniture should have an important place in preserving and transferring the wood material to future generations. During the restoration, it should be aimed to introduce surface cleaning methods that will remove the dirty and damaged area from the surfaces of the wood material and which are based on human and environmental health [17].

As a result; Precautions should be taken for the long-lasting wooden and masonry structures without disturbing the original texture of traditional Turkish houses and necessary maintenance suggestions should be made and maintained. Spatial, formal, structural features and adaptation to the environment of cultural assets should be repaired with original materials.

REFERENCES

[1] https://yandex.com.tr/gorsel/search?text=tarakl%C4%B1&stype=image&lr=103843&source=wiz

[2] F. Seymen, ''Taraklı'daki geleneksel sivil mimaride kullanılan yapım teknikleri ve Sadık Özen Evi restorasyon önerisi,'' İstanbul, 2008.

[3] https://yandex.com.tr/gorsel/search?text=tarakl%C4%B1&pos=4&img_url=https%3A%2F%2Fwww.gur bayturizm.com%2Fturresim%2F443_b.jpg&rpt=simage.

[4] S.S. Özkan, ''Taraklı'nın fiziksel ve tarihsel dokusu, sivil ve anıtsal mimarlık örnekleri Hacı Rıfatlar Konağı restorasyonu,'' İstanbul, 2008.

[5] Taraklı Belediyesi Arşivi, Taraklı, 2009.

[6] www. tr.wikipedia.org/wiki/Tarakl%C4%B1,_Sakarya, Aralık 2008.

[7] Sakarya Irmak Dergisi, 2004.

[8] www.tarakli.gov.tr/?anka.wesscom=sitesayfasi&SiteSayfaAdi=Taraklı,Ocak 2009.

[9] www.tarakli.com/mediac/400_0/media/harita1.jpg,Mart 2009.

[10]https://yandex.com.tr/gorsel/search?text=tarakl%C4%B1%20hac%C4%B1%20r%C4%B1fatlar%20kon a%C4%9F%C4%B1.

[11]https://yandex.com.tr/gorsel/search?text=tarakl%C4%B1%20fenerli%20evi

[12]https://yandex.com.tr/gorsel/search?text=tarakl%C4%B1%20%C3%A7ak%C4%B1rlar%20kona%C4% 9F%C4%B1.

[13]Tuna, F., Akçakoyunluoğlu, Yedi İklim Dergisi, Sakarya, 2004.

[14] Demir, E., ''Taraklı'da Tarihi Çevre Değerlerini Koruma Amaçlı Bir İnceleme,'' İstanbul, 1988.

[15] Taraklı Kaymakamlığı, ''Tarihin Doğayla Buluştuğu Yer Taraklı,'' Sakarya, 2003.

[16] http://sutod.selcuk.edu.tr/sutod/article/viewFile/173/262.

[17] Ahunbay, Z., Tarihi Çevre Koruma ve Restorasyon, Yapı Yayın, İstanbul, 1998.

[18] Acun, H. Sakarya ili Taraklı ilçesi ve Yunus Paşa Camii, Ankara, 1996.

[19] Şentürk, M. H., ''Osmanlılar döneminde Sakarya,'' Sakarya ili tarihi, c.1, s.181, 2005.

[20] Temel kuran, T., Çevik, M. Evliya Çelebi Seyahatnamesi, 1984.

[21] Çetin, Y. ''Sakarya'da Türk Mimari Eserleri,''2008.

[22] Ö. Özkan, ''Taraklı'daki sivil mimarlık örnekleri ile Halim Düzgün Evi'nin Proje ve Ali Pektaş Evi'nin Restorasyon Çalışmaları,'' Sakarya, 2009.

[23] https://yandex.com.tr/gorsel/search?text=tarakl%C4%B1da%20yap%C4%B1lan%20restorasyon%20uygulamalar%C4%B1&stype=image&lr=103843&source=wiz

A NOTE ON ABSOLUTE FACTORABLE MATRIX SUMMABILITY METHOD

F.Gökçe[1], M.A.Sarıgöl[2]

[1,2]*Department of Mathematic, Faculty of Arts and Sciences, Pamukkale University, Denizli, TURKEY*

E-mail: fgokce@pau.edu.tr

Abstract

In this study, we obtain necessary and sufficient conditions for $\left|A_f, \theta_n\right|_k \implies \left|B_f, \varphi_n\right|_s$ for the case $1 < k \leq s < \infty$, where θ, φ are positive sequences and $\left|A_f, \theta_n\right|_k$, $\left|B_f, \varphi_n\right|_k$ are absolute factorable summabilities. Also, in the special cases, we obtain some well-known results.

Keywords: Summability Method, Factorable matrix, Comparison of methods

1. INTRODUCTION

Let X and Y be two subspaces of ω and $A = (a_{n\nu})$ be an arbitrary infinite matrix of complex numbers. By $A(x) = \big(A_n(x)\big)$, we denote the A −transform of the sequence $x = (x_\nu)$, i.e.,

$$A_n(x) = \sum_{\nu=0}^{\infty} a_{n\nu}\, x_\nu,$$

provided that the series converges for $n \geq 0$. Then, A defines a matrix transformation from X into Y, it is written that $A \in (X, Y)$, or $A: X \to Y$, if $Ax = \big(A_n(x)\big) \in Y$ for every $x \in X$.

Let $\sum x_\nu$ be a given infinite series with its n-th partial sum s_n, θ be any positive sequence and $1 \leq p < \infty$. If

$$\sum_{n=1}^{\infty} \theta_n^{p-1} |A_n(s) - A_{n-1}(s)|^p < \infty \tag{1}$$

then, the series $\sum x_\nu$ is said to be summable $|A, \theta_n|_p$ [5].

Suppose that A and B are two summability methods. If every series summable by the method A is also summable the method B, it is said that B includes A and written that $A \Longrightarrow B$. If each method includes the other one, then we say that these methods are equivalent.

Note that if we take the weighted mean matrix instead of A in (1), the summability $|A, \theta_n|_p$ is reduced to the summability $|\bar{N}, q_n, \theta_n|_p$, $p \geq 1$, [8]. Also, using this method, the following space

$$\big| \bar{N}_q^\theta \big|_p = \left\{ x = (x_\nu) : \sum_{n=1}^{\infty} \theta_n^{p-1} \left| \frac{q_n}{Q_n Q_{n-1}} \sum_{\nu=1}^{n} Q_{\nu-1} x_\nu \right|^p < \infty \right\},$$

was introduced and studied [5]. In this situation, the series $\sum x_\nu$ is summable $|\bar{N}, q_n, \theta_n|_p$ if and only if the sequence $x = (x_\nu) \epsilon \big| \bar{N}_q^\theta \big|_p$. Further, the summability $|\bar{N}, q_n, \theta_n|_p$ was extended by Hazar and Gökçe [3] to the factorable summability $\big| A_f, \theta_n \big|_k$ as follows: The series is summable $\big| A_f, \theta_n \big|_k$ if

$$\sum_{n=1}^{\infty} \left| \theta_n^{1/k^*} \hat{a}_n \sum_{\nu=1}^{n} a_\nu x_\nu \right|^k < \infty,$$

where θ is a sequence of positive numbers. One knows that a factorable matrix A is given by

$$a_{n\nu} = \begin{cases} \hat{a}_n a_{\nu,} & 1 \leq \nu \leq n \\ 0, & \nu > n \end{cases}$$

where $(\hat{a}_n)$ and (a_v) are any sequence of real numbers.

Also, it is clear that if $\hat{a}_n = p_n/P_n P_{n-1}$ and $a_v = P_{v-1}$ ($\theta_n = P_n/p_n$ and $\theta_n = n$), then we get the summability $|\bar{N}, p_n, \theta_n|_k$ ($|\bar{N}, p_n|_k$ [2] and $|R, p_n|_k$ [7], respectively) [8].

2. MATERIAL AND METHODS

The aim of this study is to obtain necessary and sufficient conditions for $\left|A_f, \theta_n\right|_k \implies \left|B_f, \varphi_n\right|_s$ for the case $1 < k \leq s < \infty,$ where θ and φ are positive sequences. Also, in the special cases, we obtain some well-known results.

Firstly, we remind Bennett's theorem [1] which plays an important roles in proving our theorem.

Theorem A Let $1 < p \leq q < \infty$, a and b be sequences of non-negative numbers, and let A be a factorable matrix. Then the following conditions are equivalent.

(i) A maps l_p into l_q.

(ii) There exists K_1, such that, for $m = 1,2, ...,$

$$\sum_{n=1}^{m} \left(a_n \sum_{k=1}^{n} b_k^{p^*} \right)^q \leq K_1 \left(\sum_{k=1}^{m} b_k^{p^*} \right)^{\frac{q}{p}}.$$

(iii) There exists K_2, such that, for $m = 1,2, ...,$

$$\left(\sum_{n=m}^{\infty} a_n^q \right)^{1/q} \left(\sum_{k=1}^{m} b_k^{p^*} \right)^{1/p^*} \leq K_2.$$

(iv) There exists K_3, such that, for $m = 1,2, ...,$

$$\sum_{k=m}^{\infty} \left(b_k \sum_{n=k}^{\infty} a_n^q \right)^{p^*} \leq K_3 \left(\sum_{n=m}^{\infty} a_n^q \right)^{p^*/q^*},$$

[1].

3. RESULTS AND DISCUSSION

Theorem B Let $1 < k \leq s < \infty$, θ and φ be sequences of positive terms. Then, $\left|A_f, \theta_n\right|_k \implies \left|B_f, \varphi_n\right|_s$ if and only if

(i) $\left(\dfrac{\varphi_n^{\frac{1}{s^*}} b_n \hat{b}_n}{\theta_n^{\frac{1}{k^*}} a_n \hat{a}_n} \right) = O(1)$

(ii) There exists K, such that, for $m = 1,2, ...,$

$$\left(\sum_{n=m}^{\infty} \varphi_n^{\frac{s}{s^*}} \hat{b}_n^s \right)^{1/s} \left(\sum_{v=1}^{m} \frac{1}{\theta_v \hat{a}_v^{k^*}} \left(\Delta \frac{b_v}{a_v} \right)^{k^*} \right)^{1/k^*} \leq K,$$

where

$$\Delta\frac{b_v}{a_v} = \frac{b_v}{a_v} - \frac{b_{v+1}}{a_{v+1}}.$$

Proof Let $X = (X_n)$ and $Y = (Y_n)$ be the transformation sequences of the series $\sum x_v$ summable by the methods $\left|A_f, \theta_n\right|_k$ and $\left|B_f, \varphi_n\right|_s$, respectively, i.e.,

$$X = (X_n) = \left(\theta_n^{\frac{1}{k^*}}\hat{a}_n \sum_{v=1}^n a_v x_v\right),$$

$$Y = (Y_n) = \left(\varphi_n^{\frac{1}{s^*}}\hat{b}_n \sum_{v=1}^n b_v x_v\right).$$

Then, $X\epsilon l_k$ and $Y\epsilon l_s$. Now, since

$$x_n = \frac{1}{a_n}\left(\frac{X_n}{\hat{a}_n\theta_n^{1/k^*}} - \frac{X_{n-1}}{\hat{a}_{n-1}\theta_{n-1}^{1/k^*}}\right),$$

we get

$$Y_n = \varphi_n^{\frac{1}{s^*}}\hat{b}_n \sum_{v=1}^n b_v x_v = \varphi_n^{\frac{1}{s^*}}\hat{b}_n \sum_{v=1}^n b_v \frac{1}{a_v}\left(\frac{X_v}{\hat{a}_v\theta_v^{1/k^*}} - \frac{X_{v-1}}{\hat{a}_{v-1}\theta_{v-1}^{1/k^*}}\right)$$

$$= \frac{\varphi_n^{\frac{1}{s^*}}b_n\hat{b}_n X_n}{\theta_n^{\frac{1}{k^*}}a_n\hat{a}_n} + \varphi_n^{\frac{1}{s^*}}\hat{b}_n \sum_{v=1}^{n-1} \frac{1}{\theta_v^{\frac{1}{k^*}}\hat{a}_v}\left(\frac{b_v}{a_v} - \frac{b_{v+1}}{a_{v+1}}\right)X_v$$

$$= \sum_{v=1}^n c_{nv} X_v$$

where

$$c_{nv} = \begin{cases} \dfrac{\varphi_n^{\frac{1}{s^*}}\hat{b}_n}{\theta_v^{\frac{1}{k^*}}\hat{a}_v}\left(\dfrac{b_v}{a_v} - \dfrac{b_{v+1}}{a_{v+1}}\right), & 1 \le v \le n-1 \\[4mm] \dfrac{\varphi_n^{\frac{1}{s^*}}b_n\hat{b}_n}{\theta_n^{\frac{1}{k^*}}a_n\hat{a}_n}, & v = n \\[4mm] 0, & v > n. \end{cases}$$

Note that $\left|A_f, \theta_n\right|_k \Rightarrow \left|B_f, \varphi_n\right|_s$ if and only if

$$\sum_{n=1}^{\infty} |Y_n|^s < \infty \text{ whenever } \sum_{n=1}^{\infty} |X_n|^k < \infty,$$

or, equivalently $C = (c_{nv}) \epsilon (l_k, l_s)$. Also, it is clearly that

$$Y_n = \sum_{v=1}^{n-1} d_{nv} X_v + e_{nn} X_n = D_n(X) + E_n(X)$$

where

$$d_{nv} = \begin{cases} \dfrac{\varphi_n^{\frac{1}{s^*}} \hat{b}_n}{\theta_v^{\frac{1}{k^*}} \hat{a}_v} \left(\dfrac{b_v}{a_v} - \dfrac{b_{v+1}}{a_{v+1}} \right), & 1 \le v \le n-1 \\ \\ 0, & v \ge n, \end{cases}$$

$$e_{nv} = \begin{cases} \dfrac{\varphi_n^{\frac{1}{s^*}} b_n \hat{b}_n}{\theta_n^{\frac{1}{k^*}} a_n \hat{a}_n}, & v = n \\ \\ 0, & v \ne n. \end{cases}$$

So, if $D \epsilon (l_k, l_s)$ and $E \epsilon (l_k, l_s)$, then it is clear that $C \epsilon (l_k, l_s)$. Conversely, if $C \epsilon (l_k, l_s)$, then, since l_k and l_s are Banach spaces, $C : l_k \to l_s$ is a bounded linear operatör and so there exists a number M such that

$$\|C(x)\| \le M \|x\|$$

for all $x \epsilon l_k$. Now let $x = (e^{(n)}) \epsilon l_k$. It follows from the last inequality that the conditions (i) of the theorem holds, i.e., $E \epsilon (l_k, l_s)$, which implies that $D \epsilon (l_k, l_s)$. Therefore, we get $D \epsilon (l_k, l_s)$ and $E \epsilon (l_k, l_s)$ if and only if $C \epsilon (l_k, l_s)$, which completes the proof of the theorem together with Theorem A.

In the special cases, by Theorem B, we obtain some well-known results and list as follows:

Corollary 1 Let $1 < k \le s < \infty$, θ and φ be sequences of positive terms. Then, $|\bar{N}, p_n, \theta_n|_k \implies |\bar{N}, p_n, \varphi_n|_s$ if and only if

(i) $\left(\varphi_n^{\frac{1}{s^*}} \theta_n^{-\frac{1}{k^*}} \dfrac{q_n P_n}{Q_n p_n} \right) = O(1)$

(ii) $\left(\sum_{n=m}^{\infty} \varphi_n^{\frac{s}{s^*}} \left(\dfrac{q_n}{Q_n Q_{n-1}} \right)^s \right)^{1/s} \left(\sum_{v=1}^{m} \dfrac{1}{\theta_v} \left| Q_v - \dfrac{q_v P_v}{p_v} \right|^{k^*} \right)^{1/k^*} = O(1).$

Corollary 2 Let $1 < k \le s < \infty$. $|\bar{N}, p_n|_k \implies |\bar{N}, q_n|_s$ if and only if

331

$(i) \qquad (q_v/Q_v)^k (P_v/p_v)^s = O(1)$

$(ii) \qquad \displaystyle\sum_{v=1}^{m} \left| Q_v - \frac{q_v P_v}{p_v} \right|^{k^*} \frac{p_v}{P_v} = O\left(Q_m^{k^*}\right)$

where k^* is the conjugate of k.

Note that, for $p_v = 1$ for all v, the summability $|\bar{N}, p_n|_k$ is reduced to the summability $|C, 1|_k$. So the following results are immediately obtained.

Corollary 3 Let $1 < k < \infty$. *Then,* $|C, 1|_k \implies |\bar{N}, q_n|_k$ if and only if

$(i) \quad nq_n = O(Q_n) \qquad\qquad (ii) \quad \displaystyle\sum_{v=1}^{m} |Q_v - (v+1)q_v|^{k^*} \frac{1}{v} = O\left(Q_m^{k^*}\right).$

Corollary 4 Let $1 < k < \infty$. Then, $|\bar{N}, q_n|_k \implies |C, 1|_k$ if and only if

$(i) \quad Q_n = O(nq_n) \qquad\qquad (ii) \quad \displaystyle\sum_{v=1}^{m} \left| v + 1 - \frac{Q_v}{q_v} \right|^{k^*} \frac{q_v}{Q_v} = O\left(m^{k^*}\right).$

4. CONCLUSION

In this study, it is determined necessary and sufficient conditions for $\left|A_f, \theta_n\right|_k \implies \left|B_f, \varphi_n\right|_s$ for the case $1 < k \leq s < \infty$, where θ, φ are positive sequences and also, in the special cases, given some known results.

REFERENCES

[1] Bennett, G., Some elemantery inequalities, The Quarterly Journal of Mechanics and Applied Mathematics, 38, 401-425, 1987.

[2] Bor, H. , On two summability methods, Mathematical Proceedings of the Cambridge Philosophical Society, 97, 147-149, 1985.

[3] Gökçe, F. , Hazar, G. C, Compact and Matrix Operators on the Spaces $\left|A_f^\theta\right|_k$, Tbilisi Mathematical Journal (in press).

[4] Sarıgöl, M.A., On absolute factorable matrix summability methods. Bulletin of Mathematical Analysis and Applications, 8(1), 1-5, 2016.

[5] Sarıgöl, M.A., On local properties of factored Fourier series, Applied Mathematics and Computation, 216(11), 3386-3390, 2010.

[6] Sarıgöl, M.A., On inclusion relations for absolute weighted mean summability, Journal of Mathematical Analysis and Applications, 181(3), 762-767, 1994.

[7] Sarıgöl, M..A., On the absolute Riesz summability factors of infinite series, Indian Journal of Pure and Applied Mathematics, 23, 881-881, 1992.

[8] Sulaiman, W.T., On summability factors of infinite series, Proceedings of the American Mathematical Society, 115:313-317, 1992.

ON ABSOLUTE LUCAS SERIES SPACES

F. Gökçe[1], M.A. Sarıgöl[2]

[1, 2]Department of Mathematic, Faculty of Arts and Sciences, Pamukkale University, Denizli, TURKEY

E-mail: fgokce@pau.edu.tr

Abstract

In the present study, we introduce the absolute Lucas space $|L_\theta(r,s)|_p$ where $r, s \in \mathbb{R}$, θ be any positive sequence and $1 \le p < \infty$. Then, we give some topological and algebraic properties of this space such as BK-space, norm and show that the absolute Lucas space is isomorphic to the space l_p.

Keywords: Sequence spaces, BK- spaces, Lucas number

1. INTRODUCTION

Let ω be the set of all sequences of complex numbers and $l_p, p \geq 1$, be the set of all p-absolutely convergent series space. A linear subspace of ω is called a sequence spaces. Let X and Y be sequence spaces and $A = (a_{nk})$ be an infinite matrix of complex numbers. If the series

$$A_n(x) = \sum_{k=0}^{\infty} a_{nk} \, x_k$$

converges, for all $x \in X, n \in \mathbb{N}$, then, by $A(x) = (A_n(x))$ we denote the A-transform of the sequence $x = (x_k)$. Also, A defines a matrix mapping from X into Y, if $A(x) = (A_n(x)) \in Y$ for every $x \in X$ and it is shown that $A \in (X,Y)$ or $A: X \longrightarrow Y$. The domain of the matrix A in X, which is a sequence spaces, is defined by

$$X_A = \{x = (x_k) \in \omega : A(x) \in X\}.$$

If X is a complete normed space with continuous coordinates $p_n: X \rightarrow \mathbb{C}, p_n(x) = x_n$ defined by $p_n(x) = x_n$ for all $n \in \mathbb{N}$, then X is called a BK- space.

Let $\sum a_v$ be a given infinite series with its n-th partial sum s_n, θ be any positive sequence and $1 \leq p < \infty$. If

$$\sum_{n=1}^{\infty} \theta_n^{p-1} |A_n(s) - A_{n-1}(s)|^p < \infty \tag{1}$$

then the series $\sum a_v$ is said to be summable $|A, \theta|_p$.

The Lucas sequence (L_n) given by the Fibonacci recurrence relation with different initial condition is defined as follows:

$$L_0 = 2, L_1 = 1, L_n = L_{n-1} + L_{n-2}, n \geq 2.$$

Now, we mention some of the properties of the Lucas numbers [4]:

$$\sum_{k=1}^{n} L_k = L_{n+2} - 3, \quad \sum_{k=1}^{n} L_{2k-1} = L_{2n} - 2,$$

$$\sum_{k=1}^{n} L_{2k} = L_{2n+1} - 1, \sum_{k=1}^{n} L_k^2 = L_n L_{n+1} - 2,$$

$$L_{n-1} L_{n+1} - L_n^2 = 5(-1)^{n+1},$$

$$L_{n-1}^2 + L_n L_{n-1} - L_n^2 = 5(-1)^{n+1}.$$

Further, the Lucas band matrix $\hat{E}(r,s) = (e_{nk}(r,s))$ has been defined in [3] as follows

$$e_{nk}(r,s) = \begin{cases} s\dfrac{L_n}{L_{n-1}}, & k = n-1 \\[2mm] r\dfrac{L_{n-1}}{L_n}, & k = n \\[2mm] 0, & k > n \text{ or } 0 \le k < n-1 \end{cases}$$

where $r, s \in \mathbb{R}$.

The method of generating a new space by means of the matrix domain of a triangle matrix has recently been studied by several authors. In [3], Lucas difference space has been studied. Also, Kara has defined Fibonacci difference sequence space using by Fibonacci band matrix [2]. Moreover, from a different viewpoint, Gökçe and Sarıgöl have introduced absolute Fibonacci series spaces [1].

2. MATERIAL AND METHODS

Let take the Lucas matrix instead of the matrix A in (1). Then, we can write

$$A_n(s) = \sum_{k=1}^{n} e_{nk}(r,s) s_k = \sum_{k=1}^{n} e_{nk}(r,s) \sum_{v=1}^{k} x_v$$

$$= x_n e_{nn}(r,s) + \sum_{v=1}^{n-1} x_v \left(e_{n,n-1}(r,s) + e_{nn}(r,s) \right)$$

$$= x_n r \frac{L_{n-1}}{L_n} + \sum_{v=1}^{n-1} x_v \left(s \frac{L_n}{L_{n-1}} + r \frac{L_{n-1}}{L_n} \right)$$

and the matrix $L = (\ell_{nv})$ corresponding to above transformation is given by

$$\ell_{nv} = \begin{cases} r\dfrac{L_{n-1}}{L_n}, & v = n \\[2mm] s\dfrac{L_n}{L_{n-1}} + r\dfrac{L_{n-1}}{L_n}, & 1 \le v < n-1 \\[2mm] 0, & v > n. \end{cases} \qquad (2)$$

A few calculations give that

$$A_n(s) - A_{n-1}(s) = x_n r \frac{L_{n-1}}{L_n} + \sum_{v=1}^{n-1} x_v \left(s \frac{L_n}{L_{n-1}} + r \frac{L_{n-1}}{L_n} \right) - x_{n-1} r \frac{L_{n-2}}{L_{n-1}} - \sum_{v=1}^{n-2} x_v \left(s \frac{L_{n-1}}{L_{n-2}} + r \frac{L_{n-2}}{L_{n-1}} \right)$$

$$= x_n r \frac{L_{n-1}}{L_n} + x_{n-1} \left(s \frac{L_n}{L_{n-1}} + r \frac{5(-1)^{n+1}}{L_n L_{n-1}} \right) + \sum_{v=1}^{n-2} x_v 5(-1)^n \left(\frac{s}{L_{n-1} L_{n-2}} - \frac{r}{L_n L_{n-1}} \right)$$

$$= \sum_{v=1}^{n} \xi_{nv} \, x_v$$

where

$$\xi_{nk} = \begin{cases} r\dfrac{L_{n-1}}{L_n}, & v = n \\[2mm] s\dfrac{L_n}{L_{n-1}} + r\dfrac{5(-1)^{n+1}}{L_n L_{n-1}}, & v = n-1 \\[2mm] 5(-1)^n \left(\dfrac{s}{L_{n-1} L_{n-2}} - \dfrac{r}{L_n L_{n-1}} \right), & 1 \le v < n-1 \\[2mm] 0, & v > n. \end{cases}$$

So, the absolute Lucas series space can be expressed as

$$|L(r,s)|_p = \left\{ x \in \omega: \ \sum_{n=1}^{\infty} \left| \theta_n^{1/p^*} \sum_{k=1}^{n} \xi_{nk} \, x_k \right|^p < \infty \right\}$$

where p^* is conjugate of p, i.e., $1/p + 1/p^* = 1$, $p > 1$, and $1/p^* = 0$ for $p = 1$.

According to the notation of domain, the absolute Lucas series spaces can be redefined as

$$|L_\theta(r,s)|_p = (l_p)_{E^{(p)} \circ L}.$$

where the matrix $E^{(p)} = (e_{nv}^{(p)})$ is given by

$$e_{nv}^{(p)} = \begin{cases} \theta_n^{\frac{1}{p^*}}, & v = n \\[2mm] -\theta_n^{\frac{1}{p^*}}, & v = n-1 \\[2mm] 0, & v \ne n, n-1. \end{cases} \tag{3}$$

3. RESULTS AND DISCUSSION

Theorem 1 Let $1 \le p < \infty$ and $\theta = (\theta_v)$ be any positive sequence. Then, the set $|L_\theta(r,s)|_p$ is a linear spaces with coordinate-wise addition and scaler multiplication. Also, it is a BK- spaces with respect to norm

$$\|x\|_{|L_\theta(r,s)|_p} = \left\| E^{(p)} \circ L \, (x) \right\|_{l_p}.$$

Proof The proof of the first part of the theorem is a routine verification, and so it is omitted. Further, since the matrices $E^{(p)}$ and L are triangles, $|L_\theta(r,s)|_p = (l_p)_{E^{(p)} \circ L}$ and the space l_p is a BK- space, Theorem 4.3.2 of Wilansky [6] implies that the space $|L_\theta(r,s)|_p$ is a BK- space.

Theorem 2 Let $1 \leq p < \infty$ and $\theta = (\theta_v)$ be any positive sequence. Then, there exists a linear isomorphism between the spaces $|L_\theta(r,s)|_p$ and l_p.

Proof To prove this, we should show the existence of a linear bijection between the spaces $|L_\theta(r,s)|_p$ and l_p. Now, we consider the transformations $L: |L_\theta(r,s)|_p \to (l_p)_L$ and $E^{(p)}: (l_p)_L \to l_p$ defined by

$$L(x) = x_n r \frac{L_{n-1}}{L_n} + \sum_{v=1}^{n-1} x_v \left(s \frac{L_n}{L_{n-1}} + r \frac{L_{n-1}}{L_n} \right),$$

$$E^{(p)}(x) = \theta_n^{1/k^*}(x_n - x_{n-1}), n \geq 1.$$

The matrices corresponding these transformations given by (2) and (3) are triangles, it is clear that L and $E^{(p)}$ are linear bijections. So, the composite function is a linear bijection. Moreover, the norm is preserved. This completes the proof of theorem.

4. CONCLUSION

In this study, it has been aimed to introduce the absolute Lucas series space and to show existence of a linear isomorphism between the spaces l_p and $|L(r,s)|_p$.

REFERENCES

[1] Gökçe, F., Sarıgöl, M.A., Some Matrix And Compact Operators Of The Absolute Fibonacci Series Spaces, Kragujevac Journal of Mathematics, 44(2), 273–286, 2020.

[2] Kara, E. E., Some topological and geometrical properties of new Banach sequence spaces. Journal of Inequalities and Applications, 2013(1), 38, 2013.

[3] Karakaş, M., Karakaş, A.M., A study on Lucas difference sequence spaces $l_p(\hat{E}(r,s))$ and $l_\infty(\hat{E}(r,s))$, Maejo International Journal of Science and Technology , 12(1), 70-78, 2018.

[4] Koshy, T., Fibonacci and Lucas Numbers with Applications, John Wiley and Sons, New York, 2011.

[5] M. A. Sarıgöl, On the local properties of factored Fourier series, Applied Mathematics and Computation, 216(11), 3386–3390, 2010.

[6] Wilansky, A., Summability Through Functional Analysis, Mathematics Studies 85, North Holland, Amsterdam, 1984.

INEXTENSIBLE FLOWS OF TIMELIKE CURVES WITH PARALLEL TRANSPORT FRAME IN MINKOWSKI SPACE-TIME

S. Baş[1], T. Körpınar[2], R. C. Demirkol[3]

[1] *Department of Mathematics, Mus Alparslan University, Mus, TURKEY*
[2] *Department of Mathematics, Mus Alparslan University, Mus, TURKEY*
[3] *Department of Mathematics, Mus Alparslan University, Mus, TURKEY*

E-mail: slckbs@hotmail.com

Abstract

In this paper, we study inextensible flows of timelike curves in Minkowski space-time. Necessary and sufficient conditions for an inextensible curve flow are expressed as a partial differential equation involving the curvature.

Keywords: Bishop frame, Inextensible Flows, Minkowski space-time

1. INTRODUCTION

Inextensible curve flows have a significant influence both in a wide variety of applied mathematics and also in nonlinear phenomena belonging to physics. This setting contains problems in field theories, nonlinear optics, fluid dynamics, sigma models, relativity, water wave theory, and so on. A key point of the research of flows equations focuses on the fact that numerous different contexts can be obtained by solely single example. This type of universality might be exceedingly concerned about the fact that these equations generally have a concealed meaning in terms of geometrical manner.

Recently, an interest for studying the inextensible surface and curve flows in different spaces besides their properties has gained much attention. Physically, inextensible curve and surface flows are characterized by the absence of any strain energy induced from the motion. In [1], studied inextensible flows of developable surfaces and curves in R^3. Corresponding equations are derived for developable surfaces inextensible flow. Additionally, there are many works related with inextensible flows [2-12].

The Bishop frame was first proposed by Bishop in 1975 [13]. Unlike the Frenet frame, Bishop's frame is not unique and is well defined even at points where the curvature of the curve vanishes [14-16]. In [17], introduced inextensible flows of curves wtith Bishop frame. With this new concept, we derive the necessary and sufficient condition for the given curve to be the inextensible flow. Finally, we give some new characterizations for curvatures of a curve.

2. MATERIAL AND METHODS

Minkowski space-time E_1^4 is a usual vector space provided with the standard metric given by [18],

$$\langle,\rangle = -dx_1^2 + dx_2^2 + dx_3^2 + dx_4^2,$$

where (x_1, x_2, x_3, x_4) is a rectangular coordinate system in E_1^4. Any vector x in E_1^4 can be characterized as follows: the vector x is called spacelike, lightlike or timelike if $<x, x>> 0$, $<x, x>= 0$ or $<x, x>< 0$, respectively.

Theorem 2.1. *Let* $\Gamma: I \to \mathsf{E}_1^4$ *be a unit speed timelike curve, the following relations are satisfied:*

(i)

$$\frac{\partial}{\partial s}\begin{bmatrix} \mathbf{T} \\ \mathbf{N}_1 \\ \mathbf{N}_2 \\ \mathbf{N}_3 \end{bmatrix} = \begin{bmatrix} 0 & \kappa(s) & 0 & 0 \\ \kappa(s) & 0 & \tau(s) & 0 \\ 0 & -\tau(s) & 0 & \sigma(s) \\ 0 & 0 & -\sigma(s) & 0 \end{bmatrix}\begin{bmatrix} \mathbf{T} \\ \mathbf{N}_1 \\ \mathbf{N}_2 \\ \mathbf{N}_3 \end{bmatrix}, \tag{2.1}$$

(ii)

$$\frac{\partial}{\partial s}\begin{bmatrix} \mathbf{T} \\ \mathbf{M}_1 \\ \mathbf{M}_2 \\ \mathbf{M}_3 \end{bmatrix} = \begin{bmatrix} 0 & k_1(s) & k_2(s) & k_3(s) \\ k_1(s) & 0 & 0 & 0 \\ k_2(s) & 0 & 0 & 0 \\ k_3(s) & 0 & 0 & 0 \end{bmatrix}\begin{bmatrix} \mathbf{T} \\ \mathbf{M}_1 \\ \mathbf{M}_2 \\ \mathbf{M}_3 \end{bmatrix}, \tag{2.2}$$

(iii)

$$\begin{aligned} k_1(s) &= \kappa(s)\cos\alpha\cos\beta, \\ k_2(s) &= \kappa(s)(\sin\beta\cos\theta - \sin\alpha\cos\beta\sin\theta), \\ k_3(s) &= \kappa(s)(\sin\beta\sin\theta + \sin\alpha\cos\beta\cos\theta), \\ \sigma(s) &= -\frac{\alpha'(s)}{\sin\beta}, \end{aligned}$$

where $\kappa(s), \tau(s)$ and $\sigma(s)$ are curvature, first and second torsion functions and $k_1(s)$, $k_2(s)$ and $k_3(s)$ are principal curvatures of the curve Γ ccording to the parallel frame, [15].

3. INEXTENSIBLE FLOWS OF TIMELIKE CURVES WITH PARALLEL TRANSPORT FRAME IN MINKOWSKI SPACE-TIME

Let $\Gamma(u,t)$ is a one-parameter family of smooth timelike curves in $\mathbf{E}_1^4$. The flow of Γ can be represented as

$$\frac{\partial\Gamma}{\partial t} = \mu_1\mathbf{T} + \mu_2\mathbf{M}_1 + \mu_3\mathbf{M}_2 + \mu_4\mathbf{M}_3, \tag{3.1}$$

where $\mu_1, \mu_2, \mu_3, \mu_4$ are smooth functions.

Definition 3.1. A curve evolution $\Gamma(u,t)$ and its flow $\dfrac{\partial\Gamma}{\partial t}$ in $\mathbf{E}_1^4$ are said to be inextensible if

$$\frac{\partial}{\partial t}\left|\frac{\partial}{\partial u}\right| = 0. \tag{3.2}$$

Lemma 3.2. Let $\dfrac{\partial \Gamma}{\partial t}$ be a smooth flow of the timelike curve Γ. The flow is inextensible if and only if

$$\frac{\partial v}{\partial t} = -\frac{\partial \mu_1}{\partial u} - k_1 v \mu_2 - k_2 v \mu_3 - k_3 v \mu_4, \tag{3.3}$$

Proof. From the relations (2.3) and (3.2), we obtain

$$\frac{\partial v}{\partial t} = \; < \mathbf{T}, (\frac{\partial \mu_1}{\partial u} + k_1 v \mu_2 + k_2 v \mu_3 + k_3 v \mu_4)\mathbf{T} + (\frac{\partial \mu_2}{\partial u} + k_1 v \mu_1)\mathbf{M}_1 + (\frac{\partial \mu_3}{\partial u} + k_2 v \mu_1)\mathbf{M}_2 + (\frac{\partial \mu_4}{\partial u} + k_3 v \mu_1)\mathbf{M}_3 >,$$

which completes the proof.

Theorem 3.3. Let $\dfrac{\partial \Gamma}{\partial t}$ be a smooth flow of the timelike curve Γ. The flow is inextensible if and only if

$$\frac{\partial \mu_1}{\partial u} = -k_1 v \mu_2 - k_2 v \mu_3 - k_3 v \mu_4. \tag{3.4}$$

Proof. Now let $\dfrac{\partial \Gamma}{\partial t}$ be extensible. By using (3.2), we obtain

$$\frac{\partial}{\partial t} s(u,t) = \int_0^u \frac{\partial v}{\partial t} du = \int_0^u (-\frac{\partial \mu_1}{\partial u} - k_1 v \mu_2 - k_2 v \mu_3 - k_3 v \mu_4) du = 0. \tag{3.5}$$

We now restrict ourselves to arc length parameterized curves.

Lemma 3.4. Let $\dfrac{\partial \Gamma}{\partial t}$ be a smooth flow of the timelike curve Γ. Then,

$$\frac{\partial \mathbf{T}}{\partial t} = (\frac{\partial \mu_2}{\partial s} + k_1 \mu_1)\mathbf{M}_1 + (\frac{\partial \mu_3}{\partial s} + k_2 \mu_1)\mathbf{M}_2 + (\frac{\partial \mu_4}{\partial s} + k_3 \mu_1)\mathbf{M}_3$$

$$\frac{\partial \mathbf{M}_1}{\partial t} = (\frac{\partial \mu_2}{\partial s} + k_1 \mu_1)\mathbf{T} + \psi_1 \mathbf{M}_2 + \psi_2 \mathbf{M}_3,$$

$$\frac{\partial \mathbf{M}_2}{\partial t} = (\frac{\partial \mu_3}{\partial s} + k_2 \mu_1)\mathbf{T} - \psi_1 \mathbf{M}_1 + \psi_3 \mathbf{M}_3,$$

$$\frac{\partial \mathbf{M}_3}{\partial t} = (\frac{\partial \mu_4}{\partial s} + k_3 \mu_1)\mathbf{T} - \psi_2 \mathbf{M}_1 - \psi_3 \mathbf{M}_2,$$

where

$$\psi_1 = <\frac{\partial \mathbf{M}_1}{\partial t}, \mathbf{M}_2 >, \psi_2 = <\frac{\partial \mathbf{M}_1}{\partial t}, \mathbf{M}_3 >, \psi_3 = <\frac{\partial \mathbf{M}_2}{\partial t}, \mathbf{M}_3 > .$$

Proof. From definition of flow, we get

$$\frac{\partial \mathbf{T}}{\partial t} = \frac{\partial}{\partial t}\frac{\partial \Gamma}{\partial s} = \frac{\partial}{\partial s}(\mu_1\mathbf{T} + \mu_2\mathbf{M}_1 + \mu_3\mathbf{M}_2 + \mu_4\mathbf{M}_3).$$

From the (2.3) equations, we have

$$\frac{\partial \mathbf{T}}{\partial t} = (\frac{\partial \mu_1}{\partial s} + k_1\mu_2 + k_2\mu_3 + k_3\mu_4)\mathbf{T} + (\frac{\partial \mu_2}{\partial s} + k_1\mu_1)\mathbf{M}_1 + (\frac{\partial \mu_3}{\partial s} + k_2\mu_1)\mathbf{M}_2 + (\frac{\partial \mu_4}{\partial s} + k_3\mu_1)\mathbf{M}_3.$$

Using Lemma 3.2, we get

$$\frac{\partial \mathbf{T}}{\partial t} = (\frac{\partial \mu_2}{\partial s} + k_1\mu_1)\mathbf{M}_1 + (\frac{\partial \mu_3}{\partial s} + k_2\mu_1)\mathbf{M}_2 + (\frac{\partial \mu_4}{\partial s} + k_3\mu_1)\mathbf{M}_3.$$

From the above and using

$$<\frac{\partial \mathbf{M}_1}{\partial t}, \mathbf{M}_1 >=<\frac{\partial \mathbf{M}_2}{\partial t}, \mathbf{M}_2 >=<\frac{\partial \mathbf{M}_3}{\partial t}, \mathbf{M}_3 >= 0,$$

we obtain

$$\frac{\partial \mathbf{M}_1}{\partial t} = (\frac{\partial \mu_2}{\partial s} + k_1\mu_1)\mathbf{T} + \psi_1\mathbf{M}_2 + \psi_2\mathbf{M}_3,$$

$$\frac{\partial \mathbf{M}_2}{\partial t} = (\frac{\partial \mu_3}{\partial s} + k_2\mu_1)\mathbf{T} - \psi_1\mathbf{M}_1 + \psi_3\mathbf{M}_3,$$

$$\frac{\partial \mathbf{M}_3}{\partial t} = (\frac{\partial \mu_4}{\partial s} + k_3\mu_1)\mathbf{T} - \psi_2\mathbf{M}_1 - \psi_3\mathbf{M}_2,$$

where

$$\psi_1 = <\frac{\partial \mathbf{M}_1}{\partial t}, \mathbf{M}_2 >, \psi_2 = <\frac{\partial \mathbf{M}_1}{\partial t}, \mathbf{M}_3 >, \psi_3 = <\frac{\partial \mathbf{M}_2}{\partial t}, \mathbf{M}_3 >,$$

which completes the proof.

The following theorem states the conditions on the curvature and torsion for the curve flow $\Gamma(s,t)$ to be inextensible.

Theorem 3.5. Let the flow $\frac{\partial \Gamma}{\partial t} = \mu_1\mathbf{T} + \mu_2\mathbf{M}_1 + \mu_3\mathbf{M}_2 + \mu_4\mathbf{M}_3$ be a smooth flow of the timelike curve Γ. Then, the following system of partial differential equations holds:

$$\frac{\partial k_1}{\partial t} = k_2 \psi_1 + k_3 \psi_2 + \frac{\partial}{\partial s}(k_1 \mu_1) + \frac{\partial^2 \mu_2}{\partial s^2}. \tag{3.6}$$

where

$$\psi_1 = <\frac{\partial \mathbf{M}_1}{\partial t}, \mathbf{M}_2>, \psi_2 = <\frac{\partial \mathbf{M}_1}{\partial t}, \mathbf{M}_3>.$$

Proof. From our assumption, we have

$$\frac{\partial}{\partial s}\frac{\partial \mathbf{T}}{\partial t} = \frac{\partial}{\partial s}[(\frac{\partial \mu_2}{\partial s} + k_1 \mu_1)\mathbf{M}_1 + (\frac{\partial \mu_3}{\partial s} + k_2 \mu_1)\mathbf{M}_2 + (\frac{\partial \mu_4}{\partial s} + k_3 \mu_1)\mathbf{M}_3].$$

Also, we get

$$\frac{\partial}{\partial s}\frac{\partial \mathbf{T}}{\partial t} = (k_1^2 \mu_1 + \frac{\partial \mu_2}{\partial s}k_1 + k_2^2 \mu_1 + \frac{\partial \mu_3}{\partial s}k_2 + k_3^2 \mu_1 + \frac{\partial \mu_4}{\partial s}k_3)\mathbf{T}$$

$$+ (\frac{\partial}{\partial s}(k_1 \mu_1) + \frac{\partial^2 \mu_2}{\partial s^2})\mathbf{M}_1 + (\frac{\partial}{\partial s}(k_2 \mu_1) + \frac{\partial^2 \mu_3}{\partial s^2})\mathbf{M}_2$$

$$+ (\frac{\partial}{\partial s}(k_3 \mu_1) + \frac{\partial^2 \mu_4}{\partial s^2})\mathbf{M}_3.$$

On the other hand, from Bishop frame we have

$$\frac{\partial}{\partial t}\frac{\partial \mathbf{T}}{\partial s} = (-k_1^2 \mu_1 - \frac{\partial \mu_2}{\partial s}k_1 - k_2^2 \mu_1 - \frac{\partial \mu_3}{\partial s}k_2 - \mu_3 k_3^2 - \frac{\partial \mu_4}{\partial s}k_3)\mathbf{T}$$

$$+ (\frac{\partial k_1}{\partial t} - k_2 \psi_1 - k_3 \psi_2)\mathbf{M}_1 + (\frac{\partial k_2}{\partial t} + k_1 \psi_1 - k_3 \psi_3)\mathbf{M}_2$$

$$+ (\frac{\partial k_3}{\partial t} + k_2 \psi_3 + k_1 \psi_2)\mathbf{M}_3$$

This means that

$$\frac{\partial k_1}{\partial t} = k_2 \psi_1 + k_3 \psi_2 + \frac{\partial}{\partial s}(k_1 \mu_1) + \frac{\partial^2 \mu_2}{\partial s^2},$$

which completes the proof.

Theorem 3.6. Let the flow $\frac{\partial \Gamma}{\partial t} = \mu_1 \mathbf{T} + \mu_2 \mathbf{M}_1 + \mu_3 \mathbf{M}_2 + \mu_4 \mathbf{M}_3$ be a smooth flow of the timelike curve Γ. Then,

$$\frac{\partial k_2}{\partial t} = \frac{\partial^2 \mu_3}{\partial s^2} + \frac{\partial}{\partial s}(k_2 \mu_1) - \psi_1 k_1 + \psi_3 k_3. \tag{3.7}$$

where

$$\psi_1 = <\frac{\partial \mathbf{M}_1}{\partial t}, \mathbf{M}_2 >, \psi_3 = <\frac{\partial \mathbf{M}_2}{\partial t}, \mathbf{M}_3 >.$$

Proof. From the relations (2.3) and (3.6), we find

$$\frac{\partial}{\partial s}\frac{\partial \mathbf{M}_2}{\partial t} = (\frac{\partial^2 \mu_3}{\partial s^2} + \frac{\partial}{\partial s}(k_2\mu_1) - \psi_1 k_1 + \psi_3 k_3)\mathbf{T}$$

$$+ (k_1\frac{\partial \mu_3}{\partial s} + k_1 k_2 \mu_1 - \frac{\partial \psi_1}{\partial s})\mathbf{M}_1$$

$$+ (k_2\frac{\partial \mu_3}{\partial s} + k_2^2 \mu_1)\mathbf{M}_2$$

$$+ (k_3\frac{\partial \mu_3}{\partial s} + k_2 k_3 \mu_1 + \frac{\partial \psi_3}{\partial s})\mathbf{M}_3.$$

Also,

$$\frac{\partial}{\partial t}\frac{\partial \mathbf{M}_2}{\partial s} = \frac{\partial k_2}{\partial t} + (k_2\frac{\partial \mu_2}{\partial u} + k_1 k_2 \mu_1)\mathbf{M}_1$$

$$+ (\frac{\partial \mu_3}{\partial s}k_2 + k_2^2 \mu_1)\mathbf{M}_2 + (\frac{\partial \mu_4}{\partial s}k_2 + k_2 k_3 \mu_1)\mathbf{M}_3.$$

Thus

$$\frac{\partial k_2}{\partial t} = \frac{\partial^2 \mu_3}{\partial s^2} + \frac{\partial}{\partial s}(k_2\mu_1) - \psi_1 k_1 + \psi_3 k_3.$$

Corollary 3.7.

$$\frac{\partial k_3}{\partial t} = \frac{\partial}{\partial s}(k_3\mu_3) + \frac{\partial^2 \mu_4}{\partial s^2} - \psi_2 k_1 - \psi_3 k_2. \tag{3.8}$$

REFERENCES

[1] Kwon, D. Y., Park, F.C., Chi, D. P., Inextensible flows of curves and developable surfaces, Appl. Math. Lett., 18, 1156-1162, 2005.

[2] Bas, S., Korpinar, T., Inextensible Flows of Spacelike Curves on Spacelike Surfaces according to Darboux Frame in M_1^3, Boletim da Sociedade Paranaense de Matematica, 31 (2), 9-17, 2013.

[3] Bas, S., Korpinar, T., A New Characterization of One Parameter Family of Surfaces by Inextensible Flows in De-Sitter 3-Space, Journal of Advanced Physics, 7 (2), 251-256, 2018.

[4] Bas, S., A New Method For Inextensible Flows of Adjoint Curves in Space, AIP Conference Proceedings 2116, 240003, 2019.

[5] Korpinar, T., Bas, S., On evolute curves in terms of inextensible flows of in E^3, Bol. Soc. Paran. Mat., 36 (1), 117-124, 2018.

[6] Korpinar, T., Turhan, E., A New Version of Inextensible Flows of Spacelike Curves with Timelike B2 in Minkowski Space-Time E_1^4, Differ. Equ. Dyn. Syst., 21 (3), 281-290, 2013.

[7] Korpinar, T., On Inextensible flows of curves according to alternative moving frame, Journal of Dynamical Systems & Geomatric Theories, 15 (1), 15-27, 2017.

[8] Korpinar, Z., Inc, M., On the Biswas--Milovic Model with Power Law Nonlinearity, Journal of Advanced Physics, 7(2), 239-246, 2018.

[9] Korpinar, T., On Inextensible flows of curves according to alternative moving frame, Journal of Dynamical Systems & Geomatric Theories, 15 (1), 15-27, 2017.

[10] Korpinar, T., Demirkol, R. C.,, A new characterization on the energy of elastica with the energy of Bishop vector fields in Minkowski space. Journal of Advanced Physics, 6(4), 562-569, 2017.

[11] Korpinar, T., Bas, S., A new approach to inextensible flow of curves with Blaschke frame, Journal of Science and Arts, 1(46), 15-22, 2019.

[12] Korpinar, T., Bas, S., A new approach for inextensible flows of binormal spherical indicatrices of magnetic curves, International Journal of Geometric Methods in Modern Physics, 16 (2), 1950020, 2019.

[13] Bishop, L. R., There is More Than One Way to Frame a Curve, Amer. Math. Monthly, 82 (3), 246-251,1975.

[14] Bukcu, B., Karacan, M. K., Special Bishop motion and Bishop darboux rotation axis of the space curve, Journal of Dynamical Systems and Geometric Theories, 6 (1), 27-34, 2008.

[15] Erdogdu, M., Parallel frame of non-lightlike curves in Minkowski space-time, International Journal of Geometric Methods in Modern Physics, 12 (10), 1550109, 2015.

[16] Gokcelik, F., Bozkurt, Z., Ekmekci, F. N., and Yaylı, Y., Parallel transport frame in 4-dimensional Euclidean space E^4, Caspian J. Sci., 3, 91-102, 2014.

[17] Korpinar, T., Asil, V., Bas, S., On Characterization Inextensible flows of Curves According to Bishop frame in E^3, Revista Notas de Matematica, 7 (1), 37-45, 2011.

[18] O'Neill, B., Semi-Riemannian Geometry with Applications to Relativity, Academic Press, London, 1983.

INEXTENSIBLE FLOWS OF DUAL CURVES ACCORDING TO BISHOP FRAME IN DUAL EUCLIDEAN SPACE

S. Baş[1], R. C. Demirkol[2], T. Körpınar[3]

[1] *Department of Mathematics, Mus Alparslan University, Mus, TURKEY*
[2] *Department of Mathematics, Mus Alparslan University, Mus, TURKEY*
[3] *Department of Mathematics, Mus Alparslan University, Mus, TURKEY*

E-mail: slckbs@hotmail.com

Abstract

Inextensible flows of curves plays an important role in practical applications. We construct a new method for inextensible flows of dual curves in dual space D^3. In this paper, we study inextensible flows of dual curves according to Bishop frame in dual space D^3. The concepts with the inextensible flows are analyzed by using Bishop frame.

Keywords: Bishop frame, Inextensible Flows, Dual Space

1. INTRODUCTION

Dual numbers were investigated by W.K. Clifford [1] and rediscovered by Study [2]. Then he used dual numbers and dual vectors in his research on the geometry of lines and kinematics, and defined the mapping which is called by his name E. Study's mapping: the set of oriented straight lines in the Euclidean 3-space E^3 is one-to-one correspondence with the dual points on the surface of a dual unit sphere $\hat{S}^2$ in the dual space D^3 of triples of dual numbers. It can be seen that the dual number is a powerful mathematical tool for spatial mechanism design. Hence, dual numbers are analysis have important applications to differential line geometry and kinematics, [3-7].

In differential geometry, the special curves are an important subject of curve theory [8-11]. A large number of aspects of applied physics and engineering utilized gaseous and smooth flows. Gaseous flows are extremely essential in spacecraft, automobiles, and aeroplanes. The research of smooth flow is extremely important meant for the uses of naviero, just like the style of boats and various tasks in municipal design including the design of the harbor and the safety of seaside. Physically, inextensible curve and surface flows are characterized by the absence of any strain energy induced from the motion. Kwon etc [12] investigated inextensible flows of curves and developable surfaces in R^3. Then, they derived the corresponding equations for the inextensible flow of a developable surface and showed that it suffices to its evolution in terms of two inextensible curve flows. Additionally, there are many works related with inextensible flows, [13-15].

Inextensible flows of curves plays an important role in practical applications. We construct a new method for inextensible flows of dual curves in dual space D^3. In this paper, we study inextensible flows of dual curves according to Bishop frame in dual space D^3. The concepts with the inextensible flows are analyzed by using Bishop frame.

2. MATERIAL AND METHODS

We start our discussion by reviewing some of the basic concepts of dual numbers [6]. Dual numbers are the set of all pairs of real numbers written as

$$\varpi = \varpi + \varepsilon\varpi^*, \varpi, \varpi^* \in \mathsf{R},$$

where the dual unit ε satisfies the relationships

$$\varepsilon \neq 0, \varepsilon 1 = 1\varepsilon, \varepsilon^2 = 0.$$

For any $\varpi = \varpi + \varepsilon\varpi^*, \hat{n} = n + \varepsilon n^* \in \mathsf{D}^3$, the scalar product and the vector product of ϖ and $\hat{n}$ are defined as, respectively [6],

$$< \varpi, \hat{n} > = < \varpi, n > + \varepsilon(< \varpi, n^* > + < \varpi^*, n >),$$
$$\varpi \wedge \hat{n} = (\varpi_2 \hat{n}_3 - \varpi_3 \hat{n}_2, \varpi_3 \hat{n}_1 - \varpi_1 \hat{n}_3, \varpi_1 \hat{n}_2 - \varpi_2 \hat{n}_1),$$

where $\varpi = \varpi + \varepsilon \varpi^*, \hat{n} = n + \varepsilon n^* \in \mathsf{D}^3, 1 \le i \le 3$. If $x \ne 0$, the norm $\|\varpi\|$ of $\varpi = \varpi + \varepsilon \varpi^*$ is defined as

$$\|\varpi\| = \sqrt{< \varpi, \varpi >} = \|\varpi\| + \varepsilon \frac{< \varpi, \varpi^* >}{\|\varpi\|}.$$

Let $\{\hat{\mathbf{T}}, \hat{\mathbf{M}}_1, \hat{\mathbf{M}}_2\}$ be the Bishop frame of the differentiable dual curve in the dual space D^3. Then, the Bishop frame equations are [16]

$$\hat{\mathbf{T}}'(s) = \hat{k}_1(s)\hat{\mathbf{M}}_1(s) + \hat{k}_2(s)\hat{\mathbf{M}}_2(s),$$
$$\hat{\mathbf{M}}_1'(s) = \hat{k}_1(s)\hat{\mathbf{T}}(s),$$
$$\hat{\mathbf{M}}_2'(s) = \hat{k}_2(s)\hat{\mathbf{T}}(s)\hat{k}_2$$

The relation between k_1, k_2 and $\hat{k}_1, \hat{k}_2$ is given as;

$$\hat{k}_1 = \sqrt{k_1^2 + k_2^2 + 2\varepsilon(k_1 k_1^* + k_2 k_2^*)},$$
$$\hat{\theta}(s) = \arctan(\frac{k_2}{k_1} + \varepsilon \frac{k_1 k_2^* - k_1^* k_2}{k_1^2}),$$
$$\hat{k}_2(s) = \frac{d\hat{\theta}(s)}{dt}.$$

3. INEXTENSIBLE FLOWS OF DUAL CURVES WITH BISHOP FRAME IN D^3

Assume that $\hat{\chi}(u,t)$ is a one parameter family of smooth dual curves in dual space D^3.

Then, the flow of $\hat{\chi}$ can be represented as f

$$\frac{\partial \chi}{\partial t} = f\mathbf{T} + g\mathbf{M}_1 + h\mathbf{M}_2,$$
$$\frac{\partial \chi^*}{\partial t} = f\mathbf{T}^* + f^*\mathbf{T} + g\mathbf{M}_1^* + g^*\mathbf{M}_1 + h\mathbf{M}_2^* + h^*\mathbf{M}_2.$$

Definition 3.1. The flow $\frac{\partial \chi}{\partial t} + \varepsilon \frac{\partial \chi^*}{\partial t}$ in D^3 are said to be inextensible if

$$\frac{\partial}{\partial t} \left| \frac{\partial (\chi + \varepsilon \chi^*)}{\partial u} \right| = 0.$$

Lemma 3.2. Let $\dfrac{\partial \chi}{\partial t} + \varepsilon \dfrac{\partial \chi^*}{\partial t}$ be a smooth flow of the dual curve $\hat{\chi}$. The flow is inextensible if and only if

$$\frac{\partial v}{\partial t} = \frac{\partial f}{\partial u} - gvk_1 - hvk_2.$$

Proof. As $\dfrac{\partial}{\partial t}$ and $\dfrac{\partial}{\partial u}$ are commutative and $v^2 = < \dfrac{\partial \hat{\chi}}{\partial u}, \dfrac{\partial \hat{\chi}}{\partial u} >$, we have

$$\frac{\partial v}{\partial t} = < v(\mathbf{T} + \varepsilon \mathbf{T}^*), (\frac{\partial f}{\partial u} - gvk_1 - hvk_2)\mathbf{T} + (fvk_1 + \frac{\partial g}{\partial u})\mathbf{M}_1 + (fvk_2 + \frac{\partial h}{\partial u})\mathbf{M}_2$$

$$+ \varepsilon((\frac{\partial f^*}{\partial u} - k_1 vg^* - gvk_1^* - k_2 vh^* - hvk_2^*)\mathbf{T} + (\frac{\partial f}{\partial u} - gvk_1 - hvk_2)\mathbf{T}^* + (f^* k_1 v + \frac{\partial g^*}{\partial u} + fvk_1^*)\mathbf{M}_1$$

$$+ (fk_1 v + \frac{\partial g}{\partial u})\mathbf{M}_1^* + (k_2 vf^* + \frac{\partial h^*}{\partial u} + hvk_2^*)\mathbf{M}_2 + (gvk_2 + \frac{\partial h}{\partial u})\mathbf{M}_2^*) > .$$

which completes the proof.

Theorem 3.3. Let $\dfrac{\partial \hat{\chi}}{\partial t}$ be a smooth flow of the dual curve $\hat{\chi}$. The flow is inextensible if and only if

$$\frac{\partial f}{\partial u} = gvk_1 + hvk_2,$$

$$\frac{\partial f^*}{\partial u} = g^* vk_1 + gvk_1^* + k_2 vh^* + hvk_2^*.$$

Proof. Now let $\dfrac{\partial \chi}{\partial t} + \varepsilon \dfrac{\partial \chi^*}{\partial t}$ be extensible. From Lemma 3.2, we have

$$\frac{\partial}{\partial t} s(u,t) = \int_0^u \frac{\partial v}{\partial t} du = \int_0^u (\frac{\partial (f + \varepsilon f^*)}{\partial u} - (g + \varepsilon g^*)v(k_1 + \varepsilon k_1^*) - (h + \varepsilon h^*)v(k_2 + \varepsilon k_2^*)) du = 0,$$

Finally, we express the desired result.

We now restrict ourselves to arc length parametrized curves.

Lemma 3.4.

$$\frac{\partial \mathbf{T}}{\partial t} = (fk_1 + \frac{\partial g}{\partial s} - k_2 h)\mathbf{M}_1 + (gk_2 + \frac{\partial h}{\partial s})\mathbf{M}_2,$$

$$\frac{\partial \mathbf{M}_1}{\partial t} = (-fk_1 - \frac{\partial g}{\partial s})\mathbf{T} + \psi\mathbf{M}_2,$$

$$\frac{\partial \mathbf{M}_2}{\partial t} = -(gk_2 + \frac{\partial h}{\partial s})\mathbf{T} - \psi\mathbf{M}_1,$$

$$\frac{\partial \mathbf{T}^*}{\partial t} = (f^*k_1 + \frac{\partial g^*}{\partial s} + fk_1^*)\mathbf{M}_1$$

$$+ (fk_1 + \frac{\partial g}{\partial s})\mathbf{M}_1^* + (k_2 f^* + \frac{\partial h^*}{\partial s} + hk_2^*)\mathbf{M}_2 + (gk_2 + \frac{\partial h}{\partial s})\mathbf{M}_2^*,$$

$$\frac{\partial \mathbf{M}_1^*}{\partial t} = (-f^*k_1 - \frac{\partial g^*}{\partial s} - fk_1^*)\mathbf{T} - (fk_1 + \frac{\partial g}{\partial s})\mathbf{T}^* + \psi\mathbf{M}_2^* + \psi^*\mathbf{M}_2,$$

$$\frac{\partial \mathbf{M}_2^*}{\partial t} = -(-k_2 f^* - f^*k_2^* - \frac{\partial h^*}{\partial s})\mathbf{T} - (fk_2 + \frac{\partial h}{\partial s})\mathbf{T}^* - \psi\mathbf{M}_1^* - \psi^*\mathbf{M}_1,$$

where $\hat{\psi} = \psi + \varepsilon\psi^* = \left\langle \frac{\partial \hat{\mathbf{M}}_1}{\partial t}, \hat{\mathbf{M}}_2 \right\rangle$.

Proof. Using definition of $\hat{\chi}$, we get

$$\frac{\partial \hat{\mathbf{T}}}{\partial t} = \frac{\partial}{\partial s}(f\mathbf{T} + g\mathbf{M}_1 + h\mathbf{M}_2 + \varepsilon(f\mathbf{T}^* + f^*\mathbf{T} + g\mathbf{M}_1^* + g^*\mathbf{M}_1 + h\mathbf{M}_2^* + h^*\mathbf{M}_2)).$$

From the dual Bishop equations, we have

$$\frac{\partial \hat{\mathbf{T}}}{\partial t} = (\frac{\partial f}{\partial s} - gvk_1 - hvk_2)\mathbf{T} + (fk_1 + \frac{\partial g}{\partial s})\mathbf{M}_1 + (fk_2 + \frac{\partial h}{\partial s})\mathbf{M}_2$$

$$+ \varepsilon((\frac{\partial f^*}{\partial s} - k_1 g^* -)\mathbf{T} + (\frac{\partial f}{\partial u} - gk_1)\mathbf{T}^* + (f^*k_1 + \frac{\partial g^*}{\partial u} - k_2 h^* - h)\mathbf{M}_1$$

$$+ (fk_1 + \frac{\partial g}{\partial s} - k_2 h)\mathbf{M}_1^* + (g + k_2 g^* + \frac{\partial h^*}{\partial s})\mathbf{M}_2 + (gk_2 + \frac{\partial h}{\partial s})\mathbf{M}_2^*).$$

Using Lemma 3.2, we get

$$\frac{\partial \hat{\mathbf{T}}}{\partial t} = (fk_1 + \frac{\partial g}{\partial s} - k_2 h)\mathbf{M}_1 + (gk_2 + \frac{\partial h}{\partial u})\mathbf{M}_2$$

$$+ \varepsilon((f^* k_1 + \frac{\partial g^*}{\partial u} + fk_1^*)\mathbf{M}_1 + (fk_1 + \frac{\partial g}{\partial s})\mathbf{M}_1^*$$

$$+ (f^* k_2 + \frac{\partial h^*}{\partial s} + fk_2^*)\mathbf{M}_2 + (fk_2 + \frac{\partial h}{\partial s})\mathbf{M}_2^*).$$

Using $\left\langle \frac{\partial \mathbf{M}_1}{\partial t} + \varepsilon \frac{\partial \mathbf{M}_1^*}{\partial t}, (\mathbf{M}_1 + \varepsilon \mathbf{M}_1^*) \right\rangle = \left\langle \frac{\partial \mathbf{M}_2}{\partial t} + \varepsilon \frac{\partial \mathbf{M}_2^*}{\partial t}, \mathbf{M}_2 \right\rangle = 0,$ we obtain

$$\frac{\partial \mathbf{M}_1}{\partial t} = (-fk_1 - \frac{\partial g}{\partial s})\mathbf{T} + \psi \mathbf{M}_2,$$

$$\frac{\partial \mathbf{M}_1^*}{\partial t} = (-f^* k_1 - \frac{\partial g^*}{\partial s} - fk_1^*)\mathbf{T}$$

$$- (fk_1 + \frac{\partial g}{\partial s})\mathbf{T}^* + \psi \mathbf{M}_2^* + \psi^* \mathbf{M}_2,$$

$$\frac{\partial \mathbf{M}_2}{\partial t} = -(gk_2 + \frac{\partial h}{\partial s})\mathbf{T} - \psi \mathbf{M}_1,$$

$$\frac{\partial \mathbf{M}_2^*}{\partial t} = -(-f^* k_2 - fk_2^* - \frac{\partial h^*}{\partial s})\mathbf{T}$$

$$- (fk_2 + \frac{\partial h}{\partial s})\mathbf{T}^* - \psi \mathbf{M}_1^* - \psi^* \mathbf{M}_1,$$

where $\psi = \left\langle \frac{\partial \mathbf{M}_1}{\partial t}, \mathbf{M}_2 \right\rangle, \psi^* = \left\langle \frac{\partial \mathbf{M}_1}{\partial t}, \mathbf{M}_2^* \right\rangle + \left\langle \frac{\partial \mathbf{M}_1^*}{\partial t}, \mathbf{M}_2 \right\rangle,$ which completes the proof.

Theorem 3.5. Let the flow $\frac{\partial \hat{\chi}}{\partial t}$ be inextensible. Then, the following system of partial differential equations holds:

$$\frac{\partial \hat{k}_2}{\partial t} = \frac{\partial}{\partial s}(f \ \hat{k}_1) + \frac{\partial^2 h}{\partial s^2} - \hat{\psi}\hat{k}_1,$$

Proof. Assume that $\frac{\partial \hat{\chi}}{\partial t}$ is inextensibe flow. Noting that $\frac{\partial}{\partial s}\frac{\partial \hat{\mathbf{T}}}{\partial t} = \frac{\partial}{\partial t}\frac{\partial \hat{\mathbf{T}}}{\partial s}$, we have

$$\frac{\partial \hat{k}_2}{\partial t} = \frac{\partial}{\partial s}(f \ \hat{k}_1) + \frac{\partial^2 h}{\partial s^2} - \hat{\psi}\hat{k}_1,$$

which completes the proof.

REFERENCES

[1] Clifford, W. K., Preliminary Sketch of bi-quaternions, Proceedings of the London Mathematical Society, 4, 361-395, 1873.

[2] Study, E., Geometrie der Dynamen, Verlag Teubner, Leipzig, 1903.

[3] Korpinar, T., Bas, S., A new approach to inextensible flow of curves with Blaschke frame, Journal of Science and Arts, 1(46), 15-22, 2019.

[4] Bas, S., Korpinar, T., Turhan, E., Asil, V., Inextensible Flows of Dual Curves in the Dual Space D^3, World Applied Sciences Journal, 16 (11), 1489-1495, 2012.

[5] Bukcu, B., Karacan, M. K., Yuksel, N., Yuksel, On the dual Bishop Darboux rotation axis of the dual timelike space curve, Far East Journal of Mathematical Sciences, 1 (2), 301-310, 2008.

[6] Veldkamp, G. R., On the use of dual numbers, vectors and matrices in instantaneous, spatial kinematics, Mech. Mach. Theory, 11 (2), 141-156, 1976.

[7] Korpinar, T., Turhan, E., Bas, S., Characterizing of dual focal curves in D_1^3, Boletim da Sociedade Paranaense de Matematica, 31 (2),77-82, 2013.

[8] Korpinar, T., Bas, S., A new approach for inextensible flows of binormal spherical indicatrices of magnetic curves, International Journal of Geometric Methods in Modern Physics, 16 (2), 1950020, 2019.

[9] Bas, S., A New Version of Spherical Magnetic Curves in the De-Sitter Space S_1^2, Symmetry 10 (11), 606, 2018.

[10] Bas, S., Korpinar, T., Modified Roller Coaster Surface in Space, Mathematics, 7 (2), 195, 2019.

[11] Bas, S., Asil, V., Korpinar, T., A New Version of Five-Axis Motion of Spheres with Spacelike Curves in Minkowski Space, Journal of Advanced Physics, 7 (3), 366-375, 2018.

[12] Kwon, D. Y., Park, F. C., Chi, D. P., Inextensible flows of curves and developable surfaces, Appl. Math. Lett., 18, 1156-1162, 2005.

[13] Bas, S., A New Method For Inextensible Flows of Adjoint Curves in Space, AIP Conference Proceedings 2116, 240003, 2019.

[14] Bas, S., Korpinar, T., A New Characterization of One Parameter Family of Surfaces by Inextensible Flows in De-Sitter 3-Space, Journal of Advanced Physics, 7 (2), 251-256, 2018.

[15] Korpinar, T., Bas, S., On evolute curves in terms of inextensible flows of in E^3, Bol. Soc. Paran. Mat., 36 (1), 117-124, 2018.

[16] Karacan, M. K., Bukcu, B., Yuksel, N., On the dual Bishop Darboux rotation axis of the dual space curve, APPS. Applied Sciences, 10, 115-120, 2008.

CONSTRUCTION OF B-FOCAL CURVES IN MINKOWSKI SPACE

S. Baş[1], Z. Körpınar[2], R. C. Demirkol[3]

[1] *Department of Mathematics, Mus Alparslan University, Mus, TURKEY*
[2] *Faculty of Economic and Administrative Sciences, Department of Administration, Mus Alparslan University, Mus, TURKEY*
[3] *Department of Mathematics, Mus Alparslan University, Mus, TURKEY*

E-mail: slckbs@hotmail.com

Abstract

In this paper, we study timelike B-focal curves in the Minkowski 3-space E_1^3. We characterize timelike B-focal curves in terms of their focal curvatures.

Keywords: Bishop frame, Focal Curve, Minkowski 3-Space

1. INTRODUCTION

The focal curve of a smooth curve $\gamma : \mathsf{R} \to \mathsf{R}^{m+1}$, consists of the centers of its osculating hypersphere. The focal curve can be state as

$$C_\gamma = (\gamma + c_1 \mathbf{N}_1 + c_2 \mathbf{N}_2 + ... + c_m \mathbf{N}_m),$$

where $\{\mathbf{T}, \mathbf{N}_1, \mathbf{N}_2, ..., \mathbf{N}_m\}$ is the Frenet frame of γ and $c_1, c_2, ..., c_m$ are smooth functions that we call focal curvatures of γ. Vargas found an expression of the curvatures κ_i of γ; in terms of the focal curvatures of c_i and show that the focal curvatures satisfy some scalar Frenet equations in the Euclidean space. Besides, the focal curvatures of a non-lightlike curve in Minkowski (m+1)-space which satisfy the " scalar Frenet equations" [2]. The notion of the focal curve of a smooth curve of a consists of the centers of its osculating sphere. Moreover, the fundamental results of the focal curves which defined in E^n were given by favour of Darboux vector. The focal curves of a null Cartan curve was examined by [3]. Some special types of ruled surface, choosing one of the base curves or director curves as the focal curve were investigated by [4]. Lightlike hypersurfaces and lightlike focal sets of null Cartan curves in Lorentz-Minkowski spacetime were given by Liu and Wang [5]. Furthermore, different applications of focal curves were given in the studies [6-12]. In this paper, we study timelike B-focal curves in the Minkowski 3-space E_1^3. We characterize timelike B-focal curves in terms of their focal curvatures.

2. MATERIAL AND METHODS

The Minkowski 3-space E_1^3 is a real vector space E^3 endowed with the standard flat Lorentzian metric given by [13],

$$I = < ., . > = -dx_1^2 + dx_2^2 + dx_3^2,$$

where (x_1, x_2, x_3) is a rectangular coordinate system of E_1^3. Let $u = (u_1, u_2, u_3)$ and $v = (v_1, v_2, v_3)$ be arbitrary vectors in E_1^3, the

Lorentzian cross product of u and v defined by

$$u \times v = \begin{vmatrix} -i & j & k \\ u_1 & u_2 & u_3 \\ v_1 & v_2 & v_3 \end{vmatrix}.$$

The norm of $v \in E_1^3$ is defined by

$$\|v\| = \sqrt{|<v, v>|}.$$

A vector $v \in E_1^3$ is said to be spacelike if $<v, v>>0$ or $v = 0$, timelike if $<v, v><0$, and lighlike (or null) if $<v, v>= 0$ and $v \neq 0$.

Denoted the moving Frenet frame along a space curve γ by $\{\mathbf{T}, \mathbf{N}, \mathbf{B}\}$ where $\mathbf{T}, \mathbf{N},$ and $\mathbf{B}$ are tangent, principal normal and binormal vector of γ, respectively. If γ is a timelike curve, then this set of orthogonal unit vectors, known as the Frenet frame, has the following properties [13],

$$
\begin{aligned}
\mathbf{T}'(s) &= \kappa \mathbf{N}, \\
\mathbf{N}'(s) &= \kappa \mathbf{T} + \tau \mathbf{B}, \\
\mathbf{B}'(s) &= -\tau \mathbf{N},
\end{aligned}
$$

where κ is the curvature of γ and τ is its torsion and

$$
\begin{aligned}
g(\mathbf{T}, \mathbf{T}) &= -1, \ g(\mathbf{N}, \mathbf{N}) = 1, \ g(\mathbf{B}, \mathbf{B}) = 1, \\
g(\mathbf{T}, \mathbf{N}) &= g(\mathbf{T}, \mathbf{B}) = g(\mathbf{N}, \mathbf{B}) = 0.
\end{aligned}
$$

The Bishop frame or parallel transport frame is an alternative approach to defining a moving frame that is well defined even when the curve has vanishing second derivative. One can express parallel transport of an orthonormal frame along a curve simply by parallel transporting each component of the frame. The tangent vector and any convenient arbitrary basis for the remainder of the frame are used. Denote by $\{\mathbf{T}, \mathbf{M}_1, \mathbf{M}_2\}$ the moving Bishop frame along the timelike curve $\gamma(s): I \rightarrow E_1^3$ in the Minkowski 3-space E_1^3. For an arbitrary timelike curve $\gamma(s)$ in the space E_1^3, the following Bishop formula are given by [14],

$$
\begin{aligned}
\mathbf{T}'(s) &= k_1(s)\mathbf{M}_1(s) + k_2(s)\mathbf{M}_2(s), \\
\mathbf{M}_1'(s) &= k_1(s)\mathbf{T}(s), \\
\mathbf{M}_2'(s) &= k_2(s)\mathbf{T}(s).
\end{aligned}
\tag{1}
$$

Here, we shall call the set $\{\mathbf{T}(s), \mathbf{M}_1(s), \mathbf{M}_2(s)\}$ as Bishop trihedra, k_1 and k_2 as Bishop curvatures, where $\theta(s) = \arctan \dfrac{k_2}{k_1}$, $\tau(s) = \dfrac{d\theta(s)}{ds}$, $\kappa(s) = \sqrt{k_1^2 + k_2^2}$. Thus, Bishop curvatures are defined by

$$
\begin{aligned}
k_1 &= \kappa(s) \cos \theta(s), \\
k_2 &= \kappa(s) \sin \theta(s).
\end{aligned}
$$

Definition 2.1. The curve $C_\gamma : \theta \to C_\gamma(\theta) \in \mathsf{R}^{m+1}$ consisting of the centres of the osculating hyperspheres of a good curve $\gamma : \theta \to \gamma(\theta) \in \mathsf{R}^{m+1}$ is called the parametrised focal curve of γ, [1].

For a unit speed curve $\gamma = \gamma(s) : I \to \mathsf{E}^3$ the curve consisting of the centers of the osculating spheres of γ is called the parametrized focal curve of γ. The hyperplanes normal to at a point consist of the set of centers of all spheres tangent to γ at that point. Hence the center of the osculating spheres at that point lies in such a normal plane. Therefore, denoting the focal curve by C_γ we can write

$$C_\gamma(s) = (\gamma + c_1 \mathbf{N}_1 + c_2 \mathbf{N}_2)(s),$$

where the coefficients c_1, c_2 are smooth functions of the parameter of the curve γ, called the first and second focal curvatures of γ, respectively. Further, the focal curvatures c_1, c_2 are defined by

$$c_1 = \frac{1}{\kappa}, c_2 = \frac{c_1'}{\tau}; \kappa \neq 0, \tau \neq 0.$$

Theorem 2.2. Let $\gamma = \gamma(s) : I \to \mathsf{E}^3$ be a unit speed curve and

$$\mathsf{F}_\gamma^B = (\gamma + f_1 \mathbf{M}_1 + f_2 \mathbf{M}_2)(s),$$

its Bishop-focal curve on E^3. Then

$$\mathsf{F}_\gamma^B = (\gamma + p\mathbf{M}_1 + \frac{1 - pk_1}{k_2} \mathbf{M}_2)(s),$$

where p is a constant.

3. TIMELIKE B-FOCAL CURVES ACCORDING TO BISHOP FRAME IN E_1^3

Denoting the focal curve by G_γ^B, we can write

$$\mathsf{G}_\gamma^B = (\gamma + r_1 \mathbf{M}_1 + r_2 \mathbf{M}_2)(s),$$

where the coefficients r_1, r_2 are smooth functions of the parameter of the curve γ, called the first and second focal curvatures of γ, respectively.

To separate a focal curve according to Bishop frame from that of Frenet- Serret frame, in the rest of the paper, we shall use notation for the timelike focal curve defined above as timelike B-focal curve.

Theorem 3.1. Let $\gamma = \gamma(s) : I \to \mathsf{E}_1^3$ be a unit speed curve and

$$\mathbf{G}^{B}_{\gamma} = (\gamma + r_1 \mathbf{M}_1 + r_2 \mathbf{M}_2)(s),$$

its timelike B-focal curve on E^3_1. Then

$$\mathbf{G}^{B}_{\gamma} = (\gamma + p\mathbf{M}_1 - \frac{1+ak_1}{k_2}\mathbf{M}_2)(s),$$

where a is a constant.

Proof: Assume that γ is a unit speed curve and $\mathbf{G}^{B}_{\gamma}$ its focal curve on E^3_1. So, by differentiating of the formula (4), we get

$$(\mathbf{G}^{B}_{\gamma})^{'} = (1 + r_1 k_1 + r_2 k_2)\mathbf{T} + (r_1^{'})\mathbf{M}_1 + (r_2^{'})\mathbf{M}_2.$$

Using above equation, the first 2 components vanish, we get

$$\begin{aligned} r_1 k_1 + r_2 k_2 &= -1, \\ g_1^{'} &= 0. \end{aligned} \tag{2}$$

Considering second equation above system, we have

$$r_1 = a = \text{constant} \neq 0.$$

Since, we immediately arrive at

$$r_2 = -\frac{1 + r_1 k_1}{k_2}.$$

By means of obtained equations, we express (2). This completes the proof.

Corollary 3.2. Let $\gamma = \gamma(s): I \rightarrow \mathsf{E}^3_1$ be a unit speed curve and $\mathbf{G}^{B}_{\gamma}$ its focal curve on E^3_1. Then, the focal curvatures of $\mathbf{G}^{B}_{\gamma}$ are

$$\begin{aligned} r_1 &= \text{constant} \neq 0, \\ r_2 &= -\frac{1 + r_1 k_1}{k_2}. \end{aligned}$$

In the light of Theorem 3.1, we express the following corollary without proof:

Corollary 3.3. Let $\gamma = \gamma(s) : I \rightarrow \mathsf{E}_1^3$ be a unit speed curve and G_γ^B its focal curve on E_1^3. If k_1 and k_2 are constant then, the focal curvatures of G_γ^B are

$$
\begin{aligned}
r_1 &= \text{constant} \neq 0, \\
r_2 &= \text{constant} \neq 0.
\end{aligned}
$$

REFERENCES

[1] Vargas, R. U., Scalar Frenet Equations and Focal Curvatures for Curves in R^{m+1}, Institut de Mathematiques de Jussieu, Universites Paris, Preprint, 2000.

[2] Ozdemir, M., On the Focal Curvatures of Nonlightlike Curves in Minkowski $(m+1)-$Space, Firat University Journal of Science and Engineering Sciences, 16 (3), 401-409, 2004.

[3] Simsek, H., On focal curves of null Cartan curves, Turkish Journal of Mathematics, 41, 1579-1590, 2017.

[4] Alegre, P., Arslan K., Carriazo A., Murathan, C. and Öztürk, G., Some Special Types of Developable Ruled Surfaces, Hacettepe Journal of Mathematics and Statistics, 39 (3), 319-325, 2010.

[5] Liu, X., and Wang, Z., On lightlike hypersurfaces and lightlike focal sets of null Cartan curves in Lorentz-Minkowski spacetime, Journal of Nonlinear Science and Applications, 8 (5), 628-639, 2015.

[6] Asil, V., Bas, S., Korpinar, T., On Construction of D-Focal Curves in Euclidean 3-Space M^3, Bol. Soc. Paran. Mat., 31, 273-277, 2013.

[7] Bas, S., Korpinar, T., On Characterization Of B-Focal Curves In E^3, Bol. Soc. Paran. Mat., 31 (1), 175-178, 2013.

[8] Korpinar, T., Turhan, E., Bas, S., Characterizing of dual focal curves in D_1^3, Boletim da Sociedade Paranaense de Matemática, 31 (2), 77-82, 2013.

[9] Korpinar, T., Bas, S., A new approach for inextensible flows of binormal spherical indicatrices of magnetic curves, International Journal of Geometric Methods in Modern Physics, 16 (2), 1950020, 2019.

[10] Bas, S., A New Version of Spherical Magnetic Curves in the De-Sitter Space S_1^2, Symmetry 10 (11), 606, 2018.

[11] Bas, S., Korpinar, T., Modified Roller Coaster Surface in Space, Mathematics, 7 (2), 195, 2019.

[12] Bas, S., A New Method For Inextensible Flows of Adjoint Curves in Space, AIP Conference Proceedings 2116, 240003, 2019.

[13] O'Neill, B., Semi-Riemannian Geometry with Applications to Relativity, Academic Press, London, 1983.

[14] Bukcu, B., Karacan, M. K., On the Slant Helices according to Bishop Frame of the Timelike Curve in Lorentzian Space, Tamkang Journal of Math., 39, 255-262, 2008.

QUASI ADJOINT CURVES AND THEIR CHARACTERIZATIONS IN

3-DIMENSIONAL SPACE

Muhammed T. Sarıaydın[1], Talat Körpınar[2]

[1]Department of Mathematics, Faculty of Sciences, Selçuk University, Konya, TURKEY
[2]Department of Mathematics, Faculty of Art and Sciences, Muş Alparslan University, Muş, TURKEY

E-mail: talatsariaydin@gmail.com

Abstract

In this paper, we obtain some characterizations of quasi adjoint curves. The relationship between quasi adjoint curve and a spatial curve are examined according to quasi frame in three-dimensional Euclidean space. Additionally, some results and theorems are presented with special cases.

Keywords: Adjoint Curve, Line of Curvature, Quasi frame

1. INTRODUCTION

In geometry, Ruled surfaces have already been widely used in designing cars, ships, production of products and several additional areas for example movement analysis and simulation of a rigid body and model-based object recognition systems. Contemporary surface area modeling systems consist of ruled surfaces. The geometry of ruled surfaces is vital for studying kinematical and positional mechanisms in Euclidean 3-space. This surface area is often found in the scientific study from days gone by. For example, Odehnal explored subdivision algorithms ruled surfaces and Chen defined the mu-basis for a rational ruled surface, [5,10,13].

A developable surface may be formed by bending or rolling a planar surface without stretching out or tearing; in additional terms, it can become created or unrolled isometrically onto a plane. Developable surfaces are also known as singly curved surfaces since one of their principal curvatures is usually zero. Developable surfaces are broadly utilized with components that are not really responsive to extending. Applications consist of the development of ship hulls, ducts, shoes, clothing, and car parts such as upholstery, body windshields and panels, [3].

2. RESULTS AND DISCUSSION

Assume that $\alpha : s \to \alpha(s)$, which is parameterized by the arc-length parameter s is a regular curve. The derivative of the Frenet frame according to the arc-length parameter is governed by the relations;

$$T' = \kappa N,$$
$$N' = -\kappa T + \tau B,$$
$$B' = -\tau N,$$

where κ is the curvature and τ is torsion of the curve α. Now, we present an orthogonal frame $\{e_1, e_2, e_3\}$ as follows:

$$\frac{d}{ds}\begin{pmatrix} e_1 \\ e_2 \\ e_3 \end{pmatrix} = \begin{pmatrix} 0 & \kappa_1 & \kappa_2 \\ -\kappa_1 & 0 & \kappa_3 \\ -\kappa_2 & -\kappa_3 & 0 \end{pmatrix}\begin{pmatrix} e_1 \\ e_2 \\ e_3 \end{pmatrix},$$

where κ_i denotes the $q-$ curvatures satisfying, [2],

$$\kappa_1 = \kappa\,cos\phi = \langle e'_1, e_2 \rangle,$$
$$\kappa_2 = -\kappa\,sin\phi = \langle e'_1, e_3 \rangle,$$
$$\kappa_3 = d\phi + \tau = -\langle e'_3, e_2 \rangle.$$

Definition 1. Let α be a unit speed curve and $\{t,n,b\}$ is its Frenet frame in Euclidean 3-space. Then, the adjoint curve of curve α is, [12],

$$\beta(s) = \int_{s_0}^{s} b(s)ds.$$

Theorem 2. Let α be a unit speed curve, $\{t,n,b\}$ is its Frenet frame and β be adjoint curve of the curve α in Euclidean 3-space. Denote by $\{t_\beta, n_\beta, b_\beta\}$ the moving Frenet frame along the curve $\beta(s)$. Then, it can be written as, [12],

$$t_\beta = b,$$
$$n_\beta = -n,$$
$$b_\beta = t$$

and

$$\kappa_\beta = \kappa,$$
$$\tau_\beta = \tau.$$

We will describe the adjoint curve of a space curve as in [12] according to quasi frame in Euclidean 3-space.

Definition 3. Let γ be a regular curve with parametrized by arc-length and $\{t_q, n_q, b_q\}$ be its quasi frame. Then, the adjoint curve of a space curve γ according to quasi frame is

$$\sigma(s) = \int_{s_0}^{s} b_q(s)ds.$$

Theorem 4. Let γ be a unit speed curve, $\{t_q, n_q, b_q\}$ is its quasi frame and σ be adjoint curve of the curve γ in Euclidean 3-space. Denote by $\{t_\sigma, n_\sigma, b_\sigma\}$ the moving Frenet frame along the curve $\sigma(s)$. Then, it can be written as

$$\%_o = b_q\,,$$

$$\%_o = -\frac{\kappa_2 t_q + \kappa_3 n}{\sqrt{{\kappa_2}^2 + {\kappa_3}^2}}$$

$$\%_o = \frac{\kappa_3}{\sqrt{{\kappa_2}^2 + {\kappa_3}^2}} t_q - \frac{\kappa_2}{\sqrt{{\kappa_2}^2 + {\kappa_3}^2}} n_q$$

Theorem 5. A ruled surface

$$S : I \times_i \quad \rightarrow \quad E^3$$
$$(s,t) \quad \rightarrow \quad S(s,t) = \sigma(s) + t\%_o$$

for which $\sigma(s)$ is a the line of curvature of surface S, can not be described. Here σ is adjoint curve of the any space curve γ and $\%_o$ is tangent vector of curve σ in Euclidean 3-space.

Proof. Let σ be adjoint curve of a regular curve with parametrized by arc-length. If the curve σ is the line of curvature of the ruled surface S, the following equation must be provided

$$det\left(\sigma', \%_o, \%_o\right) = 0$$

and we know that σ is a line of curvature on the surface S if and only if the normal vector field $n(s,t)$ of the surface S along the curve $\sigma(s)$ is parallel to the principal normal vector field $\%_o$ of the curve σ; that is, $n(s,t) P \%_o$. But with simple operations, we have seen that $n(s,t)$ and $\%_o$ are not parallel.

REFERENCES

[1] Chen, F., Zheng, J., Sederberg, T.W., The mu-Basis of a Rational Ruled Surface, Comp. Aid. Des., 18, 61-72,2001.

[2] Dede, M., Ekici, C., Görgülü, A., Directional q-frame along a space curve. Int Jour Adv Res Comp Scie Soft Eng IJARCSSE, 5(12), 775-780, 2015.

[3] Frey, W.H., Bindschadler, D., Computer-Aid Design of a Class of Developable Bezier Surfaces, R&D Publication 8057, General Motors, 1993.

[4] Gorenstein, D., An arithmetic theory of adjoint plane curves, Transactions of the American Mathematical Society, 72(3), 414, (1952.

[5] Güven, İ.A., Nurkan, S.K., Tor, İ.A., Notes on W-direction curves in Euclidean 3-space, arXiv preprint arXiv:1506.03938, 2015.

[6] Körpınar, T., Turhan, E., On characterization of B-canal surfaces in terms of biharmonic B-slant helices according to Bishop frame in Heisenberg group Heis3. Journal of Mathematical Analysis and Applications, 382(1), 57-65, 2011.

[7] Körpınar, T., On evolute curves in terms of inextensible flows of in E^3. Boletim da Sociedade Paranaense de Matemática, 36(1), 117-124, 2018.

[8] Körpınar, T., Turhan, E., Spacelike Biharmonic New Type B-Slant Helices According to Bishop Frame in the Lorentzian Heisenberg Group H 3. Gen, 10(2), 36-42, 2012.

[9] Körpınar, T., & Turhan, E., New Approach for binormal spherical image in terms of inextensible flow in E3. Prespacetime Journal, 4(4), 2013.

[10] Kühnel, W., Curves- Surfaces- Manifolds, Diﬀerantial Geometry, Amer. Math. Soc., 2003.

[11] Mňuk, M., An algebraic approach to computing adjoint curves, Journal of Symbolic Computation, 23(2-3), 229, 1997.

[12] Nurkan, S. K., Güven, İ. A., Karacan, M. K., Characterizations of adjoint curves in Euclidean 3-space. Proceedings of the National Academy of Sciences, India Section A: Physical Sciences, 89(1), 155-161, 2019.

[13] Odehmal, B., Subdivision Algorithms for Ruled surfaces, Jour. For Geo. and Grap., 1(12), 1-18, 2008.

[14] Sendra, J.R., Sevilla, D., Radical parametrizations of algebraic curves by adjoint curves, Journal of Symbolic Computation, 46(9), 1030, 2011.

[15] Struik, J. D., Lectures on Classical Differential Geometry, Addison-Wesley Press. Inc.,Cambridge 42 Mass, 1950.

ON QUASI PEDAL CURVES AND QUASI PEDAL SURFACES IN 3-DIMENSIONAL EUCLIDEAN SPACE

Muhammed T. Sarıaydın[1], Vedat Asil[2]

[1]*Department of Mathematics, Faculty of Sciences, Selçuk University, Konya, TURKEY*
[2]*Department of Mathematics, Faculty of Sciences, Fırat University, Elazığ, TURKEY*

E-mail: talatsariaydin@gmail.com

Abstract

Notions of the pedal curves of regular curves are classical topics in differential geometry. Pedal curves are the loci of the feet of perpendiculars to the tangents of a fixed curve to a fixed point called the pedal point. In this paper, we present the concept of pedal surface of a pedal curve according to quasi frame in 3-dimensional Euclidean space. Additionally, some results and theorems are presented with special cases.

Keywords: Pedal curve, Pedal surface, Quasi frame

1. RESULTS AND DISCUSSION

Assume that $\alpha : s \to \alpha(s)$, which is parameterized by the arc-length parameter s is a regular curve. The derivative of the Frenet frame according to the arc-length parameter is governed by the relations;

$$T' = \kappa N,$$
$$N' = -\kappa T + \tau B,$$
$$B' = -\tau N,$$

where κ is the curvature and τ is torsion of the curve α. Now, we present an orthogonal frame $\{e_1, e_2, e_3\}$ as follows:

$$\frac{d}{ds}\begin{pmatrix} e_1 \\ e_2 \\ e_3 \end{pmatrix} = \begin{pmatrix} 0 & \kappa_1 & \kappa_2 \\ -\kappa_1 & 0 & \kappa_3 \\ -\kappa_2 & -\kappa_3 & 0 \end{pmatrix} \begin{pmatrix} e_1 \\ e_2 \\ e_3 \end{pmatrix},$$

where κ_i denotes the $q-$ curvatures satisfying, [1],

$$\kappa_1 = \kappa \cos\phi = \langle e'_1, e_2 \rangle,$$
$$\kappa_2 = -\kappa \sin\phi = \langle e'_1, e_3 \rangle,$$
$$\kappa_3 = d\phi + \tau = -\langle e'_3, e_2 \rangle.$$

Definition 1. Let C be a curve in E^3 and O be a fixed point not on C. The locus of the foots of perpendicular drawing from O to the tangents of C with respect to O as origin are called the pedal curve of C with respect to O, [13].

Definition 2. Let S be a smooth, convex surface in E^3 and O be a point not on S. If Ξ is position vector of a point k on S with respect to O as origin and N is the inner unit normal vector of the surface at $k \in S$, then support function h of S is defined by

$$h = -\langle X, N \rangle$$

where $\langle , \rangle$ is the usual metric in E^3, [4].

In this section, we will describe the pedal curve and the pedal cone surface as in [kasap] according to quasi frame.

Let γ be a regular curve with parametrized by arc-length and

$$S : I \times_i \quad \rightarrow \quad E^3$$
$$(s,t) \quad \rightarrow \quad S(s,t) = \gamma(s) + te_1$$

be a ruled surface in E^3. Here e_1 is unit quasi tangent vector of curve γ. In this case, the pedal curve of ruled surface S can be written as follows

$$\not\gamma(s) = \gamma(s) + q(s)e_1(s),$$

where q is the distance between the points $\gamma(s)$ and $\not\gamma(s)$.

Since

$$S_s = e_1 + t\kappa_1 e_2 + t\kappa_2 e_3,$$
$$S_t = e_1.$$

From Eq. (1), normal vector of surface S is

$$n(s,t) = t\left(\kappa_2 e_2 + \kappa_3 e_3\right).$$

Then, the ruled surface $\not{S}$ can be written by

$$\not{S}(s,u) = \not\gamma(s) + un(s,t).$$

Example 3. Let us consider the space curve α which is defined by

$$\alpha : R \rightarrow R^3$$

$$\alpha(t) = \begin{pmatrix} -\dfrac{18}{5}\sin\left(-\dfrac{t}{4}\right) + \dfrac{2}{45}\sin\left(\dfrac{9t}{4}\right), \\[3mm] -\dfrac{18}{5}\cos\left(-\dfrac{t}{4}\right) + \dfrac{2}{45}\cos\left(\dfrac{9t}{4}\right), \\[3mm] \dfrac{3}{5}\cos t \end{pmatrix}$$

Calculating the first derivative of α; one can easily see that

$$\left\| \alpha'(t) \right\| \neq 0$$

for all $t \in R$. So we can say that α is a regular space curve. In the light of the quasi formulas, one can easily obtain the quasi frame $\{t_q, n_q, b_q\}$ of α. The graphics of the curve α and its spherical images are given below.

Fig. 1. The Curve α

Fig. 2. Tangent Vector of The Curve α

Fig. 3. Pedal Curve of The Curve α , $q(t) = log(t)$

Fig. 4. Pedal Curve of The Curve α , $q(t) = sin(log(t))$

REFERENCES

[1] Dede, M., Ekici, C., Görgülü, A., Directional q-frame along a space curve. Int Jour Adv Res Comp Scie Soft Eng IJARCSSE, 5(12), 775-780, 2015.

[2] Eschenbach, P.W., Standup exercise apparatus with pedal articulation, U.S. Patent No. 6,142,915. 7, 2000.

[3] Huang, F., Su, J., Deformable pedal curves with application to face contour extraction, IEEE Computer Society Conference on Computer Vision and Pattern Recognition, 2003. Proceedings, 1,1,.2003.

[4] Kasap, E., Saraoğlugil, A., Kuruoğlu, N., The Pedal Cone Surface of a Developable Ruled Surface, Int. J. Pure and App. Mat., 2 (19), 157-164, 2005.

[5] Körpınar, T., Turhan, E., On characterization of B-canal surfaces in terms of biharmonic B-slant helices according to Bishop frame in Heisenberg group Heis3. Journal of Mathematical Analysis and Applications, 382(1), 57-65, 2011.

[6] Körpınar, T., On evolute curves in terms of inextensible flows of in E³. Boletim da Sociedade Paranaense de Matemática, 36(1), 117-124, 2018.

[7] Körpınar, T., Turhan, E., Spacelike Biharmonic New Type B-Slant Helices According to Bishop Frame in the Lorentzian Heisenberg Group H 3. Gen, 10(2), 36-42, 2012.

[8] Körpınar, T., & Turhan, E., New Approach for binormal spherical image in terms of inextensible flow in E3. Prespacetime Journal, 4(4), 2013.

[9] Lockwood, E.H., A book of curves. Cambridge University Press, 1967.

[10] Nishimura, T., Normal forms for singularities of pedal curves produced by non-singular dual curve germs in Sn, Geometriae Dedicata, 133(1), 59, 2008.

[11] Nishimura, T., Singularities of pedal curves produced by singular dual curve germs in Sn, Demonstratio Mathematica, 43(2), 447, 2010.

[12] Nishimura, T., Singularities of one-parameter pedal unfoldings of spherical pedal curves, Journal of Singularities, 2, 160, 2010.

[13] Struik, J. D., Lectures on Classical Differential Geometry, Addison-Wesley Press. Inc.,Cambridge 42 Mass, 1950.

[14] Vemuri, B.C., Guo, Y., Wang, Z., Deformable pedal curves and surfaces: Hybrid geometric active models for shape recovery, International Journal of Computer Vision, 44(2), 137, 2000

THE INVESTIGATION OF NSS, RS AND INTERFACIAL LAYER ON THE ELECTRICAL CHARACTERISTICS OF Au/ $Ca_3Co_4Ga_{0.001}O_X$ /n-Si/Au

E. MARIL

Department of Property Protection and Security, Karabük University, Karabük, TURKEY

E-mail: elifmaril@karabuk.edu.tr

Abstract

In order to determine the N_{SS}, R_s and interfacial layer on the electrical characteristics, both the c-v and G/ω-V measurements were performed at 7 and 500 kHz at room temperature. Experimental results were confirmed that the main electrical parameters such as diffusion potential (V_D), series residence (R_s), Fermi energy level (E_F), barrier height (Φ_B (C-V)) and surface states (N_{SS}) are found a strong a function of frequency and voltage. Both the R_s and N_{SS} were excepted from the Nicollian-Brews and high-low C_{HF}-C_{LF} frequency method, respectively. They show a distinctive peak at about depletion region due to surface state and interfacial layer.

Keywords: Interfacial layer, Nicollian-Brews method, High-low C_{HF}-C_{LF} frequency method

1. INTRODUCTION

Since an interfacial insulator or polymer layer inserted between metal and semiconductor, metal-semiconductor (MS) structure is converted to MIS or MPS structure or capacitor. [1-3]. Especially, the use of high-dielectric interfacial leads to improve the performance of the MS and MIS type structure [3-8]. The capacitance-voltage (C-V) and conductance-voltage (G/ω-V) measurements in the wide range of applied bias voltage can be supplied more information on the electrical characteristics of these devices. Therefore, in this study, the electrical characteristics of Au/(Ca$_3$Co$_4$Ga$_{0.001}$O$_x$)/n-Si (MPS) have been investigated by using C-V and G/ω-V measurements for at low (7 kHz) and high (500 kHz) frequencies at room temperature by taking into account density distribution of N$_{ss}$, and R$_s$ and polymer interfacial layer.

2. MATERIAL AND METHODS

In this study, Au/ Ca$_3$Co$_4$Ga$_{0.001}$O$_x$ /n-Si/Au structures were fabricated on n-Si single crystal (P-doped) with 0.001-0.005 Ω.cm resistivity, (100) orientation and ~250 µm thickness.

Firstly, wafer was ultrasonically cleaned in the various solutions, rinsed by propylene glycol and blown dry N$_2$ gas. Secondly, wafer immediately was transferred into the high vacuum metal evaporation system and then high purity Au (99.999 %) with 150 nm thickness was thermally evaporated onto the whole back side of n-Si wafer at 10-6 Torr and then was annealed at 500°C in the nitrogen ambient at 5 min to get a good ohmic contact.

After formation ohmic contact, Ca$_3$Co$_4$Ga$_{0.001}$O$_x$ interfacial layer was grown on front of the n-Si wafer by using electrospinning method. Finally, the high purity of Au dots with 1 mm diameter and at about 150 nm thickness were deposited on the (Ca$_3$Co$_4$Ga$_{0.001}$O$_x$) interfacial layer. The C-V and G/ω-V measurements were performed by using an HP 4192A LF impedance analyzer.

The VHR method arises from recording the maximum temperatures of the glow peak with different heating rates. The maximum temperature T$_m$ is associated with the heating rate β, this relation could be described in equation (1) as VHR method:

$$\ln(T_m^2 / \beta) = E / kT_m + \ln(E / ks) \qquad (1)$$

where k is Boltzmann's constant, T$_m$ is the maximum temperature of glow peak , E is the activation energy (eV) and s is the frequency factor (s^{-1}). After recording T$_m$ with a number of different heating rates, E could be calculated from the slope of the straight line obtained from the plot of the ln (T^2_m/ β) versus 1/T$_m$. The

intercept of the slope this plot gives the value of s [12, 13]. Kitis and Tuyn proposed a model to correct for the temperature lag based on TSL measurements [14]. This model is given as an equation (2):

$$T_m^b = T_m^a - c \ln\left(\frac{\beta_a}{\beta_b}\right) \tag{2}$$

where c is a constant and T_m^a and T_m^b are the maximum temperatures of glow peaks with heating rates β_a and β_b, respectively.

3. RESULTS AND DISCUSSION

Both the C-V and G/ω-V measurements of the $Au/Ca_3Co_4Ga_{0.001}O_x/n\text{-}Si/Au$ capacitor was given in Fig. 1(a) and (b), respectively. As can be seen in this figure, both the C-V and G/w-V plots have an inversion, depletion and accumulation regions at 7 and 500 kHz.

Both the values of C and G/ω show (Figs.1 (a) and (b)) quite dispersion with frequency especially in the depletion region due to the existence of Nss and surface polarization at low frequency.

On the other hand, these discrepancy in the accumulation region is the result of series resistance (Rs) and interfacial layer. Such high values of C and G/ω at low (7 kHz) were attributed to the relaxation times (t) of the charges at surface states are much larger than the measured period ($T=1/\omega=1/2pf$) and so they can follow an ac signal and polarization (surface and dipole) [1,4]. But at high frequency (500 kHz), Nss and polarization cannot an excess contribution to the measured C and G values contrary to low frequency

The main electrical parameters such as diffusion potential ($V_D = V_o + kT/q$), doping concentration of donor atoms (N_D), Fermi energy level (E_F), and barrier height (Φ_B (C-V)) were obtained from the intercept and slope of the reverse bias C^{-2} vs V plot for 500 kHz as 0.850 eV, $8.95\times10^{17}cm^{-3}$, 0.086 eV, and 0.936 eV, respectively.

Figure 1. (a) C-V and (b) G/w-V plots of Au/Ca3CO4Ga0.001OX/n-Si capacitor for 7 and 500 kHz.

$$N_D = \frac{2}{(q\varepsilon_S\varepsilon_O A^2 \tan\theta)} \tag{1}$$

$$\Phi_B = \frac{kT}{q} + V_O + \left(\frac{kT}{q}\right)\ln\left(\frac{N_C}{N_D}\right) \tag{2}$$

Figure 2. The C^{-2}-V plot of Au/Ca$_3$Co$_4$Ga$_{0.001}$O$_x$/n-Si caapcitor for 500 kHz.

The value of Nss and Rs are also very important effect on C-V and G/ω-V characteristic especially at low and high frequencies, respectively. Therefore, the voltage dependent profile of Rs and Nss were obtained by using Nicollian-Brews [1,10] ang high-low frequency capacitance method, and they represented in Figures 3 and 4, respectively.

$$N_{ss} = (qA)^{-1} \cdot [(1/C_{LF} - 1/C_i)^{-1} - (1/C_{HF} - 1/C_i)^{-1}] \tag{3}$$

As shown in the Ri-V plot (Fig. 3), the value of resistance (Ri) increase with decreasing voltage, but the real value of Rs is corresponding to the strong accumulation region.

Figure 3. The R$_s$-V Au/(Ca$_3$Co$_4$Ga$_{0.001}$O$_x$)/n-Si capacitor for 500 kHz.

[4] Tripathi, S. K., Sharma, M., Analysis of the forward and reverse bias I-V and C-V characteristics on Al/PVA: n-PbSe polymer nanocomposites Schottky diode, Journal of Applied Physics. 111, 074513, 2012.

[5] Hoque Md. M., Dutta A., Kumar Sanjay, Sinha T.P., Dielectric Relaxation and Conductivity of Ba $(Mg_{1/3}Ta_{2/3})O_3$ and Ba$(Zn1/3Ta_{2/3})O_3$, Journal of Materials Science & Technology, 30, 311-320, 2014.

[6] Cho, M. S., Park, S. Y., Hwang J. Y., Choi, H., Synthesis and electrical properties of polymer composites with polyaniline nanoparticles, Materials Science and Engineering: C, 15-18, 2004.

[7] Marıl E., Tan S. O., Altındal Ş., Uslu İ., Evaluation of Electric and Dielectric Properties of Metal–Semiconductor Structures With 2% GC-Doped-$(Ca_3CO_4Ga0,_{001}O_x)$ Interlayer, IEEE Transactions on Electron Devices, 65, 3901-3908, 2018.

[8] Marıl, E., Kaya, A., Çetinkaya, H.G., Koçyiğit, S., Altındal, Ş., On the Temperature Dependent Forward Bias Current-Voltage (I-V) Characteristics in Au/2% graphene-cobalt doped $(Ca_3CO_4Ga0,_{001}O_x)$/n-Si Structure, Materials Science in Semiconductor Processing 39, 332-338, 2015.

[9] Catagné, R., Vapaille A., Description of the SiO_2 · Si interface properties by means of very low frequency MOS capacitance measurements, Surface Science, 28, 157-193, 1971.

[10] Marıl, E., Altındal, Ş., Kaya, A., Koçyiğit, S., Uslu, İ., On Double Exponential Forward Bias Current-Voltage (I-V) Characteristics of Au/$Ca_3CO_4Ga0,_{001}O_x$/n-Si/Au (MS) Type Structures in Temperature Range of 80-340 K, Philosophical Magazine 95, 1049-1068, 2015.

THE EFFECT OF OPERATIONAL PARAMETERS ON THE PHOTOCATALYTIC DECOLORIZATION OF REACTIVE YELLOW 145

N. Turkten

¹ *Department of Chemistry, Faculty of Arts and Sciences, Kirsehir Ahi Evran University, Kirsehir, TURKEY*

E-mail: nazli.turkten@ahievran.edu.tr

Abstract

Heterogeneous photocatalysis is an advanced oxidation process and this alternative approach has gained an enormous interest to degrade organic contaminants in wastewater in recent decades. The process is based on the combined use of UV-A light and semiconductors to decompose organic pollutants. Owing to its chemical inertness, photostability, low-cost, non-toxicity and high oxidative power, TiO_2 is the most efficient photocatalyst for this process. However, TiO_2 is active under only UV light because of its wide band gap. This disadvantage, limits its usage under solar light as a renewable energy source. Overcoming this issue, TiO_2 is doped with metal or non-metal ions to improve its activity under solar light in recent years.

In this study, solar light sensitive copper doped TiO_2 photocatalyst containing 0.25 wt% Cu (0.25%Cu-TiO_2) was prepared by a simple wet-impregnation method and followed by a heat treatment. $Cu(NO_3)_2 \cdot 3H_2O$ was used as the dopant source. The photocatalytic activity of 0.25%Cu-TiO_2 photocatalyst was determined by investigating the photocatalytic decolorization of Reactive Yellow 145 under solar light irradiation. The effect of operational parameters such as amount of catalyst, the initial dye concentration, and the initial pH on the decolorization percentage of dye was also studied.

Keywords: Copper doped TiO_2, Decolorization, Photocatalysis, Reactive Yellow 145

1. INTRODUCTION

Reactive dyes are anionic dyes that extensively used especially in textile industry [1-3]. They can be expressed by chromophoric system such as azo, anthraquinone, phtahalocyanine etc. and the anchor group such as vinylsulfone, chlorotriazine etc. [4]. Azo dyes constitute an important class of pollutants in wastewater released from textile industries. Discharging of these azo dyes into water after dyeing and finishing processes in the textile industry can cause serious environmental and health problems [5-6]. Reactive azo dyes are resistant to aerobic degradation and their degradation products are highly carcinogenic.

Conventional treatment methods are either ineffective to remove them from wastewater or they only transfer them to another phase causing a secondary pollution. These synthetic dyes are resistant to microbial degradation. Thus, removal of azo dyes from wastewater of the textile industry is greatly significant and many studies are made for the development of water treatment technologies in recent years. Photocatalysis is an advanced oxidation process to destroy organic contaminants in water or air converting them to small molecules such as CO_2, H_2O and HCl. The process is based on the combined use of UV-A light and semi-conductors to decompose organic pollutants. Owing to its chemical inertness, photostability, low-cost, non-toxicity and high oxidative power the anatase form of TiO_2 is the most efficient photocatalyst for this process [7-10].

Doping TiO_2 with metal or non-metal ions to improve its activity under solar light has attracted great interest in recent years. New photocatalysts are made with using impurity doping approach to improve the photocatalytic property of TiO_2. For this reason, recent studies have focused on doping TiO_2 with metallic elements (such as Ag, Pt, Cr, V and Fe) and non-metallic elements (B, C, S, F and N) to enhance the photocatalytic activity in visible light. The doped metal ion enhances the photocatalytic activity by reducing electron–hole pair recombination and narrowing the band gap [12-22].

In the present study, visible light active photocatalyst was prepared. For this reason, copper doped TiO_2 photocatalyst containing 0.25 wt% Cu (0.25%Cu-TiO_2) was prepared by a simple wet-impregnation method and followed by a heat treatment. $Cu(NO_3)_2 \cdot 3H_2O$ was used as the dopant source. Reactive Yellow (RY 145) is a commercial azo dye widely used in dyeing process of textile The photocatalytic activity of 0.25%Cu-TiO_2 photocatalyst was determined by investigating the photocatalytic decolorization of RY 145 under solar light irradiation. The effect of operational parameters such as amount of catalyst, the initial dye concentration, and the initial pH on the decolorization of the dye was also studied.

2. MATERIAL AND METHODS

TiO_2 Evonik P25 grade with a particle size of about 21 nm and a surface area of 50 m^2 g^{-1} was used as the photocatalyst without further treatment. Evonik P25 powder, which is a mixture of anatase and rutile phases (79 % anatase, 21 % rutile) is one of the photocatalysts with high activity and has been used as a standard TiO_2 reference material. $Cu(NO_3)_2 \cdot 3H_2O$ was purchased from Merck. All the chemicals that were used in the experiments were of laboratory reagent grade and used as received without further purification. The solutions were prepared with doubly distilled water. 0.25 wt% Cu (0.25% $Cu-TiO_2$) was prepared by a simple wet-impregnation method described as follows: 10 g TiO_2 Evonik P25 and appropriate amount of $Cu(NO_3)_2 \cdot 3H_2O$ were mixed with definite volume of doubly distilled water and stirred for 1h. Evonik P25 was mixed with 15 mL of aqueous solutions of dopant and stirred for 1 h at room temperature. Then, the prepared photocatalyst was washed with water, heat-treated at 373 K for 24 h to eliminate water, calcined at 773 K for 3 h, ground and sieved [23].

Photocatalytic decolorization of RY 145 was performed in an ATLAS Suntest CPS+ simulator as solar photocatalytic reactor, equipped with an air cooled Xenon lamp (250 W m^{-2} and wavelength range of 300–800 nm) as the light source. 50 mL of 20 mg L^{-1} dye solution was put in a 150 mL cylindrical Pyrex reaction vessel and subjected to solar photocatalytic oxidation process in the presence of 0.25 mg mL^{-1} photocatalyst. An ultrasonic water bath was used for the preparation of a homogenous suspension. Continuous stirring was applied during the experiments. After the experiments, samples were filtered through 0.45 μm Millipore filters in order to remove TiO_2 specimens from the solution prior to analyses via UV-Vis spectrometer. λ_{max} value and molecular weight of RY 145 was 419 nm and 1026.2 mol.g^{-1}, respectively. The chemical structure of RY 145 is given in Figure 1.

Figure 1. The chemical structure of RY 145.

3. RESULTS AND DISCUSSION

The effect of operational parameters such as photocatalyst amount, initial concentration of RY 145 and pH of the solution was investigated.

(A)

(B)

Figure 2. The UV-Vis spectra of RY 145 with different amounts of 0.25%Cu-TiO$_2$.

Figure 2 shows the UV-Vis spectra of RY 145 with different amounts of 0.25%Cu-TiO$_2$. The dye concentration was 20 mg/L. The removal percentage was obtained 92% and 96% after irradiation 80 minutes for 0.25 gL^{-1} and 0.50 g L^{-1} of 0.25%Cu-TiO$_2$, respectively. As the amount of the photocatalyst was increased, a slight change was observed. Thus, a minimum catalyst dose, 0.25 g L^{-1} was preferred in experiments.

Removal percentages were determined from Equation (1), where C$_0$ is the initial concentration of the dye and C is the dye concentration at time t.

$$Removal \% = \frac{C_0 - C}{C_0} \ x \ 100 \tag{1}$$

In Figure 3, the effect of initial dye concentration on the removal percentages after 60 minutes irradiation time was given. The initial concentration of RY 145 was investigated in the range of 10 mg/L-40 mg/L. The results showed that the removal percentage of RY 145 depended on the initial dye concentration. For the lowest initial concentration 10 mg/L of RW 145, removal percentage was 86%. However, at higher concentrations, several layers of the RY 145 could be adsorbed on to the photocatalyst surface. This may inhibit the removal of dye with photogenerated holes or hydroxyl radicals [24-25].

Figure 3. The effect of initial dye concentration on the removal percentages of RY 145.

In this study, the effect of variation of pH on the removal percentages of RY 145 was investigated and presented in Figure 4. The best result was obtained in acidic pH=3 (92%). At almost neutral pH=6, the removal percentage for RY 145 was 81%. The removal percentage was the lowest at pH=10 (49%). The reason could be the decreasing of the oxidation potential of hydroxyl radicals [24-25].

Figure 4. The effect of pH on the removal percentages of RY 145.

4. CONCLUSION

In this study, copper doped TiO_2 photocatalyst, $0.25\%Cu\text{-}TiO_2$ was prepared by a simple wet-impregnation method and photocatalytic decolorization of RY 145 was investigated. Moreover, the effects of the amount of the photocatalyst, the initial concentration of RY 145 and the pH variation of the solution on the removal percentage of RY 145 was examined. The removal percentages of azo dyes strongly depended upon the pH of the solution. The highest removal percentage of RY 145 was obtained for pH=3.

ACKNOWLEDGMENTS

Author would like to express her gratitude to Prof. Miray Bekbolet for allowing her to conduct photocatalytic experiments at the laboratories of Boğaziçi University, Institute of Environmental Sciences.

REFERENCES

[1] Brillas, E. and Martínez-Huitle, C. A., Decontamination of wastewaters containing synthetic organic dyes by electrochemical methods. An updated review, Applied Catalysis B: Environmental, 166-167, 603-643, 2015.

[2] Forgacs, E., Cserháti, T. , Oros, G., Removal of synthetic dyes from wastewaters: a review, Environment International, 30, 953-971, 2004.

[3] Martínez-Huitle, C. A., Brillas, E., Decontamination of wastewaters containing synthetic organic dyes by electrochemical methods: A general review, Applied Catalysis B: Environmental, 87, 105-145, 2009.

[4] Bansal, P. and Sud, D., Photodegradation of commercial dye, CI Reactive Blue 160 using ZnO nanopowder: Degradation pathway and identification of intermediates by GC/MS, Separation and Purification Technology, 85, 112-119, 2012.

[5] Nilsson, R., Nordlinder, R., Wass, U., Meding, B., Belin, L., Asthma, rhinitis, and dermatitis in workers exposed to reactive dyes, Occupational and Environmental Medicine, 50, 65-70, 1993.

[6] Stylidi, M., Kondarides, D. I., Verykios, X. E., Pathways of solar light-induced photocatalytic degradation of azo dyes in aqueous TiO_2 suspensions, Applied Catalysis B: Environmental, 40, 271-286, 2003.

[7] Bahnemann, D., Bockelmann, D., Goslich, R., Mechanistic studies of water detoxification in illuminated TiO_2 suspensions, Solar Energy Materials, 24, 564-583, 1991.

[8] Liu, G., Wang, L., Yang, H. G., Cheng, H.-M., Lu, G. Q., Titania-based photocatalysts-crystal growth, doping and heterostructuring, Journal of Material Chemistry, 20, 831-843, 2010.

[9] Manso, M., Ogueta, S., García, P., Pérez-Rigueiro, J., Jiménez, C., Martínez-Duart, J. M., Langlet, M., Mechanical and in vitro testing of aerosol–gel deposited titania coatings for biocompatible applications, Biomaterials, 23, 349-356, 2002.

[10] Ollis, D. F., Pelizzetti, E., Serpone, N. Photocatalyzed destruction of water contaminants, Environmental Science & Technology, 25, 1522-1529, 1991.

[11] Xu, T., Kamat, P. V., Joshi, S., Mebel, A. M., Cai, Y., O'Shea, K. E, .Hydroxyl radical mediated degradation of phenylarsonic acid. The journal of physical chemistry. A 111, 7819-7824, 2007.

[12] Birben, N. C. et al. Comparative evaluation of anion doped photocatalysts on the mineralization and decolorization of natural organic matter, Catalysis Today, 240, Part A, 125-131, 2015.

[13] Diebold, U., The surface science of titanium dioxide. Surface Science Reports 48, 53-229, 2003.

[14] In, S., Orlov, A., Berg, R., Garcia, F., Pedrosa-Jimenez, S., Tikhov, M. S., Wright, D. S., Lambert, R. M., Effective visible light-activated B-doped and B, N-codoped TiO_2 photocatalysts, Journal of the American Chemical Society, 129, 13790-13791, 2007.

[15] Likodimos, V., Han, C., Pelaez, M., Kontos, A. G., Liu, G., Zhu, D., Liao, S., de la Cruz, A. A., O'Shea, K., Dunlop, P. S. M., Byrne, J. A., Dionysiou, D. D., Falaras, P., Anion-Doped TiO2 Nanocatalysts for Water Purification under Visible Light. Industrial & Engineering Chemistry Research, 52, 13957-13964, 2013.

[16] Lu, J., Su, F., Huang, Z., Zhang, C., Liu, Y., Ma, X., Gong, J., N-doped Ag/TiO_2 hollow spheres for highly efficient photocatalysis under visible-light irradiation, RSC Adv. 3, 720-724, 2013.

[17] Yalçın, Y., Kılıç, M., Çınar, Z. The Role of Non-Metal Doping in TiO2 Photocatalysis. Journal of Advanced Oxidation Technologies 13, 281-296 (2010).

[18] Zaleska, A. Doped-TiO_2: A Review. Recent Patents on Engineering 2, 157-164, 2008.

[19] Ho, W., Yu, J. C., Sonochemical synthesis and visible light photocatalytic behavior of CdSe and $CdSe/TiO_2$ nanoparticles. Journal of Molecular Catalysis A: Chemical 247, 268-274, 2005.11.057, 2006.

[20] Wu, L., Yu, J. C. & Fu, X. Characterization and photocatalytic mechanism of nanosized CdS coupled TiO_2 nanocrystals under visible light irradiation, Journal of Molecular Catalysis A: Chemical, 244, 25-32, 2006.

[21] Yu, C., Cai, D., Yang, K., Yu, J. C., Zhou, Y., Fan, C., Sol–gel derived S,I-codoped mesoporous TiO_2 photocatalyst with high visible-light photocatalytic activity, Journal of Physics and Chemistry of Solids, 71, 1337-1343, 2010.

[22] Gurkan, Y. Y., Kasapbasi, E., Cinar, Z., Enhanced solar photocatalytic activity of TiO_2 by selenium(IV) ion-doping: Characterization and DFT modeling of the surface, Chemical Engineering Journal, 214, 34-44, 2013.

[23] Turkten, N., Cinar, Z., Tomruk, A., Bekbolet, M., Copper-doped TiO_2 photocatalysts: application to drinking water by humic matter degradation, Environmental science and pollution research international, 2019.

[24] Buxton, G. V., Greenstock, C. L., Helman, W. P., Ross, A. B., Critical Review of rate constants for reactions of hydrated electrons, hydrogen atoms and hydroxyl radicals ($\cdot OH/\cdot O^-$ in Aqueous Solution, Journal of Physical and Chemical Reference Data, 17, 1988..

[25] Grzechulska, J. and Morawski, A. W., Photocatalytic decomposition of azo-dye acid black 1 in water over modified titanium dioxide, Applied Catalysis B: Environmental 36, 45-51, 2002.

MICELLIZATION AND THERMODYNAMIC PROPERTIES OFCATIONIC SURFACTANTCETYLTRIMETHYLAMMONIUM CHLORIDE(CTACl) IN AQUEOUS MIXTURE OF POLYVINYLPYRROLIDONE (PVP)

O.Masalcı

[1]*Department of Physics, Faculty of Sciences, Ege University, İzmir, TURKEY*

E-mail: ozgur.masalci@ege.edu.tr

Abstract

Surfactants and water-soluble polymers are of very great application. It is important that polymers are combined with surfactant in the industry and the related research has been made. Interaction between polymer and surfactant in an aqueous solution relies on the molecular aspects of the polymer and the surfactant. Moreover, polymer and surfactant mixture is effected by a variety of factors, including hydrophilic polar head group, hydrophobic hydrocarbon tail, cosurfactant, temperature, PH etc.

Thermodynamics of the micellization process of the surfactant in water with and without the polymer has been widely examined using conductometry technique. Conductometric measurements have been made to obtain a comprehensive knowledge of the interactions of the surfactant with the polymer in a solution. Considering importance of the polymer–surfactant system, intermolecular interactions of Cetyltrimethylammonium chloride (CTACl) with polymer (PVP) in the solution has been studied.

The present study has determined a critical micelle concentration(CMC), critical aggregation concentration (CAC) and degree of ionization (α) of the aqueous solution composed of CTACl surfactant and PVP by electrical conductivity at distinct temperatures. One has calculated the thermodynamic parameters (Gibbs free energy, enthalpy and entropy) of the surfactant in the absence and presence of the polymer.

Keywords: Critical Micelle Concentration(CMC), Enthalpy, Entropy, CTACl

1. INTRODUCTION

The word surfactant is an acronym for surface active agent [1]. Surface active agents are chemical compounds to affect surface tension (mostly reduce) once they have been dissolved in water or in an aqueous solution. Surfactants also influence the interfacial tension between the two liquids. Surface active agents are those which can be self-assembly consisting of hydrophilic and hydrophobic parts.

Their most explicit properties are that they accumulate on both the water-air and the water-oil surfaces when they have been added to water, the reason for which is that water molecules are closely connected to each other by means of hydrogen bonds [1, 2]. This leads to the fact that water molecules in contact with the air wrap the water surface like a stretched membrane. Therefore, the water is collected as droplets when they poured onto a surface. With the surfactant, this qualification of the water is disturbed. The polar main group of the surfactant can be decomposed in water through ionization or establishment of hydrogen bonds. However, hydrocarbon chain has no edge to hold onto the water molecules. Thus, it can be present in water only at the expense of deformation of part of the hydrogen bonds, which could just be tolerated with very low surfactant concentrations. When the concentration increases up to a given value, the majority of the surfactant molecules are aggregated in micelles and the others are pushed to the water-air interface in the forms of the head groups inside and the hydrocarbon chains outside [1, 3]. That is why, such substances are named surfactant. The concentration at which surfactant molecules begin to accumulate in micelles is called the Critical Micelle Concentration (CMC), a characteristic for each surfactant [4]. Surfactants have a cleansing impact only above the CMC.

Monomer is a phrase to refer to small molar mass chemical. They bond to each other by covalent bonds, producing larger molecules. Polymer is bigger macromolecules made up of hundreds of monomers. Use of the material is as an antiseptic, a cationic surfactant and its other uses are shampoo and cosmetic items. PVP is known to be widely utilized as a medicine in pharmacy. On the other hand, it is a potential substitute for albumin serum in the blood [5].

2. MATERIAL AND METHODS

Material

Cetyltrimethylammonium chloride (CTACl-at no: 52366 Fluka) of molecular weight 320.00g/mol is supplied by Fluka, which has been used with no processes or modifications. Polyvinylpyrrolidone (PVP), aka polyvinylpyrrolidone, is a water-soluble polymer made from the monomer N-vinylpyrrolidone.

Polyvinylpyrrolidone (PVP-cat no: 9003-39-8) with an average molar mass 10000 g/mol is obtained from Sigma-Aldrich. Deionized water has been used as the solvent medium of the experiment.

Methods

Krüss Easy Dyne tensiometer was used to measure the surface tension of the samples. For the measurements made with Wihelmy plate method, the samples were placed in a container and the plate was submerged by tensiometer in a small amount. Depending on the breakout force, the surface tension results are shown on the tensiometer display.

The system which measures the electrical conductivity is basically consist of two main parts. One of them is the WTW Cond Level 3 module to which the probe is connected. The TetraCon 325 prob convenient for our measurements, which has been coupled with the cable-galvanized module. The probe measurement range is of 5–100 °C (with an accuracy of 0.2 °C) for temperature and 1 µS/cm-2 S/cm (the accuracy is temperature dependent and 5%) for electro conductivity. The other one is the WTW Cond Level 3 terminal section where the system is managed and the measurements are displayed. A PHYWE make thermostat heater has been selected to heat the sample.

3. RESULTS AND DISCUSSION

To determine CMC is usually based on the localizing the position of a breaking point in the concentration dependencies of selected physical or chemical properties of surfactant solutions [6]. Figure 1 a exhibits characteristic plots of the surface tensions versus CTACl in water. Given the surface activity of such substances, measurement of the surface tension of surfactant solutions represents the major method to determine CMCs.

The electrical conductivity is based on discovery of a breaking point on the curves, which describes the dependence of conductivity on concentration. It is obvious that the electrical conductivity of any solution is directly proportional to the concentration of its ions. The point where the micelle formation starts is shown as a breaking point of electrical conductivity. It is easy to find the breaking point since it indicates a significant change of the linear slope of the dependence.

(a)   (b)

Figure 1. CMC value was determined as 1.7 mM at 20C **a)** by using surface tension method **b)** by using electrical conductivity method

The present study has examined the aggregation process between a cationic surfactant (Cetyltrimethylammonium Cloride_CTACl) and Polyvinylpyrrolidine (PVP) to study the energetics of the process.

(a)   (b)

Figure 2. Change in electrical conductivity of different concentrations of CTACl in PVP solutions **a)** at 30C **b)** 35 C

With the addition of PVP polymer to the solution, significant changes in slopes can be seen on the graph (Figure 2 a-b), occurring based on polymer-surfactant interaction. The breaking points are called CAC and C2 [7]. As observed on the graph, they are accounted for by strong bindings and clustering at the CAC

point in the presence of polymer. The surfactant monomer concentration and activity have increased again due to the interaction between surfactants and polymers and thus normal micelles begin to shape at C2.

Molecules accumulate around the polymer chain and begin to create pre-micelles due to hydrophobic and hydrophilic groups in the PVP/ CTACl solution, in which the molecules beginning to aggregate are surrounded by opposite charges. Such screening effect causes the CAC value to drop under the CMC value [8].

At CMC, the term Gibbs free energy is calculated with the equation (1) whereas the surfactants are aggregated with the passage of the hydrocarbon chain in the surfactant through the aqueous platform into the micelle.

$$\Delta G = (2-\propto)RT ln X_{cmc}........(1)$$

X_{cmc} is the mol amount of surfactant at the critical micelle concentration, R the general gas constant and its value R=8,31J/mol, the temperature value T in Kelvin and the degree of ionization of micelle in α. The degree of ionization of micelle α is calculated by the ratio between the slopes of the curves in the region before and after micelle formation.

The term, Gibbs free energy is calculated with equation (2) during the aggregation of surfactant in the surfactant/polymer solution. X_{cac} is the molar amount of surfactant at critical aggregation concentration.

$$\Delta G_{psi} = (2-\propto)RT ln X_{cac}........(2)$$

All the interactions exhibits that Gibbs free energy changes (Figure 3a) are negative, thus showing that the micellization process occurs spontaneously [9]. There is no regular change of free energy due to temperature increase, which emerges because the polymer does not show a regular expansion based on temperature. The increase of the hydrophobic interactions also reduces the free energy values, though the regular change was not observed.

The enthalpy is calculated with equation (3) and (4) during the aggregation of surfactants in water absence and presence polymer, respectively

$$\Delta H = -(2-\propto)RT^2 (\frac{\partial ln X_{cmc}}{\partial T})........(3)$$

$$\Delta H_{psi} = -(2-\propto)RT^2 (\frac{\partial ln X_{cac}}{\partial T})..........(4)$$

Figure 3. Variation of **a)** Gibbs Free Energy (ΔG) **b)** Enthalpy (ΔH) c) Entropy (ΔS), with temperature

Examination of the ΔH enthalpy values for the formation of micelle CTACl in water shows that ΔH enthalpy values are seen as negative (exothermic). As the temperature increases, ΔH values decrease (Figure 3b). When the PVP polymer is added into the mixture, ΔH enthalpy values become positive (endothermic). In other words, it changes from negative (exothermic) to positive (endothermic). The negative valence of ΔH associates with the London-dispersion interactions as an attractive force for micellization [10]. The positive valence of ΔH means that the structured water around the hydrophobic parts of the molecules is broken [10]. The increase of the freedom of the hydrophobic chains within the micelle originates due to the presence of a completely nonpolar part.

The entropy is calculated with equation (5) and (6) during the aggregation of surfactants in water absence and presence polymer, respectively.

$$\Delta S = \frac{\Delta H - \Delta G}{T} \dots\dots\dots\dots\dots\dots(5)$$

$$\Delta S_{psi} = \frac{\Delta H_{psi} - \Delta G_{psi}}{T} \dots\dots\dots\dots(6)$$

During the micellization of CTAC1 in pure water, entropy value of ΔS is positive (Figure 3c). As the temperature increases, the entropy value decreases and changes from positive to negative. The addition of PVP polymer into the water increases the ΔS entropy value. The positive entropy value decreases with temperature and approaches zero, but it always remains positive.

4. CONCLUSION

The present study goes to show examination of the micellization process of CTACl and its mixtures with PVP using electro conductivity techniques in aqueous media at different temperatures. From the experimental results it is concluded that interaction between CTACl and PVP exists. Although enthalpy is negative at all temperatures, entropy is positive at low temperature and negative at high temperature for CTACl micellization in water. Thus, the micellization of CTAC in water is an entropy-enthalpy controlled process at low temperatures with the increasing temperature micellization is also entropy controlled. ΔH may be negative when hydration of the hydrophilic main groups become more important than the deterioration of the water structure around the hydrophobic alkyl chain of the surfactant monomers [10]

In the presence of PVP polymer in the mixture, the ΔH value for CTACl's micellization decreases from positive to negative. The ΔS value is positive and remains positive even if it decreases with increasing temperature. Positive value of entropy refers to the significance of hydrophobic interactions [11].CTACl-PVP system's micellization process are rely on the enthalpy and entropy change.

ACKNOWLEDGMENTS

REFERENCES

[1]Jönsson, B., Lindman, B., Holmberg, K., Kronberg, B., Surfactants and Polymers in Aqueous Solution, John Wiley&Sons, Chichester, England, 1998.

[2] Israelachvili, J. N., Intermolecular and Surface Forces, Academic Press, London, England, Second Edition, 1991.

[3] Goodwin, J., Colloids and Interfaces with Surfactants and Polymers-An Introduction, John Wiley&Sons, Chichester, England, 2004

[4] Noudeh, G. D., Housaindokht, M., Bazzaz, B. S. F., The Effect of Temperature on Thermodynamic Parameters of Micellization of Some Surfactants, Journal of Applied Science, 7(1), 47-52, 2007

[5] Majhi, P.R., Moulik, S. P., Burke, S. E, Rodgers, M., Palepu, R., Physicochemical Investigation on the Interaction of Surfactants and Salts with Polyvinylpyrrolidone in Aqueous Medium, Journal of Colloid and Interface Science, 235, 227-234, 2001.

[6] Gelgec, U., Iscan, M., Interactions of Polyglycol Ethers with Anionic Surfactants in Water, Journal of Dispersion Science and Technology, 31, 1667-1672, 2010

[7] Sardar, N., Kamil, M., Kabir-ud-Din, Studies on Solution Behavior of AqueousMixtures of NonionicPolymer in Presence of CationicSurfactants, Journalof SurfactantsandDetergents, 20, 631–645, 2017.

[8] Gharibi, H., Rafat, A. A., Feizollahi, A., Razavizadeh, B. M., Safarpour, M. A., Thermodynamic studies of interaction between cationic surfactants and polyvinylpyrrolidone using potentiometric techniques, Colloids and Surfaces A: Physicochemical and Engineering Aspects, 145, 47–60, 1998.

[9] Khan, Z., Malik, M. A., AL-Thabaiti, S. A., Alshehri, A., Nabi, F., Micellization and Thermodynamic Properties of Cationic Surfactant Cetyltrimethylammonium Bromide in non-Aqueous Mixture of LauricAcid, International Journal of Electrochemical Science, 12, 4528 – 4542, 2017.

[10] Hoque, Md. A., Patoary, M. O. F., Rashid, M., Molla, M. R., Rub, M. A., Physico-chemical Investigation of Mixed Micelle Formation Between Tetradecyltrimethylammonium Bromide and Dodecyltrimethylammonium Chloride in Water and Aqueous Solutions of Sodium Chloride, Journal of Solution Chemistry, 46, 682–703, 2017.

[11] Chauhan, S., Kumar, K., Rana, D. S., Kumar, R., Chauhan, M. S. A., Comparative Study on the Aggregation and Thermodynamic Properties of Anionic Sodium Dodecylsulphate and Cationic Cetyltrimethylammonium Bromide in Aqueous Medium: Effect of the Co-solvent N-Methylacetamide, Journal of Surfactants and Detergents, 19, 193-200, 2016.

TEMPERATURE DEPENDENT CAPACITANCE AND OTHER ELECTRICAL PROPERTIES OF THE DEVICES WITH A STRUCTURE OF Al/YMn$_{0.95}$Os$_{0.05}$O$_3$/*p*-Si/Al

Fatih Mehmet Coşkun[1]

[1]*Department of Engineering Physics, Faculty of Engineering and Naturel Science, İstanbul Medeniyet University, İstanbul, TURKEY*

e-mail: fatihmehmetcoskun@gmail.com

Abstract

Al/YMn$_{0.95}$Os$_{0.05}$O$_3$/*p*-Si/Al devices were fabricated within the scope of this study. The 5% Os doped YMnO$_3$ thin layers were coated on a *p*-Si substrate by RF sputtering technique under 2 mTorr pressure, 100 W power and with a substrate temperature of 500 C. In this report, the capacitance to voltage (C-V) characteristics of those devices with varying temperature between 40 and 320 K were presented. According to this data, C^{-2} vs V characteristics plotted and the barrier heights were calculated from the intercepts of the C^{-2} vs V plot with V axis for each temperature. The temperature dependent barrier height $\Phi_{CV}(T)$ behavior was almost linear and decreased with increasing temperature. The barrier height value at 0 K was obtained as 1.85 eV. The graph of the carrier concentration N_a showed a little fluctuation; it reached a peak with a value of 9x10^{15} cm^{-3} at 75 K, and decreased linearly till 150 K, which is about 8x10^{15} cm^{-3}, then showed almost a constant value of this concentration up to 300 K and finally made a rigid peak at 350 K with a concentration of 8.8x10^{15} cm^{-3}.

1. INTRODUCTION

The perovskite oxides, which are in general form of ABO_3, have attracted considerable attention from the researchers due to their advantages in chemical and semiconductor device industries. Although perovskite oxides are most prominent and prevelant compounds in the form of perovskite structures, some other types (such as nitrides, carbides, and halides) can also be crystallized in this structure [1-3]. Some perovskites have multiferroic property, which means comprising more than one physical features at the same time. For example they may have both magnetic and ferroelectric properties. Therefore, these materials provide immense opportunities to the opto-electronic and magnetoelectric device indusrty [4,5,7-11]. Because of those properties, multiferroic perovskite oxides are preferably used by the scientists as a semiconductor in heterojunciton structures [3-5].

Figure 1. The structure of an ABO_3 perovskite with the origin centered at (a) the B-site ion and (b) the A-site ion [6]

$YMnO_3$ (YMO) , which is a rare-earth manganite, exhibits attracted multiferroic features and is studied for electronic device technology such as spintronics, data storage media, sensors, antennas and so on. Therefore this material has drawn intensive consideration among the researchers and device manfucter companies as well [12-21]. Because of those physical properties, YMO is classified as a multiferroic material by sicentists. However, in terms of the chemical structure, it is in perovskite-oxide class under the huge perovskite tree. If it is investegated as a multiferroic, it is a typical type-I multiferroic, which has a very high Curie temperature ($T_C \sim 900$ K) and a low antiferromagnetic ordering temperature ($T_N \sim 70$ K) [22,23]. Having suitable dielectric features as a powder, YMO shows a great dielectric interface layer property in semiconductor devices and this leads to an extensive research literature about YMO based devices [24-28].

In the fabrication process of YMO thin films, several methods may be used. If it is coated directly on a Si substrate, YMO possesses a great dielectric oxide layer because it does not exists volatile components. Therefore YMO is commonly used as an interface layer in many electronic and magnetic devices such as

magnetic sensors, ferroelectric random access memories, metal–ferroelectric–insulator–semiconductor field effect transistors (MFIS-FET) and so on [29-37].

In crystal structure studies, YMO has been found in hexagonal form. However, when the B site of YMO, which is Mn, is doped with other elements, it exhibits a phase transitions [38]. The oxidation state of the dopant plays an important role on the physical and chemical properties of the compouds and so on YMO. For example the ionic radius is directly affected by the oxidation state of the dopants. Such influences of the ionic radius of dopant may change the energy in the parent compound. In the literature, it has been proclaimed that such distortions in the energy modifies the electrical, magnetic, and optical properties of the materials. In this study Os has been chosen as a dopant because of its various oxidation states, which are +2, +3, +4, +6 and +8 [39]. 5% Os doped YMO, which has the chemical formula of $YMn_{0.95}Os_{0.05}O_3$ (YMOO) has been used for the device fabrication. As explained in the materials and methods part the devices were fabricated and the C^{-2} vs V characteristics were investigated. The barrier heights were calculated from the intercepts of the C^{-2} vs V plot with V axis for each temperature. The temperature dependent barrier height $\Phi_{CV}(T)$ behavior was also examined.

2. MATERIAL AND METHODS

The YMOO powder was prepared by the solid-state reaction method, which has been declared in the previous study of the author [40]. After this preparations the YMOO sputter targets, with 5 cm diameter, were pressed under 10 tones as shown in figure 2 and put into the physical vapor deposition (PVD) system.

Y_2O_3 (99.99%) + Mn_2O_3 (98%)
+
OsO_2 (85%)

→ • $YMn_{0.95}Os_{0.05}O_3$ →

Figure 2. Preparetion scheme of the YMOO target

Meanwhile, the previously Al coated *p*-type Si substrates were chemically cleaned by RCA method and they were put into PVD system as well. The chamber of the system were vacuumed to $2x10^{-7}$ mTorr

pressure. RF power was applied to the YMOO targets and after manipulations with the chamber pressure the YMOO thin films were deposited onto the p-Si substrates under 20 sccm Ar flow, 100 W RF power, 2.5 mTorr pressure and 500 °C substrate heating and rotating for 1 hour. After YMOO thin film deposition, Al was thermally evaporated on the shadow mask with dots of about 1 mm diameter in order to form Schottky contacts. Finally, the heterojunction device structure of Al/p-YMOO/p-Si/Al was fabricated. The capacitance-voltage (C-V) characterization of the fabricated device was performed in ARS 4K closed cycle helium (He) cryostat, which has LakeShore 330 temperature controller with 0.2 K temperature precision, between 30-320 K temperatures using Boonton 72B capacitance meter.

3. RESULTS AND DISCUSSION

The capacitance to voltage (C-V) characteristics of Al/YMn$_{0.95}$Os$_{0.05}$O$_3$/p-Si/Al devices are demonsrated in figure 3. In this figure the C-V characteristics of the devices from 30K to 320K are shown.

Figure 3. C-V characteristics of Al/YMn0.95Os0.05O3/p-Si/Al devices

Temperature dependent C^{-2}&V plots are shown in figure 4. As seen from the figure, at reverse bias the graph shows almost a lineer behaviour. However at about zero bias the graph deviate from the lineer form. This behavior can be attributed to the effect of carrier concentration.

Figure 4. C^{-2}-V characteristics of Al/YMn0.95Os0.05O3/p-Si/Al devices

Figure 5. Barrier Height with varrying temperature

The Barrier Height (Φ_{CV}) behaviour with varrying temperature is shown figure 5. Φ_{CV} of a device can be calculated from:

$$\Phi_{CV} = V_{D0} + V_p \tag{1}$$

where V_p is the potential difference between Fermi level and the valance band maximum in the neutral region of p-type semiconductor and is stated by the relation:

$$V_p = kTln(\frac{N_v}{N_A}) \tag{2}$$

Where;

$$N_A = \frac{2}{q\varepsilon_0 A^2} \frac{dV}{d(C^{-2})} \tag{3}$$

The values of figure 5 were calculated from the equations (1), (2) and (3). The graph in the figure was plotted according to those values and we can say that the Φ_{CV} exhibits almost a lineer behavior. The Φ_{CV} values decreases with increasing temperature.

The Carrier concentration (N_A) versus temperature calculations and plots are demonstrated in figure 6. The N_A values from 100K and 300K are almost constant. However at temperatures lower than 100K, it exhibits a fluctuation which may be attributed to the interface situations.

Figure 6. Carrier concentration versus temperature

CONCLUSION

In this study, the 5% Os doped YMOO thin films were grown on *p*-Si substrates using RF sputter technique. Electrical characterization was performed in ambient condition. The C-V measurements were done and C^{-2}-V calculations were conducted. After the calculations from C^{-2}-V characteristics, it has been seen that the barrier height of YMOO material decreases with increasing temperature. The carrier concentration remains constant between 100K and 300K – which is an expected state – but increases after 100K and 300K. This deviation can be attributed to the interface layers.

ACKNOWLEDGMENTS

REFERENCES

[1] Pena M. A. and Fierro J. L. G., Chemical Structures and Performance of Perovskite Oxides, Chem. Rev. 101, 1981, 2001.

[2] Tu L., Wang X., Wang J., Meng X., and Chu J., Adv. Electron. Mater. 4(11), 1800231, 2018.

[3] Yıldırım M., Sahin C., Altındal S., Durmuş P., Electrical and Dielectric Properties of a n-Si Schottky Barrier Diode with Bismuth Titanate Interlayer: Effect of Temperature, J. Electron. Mater. 46(3), 1895, 2017.

[4] Zhai H., Kong J., Yang J., Xu J., Xu Q., Sun H., Li A., Wu D., Resistive Switching Properties and Failure Behaviors of (Pt,Cu/Amorphous ZrO2/Pt Sandwich Structures, J. Mater. Sci.&Techn. 32, 676, 2016.

[5] Qiu J., Shang Y., Chen X., Li S., Ma W., Wan X., Yang J., Lei Y., Chen Z., Enhanced efficiency of graphene-silicon Schottky junction solar cell through inverted pyramid arrays texturation, J. Mater. Sci. & Techn. 34, 2197, 2018.

[6] Fu D. and Itoh M., Ferroelectricity in Silver Perovskite Oxides, Ferroelectrics − Material Aspects, Dr. MickaÃ«l Lallart (Ed.), ISBN: 978-953-307-332-3, InTech, Available from: http://www.intechopen.com/books/ferroelectrics-material-aspects/ferroelectricity-in-silver-perovskite-oxides. 2011.

[7] Kolisetty A., Fu Z., Koc R., Development of La(CrCoFeNi)O_3 system perovskites as interconnect and cathode materials for solid oxide fuel cells, Ceramics International 43(10), 7647, 2017.

[8] Kumar M., Phase D.M., Choudhary R.J., Upadhyay S.K., Reddy V.R., Microwave assisted radiant hybrid sintering of YMnO$_3$ ceramic: Reduction of microcracking and leakage current, Ceramics International. 44, 8196, 2018.

[9] Park J., Lee S., Kang M., Jang K.-H., Lee C., Streltsov S.V., Mazurenko V.V., Valentyuk M.V., Medvedeva J.E., Kamiyama T., Park J.-G., Doping dependence of spin-lattice coupling and two-dimensional ordering in multiferroic hexagonal $Y_{1-x}Lu_xMnO_3$($0{\le}x{\le}1$), Phys. Rev. B 82, 054428, 2010.

[10] Eslem-Kisa A. and Demircan O., Synthesis and characterization of $La_{0.595}V_{0.005}Sr_{0.4}CoO_{3-\delta}$ as a novel cathode material for solid oxide fuel cells (SOFC), J. Sol-Gel Sci. Technol. 82, 352–362, 2017.

[11] Sun B., Wu J.H., Jia X.J., Chen P., Photo-regulated magnetism and photoferroelectric effect in BiFeO$_3$ nanoribbons at room temperature, Scr. Mater. 105, 26–29, 2015.

[12] Jiang N., Woodley S.M., Richard C., Catlow A., Zhang X., Applying a new interatomic potential for the modelling of hexagonal and orthorhombic $YMnO_3$, J. Mater. Chem. C 3, 4787, 2015.

[13] Adem U., Mufti N., Nugroho A.A., Catalan G., Noheda B., Palstra T.T.M., Dielectric relaxation in $YMnO_3$ single crystals, J. Alloys Compd. 638,228, 2015.

[14] Polat O., Coskun M., Coskun F.M., Durmus Z., Caglar M., Turut A., Os doped YMnO3 multiferroic: a study investigating the electrical properties through tuning the doping level, J. Alloys Compd. 752, 274, 2018.

[15] Chen Z., Ma C.-L., Wu F.-X., Chen Y.B., Zhou J., Yuan G.-L., Gu Z.-B., Hang S.-T., Chen Y.-F., The electrical and magnetic properties of epitaxial orthorhombic $YMnO_3$ thin films grown under various oxygen pressures, Appl. Surf. Sci. 257, 8033, 2011.

[16] Wu H., Yuan J., Peng T., Pan Y., Han T., Liu C., Temperature- and fielddependent leakage current of epitaxial $YMnO_3$/GaN heterostructure, Appl. Phys. Lett. 94, 22904, 2009.

[17] Li S.Z., Yan Z.B., Wei T., Luo S.J., Liu B., Wang K.F., Liu J.-M., Preparation of epitaxial orthorhombic $YMnO_3$ thin films and the currentevoltage rectifying effect, Appl. Phys. A 94,975, 2009.

[18] Bogusz A., Bürger D., Skorupa I., Schmidt O.G., Schmidt H., Bipolar resistive switching in $YMnO_3$/Nb:SrTiO$_3$ pn-heterojunctions, Nanotechnology 27, 455201, 2016.

[19] Shin H.W., Son J.Y., Ferroelectric domain structure and polarization switching speed of highly (111)-oriented polycrystalline $YMnO_3$ thin films on glass substrates, Thin Solid Films 636, 247, 2017.

[20] Zhao Y., Rao Y., Luo B., Chen C., Xing H., Niu L., Wang J., Jin K., Electricaltransport and magnetodielectric properties in $YMnO_3$/La$_{0.67}$Sr$_{0.33}$MnO$_3$ heterostructure, J. Phys. Chem. C 120,22318, 2016.

[21] Kumar M., Phase D.M., Choudhary R.J., Upadhyay S.K., Reddy V.R., Microwave assisted radiant hybrid sintering of $YMnO_3$ ceramic: Reduction of microcracking and leakage current, Ceram. Int. 44,8196, 2018.

[22] Guo L., Zhou Z. Q., and Yuan H. M., J. Alloys Compd. 616, 454–460, 2014.

[23] Ahmed T., Walia S., Mayes E. L. H., Ramanathan R., Guagliardo P., Bansal V., Bhaskaran M., Yang J. J., and Sriram S., Appl. Mater. Today 11, 280–290, 2018.

[24] Li D., Zheng D., Jin C., Zheng W., and Bai H., ACS Appl. Mater. Interfaces 10, 19836, 2018.

[25] Chandra Sekhar M., Lee S., Choi G., Lee C., and Park J.-G., Phys. Rev. B 72 (1), 014402, 2005.

[26] Zaghrioui M., Greneche J. M., Autret-Lambert C., and Gervais M., J. Magn. Magn. Mater. 323, 509, 2011.

[27] Sharma N., Das A., S. Mishra K., Prajapat C. L., Singh M. R., and Meena S. S., J. Appl. Phys. 115, 213911, 2014.

[28] Tomczyk M., Senos A. M., Vilarinho P. M. et al., Scr. Mater. 66, 288, 2012.

[29] Vopson M. M., Crit. Rev. Solid State Mater. Sci. 40, 223, 2015.

[30] Zhang Z. and Wang S., J. Mat. Sci.: Materials in Electronics 28(15), 10940–10950, 2017.

[31] Cao Z. and Wang C., J. Chen, Mater. Res. Express 5(11), 115512, 2018.

[32] Kitahata H., Tadanaga K., Minami T., Fujimura N., and Ito T., Appl. Phys.Lett. 75(5), 719, 1999.

[33] Yi W.-C., Seo C.-S., and Kwun S.-I., Appl. Phys. Lett. 77(7), 1044, 2000.

[34] Yoo D. C., Lee J. Y., Kim I. S., and Kim Y. T., Thin Solid Films 416, 62, 2002.

[35] Parashar S., Raju A. R., Rao C. N. R., Victor P., and Krupanidhi S. B., J. Phys.D Appl. Phys. 36, 2134, 2003.

[36] Kim K.-T. and Kim C.-I., J. Eur. Ceram. Soc. 24, 2613, 2004.

[37] Ito D., Fujimura N., Yoshimura T., and Ito T., J. Appl. Phys. 94(6), 4036, 2003.

[38] Aikawa Y., Katsufuji T., Arima T., and Kato K., Phys. Rev. B 71, 184418, 2005.

[39] Polat O., Coskun M., Coskun F. M., Durmus Z., Caglar M., and Turut A., J. Alloys Compd. 752, 274, 2018.

[40] Coşkun M., Polat Ö, Coşkun F. M., Durmuş Z., Çağlar M., and Türüt A., Mater. Sci. Semicond. Process. 91, 281–289, 2019.

INVESTIGATION OF MICROSTRUCTURAL AND ELECTROCHEMICAL CORROSION BEHAVIOR OF THERMAL BARRIER COATINGS

E.Altan[1], M. Celiker[1], M. Kocabas[2], A.C. Karaoglanli[1]

[1]Department of Metallurgical and Materials Engineering, Faculty of Engineering, Bartin University, Bartin, TURKEY

[2]Department of Metallurgical and Materials Engineering, Faculty of Engineering, Konya Technical University, Konya, TURKEY

E-mail: elif.altan@ogrenci.bartin.edu.tr / elifaaltan1101@gmail.com

Abstract

The aim of this study is to determine and investigate the electrochemical corrosion behavior of thermal barrier coatings (TBCs). The electrochemical corrosion effect of the TBCs was investigated microstructurally under acidic-basic environments and seawater environments. TBC system was composed of a CoNiCrAlY bond coat and a ZrO_2–8% Y_2O_3 (YSZ) ceramic top coat on Inconel 718 nickel-based super alloy disk-shaped substrate. High-velocity oxygen fuel (HVOF) technique was used to produce CoNiCrAlY metallic bond coats. Atmospheric plasma spraying (APS) technique was used to produce ceramic YSZ top coats. Electrochemical tests were performed after the production of the coatings and structural changes of the coatings were examined. 0.1 molar NaCl (sodium chloride) solutions were prepared to immerse the samples to be corroded. Experiments were carried out at room temperature and at 3-electrode classical system. Three different corrosion tests were applied to the samples including open circuit potential (OCP), impedance measurement (EIS) and potentiodynamic polarization test (PDP). EIS analysis were performed in the frequency range of 20 kHz-10 mHz and 10 mV AC depending on the OCP test.

Keywords: Thermal barrier coatings (TBCs), Atmospheric plasma spraying (APS), High-velocity oxygen fuel (HVOF), Electrochemical corrosion.

1. INTRODUCTION

The main function of TBCs is to provide thermal insulation against hot gases in engines and turbines and to prevent the materials used in corrosive and humid environments such as salt water environments from being affected by the adverse conditions of the environment [1,2]. Understanding of damage mechanisms of thermal barrier coatings is the key factor to increase durability and reliability [3]. Electrochemical corrosion is also one of these damage mechanisms [4,5]. Offshore oil and gas production environments represent aggressive conditions in terms of erosion and corrosion [6, 7].

TBC systems are consist of a Ni-based super alloy substrate material, a ceramic overcoat providing thermal insulation, a bond coat that protects the substrate material against oxidation and a thermally grown oxide (TGO) layer formed during the coating process and growth by oxidation of the bond coat during the service life [8-12].

In high-velocity oxygen fuel (HVOF) method that used for bond coating, the process is involved with an internal combustion to rapidly heated and accelerated of powder consumable to high velocities[11-13]. The high combustion pressure and rapid exposures through a nozzle facilitated the particle velocity to reach supersonic speed before impacting on to a surface [14]. This provides excess impacting force which, results in mechanical adhesion of powders to the solid surface [13-15].

The electrochemical impedance spectroscopy (EIS) method which used for electrochemical corrosion tests is based on the application of a low amplitude alternating current voltage signal (10–20 mV) to the coated metallic sample using a conventional three-electrode electrochemical cell [16]. EIS data of the coated metals is usually presented by using Bode plot, which displays the variations of logarithm of the impedance modulus and phase angle versus the logarithm of the frequency [17,18]. The Nyquist plot is used to present the features such as diffusion effects on EIS data of the coated metals [17-19].

The general purpose of this research is to observe the effect of the applied methods on Inconel-718 nickel-based super alloy metal used as substrate material for increase the service life at intense aggressive environments. Especially in terms of the subject of the study; was investigated the effect of the electrochemical corrosion on the coating surface on the parts such as propellers used in working environments such as acidic-basic environments, seawater environments. The physical absorption of electrolyte in the coating and structural changes were estimated. Additionally, the mechanism of electrochemical reactions at the coating/metal interface was investigated by EIS. In this study, the corrosion resistance of Inconel 718 samples

that covered with HVOF sprayed CoNiCrAlY bond coatings and atmospheric plasma sprayed YSZ (ZrO_2 + Y_2O_3) top coating was evaluated using potentiodynamic polarization and EIS in 0.1 mol NaCl solution.

2. MATERIAL AND METHODS

It is safe to use EIS to provide an understanding of the mechanism of damage to TBCs by creating an artificial seawater environment. Experiments carried out under room temperature conditions provide an understanding of the quality and durability of the coating by the leakage of electrolytes. Inconel 718 nickel based superalloy disk shaped samples with a diameter of 25.4 mm and thicknesses of 4 mm, were used as substrate. HVOF technique was used to produce CoNiCrAlY metallic bond coats. APS technique was used to produce ceramic YSZ top coats the thickness of the bond coating was measured as approximately 100 μm and the thickness of the top coat was measured as 300 μm, respectively.

The electrochemical corrosion test apparatus; Gamry Instrument Model 600 (Gamry Interface 1010B) is used to characterize the samples and generate the electrical current potential curves. Then 0.1 mol of NaCl (Sodium Chloride) solution was prepared in order to immerse the samples to be corroded. Experiments were carried out in a conventional 3-electrode system at room temperature. Three different corrosion tests including open circuit potential (OCP), impedance measurement and potentiodynamic polarization test (PDP) were applied to the samples. Electrical values of the experiment was realized in the frequency range of 20 kHz-10 mHz and 10 mV AC depending on the OCP test. Gamry Echem Analyst program was used to analyze the tests. The starting potential of the curves obtained from the potentiodynamic (PDP) tests is stated as ± 250 mV and the ending potential is +1500 mV.

3. RESULTS

Corrosion potential (E_{corr}) and the corrosion current density (i_{corr}) values which is corresponding to potential can be found by drawing anodic and cathodic polarization curves between the voltages and the current logarithm for anodic and cathodic reactions. The low E_{corr} indicates that the metal subjected to electrochemical corrosion test has a higher susceptibility to corrosion. On the other hand, the decrease in the i_{corr} indicates that the corrosion resistance increases. Electrochemical corrosion values in NaCl solution are shown in Table 1. Polarization curves of samples in NaCl solution are shown in Figure 1.

Table 1. Electrochemical corrosion values in NaCl solution.

Test Samples	OCP (mV)	E_{corr} (mV)	i_{corr} (uA/cm^2)
Inconel 718 Substrate Material	-403	-435	4.8
CoNiCrAlY HVOF Bond Coat	-64	-102	0.123
HVOF + APS (TBC system)	-26	-146	0.7

Figure 1. Polarization curves of samples in NaCl solution.

Polarization curves, corrosion current density and corrosion potential values are given of these samples for uncoated, HVOF coated and HVOF + APS coated samples in the figure and table. For the results obtained; it can be said that the current density value (i_{corr}) of the uncoated Inconel 718 sample is higher than the current density values of the samples that are tested separately by HVOF and HVOF + APS method. Decreasing of the corrosion current density by coating of the material shows that the corrosion resistance is increased. The corrosion potential of the uncoated sample (E_{corr}) appears to be considerably lower than that of HVOF and HVOF + APS coated samples. The low corrosion potential indicates that the metal undergoing electrochemical corrosion test has a higher susceptibility to corrosion. Therefore, it can be said that thermal barrier coated samples are less susceptible to corrosion than uncoated sample. Electrochemical impedance spectroscopy

means measuring the resistance where the electron flux is. The nyquist graphs generated accordingly are given at Figure 2 and Figure 3.

Figure 2. Nyquist curves of samples subjected to corrosion test in NaCl solution.

Figure 3. Bode curves of samples subjected to corrosion test in NaCl solution.

Table 2. EIS data of samples in NaCl solution.

Solution Content	Condition	R_p (ohms)	R_u (ohms)	Y_0	Alpha
0.1 M NaCl Solution	Inconel 718	$16.51.10^3$	35.71	$50.35.10^{-6}$	$685.9.10^{-3}$
	Inconel 718 + HVOF	$296.9.10^3$	38.35	$18.09.10^{-6}$	$759.7.10^{-3}$
	Inconel 718 + HVOF + APS	$128.5.10^3$	373.3	$71.05.10^{-6}$	$806.9.10^{-3}$

According to the graphic; where the electron flow occurs, the sample with the shortest time and least resistance to this flow is the uncoated sample, while the HVOF coated sample shows the most resistance.

Figure 4. Uncoated Inconel 718 microstructure image.

The SEM image of the uncoated sample were subjected to electrochemical corrosion tests seen at Figure 4. Based on these image; can be seen that salt crystals used as electrolytes cause deposits in some parts of the sample surface. The seen micro-cracks can be seen in similar experiments as a result of poor cleaning of NaCl from the surface. From this, it can be said that the cracks progress and cause damage at the uncoated parts which is exposed to salt water environment for a long time.

Figure 5. Cross-sectional view of part treated with HVOF bond coat and electrochemical corrosion.

Figure 6. Cross-sectional views of the part undergoing HVOF + APS topcoat and electrochemical corrosion testing.

Figure 5 and Figure 6 on the top shows the HVOF coated sample and HVOF + APS coated sample. This may be better to have the particles adhere to each other as the deposition process is completed by climbing to supersonic levels during particle spraying in the HVOF technique. The density of surface cracks is remarkable when the surface images of APS coatings are examined.

4. CONCLUSION

It can be said that the coatings made using APS technique are more susceptible to surface cracks and dense porosity due to their low thermal conductivity and application of this method in open air environment. It cannot be said that the electrochemical corrosion test results in the formation of superficial cracks at the top coat produced using ceramic based materials. The reason of this; it does not have an ambient temperature that will cause thermal shock since no high temperatures are reached. In addition, formation of TGO layer observed at high temperatures is not seen in the electrochemical corrosion environment, because of not reached to high temperatures. As a result of the experimental studies; it was determined that the uncoated sample was affected most and primarily by the environmental conditions and the bond coated sample had higher corrosion resistance than the sample with top coating. HVOF bond coat method has higher performance and density compared to other coating methods as it seen in the literature researches.

This is related to coatings made by APS method has high porosity and low density structure because of it is a method applied in open air environment and because of the effect of high application temperature. It can be said that this reason why the bond coat is more successful in electrochemical corrosion behaviour than top coat in coating process.

REFERENCES

[1] Clarke, D. R., Oechsner, M. and Padture, N. P., Thermal-barrier coatings for more efficient gas-turbine engines, Materials Research Society, 37, 2012.

[2] Rajendran, R., Gas turbine coatings, Journal of Engineering Failure Analysis, 26: 355, 369, 2012.

[2] Mumm, D., Mechanisms controlling the performance and durability of thermal barrier coatings, Key Engineering Materials, 197:199-0, 2001.

[3] Jonnalagadda, K. P., Thermal barrier coatings failure mechanisms and life prediction, Linköping Studies in Science and Technology, Dissertation No. 1975, 2019.

[4] Ebrahimi, H. and Nakhodchi, S., Thermal fatigue testing and simulation of an APS TBC system in presence of a constant bending load, International Journal of Fatigue, 2016.

[5] Karaoğlanlı, A. C., Ogawa, K., Türk, A. and Özdemir, İ., Thermal shock and cycling behavior of thermal barrier coatings (TBCs) used in gas turbines, In Book: Progress in Gas Turbine Performance, 2013.

[6] Chen, Z. B., Wang, Z.G. and Zhu, S.J., Tensile fracture behavior of thermal barrier coatings on superalloy, Journal of Surface & Coatings Technology 205, 3931–3938, 2011.

[7] Dalkılıç, S., Tanatmış, A. A., Termal bariyer kaplama sistemlerinde yüksek sıcaklıkta düşük çevrimli yorulma şartları altında oluşan hasarların incelenmesi, Journal of Havacılık Ve Uzay Teknolojileri, 4, 2, 15-27, 2009.

[8] Karaoğlanlı, A.C., Döleker, K. M., Demirel, B. and Türk, A., Effect of shot peening on the oxidation behavior of thermal barrier coatings, Journal of Applied Surface Science, 354, 2015.

[9] Fauchais, P. and Vardelle A., Thermal sprayed coatings used against corrosion and corrosive wear, In book: Advanced Plasma Spray Applications, 2012.

[10] Zhou, C. G. and Song, Y. X., Oxidation and hot corrosion of thermal barrier coatings (TBCs), In book: Thermal Barrier Coatings, 2011.

[11] Wu, R. T., Chemical analyses of TGO layers and interfaces, In book: Thermal Barrier Coatings, 2011.

[12] Shen, Q., Yanga, L., Zhoua, Y.C., Wei, Y.G. and Wang, N.G., Models for predicting TGO growth to rough interface in TBCs, Journal of Surface & Coatings Technology 325, 219–228, 2017.

[13] Zavareh, M.A., Sarhan, A.D., Razak, B., Basirun, W.J., Electrochemical characterizations of different ceramic composite coatings on carbon steel piping using high velocity oxy-fuel spray, Proceedings of the World Congress on Engineering and Computer Science, 22-24, 2014.

[14] Mohammadi, M., Javadpour, S., Ahmad, S., Jahromi, J. and Kobayashi, A., Cyclic oxidation and hot corrosion behaviors of gradient CoNiCrAlYSi coatings produced by HVOF and diffusional processes, Journal of Oxidation of Metals, 2016.

[15] Liu, Y., Fan, X., Zeng, S., Wang, Y., Zou, B., Gu, L.,Chen, X., Khan, Z.S., Yang, D., Cao, X., Corrosion behavior of coating with plasma sprayed 8YSZ on the surface of carbon steel, Journal of Rare Earths, 30, 6, 592, 2012.

[16] Olivier, M. O., Poelman, M., Use of electrochemical impedance spectroscopy (EIS) for the evaluation of electrocoatings performances, In book: Recent Researches in Corrosion Evaluation and Protection, 2012.

[17] Olivier, M., G. and Poelman, M., Use of electrochemical impedance spectroscopy (EIS) for the evaluation of electrocoatings performances, In book: Recent Researches in Corrosion Evaluation and Protection, 2012.

[18] Eliyan, F. F., Alfantazi, A., Mechanisms of corrosion and electrochemical significance of metallurgy and environment with corrosion of iron and steel in bicarbonate and carbonate solutions, Journal of Corrosion, 70: 9, 2014.

[19] Khajezadeh, M. H., Mohammadi, M. and Ghatee, M., Hot corrosion performance and electrochemical study of CoNiCrAlY/YSZ/YSZ-La_2O_3 multilayer thermal barrier coatings in the presence of molten salt, Journal of Materials Chemistry and Physics, 220,23–34.2018

ELECTROCHEMICAL CORROSION BEHAVIOR OF YTTRIA STABILIZED ZIRCONIA THERMAL BARRIER COATINGS (TBCs)

M. Celiker[1], M. Kocabas[2], A. C. Karaoglanli[1]

[1]*Department of Metallurgical and Materials Engineering, Faculty of Engineering, Bartin University, Bartin, TURKEY*
[2]*Department of Metallurgical and Materials Engineering, Faculty of Engineering, Konya Technical University, Konya, TURKEY*

E-mail: mineceliker93@gmail.com

Abstract

Cold Gas Dynamic Spray (CGDS) and Atmospheric Plasma Spray (APS) techniques were employed to deposit the CoNiCrAlY bond coats and the ceramic top coats of thermal barrier coating (TBC) systems, respectively. Corrosion experiments were carried out electrochemically on open circuit potential (OCP) and potentiodynamic polarization (PDP) curves in 0.1 M sodium chloride (NaCl) solution at room temperature. The potentiodynamic polarization scan was started from the starting potential (-0.250 mV vs. OCP) to ending potential (+1.500 mV vs. OCP) with a scan rate of 1 mV/s. Electrochemical experiments were performed using a potentiostat/galvanostat. The study is examined the electrochemical corrosion behaviour of uncoated, and coated with different coating conditions in NaCl solution.

Keywords: Thermal Barrier Coating (TBC); Electrochemical Corrosion; Cold Gas Dynamic Spray (CGDS); Atmospheric Plasma Spray (APS); CoNiCrAlY; YSZ; NaCl

1. INTRODUCTION

Thermal barrier coatings (TBCs) are widely used in energy, aircraft, automotive and aerospace industries [1]. TBCs are applied for the protection of metallic components that are exposed to high thermal gradients in applications such as gas turbines, diesel engines, and jet engines. To ensure high engine efficiency, TBCs durability should be maintained at higher working gas temperatures without increasing component temperatures [2,3,4,5]. To obtain low thermal conductivity, TBCs are generally applied onto a superalloy substrate and composed of a metallic bond coat and a ceramic top coat. A typical metallic bond coat, which is used as an oxidation resistance layer, consists of a MCrAlY alloy (M: Co and/or Ni) [6]. Metallic bond coatings in TBC systems are produced using thermal spray methods such as Atmospheric Plasma Spray (APS), High Velocity Oxy-Fuel (HVOF) Spraying, Detonation Gun (D-Gun), and Cold Gas Dynamic Spray (CGDS). Ceramic top coatings are generally produced using processes such as APS, and Electron Beam Physical Vapor Deposition (EB-PVD) [7,8].

Since the mechanism of damage encountered in aqueous environments is electrochemical, electrochemical corrosion testing is a great alternative for the investigation of a material operating in such a corrosive environment [9]. Electrochemical corrosion occurs at the metal/solution interface in atmospheric, soil and similar aqueous environments. To evaluate degradation mechanism of TBCs in artificial seawater the electrochemical corrosion tests is a reliable method [10,11,12]. Electrochemical tests is a generally common way to characterize the reactivity of a surface, where a more reactive surface has a lower anodic open circuit potential (OCP) [13,14]. In this study, electrochemical corrosion behaviour of TBC system was investigated using open circuit potential (OCP) and potentiodynamic polarization (PDP) tests.

2. MATERIAL AND METHODS

Metallic bond material CoNiCrAlY was coated on Inconel 718 superalloy substrate material with a thickness of approximately 100 μm using CGDS method. Production of ceramic top coat, which content ZrO_2 + Y_2O_3 (YSZ), were produced by APS technique. The top coating thickness is approximately 300 μm.

Produced TBC samples and uncoated samples were subjected to electrochemical corrosion tests. Corrosion experiments were carried out electrochemically on EIS and potentiodynamic polarization curves in 0.1 M sodium chloride (NaCl) solution at room temperature. A conventional three using electrode cell, with a graphite counter electrode and a reference electrode (Ag/AgCl), and the coating as the working electrode, was employed. OCP is applied for at least 5 min. The PDP scan was started from the starting potential (-0.250 mV

vs. OCP) to ending potential (+1.500 mV vs. OCP) with a scan rate of 1 mV/s. Electrochemical experiments were performed using a Gamry Interface 1010B potentiostat/galvanostat.

3. RESULTS

The OCP results of the Inconel 718 super alloy substrate material, CoNiCrAlY metallic bond coating and YSZ ceramic top coating are given in Figure 1.

Figure 1. OCP results of Inconel 718 substrate, CoNiCrAlY bond coat and TBC system.

It is seen that the lowest OCP value in NaCl solution was obtained for Inconel 718 superalloy substrate in Table 1 and Figure 1. On the other hand, CoNiCrAlY metallic bond and YSZ ceramic top coating exhibited higher OCP value. This is due to the fact that the Inconel 718 superalloy substrate material exhibits less noble behavior (more negative) than other metal bond coat and YSZ ceramic top coat.

Table 1. Electrochemical corrosion values of Inconel 718 substrate, CoNiCrAlY bond coat and TBC system.

Test Conditions	OCP (mV)	E_{corr} (mV)	i_{corr} ($\mu A/cm^2$)
Inconel 718	-403	-435	4.8
Inconel 718 + Bond Coat	-230	-270	0.9
TBC system	-54	-182	0.18

The PDP values of the Inconel 718 super alloy substrate material, CoNiCrAlY metallic bond coating and YSZ ceramic top coating are given in Table 1 and Figure 2.

Figure 2. PDP curves of Inconel 718 substrate, CoNiCrAlY bond coat and TBC system.

It is seen that the highest i_{corr} value in NaCl solution was obtained for Inconel 718 superalloy substrate in Table 1 and Figure 2. On the other hand, CoNiCrAlY metallic bond and YSZ ceramic top coating exhibited lower i_{corr} value and higher electrochemical corrosion performance. This is related to the corrosion resistance and structural properties provided by the coating layer. The best electrochemical performance value was found in the samples of TBC system due to its superior properties.

4. CONCLUSION

In this study, the electrochemical corrosion behavior and of cold gas dynamic sprayed TBCs have been conducted and evaluated. CoNiCrAlY coatings and YSZ ceramic coatings were successfully deposited using CGDS technique for bond coat and APS technique for the top coat. TBC system with YSZ ceramic top coating and CoNiCrAlY metallic bond coating has been shown to exhibit superior electrochemical corrosion resistance compared to Inconel 718 substrate. This situation is due to the microstructural properties of the coating layers. Future studies will be carried out to determine the electrochemical properties of hot corrosion tested TBC samples and to examine the properties of the TGO layer at the interface.

ACKNOWLEDGMENTS

REFERENCES

[1] Parker, D. W., Thermal barrier coatings for gas turbines, automotive engines and diesel equipment, Materials and Design, 13(6), 345–351, 1992.

[2] Padture, N. P., Thermal barrier coatings for gas-turbine engine applications, Science, 296(5566), 280–284, 2002.

[3] Nijdam T.J., Sloof W.G., Combined pre-annealing and pre-oxidation treatment for the processing of thermal barrier coatings on NiCoCrAlY coatings, Surface and Coatings Technology, 201, 3894–3900, 2006.

[4] Li Y., Li C.J., Zhang Q., Xing K., Yang G.J., Effect of surface morphology of MCrAlY bond coats on isothermal oxidation behavior, International Thermal Spray Conference, ITSC 2010, DVS-ASM, Raffles City, Singapore, 491–497, 2010.

[5] Xie D., Xiong Y., Wang F., Effect of an enamel coating on the oxidation and hot corrosion behavior of an HVOF sprayed CoNiCrAlY coatings, Oxidation of Metals, 59, 503–516, 2003.

[6] Karaoglanli, A. C., Altuncu, E., Ozdemir, I., Turk, A., Ustel, F., Structure and durability evaluation of $YSZ+Al_2O_3$ composite TBCs with APS and HVOF bond coats under thermal cycling conditions, Surface and Coatings Technology, 205, 369–373, 2011.

[7] Burlacov, I., Jirkovský, J., Kavan, L., Ballhorn, R., Heimann, R. B., Cold gas dynamic spraying (CGDS) of TiO_2 (anatase) powders onto poly(sulfone) substrates: Microstructural characterisation and photocatalytic efficiency, Journal of Photochemistry and Photobiology A: Chemistry, 187(2-3), 285–292, 2007.

[8] Doleker, K. M., Karaoglanli, A. C., Comparison of oxidation behavior of YSZ and $Gd_2Zr_2O_7$ thermal barrier coatings (TBCs), Surface and Coatings Technology, 318, 198–207, 2017.

[9] Chao, L., Hui, H., Liyong, N., Chungen, Z., Evaluation of thermal barrier coatings exposed to hot corrosion environment by impedance spectroscopy, Chinese Journal of Aeronautics, 24: 514–519, 2011.

[10] Perez, N., Electrochemistry and corrosion science, Second Edition, Switzerland, 455 s., 2016.

[11] Wang, N., Li, C., Yang, L., Zhou, Y., Zhu, W., Cai, C., Experimental testing and FEM calculation of impedance spectra of thermal barrier coatings: Effect of measuring conditions, Corrosion Science, 107: 155–171, 2016.

[12] Barranco, V., Feliu, S., Feliu, S., EIS study of the corrosion behaviour of zinc-based coatings on steel in quiescent 3% NaCl solution, Part 1: directly exposed coatings, Corrosion Science, 46: 2203-2220, 2004.

[13] Törne, K., Örnberg, A., Weissenrieder, J., Influence of strain on the corrosion of magnesium alloys and zinc in physiological environments, Acta Biomaterialia, 48, 541–550, 2017.

[14] Chen, L., Sheng, Y., Zhou, H., Li, Z., Wang, X., Li, W., Influence of a MAO+PLGA coating on biocorrosion and stress corrosion cracking behavior of a magnesium alloy in a physiological environment, Corrosion Science, 2018.

SYNTHESIS OF METAL OXIDE NANOPARTICLES BY AN EFFECTIVE COMBUSTION METHOD

*Y. Kamaci[1], R. Tas[2], S. **Rajendrachari**[1], A.C. Karaoğlanli[1]*

[1]Department of Metallurgical and Materials Engineering, Faculty of Engineering, Architecture and Design, Bartın University, Bartın, TURKEY
[2]Department of Biotechnology, Faculty of Science, Bartın University, Bartın, TURKEY

E-mail: yasemin.kmc24@gmail.com

Abstract

Nanoparticles play an important role in the advancement of manufacturing technologies and the emergence of new synthesis methods. In this study, experimental studies have been performed in order to absolutize the stoichiometric rates of oxidizing agent and fuel by using CuO and ZnO nanoparticles and by taking literature and application studies into consideration. In order to determine their phase structures, examine their microstructural properties and both CuO and ZnO have been characterized with x-ray diffraction, scanning electron microscope (SEM).

Keywords: Combustion method, Metal oxide nanoparticles, CuO nanoparticles, ZnO nanoparticles

1. INTRODUCTION

Nanoparticles play an important role in the development of synthesis and production technologies and the emergence of new methods. With the usability of their exceptional properties and qualities in different applications, the have shown an extremely rapid technological development [1]. Thanks to the excellent properties of nanostructured particles, they are widely used in various industrial areas especially in industries electric-electronic, biomedical, automotive and chemical [2]. In recent years, synthesis of metal oxide nanoparticles has advanced with great momentum due to its ability to produce materials in nanoscale and their applications in various fields. One of the main advantages of preparing metal oxide nanoparticles is their extremely small size and high surface ratio. Due to their extremely refined size, the metal nanoparticles have unique physical and chemical properties compared with nanometals. Some of the important metal oxide nanoparticles are CuO, ZnO, TiO_2, Fe_2O_3, Al_2O_3, MgO, AgO, CeO_2, ZrO_2 etc. [3]. Among these important metal oxides, CuO and ZnO have been examined.

Copper oxide nanoparticles are one of the very useful metal oxides and they appear to be brownish-black powder. The properties like high electrical conductivity, toughness, excellent ductility, high hardness and luminescent efficiency of semiconductors have made CuO nanoparticles one of the valuable metal oxides [4]. Nano-copper oxide is a widely used material. It has been applied to the catalyst, superconducting materials, thermoelectric materials, sensing materials, glass, ceramics and other fields [5]. Another important class of metal oxide nanoparticles is zinc oxide they are available as white powders and dispersions. The general properties of ZnO nanoparticles include antibacterial, anti-corrosive, antifungal and UV filtering properties. Zinc oxide is one of the metal oxides having wide range of applications [6]. This application areas of solar cells, light-emitting device, a transparent conductive film, a UV transparent property, chemical sensors, gas sensors, bio-cells, cosmetics, antibacterial, air-conditioning, chemical, cooling, electrical and optical devices, catalysts and catalyst selection for hydrogenation of liquid phase photocatalytic, biomedical, textile, organic coatings can be shown as an example [7,8,9,10]. In this study, experimental studies have been performed in order to absolutize the stoichiometric rates of oxidizing agent and fuel by using CuO and ZnO nanoparticles.

2. MATERIAL AND METHODS

In this study, 3g zinc (II) nitrate was used as zinc source, 1.5 g urea as organic fuel and 20 ml deionized water as solvent for zinc oxide synthesis. For copper oxide synthesis, 5 g copper (II) nitrate was used as copper source, 5 g urea as organic fuel and deionized water as solvent. In the combustion synthesis of both metal

oxide nanoparticles, blend the solution for homogeneity and keep the reaction solution in a silica crucible. The reaction mixture is heated on a magnetic stirrer at 300 °C. Initially, the viscous gel undergoes dehydration and starts combustion. Black products were obtained for CuO nanoparticles while white products were obtained for ZnO nanoparticles.

3. RESULTS

3.1 X-Ray Diffraction (XRD) Analysis

Figure 1. XRD diffraction pattern of CuO nanoparticles prepared by combustion method.

Figure 1 shows the XRD diffraction pattern of CuO nanoparticles prepared by combustion method.

Figure 2. XRD pattern of ZnO nanoparticles prepared by combustion method

Similarly, the figure 2 depicts the XRD pattern of ZnO nanoparticles prepared by combustion method.

3.2 Scanning Electron Microscopy (SEM) Analysis of CuO and ZnO Particles

Figure 3. XRD pattern of nanoparticles prepared by combustion method a) CuO and b) ZnO, respectively.

Figure 3a depicts the SEM image of CuO nanoparticles prepared by combustion method. SEM image shows that CuO nanoparticles appear spongy where the nanoparticles are linked together to form agglomerates of different sizes and shapes. Ultimately, we have prepared CuO nanoparticles to exhibit both spherical and rod shapes as shown in figure 3a. Similarly, in figure 3b shows the SEM image of ZnO nanoparticles prepared by combustion method. SEM image shows that ZnO nanoparticles appear spongy and are spherical in nature linked together to form a big porous structure. Prepared ZnO nanoparticles exhibit very fine size and spherical shape as shown in figure 3b.

3.4 UV-Visible Spectroscopy Analysis of CuO and ZnO Particles

Figure 5. UV-Visible spectra of a) CuO and b) ZnO nanoparticles prepared by combustion method

420

Figure 5a depicts the UV-Visible spectra of CuO nanoparticles prepared by combustion method. Due to the presence of absorption edge, the type of transition and bandgap value can be determined [11,12]. Figure 5b depicts the UV-Visible spectra of ZnO nanoparticles prepared by combustion method. The UV-Visible spectrum shows a characteristic absorption peak of ZnO at a wavelength of 360 nm and which confirms the band gap due to the intrinsic transition of the ZnO. This intrinsic band gap absorption of ZnO is due to the electron transitions from the valence band to the conduction band [13,14].

4. CONCLUSION

The combustion method of metal oxide nanoparticle synthesis is proved to be a very simple and robust technique. CuO and ZnO nanoparticles were successfully prepared by using urea as fuel and were characterized through XRD, SEM, UV-Visible spectroscopy, particle size analyzer. According to XRD analysis results, CuO nanoparticles are monoclinic crystalline, while ZnO nanoparticles have a hexogonal crystal structure SEM images of CuO nanoparticles show both spherical and rod shaped structure, whereas, ZnO nanoparticles show only spherical structure. EDS data of both the metal oxide nanoparticles confirms that they are stoichiometric and are a good agreement with the theoretical values. UV-Visible Spectrophotometer for ZnO and CuO nanoparticles obtained the desired result. Particle size analysis of CuO nanoparticles show two strong peaks and this is due to the different shapes of prepared CuO nanoparticles (Spherical and rod shape). The particle size distribution curve of both the metal oxide nanoparticles shows a wide range of particle sizes ranging from nano to microns and this is due to the agglomeration of prepared metal oxide nanoparticles.

REFERENCES

[1] Baykara, T., Nanoteknolojiler dünyasına doğru, 1. Basım, Nobel Akademik Yayıncılık, Ankara, 437, 2016.

[2] Gürmen, S., Ebin, B., İTÜ., M., Nanopartiküller ve üretim yöntemleri 1. Metalurji Dergisi, 150, 31-38, 2018.

[3] Garcia, M.F., Rodriguez, J.A., Metal oxide nanoparticles, Brookhaven National Laboratory, BNL-79479-2007-BC, 2007.

[4] AZONano, Copper oxide (CuO) nanoparticles - properties, applications, 9th May, 2013. https:// https://www.azonano.com/article.aspx?ArticleID=3395#

[5] https://www.us-nano.com/inc/sdetail/222

[6] Shashanka, R., Chaira, D., Optimization of milling parameters for the synthesis of nano-structured duplex and ferritic stainless steel powders by high energy planetary milling, Powder Technol, 278, 35-45, 2015.

[7] Vaseem, M., Umar, A., Hahn, Y., ZnO nanoparticles: growth, properties and applications, Chapter 4. In metal oxide nanostructures and their applications, Publisher: American Scientific Publishers, pp. 1-36, 2010.

[8] Yeşiltepe, D., Gürmen S., Production of nano zinc oxide (ZnO) by hydrothermal method, TMMOB Metalurji ve Malzeme Mühendisleri Odası Bildiriler Kitabı, 18. Uluslararası Metalurji ve Malzeme Kongresi, 297-299 s., 2016.

[9] Azem, A., N.F., Birlik, I., Sol-jel yöntemi ile hazırlanmış ZnO nanopartiküllerin optimizasyonu, Dokuz Eylül Üniversitesi-Mühendislik Fakültesi Fen ve Mühendislik Dergisi, 20 (58), 121-127, 2018.

[10] Matei, A., Ţucureanu, V., Popescu, M.C., Romaniţan, C., Mihalache, I., Influence of Cu dopant on the morpho-structural and optical properties ZnO nanoparticles, Ceramics International, 1-26 p., 2019.

[11] Dhineshbabu, N. R., Rajendran, V., Nithyavathy, N., Vetumperumal, R., Study of structural and optical properties of cupric oxide nanoparticles. Appl. Nanosci., 6, 933-939, 2016.

[12] Essic, J., Mather, R., Characterization of a bulk semiconductors band gap via near-absorption edge optical transmission experiment. Am. J. Phys., 61, 646-649, 1993.

[13] Zak, A.K., Razali, R., Abd Majid, W.H., Darroudi, M., Synthesis and characterization of a narrow size distribution of zinc oxide nanoparticles. Int. J. Nanomed., 6, 1399-1403, 2011.

[14] Zak, A.K., Abrishami, M.E., Abd Majid, W.H., Yousefi, R., Hosseini, S.M., Effects of annealing temperature on some structural and optical properties of ZnO nanoparticles prepared by a modified sol-gel combustion method. Ceram Int., 37, 393-398, 2011.

DETERMINATION METHODS FOR CORROSION RATE

S. Bilgiç

Department of Chemistry, Faculty of Sciences, Ankara University, Ankara, TURKEY

E-mail: semra.bilgic@science.ankara.edu.tr

Abstract

The methodologies developed to specify the corrosion rate is divided into two distinct groups: "chemical" and "electrochemical" methods. Chemical methods are based on the detection of mass loss and atomic absorption spectroscopy analysis. However, electrochemical methods are more widely used and more important in determining the corrosion rate.

Electrochemical methods are known as (i) Tafel extrapolation, (ii) linear polarization, and (iii) impedance spectroscopy methods. The Tafel extrapolation method is based on the implementation of the Tafel equation found by Tafel. The corresponding Tafel equation is given by the following formula; $\eta = a + b\log i$; where η is overvoltage, i represents the corrosion current density, a and b are the constants. Another method used to determine the corrosion rate is named as linear polarization or polarization resistance method. The theoretical basis of this method is given by Stern-Geary equation

$$\frac{\Delta E}{\Delta i} = \frac{\beta_a \times \beta_c}{2.303 \times i_{corr} \times (\beta_a + \beta_c)}$$

In the above-given equation; ΔE and Δi signify the potential and current differences, respectively. icor represents the corrosion current density and $\beta_a - \beta_c$ define the anodic and cathodic Tafel constants. In order to determine the corrosion rate, Electrochemical Impedance Spectroscopy (EIS) could also be used to obtain accurate and error-free results. Besides, this method is also crucial for developing electroplating and electro-organic synthesis methodologies, and it provides an effective way to generate and modify high-technology semiconductors and batteries. During an EIS analysis, we measure the resistance and capacitance properties of the studied materials via the application of a sinusoidal AC excitation signal (0.2 – 10 mV). The corresponding spectrum obtained by the variation frequency in a defined range. This spectral method is more sensitive and effective than the other techniques discussed herein.

Keywords : Corrosion, Corrosion rate, Chemical methods, Electrochemical methods

1. INTRODUCTION

In general, the corrosion is defined as the chemical and electrochemical degradation of substances as a result of their interaction with their environment; this phenomenon is particularly applies for metals and alloys. The corrosion can be defined in different ways [1]. Those could be summarized as:

a) degradation and decomposition of the substances through the reactions within its environment,

b) direct decomposition of materials by non-mechanical factors,

c) reverse process of obtaining metals from oxidized minerals.

The most prominent examples of corrosion are; formation of rust and other corrosion products on iron and steel, tarnish on silver, formation of green patina on copper and brass, formation of rust, ruptures and cracks on aircrafts, cars, and ships.

Corrosion in an electrochemical event based on the exchange of electrons between the metal surface and the aqueous electrolyte solution [2].

Figure / Some examples of corrosion

In order to exemplify the nature of corrosion we could use the reaction of salt acid over zinc. Following to the immersion of a zinc piece into the aqueous salt acid solution, a severe reaction will be observed. Hydrogen gas production is observed on the zinc surface, the comcomitant step involves the dissolution of zinc metal, and result to the formation of zinc chloride. The corresponding reaction is depicted as follows:

$$Zn_{(s)} + 2\,HCl \longrightarrow ZnCl_2 + H_{2(g)}$$

Considering that the chloride ion does not change in the reaction, the equation can be simplified as follows:

$$Zn + 2H^+ \longrightarrow Zn^{2+} + H_2$$

Thus, in the acid solution, zinc reacts with the hydrogen ion to form the zinc ion and hydrogen gas is released. If the latter reaction is examined closely, it is seen that during the reaction, zinc is oxidized to form zinc ions and hydrogen ions are reduced to hydrogen. The above reaction can be divided into half-reactions. The oxidation of zinc and the reduction of hydrogen ions.

Oxidation (anodic reaction)　: $Zn \longrightarrow Zn^{2+} + 2e^-$

Reduction (cathodic reaction) : $2H^+ + 2e^- \longrightarrow H_2$

A crucial principle for corrosion can be derived from these half-reactions. The oxidation rate during the corrosion process is equal to its reduction rate. Therefore, corrosion is a hazardous problem seen in various industries such as chemical industry, petrochemical industry, construction, automotive, railways, maritime and aviation.

Corrosion wastes sources and products, stops the production and causes various accidents. In addition, corrosion also causes significant economic losses. Corrosion is an essential factor in industrial investment and production processes. In accordance with some estimations, the cost of corrosion is between 3.5-5.5% of gross national product in many countries [2, 3]. Each year, it is thought that 20% of the produced iron is lost due to corrosion.

2. MATERIAL AND METHODS

The corrosion rate determination methods are primarily classified as chemical and electrochemical methods.

Chemical methods are;

i)　*Mass-loss method*

ii)　*Atomic absorption method*

Electrochemical methods;

i)　*Tafel extrapolation method*

ii)　*Polarization resistance (linear polarization) method*

iii)　*Alternative current impedance method*

Chemical methods

i) Mass-loss method

In order to compare the corrosion resistance of metals and alloys with each other, the corrosion rate of each must be given quantitatively. As shown in Table 1, the corrosion rate is explained in various ways in literature [2]. In order to determine the corrosion resistance of a material, the mass reduction of a material

deposited in the corrosion environment can be given in grams or milligrams and as a percentage change in mass. However, this method finds very limited application area. In both ways, mass reduction is related to how much material is exposed to the corrosion environment. Furthermore, the shape of the corroded material affects the rate of corrosion.

For example, if we leave the same metal with the same mass as a sphere shape and as a thin layer for the same duration, both mass-loss and percentage change in mass will be higher for the thin layer shaped sample, because thin layer sample has a greater surface area per unit of corrosion environment. Therefore, both ways of expression should be avoided in order to avoid uncertainties and misunderstandings in defining the corrosion rate. In another definition of corrosion rate, the mass reduction was changed to the mass reduction per unit surface for unit time. In British and American literature, the commonly used definition is the daily milligram mass reduction (mdd) per square decimeter.

Table 1. Expressions used to compare corrosion rates for engineering applications.

Expression	Comment
Mass decrease in grams or milligrams, percentage mass change.	Less frequently used, the shape of the sample, the residence time in the corrosion environment, affects the result.
Daily milligram (mdd) per square decimeter, daily gram per square decimeter, hourly gram per square centimeter, hourly gram per square meter, hourly gram per square inches, hourly mol per square centimeter.	Good, but these expressions cannot express the metal thinning rate.
Inchese per year, inches per month, milimeters per year.	Better, these expressions give the metal thinning rate.
Miles per year (mpy)	Best, the metal thinning rate can be expressed with smaller numbers without decimals.

From an engineering point of view, the rate of penetration of the metal or the thinning of a component can be used directly to predict the life of the material. The last four statements give the corrosion rate directly in the thinning term; inches per year, inches per month, millimeters per year, and miles per year. Since the corrosion rate of metals used in the industry ranges from about one to two hundred mpy, in practice, the expression of shaft thinning per year is superior. If this latter statement is used, it is possible to give the corrosion data in small numbers, avoiding decimal numbers [2].

$$\text{mpy} = \frac{534\,\text{W}}{\text{D A T}}$$

W: mass-loss, mg,   D: sample density, g/cm^3,   A: sample surface, square inches,   T: time, hour

When the corrosion rate is given in other units, it must be multiplied by the following coefficients to obtain (mpy).

	factor
inches/year	1000
inches/month	12000
mg/dm^2/day	1.44 / specific mass

Corrosion rate given in miles per year is converted to metric system with the following conversions.

mpy = 0.0254 mm/year = 25.4 μm/year = 2.90 nm/h = 0.805 pm/S

(mm = 10^{-3} m, μm = 10^{-6} m, nm = 10^{-9} m, pm = 10^{-12} m)

Electrochemical methods

i) Tafel extrapolation method

$$\eta = a + b \cdot \log i \quad \text{(Tafel equation)}$$

η: overvoltage, i: current density, a and b: constants.

The anodic and cathodic curves for the corroded metal are determined experimentally, and their linear parts are lengthened, and the corrosion potential E_{corr} and corrosion rate i_{corr} are determined from the cutting points [1 – 4]. Under ideal conditions, the sensitivity of the Tafel extrapolation method is equal to or higher than the sensitivity of the mass-loss method. By applying this technique it is possible to determine meager corrosion rates and continuously monitor the corrosion rate of the system. (A polarization curve can be achieved in ten minutes or less.)

Although this method can be achieved in a short time and the degree of sensitivity is high, there are many limitations in the application of this method. In order to obtain a reasonable accuracy, the Tafel region must extend at least ten times in a current density region.

Figure 1. Experimental E-log i curves of iron in sulfuric acid solution (Tafel curves).

ii) Linear polarization (polarization resistance) method

The theoretical foundations of the method were given by Stern and Geary in 1957. According to this method, there is a linear correlation between the effect of current Δi and the potential difference ΔE formed due to the corrosion potential.

$$\frac{\Delta E}{\Delta i} = \frac{\beta_a \times \beta_c}{2.303 \times i_{corr} \times (\beta_a + \beta_c)} \quad \text{(Stern-Geary equation)}$$

β_a: anodic Tafel constant, β_c: cathodic Tafel constant. i_{corr}: corrosion current density

This linear equation applies to a maximum 10 mV. Generally after 7 mV deviation from the linearity is observed [2, 6].

In Stern-Geary equation, if B constant is defined as;

$$B = \frac{\beta_a \times \beta_c}{2.303 \times (\beta_a + \beta_c)}$$

$$i_{corr} = B \times \frac{\Delta i}{\Delta E}$$

By using this method, i – E curves can be depicted in Figures 2 and 3.

If β_a and β_c constants are unknown in a system, it can be considered as $\beta_a = \beta_c = 0.12$ V (average value for industrial metals) and therefore, B constant is accepted as 0.026 V.

Figure 2. Current-potential curve.

Figure 3. Current-potential curve.

Figure 4. Linear polarization curve.

Table 2. B constants used for some systems in determining corrosion rate according to polarization resistance method

Corrosion system	Constants for calculations	References
β_a/V/ β_c 0.12 0.12 0.12 ∞ 0.06 0.12	B = 26 mV B = 52 mV B = 17.4 mV	[5] [6]
Organic acids Fe	B ~ 90 mV	[7]
Dilute H_2SO_4 Fe pH < 3 Fe	B ~ 47 mV B = 30 mV	[8]
3% NaCl 13/1 Cr Ni 13/4 Cr Ni 14/5/1 Cr Ni No	B = 22 mV B = 36 mV B = 41 mV	[9]

Pros and Cons of The Polarization Resistance Method

Pros

- *The polarization resistance method is easy to apply.*

- *The devices used are less expensive than those used in other methods.*

- *Meager corrosion rates which cannot be determined by other methods can be measured.*

- *The average corrosion rate can be determined at any time other than the determination of the corrosion rate.*

- *Corrosion rate determinations can be made in a concise time.*

- *The corrosion rate can also be determined without removing the metal from its location.*

- *The method can be used for the determination of corrosion rate of buried underground pipes, determination of corrosion rates of metals used in surgeries and determination of corrosion rate under severe nuclear radiation.*

Cons

- *The method gives good results in neutral and acidic environments but it is not sensitive to basic environments.*

- *It gives relative corrosion rate rather than absolute corrosion rate.*

- *The β_a and β_c values cannot be reliably determined for each electrode reaction. However, data available in this field indicate that β_a values are generally between 0.06-0.12V.*

Determination of Corrosion Rate by Alternating Current Polarization Method

The main criticism of the direct current methods used to determine the corrosion rate experimentally is that the polarization of the dissolved metal leads to the removal of the corrosion potential from natural conditions. EES method is an experimental approach in response to this problem. In this method, the dissolving metal electrode is stimulated by sending a potential sinusoid with a small amplitude (5-10mV). In this embodiment, a wide frequency range is scanned.

The result obtained by interpreting the current obtained against the frequency obtained. The responses received were resistive and capacitive. Resistive ones are due to ambient resistance (R_Ω)and polarization resistance (R_P); the capacitive is due to the electrical double layer (C_{dl}) at the metal-electrolyte interface [2,3].

The time-dependent potential signal and the current response are expressed by the following equations.

$$V_t = V_0 \sin\omega t$$

$$I_t = I_0 \sin(\omega t + \theta)$$

t: time, ω: radial frequency (rad/s), θ: phase degree between V_t and I_t, ωt is given as radial unit thus, θ should also be given in radial unit.

Between the radial frequency (ω), frequency (f) and period (T), there are correlation of $\omega = 2\pi f$ and $T = 2\pi/\omega$. The relationship between V_t and I_t is a magnitude that is the function of angular frequency and is called impedance (Z). ($Z_\omega = V_t/I_t$)

Figure 5. Voltage-current relations in alternating current

a. Ohmic resistance   b. capacitive resistance circuit

$$Z_\omega = R\Omega + \frac{Rp}{1 + (\omega\,C\,R_p)^2} - j\,\frac{\omega\,C\,R_p{}^2}{1 + (\omega\,C\,R_p)^2}$$

Real impedance $Z'_\omega = R\Omega + \dfrac{Rp}{1 + (\omega\,C\,R_p)^2}$

Virtual impedance $Z''_\omega = \dfrac{\omega\,C\,R_p{}^2}{1 + (\omega\,C\,R_p)^2}$

Another approach used in presenting the impedance data is to carry log |Z| against logω or log θ against log ω. Bode diagrams gathered by both methods are shown in Figure 6b.

Figure 6. Two choices for EES data presentation

a) Nyquist   b) Bode diagrams

In this method, which is considered equivalent to the Nyquist presentation, the polarization resistance is obtained by subtrac ting the R_ω value measured at high frequency and $(R_\omega + R_p)$ measured at low frequency. The portion of the $(\log |Z| - \log \omega)$ curve recorded in the mid-size values contains a linear portion with a slope of -1.0. Two examples of Nyquist and Bode diagrams recorded under actual corrosion conditions are shown in Figures 7a and b.

Figure 7. Nyquist (a) and Bode (b) diagram examples.

Material: Carbon steel, environment: 1000 ppm chloride + sulfate and bicarbonate consisting water.

Temperature: 32°C. Warburg impedance due to concentration polarization is clearly seen in both diagrams.

3. RESULTS AND DISCUSSION

EES has significant advantages over direct current methods used to determine the corrosion rate. EES provides information about the mechanisms determining the corrosion kinetics as well as measuring the polarization resistance [3]. For example, the capacity of the electrical bilayer located at the metal-electrolyte interface can be measured by EES. However, there are some factors that limit the reliability of the impedance measurement results. In particular, if the corrosion rate does not remain constant during the extended test period at shallow values of the frequency, the impedance behavior changes. It should be added that the Warburg impedance that occurs in corrosion reactions where diffusion control is predominant. Warburg impedance prevents lossless reflection of low-frequency data on the measurement results [10, 11]. As a result,

432

it can be said that the limiting factors, which we mentioned apart, negatively affect the interpretation and usefulness of EES data. On the other hand, significant advances have been made to overcome these challenges with the strong support of digital computers and improved programs. The type of equivalent circuits that the measured impedance data are compatible with can be determined by computer programs.

REFERENCES

[1] Erbil, M., Korozyon, İlkleer ve Önlemler, Poyraz Ofset, Ankara, 2012.

[2] Üneri, S., Korozyon ve Önlenmesi, Korozyon Derneği, Poyraz Ofset, Ankara, 2011.

[3] Doruk, M., Metalik Malzemeler ve Korozyon, Korozyon Derneği, Poyraz Ofset, Ankara, 2014.

[4] Burstein, G.T. "A Century of Tafel's Equation: 1905–2005. A Commemorative Issue of Corrosion Science", Corrosion Science, 47, 2858–2870, 2005.

[5] Stern, M., Geary, A.L., "Electrochemical Polarization, I.A. Theoretical Analysis of the Shape of Polarization Curves, Journal of the Electrochemical Society, 104, 56–63, 1957.

[6] Stern, M., A Method For Determining Corrosion Rates From Linear Polarization Data Corrosion, The Journal of Science & Engineering, 14, 440Z–444Z, 1958.

[7] Neufeld, J., Application of the polarization resistance technique to corrosion monitoring, Corrosion Science, 4, 245–251, 1964.

[8] Prozák, M., and Barton, K., The estimation of corrosion velocity by measuring polarization resistance, Corrosion Science, 7, 159–163, 1967.

[9] Lots, U., Schollmaier, M., Heitz, E., Flow–dependent corrosion–II. Ferrous materials in pure and particulate chloride solutions, Materials and Corrosion, 36, 163–173, 1985.

[10] Darowicki, Corrosion Rate Measurements by non–linear Electrochemical Impedance, Spectroscopy, Corrosion Science, 37, 913–925, 1995.

[11] Brytan, Z., Niagaj, J., Reiman, Z., Corrosion studies using potantiodynamic and EIS electrochemical techniques of welded lean duplex stainless steel UNS 582441, Applied Surface Science, 388, 160–168, 2016.

PASSIVITY IN CORROSION

S. Bilgiç

Department of Chemistry, Faculty of Sciences, Ankara University, Ankara, TURKEY

E-mail: semra.bilgic@science.ankara.edu.tr

Abstract

In general terms, passivation is defined as the loss of a metal's ability to react under certain environmental conditions. Alternatively, passivation is also referred as the anodic potential applied to the system externally in order to substantially reduce the rate of corrosion or the addition of an oxidizing component to the corrosive medium in which the metal is present. The corrosion rates decrease by $10^4 - 10^6$ when the metal goes from active to passive state, and the passive state is usually unstable. The passivation state may be degraded due to electrochemical or mechanical effects. Electrochemical effects include altering the potential of the metal or its alloy, excessive oxidation, and dissolution processes. Eliminating the passivation by scraping the metal surface with a glass rod is an example of the mechanical effect. The metals that are first passivated and then reactivated are described as active-passive metals. Following the elimination of passivation, the current in the solution will start to rise, and the crude metal will dissolve again into the solution by generating its cation species but in a higher state. For example, in the beginning, if the reaction environment consists of the iron ion, which is in Fe^{+2} state, after the elimination of the metal passivation step, the metal will dissolve in +3 state. The region that occurs following the passivation is known as the transpassive region. In the case of anions such as chloride are present in the solution medium where the passivation is carried out, the degradation potential of the passivation shifts to less noble values so that the passivation zone becomes narrower, and therefore the metal will be corroded. The shape of the passivation curves depends on the type of the studied metals, the passivation medium, and the specific ion species present in this medium. For instance, in the same acidic environment, the passivation curves obtained from Ti, Cr, and stainless steel will be different from each other. Howbeit, for the same stainless steel sample, the passivation curves obtained in three different media will also be distinctive. The temperature and increase in acid concentration also affect the passivation curve of the active-passive metals.

Keywords: Metals and alloys, Corrosion, Passivation

1. INTRODUCTION

What is passivity?

Passivity is the loss of chemical activity of some metals and alloys under special environmental conditions $(1-5)$.

Passivity is very important in engineering. The passivity of many metals and alloys allows them to be used as building materials in engineering. The corrosion rate of an inactivated metal in an air-free acid solution is indicated by point A. If oxygen or Fe^{3+} is added to this solution, it is observed that the corrosion rate of the metal increases.

Figure 1. Corrosion rate of a non-passive metal dependence on the oxidation power of the solution

Corrosion in a passivating metal

The corrosion state of a passivated metal or alloy can be examined in three zones [1, 2].

a) Active region

b) Passive region

c) Transpassive region

Figure 2. Corrosion of an active-passive metal depending on the oxidation power (electrode potential) of the solution

The state of this metal in the active region is identical to that of a non-passivating normal metal.

A slight increase in the oxidation potential of the solution causes the corrosion rate to increase rapidly (the situation in Figure 1). If more oxidants are added, the corrosion rate suddenly decreases. This corresponds to the beginning of the passive region.

Increasing the oxidizing agent will slightly or does not change the corrosion rate of the metal (passivity region).

Chromates (CrO_4^-), nitrites (NO^{2-}), molybdates (MoO_4^{-2}) and tungstates (WO_4^{2-}) are used as oxidizing agents and are called passivators [6, 7].

The condition for success with passivators is that they are added to the environment in a way that exceeds the minimum amount required for passivation. The amount of passivators added below this amount causes the corrosion rate to increase rather than decrease. In the transition from active region to passive region, corrosion rate is generally reduced by $10^3 - 10^6$.

It is believed that in the passive region, a thin oxide layer is formed which is invisible on the metal surface and this layer protects the metal with a high protective concentration of the oxidizing agent.

It has been shown that in the high concentration of the oxidizer or in environments with high oxidation power, this protective layer breaks down and the metal begins to redissolve. This region, where the corrosion rate increases again, is called the transpassive region.

Some metals and alloys can be passivated by direct active–passive conversion in the immersion medium. This is called self-passivation.

In the absence of self-passivation under current conditions, active-passive conversion can be realized;

a) By adding strong passivators to the environment,

b) By lowering the passivation potential by forming alloys with high passivation metals,

c) By applying external current to increase the potential of the metal to exceed the passivation potential.

2. MATERIALS AND METHODS

Passivity is also defined as the reduction of the rate of corrosion of a metal and alloy in certain environmental conditions.

In order to indicate the nature of passivity, it is useful to look at Faraday's experiments with iron in nitric acid in 1840.

If a piece of iron or steel is immersed in a nitric acid concentration of about 70% at room temperature, no reaction is observed.

If mass losses are determined, it is seen that the corrosion rate of iron is very small and it approaches zero.

If enough water is added to this nitric acid to a dilution of about 1:1, no change is seen, or if the iron is shaken to the edges of the beaker, it is observed that nitrogen gases are released and iron dissolves in a drastic reaction (Figure 3.C).

If the iron piece is introduced directly into dilute nitric acid, it is observed that it reacts drastically in the same manner.

Figure 3. Schematic representation of Faraday's experiments on iron passivation.

Electrochemical investigations in recent years have significantly increased the knowledge of corrosion and passivity. The film is understood to be composed of metal oxides and hydroxides.

Electrochemical studies have shown that the dissolution rate of some metals in a large potential region is very small.

Not all metals show passivity, but there are many alloys that show passivity in solutions.

Fe, Cr, Ni, Ti and their alloys (for example stainless steels) are the most important of passive metals [8].

Figure 4. Two examples showing the corrosion behavior of metals in acidic environments: active dissolution of iron in HCl (no passivation) and active-passive conversion in H₂SO₄

Ensuring passivity by applying anodic current and examining regions in active-passive metals

i_{tp} net passivity current density

i_p passivation critical current density

E_{corr} corrosion potential

E_{pp} primary passivation potential

E_{tp} net passivation potential

E_p pitting potential

E_t Transpassivation potential

Figure 5. Schematic potential – log i curve for an active-passive metal.

As the potential in the active region (AB) is increased, the rate of dissolution of the metal increases, while the metal ions formed are transferred to the medium, Epp potential (B) begins to precipitate as the hydroxide or oxide on the metal surface by exceeding the solubility product of the metal hydroxide or oxide.

The current decreases between BC as the surface begins to be covered. Both the formation and deterioration of the oxide lattice causes current oscillations in this region.

438

The shapes of the passivity curves depend on the type of metal, the passivation medium, the special ions in the medium.

Figure 6. Passivity curves for Ti, Cr and stainless steel in acidic media.

If the passivity curves for the same stainless steel in different environments are examined, differences are observed.

Figure 7. Passivity curves for stainless steel in three different environments.

The potential at which the passivation begins is called Flade Potential and is symbolized by E_{pp}. This value is an important quantity for determining the corrosion conditions of active-passive metals.

Passivity dissolution current i_{pp} and critic current density i_p are two other important parameters.

The change of temperature and acid concentration affect the corrosion of active - passive metals. Anodic critical current density increases with increasing temperature and hydrogen ion concentration, other parameters change slightly.

3. RESULTS AND DISCUSSION

Three conditions are shown for an active-passive metal which yields an anodic dissolution curve in the form of S in an acid solution. In this way, there is a single reduction process, such as hydrogen discharge, only

three different equilibrium reactions are thought to be the current density. In case 1 there is only one stable intersection point (A).

Since this intersection is in the active region, a high dissolution rate is observed.

Figure 8. Effect of temperature and acid concentration on the anodic dissolution curve of an active-passive metal.

Figure 9. Behavior of an active-passive metal in corrosive environment.

It can be deduced from Figure 9 why the position of the current maximum or arch of the anodic dissolution curve is important. If the curve of the cathodic reduction event passes over the arch of the anodic dissolution curve, as in case 3, spontaneous passivation occurs. In other words, for spontaneous passivation, the rate of cathodic reduction in the primary passivation potential must be equal to or greater than the rate of anodic dissolution.

As the anodic critical current density ip is smaller, and the primary passivation potential Epp is more active of a metal or alloy, so the more easily it can be passivated. It is therefore possible to determine the

quantitative susceptibility of a metal or alloy to passivation from its anodic dissolution state, and consequently its resistance to corrosion.

Figure 10 shows the effect of E_{pp} on passivity. Schematic anodic polarization curves for two metals are shown here. The cathodic process was assumed to have the same electrochemical parameters on both metal surfaces.

Figure 10. Effect of E_{pp} on passivity.

In system 1 with higher primary passive potential, the anodic and cathodic polarization curves intersect each other in the active region A and the corrosion rate is high. On the other hand, in system 2 where the E_{pp} potential is lower, the intersection occurs in the passive region B and the corrosion rate is smaller than the other.

Figure 11 shows the effect of passivation critical current density, ip on corrosion conditions of metals showing active-passive transition. The anodic polarization curves are the same as in Figure 10.

Figure 11. Effect of critical current density on passivity.

The cathodic process is assumed to be the same for both metals, but it is diffusion-controlled. The cathodic and anodic polarization curves have only one point of intersection (A) for the metal with a smaller critical current density.

However, for metal 2, there are two stable intersection points, B and C. Since one of these points is located in the active region and the other is in the passive region, it is difficult to determine whether the metal 2 undergoes corrosion with a low corrosion rate or with a high corrosion rate.

Figure 12. Effects of H + and O2 reduction processes on corrosion of 18Cr – 8Ni Steel in acidic medium.

In the figure, the corrosion situation of 18Cr – 8Ni steel in sulfuric acid is shown schematically. If there is no oxygen in the environment, since the reduction curve of hydrogen ions HI intersects the oxidation curve of the steel JK in the active region, corrosion occurs. The situation gets worse if a small amount of oxygen is found in the environment: Reduction curve of oxygen D E F G, intersects S curve of steel at three points E, F and G (such as the case 2 in Figure 10). If abundant oxygen is present, reduction curve of oxygen A B C, intersects S curve of steel in the passivity region, B, and corrosion occurs slightly.

Deterioration of passivity

Since passivity is based on a passivating film formed by anodic oxidation or chemical oxidation on the metal surface, various factors that cause this film to partially or completely deteriorate, cause the passivity to deteriorate.

These factors may be electrochemical oxidation and reduction, excessive chemical oxidation or dissolution (acidic or basic media and complex forming anions) and mechanical [1].

Electrochemical Deterioration

If the potential of an anodically passivated metal or alloy is further increased, the current increases again in the transpassive region (DF in Figure 5). In this region, the metal can often begin to redissolve with higher valence, for example, like Fe^{3+} ion. Often this dissolution proceeds by forming pits.

The potential in which the current starts to increase in the transpassive region is called the passivity deterioration potential (E_t). Oxygen is also released in the transpassive region.

If there are activating anions such as Cl^- in the passiavation medium, this passivity distortion potential shifts to less nobel potential, so the passivity region becomes narrower, metal exposes to corrosion by forming pits. E_p is called pit potential.

If the amount of Cl^- ions is large, the passivity region may disappear completely and the metal will continue its active dissolution, i.e., corrosion occurs.

If Cl^- is added to the medium after the metal is passivated, the same effect is observed, i.e., the passivity is deteoriated [9].

Stainless steels containing large amounts of chromium dissolve easily in the transpassive region by forming chromium-VI compounds and passivity is deteoriated.

If the passivating oxides formed on the metal surface are reduced by cathodic process, the passivity is deteoriated again.

Mechanical Deterioration

The passivating oxide film can be deteoriated by bending, impact, stretching, scratching, stripping and other mechanical forces. In practice, it is desirable to maintain the passivity of electrophilic or chemically spontaneous oxide formation of the degraded sites of the passivating oxide film on the metal which is intended to be protected by passivation.

3. RESULT AND DISCUSSION

Passivity is a state in which metals and alloys are not corroded, they are desirable from the engineering point of view, but are not always continuous.

REFERENCES

[1] Üneri, S., Korozyon ve Önlenmesi, Korozyon Derneği, Poyraz Ofset, Ankara, 2011.

[2] Doruk, M., Metalik Malzemeler ve Korozyon, Korozyon Derneği, Poyraz Ofset, Ankara, 2014.

[3] Uhlig, H.H., Passivity in metals and alloys, Corrosion Science, 19, 777–791, 1979.

[4] Olsson, C.O.A., Landolt, D., Passive films on stainless steels-Chemistry, structure and growth, Electrochim. Acta, 48, 1093 (2003).

[5] Schmuki, P., From Bacon to barriers: a review on the passivity of metals and alloys, Journal of Solid State Electrochemistry, 6, 145–164, 2002.

[6] Valcarce, M.B., Vázquez, M., Carbon steel passivity examined in solutions with a low degree of carbonation: The effect of chloride and nitrite ions, Materials Chemistry and Physics, 115, 313–321, 2009.

[7] Virtamen, S., Surber, B., Nylund, P., Influence of MnO_4^- anion in the electrolyte on passivity breakdown of iron, Corrosion Science, 43, 1165–1177, 2001.

[8] Palit, G.C., Elayaperumal, K., Passivity and pitting of corrosion resistant pure metals Ta, Nb, Ti, Zr, Cr and Al in chloride solutions, Corrosion Sciene, 18, 169–179, 1978.

[9] Elfström, B.O., The effect of chloride ions on passive layers on stainless steels. Materials Science and Engineering, 42, 173–180, 1980.

INVESTIGATION OF ANNEALING OF SURFACES OF ITO and PEDOT:PSS FOR PERFORMANCE OF ORGANIC SOLAR CELLS

M. Cantürk Rodop

Department of Physics, Faculty of Arts and Sciences, Yildiz Technical University, Istanbul, TURKEY

E-mail: mcrodop@gmail.com

Abstract

In this study, the effects of thermal, UV and surface modification processes applied to ITO and PEDOT: PSS surfaces on the photovoltaic performance of P3HT:PCBM based organic solar cells were investigated. Organic solar cells were prepared and their device performances were examined. UV effect and thermal annealing were observed to improve the photovoltaic performance.

Thermal annealing was applied to ITO; also ITO and PEDOT:PSS layers were exposed to UV irradiation. As a result, it is observed that these processes have positive impacts on the photovoltaic performances of bulk heterojunction organic solar cells.

Keywords: organic solar cells, temperature annealing, P3HT:PCBM

1. INTRODUCTION

Organic solar cells have been the subject of deep research in recent years. The lightness, flexibility, ease of production and easy adjustability of chemical and physical properties of organic materials via chemical synthesis routes make them advantageous over their inorganic counterparts [1]. Organic solar cells are prepared by blending two different organic materials, one of which is a donor and the other is an acceptor, and sandwiching the resulting thin film between two metal electrodes [2-4]. Although the power conversion efficiencies of organic solar cells have increased rapidly in recent years [5-8], it is still not comparable to silicon solar cells [9], which dominate the photovoltaic market. Therefore, research and development studies to increase the efficiency of organic solar cells are of great importance [10].

In this study, the effects of thermal, UV and surface modification processes applied to ITO and PEDOT: PSS surfaces on the photovoltaic performances of organic solar cells were investigated. Organic solar cells were prepared and the device performances were examined. UV effect, thermal annealing and surface modification of PEDOT:PSS were observed to improve the photovoltaic performance.

2. MATERIAL AND METHODS

The Indium Tin Oxide (ITO) coated substrates from Kintec Company with a thickness of around 120 nm, a sheet resistance of 34 Ω/sq. and a size of 1.5×1.5 cm^2 were used as transparent oxide electrodes. One-third of ITO was patterned by etching with an acid mixture (HCl:HNO$_3$:H$_2$O) and then each substrate was cleaned with distilled water. After cleaning procedure, glass substrates were cleaned in ultrasonic bath with acetone and isopropanol at each stage for 20 minutes, respectively. P3HT:PCBM solution was prepared by dissolving P3HT and PCBM in 1 ml of chlorobenzene (CB) 2:1.1 ratio. ITO substrates and PEDOT:PSS layers were exposed to UV radiation 30 minutes for ITO and 15 minutes for PEDOT:PSS. ITO substrates were annealed 5 to 10 minutes separately. Poly(3,4-ethylenedioxythiophene)– poly(styrenesulfonate) (PEDOT:PSS) was spin coated at 2000 rpm on the glass–ITO substrates. The PEDOT:PSS layers were annealed in a furnace at 140 °C for 10 minutes. P3HT:PCBM solution was spin cast on the ITO/PEDOT:PSS substrates. P3HT:PCBM layers were annealed in a furnace at 120 °C for 4 minutes. Finally, 100 nm Al was thermally evaporated as top contact. All current–voltage (I–V) characteristics of the PV devices were measured (using a Keithley 2400) under nitrogen in a dry glove box immediately after production.

3. RESULTS AND DISCUSSION

The current density-voltage (J-V) characteristics of reference devices in the form ITO/PEDOT:PSS/P3HT:PCBM/Al is shown in figure 1. These devices were non-annealed to better understand the effect of thermal and UV annealing on the device performance. As can be seen from the figure 1, reference device exhibited a short circuit current density (J_{sc}) of 6 mA/cm^2, an open circuit voltage (V_{oc}) of 625 mV, a fill factor (FF) of 0.5 was calculated using J-V curves which led to a power conversion efficiency (PCR) of 1.8 %.

Figure 1. J-V curves of a reference device under illumination (red) and dark (black).

Figure 2 shows the J-V characteristics of devices comprising of both UV treated ITO and PEDOT:PSS in the form of ITO (UV)/PEDOT:PSS (UV)/P3HT:PCBM/Al. As can be seen from the figure 1, reference device exhibited a short circuit current density (J_{sc}) of 6.1 mA/cm^2, an open circuit voltage (V_{oc}) of 625 mV, a fill factor (FF) of 0.49 was calculated using J-V curves which led to a power conversion efficiency (PCR) of 1.9 %.

Figure 2. J-V curves of devices in the form of ITO(UV)/PEDOT:PSS(UV)/P3HT:PCBM/Al

under illumination (red) and dark (black).

Figure 3 shows the J-V characteristics of devices comprising of PEDOT:PSS treated with dimethyl sulfoxide (DMSO) in the form of ITO/PEDOT:PSS(DMSO)/P3HT:PCBM/Al. Such devices exhibited a short circuit current density (J_{sc}) of 6.7 mA/cm^2, an open circuit voltage (V_{oc}) of 575 mV, a fill factor (FF) of 0.56 was calculated using J-V curves which led to a power conversion efficiency (PCR) of 2.15 %.

Figure 3. J-V curves of devices in the form of ITO/PEDOT:PSS(DMSO)/P3HT:PCBM/Al

under illumination (red) and dark (black).

Figure 4 shows the J-V characteristics of devices comprising of UV treated ITO and both UV and DMSO treated PEDOT:PSS in the form of ITO(UV)/PEDOT:PSS(UV+DMSO)/P3HT:PCBM/Al. Such devices exhibited a short circuit current density (J_{sc}) of 6.5 mA/cm^2, an open circuit voltage (V_{oc}) of 625 mV, a fill factor (FF) of 0.55 was calculated using J-V curves which led to a power conversion efficiency (PCR) of 2.23 %.

Figure 4. J-V curves of devices in the form of ITO (UV)/PEDOT:PSS(DMSO+UV)/P3HT:PCBM/Al

under illumination (red) and dark (black).

Figure 5 shows the J-V characteristics of devices comprising of thermally treated ITO and DMSO treated PEDOT:PSS in the form of ITO(Annealing)/PEDOT:PSS(DMSO)/P3HT:PCBM/Al. Such devices exhibited a short circuit current density (J_{sc}) of 6.5 mA/cm^2, an open circuit voltage (V_{oc}) of 625 mV, a fill factor (FF) of 0.56 was calculated using J-V curves which led to a power conversion efficiency (PCR) of 2.27 %.

Figure 5. J-V curves of devices in the form of ITO (Annealing)/PEDOT:PSS(DMSO)/P3HT:PCBM/Al

under illumination (red) and dark (black).

REFERENCES

[1] Gunes, S., Neugebauer, H., Sariciftci, N.S., Conjugated polymer based organic solar cells, Chemical Reviews, 107, 1324-1338, 2007.

[2] Ganesan, S., Mehta, S., Gupta, D., Fully printed organic solar cells-a review of techniques, challenges and their solutions, Opto-Electronics Review, 27, 298-320, 2019.

[3] Kim, Y., Lim, H., Development of polymer acceptors for organic photovoltaic cells, Polymers, 6, 382-407, 2014.

[4] Ganesamoorthy, R., Sathiyan, G., Sakthivel, P., Review: fullerene based acceptors for efficient bulk heterojunction organic solar cell applications, 161, 102-148, 2017.

[5] Fan, B., Du, X., Liu, F., Zhong, W., Ying, L., Xie, R., Tang, X., An, K., Xin, J., Li, N., Ma, W., Brabec, C.J., Huang, F., Cao, Y., Fine-tuning of the chemical structure of photoactive materials for highly efficient organic photovoltaics, Nature Energy, 3, 1051-1058, 2018.

[6] Yuan, J., Zhang, Y., Zhou, L., Ulanski, J., Li, Y., Zou, Y., Single-junction organic solar cell with over 15 % efficiency using fused-ring acceptor with electron-deficient core, Joule, 3,1-12, 2019.

[7] Cui, Y., Yao, H., Zhang, J., Zhang, T., Wang, Y., Hong, L., Xian, K., Zhang, S., Peng, J., Wei, Z.,Gao, F., Hou, J., Over 16% efficiency organic photovoltaic cells enabled by a chlorinated acceptor with increased open-circuit voltages, Nature Communications, 10, 2515, 2019.

[8] Meng, L., Zhang, Y., Wan, X., Li, C., Zhang,X., Wang, Y., Ke, X., Xiao, Z., Ding, L. et. al, Organic and solution-processed tandem solar cells with 17.3 % efficiency, Science, 361, 1094-1098, 2018.

[9] Green, M., Solar cell efficiency tables (version 53), Progress in photovoltaics:research and applications, 27, 2018.

[10] Scharber, M.C., Sariciftci, N.S.,Efficiency of bulk heterojunction organic solar cells, Progress in polymer science, 38, 1929-1940, 2013.

[11] Hu, Z., Zhang, J., Zhu, Y., Effects of solvent treated PEDOT:PSS on organic photovoltaic devices, Renewable Energy, 62, 100-105, 2014.

EXAMINATION OF FACADE DAMAGES IN BUILDINGS; ZONGULDAK KARADENİZ EREĞLİ ATATÜRK CULTURE CENTER (AKM)

A. Dilaver[1], A. Özata[1], A. Bideci[2], Ö. Sallı Bideci[2]

[1]Department of Architecture, Institute of Science, Düzce University, Düzce, TURKEY
[2]Department of Architecture, Faculty of Art, Design and Architecture, Düzce University, Düzce, TURKEY

E-mail: aygun.dilaver0@gmail.com

Abstract

In this study, facade damages on Atatürk Cultural Center (AKM) building, which is a socio-cultural structure located in the coastal band of Ereğli Atatürk Boulevard in Zonguldak-Karadeniz (Kdz.), were investigated. Facade investigations were carried out in the headings of the problems caused by damages (aesthetic problems, usage and comfort problems, health and safety problems) and human faults (wrong detail design, wrong applications, wrong use and maintenance of the building) that caused damage on the facade. As a result of the study, the facade damages that occurred on the Eregli AKM facade were determined and a base was prepared to prepare the data on the measures that could be taken in order to prevent the permanent damages. Possible damage to new buildings has been identified and it has been concluded that necessary measures have to be taken during the design process.

Keywords: Atatürk Cultural Center (AKM) Building, Facade Damage, Physical Building Problems

1. INTRODUCTION

The facades of the building's shell are the structural elements that are affected most by the external conditions and other physical and mechanical factors. Therefore, many damages occur on the building facades. "Building façades must fulfill the task of providing aesthetics, economy, protection of the building from environmental influences and providing comfortable environments for the inhabitants of the building in accordance with the function they are designed. If the building facades fail to fulfill the task expected from them, they provide a comfortable environment for the inhabitants. They cause problems that do not meet the requirements of building physics. As a result, the building facades are damaged in a short time, they wear out, and the quality of the building decreases "[1].

The loss of the first effect of color, shape and texture changes on the building facade can be defined as aesthetic distortions. Use and comfort problems can be explained as the failure of the structure to meet the intended needs and rendering it unusable for the user. Deformations affecting building static balance and causing deformation of building elements are safety and health problems [2].

The problems caused by facade damage can be classified as follows (Table 1). [3]

Aesthetic Problems	Use and Comfort Problems	Health and Safety Issues
Efflorescence	Superficial deformations that may cause water, air and sound penetration into the interior	Plaster cracks
Surface distortions		Corrosion of metals
Color changes		Decay in wood
Atmospheric impurities		Surface degradation
		Bacteria and insect formation
Light abrasion	Glare on transparent surfaces	Fracture / Fall
Worn image		Algae, mold and fungus formation
Distortions due to usage errors		Cracking
Surface corrosion in metals		Abrasion

Table 1. Problems caused by facade damages.

The components and salts in the cement mortar dissolve in the presence of water and leak out of the material. The infiltrating components crystallize as a result of atmospheric interaction to form stains on the surface can be defined as efflorescence [4, 12].

Most of the physical damage caused by the facade is caused by human errors which are the primary users of the buildings. Lack of information, carelessness and lack of maintenance for the building result in damage to the facade [4].

During the facade damage process, it is possible to collect the human factor under the following headings.

a) False detail design

b) Incorrect application

c) Misuse and maintenance of the building [1, 9].

In this study, facade investigations were carried out under the titles of problems caused by damages in AKM building (aesthetic problems, usage and comfort problems, health and safety problems) and human errors (wrong detail design, wrong applications, wrong usage and maintenance of the building) causing damage to the facade.

2. MATERIAL AND METHODS

2.1 Material

The building where the facade damages are examined is a building belonging to the public institution located in Kdz Eregli district of Zonguldak province. Kdz Eregli Orhanlar Neighborhood 160 is located on the parcel of the island 7 is located on the shore band of Ataturk Boulevard, 50 m away from the sea (Figure 1). AKM Building consists of ground floor and 1st floor. Kdz Ereğli has been in service since 1996 and has 3 cinema halls, 2 exhibition halls, 1 public library, 1 wedding hall, 1 city council hall and 1 cafeteria. The building was constructed as reinforced concrete and no thermal insulation (Figure 2).

2.2. Metod

Kdz. Investigations were carried out on the facade damages on the AKM building, a socio-cultural structure located on the coastal line of Ereğli Atatürk Boulevard. The damages of the facade in AKM building were examined by visual analysis. The research is mainly focused on research, examination and visual. The facade damages in the AKM building were photographed and the subject was discussed and photographs of the factors causing the damage to the facade were interpreted.

3. RESULTS AND DISCUSSION

Figure 1. Location of Kdz Ereğli Atatürk Culture Center.

Figure 2. Kdz Ereğli Atatürk Cultural Center.

3.1. Damages Caused by Incorrect Detail Design

In the sections where the structures join the ground, algae formations have been seen due to material breakage on the facade and lack of necessary water insulation due to lack of insulation or removal of water from the structure. The facade of the building is under the influence of sea salts due to the winds blowing from the sea due to its proximity to the sea. Sea salts are thought to cause effloresence on the facade. For this purpose, necessary laboratory tests should be performed (Photo 1).

Photo 1. Damage to the facade exposed to water.

Rain water accumulated on the roof should be removed as soon as possible and correctly. Parapet dropper should be designed to remove the accumulated water from the structure due to rainfall. Material spills and material discolorations occurred in the parapet due to incorrect detailing. Water acting along the surface of the parapet may seep into the material and cause corrosion in the floor reinforcement. Material spillage under the observed (Photo 2).

In roof design, water cannot be removed from the structure quickly and accurately. and over time, the water leaked through these cracks caused efflorescence.

Building facades are under the influence of water as a result of condensation of water vapor and freezing of ice due to leakage of ground water through precipitation. Disturbances occur in the structure and building materials with the effect of water [1,8]. The presence of water is a danger to buildings. Necessary precautions should be taken by considering the factor of water in building design. Failure to take the necessary precautions for water on the facade of the AKM building was observed to cause cracks and efflorescence on the facade (Photo 3).

Photo 3. Cracks and effloresence on the facade

3.2.Damages Caused by İmproper Applications

As a result of water leakage and incorrect combination of rain pipes, rain water leaks, causing structural damage on the facade. The water coming into contact with the facade building material is absorbed into the material and interacts with the components in the building. In addition, freezing and thawing occurs as a result of the temperature differences of the water filling the cracks on the surface of the building day and night. Distortion occurs on the building surface. Water leaks have occurred as a result of improper application of rain downpipes [6]. Algae formations where water is active on the facade were observed (Photo 4).

Photo 4. Moss formation on the facade.

With the incorrectly applied window sill detail, cracks in the building which may cause problems in terms of safety and health were observed (Photo 5). ilure to ensure proper integration of building elements with joints and insulations caused serious structural cracks. Visual contamination under windows caused by incorrectly applied dropper.

Photo 5. Incorrectly applied sills detail.

459

Some of the devices added to the structure (usually air conditioning) added to the surface of the facade errors made in the form of growing damage over time. The air conditioning pipes are arranged randomly. Water leaked in the air conditioning pipes caused aesthetic deterioration such as color change on the facade [6]. The pipes of the air conditioner should be placed in the water channels with appropriate details (Photo 6).

Photo 6. Incorrectly applied air conditioning application.

3.3. Damages Due to Misuse of the Building and Lack of Maintenance

During some installation works that were added to the building, physical damage was caused to the building facade (Photo 7). Failure to perform the necessary maintenance and repair as a result of the damage has caused damage that may cause serious health and safety problems in the future. Due to this damage to the structural element of the structure, reinforcement corrosion has occurred as a result of the direct contact of the reinforcement with the atmosphere.

Photo 7. Damage due to building renovation.

Lack of necessary maintenance and insulation in the structure caused spilling and flowering on the facade (Photo 8). Building materials and building elements in the facade are exposed to constant wetting and drying as a result of rainfall. Precipitation waters affect the structural elements and materials, causing biological and chemical damage. Necessary insulation should be made for thermal changes and water-induced damages that may occur on the facades.

Photo 8. Damage to the facade exposed to rainwater

4. CONCLUSION

As a result of the facade investigations carried out in Karadeniz Eregli AKM Building, it was observed that damages occurred in the facade cladding materials and carrier elements. The evaluation of the damages on the building facade and suggestions for solutions are given below.

- As a result of the investigations, biological and chemical deterioration was observed on the facade. Material breaks and chemical deterioration have occurred due to improper application of waterproofing from the ground on the facades. Ground water insulation should be done correctly and the water should be removed from the ground correctly in order to prevent the water from being absorbed by the building.

- Rain downpipes where serious damages are detected as a result of the contact of the structure with water should be applied by detailing as required. Water leakage in rain pipes should be prevented by timely intervention and maintenance and repair.

- The elements that are subsequently assembled to the structure must be detailed so as to prevent damage Before installation, the necessary material selection should be done and planning should be prevented.

- Attention should be paid to the installation of ait conditioning and air conditioning pipes. Air conditioning water should be removed from the facade without damaging the facade with appropriate details.

- User-induced damage to the facade should be corrected by making necessary repairs. Thus, durability problems that may occur will be prevented.

As a result of the study; the facade damages on the Kdz Ereğli AKM facade were determined and was prepared data for the measures that can be taken in order to prevent permanent damages. The possible damages in new buildings were determined and necessary precautions should be taken during the design process. Due to various reasons arising from the design, application and usage phases of the structure, it is possible to solve the damages caused by external factors by eliminating the factors causing the damages. Thus, healthy conditions can be created for the structure and users.

REFERENCES

[1] Koçu Nazım 2008, "Yapı Cephelerinde Görsel Yönden Olumsuz Olarak Etkileyen Sorunlar ve Nedenlerin Analizi", 4. Ulusal Çatı & Cephe Kaplamalarında Çağdaş Malzeme ve Teknolojiler" Sempozyumu, İTÜ Mimarlık Fakültesi Taşkışla, İstanbul. (In Turkish)

[2] Esener N. Özge, 2018, "Bina Cephelerinde Oluşan Tasarım Kaynaklı Bozulmaların İncelenmesi", 9. Ulusal Çatı & Cephe Konferansı, İstanbul. (In Turkish)

[3] Erturan Banu,2017"Bina Cephelerinin Yenilemesine Karar Vermek İçin Kullanılabilecek Bir Değerlendirme Modeli", Mimar Sinan Güzel Sanatlar Üniversitesi, Mimarlık Anabilim Dalı, Yapı Bilgisi Programı, İstanbul. (In Turkish)

[4] Yıldırım Korkmaz, "Yapı Fiziği Açısından Yapı Elemanlarında Dayanıma Etki Eden Çiçeklenme Olayı ve Korunma Yöntemleri", Adnan Menderes Üniversitesi, Aydın Meslek Yüksekokulu Efeler/Aydın. (In Turkish)

[5] Güler Hande,2010" Binalarda Yapı Fiziği Problemleri: Bursa'da Bir Kamu Kurumu Örneği", Uludağ Üniversitesi Mühendislik-Mimarlık Fakültesi Dergisi, Bursa. (In Turkish)

[6] Dereli Mustafa,2018"Yapıların Cephe Kaplama Malzemelerinde Hasar Oluşturan Etkilerin Tespiti ve Çözüm Önerileri – Konya Ptt Hizmet Binası Örneği",Selçuk Üniversitesi, Mimarlık Fakültesi, Mimarlık Bölümü, Konya. (In Turkish)

[7] Şirin Cemal,2006, "Yapılarda Oluşan Hasar Biçimleri ve Nedenleri ve Yapıların Onarım ve Güçlendirilmesi Teknikleri ile Bir Yapının Güçlendirilmesi", İstanbul Teknik Üniversitesi □ Fen Bilimleri Enstitüsü, İstanbul. (In Turkish)

[8] Güzelçoban Mayuk Seher, 2014, "Dış Etkenler Sonucu Yapılarda Oluşan Hasarların Nedenlerinin Belirlenmesi", 1. Ulusal Yapı Fiziği ve Çevre Kontrolü Kongresi, İTÜ Mimarlık Fakültesi, İstanbul. (In Turkish)

[9] E. Avlar, "Yapılarda Su ve Nem Korunumu",2000, Yıldız Teknik Üniversitesi Basım/Yayın Merkezi.. (In Turkish)

[10] Gür Hande, 2013, "Tarihi Kârgir Yapıların Cephelerindeki Hasar ve Bozulmaların Tespiti ve İfadelendirilmesi İçin Bir Model Önerisi ve Modelin Galata-Pera Bölgesindeki 19. Yüzyıl Yapılarında Sınanması"1, M. Tanrıkulu, 2013, Harita'ya Davet, Yeditepe Yayınevi, İstanbul, s. 251. (In Turkish)

[11] Güneş Sinan,2018, "Kentsel Dönüşüm Kararı Alınmasında Yapı Hasarlarının Etkisi: Ankara Örneği", Akademik Sosyal Araştırmalar Dergisi, Yıl: 6, Sayı: 64, Ocak 2018, s. 636-650. (In Turkish)

[12] Akan, A. Örmecioğlu, H. Brüt Beton Yapıların Kullanım Ömrü ve Onarım Teknikleri, Mimarlık Dergisi, Temmuz-Agustos,2012. (In Turkish)

PREDICTING 2H-PHASE MONOLAYERS OF MXENES

B. Akgenc

Department of Physics, Faculty of Arts and Sciences, Kırklareli University, Kırklareli, TURKEY

E-mail: berna.akgenc@klu.edu.tr

Abstract

In the past decade, many MXenes are intensively investigated due to their high surface area and unique properties in various field. Using a set of first-principle calculations, we have studied structural, magnetic and electronic properties of 2H-phase monolayers of MXenes. We have established 2H-phase MXenes (Cr_2C, Mo_2C, V_2C and Nb_2C). Our electronic structure calculations indicate that 2H-phase monolayers of MXenes exhibit metallic properties. We have also demonstrated that these MXenes are thermodynamically stable. This research will deepen understanding of the electronic properties of 2H-phase monolayers of MXenes.

Keywords: MXenes, Density Functional Theory, Electronic Properties, Ab-initio Molecular Dynamic.

1. INTRODUCTION

Due to fact that lack a degree of freedom, which always results in impressive changes in electronic and magnetic properties in two-dimensional (2D) material differ from those of their 3D precursors. Since the discovery of graphene [1-2], finding and designing 2D materials has become important in the research area. Very recently, a family of 2D materials have increased with a new member, which called as MXenes [3]. The MXenes are synthesized by chemical exfoliation from the transition metal carbides/nitrides, which belong to MAX phase using hydrofluoric acid. Basically, they are produced by selectively "A" layers out from MAX bulk. Their chemical formula is given with $M_{n+1}AX_n$ (n= 1,2,3), where M is early transition metal, A is an element from group IIIA or IVA, and X is carbon or nitrogen. The MXenes attract great attention due to their potential applications in sensors, catalysis, energy storage and nanoelectronics. Most of previous studies showed the MXenes are synthesized with 1T-configuartion. Further more from these general studies, monolayer Mo_2C MXenes showed ground state in the 2H-configuration. Moreover, $2H$-Mo_2C was found metallic behavior regardless of whether surface functionalization exists or not. It is well known that 1T-phase MXenes' electronic properties or mechanical behaviour strongly depend on surface functionalization [4]. The electronic band structure of V_2C is indicated that metallic as well as the corresponding functionalized system for 1T-V_2C by Champagne et al.. [5] Besides, 1T-Cr_2C MXene showed that half-metallic ferromagnetic behaviour with a large half-metallic gap [6]. Nb_2C behaves electrochemically more like a supercapacitor than a battery, and its 2H phase should be investigate [7]. The studies showed that structural configuration is critical on MXenes. Besides of this study, we were motivated by the question of investigating the 2H phases of "other" MXenes.

2. MATERIAL AND METHODS

The structural, magnetic and electronic properties are calculated using the DFT as implemented in the Vienna ab-inito simulation package (VASP) [8]. Electron- ion interactions were described using standard PAW potentials. The generalized gradient approximation (GGA) with the format of Perdew-Burke-Ernzehof (PBE) was applied for the exchange-correlation functional [9]. Since traditional DFT calculations at the PBE level cannot correctly include the nonlocal van der Waals interactions, the calculations with dispersion corrections may affect the adsorption energies of small molecules. In this regard, the DFT-D3 method was used for dispersion corrections here [10]. A plane-wave basis set with the cut-off kinetic energy of 600 eV and the Gamma-centered ($16x16x1$) k-point grids are utilized for structural optimization and static self-consistent calculations of 2H-phase of MXene. All the atoms were allowed to relax until the Hellmann-

Feynman forces were smaller than 0.02 eV/Å, and the convergence criterion for the self-consistent electronic optimization loop was set to 10^{-5} eV. Our calculations were performed with a large unit cell, which are limited with 20 Å vacuum region along the out-of-plane direction.
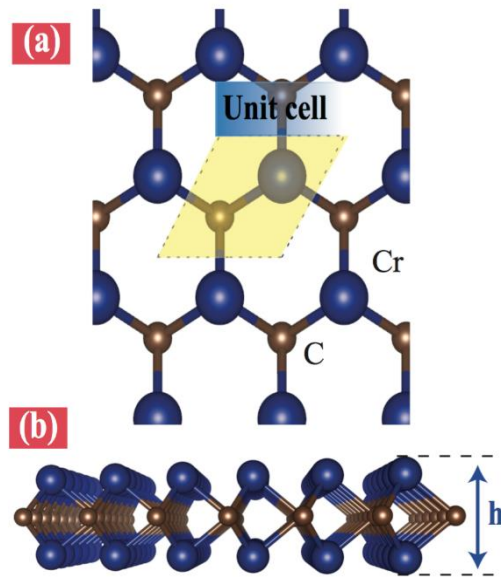
3. RESULTS AND DISCUSSION

Although 1T phase is the most common crystal structure for MXenes, structural and electronic properties of 2H-MXene. The optimized atomic structures of monolayers of MXene forming 2H polytypes is shown in Figure 1 (a) and (b). 2H-phase of MXenes belong to *P6m2* space groups, with the hexagonal Bravais lattice. Lattice parameters, bond distances between transition metal atoms (Mo, Cr, V and Nb) and C atom, and thickness of optimized crystal structure of primitive cell are defined in Table 1. The primitive cell of the 2H-MXene contains three atoms with the two layers. The thicknesses of 2H-MXene structures were determined by the uppermost and lowermost atomic layers along the z-direction. The cohesive energy per atom was calculated by using the formula as:

$$E_{coh} = (n_M E_M + n_C E_C) - E_{M_2 C}/3$$

where E_M and E_C represent the energies of isolated single transition metal atom and carbon atom; $E_{M_2 C}$ represents the total energy of $M_2 C$, n_M and n_C stand for number of transition atom and carbon atom, respectively. We have also calculated spin-polarized and spin-unpolarized states. We have spin polarized case found ground state in 2H-Cr_2C and 2H-V_2C. The energy difference between the spin polarized and spin-unpolarized state are found 0.95 eV for 2H-Cr_2C, 40 meV for 2H-V_2C. We have found that non-magnetic ground state for 2H-Nb_2C and 2H-Mo_2C.

Table 1. The calculation results on optimized structure of pristine 2H-phase MXenes .

	a (Å)	d (Å)	h (Å)	E_{coh} (eV)	E_{tot} (eV)	μ_B
Cr_2C	2.62	2.51	2.50	-4.80	-26.54	0.00
Mo_2C	2.84	2.71	2.70	-6.41	-29.68	0.00
V_2C	2.75	2.55	2.55	-5.78	-25.86	1.66
Nb_2C	2.95	2.79	2.80	-7.03	-28.78	0.58

Figure 1. Top (a) and side (b) views of geometric structures of 2H-MXenes. Dark blue balls show Cr, Mo,V or Nb , brown balls represents C atom.
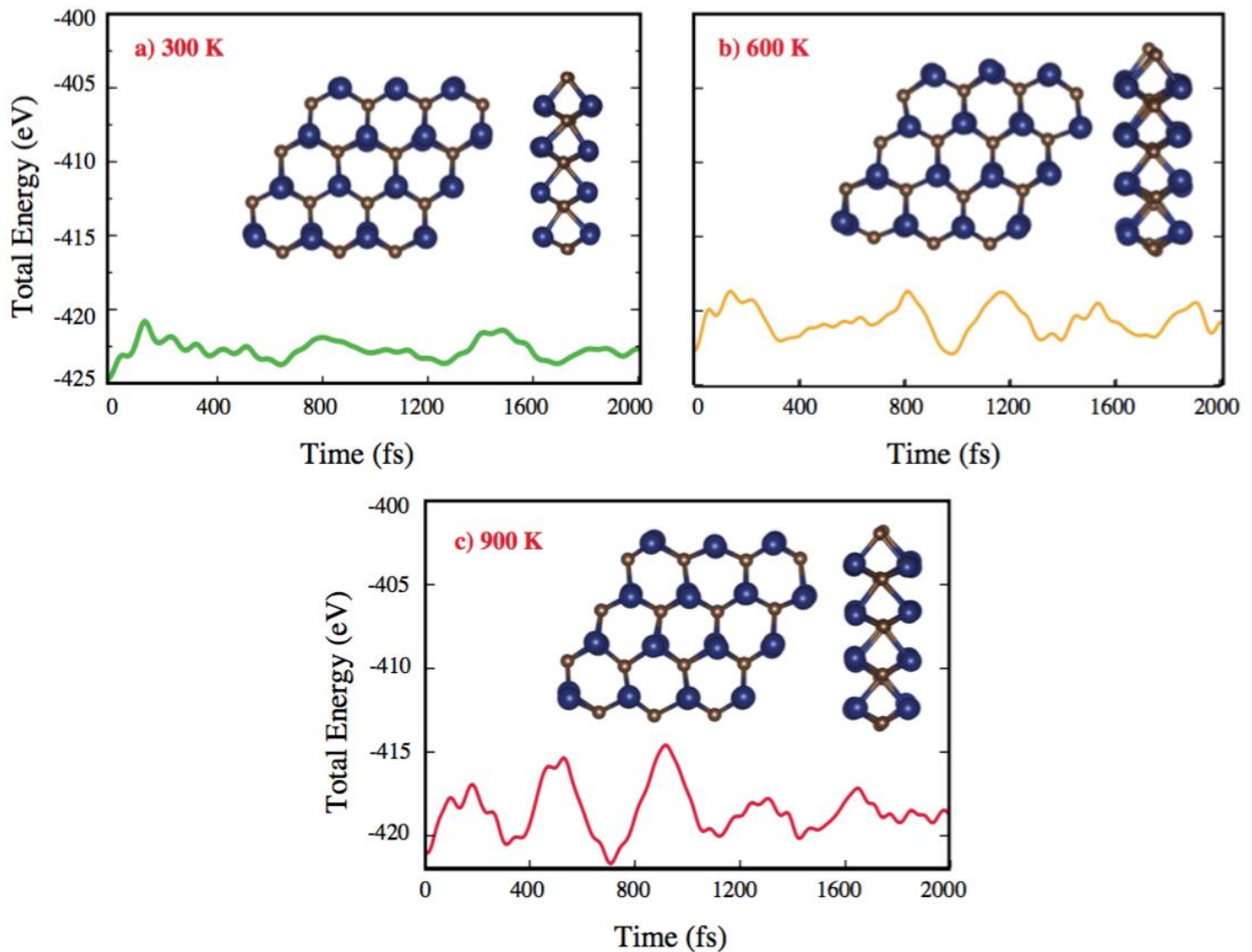

Figure 2. The electronic band structure of 2H- (a) Cr_2C, (b) Mo_2C, (c) V_2C and (d) Nb_2C. Fermi level is set to zero.

The thermal stability investigations were achieved by the ab-initio molecular dynamic (AIMD) simulation. The calculations are carried out on a $4x4x1$ supercell which containing 48 atoms and a $4x4x1$ k-points. AIMD calculation were performed in the NVT ensemble with fixed particle number, volume and temperature. The time step was set to 2 fs (1000 steps) with a total simulation time of 2 ps. The temperature was increased to 900 K with 300 K steps. The structure snapshots are taken at the end of the each simulation in every temperature steps; 300 K, 600K, and 900 K. The simulation has been finished at 6 ps for all different temperature. The evolution of free energy for 2H-MXene during the simulation time is shown in Figure 3. As

an example, 2H-phase Cr_2C shows thermal dynamic stability till 900 K. Our results show that they are promising monolayer MXenes with a good thermal stability.

Figure 3. Snapshots of for AIMD simulation of geometrical structure for the 2H-Cr_2C at the temperature of (a) 300 K, (b) 600 K and (c) 900 K during the timescale of 2 ps.

4. CONCLUSION

By employed density functional theory calculations with ab-initio molecular dynamic simulation, a pristine two-dimensional MXenes are theoretically predicted with 2H symmetry. The electronic band structure results showed that they have metallic feature, while AIMD calculations suggest that 2H-MXenes possess good thermal stability. We expect that this theoretical study will stimulate further experimental research on this material in the future.

ACKNOWLEDGMENTS

REFERENCES

[1] Novoselov, K. S., Geim, A.K., Morozov, S.V., Jiang, D., Zhang, Y., Dubonos, S.V., Grigorieva, I.V., Firsov, A.A., Electric field effect in atomically thin carbon films, Science 306, 666-669, 2004.

[2] Novoselov, K.S., Geim, A.K., The rise of graphene, Nat. Mater, 6(3), 183-191, 2007.

[3] Urbankowski, P., Anasori, B. Makaryan, T., Er, D., Kota, S., Walsh, P.L., Zhao, M., Shenoy, V.B., Barsoum, M.W., Gogotsi, Y., Synthesis of two-dimensional titanium nitride Ti_4N_3 (MXene), Nanoscale 8 (22) 11385–11391, 2016.

[4] Lei, J., Kutana, A. and Yakobson, B.I., 2017. Predicting stable phase monolayer Mo_2C (MXene), a superconductor with chemically-tunable critical temperature, Journal of Materials Chemistry C, 5(14), 3438-3444, 2017.

[5] Champagne, A., Shi, L., Ouisse, T., Hackens, B. and Charlier, J.C., Electronic and vibrational properties of V_2C-based MXenes: From experiments to first-principles modeling, Physical Review B, 97(11), p.115439, 2018.

[6] Si, C., Zhou, Surresh,J., Sun, Z., Half-metallic ferromagnetism and surface functionalization-induced metal-insulator transition in graphene-like two-dimensional Cr_2C crystals, ACS Appl. Mater. Interfaces, 7, 17510-17515, 2015.

[7] Mashtalir, O., Lukatskaya, M.R., Zhao, M.Q., Barsoum, M.W. and Gogotsi, Y., Amine-assisted delamination of Nb_2C MXene for Li-ion energy storage devices, Advanced Materials, 27(23), pp.3501-3506, 2015.

[8] Kresse, G., Furthmüller, J., Efficient iterative schemes for ab initio total-energy calculations using a plane-wave basis set. Physical review B, 54(16), 11169, 1996.

[9] Perdew, J.P., Burke, K., Ernzerhof, M., Generalized gradient approximation made simple. Physical review letters, 77(18), 3865, 1996.

[10] Grimme, S., Semiempirical GGA-type density functional constructed with a long-range dispersion correction. Journal of computational chemistry, 27(15), 1787-1799, 2006.

Mo₂C-BASED DOUBLE-M ELEMENTS MXENES IN THE 1T- AND 2H- PHASE

B. Akgenc

Department of Physics, Faculty of Arts and Sciences, Kırklareli University, Kırklareli, TURKEY

E-mail: berna.akgenc@klu.edu.tr

Abstract

Graphene-like two-dimensional materials have garnered tremendous interest as emerging device materials in the field of material science and engineering due to their remarkable properties. Based on recent experimental and theoretical findings of transition metal carbides/nitrides (also known as MXene), we have performed the structural, electronic, magnetic, vibrational properties of alloy forms of MXenes by using first-principle calculations. Performance in device applications that used MXenes is directly related to electronic and magnetic properties. To further improve performance, there is a need to increase MXenes' electronic conductivity. For the motivation, we also investigated the effect of double M-elements on Mo_2C based MXene in 1T- and 2H- phase to understand their role in manipulating its electronic, magnetic and vibrational properties. Moreover, ab-initio molecular dynamic simulations (AIMD) are also performed to check the thermal stability of these MXenes. Our results highlight a new promising material with tunable magnetic and electronic properties toward nanoscale spintronics and electronics applications.

Keywords: DFT, First-principle calculations, Double-M ordered MXenes, Structural properties, Electronic properties, Dynamical properties.

1. INTRODUCTION

Since the successful discovery of graphene [1] from its bulk counterpart, two-dimensional (2D) materials have received immerse interest in material science and device technology due to their unique electronic, optical, mechanical and thermal properties. These unique properties are the result of quantum confinement effect in 2D materials and they are strongly dependent on the layer thickness and composition. The hottest subject in the field of 2D material is the tunable engineering [2]. Many effort such as defects, dopants or external electric field have been put forward to design of 2D-material based devices [3,4].

Very recently, a new member of 2D early transition metal carbides and/or nitrides just entered the research area [5]. M. Naguib have reported that they obtained compose of a few Ti_3C_2 layers and canonical scrolls produced by exfoliation of Ti_3AlC_2 in hydrofluoric acid at the room temperature. These new 2D materials occur when Al atoms are extracted from Ti_3AlC_2, which was proposed to be called "MXene" to emphasize its graphene-like morphology. Their general formula consist of $M_{n+1}AX_n$ (n=1,2,3), M, A and X represent early transition metal, A-group elements and C and/or N, respectively. They were produced by selectively etching "A" layers out of the MAX bulk. After their exfoliation from the MAX phase, MXenes are fully surface terminated by functionalized groups. Various MXenes were already prepared experimentally from parent MAX phase materials. The MXenes possess great attention due to their potential applications in sensors, catalysis, energy storage and nanoelectronics.

2D layered Mo_2C as a new member of MXenes was formed from Mo_2Ga_2C thin films, it can be produced by selectively etching the Ga layer. Among the three candidate structures (alpha, 1T, 2H), the most stable form is found to be 2H. Monolayer Mo_2C is found non-magnetic and appears strong metallicity [6]. This two properties are different from the other MXenes and we have motivated to investigated Mo_2C-based double-M elements MXenes in the 1T- and 2H-phase .

The other interesting MXenes should be cite here: Cr_2C MXene exhibits half-metallic ferromagnetic behaviour with a large half-metallic gap of 2.85 eV stem from itinerant Cr d electrons which are 100% spin-polarized around the Fermi surface. It introduces a promising material in the Mxenes family, with tunable magnetic and electronic properties by Si et al. [7] V_2C and Ti_2C is also considered non-magnetic MXenes because of very small magnetic moment around 0.14 μ_B and 0.15 μ_B, respectively [8,9]. Given that there is no experimental evidence of magnetic properties for these system as confirmed by the ab-initio simulations.
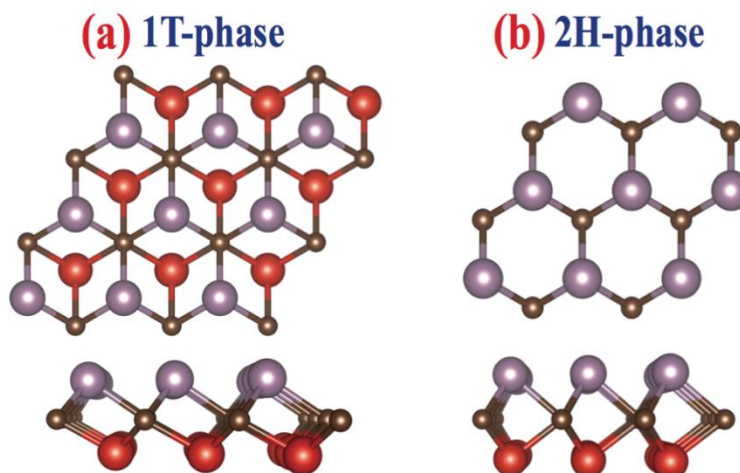
2. MATERIAL AND METHODS

The density functional theory (DFT) calculations were performed using the Vienna ab initio Simulation Package (VASP) by using the plane-wave basis projector augmented wave (PAW) method [10]. For exchange-correlation potential, the generalized gradient approximation (GGA) in Perdew-Burke-Ernzerhof (PBE) for was employed in all the calculations [11]. The vdW correction to GGA functional was included by using DFT-D2 method of Grimme [12]. The cutoff kinetic energy for plane waves was set to 600 eV. The total energy was minimized until the energy variation in successive steps became less than 10^{-5} eV in the geometrical optimization. The converge criterion was taken to be 10^{-5} eV/A for Hellmann-Feynman forces. A Gamma k-point mesh of $16x16x1$ was used to sample the Brillouin zone for geometry optimization. To hinder interactions between the adjacent cells, vacuum spacing was set to 20 A along the z-direction. Gaussian smearing factor was used and pressures on the unit cell were decreased to a value of less than 1.0 kBar in all three directions. Geometrical and electronic relaxations of the structures were performed by considering a unit cell which contain two transition metal atoms (Cr, Ti, V, Nb) and one carbon (C) atom.

3. RESULTS AND DISCUSSION

We firstly discuss the stucture properties of systematically 1T- and 2H- phase Mo_2C-based double-M elements MXenes. Monolayer M_2X is composed of triple layers, in which the X layer is sandwiched between two M layers in Fig 1(a) and (b) shows the top and side views of the possible configurations of monolayer M_2C. Both 1T- and 2H- MXenes are with hexagonal lattices. The optimized structural properties are given in Table 1.

Figure 1. Top and side views of 1T- (a) and 2H- (b) phase structure of Mo_2C-based double-M elements MXenes. Purple and brown ball represents Mo, and C atoms. Red balls shows double M element (Cr,Nb,Ti, and V)

Table 2. The strcutural parameters, total energy (eV) for both 1T- and 2H- structures of Mo_2C-based double M-elements. GS represents ground state corresponding to the most stable structure.

		a (Å)	d (Å)	E_{tot} (eV)	μ_B	
Mo_2C	1T	2.89	2.57	-29.39	0.00	-
	2H	2.84	2.70	-29.68		GS
MoCrC	1T	2.95	2.16	-27.95	1.50	-
	2H	2.75	2.58	-28.02	0.15	GS
MoVC	1T	2.99	2.14	-28.20	0.00	GS
	2H	2.79	2.63	-27.86	0.73	-
MoTiC	1T	3.03	2.28	-27.62	0.63	GS
	2H	2.87	2.70	-26.98	1.15	-
MoNbC	1T	3.12	2.24	-29.59	0.00	GS
	2H	2.87	2.78	-29.30	0.00	

We have systematically investigated double M elements in both 1T- and 2H- MXenes. While pristine Mo_2C ha shown ground state in 2H- phase, MoNbC, MoTiC and MoVC have 1T-phase ground state. MoCrC has kept its ground state configuration in 2H-phase. Our results show that these MXenes show metallic character. The band structure of Mo_2C-based double-M elements MXenes are given in Figure 2.

The dynamical stability of each 1T and 2H- phase of Mo_2C-based double-M elements MXenes are examined by calculating the corresponding phonon band structure through the whole BZ in Figure 3. It is clearly show that, these MXenes are dynamically stable with no significant imaginary frequencies. Additionally, thermal stability of Mo_2C-based double-M elements MXenes are further examined by the ab-inito molecular dynamic (AIMD) simulation. The calculations are carried out on 4x4x1 supercell. They kept their original structure at given temperature.
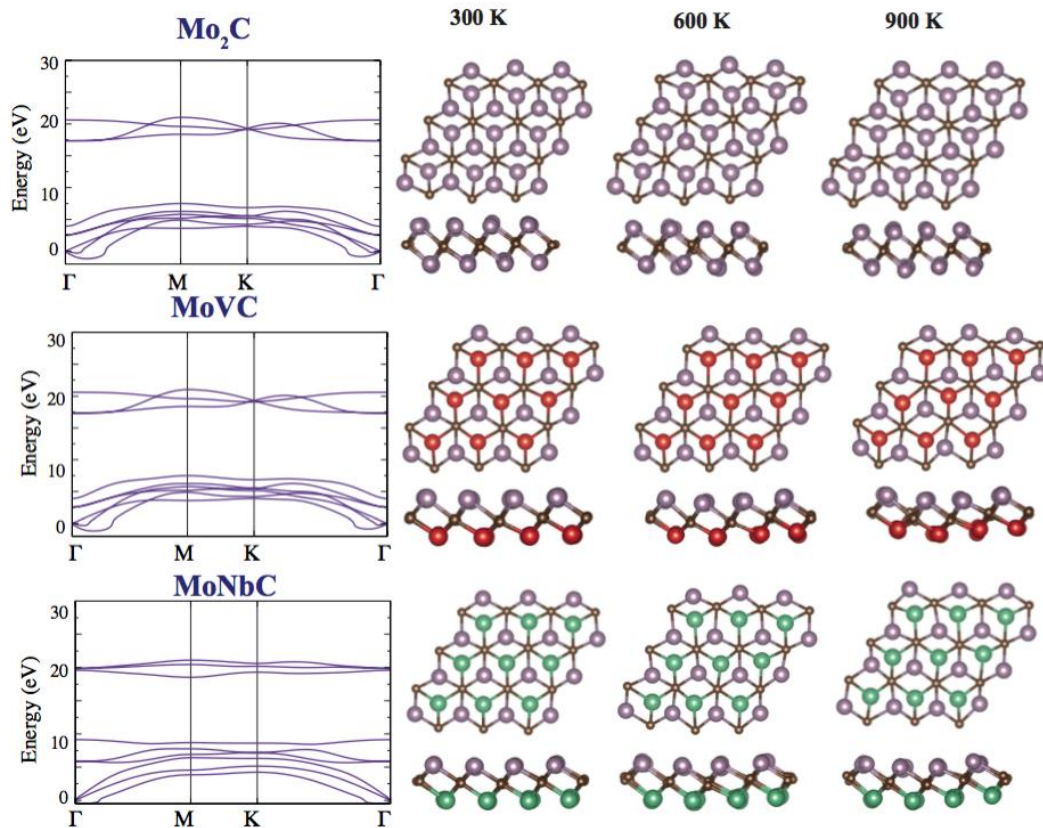
4. CONCLUSION

By employing DFT calculations including AIMD, pristine Mo_2C and Mo_2C-based double-M elements MXenes are theoretically predicted with 1T- and 2H- symmetries. The electronic structure results showed that metallic feature. AIMD calculations suggest that they posses good thermal stability.

Figure 2. Band structure of Mo₂C-based double-M elements MXenes. The Fermi level is at zero.

Figure 3. Phonon dispersion of 1T- phase of Mo_2C-based double-M elements MXenes and the snapshots of for AIMD simulation of geometrical structure at the temperature of 300 K, 600 K, and 900 K.

REFERENCES

[1] Novoselov, K.S., Geim, A.K., The rise of graphene, Nat. Mater, 6(3), 183-191, 2007.

[2] Mak, K.F., Shan, J., Photonics and optoelectronics of 2D semiconductor transition metal dichalcogenides. Nature Photonics, 10(4), 216, 2016.

[3] Yagmurcukardes, M., Monolayer fluoro-InSe: Formation of a thin monolayer via fluorination of InSe. Physical Review B, 100(2), 024108, 2019.

[4] Akgenc, B., Intriguing of two-dimensional Janus surface-functionalized MXenes: An ab initio calculation. Computational Materials Science, 171, p.109231, 2020.

[5] Naguib, M., Mochalin, V.N., Barsoum, M.W., Gogotsi, Y., 25th anniversary article: MXenes: a new family of two-dimensional materials, Advanced Materials 26 (7), 992–1005, 2014.

[6] Lei, J., Kutana, A. and Yakobson, B.I., Predicting stable phase monolayer Mo_2C (MXene), a superconductor with chemically-tunable critical temperature. Journal of Materials Chemistry C, 5(14), pp.3438-3444, 2017.

[7] Si, C., Zhou, Surresh,J., Sun, Z., Half-metallic ferromagnetism and surface functionalization-induced metal-insulator transition in graphene-like two-dimensional Cr_2C crystals, ACS Appl. Mater. Interfaces, 7, 17510-17515, 2015.

[8] Hu, J., Xu, B., Ouyang, C., Yang, S. A., Yao, Y., Investigations on V_2C and V_2CX_2 (X=F,OH) monolayer as a promising anode material for Li ion batteries from first-principles calculations, J. Phys. Chem. C, 118, 24274-24281, 2014.

[9] Gao, G., Ding, G., Li, J., Yao, K., Wu, M. Qian, M., Monolayer Mxenes: promising half-metals and spin gapless semiconductors, Nanoscale, 8, 8986-8994, 2016.

[10] Kresse, G., Furthmüller, J., Efficient iterative schemes for ab initio total-energy calculations using a plane-wave basis set. Physical review B, 54(16), 11169, 1996.

[11] Perdew, J.P., Burke, K., Ernzerhof, M., Generalized gradient approximation made simple. Physical review letters, 77(18), 3865, 1996.

[12] Grimme, S., Semiempirical GGA-type density functional constructed with a long-range dispersion correction. Journal of computational chemistry, 27(15), 1787-1799, 2006.

APPLICATION OF RADIO OVER FIBER MODULATION TECHNIQUES IN INTELLIGENT TRANSPORTATION SYSTEMS

T. Açıkgöz[1], N. Ö. Ünverdi[2]

[1]Department of Electronics and Communication Engineering, Faculty of Engineering, Yıldız Technical University, İstanbul, TURKEY
[2]Department of Electronics and Communication Engineering, Faculty of Engineering, Yıldız Technical University, İstanbul, TURKEY

E-mail: tuce_ackgz@hotmail.com, unverdi@yildiz.edu.tr

Abstract

Today, the rapid development of communication and information technologies has a positive effect on transportation systems. Intelligent Transportation Systems, ITS, utilize this to shorten travel times and increase traffic safety. Intelligent Transportation Systems facilitate more rapid thinking and decision-making than individuals. By using ITS, The International Road Federation (IRF) aims at achieving increased driving safety and sustainable road transport by means of automatic data collection, transfer, processing and analyses which are necessary elements for conscious decision making. Radio over Fiber (RoF) technology is an integration of microwave communications and optical networks. It has been emerged as a potential tool for rising capacity and mobility as well as reducing costs of the broadband access network. RoF technology is based on transmitting information over optical fibers by modulating light with radio frequency signal (RF) to take advantage of the low loss characteristic of an optical fiber. Therefore, in this study, RoF structures which are beginning to be used in intelligent transportation systems to gain great advantages are introduced and their superiority is emphasized.

Keywords: Communication Technologies, Optical Communications, Radio over Fiber, Intelligent Transportation Systems, Optical Fiber, Modulation.

1. INTRODUCTION

The objectives of Intelligent Transportation Systems, ITS, include obtaining standardized data transmission in multidimensional data exchange among humans and vehicle-infrastructure-center, controlling the traffic flow according to the capacities of rail roads, thereby improving traffic safety, enhancing mobility and reducing harmful environmental effects by means of energy efficient systems.

Fiber optical communication systems are important in monitoring and controlling rail systems by facilitating accurate and rapid transmission of data. Recently introduced Radio over Fiber (RoF) technology is based on analog optical communications that transmit modulated RF signals from a central location to remote antenna units by means of optical fiber connections. Due to the low loss of optical fiber and ultra-wide bandwidth of intelligent transportation systems, RoF systems with high data rates have begun to be preferred for wireless broadband communications [1, 2]. Radio over Fiber technology, which is based on hybrid systems combining fiber and radio technologies, is used to enlarge the coverage of the wireless millimeter-wavelength signals. RoF is an analog transmission system in which the radio signals are only transposed onto an optical carrier by modulating the light intensity of an optical source, without changing the modulation format. This technology conveys the information over long distances with a low cost and high performance provided by the optical fiber. The structure of the RoF system is shown in Fig. 1.

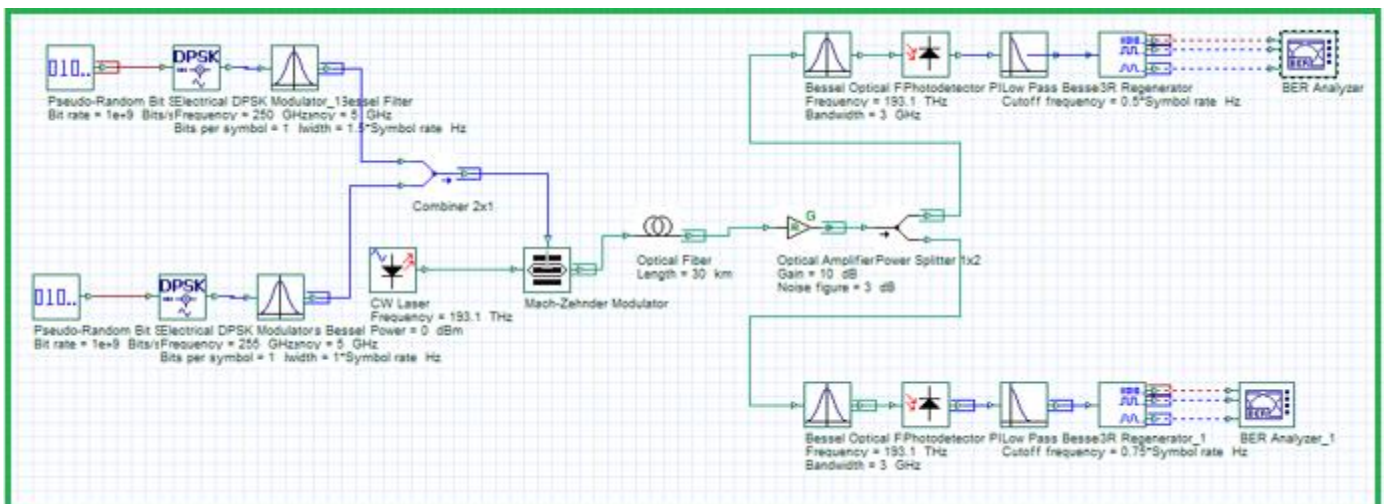Fig 1. Fundamental structure of basic RoF system [3]

2. MATERIAL AND METHODS

In this study, a fiber optical system is analyzed by means of OptiSystem 7.0 tool for different modulation techniques and the most suitable modulation method is determined. As shown Fig. 2, two random bit sequence generators are implemented to modulate two different data signals. This data is used to modulate two different electrical carrier frequencies. After passing through the optical band pass filter, the signals are combined by means of an electrical power combiner, and then the combined signal modulates an optical carrier by means of a Mach-Zehnder modulator. These optical signals are then fed to a Bessel optical filter. Thereafter filtered signals are fed to a photodetector which converts optical signals directly to base-band signals. Finally the initially transmitted data is recovered by filtering high frequency components by low pass filters.

3. RESULTS AND DISCUSSION

In this study, Q-factor (quality factor) and BER (Bit Error Rate) parameter of the systems with DPSK (Differential Phase Shift Keying), CPSK (Continuous Phase Shift Keying), PAM (Pulse Amplitude Modulation), FSK (Frequency Shift Keying) and QAM (Quadrature Amplitude Modulation) modulation techniques are calculated and the results are compared. As a result of this study, it is found that performance of RoF systems is enhanced by implementing DPSK modulation technique because of its higher quality factor and low Bit Error Rate. The results reveal that the proposed system has great potential for future broadband multimedia applications in intelligent transportation systems.

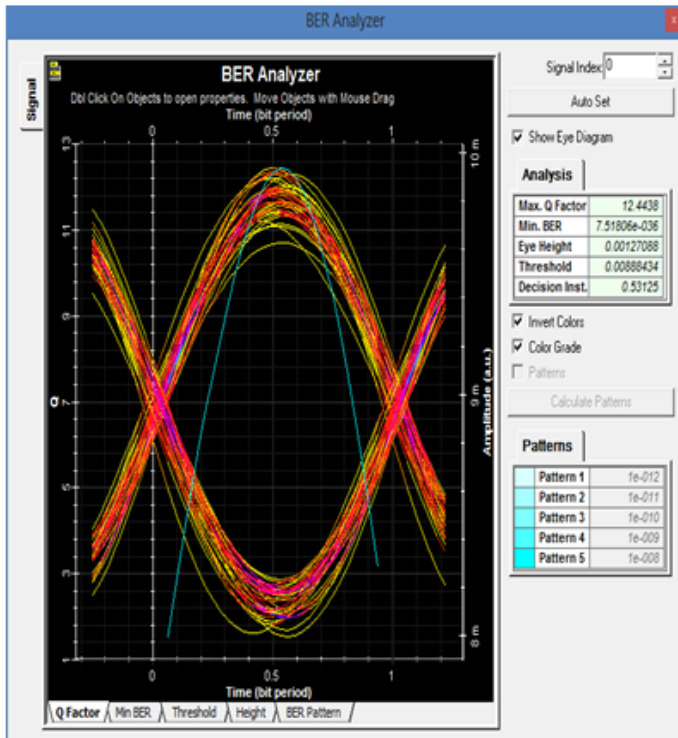**Fig 2**. DPSK based RoF system design
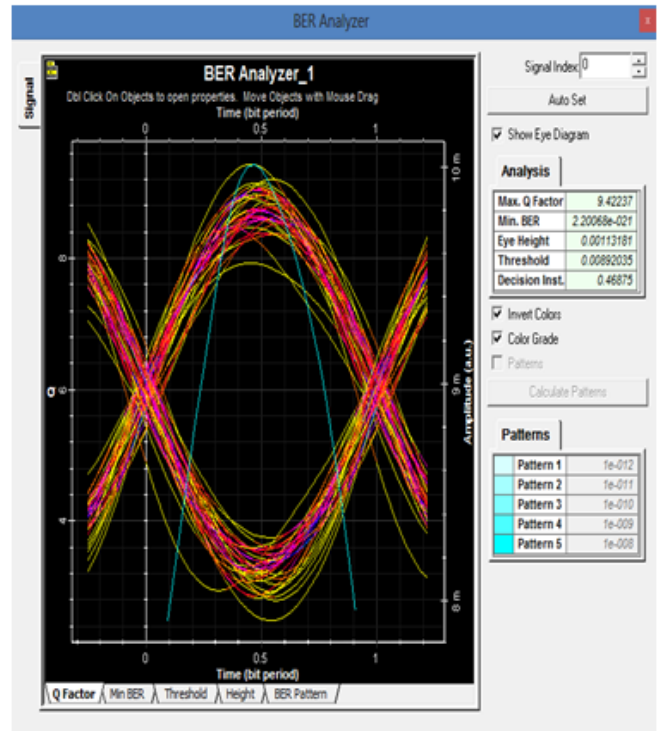
Fig 3. FSK modulation result
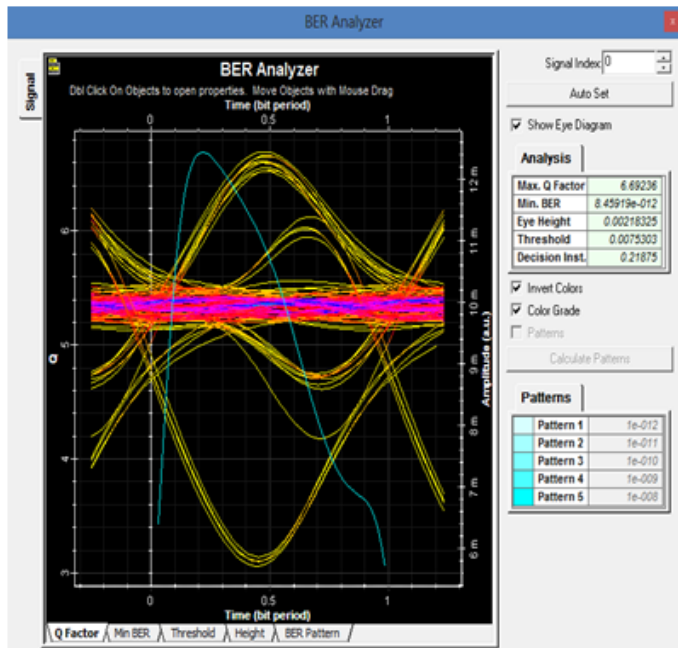

Fig 4. CPFSK modulation result

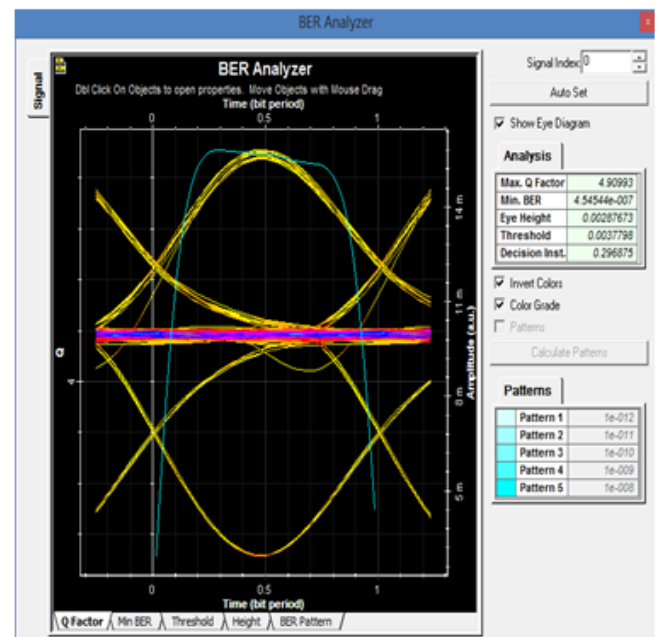**Fig 5.** PAM modulation result

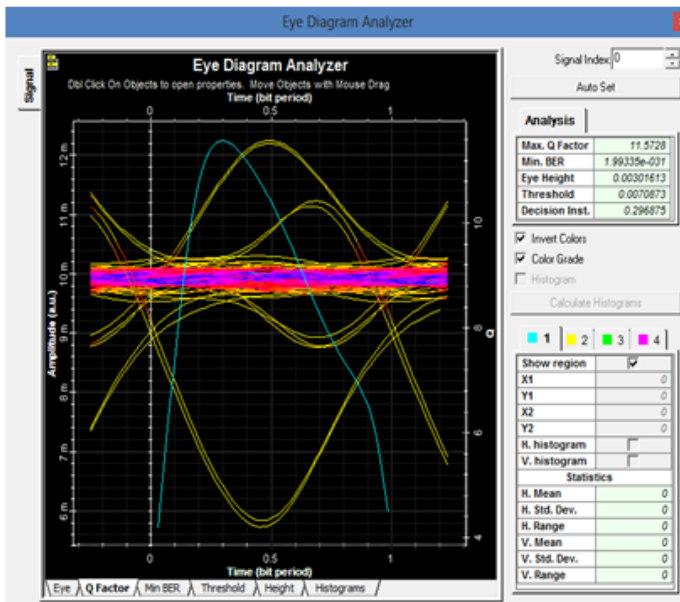**Fig 6.** QAM modulation result
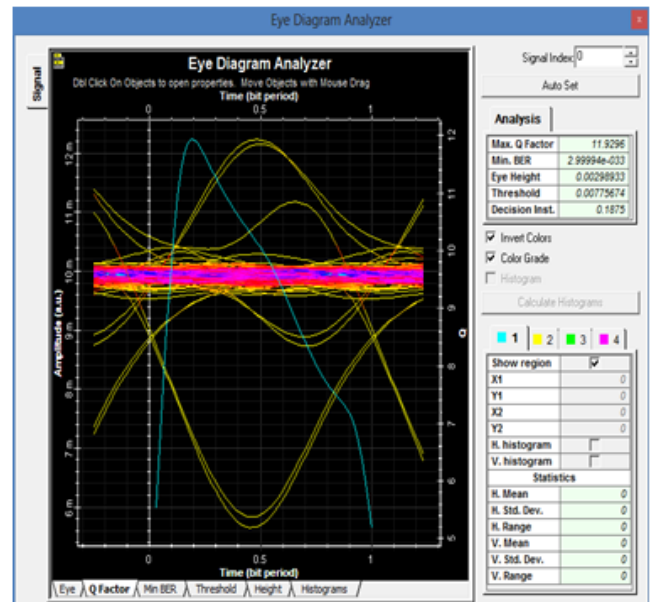
Fig 7. PSK modulation result

Fig 8. DPSK modulation result

The simulation results for different modulation schemes, namely FSK, CPFSK, PAM, QAM, PSK and DPSK, are shown as eye diagrams, which give performance matrices in terms of the quality factor and Bit Error Rate analyses results of the systems, in Fig. 3 to Fig. 8.

i. Bit Error Rate

Bit error rate is the number of received bits of a data stream over a communication channel that have been altered due to noise, interference, distortion or bit synchronization errors [1].

ii. Quality Factor

Q-factor is a parameter which shows the quality of an optical communication system directly. It shows how beneficial, i.e low loss, the system is. The higher the value of Q is, the better the quality of the system [4].

iii. Eye Diagram

Q-factor symbolizes the quality of the SNR in the "eye" of a digital signal – the "eye" being the human eye shaped pattern on an oscilloscope which shows the performance of a transmission system. The best place for assigning whether a given bit is a "1" or a "0" is the sampling phase with the biggest "eye opening." The larger the eye is, the greater the gap between the mean values of the signal levels for a "1" and a "0". The bigger the gap is, the higher the Q-factor and the better the BER performance. An open eye pattern indicates minimal

signal defect. Deterioration of the signal waveform due to inter-symbol interference and noise is manifested by decreased enclosure of the eye pattern [5].

iv. Eye Height and Threshold

In a digital optical telecommunications receiver, the contingent signals are sampled in the centre of the bit period and the sampled level is contrasted to a threshold to appoint the existence of a one or zero. With threshold identification of this nature errors arise when noise in the system pulls a one signal level below threshold at the sampling point and pushes a zero above threshold [6]. Simulation results of modulation schemes of the proposed RoF system are shown in Table 1.

Table 1. Simulation results of Modulation Schemes of the Proposed RoF system

Modulation Scheme						
Parameters	PSK	DPSK	FSK	CPFSK	PAM	QAM
Q-Factor	11.572	11.929	12.443	9.422	6.692	4.909
BER	1.99e-031	2.99e-033	7.51e-036	2.20e-021	8.45e-012	4.54e-007
Threshold	0.00708	0.00776	0.00127	0.00113	0.00753	0.00377
Eye Height	0.003	0.002	0.008	0.008	0.218	0.296

4. CONCLUSION

In this study, Q-factor and BER parameter of the systems with PSK, DPSK, FSK, CPFSK, PAM and QAM modulation techniques are calculated and the results are compared. It is found that performance of a RoF system is enhanced by implementing DPSK modulation technique because of its higher quality factor and low Bit Error Rate. The results reveal that the proposed system has great potential for future broadband multimedia applications in intelligent transportation systems.

REFERENCES

[1] Srivastava, N. K., Jaiswal, A. K., Kumar, M. (2014), Design and performance analysis of radio over fiber system incorporating differential phase shift keying modulation in high speed transmission system, *IOSR Journal of Electronics and Communication Engineering*, *9*(2), 37-42.

[2] Sharma, S. R. A., Rana, S. (2017), Comprehensive study of radio over fiber with different modulation techniques–a review, *International Journal of Computer Applications*, *170*(4), 22-25.

[3] Johny, J., Shashidharan, S. (2012, October), Design and simulation of a Radio over Fiber system and its performance analysis, *IV International Congress on Ultra Modern Telecommunications and Control Systems* (pp. 636-639), IEEE.

[4] Mehra, R., Joshi, V. (2014), Effect on Q Factor of Fixed Bit Pattern and Encoding Techniques in Intensity Modulated Optical Networks, *International Journal of Computer Applications*, *106*(13).

[5] Miller, C. M. (1994), High-speed digital transmitter characterization using eye diagram analysis, *Hewlett Packard Journal*, *45*, 29-29.

[6] Verma, A. S., Jaiswal, A. K., Kumar, M. (2013), An improved methodology for dispersion compensation and synchronization in optical fiber communication networks, *International Journal of Emerging Technology and Advanced Engineering*, *3*(5), 769-775.

ASSESSMENT OF LONG-RANGE CORRECTED (LC) PARAMETERS FOR PREDICTION OF ELECTRONIC STRUCTURE OF CARBAZOLE

Mustafa Kurban

Department of Electronics and Automation, Kırşehir Ahi Evran University, Kırşehir, TURKEY

E-mail: mkurbanphys@gmail.com

Abstract

The electronic structure of materials is significantly tunable as a function of many factors such as temperature, an atom substitution or using different theoretical and experimental methods, etc. Thus, the changes in the bandgap and photophysical properties of **carbazole organic molecule** have been investigated using the self-consistent charge density functional based tight-binding (SCC-DFTB) which is based on the density-functional theory (DFT). Firstly, some benchmarks were carried out on carbazole by Slate-Koster parameters including DFTB3 and long-range corrected (LC) parameters. Later, the electronic and optical properties of carbazole by substitution of Oxygen (O) atom was performed. HOMO, LUMO and bandgap energies, dipole moments, and Fermi levels were investigated. Absorption spectral analysis has also been obtained by time-dependent (TD)-DFTB calculations-based on the Casida's approach. The obtained results were compared to experimental and DFT data. The HOMO energy level of carbazole from SCC-DFTB and DFT calculations was found -5.49 and -5.68 eV, respectively, which are compatible with experimental HOMO (-5.40 eV) energy level. The band energy is 4.13 eV wide i.e. smaller 0.52 eV from DFT result (4.65 eV). The gap energy of carbazole decreases from 4.13 eV to 4.02 eV when it comes to O-doped carbazole which is about 0.11 eV smaller than that of carbazole. SCC-LC-DFTB results also compared with DFT, SCC-DFTB and experimental data. The calculated maximum absorbance peak is 239 nm which is close to experimental value (291 nm).

Keywords: Carbazole, Bandgap, Electron transport, LC-DFTB, DFT

1. INTRODUCTION

Recently, organic semiconductors (OSs) are finding use in many applications, especially, electronic and photonic applications [1, 2]. Among them, the chemistry and biology of Carbazole have attracted increasing interest over the last 50 years because it possesses desirable electronic and charge transport properties, as well as a large π-conjugated system. This enables various functional groups to be easily introduced into the structurally rigid carbazolyl ring. These characteristics result in the extensive potential application of Carbazole in the field of chemistry (photoelectrical material, dyes, supramolecular recognition) and medicinal chemistry (antitumor, anti-inflammatory, antimicrobial, psychotropic, anti-oxidative) [3-6]. These Carbazole-based compounds are also considered to be potential candidates for electronic applications, such as color displays, organic semiconductors, lasers, and solar cells, as they demonstrate electroactivity and luminescence [7,8].
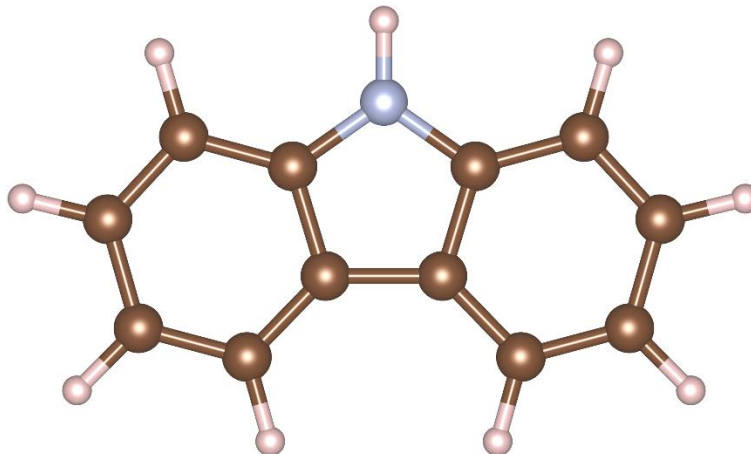
The electronic structure of materials is significantly tunable as a function of temperature and an atom substitution [9, 10]. In these regards, in this study, the changes in the bandgap and photophysical properties of **carbazole** have been investigated using the self-consistent charge density-functional based tight-binding (SCC-DFTB) which is based on the density functional theory (DFT). Firstly, some benchmarks were carried out on carbazole organic compound using Slate-Koster parameters including DFTB3 and long-range corrected (LC) parameters. Later, the electronic and optical properties of carbazole by substitution of Oxygen (O) atom was performed. HOMO, LUMO and bandgap energies, dipole moments, and Fermi levels were investigated. Absorption spectral analysis has also been obtained by time-dependent (TD)-DFTB calculations.

2. MATERIAL AND METHODS

The electronic structure and optical properties of undoped and O-doped carbazoles organic molecule have been examined using DFTB implemented in DFTB+ code [11] with the matsci/matsci-0-3 [12] and ob2-1-1/base [13] sets of Slater Koster parameters. Firstly, some benchmarks were carried out on carbazole organic compound using Slate-Koster parameters including DFTB3 and long-range corrected (LC) parameters. Later, the electronic and optical properties of carbazole by substitution of Oxygen (O) atom was performed. HOMO, LUMO and bandgap energies, dipole moments, and Fermi levels were investigated. Absorption spectra have also been obtained by TD-DFTB calculations-based on Casida's approach [14].

3. RESULTS AND DISCUSSION

The picture of the optimized geometry of the carbazole organic molecule is indicated in Fig. 1.
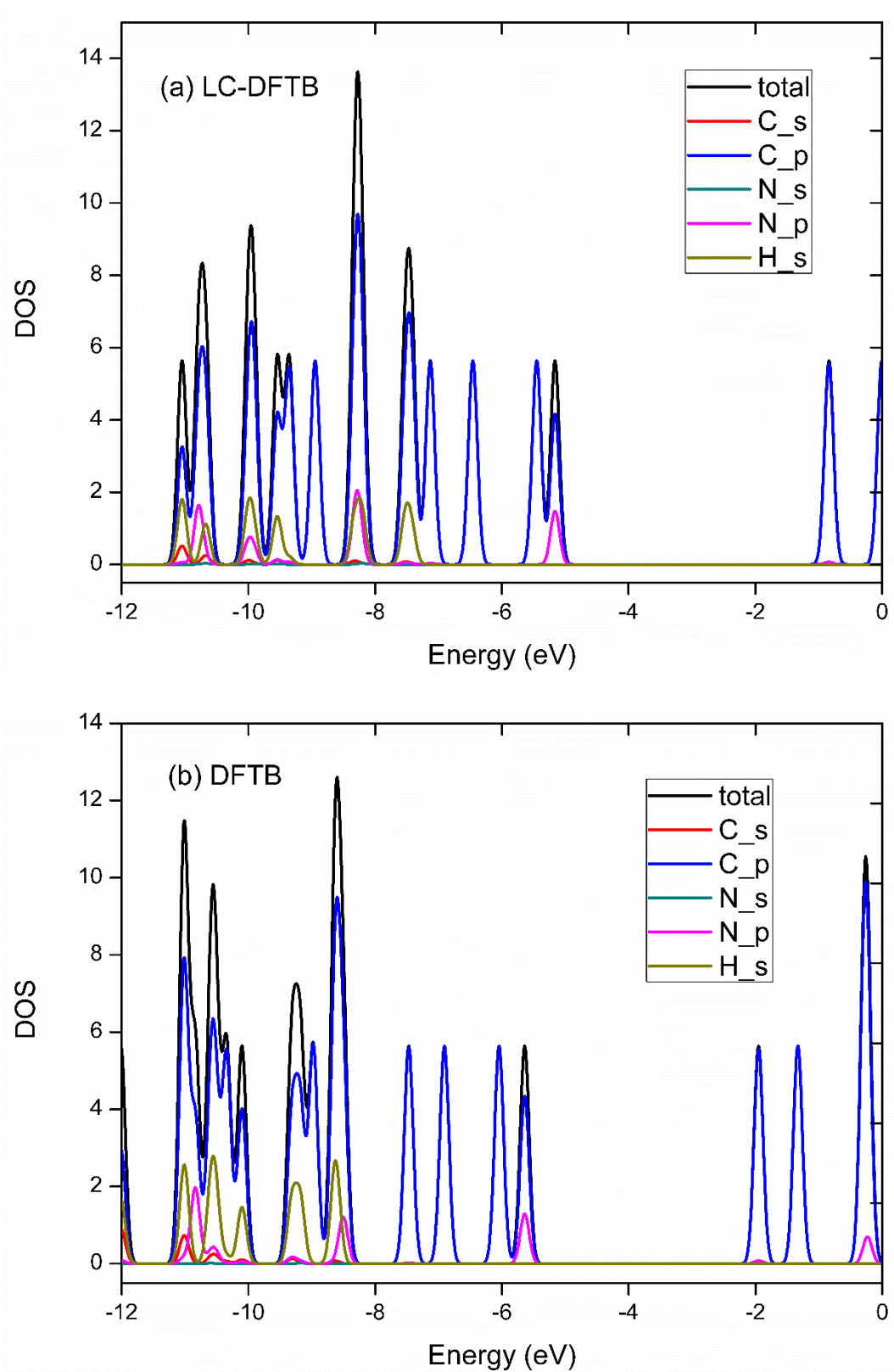

Figure 1. The optimized geometry of carbazole organic molecule. (Blue is Nitrogen, purple is Hydrogen and brown is Carbon).

To get detailed information on electronic states in carbazole organic semiconductor, firstly, the results of the electronic total and partial DOS of carbazole based on the LC-DFTB and DFTB methods as seen in Fig. 2. The most contribution of the density of localized states comes from p orbital of C atoms for both methods, but they are greater for the LC-DFTB method. These fluctuations progressively increase from LC-DFTB to DFTB method also there is a considerable shift in energy values. The density of localized states has a sharply increasing tendency to occur in the region of between -10 and -8 eV. The DOS analysis also indicates that carbazole has the energy gap, so, all the nanoparticles show semiconductor character. There is an increase in HOMO and LUMO energy levels form DFTB to LC-DFTB method.

The obtained results were also compared to experimental and DFT data. The HOMO energy level of carbazole from SCC-DFTB and DFT calculations was found -5.49 and -5.68 eV, respectively, which are compatible with experimental HOMO (-5.40 eV) energy level [15]. The band energy is 4.13 eV wide i.e. smaller 0.52 eV from DFT result (4.65 eV). The SCC-LC-DFTB calculations show that the HOMO and LUMO levels are -5.14 eV and -0.83 eV, respectively, which are more convenient with experimental data.

Figure 2. The total and partial density of states (DOS) of carbazole based on (a) LC-DFTB and (b) DFTB methods.
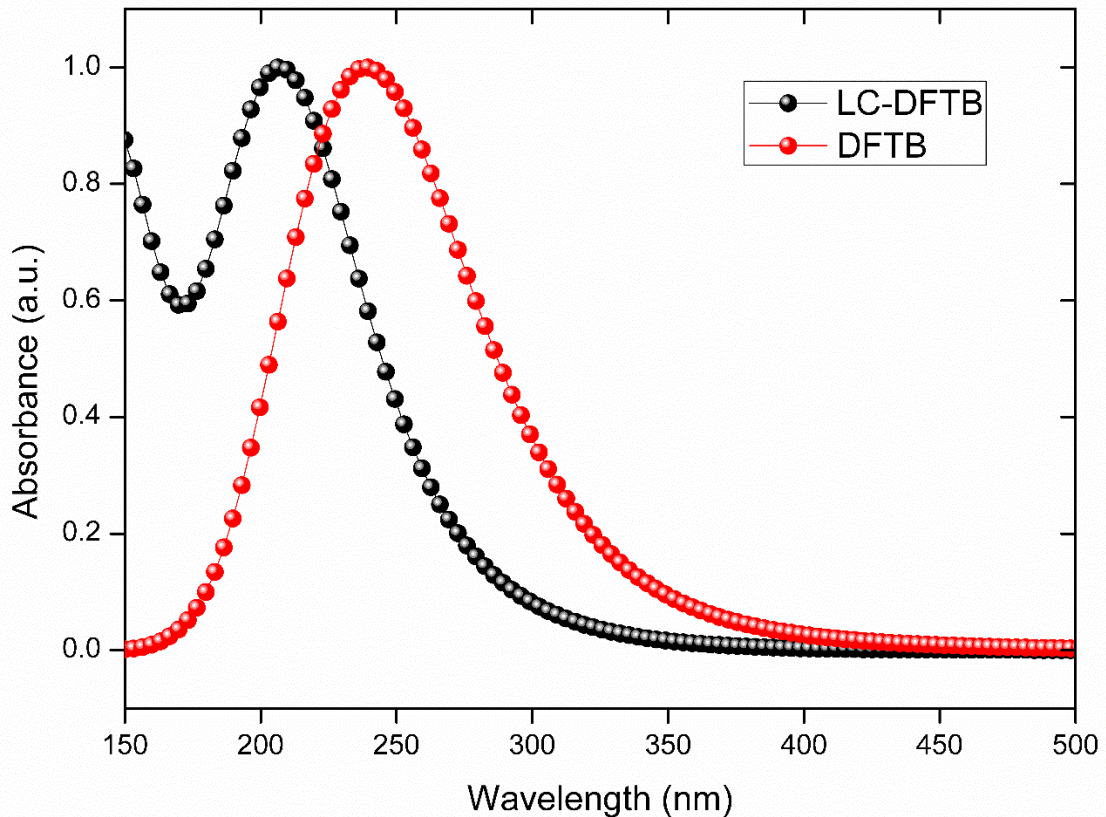
On the other hand, the energetic properties of O-doped carbazole have been investigated. The HOMO, LUMO, Fermi energy levels and HOMO-LUMO gap were tabulated in Table 1. The gap energy of carbazole decreases from 4.13 eV to 4.02 eV when it comes to O-doped carbazole which is about 0.11 eV smaller than that of carbazole. It is interesting to note that it was predicted that there is the *p-* to *n-type* transition with a single atom substitution due to the Fermi energy level close to the conduction band rather than the valance band.

Table 1. The electronic structure data undoped and O-doped carbazole based on different methods.

	HOMO	LUMO	Energy gap	Fermi energy
SCC-DFTB	-5.878	-2.444	3.434	-4.161
SCC-LC-DFTB	-5.140	-0.836	4.304	-2.988
DFT	- 5.686	-1.034	4.652	-
Experiment [15]	-4.797	-3.130	1.667	-
O-doped	-5.216	-1.187	4.029	-1.186

The dipole moment (D_M) results from differences in electronegativity. The bigger D_M means stronger intermolecular interaction. The component of D_M along the y-axis (4.39 Debye) gives rise to the largest positive charge separation in the y-direction obtained from SCC-DFTB. D_M decreases along x- and y-directions when using the SCC-LC-DFTB method; it increases along the z direction. When it comes to total D_M, DFT calculations show that it is 1.66 Debye i.e. smaller 2.73 Debye than SCC-DFTB and 1.59 Debye than SCC-LC-DFTB calculations. These values are comparable with the bandgap energy because the lowest gap energy of carbazole obtained from SCC-DFTB means that electrons easily transfer from HOMO to LUMO. In this regard, there is a highly relevant correlation between D_M and the energy gap of carbazole. Thus, it can be concluded that the large D_M has a small energy gap.

Absorbance spectra of carbazole in terms of different DFTB methods were depicted in Fig. 3. The carbazole exhibits the maximum peaks 6.10 eV (209 nm) and 5.18 eV (239 nm) from the LC-DFTB and DFTB calculations, respectively, which correspond to the near ultraviolet (UV) region, which is well-matched with experimental data 4.26 eV (291 nm) [16].

Figure 3. Absorbance spectra of carbazole based on the SCC-DFTB and LC-DFTB methods.

4. CONCLUSION

The electronic and photophysical properties of **carbazole organic semiconductor**-based on a single atom substitution and DFT, SCC-DFTB, and SCC-LC-DFTB methods. The HOMO energy level of carbazole from SCC-DFTB and DFT calculations was found -5.49 and -5.68 eV, respectively, which are compatible with experimental HOMO (-5.40 eV) energy level. The band energy is 4.13 eV wide i.e. smaller 0.52 eV from DFT result (4.65 eV). The gap energy of carbazole decreases from 4.13 eV to 4.02 eV when it comes to O-doped carbazole which is about 0.11 eV smaller than that of carbazole. SCC-LC-DFTB results also compared with DFT, SCC-DFTB and experimental data. The component of D_M along the y-axis (4.39 Debye) gives rise to the largest positive charge separation in the y-direction obtained from SCC-DFTB. The calculated maximum absorbance peak is 239 nm obtained from the SCC-DFTB method which is close to experimental value (291 nm).

REFERENCES

[1] C. Xie, P. You, Z. Liu, L. Li, F. Yan, Light Sci. Appl. 6, e1702 (2017).

[2] A. D. Sio, C. Lienau, Phys. Chem. Chem. Phys. **19,** 18813 (2017).

[3] F. F. Zhang, L. L. Gan, C. H. Zhou, Bioorg. Med. Chem. Lett. 20, 1881-4 (2010).

[4] B. C. Nandy, A. K. Gupta, A. Mittal, V. Vyas, J. Biomed. Pharm. Res. 3, 42-8 (2014).

[5] P. Ravichandiran, A. Jegan, D. Premnath, V. S. Periasamy, et al., Bioorg. Chem. 53, 24 (2014).

[6] P. Ravichandiran, D. Premnath, S. V. Kumar, Int. J. Pharm. Sci. 6, 244 (2014).

[7] Q. Zhang, C. Jiangshan, C. Yanxiang, W. Lixiang, M. A. Dongge, et al., J. Mater. Chem. 14, 895 (2004).

[8] R. H. Friend, R. W. Gymer, A. B. Holmes, J. H. Burroughes, R. N. Marks, et al., Nature 397, 121 (1999).

[9] M. Kurban, Optik, 172, 295 (2018).

[10] M. Kurban, O. B. Malcıoğlu, Ş. Erkoç, Chem. Phys. 464, 40 (2016).

[11] B. Aradi, B. Hourahine, T. Frauenheim, J. Phys. Chem. A 111, 5678 (2007).

[12] N. Jardillier, PhD Thesis, Universite Montpellier II, 2006, online:http://nicolas.jardillier.free.fr

[13] V. Q. Vuong, J. A. Akkarapattiakal, M. Kubillus, J. Kranz, T. A. Mast, et al., J. Chem. Theory. Comput. 14, 115 (2018).

[14] H. C. Andersen, J. Chem. Phys. 72(4), 2384 (1980).

[15] Y. Mizuno, I. Takasu, S. Uchikoga, et al., J. Phys. Chem. *C* 116, 20681 (2012).

[16] M. Rahimi-Nasrabadi, M. M. Zahedi, S. M. Pourmortazavi, et al., Microchim Acta 177, 145 (2012).

BAND ENGINEERING AND PHOTOPHYSICAL PROPERTIES OF C-DOPED F8T2 ORGANIC COMPOUND

Mustafa Kurban[1,*], Burhan Coşkun[2]

[1]Department of Electronics and Automation, Kırşehir Ahi Evran University, Kırşehir, TURKEY
[2]Department of Physics, Faculty of Science, Kırklareli University, Kırklareli, Turkey

E-mail: mkurbanphys@gmail.com

Abstract

The electronic and optoelectronic properties of materials are considerably tunable as a function of an atom substitution. Herein, the changes in the bandgap and photophysical properties of **F8T2** have been investigated using the self-consistent charge density-functional based tight-binding (SCC-DFTB) which is based on the density functional theory (DFT). Later, the electronic and optical properties of F8T2 by substitution of Carbon (C) single atom were performed. The HOMO, LUMO and bandgap energies, dipole moments, refractive index and Fermi levels were investigated. Absorption spectral analysis has also been obtained by time-dependent (TD)-DFTB calculations-based on the Casida's approach. Our results show that the HOMO and LUMO energy levels of F8T2 were found -5.045 and -2.729 eV, respectively, which are compatible with experimental HOMO (-5.44 eV) and LUMO (-2.95 eV) energy levels. The band energy (2.32 eV) is also consistent with experimental findings (2.49 eV). The gap energy for F8T2 decreased from 2.32 eV to 0.13 eV which is about 2.19 eV shorter than that of F8T2. The calculated maximum absorbance peak of F8T2 is 437 (2.83 eV) nm which is shorter 266 nm (4.66 eV) than that of C-doped F8T2 (703 nm; 1.76 eV).

Keywords: F8T2, Bandgap, Electron transport, DFTB.

1. INTRODUCTION

Recently, organic semiconductors have been of important attention in many applications, especially, electronic and photonic applications [1, 2]. Among them, poly[(9,9-dioctylfluorenyl-2,7-diyl)-co-bithiophene] (F8T2), especially, is a promising class in organic field effect phototransistors as the active material due to its high ionization potential (5.5 eV). Besides, the transistors show highly stable and reproducible performance under heat treatment [3, 4].
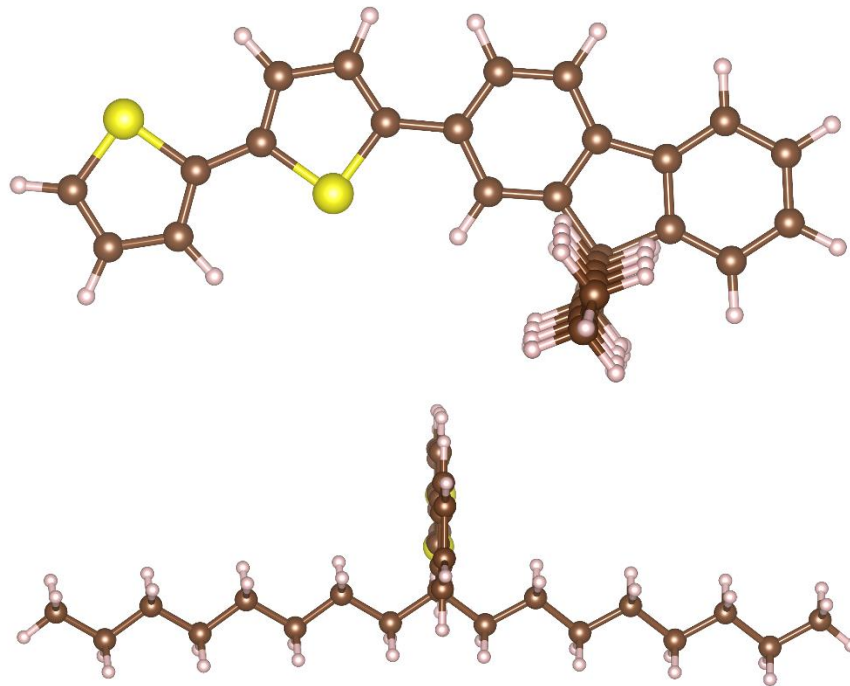
The electronic structure of materials is significantly tunable as a function of an atom substitution or temperature [5, 6]. Thus, in this study, the changes in the bandgap and photophysical properties of undoped and C-doped **F8T2** organic molecule have been carried out by the self-consistent charge density-functional based tight-binding (SCC-DFTB) which is based on the density functional theory (DFT) [7, 8]. First of all, the electronic and optical properties of F8T2 by substitution of O-doped F8T2 were performed. HOMO, LUMO and bandgap energies, dipole moments, and Fermi levels were investigated. Absorption spectral analysis has also been performed using time-dependent (TD)-DFTB.

2. MATERIAL AND METHODS

The electronic structure and optical properties of undoped and Carbon (C)-doped F8T2 organic molecule have been examined using DFTB implemented in DFTB+ code [11] with the 3ob/3ob-3-1 [9, 10] set of Slater Koster parameters. Firstly, some benchmarks were carried out on F8T2 organic compound using Slate-Koster parameters including DFTB3 parameters. Later, the electronic and optical properties of F8T2 by substitution of C atom was performed. HOMO, LUMO and bandgap energies, dipole moments, and Fermi levels were investigated. Absorption spectra have also been obtained by TD-DFTB calculations-based on Casida's approach [11]. The detailed descriptions of theoretical aspects and performance of the DFTB approach, as well as advances in theoretical development and application have been studied in Refs [12-15].
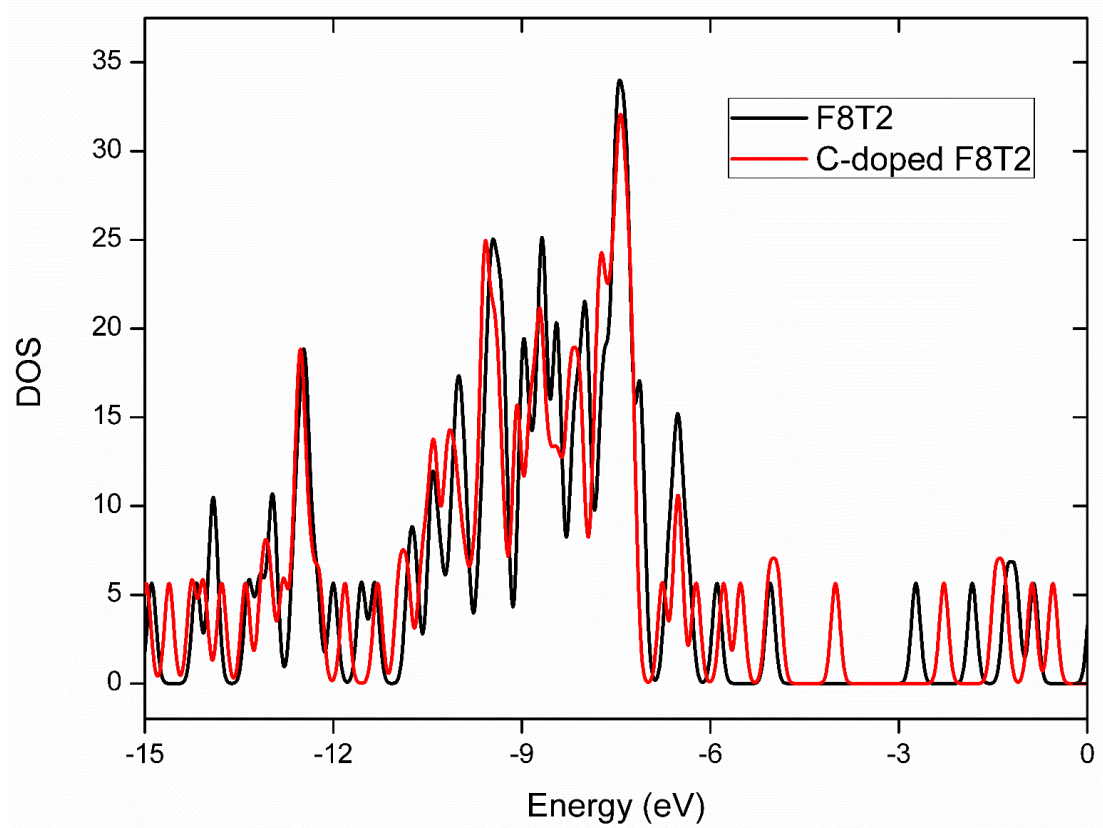
3. RESULTS AND DISCUSSION

The picture of the optimized geometry of the F8T2 organic molecule is indicated in Fig. 1. The F8T2 molecule is composed of two symmetric chains as shown in Fig. 1.

Figure 1. Different views of the optimized geometry of F8T2 organic molecule. (Yellow is Sulfur, purple is Hydrogen and brown is Carbon).

To predict the electronic states in F8T2 organic semiconductor, firstly, the results of the electronic total DOS of undoped and C-doped F8T2 as seen in Fig. 2. The contribution of the density of localized states of undoped F8T2 is greater than that of C-doped F8T2. These fluctuations progressively increase from 0 eV to -15 eV and also there is a considerable shift in energy values. The density of localized states has a sharply increasing tendency to occur in the region of between -9 and -6 eV. The DOS analysis also indicates that F8T2 has the energy gap, so, all the nanoparticles show semiconductor character. There is an increase in HOMO energy levels, but a decrease in LUMO level.

The obtained results were also compared to experimental and DFT data. The results show that the HOMO and LUMO energy levels of F8T2 were found -5.045 and -2.729 eV, respectively, which are compatible with experimental HOMO (-5.44 eV) and LUMO (-2.95 eV) energy levels [16]. The band energy (2.32 eV) is also consistent with experimental findings (2.49 eV). The gap energy for F8T2 decreased from 2.32 eV to 0.13 eV for C-doped F8T2 which is about 2.19 eV shorter than that of F8T2. The obtained energy values were indicated in Table 1.

Figure 2. The total density of states (DOS) of undoped and C-doped F8T2 organic molecule.

Table 1. The electronic structure data undoped and C-doped F8T2.

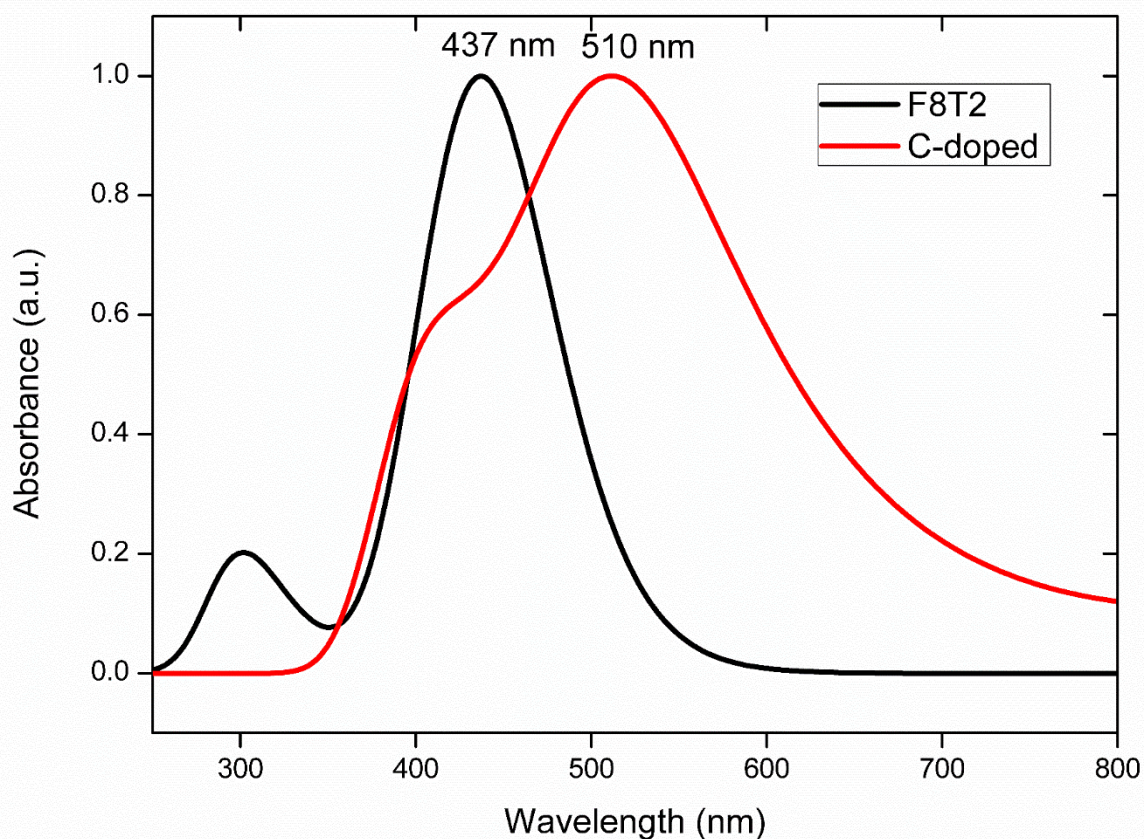|	HOMO	LUMO	Energy gap	Fermi energy
F8T2	-5.045	-2.729	2.316	-3.887
Experiment [16]	-5.440	-2.950	2.490	-
C-doped F8T2	- 5.032	-4.895	0.137	-4.963

The dipole moment (D_M) results from differences in electronegativity. The bigger D_M means stronger intermolecular interaction. The component of D_M along the z-axis (-0.48 Debye) gives rise to the largest negative charge separation in the z-direction. D_M increases along x- and y-directions when it comes to a carbon substitution on the F8T2; it decreases along the z direction. It is found 1.43 and 1.87 Debye along with x and y-directions, respectively. These values are comparable with the bandgap energy because the lowest gap energy of F8T2 obtained from SCC-DFTB means that electrons easily transfer from HOMO to LUMO. Also,

494

there is a highly relevant correlation between D_M and the energy gap of F8T2. Thus, it can be concluded that the large D_M has a small energy gap.

Absorbance spectra of undoped and C-doped F8T2 organic molecule were depicted in Fig. 3. The calculated maximum absorbance peak of F8T2 is 437 (2.83 eV) nm which is shorter than that of C-doped F8T2 (510 nm; 2.43 eV) [16].

Figure 3. Absorbance spectra of undoped and doped F8T2 molecule.

4. CONCLUSION

The electronic and photophysical properties of **F8T2 organic semiconductor**-based on a single atom substitution. Our results show that optoelectronic properties, optoelectronic parameters can be controlled with a single atom substitution. C-doped on F8T2 significantly improve the photophysical properties of F8T2. The gap energy for F8T2 decreased from 2.32 eV to 0.13 K. The results obtained from DFTB calculations are good agreement with experimental data.

ACKNOWLEDGMENTS

REFERENCES

[1] C. Xie, P. You, Z. Liu, L. Li, F. Yan, Light Sci. Appl. 6, e1702 (2017).

[2] A. D. Sio, C. Lienau, Phys. Chem. Chem. Phys. **19,** 18813 (2017).

[3] X. Wang, K. Wasapinyokul, W. D. Tan, R. Rawcliffe, et al., J. Appl. Phys. 107, 024509 (2010).

[4] H. Sirringhaus, T. Kawase, R. Friend, H. T. Shimoda, et al., Science 290, 2123 (2000).

[5] M. Kurban, Optik, 172, 295 (2018).

[6] M. Kurban, O. B. Malcıoğlu, Ş. Erkoç, Chem. Phys. 464, 40 (2016).

[7] B. Aradi, B. Hourahine, T. Frauenheim, J. Phys. Chem. A 111, 5678 (2007).

[8] M. Elstner, D. Porezag, G. Jungnickel, J. Elsner, M. Haugk, et al., Phys. Rev. B 58, 7260 (1998).

[9] M. Gaus, A. Goez, M. Elstneri, J. Chem. Theory Comput. 9, 338 (2013).

[10] M. Kubillus, T. Kubař, M. Gaus, J. Řezáč, M. Elstner, J. Chem. Theory Comput. 11, 332 (2015).

[11] H. C. Andersen, J. Chem. Phys. 72(4), 2384 (1980).

[12] M. Shahidul, R. Islam Pierre-Nicholas J. Chem. Theory Comput. 87, 2412 (2012).

[13] M. A. Addicoat, R. Stefanovic, G.B. Webber, R. Atkin, A.J. Page J. Chem. Theory Comput. 10(10) 4633 (2014).

[14] T. Frauenheim, G. Seifert, M. Elsterner, Z. Hajnal, G. Jungnickel, D. Porezag, S. Suhai, R. Scholz Phys. Status Solidi B 217, 41 (2000).

[15] M. Kurban, J. Alloys Compd. 791, 1159 (2019).

[16] O. Kettner, A. Pein, G. Trimmel, P. Christian, C. Röthel, et al., Synth. Met. 220, 162 (2016).

SIZE DEPENDENT ELECTRONIC STRUCTURE AND STRUCTURAL PROPERTIES OF CUPRIC OXIDE (CuO) NANOPARTICLES

Hasan Kurban[1,3], Mustafa Kurban[2] and Mehmet Dalkılıç[1]

[1]*Computer Science Department, Indiana University, Bloomington, 47405 Indiana, USA.*
[2]*Department of Electronics and Automation, Kırşehir Ahi Evran University, 40100 Kırşehir, Turkey.*
[3]*Computer Engineering Department, Siirt University, 56100 Siirt, Turkey.*

E-mails: mkurbanphys@gmail.com; hakurban@gmail.com

Abstract

We performed the electronic and structural properties of CuO nanoparticles (NPs) using the density functional tight-binding (DFTB) method. An increase in the size of the CuO NPs, the number of bonds, segregation phenomena and radial distribution function (RDF) of two-body interactions such as Cu-Cu, Cu-O and O-O were investigated using new algorithms. The results reveal that the number of Cu-Cu bonds is larger than that of Cu-O and O-O bonds; thus, it appears that Cu atoms have a greater preference for Cu or O atoms. The RDFs of Cu and O atoms decrease based on the increase in the size. The segregation of Cu and O atoms show that O atoms tend to co-locate at the center, while Cu atoms tend to reside on the surface in general. CuO NPs shows a semiconductor character that is compatible with experimental data. The HOMO-LUMO energy gap decrease with an increase in size. We can conclude that the stabilization of CuO NPs decreases with increasing NP size because of a decrease in the energy gap.

Keywords: CuO, Nanoparticles, Electronic structure, Segregation phenomena.

1. INTRODUCTION

Nanoparticles (NPs) have attracted very wide interests in many applications including energy, electronics, biomedical and optical fields due to their excellent size and shape dependence properties comparing with their bulk materials. Taking into consideration the various types of NPs such as metal, semiconductor, and insulator, semiconductor NPs have been widely investigated because the materials have been found useful in important applications [1-3].

Metal oxide NPs have a very important place in material science. Among them, for instance, cupric oxide (CuO) NPs have been the hot topic because of their monoclinic structure, narrow bandgap with p-type and semiconducting properties [4, 5]. They are prominent due to their diverse applications such as photodetector [6], energetic materials [7], supercapacitors [8]. The factors including size, shape and composition of NPs affects the interaction between the NPs and living cells [9].

In this study, a density functional based tight-binding (DFTB) which is based on the density functional theory (DFT) have been performed to study the size-dependent electronic structure properties such as HOMO, LUMO and bandgap energies, total energies, dipole moments and Fermi levels. The results were compared with experimental results and discussed in detail. Besides, we have performed the structural analysis using R which is an open-source programming language. To make the program more accessible, we have designed and implemented R programs to simplify structural analysis [10]. These include functions to analyze the number of bonds, segregation phenomena, and RDF of the CuO NPs based on the size. We also have made the code open source freely available online (https://github.com/hasankurban/Structural-Analysis-NanoParticles). Moreover, these programs include high-resolution visualizations to plot data.
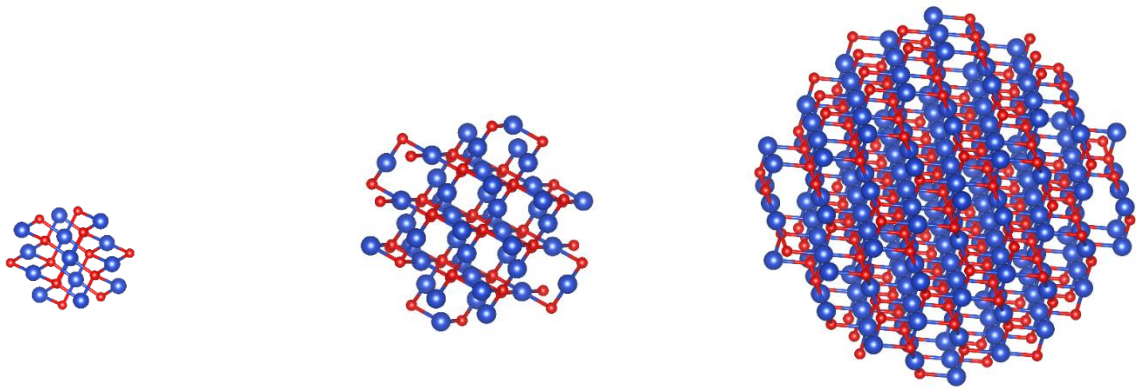
2. MATERIAL AND METHODS

The structural and electronic structure analysis of CuO NPs molecule have been examined using DFTB implemented in DFTB+ code [11] with the matsci/matsci-0-3 [12] set of Slater Koster parameters. Firstly, some benchmarks were carried out on CuO NPs using Slate-Koster parameters including DFTB3 parameters. Later, the electronic and optical properties such as HOMO, LUMO and bandgap energies, dipole moments, and Fermi levels were investigated. We do not explain the procedure of DFTB calculations in detail because there currently exist several studies available with detailed descriptions of theoretical aspects and performance of the DFTB approach, as well as advances in theoretical development and application [13-16].

3. RESULTS AND DISCUSSION

The initial picture of the CuO NPs according to the size is indicated in Fig. 1. The CuO NPs were characterized by 30×30×30 supercells of the monoclinic structure (space group *C2/c,#15*). The constant volume has been performed to construct the NP models.

Figure 1. Some initial structures of CuO NPs for 0.4, 0.6 and 1.0 nm from left to right, respectively. (Blue is Copper, red is Oxygen).

The number of the nearest neighbor contacts (n_{ij}), that is the number of bonds, is generally adopted to distinguish the degree of packing, which is an important property of NP. The number n_{ij} [17] for the NP is given by
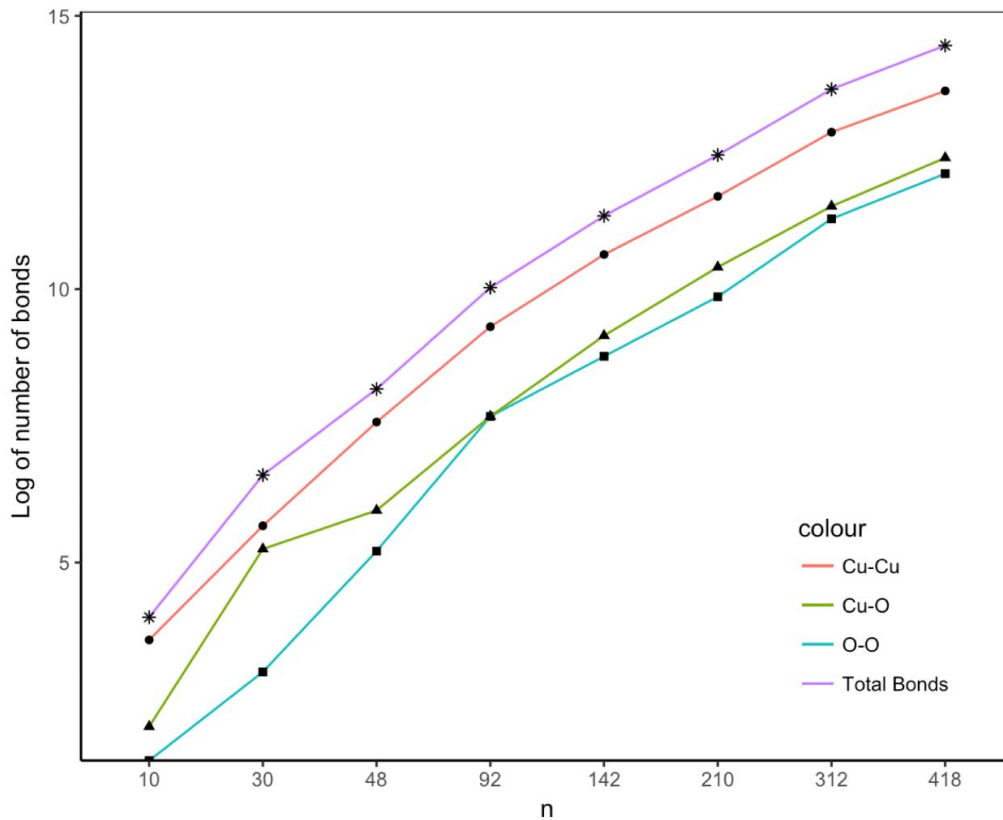
$$n_{ij} = \sum_{i<j} \delta_{ij} \qquad (1)$$

where $\delta_{ij} = \begin{cases} 1, r_{ij} \leq 1.2 r_{ij}^{(0)} \\ 0, r_{ij} > 1.2 r_{ij}^{(0)} \end{cases}$ $i,j =$ Cu or O, r_{ij} is the distance between atom i and j and $r_{ij}^{(0)}$ is a nearest

neighbor criterion derived by fitting the experimental data [18, 19]. Fig. 2 indicates the numbers of bonds in the CuO NPs. From the Fig. 2, the number of Cu-Cu, Cu-O and O-O bonds increase gradually in terms of an increase in the size in the CuO NP. Moreover, the number of Cu-Cu bonds is relatively smaller than total bonds, while O-O bonds are the smallest. Thus, Cu atoms tend to form more bonds with Cu and O atoms: that Cu_2 tends to scatter on the surface can likewise be inferred. Moreover, the number of Cu-Cu bonds is larger

than that of Cu-O and O-O bonds; thus, it appears that Cu atoms have a more preference to O atoms rather than Cu atoms with the increase of CuO NP size.

Figure 2. Variation of number of bonds of binary Cu-Cu, Cu-O and O-O interactions based on the content of N atoms in the CuO NPs.

The order parameter $\left(R_{T_i} \right)$ is calculated to determine the stable structure in the NPs by analyzing the distribution of the different types of atoms [20]. R_{T_i} is identified by the average distance of a type T_i atoms in accordance with the center of a nanoparticle,

$$R_{T_i} = \frac{1}{n_{T_i}} \sum_{i=1}^{n_{T_i}} r_i \tag{2}$$

where n_{T_i} is the number T_i type atoms in the ternary ABC NPs, and r_i is the distance of the atoms to the coordinate center of the nanoparticle. If an ϵ distance from center of nanoparticle to a reference point is defined to show the location of atoms; if $R_{T_i} < \epsilon_{min}$ (a "small" value) , it means that the T_i type atoms are at the center, and if $R_{T_i} > \epsilon_{max}$ (a "large" value), it means that the T_i type atoms are at the surface region of

nanoparticle. If neither is true, *i.e.*, if $\epsilon_{min} \leq R_{T_i} \leq \epsilon_{max}$ (a "medium" value), it means a well-mixed nanoparticle.

The variations of R of Cu and O atoms depend on the size of CuO NP were shown in Fig. 3. The segregation of atoms in the CuO NPs is carried out by the R which indicates that Cu atoms tend to locate at the center, while O atoms tend to occupy the surface as a general trend. The segregation of O atoms to the surface is due to its lower cohesive energy. The R shows different characteristics with the increase in the size of the CuO NPs. For example, R_{Cu} values sharply increase after an increase in the size of CuO NPs with 0.4 nm and R_O smoothly decrease.
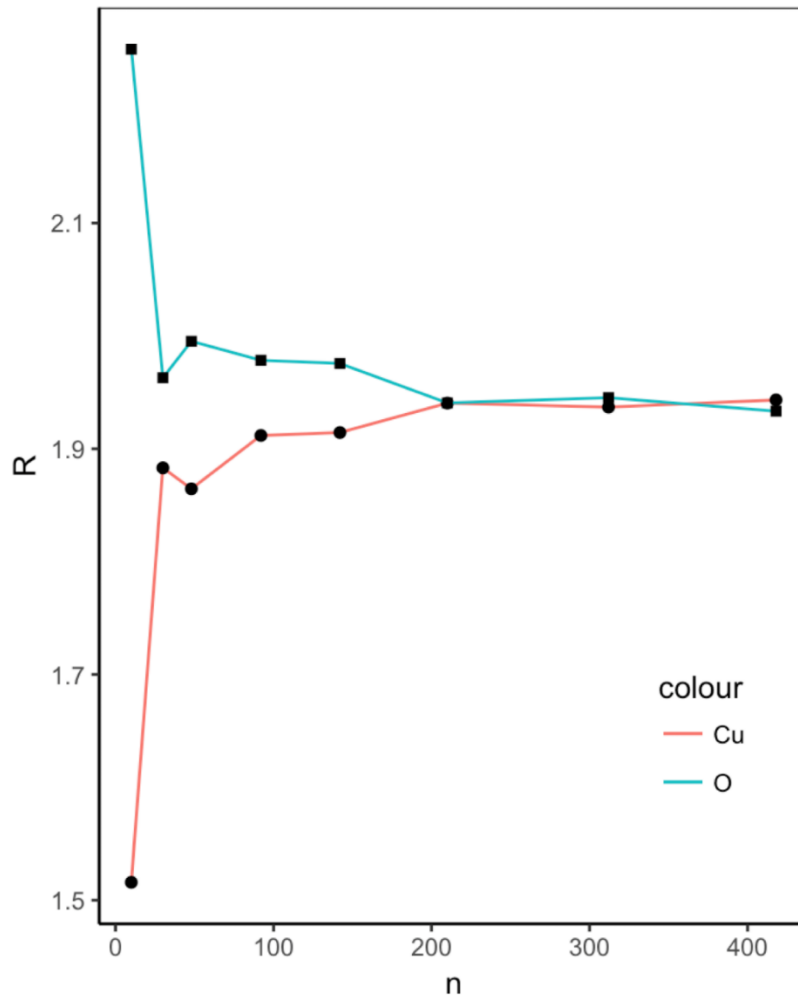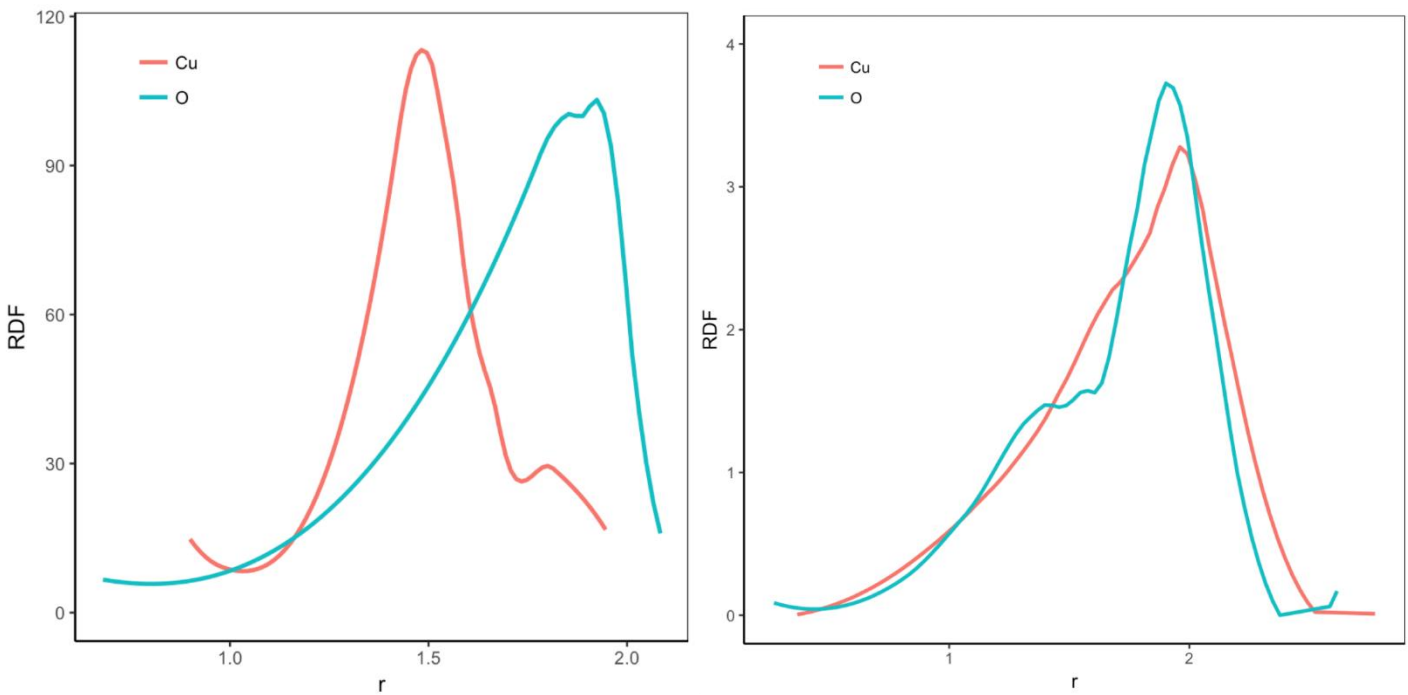

Figure 3. Variation of the order parameter of Cu and O atoms in the CuO NPs.

The Radial Distribution Function (RDF) is a significant parameter that defines the probability of finding a particle at a distance r from another tagged particle. The RDF is mathematically defined as $g_{(r_i)} = n_{(r_i)}/(|\Delta| \times V_s \times V_d)$ where $n_{(r_i)}$ is the mean number of atoms in a shell of width dr at distance r_i, $|\Delta|$ represents total atom number and V_s is the volume of the spherical shell and V_d is the mean atom density. Fig. 4 shows the RDF Cu-Cu and O-O binary interactions in CuO NPs. The RDFs are calculated for each atomic pair of optimized structures. Cu-Cu has a narrower and higher distribution than O-O interactions. When it comes to an increase in the size of CuO NPs, the peaks for both pairs decrease with increasing of the size of CuO NP. Moreover, the RDF of O-O interactions increases with raising the size of the CuO NP.

Figure 4. Radial distribution function of R4 (left) and R10 (right) CuO NPs.

3.2. Electronic structure

To predict the electronic states of the CuO NP, we analyzed the results of the HOMO, LUMO and Fermi energy levels based on the size as seen in Fig.5. Our results indicate that the CuO NPs have the energy gap, so it shows semiconductor character.

There is a considerable increase in LUMO and Fermi energy with increasing temperature, the HOMO level decreases. The HOMO value for CuO NP with R3 is -4.385 eV, *i.e.*, about 0.65 eV greater than that of R10. R9 has the lowest HOMO value (-3.58 eV) and is less reactive while being more stable than that of the other NP models (see Fig. 5). Fermi energy levels are found to be the middle of the valence and conduction band. The HOMO-LUMO energy gap of CuO NP is 0.55 eV, which decreases from 0.55 eV to 0.11 eV (see Fig. 6) except for R7 which has a bandgap 0.3 eV. It is clear then that an increase in the size of CuO NP contributes to the destabilization due to a decrease in the energy gap. Lowering of the bandgaps can be preferred for optoelectronic applications or devices, which prefer lower band gaps because the electronic transfer is easier.

The dipole moment (D_M) results from differences in electronegativity. The bigger D_M means stronger intermolecular interaction. The component of D_M along the z-axis (-104.26 Debye) gives rise to the largest negative charge separation in the z-direction for R7. All the NP models show different characteristics in terms of size. These values are comparable with the bandgap energy because there is a highly relevant correlation between D_M and the energy gap of the material. Thus, it can be concluded that the large D_M has a small bandgap.
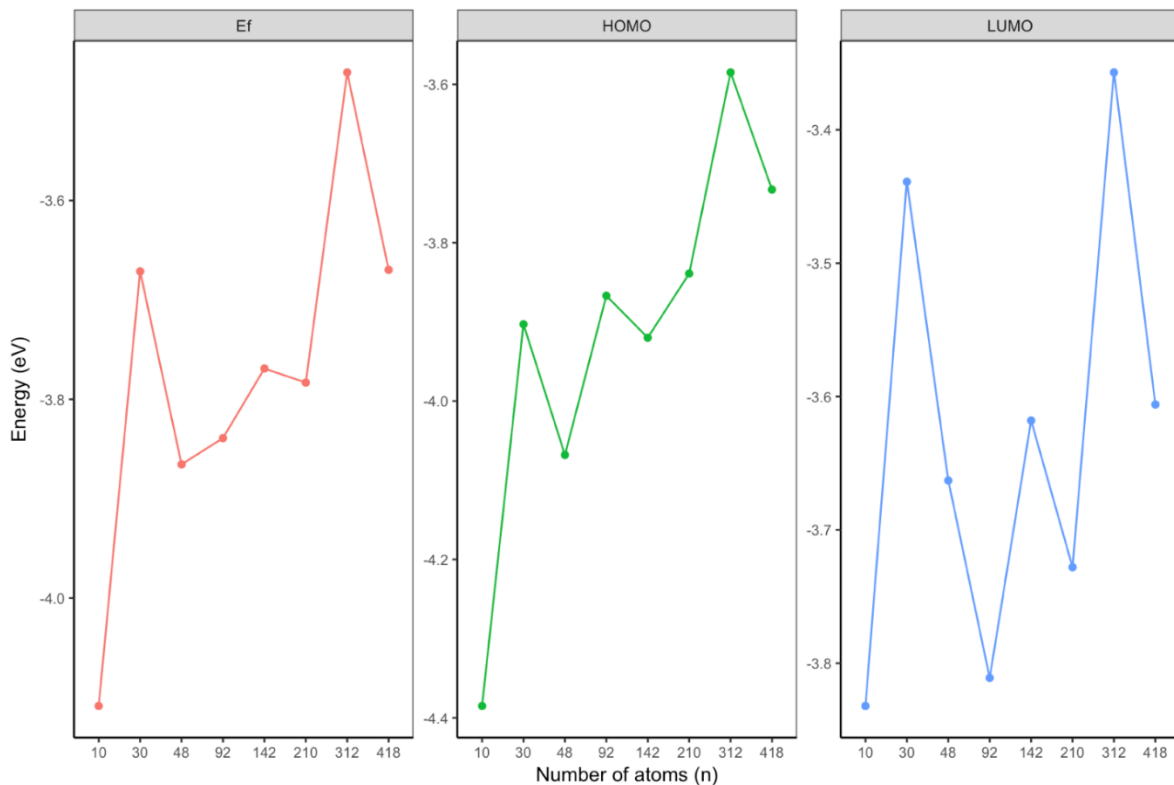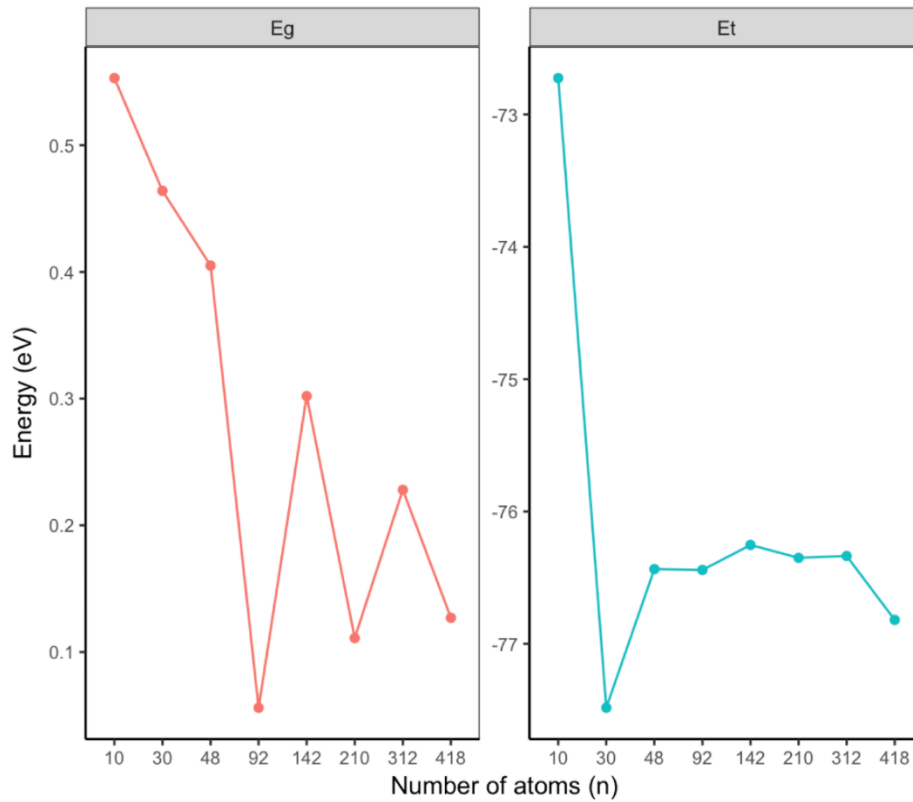

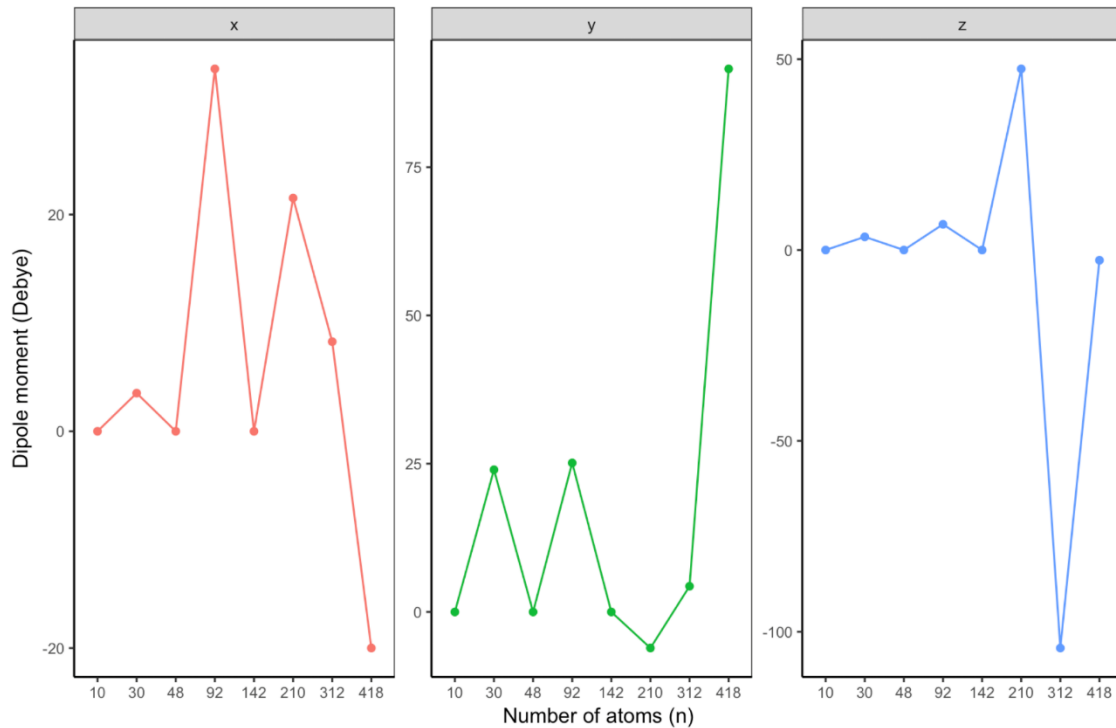**Figure 5.** HOMO, LUMO and Fermi energies of CuO NP in terms of the size.

503

Figure 6. HOMO-LUMO energy gap and total energy CuO NP in terms of the size.

Table 1. The electronic structure data of CuO NPs with different size

Models	HOMO	LUMO	Energy gap	Fermi energy
R3-10 atoms	-4.385	-3.832	0.55300	-4.1086
R4-30 atoms	-3.903	-3.439	0.46400	-3.6713
R5-48 atoms	-4.068	-3.663	0.40500	3.8655
R6-92 atoms	-3.867	-3.811	0.05600	-3.8391
R7-142 atoms	-3.920	-3.618	0.30200	-3.7691
R8-210 atoms	-3.839	-3.728	0.11100	-3.7832
R9-312 atoms	-3.585	-3.357	0.22800	-3.4711
R10-418 atoms	-3.733	-3.606	0.12700	-3.6698

Figure 7. Dipole moments of CuO NPs in the x-, y- and z- directions.

4. CONCLUSION

This work examines the structural and electronic properties of a CuO NPs with different sizes, using DFTB method. To get insight about structural properties of CuH NPs, we analyzed the number of bonds, segregation phenomena, and RDFs of binary interactions in the CuO NPs. Our results show that the number of Cu-Cu bonds is larger than that of Cu-O and O-O bonds. The segregation of Cu and O atoms indicates that O atoms tend to locate at the center, while Cu atoms tend to occupy the surface as a general trend. The HOMO energy level decreases; however, the LUMO level increase, thus the HOMO-LUMO band gap decreases from 0.55 to 0.05 eV. The decrease in the HOMO levels contributes to the stabilization of the CuO NPs. The CuO NP with 92 atoms is more desirable in energy. The component of D_M along the z-axis (-104.26 Debye) gives rise to the largest negative charge separation for CuO NP with 312 atoms in the z-direction.

ACKNOWLEDGMENTS

REFERENCES

[1] C. L. Wang, et al., J. Phys. Chem. C111, 2465 (2007).

[2] P. Yang, et al., J. Chem. Phys. 129, 074709 (2008).

[3] A. K. Kushwaha, Comp. Mater. Sci. 65, 315 (2012).

[4] A. H. MacDonald Nature 414, 409 (2001).

[5] Y. Liu, Y. Chu, Y. Zhuo, M. Li, L. Li, L. Dong, Cryst. Growth Des. 7, 467 (2007).

[6] S. B. Wang, C. H. Hsiao, S. J. Chang, K. T. Lam, et al., Sens. Actuators A—Phys.171**,** 207 (2011).

[7] C. Rossi, K. Zhang, D. Esteve P. Alphonse, P. Tailhades, J. Microelectromech. Syst. 16, 919 (2007).

[8] X. Zhang, W. Shi, J. Zhu, D. J. Kharistal, W. Zhao, B. S. Lalia, et al., ACS Nano 5, 2013 (2011).

[9] X. M. Li, L. Wang, Y. B. Fan, Q. L. Feng, F. Z. Cui, J. Nanomater. 2012, 1 (2012).

[10] H. Kurban, M. Kurban, M. Dalkılıç, Mater. Today Commun. 21, 100648 (2019).

[11] B. Aradi, B. Hourahine, T. Frauenheim, J. Phys. Chem. A 111, 5678 (2007).

[12] N. Jardillier, PhD Thesis, Universite Montpellier II, 2006, online:http://nicolas.jardillier.free.fr

[13] M. Shahidul, R. I. Pierre-Nicholas, J. Chem. Theory Comput., 87 (2012), p. 2412.

[14] M. A. Addicoat, R. Stefanovic, G. B. Webber, R. Atkin, A. J. Page J. Chem. Theory Comput. 10(10), 4633 (2014).

[15] T. Frauenheim, G. Seifert, M. Elsterner, Z. Hajnal, G. Jungnickel, D. Porezag, S. Suhai, R. Scholz Phys. Status Solidi B, 217, 41 (2000).

[16] M. Kurban, J. Alloys Compd., 791, 1159 (2019).

[17] X. Wu, Z. Wei, Q. Liu, T. Pang, G. Wu, J Alloy. Compd. 687, 115 (2016).

[18] Web page. Experimental bond lengths. https://cccbdb.nist.gov/expbondlengths1.asp.

[19] M. A. Czajkowski, J. Koperski, Spectrochim. Acta, Part A 55, 2221 (1999).

[20] M. Kurban, O. B. Malcıoğlu, Ş. Erkoç, Chem. Phys. 464, 40 (2016).

BACTERIAL SYNTHESIS OF COMPLEX GO: Cu: In NANOPARTICLES AND THEIR USE AS THIN FILM IN Au / GO: Cu: In / p-Si STRUCTURE

T. Çakıcı[1], M. Özdal[2], M. Kundakçı[3]

[1]Department of Electric and Energy, Ispir Hamza Polat Vocational High Scholl, Ataturk University, Erzurum, TURKEY
[2]Department of Biology, Faculty of Science, Ataturk University, Erzurum, TURKEY
[3]Department of Physics, Faculty of Science, Ataturk University, Erzurum, TURKEY

E-mail: tuba.cakici@atauni.edu.tr

Abstract

A novel approach bacterial biosynthesis of complex nanoparticles is simple, eco-friendly and economic. In this research, complex graphene doping cooper and indium metals (GO: Cu: In) reduced together via a special type of bacteria in the Luria-Bertani medium under dark conditions for the first time. The synthesized by GO: Cu: In nanoparticles in solution dropped on glass and p-Si substrates and then they were dried for the formation thin film structure in 300°C temperature. Optical properties of the GO: Cu: In thin film have been investigated by UV-Vis. Spectrophotometer method. The indirect band gap of GO:Cu:In thin film obtained as 1.75 eV. Structural characterization of the thin film was investigated by X-ray diffraction (XRD) and Field-emission scanning electron microscopy (FE-SEM) with energy dispersive techniques (EDS) techniques. GO: Cu: In thin film had good nano-crystalline nature. Then rectifying (Au) and ohmic (Al) metal contacts were performed on direct GO: Cu: In thin film and p-Si substrate, respectively. Au/ GO: Cu: In /p-Si/Al structure was obtained and its electrical properties were investigated by current-voltage (I-V) measurements. Some electrical parameters of the Au/ GO: Cu: In /p-Si/Al structure as ideality factor (n), saturation current (I_o) and potential barrier height (Φ_b) were calculated.

Keywords: GO:Cu:In, Complex nanoparticles, Bacterial Synthesis, Thin Films

1. INTRODUCTION

Plants, bacteria, fungi, and algae are used for green synthesis of metallic nanoparticles. Biological approaches are easy, eco-friendly and low cost. Physical and chemical methods used for nanoparticle synthesis are toxic lead to non-environmentally friendly by-products and using expensive high vacuum systems. Also, researchers are used many different methods (chemical, physical, and biological) to synthesis nanoparticles which are of the required composition, shape, and size because these factors significantly affect the properties of the material. It is advantageous over chemical and physical methods as it is safe, simple, eco-friendly, cheap, reproducible, and often results in more stable materials [1-2]. A variety of metal nanomaterial (magnesium, gold, graphene, selenium, copper, zinc, silver, iron, titanium, cadmium, etc.) is being produced for the use of electronic, textile, energy, computer, medical, food, optic and space industries. Bacterial synthesis method, some special ones are unique to tolerate high chemical concentration. [1-3]. Among the different synthesis methods, using microorganisms for nanoparticle synthesis can be suitably scaled up for large-scale synthesis of nanoparticles.

Copper nanoparticles have various properties such as optical, catalytic, anti-bacterial, anti-fungal and anti-cancerous ones [3-4]. GONPs have been proposed to be incorporated into heavy metal detecting sensors [5], electrodes [6], and biomedical applications [7]. The excellent tensile and compressive strengths, high hardness, and good electrical conductivity have been obtained simultaneously in the RGO-Cu composites [8].

Metal elements have been synthesized by using bacteria in the literature. However, the production of the compound and complex nanoparticles have already not studied in the literature. Furthermore, it is very difficult to fabricate directly high-quality complex GO:Cu:In thin films by using chemical and physical methods based on the growth mechanism. In this study, we report firstly eco-friendly approach microbial biosynthesized complex GO:Cu:In nanoparticles and also we sintered these nanoparticles used as metal-semiconductor interlayer thin films for the first time in the literature. GO:Cu:In/p-Si heterojunction was fabricated and current-voltage characteristics of Au/GO:Cu:In/p-Si/Al were investigated.

2. MATERIAL AND METHODS

2.1 Obtaining Complex GO:Cu:In NP by Bacterial Synthesized method

P. aeruginosa bacteria, first, as mentioned in our previous studies, was cultured [9-10]. The cell suspension (100 μl, OD_{600} 1) was taken from inoculums and inoculated into the Luria Bertani Broth medium (20 mL) and added 1 mM $CuSO_4$, 1 mM Graphene oxide and 1 M $InSO_4$ into this medium. Complex GO:Cu:In

nanoparticles, biosynthesis was conducted at 30 °C for a period of 96 h on rotating shaker (150 rpm) in dark condition. Control experiments without $CuSO_4$, Graphene oxide, and $InSO_4$ were performed, simultaneously. It was observed that the color of the reaction mixtures was changed during the biosynthesizing process.

Complex GO:Cu:In nanoparticles were cleaned and removed from the bacteria cellular impurities by following a procedure modified from Oremland et al. [11-13] in the form of a solution. This process is described in detail in our previous studies [9- 10]. After this process, only complex GO:Cu:In nanoparticles suspended in solution. The solution of complex GO:Cu:In nanoparticles were directly dropped on the surface of the p-Si and glass substrates and then they were dried on a heater plate at 300°C for 60 min. Hence, complex GO:Cu:In thin films were synthesized on both glass and p-Si substrates. Thus, GO: Cu:In thin films were obtained.
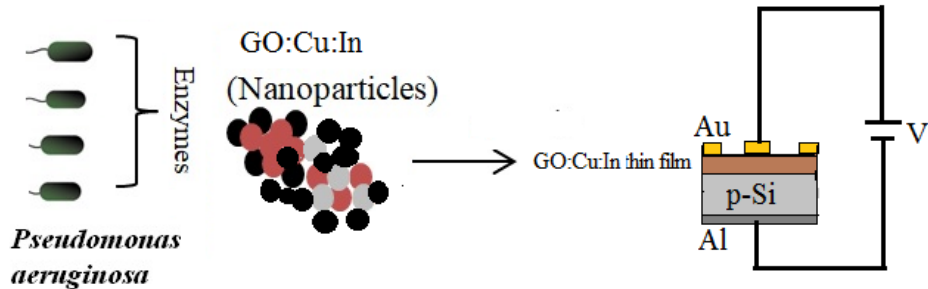
2.2. Obtaining Complex GO:Cu:In the thin film on glass and p-Si substrates and Characterizations

Size determination of complex GO:Cu:In nanoparticles was performed by using transmission electron microscopy (TEM Hitachi HighTech HT7700) image. After completing the fabrication of the samples, we performed the characterization of the thin film samples. We determined the optical properties, crystal structures, surface morphology, and qualitative analysis of GO:Cu:In thin films by using UV-VIS spectrometer (Perkin-Elmer Lambda 2S UV-Visible spectrometer), X-rays diffractometer (XRD Bruker D2, Kα, λ=1.54 A, Scanning angle 70°), Scanning electron (FE-SEM) (Sigma 300 Model Zeiss Gemini) and electron diffusion X-ray (EDX associated with FE-SEM), respectively.

2.3. Obtaining Au/GO:Cu:In/p-Si/Al device

Au/ GO:Cu:In /p-Si/Al and device structures used in this study were fabricated on p-type Si wafer with (100) surface orientation and glass.

Process of converting bacterial metal salts into complex GO:Cu:In nanoparticles and fabricating device structure (Au/ GO: Cu: In /p-Si/Al) was shown in Figure 1.
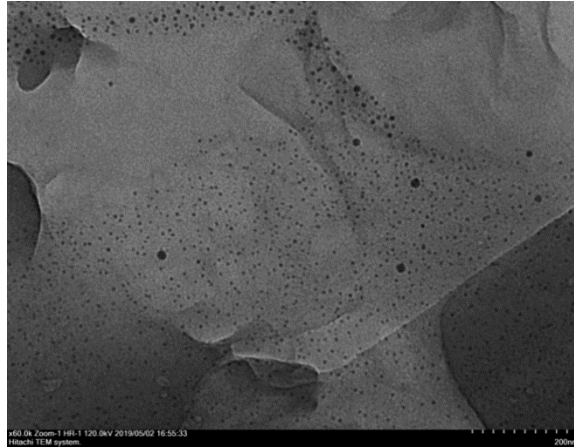
Figure 1. Process of converting bacterial metal salts into complex GO:Cu:In nanoparticles and fabricating device sturucture.

The p-Si wafer Si was sliced to pieces and they were degreased acetone and methanol in an ultrasonic cleaner for 10 min and consecutively they were etched in a sequence of $H_2O:H_2O_2:HNO_3$ (6:1:1) at 60°C, 20% HF and a solution of $H_2O:H_2O_2$: HCl (6:1:1) at 60°C, 20% HF. Finally, the substrates were rinsed thoroughly in de-ionized water with resistivity of 18 MΩ cm. An ohmic contact was formed by thermally evaporating Al onto the backside of this substrate in a vacuum system with a pressure of 1×10^{-5} Tor. In order to obtain low resistivity back ohmic contact, p-Si/Al structure was annealed at about 550 ^{o}C for 3 min in flowing dry nitrogen ambient. At the end, another Au metal was again directly evaporated on the GO:Cu:In thin films surfaces as rectifying contact with shadow mask cylindrical geometry of 1.00 mm diameter in vacuum pump (1.5 10-5 Torr). Au/ GO:Cu:In /p-Si/Al device were fabricated and the electrical properties of the device were obtained by Keithley 2400 Picoammeter/Voltage Source meter at 300 K.

3. RESULTS AND DISCUSSION

Figure 1 shows the TEM image of GO:Cu:In nanoparticles at the race of 100 nm, respectively. In Fig. 1 (a), it can see a uniform relatively dispersion of GO:Cu:In nanoparticles with an average particle size of about 15–30 nm. TEM investigation for the GO:Cu:In nanoparticles indicates that the nanoparticles are well separated and tend to form a nano sheeted structure.
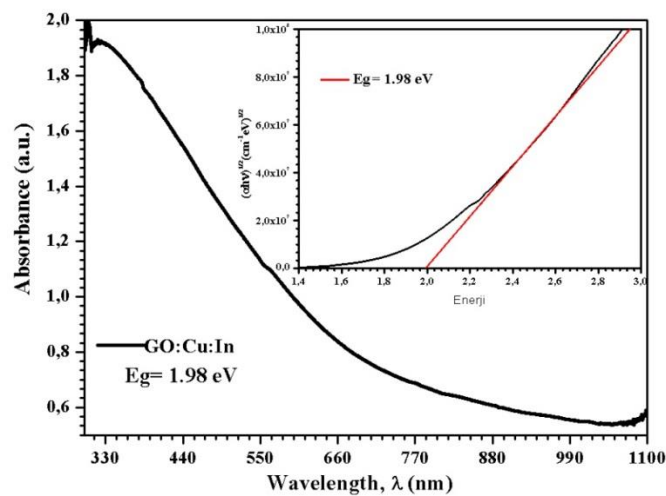
Figure 1. The TEM image of Complex GO:Cu:In nanoparticles (200 nm).

Figure 2 shows the optical absorption spectra measured between 300 nm and 1000 nm for GO:Cu:In thin film. The absorption coefficient and the optical band gap values were determined from the transmission data. The optical band gap energy (E_g) value of the thin film sample is calculated substituting the values of absorption coefficients, α, corresponding to each wavelength into Equ. 1 given as following:

$$ahv = A\,(hv - E_g)^n \tag{1}$$

where A, h, Eg, hυ, and n are α absorption coefficient values constant related to the effective masses of charge carriers, the Planck constant, the band gap energy, the energy of the photon, and the exponent that depends on the nature of the optical transition. The band gap energy of GO:Cu:In thin film have been determined as 1.98 eV by the extrapolation of the linear region on the energy axis (hυ) as shown in Fig. 2.

Figure 2. Optical absorbance versus the wave-length of incident photons and $(\alpha h v)^2$ plot versus photon energy (hυ) and the band gap energy (E_g) determined by extrapolation for GO:Cu:In thin film

XRD peaks of the GO: Cu:In/glass (red line), GO: Cu/p-Si (blue line), GO: Cu:In /p-Si (green line) and are shown in Figure 3. Herein, the strongest peaks appearing at $2\theta \sim 33$, ~61 and ~70° and directed as (100) correspond p-Si (100). Table 1 shows the structural parameters of published in our previous research GO:Cu thin film on the p-Si substrate [9]. All of the peaks shift to bigger 2θ angles with indium (In) deposition in GO:Cu thin film. Table 2 shows the structural parameters of GO: Cu:In /p-Si structure.

Figure 3. XRD patens of the GO:Cu:In thin film grown on p-Si and glass substrates.

According to XRD pattern of GO: Cu/p-Si (blue line) and GO: Cu:In /p-Si (green line) peaks at about 28.27° and 28.21° belongs to (002) plane of graphide, and they have 0.38 nm and 0.32 nm interlayer distance, respectively. The strong peaks of GO: Cu/p-Si (blue line) and GO: Cu:In /p-Si (green line at about 9.36° and 10.46 ° shows (002) plane of graphene oxide with 0.94 nm and 0.85 nm interlayer distance, respectively. The increase at the interlayer distance of the GO can be attributed to presence of the oxygen-containing functional groups and some other structural defects [14-15]. Also, the peaks of GO: Cu/p-Si (blue line) and GO: Cu:In /p-Si (green line) at 45.02° and 44.96° angles corresponds to graphene oxide phase with 0.2 nm interlayer distance, respectively.

The peaks of GO: Cu/p-Si (blue line) and GO: Cu:In /p-Si (green line) at 31.31° and 31.25° 2θ angles corresponds to CuO cubic phases, respectively. The peak of GO: Cu:In /p-Si (green line) at 35.34° at 2θ angle corresponds to the InO phase.

Table 1. The structural parameters of GO:Cu thin film on the p-Si substrate [9]

(hkl)	FWHM	Intensity (a.u.)	2θº (Observed)	d-values (nm)	Crystal size (D) nm	Crystal
(002)	3.58	4745.10	9.36	0,94	2,23	GO
(101)	0,38	383,16	28.27	0,35	21,60	Graphite
(110)	0.20	2467.33	31.31	0.29	41.51	CuO
(200)	0.255	790.87	45.02	0.20	33.73	GO

Table 2. The structural parameters of GO:Cu:In thin film on the p-Si substrate

(hkl)	FWHM	Intensity (a.u.)	2θº (Observed)	d-values (nm)	Crystal size (D) nm	Crystal
(002)	0,52	2784,18	10,46	0,85	35,23	GO
(101)	0,45	66,42	28,21	0,32	25,60	Graphide
(110)	0,19	1164,59	31,25	0.29	45.51	CuO
(111)	0,37	78,40	35,34	0.25	22.03	InO
(200)	0.26	252,13	44,96	0.20	33.73	GO

The surface morphology and thin film composition of the prepared sample were obtained from the FE-SEM and EDX analysis techniques. Figure 4 (a) shows the FE-SEM image of prepared GO:Cu:In/p-Si structure, it can be observed that the GO:Cu:In thin film exhibits sheeted structure with nanometer-scale well cover the substrate and distribution of the crystallites are very uniform. As indicated in the literature, the image indicates graphene oxide typically sheeted layers [15].

Figure 4 (b) shows the EDX results of complex GO:Cu:In /p-Si structure and component elements percentages are given in the list, taking place in the composition of GO:Cu:In /p-Si structure. According to this list, it has consisted of expected elements for GO:Cu:In /p-Si structure, O, Cu, C, In, and Si.

| | (a) | | (b) |

Figure 4. FE-SEM image and EDX spectrum of GO:Cu:In/p-Si structure a) FE-SEM image with magnification scale (100nm), b) EDX spectrum

Figure 5 presents the I-V characteristics graph of Au/GO:Cu:In/p-Si/Al devices for darkroom conditions. The devices exhibit good rectifying properties. According to the thermionic emission theory (V≥3kT/q), the current, I, is expressed as follows:

$$I = I_0 \left[exp\left(\frac{qV}{nkT}\right) - 1 \right] \qquad (3)$$

Herein, I_0 is saturation current which is obtained by the intercept of the linear region at the I-V graph. Saturation current is given as an equation (4):
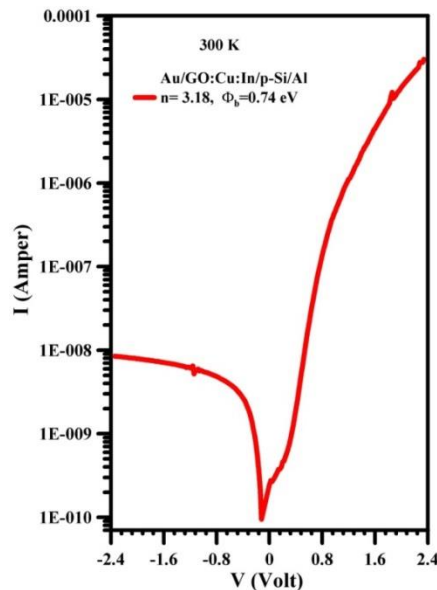
$$I_0 = AA^* T^2 exp\left(\frac{q\phi_b}{nkT}\right) \qquad (4)$$

Au/GO:Cu:In/p-Si/Al device has 1.50×10^{-10} A saturation current value at room temperature. Ideality factor and barrier height values for V≥3kT/q are derived from the equation (5). They can be rearranged as below:

$$n = \frac{q}{kT} exp\left(-\frac{dV}{dlnI}\right) \qquad (5)$$

$$\phi_b = \frac{kT}{q} ln\left(-\frac{AA^* T^2}{I_0}\right) \qquad (6)$$

Ideality factor, n, and barrier height, ϕ_b values of Au/GO:Cu:In/p-Si/Al structure are calculated from equation (5) and (6) of 3.18 and 0.74 eV, respectively. Higher ideality factor values in the study can be attributed to barrier inhomogeneity and non-uniform distribution of the carriers in the interface [16].

Figure 5. Current-Voltage (I-V) characteristic pilot of Au/ GO:Cu:In /p-Si/Al structure

4. CONCLUSION

In this report, complex GO:Cu:In nanoparticles synthesized via the microbial green method for the first time and used these as an interfacial thin film on Au/GO:Cu:In/p-Si/Al device structure. Size of complex GO:Cu:In nanoparticles were determined by TEM image of 15-30 nm. GO:Cu: In thin film deposited on p-Si and glass substrates by sintering at 300^oC. Thin film properties were investigated UV-Vis. Spectrophotometer method, XRD, FE-SEM with EDS and these results showed that GO:Cu:In thin film were obtained successfully. XRD graph indicates that GO:Cu:In thin film have a polycrystalline structure. FE-SEM image revealed that the GO:Cu thin film has a nano-sheeted structure and the structures composed to expected elements checked with EDS. The GO:Cu:In thin film inserted between the Au metal and p-type Si, and Au/GO:Cu:In /p-Si/Al device was obtained. The device tested by I-V measurements under dark. The obtained device has 3.18 ideality factor and 0.74 eV barrier height according to the thermionic emission theory. The device has good and stabile rectifying properties.

REFERENCES

[1] Shah, M., Fawcett, D., Sharma, S., Tripathy, S. K., Poinern, G. E. J., Green synthesis of metallic nanoparticles via biological entities, Materials, 8(11), 7278-7308, 2015.

[2] Hulkoti, N. I., Taranath, T. C., Biosynthesis of nanoparticles using microbes—a review. Colloids and Surfaces B: Biointerfaces, 121, 474-483, 2014.

[3] Khanna, P. K., Gaikwad, S., Adhyapak, P. V., Singh, N., Marimuthu, R., Synthesis, and characterization of copper nanoparticles, Materials Letters, 61(25), 4711-4714, 2007.

[4] Rasool, U., Hemalatha, S., Marine endophytic actinomycetes assisted the synthesis of copper nanoparticles (CuNPs): Characterization and antibacterial efficacy against human pathogens, Materials Letters, 194, 176-180, 2017.

[5] Li J.-L., Hou X.-L., Bao H.-C., Sun L., Tang B., Wang J.-F., Wang X.-G., and Gu M., Graphene oxide nanoparticles for enhanced photothermal cancer cell therapy under the irradiation of a femtosecond laser beam, J. Biomed. Materials Res. 2013b.

[6] Chen, D., Feng H.B., and Li J.H., Graphene oxide: preparation, functionalization, and electrochemical applications, Chem. Rev. 112, 6027, 2012a.

[7] Li M., Gou H., Al-Ogaidi I., Wu N., Nanostructured sensors for detection of heavy metals: A review, ACS Sustain. Chem. Eng. 1, 713, 2013a.

[8] Wang, L., Yang, Z., Cui, Y., Wei, B., Xu, S., Sheng, J., ... Fei, W., Graphene-copper composite with micro-layered grains and ultrahigh strength, Scientific reports, 7, 41896. 2017.

[9] Çakıcı, T., Investigation of Go:Cu nanoparticles produced by green synthesization method and fabrication of Au/Go:Cu/p-Si/al diode, Journal of Molecular Structure, 1199, 126945, 2020.

[10] Çakıcı, T., Özdal,M., Kundakcı, M., Kayalı, R., ZnSe and CuSe NP's by microbial green synthesis method and comparison of I-V characteristics of Au/ZnSe/p-Si/Al and Au/CuSe/p-Si/Al structures Materials Science in Semiconductor Processing, 103, 104610, 2019.

[11] Oremland, R.S., Herbel, M.J., Switzer-Blum, J., Langley, S., Beveridge, T.J., Ajayan PM, Sutto T, Ellis AV, Curran S., Structural and spectral features of selenium nanospheres produced by Se-respiring bacteria, Applied and Environmental Microbiology, 70(1), 52-60, 2004.

[12] Yoshida, N., Miyata, Y,, Doi, K., Goto, Y., Nagao, Y., Tero, R., Hiraishi, A., Graphene oxide-dependent growth and self-aggregation into a hydrogel complex of exoelectrogenic bacteria, Scientific reports, 6, 21867, 2016.

[13] Wadhwani, S.A., Gorain, M., Banerjee, P., Shedbalkar, U.U., Singh, R., Kundu, G.C., Chopade, B.A., Green synthesis of selenium nanoparticles using Acinetobacter sp. SW30: Optimization, characterization and its anticancer activity in breast cancer cells, International journal of nanomedicine, 12, 6841, 2017.

[14] Wang, X., Zhi L., Müllen, K., Transparent, conductive graphene electrodes for dye-sensitized solar cells, Nano letters, 8(1), 323-327. 2008.

[15] Karteri, İ., Güneş M., Synthesis of reduced graphene oxide-phosphorus nanocomposites with a new approach for dye sensitized solar cells applications. Journal of Materials Science: Materials in Electronics, 27(11), 11502-11508. 2016.

[16] Çakıcı, T., Güzeldir, B., Sağlam, M., Temperature-dependent of electrical characteristics of Au/n-GaAs/In Schottky diode with In_2S_3 interfacial layer obtained by using spray pyrolysis method, Journal of Alloys and Compounds, 646 954-965, 2015.

INVESTIGATION OF BACTERIAL SYNTHESIZED COMPLEX CuZnSe NANOPARTICLES AND FABRICATION OF CuZnSe THIN FILM

T. Çakıcı[1], M. Özdal[2], M. Kundakçı[3]

[1]*Department of Electric and Energy, Ispir Hamza Polat Vocational High Scholl, Ataturk University, Erzurum, TURKEY*
[2]*Department of Biology, Faculty of Science, Ataturk University, Erzurum, TURKEY*
[3]*Department of Physics, Faculty of Science, Ataturk University, Erzurum, TURKEY*

E-mail: tuba.cakici@atauni.edu.tr

Abstract

Many different methods such as chemical, physical, and biological methods are used to synthesis nanoparticles. Among the different synthesis methods, using microorganisms for nanoparticles synthesis can be suitably scaled up for large-scale synthesis of nanoparticles.

In this research CuZnSe nanoparticles were synthesized by using selected special bacterium under dark conditions for the first time. The synthesized CuZnSe nanoparticles were characterized by transmission electron microscopy (TEM). Then their solution dropped on different substrates (glass and p-Si) and then they were dried at 65°C. Optical properties of the CuZnSe thin film was investigated by UV-Vis. Spectrophotometer method. Structural properties of CuZnSe thin film were characterized X-ray diffraction (XRD), Atomic force microscopy (AFM) and Field-emission scanning electron microscopy (FE-SEM) with energy dispersive X-ray spectroscopy (EDS) techniques. CuZnSe

Keywords: Bacterial synthesized, Complex nanoparticles, CuZnSe, Thin film

1. INTRODUCTION

Bacterial synthesis of nanoparticles is a green chemistry approach that non-toxic and economic. Among the bacteria, some special bacteria is unique to tolerate high chemical concentration [1-2].

Nowadays, nanoparticles (NPs) have a great interest due to their matchless physicochemical structures and photoluminescence, electronic, optical, and photocatalytic properties they have prominent potential applications in a wide variety fields such as nanotechnology, industry, electro-optics, optoelectronics, lasers, photovoltaic cells, light emitting diodes, and sensors [3]. Many researchers studied different nanoparticles produced from different materials and applied methods using different systems or chemical and physical, methods. These have performed the different methods used for the production of the nanoparticles are based on the chemical and physical processes in the literature [4-8]. However these processes have many disadvantages and difficulties such as non-ecofriendly, non-economical, non-cleanly, and toxicity and need highly advanced experimental instruments. Therefore, researchers focused on new methods that do not have the disadvantages mentioned above for the production of nanoparticles and considered the biological synthesizing method as a new method that will be an eco-friendly alternative candidate instead of these methods. Many researchers concentrate on studies involving biosynthesis methods for the production different types of nanoparticles [9] which have produced using bacteria [10], fungi [11], enzyme [12], and plant [13].

In this study, we focused on the production of complex CuZnSe nanoparticles via ecofriendly biosynthesizing method using a special bacterium for the first time. Also, these nanoparticles were also deposited as CuZnSe thin films on glass and p-Si substrates and performed their characterizations.

2. MATERIAL AND METHODS

Two different types of substrates (glass and p-Si) with sliced as 15mm×10mm pieces were prepared. These substrates were chemically cleaned separately. Firstly, p-Si substrates were cleaned as following; these substrates were decreased for 10 min, acetone, and methanol in an ultrasonic cleaner, consecutively and then etched in a sequence of $H_2O:H_2O_2:HNO_3$ (6:1:1) at 60°C, 20% HF, a solution of $H_2O:H_2O_2: HCl$ (6:1:1) at 60°C, 20% HF. The p-Si substrates were rinsed thoroughly in de-ionized water with a resistivity of 18 MΩ cm. After completing the cleaning of p-Si substrates, the glass substrates cleaned using piranha solution.

2.1. Production of complex CuZnSe nanoparticles

In order to obtain CuZnSe nanoparticles, the selected special bacterium was used. Pseudomonas sp. OG1 was cultured in the Tryptic Soya Broth for 24 h at 150 rpm and 30 °C. The cell suspension (100 μl, $OD_{600}1$) was inoculated into the Luria Bertani Broth medium (20 mL) containing 0.5 mM $CuSO_4$ + 0.5 mM $ZnSO_4$ + Na_2SeO_3. All the nanoparticles biosynthesis was conducted at 30 °C for a period of 96 h on rotating shaker (150 rpm) at dark conditions. Then nanoparticles were cleaned from the broth medium by using a procedure modified by Oremland et al. [14]. After this process, cleaned CuZnSe nanoparticles were suspended in deionized water. These nanoparticles characterized by using the TEM technique.

Solutions of CuZnSe nanoparticles were dropped and distributed homogeneously on p-Si and glass substrates (50cc solution) and they were dried on the hot plate at 75°C for 60 min. Thus, ZnSe and CuSe thin films were formed on p-Si and glass substrates.
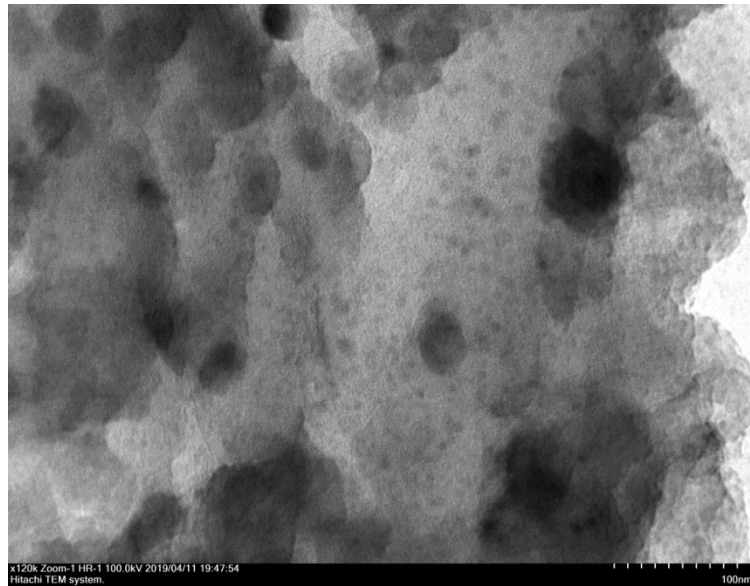
2.2. Characterization of CuZnSe thin film

The optical properties, crystal structures, surface morphology, and qualitative analysis of CuZnSe thin film were determined by using UV-VIS spectrometer (Perkin-Elmer Lambda 2S UV-Visible spectrometer and in these measurements CuZnSe thin film formed on glass substrates were used), X-rays diffractometer (XRD Bruker D2, $K_α$, λ=1.54 A, Scanning angle 70°), scanning electron (FE-SEM) (Sigma 300 Model Zeiss Gemini) and electron diffusion X-ray (EDX associated with FE-SEM), respectively.

3. RESULTS AND DISCUSSION

3.1. TEM results of CuZnSe nanoparticles

Fig. 1 shows TEM images of CuZnSe nanoparticles at the race of 100 nm. In Fig. 1, it can clearly see a uniform dispersion of CuZnSe nanoparticles with an average particle size of about 10–30 nm. Also in Fig.2, it can say a uniform dispersion of CuSe nanoparticles with an average particle size of about 20–45 nm.
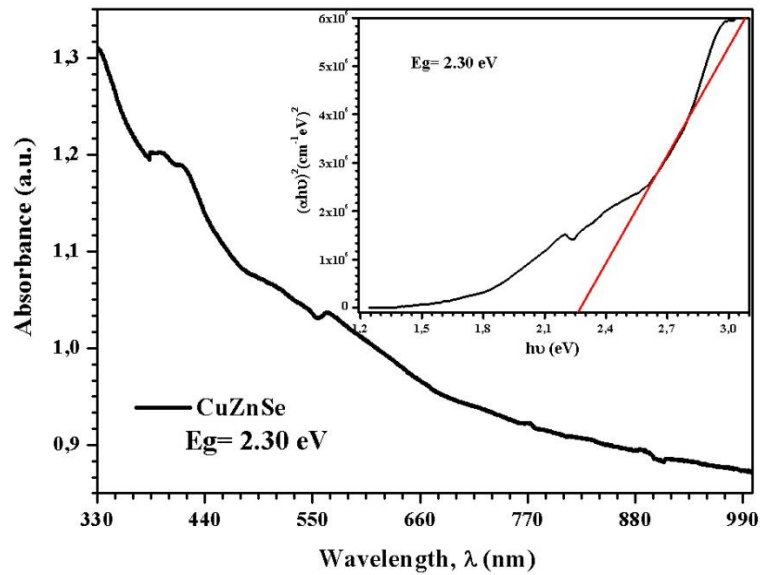
Figure 1. TEM image of complex CuZnSe nanoparticles

3.2. Optical and structural characterisation of CuZnSe thin film

As seen in Fig. 2, to calculate the energy band gap of CuZnSe thin film, absorption vs. wavelength and $(\alpha h\upsilon)^2$ vs. $h\upsilon$ graphs were plotted. The band gap energy of film has been determined as 2.30 eV by the extrapolation of the linear region on the energy axis ($h\upsilon$) set in Fig. 2. The optical band gap (Eg) values were determined from the commonly known equation:
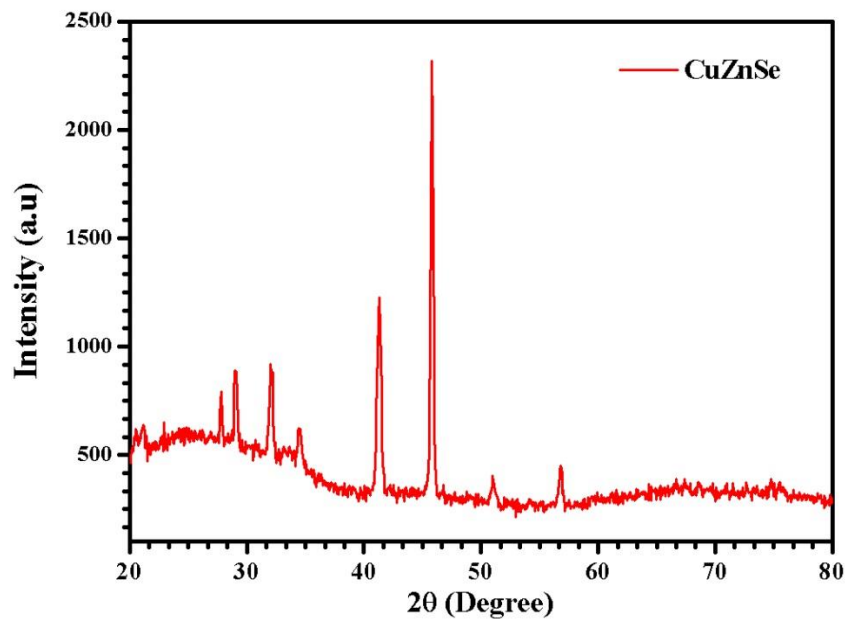
$$\alpha h\upsilon = B\,(h\upsilon - E_g)^n \tag{1}$$

where A is a constant related to the effective masses of charge carriers, h is the Planck constant, Eg is the band gap energy, hy is the incident photon energy, and n is the exponent that depends on the nature of the optical transition (n = 0.5 and 2 for direct and indirect transition, respectively) [15].

Figure 2. . Plots of αhυ)^2 vs. hυ and variation of optical absorbance versus the wavelength of incident photons of the CuZnSe thin film on the glass substrate

Fig. 3 shows the XRD pattern of an CuZnSe thin film deposited on the glass substrate. The six XRD peaks located at 2Θ angles, shown in Table 1, are clearly identified and matchwell with the JCPDS 00-021-1016 pattern corresponding to a tetragonal phase of CuZnSe thin film. It can be seen that the CuZnSe film is found to have polycrystalline nature and grown inthe tetragonal crystal structure with nano-cristallyn natüre.

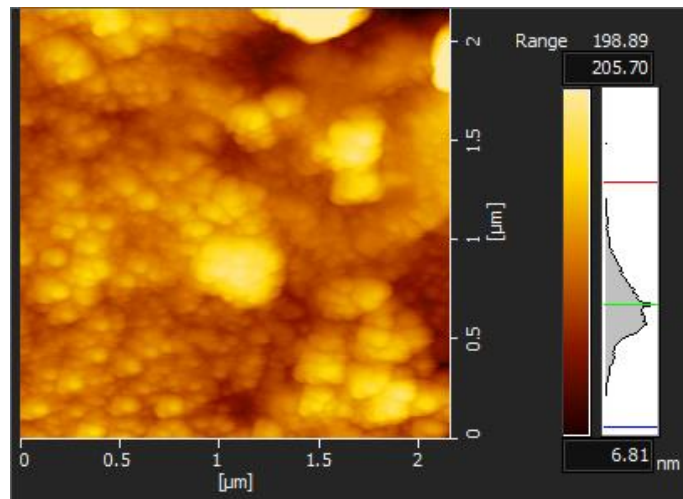**Figure 3.** .XRD pattern of CuZnSe thin film deposited on glass substrate

Table 2. XRD parameters of the CuZnSe thin film.

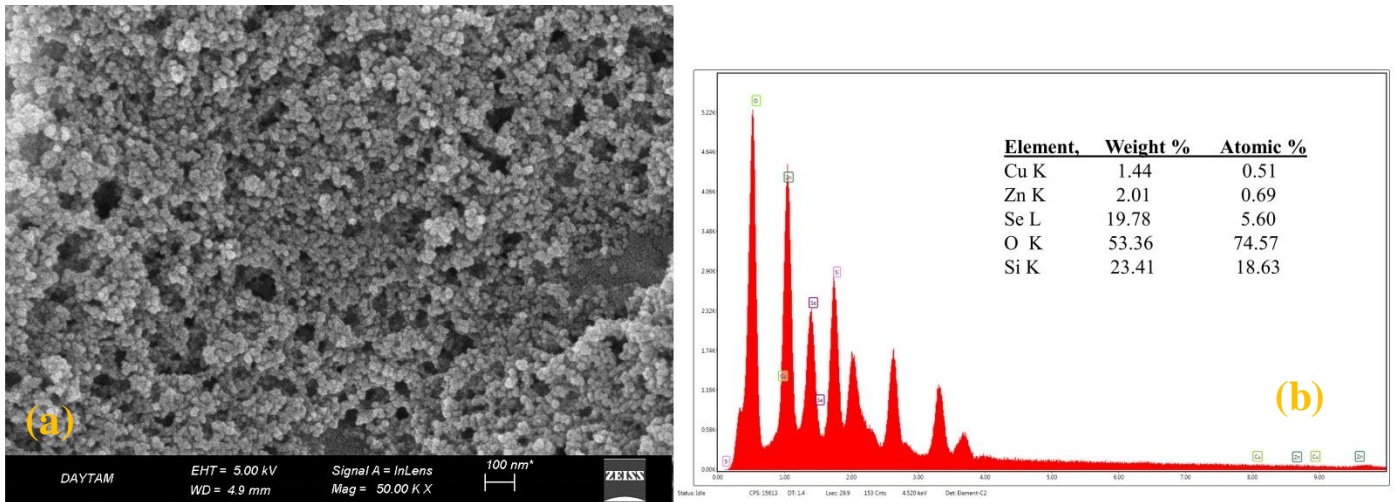| (hkl)	FWHM	Intensity (a.u.)	$2\theta^o$ (Observed)	d-values (nm)
(111)	0.1624	202.01	27.68	3.2269
(220)	0.2165	273.64	28.84	3.0959
(200)	0.1624	601.10	32.01	2.7963
(042)	0.3788	860.29	40.98	2.2023
(220)	0.2165	1902.29	45.74	1.9836
(222)	0.3960	119.20	56.75	1.6208

The one-dimensional cross section image (1D) of surface profile is plotted in Fig. 4 for CuZnSe thin film. As can be see that the granules of same scales exist in the film and are distributed evenly in same ranges. Also, the granules have relatively regular spherical shapes, sizes, and separations. The interconnected cylinder type grains are observed in Figure 4, such type of morphology may be employed in many optoelectronic devices.

Figure 4.. AFM image of CuZnSe thin film with scale 2μ×2μ

Fig. 5 (a) shows the FE-SEM image of prepared CuZnSe thin film, it can be observed that the CuZnSe thin film is uniform and cover the substrate well. In Fig. 5 (a), it is clear that the films were composed single type of small densely packed nanocrystals. The grains are well defined, spherical, of almost similar size, which were uniformly distributed. The average diameter of spherical particles is about 20-40 nm. XRD, AFM and

FESEM results are well-matched. It is determined that CuZnSe thin film has a high quality nanocrystalline structure Figure 5 (b) shows that EDX spectrum for the CuZnSe thin film, deposited on p-Si substrate

Element,	Weight %	Atomic %
Cu K	1.44	0.51
Zn K	2.01	0.69
Se L	19.78	5.60
O K	53.36	74.57
Si K	23.41	18.63

Figure 5. FE-SEM image and EDX spectrum of CuZnSe thin film (a) FE-SEM image with magnification scale (100nm) (b) EDX spectrum

4. CONCLUSION

CuZnSe complex nanoparticles are synthesized via bacterial green biosynthesis method for the first time and they have characterized by the TEM analysis method. CuZnSe complex nanoparticles size has determined of 20-45 nm range and these are deposited as thin films on glass and p type Si substrates at 75°C.

CuZnSe thin film properties were detailed investigated UV-Vis. Spectrophotometer method, XRD, AFM, FE-SEM with EDS techniques and these results showed that CuZnSe thin film were obtained successfully nanocrystalline nature and high quality. XRD graph indicates that CuZnSe thin films have polycrystalline structure. FE-SEM and AFM images revealed that the CuZnSe thin film has nano granular structure and the structures composed to expected elements checked with EDS.

ACKNOWLEDGMENTS

REFERENCES

[1] Hulkoti N. I., Taranath, T. C., Biosynthesis of nanoparticles using microbes—a review, Colloids and Surfaces B: Biointerfaces, 121, 474-483, 2014.

[2] Ocsoy, I., Tasdemir, D., Mazicioglu, S., Celik, C., Katı A., Ulgen, F., Biomolecules incorporated metallic nanoparticles synthesis and their biomedical applications, Materials Letters, 212, 45-50, 2018.

[3] Hasan, S., A Review on Nanoparticles: Their Synthesis and Types, Research Journal of Recent Sci. 1-3, 2277-2502, 2015

[4] Yang, G., Zhong, H., Liu, R., Li, Y., Zou, B., In Situ Aggregation of ZnSe Nanoparticles into Supraparticles: Shape Control and Doping Effects, Ameri. Chem. Soci., 29 (6), 1970–1976, 2013.

[5] Sobhani, A., Salavati-Niasari, M., Optimized synthesis of ZnSe nanocrystals by hydrothermal method, J. of Mater. Sci.: Materials in Elect. 27 (1), 293–303, 2016

[6] Wang, H. I., Tsung Tang, W., Liao, L. W., Tseng, P. S., Luo, C. W., Yang, C. S., Kobayashi, T., Femtosecond Laser-Induced Formation of Wurtzite Phase ZnSe Nanoparticles in Air, J. Nanomaterials, 278364, 2012.

[7] Chong, W. S. (2011). Synthesis and characterization of copper selenide nanoparticles via emulsion technique, (Doctoral dissertation, UTAR).

[8] Petrovic, M., Gilić, M., Ćirković, J., Romčević, M., Romčević, N., Trajić, J., Yahia, I., Optical Properties of CuSe Thin Films – Band Gap Determination, Sci. of Sint. 49 167-174, 2017.

[9] Mittal, A.K., Bhaumik, J., Kumar, S., Banerjee, U.C., Biosynthesis of silver nanoparticles: Elucidation of prospective mechanism and therapeutic potential, J. Colloid Interface, Sci. 415, 39–47, 2014.

[10] Singh, P., Kim, Y. J., Zhang, D., Yang, D. C., Biological synthesis of nanoparticles from plants and microorganisms, Trends in biotech. 34 (7), 588-599, 2016.

[11] Kitching, M., Ramani, M., Marsili, E., Fungal biosynthesis of gold nanoparticles: mechanism and scale up Microbial biotech., 8 (6), 904-917, 2015.

[12] Kumar, S. A., Abyaneh, M. K., W.Gosavi, S., Kulkarni, S. K., Pasricha, R., Ahmad, A., Khan, M. I., Nitrate reductase-mediated synthesis of silver nanoparticles from AgNO3. Biotech. letter., 29 (3) 439-445, 2007.

[13] Depuydt, J.M., Haase, M.A., Guha, Qiu, J., Cheng, H., Wu, B.J., Hofler, G.E., Meis-Haugen, G., Hagedorn, M.S., Baude, P.F., Room temperature II-VI lasers with 2.5 mA threshold, J. Cryst. Growth. 138 (1-4), 667-676.

[14] Oremland, R.S., Herbel, M.J., Switzer-Blum, J., Langley, S., Beveridge, T.J., Ajayan, P.M., Sutto, T., Ellis, A.V., Curran, S., Structural and spectral features of selenium nanospheres produced by Se-respiring bacteria. Applied and Environmental Microbiology, 70(1), 52-60, 2004.

[15] Çakıcı, T., Özdal,M., Kundakcı, M., Kayalı, R., ZnSe and CuSe NP's by microbial green synthesis method and comparison of I-V characteristics of Au/ZnSe/p-Si/Al and Au/CuSe/p-Si/Al structures Materials Science in Semiconductor Processing, 103, 104610, 2019.

THE EFFECT OF PEG-40S SURFACTANT CONCENTRATION ON THE STABILITY OF ALGINATE MICROBUBBLES PRODUCED BY T-SHAPED MICROFLUIDIC JUNCTION DEVICE METHOD

I.Kucuk

Institute of Nanotechnology, Gebze Technical University, Gebze, TURKEY

E-mail: i.kucuk@gtu.edu.tr

Abstract

Preparation of porous alginate films with a well-controlled architecture useful for tissue engineering is still a challenge. Here, T-shaped microfluidic junction device method is utilized to design highly monodispersed porous alginate scaffolds with a contribution of PEG-40S surfactant. The mechanism of pore formation is studied considering two factors affecting the pore size: i) stability of bubbles and ii) evaporation of solvent during the drying environment and time. Microbubble stability can achieve a control in determining coating surface morphology because the microbubbles often get destroyed during the drying process in coating formation. Optimizing the concentration of the surfactants on its shell layer is crucial for minimizing microbubble destruction. Presence of surfactants greatly influence the size and stability of the microbubbles and thus different surfactant concentrations and alginate polymeric solution concentrations were examined. This could potentially determine duration of microbubble destruction time and affect surface morphology of alginate film structures.

Keywords: Surfactant, Microbubbles, Microfluidics, Scaffolds

1. INTRODUCTION

Microbubbles have gained the great interest for their application in cosmetics, food, biomedical, and chemical industries [1-3]. Controllable size and size distribution of microbubbles plays a vital role to meet the demands of all of these applications [1, 4]. Precise control in space and time over the transport of fluids as well as their easy-going production enabled by microfluidics, making microfluidic techniques a highly promising production way for monodisperse microbubbles [5, 6].

Microbubbles may have the ability to generate new alternative materials and make them easier to use as scaffolds for photonics, microporous media, drug delivery and tissue engineering [7]. Microbubbles also have various other applications between bacteria and protein separation and contaminated water treatment [5, 8]. Microbubbles are widely used for the abovementioned applications because of their stability for enhanced mass transfer, the adsorption of particles at the microbubble interface, and their large interfacial area [1, 4]. Microfluidic devices play an important role to form such materials, enabling the desired level of control over the physical properties of them [9, 10].

Generation of microbubbles and enhancing the stability of the bubbles formed can be precisely controlled by using surfactants [4]. Surfactants are available to produce highly stable aqueous microbubble clusters when they are incorporated into the liquid phase. They may minimize an interfacial tension between the gas-liquid interface and influence on microchannel's internal surface characteristics to control whether it is hydrophilic or hydrophobic [11]. The physical characteristics of polymeric liquid phase depend upon surfactant material's concentration and molecular structure and both will influence bubble generation and play a vital role to indicate bubble stability. Changing the surfactant concentration can thus have a significant effect on microbubble behaviour as various surfactant concentrations have different characteristics. To achieve the demanded microbubble characteristics, the decision of surfactant concentration has thus a crucial role.

In the present study, microbubbles prepared by a T-shaped microfluidic junction device technique was used. In this work, the microbubble stability and bubble size and distribution investigation were performed to indicate the influence of varying surfactant concentrations in the microfluidic system constructed. It was observed that the larger diameter of microbubbles and most stable bubbles were obtained when an increase in surfactant concentration in a constant alginate aqueous solution at a constant feeding liquid's flow rate and gas pressure.

2. MATERIAL AND METHODS

An aqueous polymeric solution of sodium alginate (Sigma Aldrich, UK) was prepared to achieve 1 wt. % sodium alginate concentration. Polyoxyethylene glycol 40 stearate surfactant (PEG-40S purchased from Sigma Aldrich, UK)) was added to the aqueous 1 wt.% alginate solution in varying concentrations (0, 0.25, 0.50 and 0.75 wt. %) under vigorous stirring to facilitate bubble formation and investigate the effect of liquid surface tension and surfactant concentration on the size and stability of the bubbles produced. Nitrogen inert gas was used as the dispersed phase in the experimental work. Table 1 shows the physicochemical characteristic of the PEG-40S surfactant and properties of the different solutions.

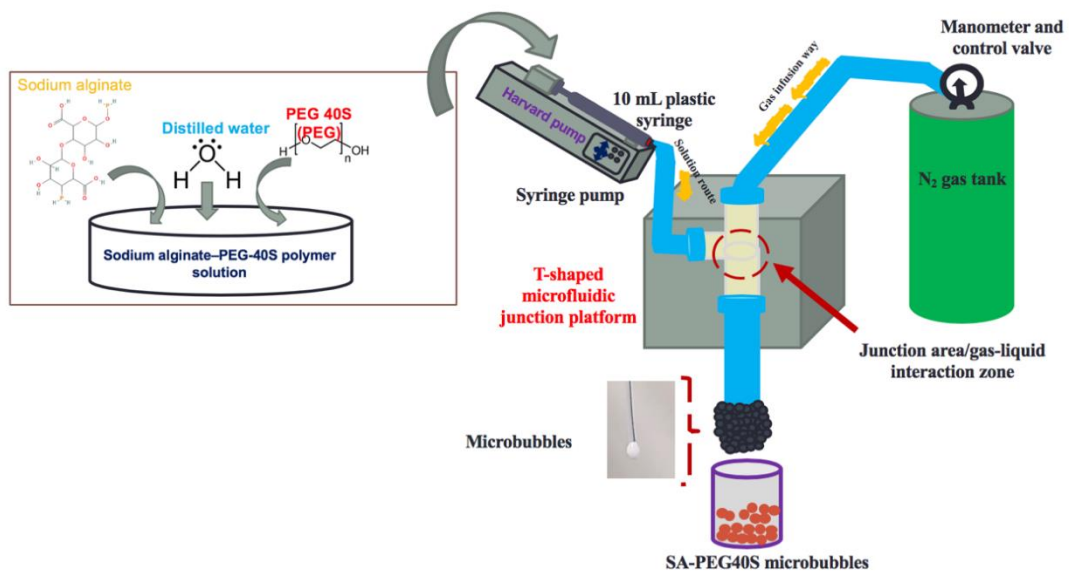**Table 1.** Physical properties of the solutions used in this experimental work at ~23 °C.

Solution ID	Polymer concentrations		Physical properties	
	Alginate (wt. %)	PEG-40S (wt. %)	Viscosity (mPa s)	Surface tension (mN/m)
1	1	-	12.4 ±0.03	70.7 ±0.80
2	1	0.25	14.6 ±0.03	56.3 ±0.40
3	1	0.50	15.1 ±0.03	53.8 ±0.20
4	1	0.75	16.3 ±0.03	51.5 ±0.30

Viscosity was measured using an Oswalt's U-tube viscometer (BS/E type, VWR, UK). The surface tension for the solutions prepared was measured with an error of ±0.03% using a One Attension Theta Lite System (Biolin Scientific, Gothenburg, Sweden). Calibration was carried out with pure water and ethanol. All the measurements, presented in Table 1, were carried out in triplicate under ambient conditions after calibrating the equipment using distilled water.

In order to investigate the resultant bubble size and size distribution, microbubbles were collected on microscope slides from the outlet of the device and immediately observed under an optical microscope (Zeiss Axio Imager M1m) fitted with a camera (Axiocam). Also, microbubbles were collected in vector test tubes to determine stability of the alginate-PEG-40S aqueous solutions with a change in surfactant concentrations.

The experiments were conducted using the T-shaped microfluidic junction device designed to generate microbubbles. The T-shaped microfluidic junction device details are shown in Figure 1. The device consisted of three teflon fluorinated ethylene polypropylene (FEP) capillaries embedded into a transparent

polydimethylsiloxane (PDMS) platform (100 × 100 × 10 mm) as inlet and outlet channels. The internal diameter for all of the capillaries was fixed at 100 μm. The top capillary (Inlet 1) was connected to a gas regulator fitted to a nitrogen gas tank via 6 mm diameter tubing, where the gas was supplied to the junction at constant pressure of 0.8 mbar. The liquid feeding capillary (Inlet 2) perpendicular to the capillary supplying air was connected to a 10 ml BD plastic syringe (Becton, Dickinson and Company, NJ, USA). A Harvard syringe pump Elite 11 (Harvard, Holliston MA, USA) was used to insert polymeric solution through the capillaries at a constant flow rate of 350 μl.min^{-1}. A third FEP capillary (Outlet) was fitted in the PDMS platform aligned with the gas inlet channel distance to create the junction where the two phases meet. All experiments were performed in triplicate wells for each set to confirm the reproducibility of the resultant bubbles with a mean diameter which was calculated to be approximately between 2 and 5%.
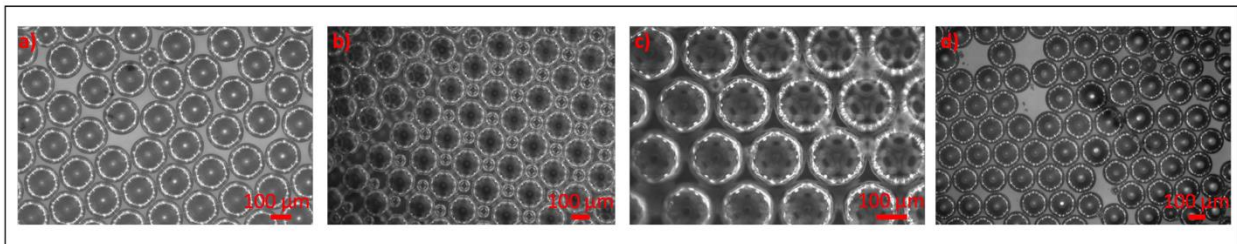

Figure 1. Schematic view of the T-shaped microfluidic junction microfluidic device setup to generate microbubbles in vector test tubes.

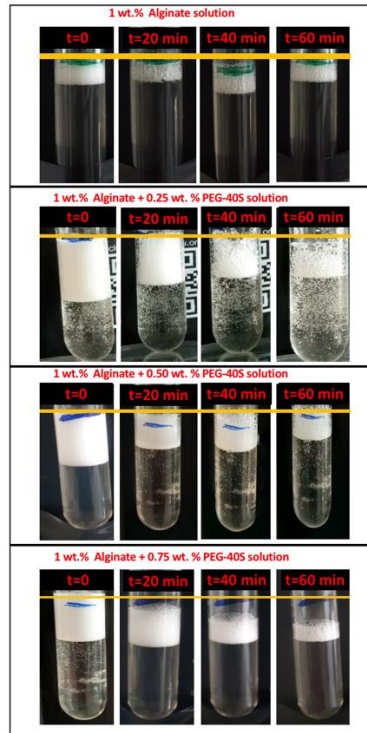## 3. RESULTS AND DISCUSSION

The effect of PEG-40S surfactant in 1 wt. % alginate aqueous polymer solution was investigated with concentrations of 0, 0.25, 0.50 and 0.75 wt. %. Bubble size distribution and mean diameter of the microbubbles collected were measured for surfactant's different concentrations are presented in Figure 2. The mean diameter values of the microbubbles obtained at 0 (Figure 2a), 0.25 (Figure 2b), 0.50 (Figure 2c) and 0.75 (Figure 2d) wt. % PEG-40S concentrations were approximately 150±6, 180±3, 189±6, and 190±5 μm, respectively. For the given PEG-40S surfactant concentrations at constant alginate concentration, gas pressure and polymeric

solution feeding rate, the bubbles produced with the solely alginate solution were generally the smallest, followed by the solution containing 0.25 wt. % PEG-40S. It was shown that for a given gas pressure, flow rate and low surfactant concentration smaller microbubbles were produced at higher surface tension and lower viscosity for the PEG-40S surfactant, while the higher surfactant concentration produced the largest bubbles due to lower surface tension and higher viscosity (Table 1). Previous studies conducted by Takagi S. et al. and Beneventi D. et al. indicated the effect that surfactants have on the dynamics of bubble formation by influencing the wettability of the channel surface, the dynamic adsorption of surfactant molecules on the liquid–solid and liquid–gas interfaces in the microchannels and the physical properties of the liquid phase [5, 8]. Wetting characteristics of the channel wall surface was found to be key factor in determining the size of microbubbles. The diameter and size distribution of microbubbles generated by a T-shaped microfluidic junction device may be depending on solution's physical properties, particularly surface tension and viscosity.

Figure 2. Changes of microbubble (mb) diameter as a function of the PEG-40S surfactant concentrations at both constant 0.8 bar N_2 gas pressure and 1 wt. % alginate aqueous polymer solution's 350 μl min^{-1} flow rate.

Microbubble stability length was observed as a function of time *via* digital camera imaging. Microbubbles from each sample collected in 1.5 cm length the vector test tubes (2 samples for concentrations) were studied and measured every 20 min for an hour. For the purpose of comparison, 1 wt. % concentration of alginate aqueous solution was set. As shown in Figure 3, microbubbles produced with solely 1 wt. % alginate solution was the least stable, and over the course of 60 minutes at the ambient temperature and flow rate and gas pressure, the size distribution of the bubbles broadened greatly bubble coalescence observed finally more bursting occurred was indicated. Microbubbles produced with both 0.5 and 0.75 wt. % PEG-40S surfactants were the most stable for 1 wt.% alginate aqueous solutions studied herein this study. Alginate solution with 0.75 wt.% PEG-40S surfactant had a lower surface tension then the other solutions used, and it produced the most stable large bubbles in this study. Previous studies conducted by Atta K. et al. and Stride E. et al. indicated the more closely packed the surface monolayer at the interface, the more the diffusion of the encapsulated gas into the surrounding is limited and therefore bubbles become more stable [6, 10].Thus, this could be attributed to steric stabilization by the non-ionic surfactant PEG-40S at the adjacent bubbles.

Figure 3. Vector test tube captures of microbubbles generated from 1 wt. % Alginate aqueous solution with PEG-40S surfactant in varying concentrations at time of collection, 20 mins, 40 mins and 60 mins after collection.

4. CONCLUSION

Investigation of the effect of the concentration of PEG-40S surfactant on the formation and stability of microbubbles using the T-shaped microfluidic junction device method was conducted. For all surfactant concentrations, significant changes in the bubble diameter and distribution, and stability were observed by increasing the concentration of the PEG-40S surfactant. It was noted that microbubbles produced with solutions containing the nonionic surfactant PEG-40S were generally larger, with 0.75 wt. % PEG-40S producing the largest bubble size of $\sim$190 μm for fixed alginate concentration and processing parameters. Analysis of microbubble stability was also performed and it was found that the solution containing 0.50 and 0.75 wt. % PEG-40S produced microbubbles that were highly stable, busting less bubbles (the length of the study). On the other hand, the microbubbles produced with solely 1 wt. % alginate were the least stable. Increasing the PEG-40S surfactant concentration did significantly change the microbubble stability.

ACKNOWLEDGMENTS

REFERENCES

[1] Parhizkar, M., Edirisinghe M., Stride E., The effect of surfactant type and concentration on the size and stability of microbubbles produced in a capillary embedded T-junction device, RSC Advances, 5, 14, 10751-10762, 2015.

[2] Davarcı, F., Turan, D., Ozcelik, B., Poncelet, D., The influence of solution viscosities and surface tension on calcium-alginate microbead formation using dripping technique, Food Hydrocolloids, 62, 119-127, 2017.

[3] Jung, J., Hu, J., Characterization of polyethylene oxide and sodium alginate for oil contaminated-sand remediation, Sustainability, 9, 1, 62, 2017.

[4] Azmin, M., Mohamedi, G., Edirisinghe, M., Stride, E., Dissolution of coated microbubbles: the effect of nanoparticles and surfactant concentration, Materials Science and Engineering: C, 32, 8, 2654-2658, 2012.

[5] Takagi, S., Matsumoto, Y., Surfactant effects on bubble motion and bubbly flows, Annual Review of Fluid Mechanics, 43, 615-636, 2011.

[6] Atta, K.R., Gavril, D., Loukopoulos, V., Karaiskakis, G., Study of the influence of surfactants on the transfer of gases into liquids by inverse gas chromatography, Journal of Chromatography A, 1023, 2, 287-296, 2004.

[7] Sergeeva, A., Feoktistova, N., Prokopovic, V., Gorin, D., Volodkin, D., Design of porous alginate hydrogels by sacrificial CaCO3 templates: Pore formation mechanism, Advanced Materials Interfaces, 2, 18, 1500386, 2015.

[8] Beneventi, D., Carre, B., Gandini, A., Role of surfactant structure on surface and foaming properties, Colloids and Surfaces A: Physicochemical and Engineering Aspects, 189, 1-3, 65-73, 2001.

[9] Stride, E. and Edirisinghe, M., Novel microbubble preparation technologies, Soft Matter, 4, 12, 2350-2359, 2008.

[10] Stride, E., The influence of surface adsorption on microbubble dynamics, Philosophical Transactions of the Royal Society A: Mathematical, Physical and Engineering Sciences, 366, 1873, 2103-2115, 2008.

[11] Owen, J., Kamila, S., Shrivastava, S., Carugo, D., Bernardino de la Serna, J., Mannaris, C., Pereno, V., Browning, R., Beguin, E., McHale, A.P., The Role of PEG-40-stearate in the production, morphology, and stability of microbubbles, Langmuir, 35, 31, 10014-10024, 2019.

COPPER(%1)@STARCH NANOPARTICLES: SYNTHESIS AND CATALYTIC ACTIVITY OF GREEN DEHYDROGENATION OF DIMETHYLAMINE BORANE

S. Duman

Department of Chemistry, Faculty of Arts and Sciences, Bingol University, Bingol, TURKEY

E-mail: sduman@bingol.edu.tr

Abstract

In the scope of this study, it has been investigated; (i) *in situ* synthesis of Cu(%1)@Starch nanoparticles (NPs) in the green (solventless) dehydrogenation of dimethylamine borane, (ii) effect of extensive kinetic data under stirring conditions depending on the substrate and catalyst concentrations to define the rate law of Cu(%1)@Starch NPs catalyzed dehydrogenation of DMAB at 35.0 ± 0.1°C, (iii) determination of activation parameters (E_a, $\Delta H^{\#}$ and $\Delta S^{\#}$) for Cu(%1)@Starch NPs catalyzed green dehydrogenation of DMAB; (iv) demonstration of the catalytic lifetime of Cu(%1)@Starch NPs in the green dehydrogenation of DMAB at 35.0 ± 0.1°C, (v) quantitative carbon disulfide (CS_2) poisoning experiments to find a corrected TTO and TOF values on a per-active-copper-atom basis, (vi) testing isolability and reusability of Cu(%1)@Starch NPs in the green dehydrogenation of DMAB at 35.0 ± 0.1°C.

Keywords: Copper, starch, heterogeneous, dimethylamine-borane, green dehydrogenation.

1. INTRODUCTION

Today's biggest and most important problems include the production and storage of green energy. Hydrogen is one of the most important alternative energy sources due to its properties. Nevertheless, difficulties remain with regard to the safe and efficient storage of hydrogen. For this purpose, studies on the economical, safe, effective, inexpensive and easy storage materials of hydrogen are continuing. Recently, ammonium borane and its derivatives are among the most preferred hydrogen materials owing to their simple handling, easy storage, low cost and high efficiency. Ammonium boranes (AB) or dimethylamine boranes (DMAB), methylamine boranes (MAB), hydrazine boranes (HB) have significant hydrogen content, but hydrogen production from these materials can be occurred in the presence of a suitable nano-catalyst. Nanocatalysts have high catalytic activities, highly stable structures, reusability, very small particle size, thus ensuring high efficiency in their reaction. To date, many different nanocatalysts / catalysts have been designed and used to expose hydrogen trapped in the structure of dimethylamine boranes [1,2,3,4,5].

In this study, a starch supported copper (Cu(%1)@Starch) nanoparticles (NPs) was prepared for dehydrogenation of DMAB. The catalytic activity of the prepared nanoparticles was also investigated for dehydrogenation of DMAB. As a result, it was observed that the Cu(%1)@Starch NPs had high catalytic performance.

2. MATERIAL AND METHODS

Copper(II) acetylacetonate (Cu(acac)$_2$), starch, dimethylamine-borane complex (DMAB, Me$_2$NHBH$_3$, 97%), 1,10-Phenanthroline ($\geq$99%) and hexane (99%) were purchased from Sigma-Aldrich®. All glassware and Teflon-coated magnetic stir bars were cleaned with acetone, followed by copious rinsing with distilled water before drying at 150ºC in oven for a few hours.

The experimental setup used for performing the dehydrogenation of DMAB borane under argon or nitrogen atmospheres and measuring the hydrogen gas generated from the reaction consists of a 50 mL jacketed reaction flask containing a Teflon-coated stir bar placed on a magnetic stirrer (IKA®RCT Basic) and thermostated by circulating water through its jacket from a constant temperature bath (RL6 LAUDA water bath). A graduated glass tube (50 cm in height and 2.5 cm in diameter) filled with water was connected to the reaction flask to measure the volume of the hydrogen gas to be evolved from the reaction. The temperature was also controlled via a thermocouple placed inside the reactor. Measuring the total turnover number (TTO)

was performed under argon or nitrogen atmospheres in a stirred reactor with a circulating water-bath for constant temperature control.

Before determining the catalytic activity of Cu(0) NPs in presence of starch in the dehydrogenation of DMAB, Reaction mixture was prepared as described above: In order to study the effect of starch concentration on the catalytic activity of copper nanoparticles in the dehydrogenation of DMAB (2.0 mmol), five sets of experiments were performed at 35.0 ± 0.1ºC by using copper nanoparticles prepared with different starch amounts (30-70 mg). All these tests were performed in the same conditions as described above with copper and DMAB concentrations kept constant (%Cu = 4.0, DMAB= 2.0 mmol in solvent-less medium) at 35.0 ± 0.1ºC. The good stability and the highest activity of copper nanoparticles in the dehydrogenation of DMAB were achieved at the starch amount 50 mg. Thus, 50 mg starch was selected for the further experiments.

In order to study the kinetics of dehydrogenation of DMAB catalyzed by Cu(%1)@Starch NPs, all reactions were performed in solvent-less medium in which DMAB (in the range of 1.0-3.0 mmol) and $Cu(acac)_2$ (in the percentage of 0.5-6.0%) (plus 50 mg of starch) are mixed. Then, all reactions were started by closing the reactor and turning on the stirrer at 1000 rpm simultaneously. The hydrogen generation was measured by recording the water level in graduated glass tube, which is connected to the reaction flask, in every 5 min.

Kinetics of the dehydrogenation of DMAB catalyzed by Cu(%1)@Starch NPs were studied depending on substrate concentration, catalyst concentration and the temperature. In a set of experiments, DMAB concentration was held constant at 2.0 mmol and $Cu(acac)_2$ percentage (plus 50 mg of starch) was varied in the range of 0.5-6.0% at $35.0.0 \pm 0.1$ºC. The hydrogen generation was measured for each set by recording the water level in graduated glass tube, which is connected to the reaction flask, in every 5 minutes. In the second set of experiments, $Cu(acac)_2$ percentage (plus 50 mg of starch) was held constant at 1.0%, while DMAB concentration was varied in the range of 1.0-3.0 mmol at $35.0.0 \pm 0.1$ºC. In the third set of experiments, the catalytic dehydrogenation of DMAB with $Cu(acac)_2$ percentage of 1.0% (plus 50 mg of starch) was performed by keeping DMAB concentration constant at 2.0 mmol at various temperatures in the range of 35-50ºC. The values of the observed rate constant k_{obs} were determined from the slope of the linear portion of the dehydrogenation curve used to obtain the activation energy E_a by using an Arrhenius plot [6]. The pressure versus time data was processed using Microsoft Office Excel 2010 and Origin 8.0 and then converted into the values in the proper unit, volume of hydrogen (mL).
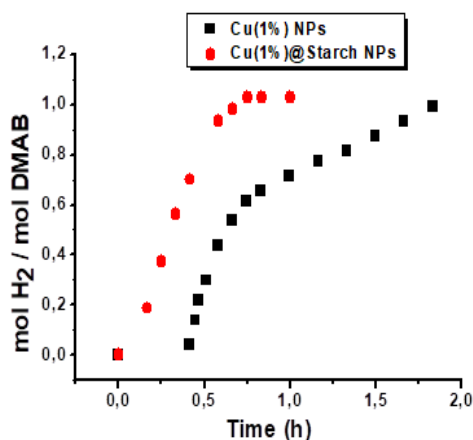
The catalytic lifetimes of Cu(%1)@Starch NPs in the dehydrogenation of DMAB were determined by measuring the total turnover number (TTO). Such a lifetime experiment was started with 1.0% copper plus 50 mg of starch and 10.0 mmol DMAB. When the complete conversion was achieved, more DMAB was added and the reaction was continued in this way until no hydrogen gas evolution was observed.

For poisoning experiment, copper nanoparticles plus 1,10-phenanthroline in the dehydrogenation of DMAB starting with Cu(%1)@Starch NPs was performed, as detailed above: A quantitative, predetermined amount of 1,10-phenanthroline [7] was added to solution after the 50% conversion. For this purpose, 0.1 equiv 1,10-phenanthroline per total copper was added for poisoning experiment. The catalytic activity was measured by monitoring the rate of hydrogen generation before and after the addition of 1,10-phenanthroline. When no more hydrogen generation was observed the experiment was stopped.

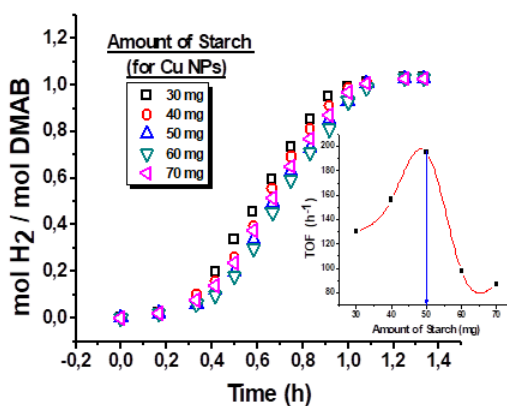## 3. RESULTS AND DISCUSSION

Cu(%1)@Starch NPs was synthesized in situ from the reduction of copper(II) acetylacetonate during the dehydrogenation of DMAB in solvent-less medium at $35.0 \pm 0.1°C$. Cu(%1)@Starch NPs was higher active and stable solution (no precipitation of copper from the solution was observed even after several weeks of storage) than Cu(0) NPs in absence of starch. Bulk metal formation was observed towards the end of dehydrogenation reaction for Cu(0) NPs in absence of starch and this result demonstrate that Cu(0) NPs in absence of starch were active but unstable. This behavior indicates the efficiency of starch in the stabilization of copper nanoparticles. Addition of starch as stabilizer to $Cu(acac)_2$ has been found to significantly increase the rate of the dehydrogenation reactions in all cases [8].

Copper nanoparticles are highly active catalyst in the dehydrogenation of DMAB; totally one equivalent of hydrogen gas per DMAB are generated at all catalyst concentration. The one equivalent of H_2 generation from DMAB is completed in ~1 h and 2 h from the dehydrogenation of DMAB catalyzed by copper nanoparticles in the presence and absence of starch, respectively (1.0wt% Cu). The initial turnover frequencies of catalytic dehydrogenation of DMAB catalyzed by copper nanoparticles in the presence and absence of starch were measured to be $51 \, h^{-1}$ and $25 \, h^{-1}$ at $35.0 \pm 0.1°C$, respectively (Figure 1).

Figure 1. Plots of equivalent H$_2$ per mole of DMAB versus time for the green dehydrogenation of DMAB in the presence of Cu(1%)@Starch (red circle) and Cu(1%) (black square)NPs at 35.0 ± 0.1°C.
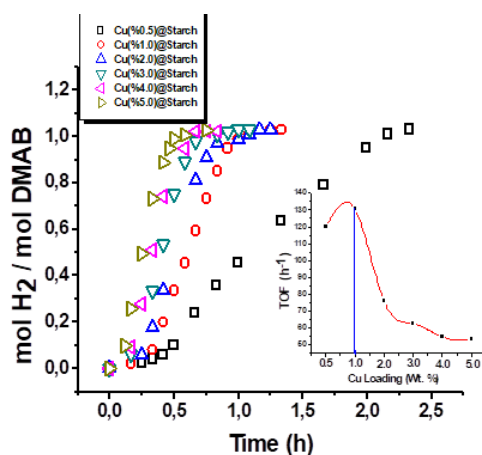
The next issue is to determine the optimum amount of starch for obtaining the highest catalytic activity and stability. In order to pick out the best starch amount in terms of activity to conduct the remainder of the study, we investigated the effect of starch amount on the catalytic activity by performing the catalytic dehydrogenation of DMAB ([DMAB] =2.0 mmol) with 30-70 mg starch at 35.0 ± 0.1°C. We observe that the TOF increases with the starch amount until the highest TOF value of 200 mol H$_2$ (Cu^{-1}h^{-1}) obtained for an amount of 50 mg but decreases for higher amount (Figure 2). However, as the starch amount increases, the nanoparticle surface is more covered by the stabilizer causing a significant decrease in the catalytic activity. In the present study, the maximum catalytic activity is achieved with the amount of 50 mg starch. Therefore, in all tests reported hereafter the catalyst prepared with amount of 50 mg starch is used, unless otherwise stated.

Figure 2. Plots of equivalent H$_2$ per mole of DMAB versus time (h) for the dehydrogenation of DMAB in the presence of Cu(1%)@Starch NPs (Inset shows TOF versus amount of starch in NPs).
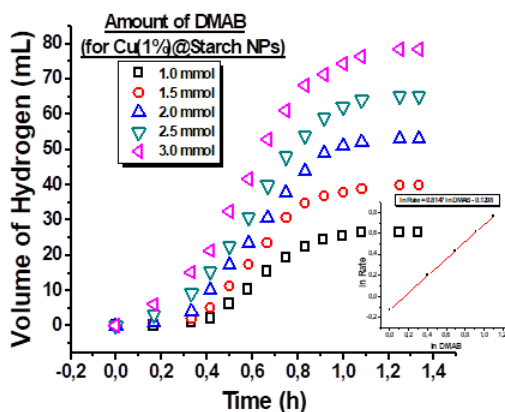
Kinetic studies in the dehydrogenation of DMAB catalyzed by Cu(1%)@Starch NPs were studied by monitoring hydrogen generation depending on catalyst concentration, substrate concentration and temperature. Catalytic activities of the systems Cu(1%)@Starch NPs in the dehydrogenation of DMAB show expectedly dependence on the copper concentration. Figure 3 depicts the plots of mole hydrogen per mole DMAB versus time during dehydrogenation of DMAB performed starting with constant substrate concentrations of 2.0 mmol and various percentage of $Cu(acac)_2$ in presence of 50 mg starch at $35.0 \pm 0.1°C$. After the induction time ($\square 25$ min), the rate of hydrogen generation, obtained from the slope of the linear portion of plots, increases with the increasing concentration of $Cu(acac)_2$ in presence of starch. Inset in Figure 3 shows the plot of TOF versus the initial loading of copper. We observe that the TOF increases with the loading of copper until the highest TOF value of 100 mol H_2 ($Cu^{-1}h^{-1}$) obtained for a percentage of 1% Cu but decreases for higher amount.

Figure 3. Plots of equivalent H_2 per mole of DMAB versus time (h) for the dehydrogenation of DMAB in the presence of Cu(1%)@Starch NPs (Inset shows TOF versus metal loadings in NPs).

The effect of substrate concentration on the hydrogen generation rate was also investigated by varying the concentration of DMAB (1.0-3.0 mmol) at constant copper percentage of 1.0% copper in presence 50 mg starch at $35.0\pm0.1°C$. The plots of initial rate of hydrogen generation versus DMAB concentration in the inset of Figure 4 gives straight line with slope of about 0.81. This indicates that dehydrogenation of DMAB is also first-order with respect to the substrate concentration.
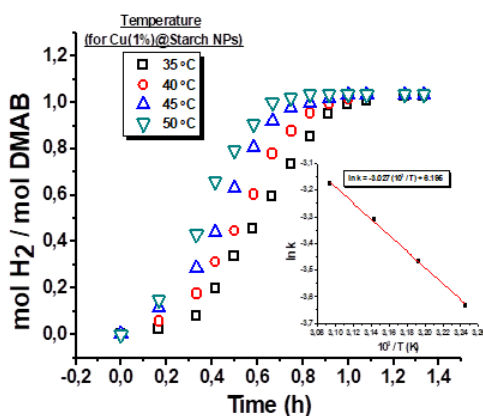
Figure 4. Plots of equivalent H$_2$ per mole of DMAB versus time (h) for the dehydrogenation of DMAB in the presence of Cu(1%)@Starch NPs (Inset shows initial ln rate versus ln DMAB).

Dehydrogenation of DMAB was carried out at various temperatures in the range 35-50°C starting with 2.0 mmol DMAB and 1.0% copper in presence of 50 mg starch. The values of the rate constant k were determined from the linear portion of the plots after induction period and used for the calculation of the activation parameters for the catalytic dehydrogenation of DMAB by using Arrhenius plot (inset in Figure 5). The Arrhenius activation energy is found to be Ea= 25 ± 2 kJmol^{-1}for the catalytic dehydrogenation of DMAB starting with 1.0% copper in presence of 50 mg starch.

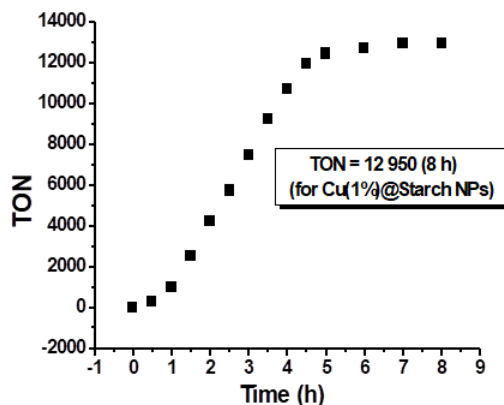**Figure 5.** Plots of equivalent H$_2$ per mole of DMAB versus time (h) for the dehydrogenation of DMAB in the presence of Cu(1%)@Starch NPs (Inset shows ln k versus 10^3/T (K), Arrhenius plots).

A catalyst lifetime experiments (starting with 1.0% Cu(0) NPs in the presence of 50 mg starch and 5.0 mmol of DMAB at 35.0±0.1°C) reveal record total turnover (TTO) values of 12,950 in the dehydrogenation
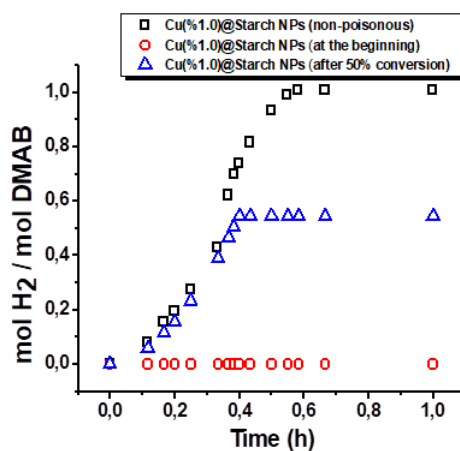
of DMAB over 8 h (Figure 6) before deactivation occurs due to aggregation into bulk copper. This TTO value is higher than the most of the catalysts.

Figure 6. Plot of turnover number versus time (h) for the dehydrogenation of DMAB in the presence of Cu(1%)@Starch NPs.

All poisoning experiments, 1,10-phenanthroline was added after ~50% of conversion was achieved to effect fully evolved sample of catalyst. It observed that the addition of 0.1 equiv of 1,10-phenanthroline per total copper did strongly slow the initial catalytic activity for Cu(1%)@Starch NPs (see Figure 7) [9]. To investigate the possibility of any homogeneous complex that can contribute to the observed activity in the dehydrogenation of DMAB was performed filtration experiments. For this aim, we filtered the reaction solution obtained after the formation of bulk copper through a micropore filter (200 nm) to remove any traces of bulk copper metal. Then, we tested the catalytic activity of the filtrate by the addition of fresh substrate in the dehydrogenation of DMAB, but we didn't observe any activity in the dehydrogenation of DMAB. This result shows that there is active heterogeneous catalyst under our reaction conditions.

Figure 7. The plots of mol H_2/mol DMAB versus time for 1,10-phenonethroline poisoning experiments starting with 2.0 mmol DMAB and Cu(1%)@Starch NPs at $35.0 \pm 0.1°C$; in absence of 1,10-phenonethroline; after the addition of 0.1 equiv. of 1,10-phenonethroline when 50% of conversion achieved; starting with 0.1 equiv 1,10-phenonethroline.

4. CONCLUSION

In summary, main findings of this work as well as implications or predictions can be summarized as follows:

(i) In this work, active, cheap and readily available metal catalyst like Cu(acac)$_2$ in the presence of 50 mg starch was used for the deydrogenation of DMAB at $35.0\pm0.1°C$. We found that dehydrogenation of DMAB catalyzed by Cu(0) NPs in absence of starch is very slow, with one equivalent of H_2 released in 2 h when more rapid H_2 loss in 1 h was observed from dehydrogenation of DMAB catalyzed by Cu(1%)@Starch NPs.

(ii) Kinetic studies on varying catalyst and substrate concentrations reveal that dehydrogenation of DMAB catalyzed by Cu(1%)@Starch NPs are first-order with respect to both catalysts and DMAB concentrations.

(iii) The temperature dependence of hydrogen generation rate from Cu(1%)@Starch NPs catalyzed dehydrogenation of DMAB was also investigated by performing these catalytic reactions at different temperatures. The activation parameter for Cu(1%)@Starch NPs is $E_a=25\pm2$ kJ mol^{-1}, indicate that Cu(1%)@Starch NPs catalyzed dehydrogenation of DMAB proceeds via an associative mechanism.

(iv) Moreover, the catalytic lifetime experiment showed that Cu(1%)@Starch NPs is the longest-lived catalyst with TON value of 12950 over 8 h before deactivation in the dehydrogenation of DMAB at $35.0\pm0.1°C$.

ACKNOWLEDGMENTS

REFERENCES

[1] Ozturk, Z., Sen, F., Sen, S., Gokagac, G., The preparation and characterization of nano-sized Pt–Pd/C catalysts and comparison of their superior catalytic activities for methanol and ethanol oxidation, Journal of Materials Science, 47, 8134-8144, 2012.

[2] Gratzel, M., Photoelectrochemical cells, Nature 414, 338-344, 2003.

[3] Jose, R., Thavasi, V., Ramakrishna, S., Metal oxides for dye- sensitized solar cells, Journal of the American Ceramic Society, 92, 289-301, 2009.

[4] Zhu, R., Jiang, C.Y., Liu, B., Ramakrishna, S., Highly efficient nanoporous TiO_2- polythiophene hybrid solar cells based on interfacial modification using a metal- free organic dye, Advanced Materials, 21, 994-1000, 2009.

[5] Liu, X.Z., Zhang, W., Uchida, S., Cai, L.P., Liu, B., Ramakrishna, S., An efficient organic- dye-sensitized solar cell with in situ polymerized poly (3, 4- ethylenedioxythiophene) as a hole- transporting material, Advanced Materials, 22, 150-155, 2010.

[6] Laidler, K.J., Chemical Kinetics, 3rd edn, Benjamin-Cummings UK, 1997.

[7] Zahmakıran, M., Philippot, K., Ozkar, S., Chaudret, B., Size-controllable APTS stabilized ruthenium(0) nanoparticles catalyst for the dehydrogenation of dimethylamine–borane at room temperature, Dalton Transactions, 41, 590-598, 2012.

[8] Özkar, S, Finke, R.G., Nanocluster formation and stabilization fundamental studies: Ranking commonly employed anionic stabilizers via the development, then application, of five comparative criteria, Journal of the American Chemical Society, 124, 5796-5810, 2002.

[9] Lin, Y., Finke, R.G., A more general approach to distinguishing "Homogeneous" from "Heterogeneous" catalysis: Discovery of polyoxoanion- and Bu4N+-stabilized, ısolable and redissolvable, high-reactivity Ir.apprx.190-450 nanocluster catalysts, Inorganic Chemistry, 33, 4891-4910, 1994.

CATALYTIC ACTIVITY OF GREEN DEHYDROGENATION OF DIMETHYLAMINE BORANE BY CATALYZED RUTHENIUM(4%)@CELLULOSE NANOPARTICLES

S. Duman

Department of Chemistry, Faculty of Arts and Sciences, Bingol University, Bingol, TURKEY

E-mail: sduman@bingol.edu.tr

Abstract

Ru(4%)@Cellulose nanoparticles which was isolated after finishing the catalytic dehydrogenation of dimethylamine-borane starting with Ru(acac)$_3$ and cellulose compounds, were used as catalyst and tested for dehydrogenation of dimethylamine borane. Kinetics of dehydrogenation of dimethylamine borane catalyzed by Ru(4%)@Cellulose nanoparticles were studied depending on catalyst concentration, substrate concentration and temperature. The experimental results demonstrated that hydrogen release rate from Ru(4%)@Cellulose nanoparticles (TOF=122.56 mol H$_2$/(molRu*h)) in the dehydrogenation of dimethylamine borane is over 3 times higher than from sole Ru(acac)$_3$ (TOF=44.91 mol H$_2$/(molRu*h)). Similarly, deactivation studies carried out both at constant temperature (35.0 $\pm$ 0.1 °C) and in retardation experiments, reveal that Ru(4%)@Cellulose nanoparticles is the most stable catalyst. To determine whether the dehydrogenation of dimethylamine borane catalyzed by Ru(4%)@Cellulose nanoparticles is homogeneous or heterogeneous, poisoning experiments were performed and observed that this nanoparticles were heterogeneous catalyst in the dehydrogenation of dimethylamine borane.

Keywords: Ruthenium, cellulose, heterogeneous, dimethylamine borane, green dehydrogenation.

1. INTRODUCTION

Hydrogen has been considered as one of the best alternative energy carriers to satisfy the increasing demand for an efficient and clean energy supply because of its abundance, high-energy density, and environmental friendliness. Various materials such as metal hydrides [1], carbon based materials (carbon nanotubes, graphene) [2], metal organic frameworks [3] are under investigation as hydrogen storage materials. However, the gravimetric hydrogen storage of most of these materials is less than the U. S. Department of Energy (DOE) target (2015) of 9 wt%. B-N compounds are attracting more attention in recent times because of their larger hydrogen content [4]. Containing both protic N-H and hydridic B-H hydrogen within the same molecule, dimethylamine borane appears ripe for dehydrogenation. Chemical hydrogen storage, wherein hydrogen is stored in a chemical compound and released via a reversible chemical reaction, is a promising strategy [3, 4]. However, efficient and reversible H_2 release from dehydrogenation of dimethylamine borane requires a suitable catalyst [5, 6]. Many transition metals can catalyse the dehydrogenation of dimethylamine borane [7]. [(1-Methylborabenzene)$_2$YR] [8], [Ir(1,5-cod)(μ-Cl)]$_2$ [9], [Rh(1,5-cod)(μ-Cl)]$_2$ [10], Rh(0)/[N(oct)$_4$]Cl [11], RhCl$_3$ [9], [RhCl(PHCy$_2$)$_3$] [12], Rh(0) Nanoclusters [13], [Ru(H)(PMe$_3$)(N(C$_2$H$_4$P^{i}Pr$_2$)$_2$] [11], Ru(0) NPs /OAm [14], Ru(0) NPs /APTS [15], Pd(0) NPs /MOF [16], Pt(0) NPs /TBA [17], Pt(0) NPs/AA [18], Pt(0) NPs/DPA@GO [19], [ReBr$_2$(NO)(P^{i}Pr$_3$)$_2$(CH$_3$CN)] [20], Cp$_2$Ti [21,22], [η^5-C$_5$H$_3$-1,3-(SiMe$_3$)$_2$Ti]$_2$ [**Hata! Yer işareti tanımlanmamış.**], Ni(0) [23], Ru@PVP, Ru@PS-co-MA and Ru@Al$_2$O$_3$ nanoparticles (NPs) [24]. However, in literature, first time, we reported concerning the use of cellulose as a stabilizing agent for heterogeneous catalysis leading to adsorption of cellulose to metal.

Herein, for the first time, we report the use of cellulose as adsorption agent in catalytic dehydrogenation of dimethylamine borane starting with Ru(acac)$_3$ which lead to formation of a novel ruthenium heterogeneous catalyst containing cellulose natural polymer, Ruthenium(4%)@Cellulose nanoparticles. Besides, it is aimed with this study that generation of hydrogen from suitable solventless catalytic dehydrogenation of dimethylamine borane to green synthesis principles using simple mechanical stirring technique, definition of many parameters (ratio of amine borane/catalyst, catalytic activity, temperature, time, activation energy, reusability, TOF etc) of active Ruthenium(4%)@Cellulose nanoparticles as catalyst.

2. MATERIAL AND METHODS

Ruthenium(III) acetylacetonate (97%), cellulose, dimethylamine borane complex (97%) were purchased from Sigma-Aldrich®. All glassware and Teflon-coated magnetic stir bars were cleaned with acetone, followed by copious rinsing with distilled water before drying at 150 ºC in oven for a few hours.

The experimental setup used for performing the dehydrogenation of dimethylamine borane was performed under argon or nitrogen atmospheres and measuring the hydrogen gas generated from the reaction consists of a 50 mL jacketed reaction flask containing a Teflon-coated stir bar placed on a magnetic stirrer (IKA® RCT Basic) and thermostated to 35.0 ± 0.1 ºC by circulating water through its jacket from a constant temperature bath (RL6 LAUDA water bath). A graduated glass tube (50 cm in height and 2.5 cm in diameter) filled with water was connected to the reaction flask to measure the volume of the hydrogen gas to be evolved from the reaction. Measuring the total turnover number (TTO) was performed under argon or nitrogen atmospheres with a circulating water-bath for constant temperature control. The temperature was also controlled via a thermocouple placed inside the reactor.

Kinetics of the dehydrogenation of dimethylamine borane catalyzed by Ruthenium(4%)@Cellulose nanoparticles was studied depending on substrate concentration, catalyst concentration and the temperature. In a set of experiments, dimethylamine borane concentration was held constant at 2.0 mmol and $Ru(acac)_3$ concentration was varied in the range of 1.0%-5.0% at 35.0 ± 0.1ºC. The hydrogen generation was measured for each set by recording the water level in graduated glass tube, which is connected to the reaction flask, in every 5 minutes. In the second set of experiments, $Ru(acac)_3$ concentration was held constant at 4%, while dimethylamine borane concentration was varied in the range of 1.0-3.0 mmol at 35.0 ± 0.1ºC. In the third set of experiments, the catalytic dehydrogenation of dimethylamine borane with $Ru(acac)_3$ concentration of 4% was performed by keeping dimethylamine borane concentration constant at 2.0 mmol, at various temperatures in the range of 35-50ºC in order to obtain the activation energy (E_a), enthalpy of activation ($\Delta H^{\#}$) and entropy of activation ($\Delta S^{\#}$). The pressure versus time data was processed using Microsoft Office Excel 2003 and Origin 7.0 and then converted into the values in the proper unit, volume of hydrogen (mL).

The catalytic lifetime of Ruthenium(4%)@Cellulose nanoparticles in the dehydrogenation of dimethylamine borane was determined by measuring the total turnover number (TTO). Such a lifetime experiment was started with 4% mM $Ru(acac)_3$ on 50 mg cellulose and 2.0 mmol dimethylamine borane at 35.0 ± 0.1ºC. When the complete conversion is achieved, more dimethylamine borane was added and the reaction was continued in this way until no hydrogen gas evolution was observed.
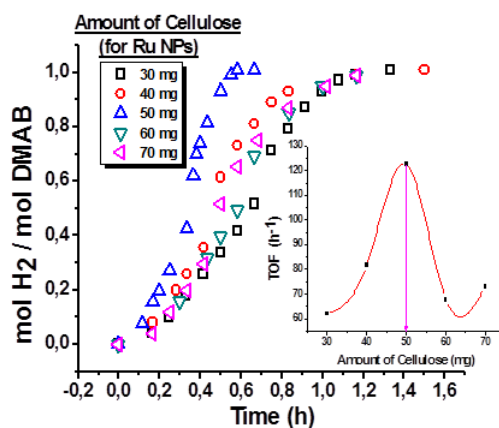
To determine whether the dehydrogenation of dimethylamine borane catalyzed by Ruthenium(4%)@Cellulose nanoparticles is homogeneous or heterogeneous, 1,10-phenonthroline poisoning experiments were performed [25]. To the reaction solution started with dimethylamine borane and Ruthenium(4%)@Cellulose nanoparticles were added 3.0 equivalent of 1,10-phenonthroline per ruthenium after the 50% conversion and at the beginning. The hydrogen generation rates were not changed after the addition of 1,10-phenonthroline, indicating that these reactions are indeed a heterogeneous catalysis.
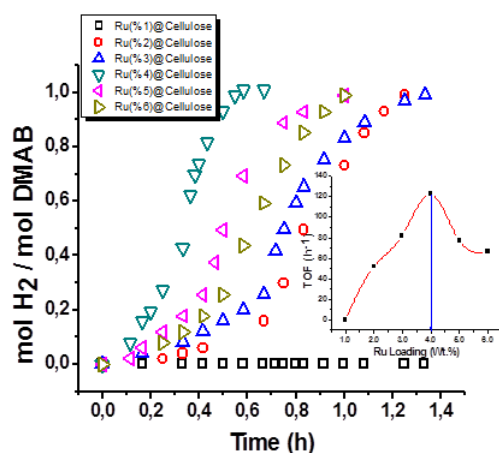
3. RESULTS AND DISCUSSION

A recent study [**Hata! Yer işareti tanımlanmamış.**] has shown that ruthenium(III) acetylacetonate acts as heterogeneous catalyst at near room temperature in the dehydrogenation of dimethylamine borane in presence of Polyvinylpyrrolidone (PVP), polystyrene co maleic anhydride (PS-co-MA) and alumina (Al_2O_3). Comparable to the dehydrogenation of dimethylamine borane, catalytic activities of these in-situ ruthenium nanocatalysts containing polymer, Ru@PVP, Ru@PS-co-MA and Ru@Al_2O_3 NPs, are higher than sole Ru(acac)$_3$ and for that reason we decided to test other suitable stabilizing agents such as natural polymer cellulose to see whether there is any possibility to be adsorbed cellulose to ruthenium and evaluate the potential effect on the catalytic activity of stabilized ruthenium catalyst by cellulose.

Before starting the kinetic studies with Ru(acac)$_3$ and cellulose system, one question needed to be addressed regarding the effect of varying amount of cellulose per ruthenium on the rate enhancement of hydrogen evolution. In order to answer this question, a series of experiments were performed starting with 2.0 mmol of dimethylamine borane, 4% Ru(acac)$_3$ and different concentrations of cellulose in the range of 30-70 mg at 35.0 ± 0.1°C (Figure 1). The rate of hydrogen generation obtained from the linear portion of curves is plotted against the amount of cellulose to TOF (inset of Figure 1). However, 50 mg of cellulose was used for further experiments concerning the kinetic study.
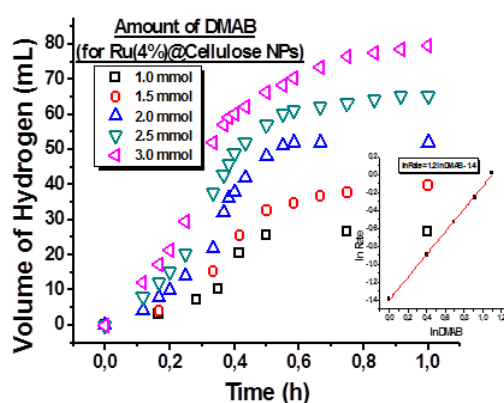
Figure 1. Plots of equivalent H_2 per mole of dimethylamine borane versus time (h) for the dehydrogenation of dimethylamine borane in the presence of Ru(4%)@Cellulose (Inset shows TOF versus amount of cellulose in NPs).

Kinetics of the dehydrogenation of dimethylamine borane in the presence of Ruthenium(4%)@Cellulose NPs was studied by monitoring hydrogen generation depending on catalyst concentration, substrate concentration and temperature. Figure 2 shows the volume of hydrogen versus time plots during dehydrogenation of dimethylamine borane (2.0 mmol) catalyzed by Ru(acac)$_3$ plus 50 mg cellulose in different ruthenium percentages at $35.0 \pm 0.1°C$. After the induction time (~15 min.), the rate of hydrogen generation, obtained from the slope of the linear portion of plots, increases with the increasing concentration of Ru(acac)$_3$ up to 6% shown in the inset of Figure 2. Accordingly, hydrogen evolution rate shows first-order dependency on the ruthenium concentration (in the range of 1-6%).
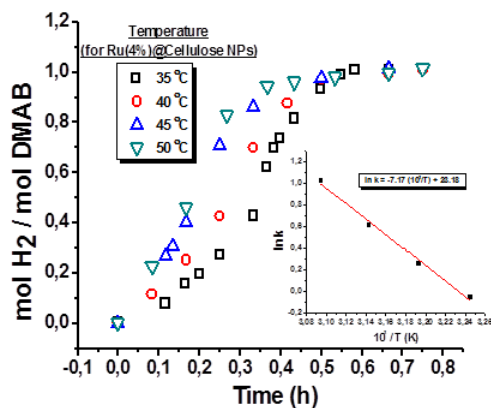

Figure 2. Plots of equivalent H_2 per mole of dimethylamine borane versus time (h) for the dehydrogenation of dimethylamine borane in the presence of Ru(4%)@Cellulose NPs (Inset shows TOF versus metal loading in NPs).

The effect of substrate concentration on the hydrogen generation rate was determined by varying the concentration of dimethylamine borane at constant ruthenium percent of 4% presence of 50 mg cellulose and temperature of $35.0 \pm 0.1°C$ based on Figures 3. The plot of hydrogen generation rate versus dimethylamine borane concentration in inset of Figure 3 gives a straight line with a slope of about 1.2. This indicates that dehydrogenation of dimethylamine borane is first order with respect to the substrate concentration, at least in the range of 1.0-3.0 mmol dimethylamine borane, in the presence of 4% ruthenium and 50 mg cellulose.
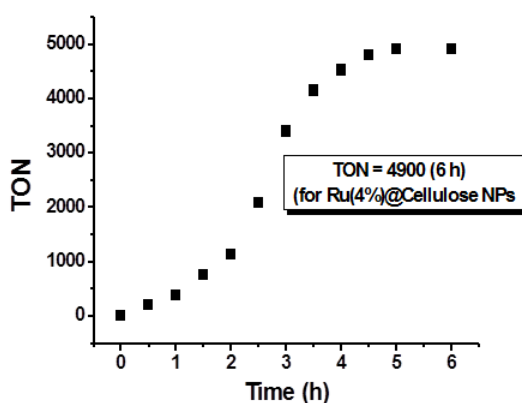

Figure 3. Plots of equivalent H_2 per mole of dimethylamine borane versus time (h) for the dehydrogenation of dimethylamine borane in the presence of Ru(4%)@Cellulose NPs (Inset shows TOF versus amount of DMAB).

Dehydrogenation of dimethylamine borane was carried out at various temperatures in the range of 35 to $50.0 \pm 0.1°C$ starting with 2.0 mmol dimethylamine borane and 4% Ru(acac)$_3$ in presence of 50 mg cellullose based on Figures 4. After the induction time, the values of the rate constant k were determined from the linear part of the plots considering the rate dependency on ruthenium or substrate concentration at four different temperatures in order to attain the activation parameters for the catalytic dehydrogenation of dimethylamine borane by using Arrhenius plot (inset of Figure 4). The Arrhenius activation energy was found to be 43 ± 2 kJ.mol^{-1} for the catalytic dehydrogenation of dimethylamine borane starting with 4% Ru(acac)$_3$.

Figure 4. Plots of equivalent H_2 per mole of dimethylamine borane versus time (h) for the dehydrogenation of dimethylamine borane in the presence of Ru(4%)@Cellulose NPs (Inset shows ln k versus $10^3/T$ (K), Arrhenius plots).

The system comprising Ru(acac)$_3$ and cellulose appears to be stable and long-lived catalyst in dehydrogenation of dimethylamine borane. Lifetime of the catalyst was measured by determining the total turnover number (TTO) in hydrogen generation from dehydrogenation of dimethylamine borane at $35.0 \pm 0.1°C$ as observed in Figure 5. The TTO value and the higher value of initial turnover frequency (TOF) for the active catalyst Ru(4%)@Cellulose NPs are 4900 (over 6 h) and 122.56 mol H_2/(molRu*h), respectively, in dehydrogenation of dimethylamine borane at $35.0 \pm 0.1°C$.
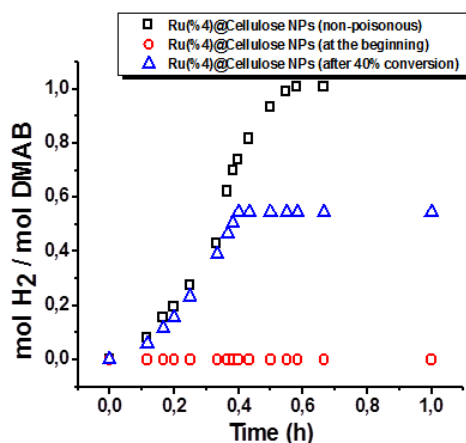

Figure 5. Plot of turnover number versus time (h) for the dehydrogenation of dimethylamine borane in the presence of Ru(4%)@Cellulose NPs.

1,10-phenonthroline poisoning experiment was performed in order to show whether the catalytic dehydrogenation of dimethylamine borane starting with Ru(4%)@Cellulose NPs is homogeneous or

heterogeneous [**Hata! Yer işareti tanımlanmamış.**]. The hydrogen generation rate in the system active catalyst, Ru(4%)@Cellulose, was stopped by the addition of 0.1 equivalent of 1,10-phenonthroline to the reaction solution after 50% conversion of dimethylamine borane and at the beginning of reaction. This observation indicates that the catalytic reaction is heterogeneous (Figure 6).

Figure 6. The plots of mol H_2/mol dimethylamine borane versus time for 1,10-phenonethroline poisoning experiments starting with 2.0 mmol dimethylamine borane catalyzed by Ru(4%)@Cellulose NPs at $35.0 \pm 0.1°C$; in absence of 1,10-phenonethroline; after the addition of 0.1 equiv. of 1,10-phenonethroline when 50% of conversion achieved; starting with 0.1 equiv 1,10-phenonethroline.

4. CONCLUSION

In summary, our study on ruthenium(III) acetylacetonate pre-catalyst and ruthenium(III) acetylacetonate plus cellulose natural polymer in dehydrogenation of dimethylamine borane leads to the following conclusions and insights, some of which were previously unavailable: (*i*) Similar to the dehydrogenation of dimethylamine borane catalyzed by Ru(acac)$_3$ and cellulose, Ru(4%)@Cellulose NPs, was isolated after catalytic dehydrogenation of dimethylamine borane starting with Ru(acac)$_3$ and cellullose. (*ii*) Ru(4%)@Cellulose NPs is formed in-situ during catalytic dehydrogenation of dimethylamine borane, has higher catalytic activity in comparison with Ru(acac)$_3$ alone. (*iii*) Ru(4%)@Cellulose NPs is a very long-lived catalyst providing a total turnover number of 4900 over 6 hours. (*iv*) Dehydrogenation of dimethylamine borane catalyzed by Ru(4%)@Cellulose NPs, is first order regarding ruthenium concentration and first order with respect to substrate concentration. (*v*) It is clearly seen that the reaction is entirely ceased upon addition of 0.1 equiv. 1,10-phenanthroline per mole of ruthenium catalyst in a very short time which indicates that the

dehydrogenation of dimethylamine borane catalyzed by Ruthenium nanoparticles supported on natural polymer is indeed heterogeneous catalysis.

ACKNOWLEDGMENTS

REFERENCES

[1] Jaska, C.A., Clark, T.J., Clendenning, S.B., Grozea, D., Turak, A., Lu, Z-H., Manners I., Poisoning of heterogeneous, late transition metal dehydrocoupling catalysts by boranes and other group 13 hydrides, Journal of the American Chemical Society, 127, 5116-5124, 2005.

[2] Jaska, C.A., Manners, I., Heterogeneous or homogeneous catalysis? Mechanistic studies of the rhodium-catalyzed dehydrocoupling of amine-borane and phosphine-borane adducts, Journal of the American Chemical Society, 126, 9776-9785, 2004.

[3] Jaska, C.A., Manners, I., Ambient temperature, tandem catalytic dehydrocoupling−hydrogenation reactions using Rh colloids and $Me_2NH·BH_3$ as a stoichiometric H_2 source, Journal of the American Chemical Society, 126, 2698-2699, 2004.

[4] US Department of Energy (DOE). Basic research needs for the hydrogen economy, report of the basic energy sciences workshop on hydrogen production, storage and use. https://www.energy.gov/, 2015.

[5] Pun, D. Lobkovsky, E., Chirik, P.J., Amine borane dehydrogenation promoted by isolable zirconium sandwich, titanium sandwich and N_2 complexes, Chemical Communications, 3297-3299, 2007.

[6] Turner, J., Sverdrup, G., Mann, M.K., Maness, P.G., Kroposki, B., Ghirardi, M., Evans, R.J., Blake, D., Renewable hydrogen production. International Journal of Energy Research, 32, 379-407, 2008.

[7] Ozkar, S., Transition metal nanoparticles as catalyst in hydrogen generation from the boron based hydrogen storage materials, in: S. L. Suib (Ed.), New and Future Developments in Catalysis. Batteries, Hydrogen Storage and Fuel Cells, Elsevier, 165 (Chapter 7), 2013.

[8] Lu, E., Yuan, Y., Chen, Y., Xia, W., 1-Methyl boratabenzene yttrium alkyl: A highly active catalyst for dehydrocoupling of $Me_2NH·BH_3$, ACS Catalysis, 3, 521-524, 2013.

[9] Jaska, C.A., Temple, K., Lough, A.J., Manners, I., Transition metal-catalyzed formation of boron-nitrogen bonds: catalytic dehydrocoupling of amine-borane adducts to form aminoboranes and borazines, Journal of the American Chemical Society, 125, 9424-9434, 2003.

[10] Jaska, C.A., Temple, K., Lough, A.J., Manners, I., Rhodium-catalyzed formation of boron–nitrogen bonds: a mild route to cyclic aminoboranes and borazines, Chemical Communications, 11, 962-963, 2001.

[11] Friedrich, A., Drees, M., Schneider, S., Ruthenium- catalyzed dimethylamineborane dehydrogenation: stepwise metal- centered dehydrocyclization, Chemistry – A European Journal, 15, 10339-10342, 2009.

[12] Sloan, M., Clark, T.J., Manners, I., Homogeneous catalytic dehydrogenation/dehydrocoupling of amine-borane adducts by the Rh(I) Wilkinson's complex analogue $RhCl(PHCy_2)_3$ (Cy = cyclohexyl), Inorganic Chemistry, 48, 2429-2435, 2009.

[13] Zahmakiran, M., Ozkar, S., Dimethylammonium hexanoate stabilized Rhodium(0) nanoclusters identified as true heterogeneous catalysts with the highest observed activity in the dehydrogenation of dimethylamine−borane, Inorganic Chemistry, 48, 8955-8964, 2009.

[14] Duman, S., Ozkar, S., Oleylamine-stabilized ruthenium(0) nanoparticles catalyst in dehydrogenation of dimethylamine-borane, International Journal of Hydrogen Energy, 38, 10000-10011, 2013.

[15] Zahmakiran, M., Philippot, K., Ozkar, S., Chaudre, B., Size-controllable APTS stabilized ruthenium (0) nanoparticles catalyst for the dehydrogenation of dimethylamine−borane at room temperature Dalton Transactions, 41, 590-598, 2012.

[16] Gulcan, M., Zahmakiran, M., Ozkar, S., Palladium (0) nanoparticles supported on metal organic framework as highly active and reusable nanocatalyst in dehydrogenation of dimethylamine-borane, Applied Catalysis B: Environmental, 147, 394-401, 2014.

[17] Rosello-Merino, M., Lopez-Serrano, J., Conejero, S., Dehydrocoupling reactions of dimethylamine-borane by Pt (II) complexes: a new mechanism involving deprotonation of boronium cations, Journal of the American Chemical Society, 135, 10910-10913, 2013.

[18] Sen, F., Karatas, Y., Gulcan, M., Zahmakiran, M., Amylamine stabilized platinum (0) nanoparticles: active and reusable nanocatalyst in the room temperature dehydrogenation of dimethylamine-borane, RSC Advances, 2014, 4, 1526-1531.

[19] Celik, B., Baskaya, G., Sert, H., Karatepe, O., Erken, E., Sen, F., Monodisperse Pt (0)/DPA@ GO nanoparticles as highly active catalysts for alcohol oxidation and dehydrogenation of DMAB, International Journal of Hydrogen Energy, 41, 5661-5669, 2016.

[20] Jiang, Y., Berke, H., Dehydrocoupling of dimethylamine-borane catalysed by rhenium complexes and its application in olefin transfer-hydrogenations, Chemical Communications, 34, 3571-3573, 2007.

[21] Clark, T.J., Russell, C.A., Manners, I., Homogeneous, titanocene-catalyzed dehydrocoupling of amine− borane adducts, Journal of the American Chemical Society, 128, 9582-9583, 2006.

[22] Sloan, M.E., Staubitz, A., Clark, T.J., Russell, C.A., Lloyd-Jones, G.C., Manners, I., Homogeneous catalytic dehydrocoupling/dehydrogenation of amine− borane adducts by early transition metal, group 4 metallocene complexes, Journal of the American Chemical Society, 132, 3831-3841, 2010.

[23] Demir, H., Duman, S., Monodisperse nickel nanoparticles in the solvent-free dehydrogenation of dimethylamine borane, International Journal of Hydrogen Energy, 40, 10063-10071, 2015.

[24] Bukan, B., Duman, S., Green dehydrogenation of dimethylamine-borane catalyzed by in situ generated ruthenium nanoclusters in presence of various supporters and its comparison with classical methods, International Journal of Hydrogen Energy, 43 (17), 8278-8289, 2018.

[25] Widegren, J.A., Finke, R.G., A review of the problem of distinguishing true homogeneous catalysis from soluble or other metal-particle heterogeneous catalysis under reducing conditions, Journal of Molecular Catalysis A: Chemical, 198, 317-341, 2003.

GROWTH AND CHARACTERIZATION OF HYBRID STRUCTURES FOR HIGH EFFICIENCY SOLAR CELLS

S. Türkdoğan1, B. Kılıç2

¹ Department of Electrical and Electronics Engineering, University of Yalova, Yalova 77200, Turkey
2 Department of Energy Systems Engineering, University of Yalova, Yalova 77200, Turkey

E-mail: sunay.turkdogan@yalova.edu.tr

Abstract

In this study, the growth of full composition graded ZnCdSSe thin film structures on a single substrate is presented and 3D junction based solar cells with enhanced solar conversion efficiency will be proposed. All these were realized by a temperature dependent composition deposition method using a CVD reactor. Along with thin film growth, nanowires on top of various compositional thin films within the ZnCdSSe material system were also grown. After the successful growth of those materials we proposed a method to build thin film/nanowire hybrid structures to form 3D junctions for enhanced solar conversion efficiencies in solar cells.

Keywords: Nanostructures, Hybrid Materials, 3D Junction, Photovoltaic Cells, Optoelectronics

1. INTRODUCTION

The increasing demand of energy and the limited reserves of fossil fuels require the development of renewable energy sources such as solar, wind, geothermal, and etc. Solar among the others is the most promising one as it provides 1400 times more energy than what the whole world currently consume in a year [1]. The best way to capture the solar energy is the photovoltaic cells and those are composed of various semiconductors with different properties. It has been a great research area to grow semiconductors with proper bandgap energy values making them suitable for solar cell applications. II-VI materials ZnS and CdSe can be used to form quaternary alloys and their full compositions can cover a wide range of the spectrum [2] and can be utilized for solar cell application.

Our aim is to grow hybrid structures having bandgap energy suitable for solar cell applications and then build 3D junction based solar cell for enhanced solar conversion efficiencies.

2. MATERIAL AND METHODS

Producing planar junctions with conventional methods for bulk materials are easy; however creating 3D junctions require a dozens of steps taken in clean room environment. By utilizing bottom-up approach we can easily form 3D junctions and problems related to the limited diffusion length can be solved through our proposed method with minimum number of steps.

Single crystal wide composition graded ZnxCd1-xSySe1-y quaternary alloy thin films on a single substrate were grown via vapor-solid (VS) growth mechanism using a single zone chemical vapor deposition (CVD) reactor [2]. Growth was carried out utilizing the temperature dependent composition deposition [3-4] and CdSe and ZnS powders were used as source materials. By placing the precursors and substrate at the right position full composition graded quaternary films can be grown on the substrate as various compositions prefer distinctive growth temperatures.

3. RESULTS AND DISCUSSION

By using various growth parameters we demonstrated the growth of full composition graded ZnCdSSe thin films on a single substrate and all the characterizations results revealed that those materials can be grown in high crystal quality and exhibit promising optical features. The detailed analysis results can be found in recently published article [2]. In addition to the thin film growth we have also grown hybrid structures with thin film at the bottom and nanowires on top. From the full composition graded thin film growth study, we know what position favors for what chemical composition of ZnCdSSe. Therefore we can easily grow

554

structures with any desired composition just by changing the position of the substrate. In order to grow hybrid structures we coated the pre grown thin film layer with catalyst material and then the growth was taken place at the right position to grow CdSe-rich nanowire structures. Figure 1(b) illustrates this procedure in detail. As a result of that pin brush-like materials were obtained as seen in the SEM images in Fig.1 (c,d).
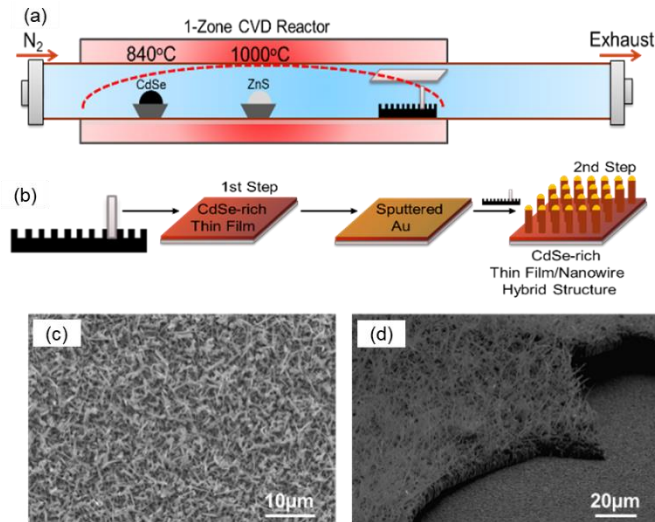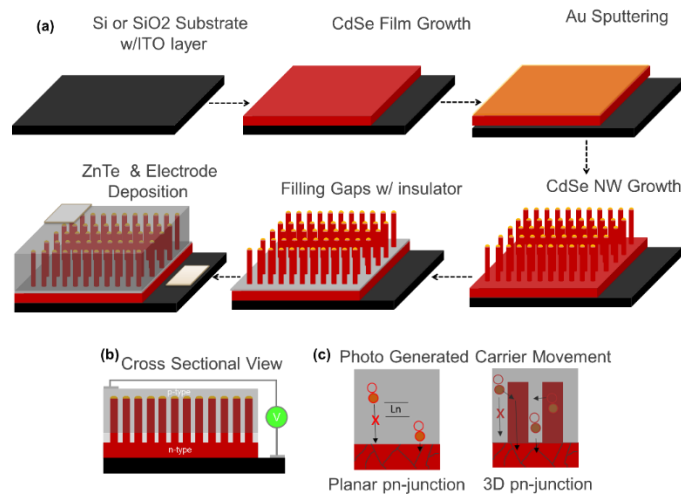

Figure 1-) **.** (a) Schematic view of the growth setup. (b) Illustration of the procedure applied to grow brush-like structures. (c) Top-view SEM image of brush-like structure (d) 60 degree tilted SEM images of a spot on same substrate.

After we obtain brush-like structures, a thin layer of insulator material can be spin coated to close any gaps to hinder the short circuiting. After that we can deposit p-type material to create 3D pn junctions as CdSe is inherently n-type. Figure 2 shows the procedure in detail. If we design a solar cell based on 3D pn junctions we can eliminate the short diffusion length problem of the carrier because photo generated carriers can become majority carrier by moving in the perpendicular direction to the substrate as seen in Fig. 2(c). By this way external quantum efficiency of the cells might be greatly enhanced and our future work will be the production of planar and 3D junction solar cells and make the comparison between those.

Figure 2-) (a) Schematic illustration of the fabrication steps for the proposed thin film/nanowire hybrid 3D junction solar cells. (b) Cross-sectional view of the device. (c) Movement of minority carrier in both planar and 3D pn-junction.

4. CONCLUSION

In conclusion, wide composition graded quaternary alloy thin films grown by a facile method based on the temperature dependent composition deposition was demonstrated. The emission of those materials lies in between the wavelength range of 400nm-700nm and therefore making the structures key material for various photonics applications. We also grew pin brush-like thin film/nanowire hybrid structures for the first time with a single growth steps to potentially create 3D pn junctions. Since our proposed device structure can reduce the carrier recombination in the device and collects more photo-generated carriers high efficiency full spectrum solar cells can be realized. Along with device application, the growth method can be also adopted for other important material systems besides ZnS-CdSe to develop novel photonic applications.

REFERENCES

[1] R. Perez and M. Perez. A fundamental look at energy reserves for the planet. The IEA SHC Solar Update vol. 50, 2 (2009).

[2] Turkdogan, S. (2018). Composition and Bandgap-Graded ZnCdSSe Thin Films and Thin Film/Nanowire Hybrid Structures for Potential Optoelectronic Applications. *Journal of Nanoelectronics and Optoelectronics*, *13*(3), 340-348.

[3] Z. Yang, J Xu, P. Wang, X. Zhuang, A. Pan, L. Tong, Nano Lett. **2011**, 11(11), 5085-5089.

[4] Y.I. Liu, J.A. Zapien, Y.Y. Shan, C.Y. Geng, C.S. Lee, S.T. Lee, Adv. Mater. **2005**, 17(11), 1372-1377.

NANOSHEET HETEROSTRUCTURE BASED CORRELATED COLOR TEMPERATURE (CCT) TUNABLE LIGHT EMITTERS

S. Türkdoğan[1], B. Kılıç[2]

[1] *Department of Electrical and Electronics Engineering, University of Yalova, Yalova 77200, Turkey*
[2] *Department of Energy Systems Engineering, University of Yalova, Yalova 77200, Turkey*

E-mail: sunay.turkdogan@ yalova.edu.tr

Abstract

In this study, growth and characterization of monolithic nanostructures with multiple segments having dissimilar chemical compositions is presented. We realize it by a novel growth method using chemical vapor deposition system and we have demonstrated tuning of correlated color temperature of trichromatic white light emission using a single quaternary alloy nanosheet. In addition to controlling correlated color temperature from warm white to cool white, we also demonstrated emission of some intermediate colors formed by pumping each segment with different pumping power.

Keywords: Nanomaterials, LEDs, Light Emitters, Nanotechnology, Semiconductors

1. INTRODUCTION

Development of LEDs for various applications such as lighting and displays has been a very attractive research area for over 50 years and has greatly intensified over the last two decades due to their low power consumption, long lifetime, high efficiency and small footprint. Especially the development of blue LEDs has been a big breakthrough as 2014 Nobel Prize in Physics was given to the inventers of blue LEDs for leading highly efficient and less power consumed white LEDs [1]. In our daily life, we see RGB and white LEDs almost everywhere and makes our life very colorful. They are expected to completely replace incandescent and fluorescent lamps in the near future. Although there are two ways of producing white LEDs: either all-semiconductor LED based approach or semiconductor LED combined with phosphorus coating, more than 90% of the white LEDs in commercial market uses the latter approach [2]. However, due to the degradation of the phosphors over time and the energy efficiency losses caused by the Stokes shift [3] where part of the high energy photons (blue) is consumed by the phosphorus layer, makes this choice non-ideal.

Our aim in this work is to build CCT tunable light emitters based on all semiconductor materials in a single body and present an ideal material for personalized lighting.

2. MATERIAL AND METHODS

Producing white LEDs based on all semiconductors is very difficult since it requires to grow epitaxial materials with dissimilar chemical compositions on a single substrate. Due to the lattice mismatch of different compositional materials it is unlikely to be grown on a single chip. Although there are some approaches such as die transfer, they increases the cost of LEDs tremendously and make it impractical.

In this work, nanotechnology plays a crucial role and we have achieved growing single nanostructures with multiple segments possessing dissimilar chemical compositions [4-7]. This is realized by a unique growth method using chemical vapor deposition and we have demonstrated tuning and control of correlated color temperature of trichromatic white light emission from a single ZnCdSSe nanosheet. The nanosheets have thicknesses in the range of 60-350 nm and lateral dimensions of tens of microns. Our growth procedure utilizes temperature-dependent composition deposition [8-10] and by changing the position of substrate during a single growth run we can grow multiple segments with various chemical compositions of ZnCdSSe quaternary alloys. The width of each segment in nanosheet structures can be controlled by the growth time at a specific position. Such controls determine the chemical composition (therefor emission color) and relative intensity of

each segment, and thus resulting in the tuning of the color temperature of the white light, or in the realization of any visible colors.

3. RESULTS AND DISCUSSION

By using various growth parameters we demonstrated trichromatic white light emission with the CCT ranging from 2700K to 14400K. It was also shown that by adjusting the growth parameters and growth paths we can grow any number of segments in a monolithic structure and color can be tuned by segment width or pumping power density. As illustrated in Fig. 1 the growth range of our materials lies between positions P1 and P3. By changing the substrate position during the growth we can grow a new segment with position defined chemical composition. In case of using a number of steps as illustrated, we can grow nanosheet structures with a number of segments able to emitting any color in the visible spectra. This makes our growth strategy very unique because by using some other techniques MBE, MOCVD, etc.. this cannot be realized.
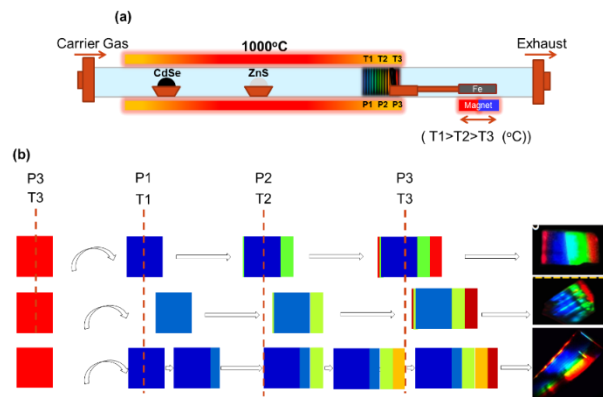

Figure 1-) (a) Schematic view of the growth setup (b) Illustration of resulted products when different growth positions used. Right hand side images are the PL image of such materials.

In Fig. 2, there a number of structures' PL images grown using various growth parameters. For those materials mainly 3 different growth position used but for each growth these three position were different, but in the range of P1-P3. Since we utilize temperature dependent composition deposition, this resulted multisegment nanosheet structures with different chemical composition for each segment. PL spectra was also taken using a homemade μPL setup under 405nm laser diode pumping and results show that each segment gives off different wavelength of light. It is also important that in our growth strategy growth time determines the width of the segments and width directly affects the emission intensity. In PL spectra, we see some segments have stronger light emission but some weaker. The reason is just as explained. After calculating the CCT value using the data (Fig.2 (a)) taken by spectrometer, we placed the combination of each spectra on CIE 1931

chromaticity diagram and as seen in Fig. (b) we can tune our white light in a wide CCT range. It is obviously seen that we can gather white light from warm to cool and this can be tuned by our growth parameters.
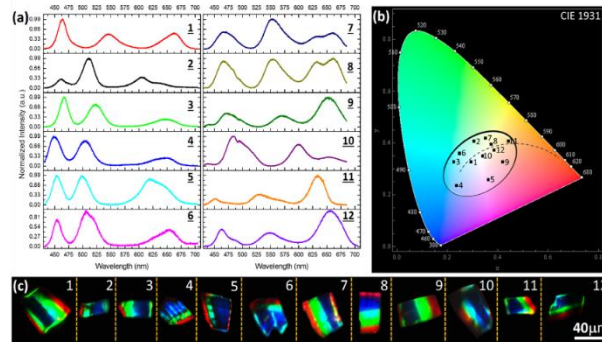

Figure 2-) (a) PL spectra (b) CIE 1931 Chromaticity diagram position (c) PL images of a number of structures grown in a separate growth run using different growth positions and growth time for each step.

As mentioned previously, we are not only able to get CCT tunable white light emission, but also get any intermediate color emissions using our materials. Figure 3 shows the capacity of our materials emitting intermediate colors. Since RGB are the main colors in the vision and any intermediate colors can be obtained mixing them partially, we can pump each segment of our structures with different pumping power to obtain the intermediate colors. For the sake of easiness, we used laser beam sweeping method as illustrated in Fig. 3. In this method, we started to project our laser beam mostly on the blue emitting segments and in an order we move it towards the upper segment. In each movement we can different light inbtensity from each segment and therefore we automatically tuned the resulted colors. In this example, we were able to get blue, cyan, white, yellow and orange, but by using a more advanced pumping method we are unlimited in the CIE 1931 Chromaticity diagram seen in Fig. 2(b).
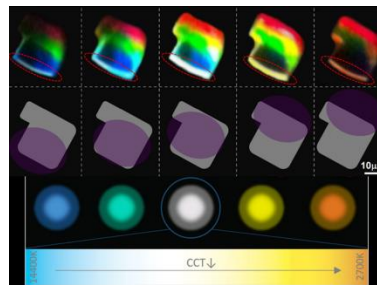

Figure 3-) Illustration of laser beam sweeping method to obtain intermediate colors using our multisegment structures.

4. CONCLUSION

All the presented results pave the way for various applications in solid state lighting and displays. By tuning the relative emission intensity of different segments either by optical pumping or electrical injection we can change the warmness of the white light emission. People can choice their favorite type of white light in a wide range of CCT by utilizing this technology and therefore we can call it personalized white light. It is also important to note that our approach meets the Solid state lighting requirements for CCT tunable, and phosphor-free white light emission from a single structure grown using a single ZnCdSSe material system. These results show great potential for various types of device applications in optoelectronic and photonics fields.

REFERENCES

[1] Nakamura, Shuji. "Nobel Lecture: Background story of the invention of efficient blue InGaN light emitting diodes." *Reviews of Modern Physics* 87.4 (2015): 1139.

[2] M.H. Crawford, IEEE J. Sel. Topics Quantum Electron. **2009**, 4, 1028-1040.

[3] E.F Schubert, J.K Kim, Science. **2005**, 308(5726), 1274-8.

[4] Fan, F., Turkdogan, S., Liu, Z., Shelhammer, D., & Ning, C. Z. (2015). A monolithic white laser. *Nature nanotechnology*, *10*(9), 796.

[5] Turkdogan, S., Fan, F., & Ning, C. Z. (2016). Color- Temperature Tuning and Control of Trichromatic White Light Emission from a Multisegment ZnCdSSe Heterostructure Nanosheet. *Advanced Functional Materials*, *26*(46), 8521-8526.

[6] Turkdogan, Sunay. *Growth and Characterization of Multisegment Chalcogenide Alloy Nanostructures for Photonic Applications in a Wide Spectral Range*. Arizona State University, 2015.

[7] Turkdogan, Sunay. *Nanowire Synthesis and Characterization: Erbium Chloride Silicate and Two Segment Cadmium Sulfide-Cadmium Selenide Nanowires and Belts*. Arizona State University, 2012.

[8] Z. Yang, J Xu, P. Wang, X. Zhuang, A. Pan, L. Tong, Nano Lett. **2011**, 11(11), 5085-5089.

[9] Y.I. Liu, J.A. Zapien, Y.Y. Shan, C.Y. Geng, C.S. Lee, S.T. Lee, Adv. Mater. **2005**, 17(11), 1372-1377.

[10] Turkdogan, S. (2018). Composition and Bandgap-Graded ZnCdSSe Thin Films and Thin Film/Nanowire Hybrid Structures for Potential Optoelectronic Applications. *Journal of Nanoelectronics and Optoelectronics*, *13*(3), 340-348.

ON THE GLOBAL STABILITY ANALYSIS OF SOME RATIONAL DIFFERENCE EQUATIONS

E.Taşdemir[1], Y. Soykan[2]

[1]Pınarhisar Vocational School of Higher Education, Kırklareli University, Kırklareli, TURKEY
[2]Department of Mathematics, Faculty of Art and Science, Zonguldak Bülent Ecevit University, Zonguldak, TURKEY

E-mail: erkantasdemir@hotmail.com, yuksel_soykan@hotmail.com

Abstract

In this paper, we investigate the global character of following rational difference equation $x_{n+1} = \frac{\beta x_n}{A + D x_{n-2}}$ where β, A, D positive parameters and the initial conditions positive numbers. We also study the bounded or unbounded solutions of related difference equation. In addition, our study gives answer to Conjecture 5.25.1 asserted by Camouzis and Ladas in their book (Dynamics of third order rational difference equations with open problems and conjectures. CRC, Boca Raton, 2008).

Keywords: Difference equation, stability, global stability, boundedness

1. INTRODUCTION

Due to the fact that most mathematical models need discrete variables, difference equations have great interest in among fields of science. Because, all of difference equations consist of these discrete variables. In additions to this, mathematical models apply to different fields in science such as physics, economy, engineering, etc. In [1], Camouzis and Ladas investigated the global behaviours of solutions of the following difference equations

$$x_{n+1} = \frac{\alpha + \beta x_n + \gamma x_{n-1} + \delta x_{n-2}}{A + B x_n + C x_{n-1} + D x_{n-2}}, n = 0,1,\cdots. \quad (1)$$

with nonnegative parameters $\alpha, \beta, \gamma, \delta, A, B, C, D$ and with arbitrary nonnegative initial conditions x_{-2}, x_{-1}, x_0 such that the denominator is always positive.

Moreover many authors have studied the dynamical behaviours of some difference equations (see [1]-[9]), for examples:

In [2], Göcen et al. studied global attractivity of following rational difference equations:

$$x_{n+1} = \frac{\alpha + \beta x_n + \gamma x_{n-1}}{C x_{n-1} + D x_{n-2}}.$$

In [3], Dekkar et al. investigated dynamics of the following two rational difference equations:

$$y_{n+1} = \frac{\alpha_n + y_n}{\alpha_n + y_{n-1}} \text{ and } y_{n+1} = \frac{\alpha_n + y_n}{\alpha_n + y_{n-2}}.$$

In this study we investigate the stability of following rational difference equations:

$$x_{n+1} = \frac{\beta x_n}{A + D x_{n-2}}, n = 0,1,\dots \qquad (2)$$

where β, A, D positive parameters and the initial conditions positive numbers.

2. PRELIMINARIES

Definition 1. Let I be some interval of real numbers and let $f: I^{k+1} \to I$ be a continuously differentiable function. A difference equation of order $(k+1)$ is an equation of the form

$$x_{n+1} = f(x_n, x_{n-1}, \cdots, x_{n-k}), \qquad n = 0,1,\cdots. \quad (3)$$

A solution of Eq.(3) is a sequence $\{x_n\}_{n=-k}^{\infty}$ that satisfies Eq.(3) for all $n \geq -k$.

As a special case of Eq.(3), for every set of initial conditions $x_{-2}, x_{-1}, x_0 \in I$, the third order difference equation

$$x_{n+1} = f(x_n, x_{n-1}, x_{n-2}), \qquad n = 0,1,\cdots. \qquad (4)$$

has a unique solution $\{x_n\}_{n=-2}^{\infty}$.

Definition 2. A solution of Eq.(3) that is constant for all $n \geq -k$ is called an equilibrium solution of Eq.(3). If

$$x_n = \bar{x}, for \ all \ n \geq -k$$

is an equilibrium solution of Eq.(3), then $\bar{x}$ is called an equilibrium point, or simply an equilibrium of Eq.(3).

So a point $\bar{x} \in I$ is called an equilibrium point of Eq.(3) if

$$\bar{x} = f(\bar{x}, \bar{x}, \cdots, \bar{x}),$$

that is,

$$x_n = \bar{x}, for \ n \geq -k$$

is a solution of Eq.(3).

Definition 3. Suppose that the function f is continuously differentiable in some open neighborhood of an equilibrium point $\bar{x}$. Let

$$q_i = \frac{\partial f}{\partial u_i}(\bar{x}, \bar{x}, \cdots, \bar{x}), for \ i = 0,1,2,\cdots, k$$

denote the partial derivative of $f(u_0, u_1, \cdots, u_k)$ with respect to u_i evaluated at the equilibrium point $\bar{x}$ of Eq.(3).

The equation

$$z_{n+1} = q_0 z_n + q_1 z_{n-1} + \cdots, q_k z_{n-k}, k = 0,1,\cdots. \qquad (5)$$

is called the linearized equation of Eq.(3) about the equilibrium point $\bar{x}$.

Definition 4. The equation

$$\lambda^{k+1} - q_0 \lambda^k + q_1 \lambda^{k-1} + \cdots, q_k = 0 \qquad (6)$$

is called the characteristic equation of Eq.(5) about $\bar{x}$.

Definition 5. Let $\bar{x}$ an equilibrium point of Eq.(3).

(a) An equilibrium point $\bar{x}$ of Eq.(3) is called locally stable if, for every $\varepsilon > 0$; there exists $\delta > 0$ such that if $\{x_n\}_{n=-k}^{\infty}$ is a solution of Eq.(3) with

$$|x_{-k} - \bar{x}| + |x_{1-k} - \bar{x}| + \cdots + |x_0 - \bar{x}| < \delta$$

then

$$|x_n - \bar{x}| < \varepsilon, for\ all\ n \geq -k.$$

(b) An equilibrium point $\bar{x}$ of Eq.(3) is called locally asymptotically stable if, it is locally stable, and if in addition there exists $\gamma > 0$ such that if $\{x_n\}_{n=-k}^{\infty}$ is a solution of Eq.(3) with

$$|x_{-k} - \bar{x}| + |x_{1-k} - \bar{x}| + \cdots + |x_0 - \bar{x}| < \delta$$

then we have

$$\lim_{n \to \infty} x_n = \bar{x}.$$

(c) An equilibrium point $\bar{x}$ of Eq.(3) is called a global attractor if, for every solution $\{x_n\}_{n=-k}^{\infty}$ of Eq.(3), we have

$$\lim_{n \to \infty} x_n = \bar{x}.$$

(d) An equilibrium point $\bar{x}$ of Eq.(3) is called globally asymptotically stable if it is locally stable, and a global attractor.

(e) An equilibrium point $\bar{x}$ of Eq.(3) is called unstable if it is not locally stable.

Theorem 1 (The Linearized Stability Theorem). Assume that the function F is a continuously differentiable function defined on some open neighborhood of an equilibrium point $\bar{x}$. Then the following statements are true:

(a) When all the roots of Eq.(6) have absolute value less than one, then the equilibrium point $\bar{x}$ of Eq.(3) is locally asymptotically stable. Moreover, in this here the equilibrium point $\bar{x}$ of Eq.(3) is called sink.

(b) If at least one root of Eq.(6) has absolute value greater than one, then the equilibrium point $\bar{x}$ of Eq.(3) is unstable.

(i) The equilibrium point $\bar{x}$ of Eq.(3) is called hyperbolic if no root of Eq.(6) has absolute value equal to one.

(ii) If there exists a root of Eq.(6) with absolute value equal to one, then the equilibrium $\bar{x}$ is called nonhyperbolic.

(iii) An equilibrium point $\bar{x}$ of Eq.(3) is called a saddle point if it is hyperbolic and if there exists a root of Eq.(6) with absolute value less than one and another root of Eq.(6) with absolute value greater than one.

(iv) An equilibrium point $\bar{x}$ of Eq.(3) is called a repeller if all roots of Eq.(6) have absolute value greater than one.

Theorem 2 ([1], p14).

(i) $f \in C\left((0,\infty)^3, (0,\infty)\right)$ and f is strictly monotonic all of its arguments.

(ii) For each $m \in (0,\infty)$ and $M > m$, we assume that

either

$$(f(M,M,M) - M)(f(m,m,m) - m) > 0$$

or

$$f(M,M,M) - M = 0,$$

$$f(m,m,m) - m = 0.$$

(iii) The function f is strictly increasing in x_n or x_{n-2}, or strictly decreasing in x_{n-1}.

If (i), (ii) and (iii) hold then every solution of Eq.(4) bounded by positive constants and every solution of Eq.(4) converges to a finite limit.

3. MAIN RESULTS

Now, we present some results given by Camouzis and Ladas in [1] p.166.

We know that from [1], p.166, with arbitrary nonnegative initial conditions and positive parameter β, the normalized form Eq.(2) is

$$x_{n+1} = \frac{\beta x_n}{1 + x_{n-2}}, n = 0,1,\cdots. \qquad (7)$$

Beside the equilibrium point of Eq.(7) is $\bar{x} = \beta - 1$. Further, if $1 < \beta < \frac{3+\sqrt{5}}{2}$

holds then the equilibrium point $\bar{x} = \beta - 1$ of Eq.(7) is locally asymptotically stable.

Theorem 3. Let the initial conditions $x_{-2}, x_{-1}, x_0 \geq 0$ and $1 < \beta < \frac{3+\sqrt{5}}{2}$. Thus Eq.(7) is bounded from

below with $x_n \geq 0$ for all $n \geq -2$.

Proof. Let $x_{-2}, x_{-1}, x_0 \geq 0$ and $1 < \beta < \frac{3+\sqrt{5}}{2}$. \ Hence, we have from Eq.(7),

$$x_1 = \frac{\beta x_0}{1 + x_{-2}} \geq \frac{x_0}{1 + x_{-2}} \geq 0,$$

$$x_2 = \frac{\beta x_1}{1 + x_{-1}} \geq \frac{x_1}{1 + x_{-1}} \geq 0,$$

and by induction, we get

$$x_n = \frac{\beta x_{n-1}}{1 + x_{n-3}} \geq \frac{x_{n-1}}{1 + x_{n-3}} \geq 0,$$

for all $n \geq -2$. So, the proof is complete as desired.

Theorem 4 (Conjecture 5.25.1 of [1]). $1 < \beta < \frac{3+\sqrt{5}}{2}$ holds. Then every positive solutions of Eq.(7)

converges to the positive equilibrium, $\bar{x} = \beta - 1$.

Proof. Now we apply to Theorem 2 for Eq.(7). Assume that $f: (0, \infty)^3 \to (0, \infty)$ is a function defined

by

$$f(x_n, x_{n-1}, x_{n-2}) = \frac{\beta x_n}{1 + x_{n-2}}, \qquad (8)$$

(i) Here, we calculate the partial derivative of (8):

$$\frac{\partial f(x_n, x_{n-1}, x_{n-2})}{\partial x_n} = \frac{\beta}{1 + x_{n-2}} > 0, \qquad (9)$$

$$\frac{\partial f(x_n, x_{n-1}, x_{n-2})}{\partial x_{n-1}} = 0, \qquad (10)$$

$$\frac{\partial f(x_n, x_{n-1}, x_{n-2})}{\partial x_{n-2}} = -\frac{\beta x_n}{(1 + x_{n-2})^2} < 0. \qquad (11)$$

So, f is strictly monotonic all of its arguments.

(ii) Assume that $m \in (0, \infty)$ and $M > m$,

$$\left(f(M, M, M) - M\right)\left(f(m, m, m) - m\right) = \left(\frac{\beta M}{1 + M} - M\right)\left(\frac{\beta m}{1 + m} - m\right)$$

$$= M\left(\frac{\beta - 1 - M}{1 + M}\right)m\left(\frac{\beta - 1 - m}{1 + m}\right)$$

From $\beta > 1$, we have

$$M\left(\frac{\beta - 1 - M}{1 + M}\right)m\left(\frac{\beta - 1 - m}{1 + m}\right) > M\left(\frac{-M}{1 + M}\right)m\left(\frac{-m}{1 + m}\right) = \frac{M^2}{1 + M}\frac{m^2}{1 + m} > 0.$$

Moreover, from (9), function f is strictly increasing in x_n.

So, according to Theorem 2 that every solution of Eq.(7) bounded from below and above by positive constants and every solution of Eq.(7) converges to a finite limit.

Example 1. Consider the Eq.(7) with initial conditions $x_{-2} = 0.75$, $x_{-1} = 0.1$, $x_0 = 1$ and $\beta = 2.15$. Thus, every positive solutions of Eq.(7) converges to the equilibrium point $\bar{x} = \beta - 1 = 1.15$. The following figure verifies our theoretical results.
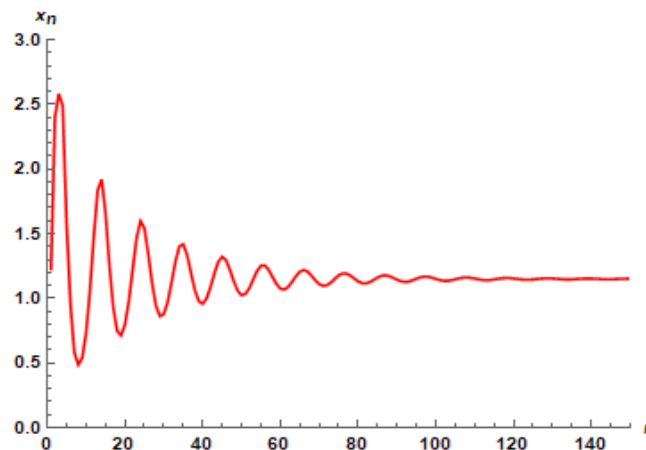

Figure: Plot of Eq.(7) for $\beta = 2.15$.

REFERENCES

[1] Camouzis, E., Ladas, G., Dynamics of third order rational difference equations with open problems and conjectures, volume 5 of Advances in Discrete Mathematics and Applications, Chapman & Hall/CRC, Boca Raton, FL, 2008.

[2] Göcen, M., Güneysu, M., The Global Attractivity Of Some Rational Difference Equations, J. Comput. Anal. Appl., 25(7), 1233-1243, 2018.

[3] Dekkar, I., Touafek, N., Din, Q., On the global dynamics of a rational difference equation with periodic coefficients, J. Appl. Math. Comput. 2018, 1-22, 2018.

[4] Kulenovic, M.R.S., Ladas, G., Dynamics of second order rational difference equations with Open Problems and Conjectures, Chapman & Hall/CRC, Boca Raton, FL, 2002.

[5] Elaydi, S., An Introduction to Difference Equations, Springer-Verlag, New York, Inc, 1996.

[6] Taşdemir, E., Soykan, Y., On the Periodicies of the Difference Equation $x_{n+1}=x_{n}x_{n-1}+\alpha$, Karaelmas Science and Engineering Journal, 6(2), 329-333, 2016.

[7] Taşdemir, E., Soykan, Y., Long-Term Behavior of Solutions of the Non-Linear Difference Equation $x_{n+1}=x_{n-1}x_{n-3}-1$, Gen. Math. Notes, 38(1), 13-31, 2017.

[8] Taşdemir, E., Soykan, Y., Stability of Negative Equilibrium of a Non-Linear Difference Equation, J. Math. Sci. Adv. Appl. 49(1), 51-57, 2018.

[9] Taşdemir, E., Soykan, Y., Dynamical Analysis of a Non-Linear Difference Equation, J. Comput. Anal. Appl., 26(2), 288-301, 2019.

ON THE STABILITY OF A NON-SYMMETRIC SYSTEM OF DIFFERENCE EQUATIONS

E.Taşdemir

[1]Pınarhisar Vocational School of higher Education, Kırklareli University, Kırklareli, TURKEY

E-mail: erkantasdemir@hotmail.com

Abstract

In this study, we deal with the global asymptotic stability of following non-symmetric rational difference equations $x_{n+1} = 2 + \frac{y_{n-1}}{y_n}, y_{n+1} = 3 + \frac{x_{n-1}}{x_n}$ with positive initial values. We also investigate the boundedness of related system.

Keywords: Difference equation, stability, global stability, boundedness, non-symmetric system

1. INTRODUCTION AND PRELIMINARIES

Nowadays, investigation of dynamic behaviour of recursive sequences (also called difference equations) have attracted significant interest. Especially researchers have studied the stability, boundedness and oscillatory behaviour of system of difference equations [1]-[16].

In [16], Amleh et al studied the global stability, the boundedness and periodicity nature of positive solutions of difference equation

$$x_{n+1} = \alpha + \frac{x_{n-1}}{x_n}.$$

Moreover, in [4], Hamza studied the global stability, the permanence and the oscillation character of related difference equation.

In [14], Zhang et al studied the behaviour of the following symmetrical system of rational difference equation

$$x_{n+1} = A + \frac{y_{n-k}}{y_n}, y_{n+1} = A + \frac{x_{n-k}}{x_n}.$$

Additionally, in [5], Gümüş studied both the global asymptotic stability of positive equilibrium point and the rate of convergence of positive solutions of the related system.

In this study we investigate the global asymptotically stability of unique positive equilibrium point of following non-symmetric system of rational difference equations

$$x_{n+1} = 2 + \frac{y_{n-1}}{y_n}, y_{n+1} = 3 + \frac{x_{n-1}}{x_n}. \qquad (1)$$

where the initial values x_{-1}, x_0, y_{-1}, y_0 are positive real numbers.

Firstly, we give some definitions and significant theorems which are used during this study.

The form of a four-dimensional discrete dynamical system is

$$x_{n+1} = f(x_n, x_{n-1}, y_n, y_{n-1}), y_{n+1} = g(x_n, x_{n-1}, y_n, y_{n-1}), \qquad (2)$$

$n = 0,1,\dots$ where $f: I^4 \times J^4 \to I$ and $g: I^4 \times J^4 \to J$ are continuously differentiable functions and I, J are some intervals of real numbers. Moreover, a solution $\{(x_n, y_n)\}_{n=-1}^{\infty}$ of system (2) is uniquely determined by initial values $(x_i, y_i) \in I \times J$ for $i \in \{-1, 0\}$.

Definition 1. Along with the system (2), we consider the corresponding vector map

$$F = \{f, x_n, x_{n-1}, g, y_n, y_{n-1}\}.$$

A point $(\bar{x}, \bar{y})$ is called an equilibrium point of the system (2) if

$$\bar{x} = f(\bar{x}, \bar{x}, \bar{y}, \bar{y}), \bar{y} = g(\bar{x}, \bar{x}, \bar{y}, \bar{y}).$$

The point $(\bar{x}, \bar{y})$ is also called a fixed point of the vector map F.

Definition 2. Let $(\bar{x}, \bar{y})$ be an equilibrium point of the system (2).

    i.   An equilibrium point $(\bar{x}, \bar{y})$ of system (2) is called stable if, for every $\varepsilon > 0$, there exists $\delta > 0$ such that, for every initial value $(x_i, y_i) \in I \times J$, with

$$\sum_{i=-1}^{0} |x_i - \bar{x}| < \delta, \sum_{i=-1}^{0} |y_i - \bar{y}| < \delta,$$

implying $|x_n - \bar{x}| < \varepsilon|$ and $|y_n - \bar{y}| < \varepsilon$ for $n \in \mathbb{N}$.

    ii.   An equilibrium point $(\bar{x}, \bar{y})$ of system (2) is called unstable, if it is not stable.

    iii.   An equilibrium point $(\bar{x}, \bar{y})$ of system (2) is called locally asymptotically stable if it is stable and if, in addition, there exists $\gamma > 0$ such that

$$\sum_{i=-1}^{0} |x_i - \bar{x}| < \gamma, \sum_{i=-1}^{0} |y_i - \bar{y}| < \gamma,$$

and $(x_n, y_n) \rightarrow (\bar{x}, \bar{y})$ as $n \rightarrow \infty$.

    iv.   An equilibrium point $(\bar{x}, \bar{y})$ of system (2) is called a global attractor if $(x_n, y_n) \rightarrow (\bar{x}, \bar{y})$ as $n \rightarrow \infty$.

    v.   An equilibrium point $(\bar{x}, \bar{y})$ of system (2) is called globally asymptotically stable if it is stable and a global attractor.

Definition 3. Let $(\bar{x}, \bar{y})$ be an equilibrium point of the map F where f and g are continuously differentiable functions at $(\bar{x}, \bar{y})$. The linearized system of system (2) about the equilibrium point $(\bar{x}, \bar{y})$ is

$$X_{n+1} = F(X_n) = BX_n, \qquad (3)$$

where

$$X_n = \begin{pmatrix} x_n \\ x_{n-1} \\ y_n \\ y_{n-1} \end{pmatrix}$$

and B is a Jacobian matrix of system (2) about the equilibrium point $(\bar{x}, \bar{y})$.

Theorem 4. (Linearized Stability Theorem [3], p.11) Assume that

$$X_{n+1} = F(X_n), \quad n = 0,1, ...,$$

is a system of difference equations such that X is a fixed point of F.

     i.   If all eigenvalues of the Jacobian matrix B about X lie inside the open unit disk $|\lambda|<1$, that is, if all of them have absolute value less than one, then X is locally asymptotically stable.

     ii.   If at least one of them has a modulus greater than one, then X is unstable.

Definition 5. (See [3], p.10) The characteristic equation of linear equation (3) is

$$\lambda^{k+1} - q_0 \lambda^{k-1} - q_1 \lambda^{k-2} - \cdots - q_k = 0. \qquad (4)$$

Definition 6. A solution $\{(x_n, y_n)\}_{n=-1}^{\infty}$ of system (2) is bounded and persists if there exist constants M, N such that $M<N$ and

$$M < x_n, y_n < N, \quad n = -m, -m + 1, ...$$

2. EQUILIBRIUM POINT OF SYSTEM (1)

The next theorem shows that system (1) has a unique positive equilibrium point.

Theorem 6. The unique equilibrium point of system (1) is $(\bar{x}, \bar{y})=(3,4)$.

Proof Let $x_n = \bar{x}$ and $y_n = \bar{y}$ for all n≥-1. Thus, we can easily obtain from system (1):

$$\bar{x} = 2 + \frac{\bar{y}}{\bar{y}} = 3,$$

$$\bar{y} = 3 + \frac{\bar{x}}{\bar{x}} = 4.$$

3. BOUNDEDNESS OF SOLUTIONS OF SYSTEM (1)

Now we study the boundedness of solutions of system (1).

Theorem 7. The every positive solutions of system (1) is bounded and persist.

Proof Let $\{(x_n, y_n)\}_{n=-1}^{\infty}$ be an arbitrary positive solution of system (1). We know from system (1) $x_n > 2$ and $y_n > 3$ for $n = 0,1,2, \dots$. Therefore we have

$$x_i, y_i \in \left[L, \frac{L}{L-3}\right], i = 1,2, \dots,$$

where $L = min\left\{a, \frac{b}{b-3}\right\}$, $a = min\{x_i, y_i\}$ and $b = max\{x_i, y_i\}$.

Hence we get

$$L = 2 + \frac{L}{\frac{L}{L-2}} \leq x_3 = 2 + \frac{y_1}{y_2} \leq 2 + \frac{\frac{L}{L-2}}{L} \leq \frac{L}{L-2} \leq \frac{L}{L-3},$$

$$L = 3 + \frac{L}{\frac{L}{L-3}} \leq y_3 = 3 + \frac{x_1}{x_2} \leq 3 + \frac{\frac{L}{L-3}}{L} \leq \frac{L}{L-3}.$$

So we obtain from induction

$$x_i, y_i \in \left[L, \frac{L}{L-3}\right], i = 1,2, \dots, \quad (5)$$

4. GLOBAL STABILITY ANALYSIS OF SYSTEM (1)

In this here, we investigate the stability analysis of unique equilibrium point of system (1).

Theorem 7. The equilibrium point $(\bar{x}, \bar{y}) = (3,4)$ of system (1) is locally asymptotically stable.

Proof Firstly we study linearized form of system (1). For this, we conceive the transformation:

$(x_n, x_{n-1}, y_n, y_{n-1}) \rightarrow (f, f_1, g, g_1)$, where

$$f = 2 + \frac{y_{n-1}}{y_n},$$

$$f_1 = x_n,$$

$$g = 3 + \frac{x_{n-1}}{x_n},$$

$$g_1 = y_n.$$

Therefore we have the Jacobian matrix about equilibrium point $(\bar{x}, \bar{y})$:

$$B(\bar{x}, \bar{y}) = \begin{pmatrix} 0 & 0 & -\frac{1}{\bar{y}} & \frac{1}{\bar{y}} \\ 1 & 0 & 0 & 0 \\ -\frac{1}{\bar{x}} & \frac{1}{\bar{x}} & 0 & 0 \\ 0 & 0 & 1 & 0 \end{pmatrix}$$

Thus, the linearized system about the equilibrium point $(\bar{x}, \bar{y}) = (3,4)$ is $X_{n+1} = B(\bar{x}, \bar{y})X_n$ where $X_n = \big((x_n, x_{n-1}, y_n, y_{n-1})\big)^T$ and

$$B(\bar{x}, \bar{y}) = \begin{pmatrix} 0 & 0 & -\frac{1}{4} & \frac{1}{4} \\ 1 & 0 & 0 & 0 \\ -\frac{1}{3} & \frac{1}{3} & 0 & 0 \\ 0 & 0 & 1 & 0 \end{pmatrix}$$

So, the characteristic equation of $B(\bar{x}, \bar{y})$ is

$$\lambda^4 - \frac{\lambda^2}{12} + \frac{\lambda}{6} - \frac{1}{12} = 0. \qquad (6)$$

Thus we obtain the four roots of characteristic equation (6):

$$|\lambda_1| = |0.14434 - 0.51753i| = 0.53728,$$

$$|\lambda_2| = |0.14434 + 0.51753i| = 0.53728,$$

$$|\lambda_3| = |-0.70067| = 0.70067,$$

$$|\lambda_4| = |0.41200| = 041200.$$

So, all roots of roots of characteristic equation (6) lie inside unit disk.

The next theorem presents that the unique positive equilibrium point of the system (1) is globally asymptotically stable.

Theorem 8. The every positive solution of system (1) converges to the equilibrium point $(\bar{x}, \bar{y}) = (3,4)$.

Proof We have from (5),

$$M_1 = \lim \sup x_n > 2 > 1,$$

$$m_1 = \lim \inf x_n > 2 > 1,$$

$$M_2 = \lim \sup y_n > 3 > 1,$$

$$m_2 = \lim \inf y_n > 3 > 1.$$

From there we obtain

$$M_1 \leq 2 + \frac{M_2}{m_2}, \qquad M_2 \leq 3 + \frac{M_1}{m_1},$$

$$m_1 \geq 2 + \frac{m_2}{M_2}, \qquad m_2 \geq 3 + \frac{m_1}{M_1}.$$

Therefore we have

$$3M_1 + m_1 \leq m_2 M_1 \leq 2m_2 + M_2,$$

$$2M_2 + m_2 \leq m_1 M_2 \leq 3m_1 + M_1.$$

Hence we can be written as

$$(3M_1 + m_1) + (2M_2 + m_2) \leq (2m_2 + M_2) + (3m_1 + M_1)$$

$$2(M_1 - m_1) + (M_2 - m_2) \leq 0$$

So we obtain $M_1 = m_1$ and $M_2 = m_2$. Thus $\lim x_n$ and $\lim y_n$ exist. Now we assume that $\lim x_n = L_1$ and $\lim y_n = L_2$. Letting $n \to \infty$ in system (1), we have

$$L_1 = 2 + \frac{L_2}{L_2} = 3,$$

$$L_2 = 3 + \frac{L_1}{L_1} = 4.$$

This system has the unique equilibrium point $(\bar{x}, \bar{y}) = (3,4)$. So every positive solution of system (1) converges to the equilibrium point $(\bar{x}, \bar{y}) = (3,4)$ as $n \to \infty$ as desired.

5. NUMERICAL EXAMPLE

In this section, we give some numerical examples so as to verify our theoretical results.

Example Consider the system (1) and the initial values $x_{-1} = 1, x_0 = 0.4, y_{-1} = 2$ and $y_0 = 0.2$. According to Theorem 8, the unique equilibrium point $(\bar{x}, \bar{y}) = (3,4)$ of the system (1) is globally asymptotically stable. The following figure verifies our theoretical results.
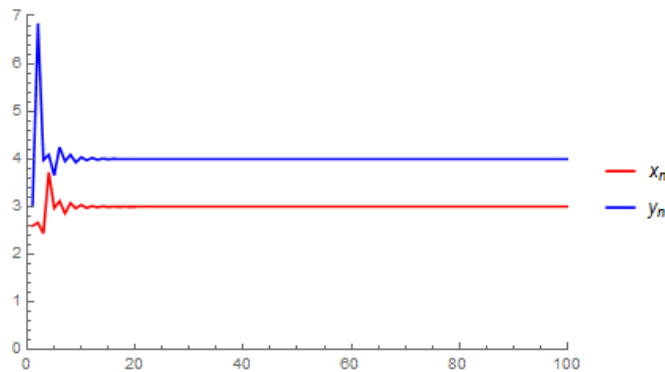

Figure 1: The plot of system (1).

6. CONCLUSIONS

This paper we investigated the stability analysis of system (1). Moreover we obtained that unique equilibrium point of system (1) is globally asymptotically stable.

REFERENCES

[1] R.P. Agarwal, P.J. Wong, Advanced topics in difference equations (Vol. 404), Springer Science & Business Media, (2013).

[2] S. Elaydi. An Introduction to Difference Equations, Springer-Verlag, New York, Inc, 1996.

[3] V.L. Kocic, G. Ladas. Global behavior of nonlinear difference equations of higher order with applications. Vol. 256. Springer Science & Business Media, 1993.

[4] A.E. Hamza, On the recursive sequence x_{n+1}=α+x_{n-1}/x_{n}, J. Math. Anal. Appl. 322, 2006, 668-674.

[5] M. Gümüş, The global asymptotic stability of a system of difference equations, J. Difference Equ. Appl. 24(6), 2018, 976-991.

[6] E. Taşdemir, On The Dynamics of a Nonlinear Difference Equation, Adıyaman University Journal of Sciences 9(1) (2019) 190-201.

[7] E. Taşdemir, On the Asymptotically Periodic Solutions of A Fifth Order Difference Equation, J. Math. Anal. 10(3) (2019) 100-111.

[8] E. Taşdemir, Y. Soykan, On the Periodicies of the Difference Equation $x_{n+1}=x_{n}x_{n-1}+\alpha$, Karaelmas Science and Engineering Journal, 6(2):329-333, 2016.

[9] E. Taşdemir, Y. Soykan, Long-Term Behavior of Solutions of the Non-Linear Difference Equation $x_{n+1}=x_{n-1}x_{n-3}-1$, Gen. Math. Notes, 38(1):13-31, 2017.

[10] E. Taşdemir, Y. Soykan, Stability of Negative Equilibrium of a Non-Linear Difference Equation, J. Math. Sci. Adv. Appl., 49(1):51-57, 2018.

[11] E. Taşdemir and Y. Soykan, Dynamical Analysis of a Non-Linear Difference Equation, J. Comput. Anal. Appl., 26(2):288-301, 2019.

[12] M. Göcen, M. Güneysu, The global attractivity of some rational difference equations, J. Comput. Anal. Appl., 25(7):1233-1243, 2018.

[13] E.M. Elsayed, T.F. Ibrahim, Solutions and periodicity of a rational recursive sequences of order five, Bull. Malays. Math. Sci. Soc. 38(1) (2015) 95-112.

[14] D. Zhang, W. Ji, L. Wang, X. Li, On the Symmetrical System of Rational Difference Equation $x_{n+1}=A+y_{n-k}/y_{n}, y_{n+1}=A+x_{n-k}/x_{n}$, Applied Mathematics, 4(5), 2013, 834-837.

[15] G. Papaschinopoulos, B.K. Papadopoulos, On the fuzzy difference equation $x_{n+1}=A+x_{n}/x_{n-m}$, Fuzzy Sets and Systems, 129, 2002, 73-81.

[16] A.M. Amleh, E.A. Grove, G. Ladas, D.A. Georgiou, On the recursive sequence $x_{n+1}=\alpha+x_{n-1}/x_{n}$, J. Math. Anal. Appl., 2, 1999, 790-798.

FREQUENCY BEHAVIOUR ANALYSIS AND TEST OF PORTABLE MEASURING DEVICE: Cartesian Magnetic Flux Mapper Example

U. Akoguz[1], H. Karagulle[2], S. Yavuz[3]

[1] *The Graduate School of Natural and Applied Sciences, Dokuz Eylul University,Tinaztepe Campus, Buca-İzmir, TURKEY*
[2]*Department of Mechanical Engineering, Dokuz Eylul University, Tinaztepe Campus, Buca-İzmir, TURKEY*
[3]*Department of Mechanical Engineering, Dokuz Eylul University, Tinaztepe Campus, Buca-İzmir, TURKEY*

E-mail: akoguz.ufuk@gmail.com

Abstract

Portable yet precise robot manipulators are needed for field applications when phenomena or source of it which is wanted to measure is not able to carry to laboratories or measuring rooms or just need to on field measurement. Precision in the design of such machines should be considered according to the characteristics of the sensor to be used. In this paper "Cartesian Magnetic Flux Mapper" is studied. Measuring of magnetic flux is important to find force index in specifics distance from magnetic circuit and find to find broken magnets. In this study Solidworks has been used for developing design and run for analysis. At the end the cartesian robot has been assembled, tested and operated.

Keywords: Permanent magnet, cartesian, quality control

1. INTRODUCTION

Magnetic Circuit (MCs) are commonly used in Magnetic Separators (MSs). MSs have wide range of uses in many industrial applications such as Recycling, Food Processing, Construction, Casting, etc[1]. MS branches two main branches, those are Permanent Magnetic Separators (PMSs) and Electromagnetic Separators (ESs). In this paper chassis of Magnetic Flux Mapper (MFM) for use of quality control and measure of PMS is studied.
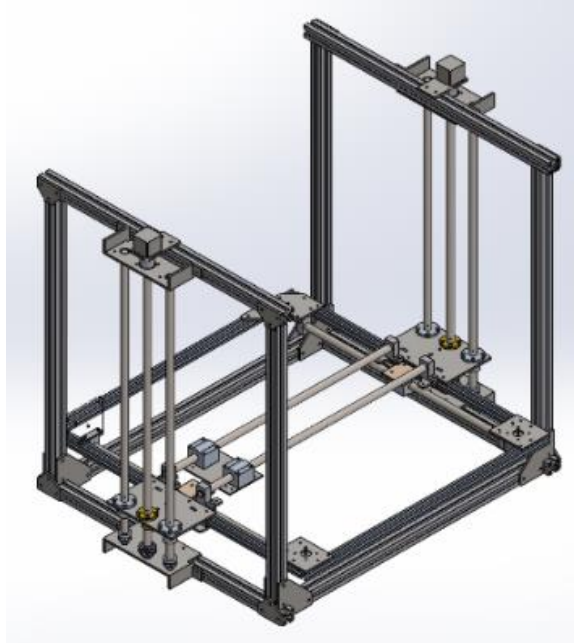
When designing or building of MC those are inside of MSs, MCs are designed to achieve to Force Index (FI) at the desired distance to attract ferrous object to separate from bulk. Any failure on manufacturing MC will affect FI [2] thus brings failure on separation process.

Cartesian movement is very suitable for the application, because general geometry of MS ar rectangular. There is also cylindrical shaped MSs but with a few adjustments to cartesian robot such as dividing head, the robot also measures cylindrical ones. In this paper, FI and the way of calculation has been mentioned but structural behaviour of robot is studied.

The study of structural behaviour of the chassis of MFM, Solidworks "Frequency Analysis" is used and also analysed several positions of the robot, "Impact Hammer Modal Test" is performed by hammering in line with the x and y axes and acceleration data obtained by wireless accelerometer. And the data is studied on MATLAB to gathering visualized information by using signal processes tool called Fast Fourier Transform (FFT). After analysis results and test results are compared.

2. DESING

Generally, design is inspired from CMM (Coordinate Measuring Machine) and 3D Printers [3]. To achieve lightweight construction and avoiding deflection of the magnetic flux, the construction is design for made by aluminium.
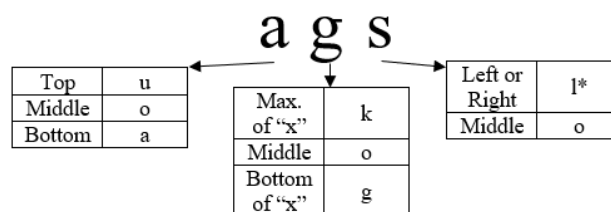
Figure 1. Design of Cartesian Magnetic Flux Mapper.

2.1 Analysis And Test

Before starting of analysis, positions of end effector are decided and named systematically.

2.1.1 Naming Of Positions

The First Letter of code refers to position of end effector (EE) along the "z" axis. For this letter there are three alternatives "d" for bottom" for middle, and "u" for top position. The Second Letter refers to position of EE along the "x" axis. For this letter there are three alternatives "s" for maximum value of "x" it refers to "south ", "m" for middle, and "n" for minimum value of "x" it refers to "north".The Third Letter of code refers to position of EE along to "y" axis. For this letter there are two alternatives "l" for maximum and minimum value of "y" and "m" for "middle". There is only one letter for maximum and minimum of "y", because construction has a symmetry plane parallel to "xz" plane.So there will be same vibrations characteristic(Figure 2).

Figure 2. Naming methodology schema of positions.

2.1.2 Deciding Critical Positions According to Mode Shapes

Due to named positions, modal frequency analysis are done in Solidworks and data gathered from that set of analysis a table developed below (Table 1).

Figure 3. The mode shapes of the system (Left to right are F1 to F5).

Table 1. Mode shape frequencies those are gathered from modal analysis for specific positions.
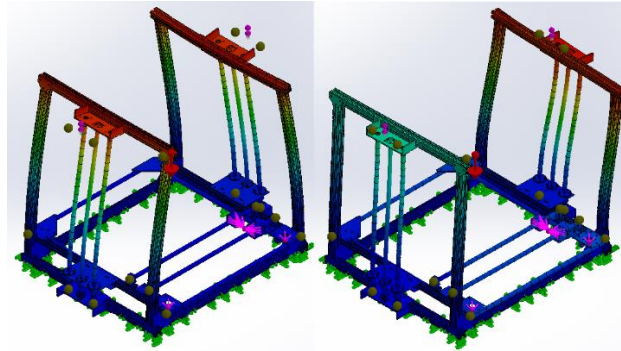
	ags	ako	aks	aoo	Aos	ogs	oko	oks	ooo	oos	ugs	uko	uks	uoo	uos
F1	38.96	39.58	40.1	45.12	45.73	38.57	39.12	39.64	44.7	45.22	52.78	53.54	52.72	51.16	51.14
F2	22.49	22.49	22.49	22.48	22.48	30.7	30.68	30.68	30.53	30.52	21.25	21.25	21.26	21.24	21.25
F3	34.76	34.76	34.76	34.78	34.78	34.8	34.81	34.85	34.88	35.93	28.07	30.23	27.96	30.77	28.24
F4	34.81	34.81	34.8	34.81	34.81	38.03	38.91	38.02	39.21	38.18	38.33	38.93	39.43	44.41	45.01
F5	38.96	39.58	40.1	45.12	45.73	38.57	39.12	39.64	44.7	45.22	52.776	53.54	52.72	51.16	51.14

On that "Table 1" Above 30 Hz are displayed with ligth green background color and bellow of 30 Hz are displayed in light red bachground color. And maximums and minumums are displayed dark shades. In this case some of positions there are bellow 30 Hz [4] mode shape frequencies according to "Table 2". Most of bellow 30 Hz situations are seen at second mode shapes.

According to Table 1's the second column, the common feature of critical positions is that the end effector is at the top or at the bottom.

The most generalized positions considered to be critical according to the second and third rows of Table 1 are shown in Figure 4.

Figure 4. The critical mode shapes according to Table 2.

3.1.3 Performing Impact Hammer Test And Processing The Results

After the chassis is assembled. The chassis was bolted to a rigid surface in accordance with the boundary conditions in the modal analysis. The Impact Hammer Modal [5] Test was performed similar to to Schwarz and Richardson's 1999 work by hammering the directions of x and y axis (Figure 1). The transmission information obtained during the test was recorded by a computer using a wireless accelerometer. FFT Analysis was performed by using Matlab "Signal Processing" library, then the information obtained was visualized and graphs to be compared with the results obtained from Modal Analysis [6] were obtained. The results of this phase are shown at Table 2.

Table 2. The impact hammer test results.

	Impact Direction	X		Y(Hz)	
ags	x	25.6	30.4	-	-
	y	25.9	30.8	41	-
ako	x	25.6	31	-	-
	y	30.8	-	41	-
aks	x	25.6	31	-	-
	y	25.6	30.8	41	-
aoo	x	25.3	30.8	-	-
	y	25.6	30.8	41.3	-
aos	x	Not Mesured*			
	y				
ogs	x	22.9	39.5	-	-
	y	22.9	39.5	35.3	-
oko	x	23.2	39.2	-	-
	y	23.5	39.8	36.5	-
oks	x	23.5	39.8	-	-
	y	23.5	52.8	35.9	-
ooo	x	23.2	38.6	-	-
	y	23.4	38.6	36.8	-
oos	x	Not Mesured*-			
	y				
ugs	x	18.4	-	29.6	-

	y	18.4	-	25	29.5
uko	x	18.4	49.1	29.5	-
	y	18.4	-	29.8	-
uks	x	18.4	-	29.5	-
	y	18.4	-	25.3	29.5
uoo	x	Not Mesured*			
	y				
uos	x				
	y				

The unmeasured parts in Table 2 are not measured because they show close values according to the information in Table 1.

Comparing of Table 1 and Table 2 Shows us in the world conditions the higher the elevator part, the lower

the frequency. Such as reverse pendulum. At the miniumum measured frequency to resonate the system you need

18 Hz of vibration or 1104 rpm of motor movement.

3.1.4 Performing Movement Test And Processing The Results

While performing this test, the "end effector" was moved for 10mm by the velocity profile [7-9] given below (Figure 5) and specs according to Table 3. And with the wireless accelerometer placed on the "end effector", the data was recorded on the computer. Matlab "Signal Processing" library FFT analysis was performed. The results were visualized and examined.
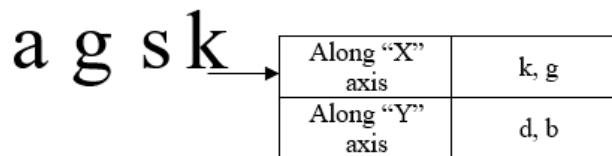

Figure 5. Velocity profile of test movement.

Table 3. The impact hammer test results.

Variable	Value	Comment
V_{max}	153.5[mm/s]	Maximum Velocity Value
Acc.	3000[mm/s^2]	Acceleration Value
Disp.	10[mm]	Desired Displacment
T_j	0.025[s]	Jerk Time
T_s	0.025[s]	Snap Time

In these measurements, to name test movements the letter coding used for naming positions was used. In addition, the letter was added to indicate the direction of movement (Figure 6).

Figure 6. Naming methodology of test movements.

In this step, measurements were taken for the positions mentioned in Table 4 in accordance with the velocity profile in Figure 6 in the x axis and y axis direction. Since it was decided that the positions at the top were critical, the focus was on the data of movements with the initial letter "u".

Table 4. The movement test results.

Positions	Graphs	Comments
ugsd		There was no significant peak.

ugsk		A peak at 25.31 Hz was seen along the y axis.
ukod		Harmonic peaks were observed starting at 4.5 Hz with approximately 10 Hz intervals. It is likely that there is a mechanical gap due to the alignment of the stepper motors in this section.
ukog		A peak at 24.1 Hz was seen along the y axis. A peak at 19.28 Hz was seen along the x axis.
uksd		Peaks were seen at 18.98 Hz and 29.22 Hz along the x axis.

uksg		A peak at 24.1 Hz was seen along the y axis. A peak at 19.28 Hz was seen along the x axis.

3. CONCLUSION AND FUTURE PERSPECTIVE

Critical positions were determined by modal frequency analysis, "Impact Hammer Test" was applied in these positions. Since the accelerometer used in the experimental setup could measure the translational acceleration, only translational vibrations could be measured, and torsional vibrations could not be measured. The translational vibrations were observed in the second, third and fourth mode shapes in the modal analysis. The frequencies obtained were confirmed by testing with a difference of about 4 Hz.

Critically determined positions are "uks, uko, ugs". Among the test movements, "ukod" movement was the most critical.

By adding beams to the top of the design, the weak points of the design can be strengthened. However, in this design, the chassis is not intended to be weighed further. Considering this situation and eliminating these weaknesses in future designs, lighter chassis designs will be made. However, in order to rethink these, it is necessary to learn the use of this design and its disadvantages.

ACKNOWLEDGMENTS

REFERENCES

[1] Svobodaa, T. F, Recent developments in magnetic methods of material separation, Minerals Engineering Volume 16, Issue 9, 785-792, 2003.

[2] Goudsmith Magnetics Knowledge Base, "https://www.goudsmitmagnets.com/en/wiki/88/force-index", 2019.

[3] https://reprap.org/wiki/RepRap_Options, 2019.

[4] Rao, S. S., Mechanical Vibration, 4th Edition, Pearson Education Press, 2004.

[5] Experimental Modal Analysis By Brian J. Schwarz & Mark H. Richardson Vibrant Technology, Inc. Jamestown, California 95327, CSI Reliability Week, 1999

[6] Karagülle, L. M., Analysis of End Point Vibrations of a Two-Link Manipulator by Integrated CAD/CAE Procedures" Finite Elements in Analysis and Design, vol:40 (2004) ,2049-2061, 2004.

[7] http://marlinfw.org, 2019.

USING CONVOLUTIONAL NEURAL NETWORK AS A FEATURE SELECTION METHOD FOR MULTI-FINGERED ROBOT HAND PRESHAPING

G. B. ERGÜN[1], S. NAZLIBİLEK[2], S. GÜNEY [3]

[1]Department of Electrical and Electronic Engineering, Başkent University, Ankara, TURKEY

E-mail: gbcangoz@baskent.edu.tr

Abstract

In this study, the aim is to extract the features from an object image in order to develop a decision making mechanism for multi-fingered robot hand which is capable of deciding automatically its hand grasping shapes based on the images taken by a camera from a work space. A hand has an action for grasping that consists of first deciding how to grasp an object and then activating the fingers to shape the hand which is appropriate for grasping. This study covers the process which consists of extracting the most effective image features for classification. Due to accomplish this task, one of the most popular deep learning method is used: convolutional neural network (CNN). On the other side, we utilized as a classifier Support Vector Machine (SVM).

Keywords: classification, convolutional neural network, deep learning, feature selection, multi fingered robot hand, image processing.
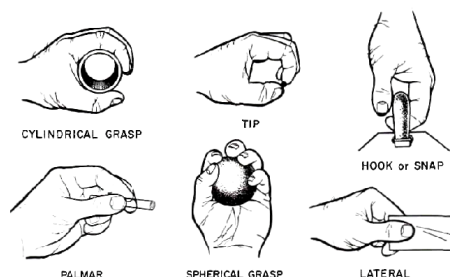
1. INTRODUCTION

Although numerous feature extraction and selection methods are exiting, even the best researchers cannot be certain about which method is appropriate for their dataset. It seems fair enough when the various data types and the aim of the studies are considering. Hence countless academic works are conducted so far [1-3].

On the other hand, when regarding some datasets like images, dimension of the data may be a problem. To overcome this difficulty, dimension reduction techniques are utilized and the most popular one is principal component analysis (PCA) [4-7].

From another perspective, working with the big data leads us to deep learning systems, for instance, convolutional neural networks (CNN), deep belief networks (DBN), and recurrent neural networks (RNN). These networks are handling the decision making process very well [8-11]. Nevertheless, these networks for very big data analysis. On account of our dataset which consisted of only fifty images, rather than these networks we tried conventional classifier: support vector machines (SVM) [12,13]. Still, instead of classification, we used CNN as a feature extraction method. So this pre-study only covers investigation of the feature extraction and classification parts. Our main purpose is to develop a multi-fingered robot hand which can decide its hand grasping shapes according to images. In order to accomplish this purpose, hundreds of images are going to studied. Thus, we intent to investigate these deep structures, yet this intention belongs to the future task.

Several works have been done about multi-fingered robot hand, but for the first time of the literature hand grasping shapes were divided into six categories by Schlesinger. In this way, we tagged our data based on these six categories, with the exception of one: lateral grasp. The labels we used for the classification are cylindrical, spherical, tip, hook and palmar grasps. The hand grasping shapes that we considered in our work are given Fig. 1 [14].

Figure 1. Hand grasping shapes: cylindrical grasp, tip grasp, hook or snap grasp, palmar grasp, spherical grasp respectively [15]

2. MATERIAL AND METHODS

A.   Dataset

Our dataset is consisting of fifty images total. We took ten photographs for each classes. The classes are determined according to the hand grasping shapes. We decided to use five hand grasping shapes: cylindrical, spherical, tip, hook and palmar grasping. The dataset is formed by images that different kind and brand of pencils, pens, pencil cases, mugs, glasses, erasers, pencil sharpeners, boxes, balls, apples, bags, etc. A visual example of our dataset is shown in Fig 2.

Figure 2. Several images from the dataset

B.   Convolution Neural Network

Although, number of the images of our dataset is not many, still processing a hundred-thousand-dimension matrixes is needed. To cope with this numerous data in matrix which some of them are not relevant, CNN is performed.

CNN is a deep learning algorithm which is generally using for classification process [16,17]. It is quite popular now because of its powerful performance. Its power is based on using a pre-trained network as a feature extractor instead of wasting time for training process. There are lots of pre-trained networks and most of them have been trained on the ImageNet dataset, which has 1000 object categories and 1.2 million images [18]. In our study, we used Residual Network-50 (ResNet-50). ResNet-50 is the network can learn several features at the end of its layers and the network has 50 layers total [19].

In CNN network, there are convolutional layer, rectified linear units (ReLU) layer, max-pooling layer and fully-connected layer. The basic architecture of CNN is given Fig. 3. However, there are only a few layers are useful for extracting features. In deeper layers, these primary features are operating and this deeper processes are ended up with classification with softmax function.

At the beginning of the network, basic image features are extracted for instance edges, lines, corners and blobs [19]. After performing CNN algorithm, the first convolutional layer's output is given Fig. 4. By observing this figure, we can say that primary features are captured successfully.

Fig. 3. Basic CNN Structure [20]

C.   Classification

In order to classify our dataset according to the assigned labels as a hand grasping shape, we applied SVM algorithm. It is because SVM algorithm is working well with images, texts and audios [21-23].

Our first goal is to extract features from the images with CNN network and the other goal is to classify data according to hand grasping shapes. After choosing the training and the test data sets, we obtained classifier's accuracy for both raw and the reduced data with CNN. The results are shown in Table I. According to the results, CNN as a feature extractor is suitable for our dataset.

Fig. 4. First Convolutional Layer Output

3. RESULTS AND DISCUSSION

The outcomes show us how CNN network is successful. It is a clear fact that CNN has a huge impact on classifier's accuracy. Besides, employing less data after CNN increasing the SVM algorithm's speed. On the other side, SVM may seem suitable classifier but, the process may continue by trying out other classifiers for future studies.

Table 1. Classification Successes.

Dataset	Classifier Success (%)
Raw Data	30
Reduced Data with CNN	92

From Table I, classifier's accuracy is only 30% for raw data. Because the dataset is created by aggregated only fifty images and like this number of images, it is tough to learn for a classifier. Whereas, classification accuracy after CNN is spectacular.

So this study is a pre-study for realizing our major goal in the near future. In the meantime, we are progressing the hardware part which is given a visual example in Fig. 5.

Fig. 5. Robot hand

4. CONCLUSION

This study is comprised of extracting the most effective features from images with convolutional neural network (CNN) which is one of the most popular deep learning method and classifying the images with Support Vector Machine (SVM) algorithm. The study is a pre-study for realizing our main goal and its results are very promising.

In a nutshell, while we are dealing with the hardware part, we expanded our dataset for better learning and we consider CNN algorithm for feature selection and may be a classifier for larger dataset. Ultimately, multi-fingered robot hand will detect the object from images automatically and it will be ready for holding the object in the image.

REFERENCES

[1]   A. Jović, K. Brkić, N. Bogunović, "A review of feature selection methods with applications", 38th International Convention on Information and Communication Technology, Electronics and Microelectronics (MIPRO), 2015.

[2]   X. Wu, V.Kumar, J.R.Quinlan, J.Ghosh, Q.Yang, H.Motoda, G.J. McLachlan, A.Ng, B.Liu, P.S. Yu, Z. Zhou, M.Steinbach, D.J. Hand, D.Steinberg, "Top 10 algorithms in data mining", Knowledge and Information Systems, vol.14, pp.1-37, 2008.

[3] Y. Wang, Z. Zhou, S. Jin, D. Liu and M. Lu, "Comparisons and selections of features and classifiers for short text classification", IOP Conf. Series: Mater. Sci. Eng., vol.261, 2017.

[4] G. Ivosev, L. Burton and R. Bonner, "Dimensionality reduction and visualization in principal component analysis", Anal. Chem., vol.80, pp.4933-4944, 2008.

[5] S. C. Ng, "Principal component analysis to reduce dimension on digital image", Procedia Computer Science, vol.111, pp.113-119, 2017.

[6] S.Khalid,T.Khalil and S.Nasreen, "A survey of feature selection and feature extraction techniques in machine learning", Proceedings of 2014 Science and Information Conference, pp. 372-378, 2014.

[7] J.Fu, C.Huang, J.Xing and J.Zheng, "pattern classification using an olfactory model with PCA feature selection in electronic noses: Study and application", Sensors, vol.12, pp: 2818-2830, 2012.

[8] J.Schmidhuber, "Deep learning in neural networks: An overview", Neural Networks, vol.61, pp.85-117, 2015.

[9] J.Qiu, Q.Wu, G.Ding, Y.Xu and S.Feng, "A survey of machine learning for big data processing", EURASIP Journal on Advances in Signal Processing, vol.2016, p.67, 2016.

[10] C.L.P.Chen and C.Y.Zhang, "Data-intensive applications, challenges, techniques and technologies: A survey on Big Data", Information Sciences, vol.275, pp.314-347, 2014.

[11] J.Li, H. Liu, "Challenges of feature selection for big data analytics", IEEE Intelligent Systems, vol. 32, 2016.

[12] T. Cover and P. Hart, "Nearest neighbor pattern classification", IEEE Transactions on Information Theory, vol.13, pp. 21-27, 1967.

[13] S. B. Kotsianti, "Decision trees: a recent overview", Artificial Intelligence Review, vol. 39, pp 261–283, 2013.

[14] G.Schlesinger, "The mechanical structure of the artificial limbs" Ersatzglieder and Arbeitshilfen. Springer, Berlin, Heidelberg, 1919.

[15] C.L.Taylor and R.J.Schwarz, "The anatomy and mechanics of the human hand", Artif Limbs, vol.2, pp.22–35, 1955.

[16] K. Fukushima, "Neocognitron: A self-organizing neural network model for a mechanism of pattern recognition unaffected by shift in position", Biological Cybernetics, vol.36, pp. 193-202, 1980.

[17] K. Fukushima, "Neocognitron: A hierarchical neural network capable of visual pattern recognition", Neural Networks, vol. 1, pp. 119-130, 1988.

[18]   J. Deng et al., "Imagenet: A large-scale hierarchical image database", Computer Vision and Pattern Recognition, CVPR IEEE Conference, 2009.

[19]   Mathworks, Image Category Classification Using Deep Learning, Online; accessed March 26, 2019. https://www.mathworks.com/help/vision/examples/image-category-classification-using-deep-learning.html

[20]   Understanding Convolutional Neural Networks for NLP, Online; accessed March 27, 2019. https://www.kdnuggets.com/2015/11/understanding-convolutional-neural-networks-nlp.html

[21]   J. Sonali, "A Machine Learning Approach: SVM for image classification in CBIR", International Journal of Application or Innovation in Engineering & Management, vol.2, 2013.

[22]   X. Sun, "Image classification via support vector machine", 4th International Conference on Computer Science and Network Technology (ICCSNT), 2015.

[23]   P.Dhanalakshmi, S.Palanivel, V.Ramalingam "Classification of audio signals using SVM and RBFNN", Expert Systems with Applications, vol.36, pp. 6069-6075, 2009.

PREDICTION OF THE ISE100 INDEX USING PATTERN RECOGNITION ALGORITHMS

K. Güven[1], S. Güney[2]

[1]*Department of Mechanical Engineering, Faculty of Engineering, Başkent University, Ankara, TURKEY*
[2] *Department of Electrical and Electronics Engineering, Faculty of Engineering, Başkent University, Ankara, TURKEY*

E-mail: kemalguven@baskent.edu.tr, seldaguney@baskent.edu.tr

Abstract

In this study, models have been developed to predict the daily changes of the ISE100 index. First, raw data is trained without any pre-processing. K-Nearest-Neighbor, Naive Bayes, Support Vector Machines and Neural Networks have been used. In order to increase the success of the model, from the feature extraction algorithms, Principal Component Analysis and Independent Component Analysis were selected. The results of algorithms and the contribution to the models of the feature extraction methods were investigated.

Keywords: k-Nearest-Neighbors; Naive Bayes; Neural Networks; Support Vector Machines; Principle Component Analysis; Independent Component Analysis

1. INTRODUCTION

Stock market movements are one of the difficult processes to predict. The fact that the stock market is one of the investment instruments makes this problem more important. In order to estimate the direction of movement of the stock market, a number of algorithms, based on statistical and artificial intelligence, are used. Statistical models are based on the assumption that there is a linear correlation structure between time series values. Therefore, solutions of non-linear problems are not possible in these models [1]. This deficiency in statistical models intensified researchers in artificial intelligence methods. These methods include genetic algorithms, artificial neural networks and various algorithms.

One of the first applications was announced by Graham and Todd in 1934 [2]. Armano et al. have developed a hybrid method for forecasting stock market movements. In the method they developed, they combined the genetic algorithm with the feed forward neural network. [3] Probabilistic Neural Networks were used in another study using the Taiwan stock exchange data [4]. Compared to the results of the statistical models, the predictors have higher accuracy. As well as Artificial Neural Networks, one of the main methods used are Support Vector Machines. Madge has achieved an accurate estimate of 40% by using SVM [5]. Karathanasopoulos et al. introduced a new model by combining genetic algorithm and SVM [6]. With this method, even in the times of financial crisis, model gives successful results. In another SVM application, attributes were prepared using single spectrum analysis and the success was increased [7]. In addition to the trained models, this problem can be solved by the algorithms that do not require training. Alkhatib and his friends have used the K Nearest Neighbor algorithm to predict the stock market movement [8]. They have achieved an acceptable error rate.

Besides the methods of estimation and classification, it is necessary to arrange the attributes to be used in the model's training. To eliminate noise and reduce the size of raw data Principal Component Analysis (PCA) [9], Core Principle Component Analysis [10], Continuous Points of Interest [11], Partial Aggregate Approach [12], Single Spectral Analysis [13], Discrete Fourier Transform, Discrete Wavelet Transform [14], Central model [15] and Random Matrix Theory [16] methods has been proposed. Kim and Han used the genetic algorithm for their financial data [17]. The most common method used on financial data is independent component analysis.

In this study, models were developed for daily estimation of ISE100 index. The dataset was trained with and without pre-processing and the results were compared. In the pre-processing stage, feature extraction methods were added to the model.

2. DATASET

The data is collected from imkb.gov.tr and finance.yahoo.com [18]. Data associated with work days at the Istanbul Stock Exchange were arranged. There are 536 samples with 8 attributes.

date	ISE	ISE	SP	DAX	FTSE	NIKKEI	BOVESPA	EU	EM
5-Jan-09	0.0357537	0.03837619	-0.00468	0.002193	0.003894	0	0.03119	0.012698	0.028524

Figure 1. Data sample

The dataset is arranged in binary system before the training process. If the stock market is decreasing, its value is 0 and it is increasing, its value becomes 1.

Table 1. Dataset information

Attribute	Description
ISE100	Istanbul stock exchange national 100 index
SP	Standard & poor's 500 return index
DAX	Stock market return index of Germany
FTSE	Stock market return index of UK
NIK	Stock market return index of Japan
BVSP	Stock market return index of Brazil
EU	MSCI European index
EM	MSCI emerging markets index

3. METHOD

In order to estimate the movement of the Istanbul stock exchange, K Nearest Neighborhood, Artificial Neural Networks, Naive Bayes and Support Vector Machines were used. First, the dataset was applied to the algorithms as raw. Then, the size and noise of the attributes were reduced by using Principal Component Analysis and Independent Component Analysis methods and re-trained.

To reduce the impact of the periodic changes of the stock data on the model, the training set was divided into the previous 250 days for the 20-day to forecast. The accuracy of the models was calculated and compared. While calculating the accuracy of the models, the success of the periods was utilized.

K Nearest Neighbors algorithm is one of the algorithms frequently used in classification problems. The algorithm uses the distance from the labelled data to classify new data. Therefore, how many neighbors are used and how to formulate the distance from that data directly affects the success of the algorithm. Thus, the most appropriate k parameter and distance formula was tried to be found in this study. For this, the graph showing the accuracy of the model for each k parameter was used with the Euclidean distance formulas because of the best accuracy obtained with this distance. In the model using Euclidean distance, the highest value of k was found to be 7 in the Fig. 2.

Figure 2. Accuracy of k-NN with Euclidean distance.

Although the success rate of Minkowski and Manhattan distances was reduced by 0.1%, the best k value was obtained as 7.

Another algorithm used frequently in classification problems is the Naive Bayes algorithm. It has been seen that the classification problems have been solved successfully with this statistical based algorithm. Kane and Khanna used the Naive Bayes algorithm to describe hand movements in their study [19].

To increase the success of the Naive Bayes classifier, the possibilities of the attributes can be given to the model first. In addition, specifying the distribution of attributes affects the success of the system. Table 2

shows the distributions used for each attribute. Table 3 is the success of the classifications using these distributions.

Table 2. Feature distribution.

No	Att1	Att2	Att3	Att4	Att5	Att6	Att7
1	normal	normal	normal	normal	normal	normal	normal
2	normal	normal	kernel	kernel	normal	kernel	kernel
3	kernel	kernel	kernel	kernel	kernel	kernel	kernel
4	kernel	normal	kernel	kernel	kernel	kernel	kernel
5	kernel	normal	normal	normal	normal	normal	kernel
6	normal	normal	normal	normal	normal	normal	normal
7	mvnn	mvnn	normal	normal	normal	normal	mvnn
8	mvnn	mvnn	mvnn	mvnn	mvnn	mvnn	mvnn
9	mvnn	mvnn	mvnn	normal	normal	normal	normal

Table 3. Performance of Naïve Bayes.

No	1	2	3	4	5	6	7	8	9
Accuracy	0.7238	0.7345	0.7321	0.7311	0.7231	0.7115	0.7366	0.7310	0.7290

One of the algorithms used in this study is Support Vector Machines. The kernel function used in this method, which classifies the data according to the support vectors it creates, greatly changes the classification success. Therefore, the kernel function should be chosen according to the problem. Table 4 shows the kernel functions and achievements.

The most appropriate kernel function for this study was found to be linear kernel function.
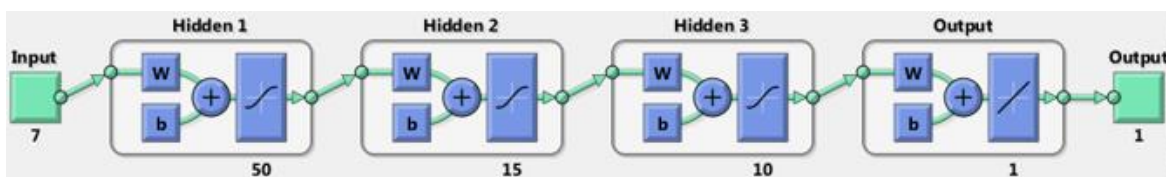
Table 4. Performance of SVM.

Kernel Function	polynomial	rdf	linear
Accuracy	0.7068	0.7104	0.7688

In recent years, the developing technology has facilitated the training processes of neural networks and led to the top of the algorithms which have the highest success in classification problems. Two of the parameters that directly affect the success of the model in the ANN are the number of layers and the number of neurons in the layers. The structure of ANN used in this study is shown in the Fig. 3.

Table 5. Performance of Neural Networks.

	Hidden Layers				Accuracy
	Layer-1	Layer -2	Layer -3	Layer -4	
Number of Neuron	25	-	-	-	0.604
	50	15	-	-	0.629
	10	8	3	-	0.628
	22	8	3	-	0.638
	12	15	10	-	0.637
	50	**15**	**10**	**-**	**0.642**
	12	15	10	5	0.634

It is seen from Table 5 that the model which has 3 hidden layers and has 50, 15 and 10 neurons respectively, has the highest accuracy.
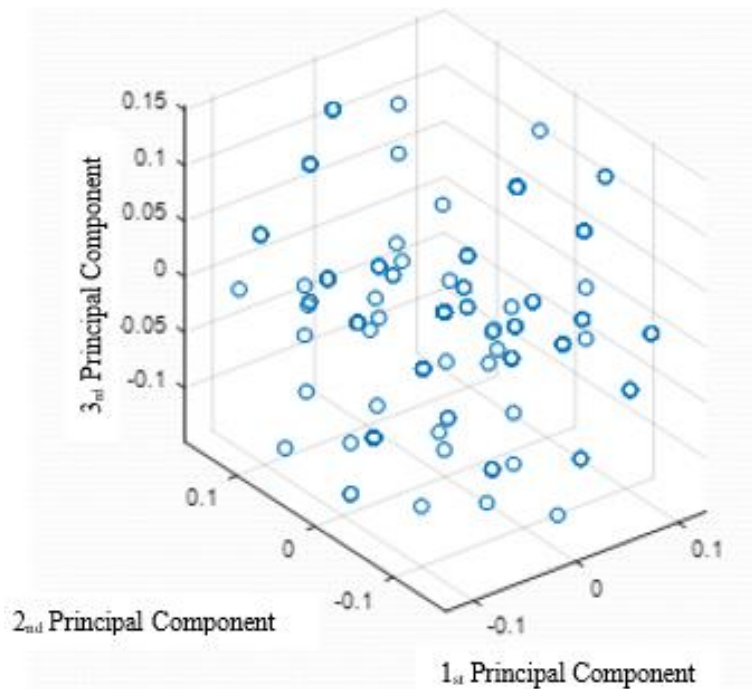

Figure 3. ANN Model.

4. FEATURE EXTRACTION

One of the methods frequently used to improve the success of pattern recognition algorithms is feature extraction. Here, the raw data is prepared through a series of operations. One of these processes is defined as

attribute extraction. In this study, Principal Component Analysis and Independent Component Analysis algorithms were used.

PCA is a method used to reduce the number of attributes in data sets that have a high number of attributes. It aims to represent the main components of the data set and to represent the data with these components in the Fig. 4.

Figure 4. Three of principal components.

The first 3 components were selected which can represent 84% of the data (Table 6).

Table 6. Variations of the principal components.

Principal Component	1	2	3	4	5	6
Variation	50.49	22.15	11.20	8.84	6.2	1.12

Despite the decrease in the success of kNN and Naive Bayes algorithms in the models trained using the first three components, it was observed that accuracies of SVM and ANN increased.

Another feature extraction algorithm used is Independent Component Analysis. ICA is generally used in signal processing and is used to separate signals from a mixture of independent signals.

When training attributes obtained using ICA were trained, only k-NN performance decreased in the Table 7.
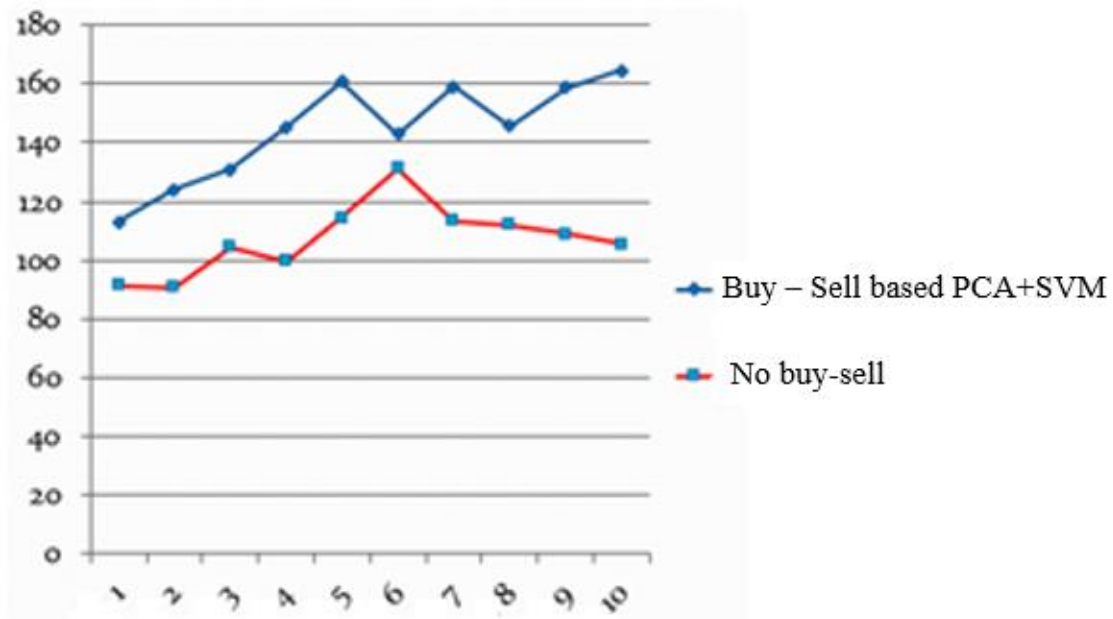
The performance of algorithms based on stock market data is measured by taking into account the financial return. An investor who redirected $ 100 by using the model developed using PCA and SVM has obtained 163 dollars at the end of 250 days. Anyone who didn't make any investment would have $ 104 can be seen in the Fig. 5.

Table 7. Performance of algorithms.

Algorithm	Raw	PCA	ICA
k-NN	76.00	54.68	68.93
Naive Bayes	73.66	60.38	73.80
SVM	76.88	77.20	76.98
ANN	64.20	71.70	71.80

Figure 5. Status of $100 investment.

5. CONCLUSION

In this study, for the ISE100 index estimation, raw data was used firstly in the trainings. The most successful methods were seen in kNN and SVM. New models have been created with new attributes obtained

by using PCA and ICA, which are attribute algorithms. The model used together with PCA and SVM was the most successful model with 77.2%.

When the PCA and SVM algorithms applied to the stock market data is measured by taking into account the financial return, an investor has obtained 163 dollars at the end of 250 days. It is seen from our suggestion that by using the proposed algorithm, earning of investors increases.

PCA and ICA increased the accuracy of ANN. Performance can be increased by using different network structures. In future studies, it is aimed to increase the success by using higher layer and neuron numbers.

REFERENCES

[1] J.-J. Wang, J.-Z. Wang, Z.-G. Zhang and S.-P. Guo, "Stock index forecasting based on a hybrid model," Omega 40(6), p. 758–766, 2012.

[2] B. Graham and D. Dodd, Security Analysis, New York: McGraw-Hill, 1934.

[3] M. M. M. A. Armano G, " A hybrid genetic-neural architecture for stock indexes forecasting.," Information Sciences 170(1, p. 3–33, 2005.

[4] L. M. D. H. Chen AS, "Application of neural networks to an emerging Application of neural networks to an emerging," Computer and Operations Research, p. 30:901–23, 2003.

[5] S. Madge, "Predicting Stock Price Direction using Support Vector Machines," Independent Work Report, New Jersey, 2015.

[6] A. Karathanasopoulos, K. A. Theofilatos, G. Sermpinis, C. Dunis, S. Mitra and C. Stasinakis, "Stock market prediction using evolutionary support vector machines: an application to the ASE20 index," The European Journal of Finance, pp. 1145-1163, 2015.

[7] F. WEN , X. Jihong, H. Zhifang and X. GONG , "Stock Price Prediction Based on SSA and SVM," Procedia Computer Science 31 , p. 625 – 631, 2014 .

[8] K. Alkhatib, H. Najadat, I. Hmeidi and M. K. A. Shatnawi , "Stock Price Prediction Using K-Nearest Neighbor (kNN) Algorithm," International Journal of Business, Humanities and Technology , pp. 32-44, 2013.

[9] F. D. Verleysen M, "The curse of dimensionality in data mining and time series prediction," in International Conference on Artificial Neural Networks:computational Intelligence and Bioinspired Systems, Berlin, 2005.

[10] T. T. Ince H, "Kernel principal component analysis and support vector machines for stock price prediction," IIE Transactions , p. 629–637, 2007.

[11] C. F. N. V. L. R. Fu T, "Pattern discovery from stock time series using self-organizing maps," In Workshop Notes of KDD2001 Workshop on Temporal Data Mining, p. 27–37, 2001.

[12] C. K. P. M. M. S. Keogh E, "Dimensionality reduction for fast similarity search in large time series databases," Knowledge and Information Systems, p. 263–286, 2000.

[13] M. F. K. F. M. K. Bunau PV, "Finding stationary subspaces in multivariate time series," Physical review letters , p. 103(21): 214101, 2009.

[14] H. M. Batal I, "A supervised time series feature extraction technique using DCT and DWT," in In International Conference on Machine Learning and Applications, Miami Beach, Florida, 2009.

[15] W. H. Z. S. P. D. Perng CS, "Landmarks: A new model for similarity-based pattern querying in time series databases," in In 16 International Conference on Data Engineeringg, IEEE ICDE, 2000.

[16] C. P. B. J. P. M. Laloux L, "Noise dressing of financial correlation matrices,," Phys. Rev. Lett. 83(7):, p. 1467–1470, 1999.

[17] H. I. Kim KJ, "Genetic algorithms approach to feature discretization in artificial neural networks for the prediction of stock price index," Expert Systems with Applications, p. 125–32, 2000.

[18] O. Akbilgic, H. Bozdogan and M. E. Balaban, "A novel Hybrid RBF Neural Networks model as a forecaster," Statistics and Computing, pp. 365-375, 2014.

[19] L. Kane and P. Khanna, "Depth matrix and adaptive Bayes classifier based dynamic hand gesture recognition," Pattern Recognition Letters, pp. 24-30, 2019.

THE EFFECT OF THE ETCHING RATE ON THE MAIN ELECTRICAL PROPERTIES OF p-Si

Y. Azizian-Kalandaragh [1,2], G. Pirgholi-Givi [1], J. Farazin [1,2]

[1] *Department of Physics, University of Mohaghegh Ardabili, P.O. Box 179, Ardabil, Iran*
[2] *Department of Engineering Sciences, Sabalan University of Advanced Technologies (SUAT), Namin, Iran*

E-mail: yashar.a.k@gmail.com

Abstract

In this research, the electrochemical etching process has been used for surface modification of p-Si semiconductor material and their morphological and electrical properties have been investigated. Five regions of porous silicon with different etching rates are selected for comparison and called P_1, P_2, P_3, P_4, and P_5. The purity, Surface morphology and roughness of the prepared samples have been investigated by Energy-dispersive X-ray spectroscopy (EDX) and Field Emission Scanning Electron Microscopy (FE-SEM) and the results show a meaningful effect of the etching on the porosity. The electrical parameters of the porous silicon (PS) at different etching conditions have been investigated by the I-V characteristic in the range of voltage (1.5V). The ideality factor (n), barrier height in zero bias (φ_0), voltage-dependent barrier height (φ), saturation current (I_0), resistance in forwarding bias (R_s), resistance in inverse bias (R_{sh}) and rectifying rate (RR) in different etching conditions have been investigated. The Rs value of the different regions of PS has obtained from different methods such as Ohm's law and Cheung method and compared to each other. The surface states (N_{ss}) versus energy (E_{ss}- E_v) plots were obtained from the forward bias I-V data by considering the voltage dependence of BH and n. The results obtained from electrical characteristics show that, by increasing the etching process, the performance and rectifying of the Schottky structures are improved.

Keywords: p-Si, porous silicon(PS), etching process, electrical properties

1. INTRODUCTION

In recent decades semiconductor nanostructures have been considered much attention due to their structural, optical, electrical, mechanical and thermal properties [1-9]. Between different semiconductor materials, silicon is one of the oldest and low-cost materials, which has many applications in various fields, especially in electronics and semiconductor device fabrication technology [10-13]. The unique characteristics of silicon are more evident when its dimensions are reduced. By reducing the size and dimension of silicon, its physical and chemical properties change due to the quantum confinement effect [14, 15]. There are different methods which used for manipulation of Si nanostructures to change its physical properties such as doping by other materials [16, 17], thermal annealing [18, 19], plasma treatment [20, 21] and electrochemical etching [6, 7]. One of these types of manipulations is to create of the porosity in silicon structure and the production of porous silicon (PS). Porous silicon is a dielectric material composed of silicon dioxide and air, which has a structural heterogeneity much smaller than normal light wavelength [22]. Between different above-mentioned methods, electrochemical etching is one of the most widely used methods for surface treatment of Si wafers. In this method, the surface morphology of the samples has changed with the condition of the electrochemical etching [6, 7, 23]. Surface treatment contain formation of porosity in the structures of the silicon semiconductors have different applications such as nonlinear optics [24, 25], biology, solar cells and fabrication of Bragg reflectors [26, 27], microelectronics[28], waveguides[29], optical filter [30], gas sensors [31, 32], photoluminescence devices in visible region [33-35], energy [36], drug industry [37], biotechnology [37] and some other complex optical devices [14] due to its high surface-to-volume ratio, high reactivity, luminescence properties at room temperature and its adaptive nature. There are several works about the optical and structural applications of porous silicon (PS) reported by researchers [22, 38, 39].

The electrical and dielectric characteristics of metal-semiconductor (MS) type Schottky barrier diodes (SBDs) have been extensively investigated due to their importance in technological applications. The current conduction mechanism (CCM) and formation of barrier height (BH) in MS are dependent on various parameters such as intrinsic layer at M/S interface, doping acceptor/donor concentration of atoms(N_a or N_d), density of interface states (N_{ss}), the homogeneity and thickness of barrier height (BH) and interfacial layer, series resistances (R_s) of the diode, sample temperature and applied bias voltage [13, 40].

In recent years, extensive studies have been carried out to control the modification of electronic and transport properties of conventional metal/semiconductor structures by using an organic interfacial insulator or polymer layer. by inserting an insulator or organic layer at M/S interface, MS type diode converts to the

MIS or MPS type diode. The presence of the insulating layer in MIS type diode reduces the leakage current, series resistance and density of surface states and thus enhances the device performance [41-44].

As our knowledge, the study of electrical properties of porous silicon structures has not been seriously investigated. Therefore, this research has been conducted to control the main electrical parameters of the metal-semiconductor structure by modifying the surface morphology of silicon using the etching process. For this aim, the forward and reverse bias I-V characteristics in the range of voltage (1.5V). The results show that the etching process has a significant effect on the electrical parameters of the (MS) Schottky diode, and the diode performance has been greatly improved by increasing the amount of etching process.

2. MATERIAL AND METHO-DS

The porous silicon wafer was purchased from Russia and was used as a metal-semiconductor (MS) Schottky diode without any contact. The surface morphology of the modified p-Si was analyzed by field emission scanning electron microscopy (FE-SEM, TeScan - Mira III, Czech Republic). The Keithley 2450 SourceMeter I-V characteristics system (USA) has been used for electrical properties of the sample. Kinetic parameters such as kinetic order, activation energy and the frequency factor have a remarkable influence on the thermoluminescence characterization of a phosphor. Hence, knowledge of these parameters has critical importance for understanding the thermoluminescence phenomenon in the phosphor, and there have been many methods for determining these parameters experimentally [11].
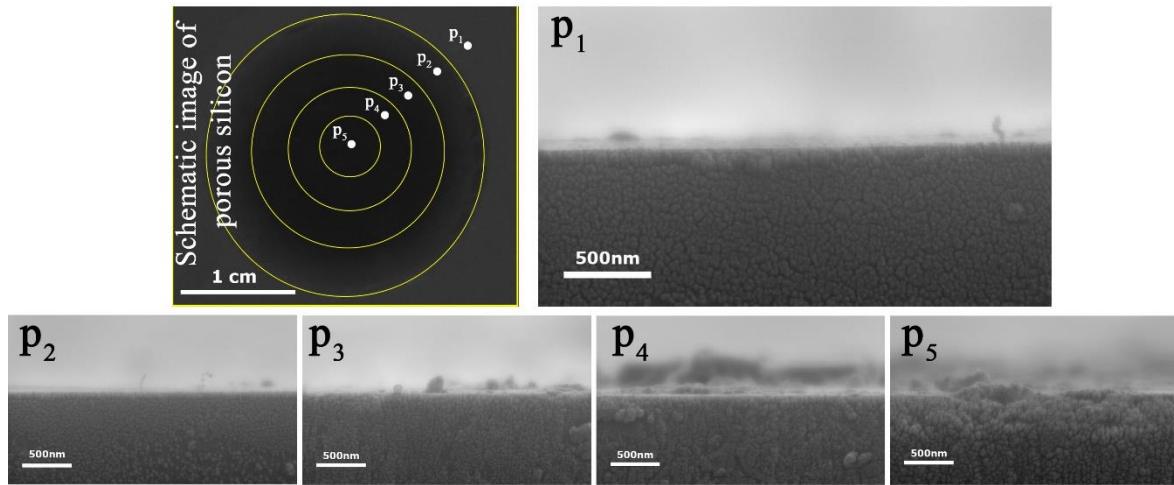
3. RESULTS AND DISCUSSION

3.1 FE-SEM AND EDX ANALYSIS

Figure 1 shows a schematic image of different porous silicon(PS) regions and shows the related to the cross-section images of PS with different levels of etching process of the p-Si surface obtained from field emission scanning electron. In Fig. 1, the area P_1 is related to the normal silicon region without manipulation, and the P_2 to P_5 regions respectively correspond to the regions of the least to the highest amount of etching process performed on the surface of the silicon. As can be seen from Fig.1, by increasing the amount of etching process, the porosity increase, so that the average value of porosity size has changed from the 300 nm for the least amount of etching (P_2) up to 2 µm for the maximum amount of etching (P_5). The mean size of different regions of silicon tabled in the table (1).
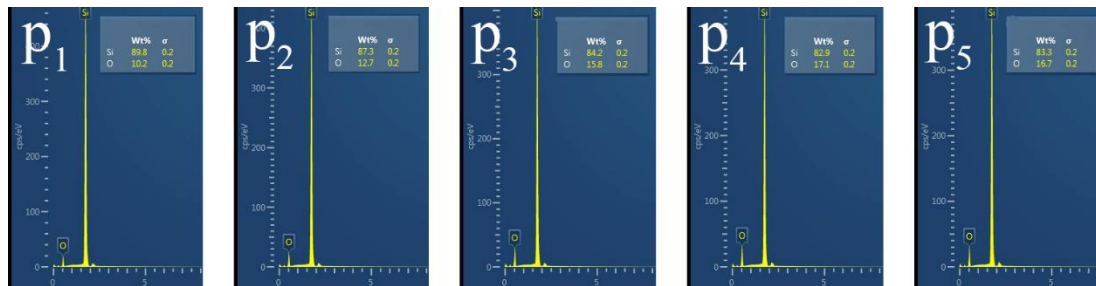
Table 1: Average diameter of different regions of PS.

sample	P_2	P_3	P_4	P_5
Size(nm)	300	700	1500	2000

Figure 1. The schematic image of different porous silicon regions, FE-SEM images of the electrochemically etched p-Si (P1 to P5).

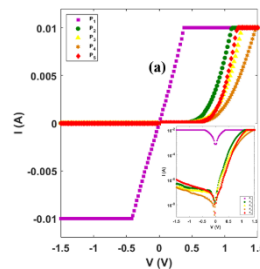The EDX profile of the different region of PS with different etching rate shown in Fig .2.

Figure 2. EDX profiles of a different region of porous silicon.

As can be seen from Fig. 2, the whole region of porous silicon includes the silicon and oxygen atoms and no impurities or other compounds have been introduced in the prepared samples. Also, the silicon content of different regions of PS are upper than 80 % and the oxygen content is less than 20 %.

3.2 ELECTRICAL PROPERTIES

The normal and semi-logarithmic forward and reverse bias I-V characteristics of the different regions ($P_1 - P_5$) of a p-type silicon wafer as shown in Fig.3.

Figure 3. The normal and semi-logarithmic plot of I-V for all region of PS.

As shown from Fig.3, the P_1 region lacking the etching process has a near-ohmic behavior, and gradually, by increasing the amount of the etching process, the I-V plot of the P_2 to P_5 regions exhibits diode's behavior. The least rectifier rate (RR) is 25.5 for P_2 region with the least porosity, and the highest is 47.2 for P4 and its amount is 9.7 related to P_5 that decreases with increasing porosity. In addition, the ideality factor (n) of the P_2 region is 2.6 and its value equal 2.4 has reached least value at P_4 and then increased in P_5 region. Also, the values of saturation current(I_0) in P_2, P_3, P_4 and P_5 region are 99.8 nA, 62.3 nA, 13.4 nA, and 15.2 nA respectively.

The ideality factor (n), barrier height in zero bias (φ_0), saturation current (I_0), resistance in forwarding bias (R_s), resistance in inverse bias (R_{sh}) and rectifying rate (RR) of a different region of PS are given in Table (2).

Table 2: Main electrical parameters of all regions of PS obtained from the I-V method.

Samples	I_o(nA)	n	Φ_{Bo}(eV)	RR	R_s(Ω)	R_{sh}(MΩ)
P_2	99.8	2.6	0.71	25.5	111	3.36
P_3	62.3	2.5	0.72	41.9	202	5.60
P_4	13.4	2.4	0.76	47.2	370	8.06
P_5	15.2	2.7	0.76	9.7	162	2.07

As shown in Table (2), P4 has the least n, I0 and Rsh and highest R_s, RR, and Φ_{B0}. Therefore, increasing the etching process (up to P_4 region) improves the performance of the diode and after that, the performance of the diode decreased with increasing porosity. Both of R_s and R_{sh} values increase by increasing the porosity. Increasing the R_{sh} value reduces the leakage current of the diode and enhancement diode rectification.

The main electrical parameter can be an extract of I-V characteristics that analyzed using thermionic emission theory. the relationship between current and applied bias voltage in terms of thermionic emission is given as [45, 46]:

$$I = AA^* \exp(-\frac{q\phi_{B0}}{kT})[\exp(\frac{q(V-IR_s)}{nkT})-1] \tag{1}$$

Where R_s, q, k, T, n, ϕ_{B0}, A^*, V, I and A are the series resistance, electronic charge, Boltzmann constant, absolute temperature in Kelvin, ideality factor, zero bias barrier height, effective Richardson constant, applied bias voltage, current, and rectifier contact area. Also, the reverse saturation current (I_0) and ideality factor (n) can be obtained from the intercept at zero bias and slope of the linear region of LnI-V plot and given by:

$$I_0 = AA^*T^2 \exp(-\frac{q\phi_{B0}}{kT}) \tag{2}$$

$$n = \frac{q}{kT}(\frac{dV}{d(LnI)}) \tag{3}$$

As shown in Table 2, the ideality factor of all region of silicon greater than unity related to several effect such as series resistance, barrier inhomogeneity, interface traps (D_{it}) and interface stats (N_{ss}) at metal/semiconductor interface [47-49], which indicate the deviation of experimental I-V information from ideal thermodynamic theory.

Other important parameters of the Schottky diodes are the series (R_s) and shunt (R_{sh}) resistance that results from the resistance of bulk semiconductor, ohmic contact and non-uniform doped atoms in the semiconductor, which it can cause errors in the extracted electrical parameters. There are several methods to the determination of the Rs from the forward bias I-V data such as Ohm's law, Norde, Cheung, and modified Norde functions by Bohlin [38]. The Rs values were obtained using Ohm's law and Cheung methods and compared with each other.

In addition, the value of Rs can also be calculated from Cheung functions developed by Cheung [50]. As follows from equation 4(a) to 4(c):

$$\frac{dV}{d(LnI)} = IR_s + n(\frac{kT}{q}) \tag{4 a}$$

$$H(I) = V - n(\frac{kT}{q})Ln(\frac{I}{AA^*T^2}) \tag{4 b}$$

$$H(I) = IR_s + n\phi_B \tag{4 c}$$

Where IRs is the voltage drop across the series resistance of the SBD. the functions of dV/d(LnI) and (H(I)) were obtained from I-V characteristics. Experimental dV/d(LnI) and (H(I)) vs I plot of a different region of PS are shown in Fig. 4. After fitting the curve to a straight line and using equation 4(a), Rs and n can be
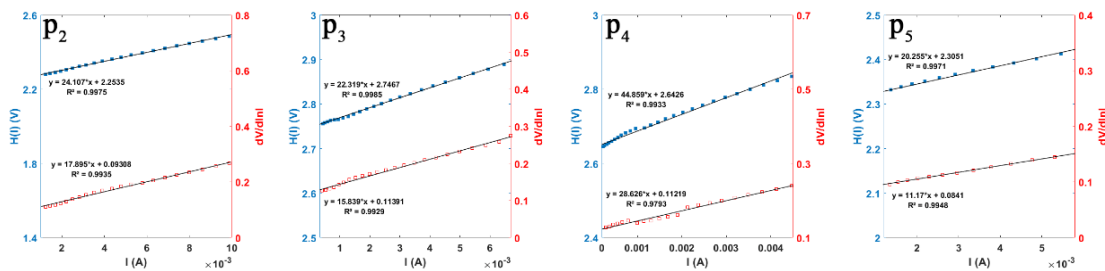
extracted from the slope and the intercept of the line. The Cheung functions were also used for the determination of R_s and Φ_B values. These values were derived from the slope and intercept of the H(I)-I curve and reported in table 3.

Table 3. Some electrical parameters extracted from the different methods for all regions of PS.

Region	n		$R_s(\Omega)$			$\Phi_B(eV)$	
	$\partial V/\partial I$	dV/d Ln(I)	$\partial V/\partial I$	dV/d Ln(I)	H(I)	I-V	H(I)
P_2	2.6	3.6	111	17.9	24.2	0.69	0.65
P_3	2.5	4.4	202	15.8	22.3	0.70	0.63
P_4	2.4	4.0	370	28.6	44.9	0.74	0.63
P_5	2.7	3.4	162	11.2	20.3	0.73	0.69

The Rs values obtained from dV/d(LnI) vs I and H(I) vs I plot for P_4 region are 28.6 Ω and 44.9 Ω. As shown in Table 3, the obtained value of HB and Rs values from Norde and I-V methods have good agreements with each other. Also, the obtained results from both methods show that the increasing porosity of silicon wafer improves the performance and rectifying of SDs.

Figure 4. The plots of dV/d Ln(I)-I and b) H(I)-I for all regions of PS.

The Peak Shape method developed by Chen, which takes into account the peak shape or geometrical properties of a well-known method of TL glow curve analysis, has been applied [22]. According to this method, the average activation energy (E) was found to be 1.11 eV and average frequency factor (s) $1.80 \times 10^{+10}$ s^{-1} according to the peak shape method of high-temperature peak (501 K) which can be taken as a dosimetric peak.
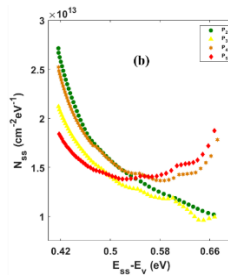
In Schottky diodes, both MS or MIS type, many surface states/traps (N_{ss} or D_{it}) are created between interfacial layer and semiconductor in the forbidden band gap of semiconductor during fabrication process [35,38]. These traps, as recombination centers, can store and release the electronic charges under the bias voltage. Therefore, the profile of surface states vs energy for all regions of PS was obtained from the forward bias I–V data by taking into account both the voltage-dependent ideality factor n (V) and barrier height (Φ_B).

The expression for the density of the interface states as deduced by Card and Rhoderick [51] can be reduced to:

$$N_{ss}(V) = \frac{1}{q}\left[\frac{\varepsilon_i}{\delta}(n(v)-1) - \frac{\varepsilon_s}{w_D}\right] \tag{7}$$

Here, ε_s (=11.8ε_o), ε_i (=4ε_o) and ε_o (=8.5 × 10-14 F/cm) is the permittivity's of the semiconductor, intrinsic interlayer, and free space, respectively. WD and δ are the depletion layer width and the thickness of the interlayer[52].

Figure 5. Energy density distribution of the surface states for all regions of PS.

For p-type semiconductors, the energy level of traps/states (E_{ss}) with respect to the bottom of the valance band (E_v) at the surface of the semiconductor is expressed as [38].

$$E_{ss} - E_v = q(\Phi_e - V) \tag{8}$$

Here; V is the voltage drop across depletion layer and Φ_e is the effective barrier height.

Thus, N_{ss} vs (E_{ss}- E_v) profile of the different region of PS were obtained from Equations 7 and 8 are shown in Fig. 5(b). As shown in Fig. 5(b), the energy values of the N_{ss} of P_2, P_3, P_4, and P_5 region are in the range of 0.42 eV-E_v to 0.67 eV-E_v. The magnitude of N_{ss} at 0.42 eV-E_v are 1.8× 1013 eV- 1 cm^{-2}, 2.1× 1013 eV-1 cm^{-2}, 2.6× 1013 eV- 1 cm^{-2} and 1.8× 1013 eV- 1 cm^{-2} for MS and 2.0× 1013 eV^{-1} cm^{-2} , and its value at 0.67 eV-E_v are 8.6× 1012 eV- 1 cm^{-2}, 9.9× 1012 eV- 1 cm^{-2}, 1.6× 1013 eV- 1 cm^{-2} and 1.9× 1013 eV- 1 cm^{-2} for P_2, P_3, P_4 and P_5 region of PS, respectively. As can be seen clearly from Fig. 5 (b), due to being the same as the intrinsic interlayer for all regions, the magnitude of N_{ss} for all regions is approximately the same. But the energy dependence of the N_{ss} in different regions is different. At low porosity region(P_2), the density of states

decreased with increasing energy, while in high porosity region, with increasing energy, the N$_{ss}$ decreased and then increased again after a minimum value.

4. CONCLUSION

In this study, the effect of the etching process on electrical parameters of porous p-Si has investigated using forward and reverse bias I-V in a wide range of applied bias voltage. In this way, the values of n, BH and Rs were obtained from the forward and reverse bias I-V data by using the different experimental measurement methods and also calculated methods namely TE theory and Cheung's methods and compared with each other. The energy-dependent profile of N$_{ss}$ was extracted from the forward bias I-V data by considering voltage-dependent of BH and n. the obtained results of both methods are confirmed that the increasing porosity of silicon wafer improves the performance and rectifying of SD in the respect of a decreases in n and leakage current and increase in rectifying rate (RR) and BH.

REFERENCES

[1] Sharma, H., et al., Effect of ratios of Cd: Se in CdSe nanoparticles on optical edge shifts and photoluminescence properties. Physica E: Low-dimensional Systems Nanostructures, 2006. **31**(2): p. 180-186.

[2] Baskoutas, S. and A.F. Terzis, Size-dependent band gap of colloidal quantum dots. Journal of applied physics, 2006. **99**(1): p. 013708.

[3] Kolahi, S., S. Farjami-Shayesteh, and Y. Azizian-Kalandaragh, Comparative studies on energy-dependence of reduced effective mass in quantum confined ZnS semiconductor nanocrystals prepared in polymer matrix. Materials Science in Semiconductor Processing, 2011. **14**(3-4): p. 294-301.

[4] Azizian-Kalandaragh, Y., et al., Strong quantum confinement effects in SnS nanocrystals produced by ultrasound-assisted method. Journal of nanoparticle research, 2013. **15**(1): p. 1388.

[5] Azizian-Kalandaragh, Y. and N. Alizadeh-Siakeshi, Comparison of quantum confinement effect on the reduced effective mass of CdSe nanocrystals prepared by different methods. JOURNAL OF OPTOELECTRONICS ADVANCED MATERIALS, 2014. **16**(3-4): p. 345-350.

[6] Zabotnov, S.V., et al., Modification of cubic susceptibility tensor in birefringent porous silicon. physica status solidi, 2005. **202**(8): p. 1673-1677.

[7] Gayvoronsky, V.Y., et al., Enhancement of two-photon absorption in anisotropic mesoporous silicon. Laser Physics Letters, 2008. **5**(12): p. 894.

[8] Woggon, U., Optical properties of semiconductor quantum dots. 1997: Springer.

[9] Bruchez, M., et al., Semiconductor nanocrystals as fluorescent biological labels. science, 1998. **281**(5385): p. 2013-2016.

[10] Werber, A. and H. Zappe, Tunable, membrane-based, pneumatic micro-mirrors. Journal of Optics A: Pure Applied Optics, 2006. **8**(7): p. S313.

[11] Kudo, H., et al., A flexible and wearable glucose sensor based on functional polymers with Soft-MEMS techniques. Biosensors Bioelectronics, 2006. **22**(4): p. 558-562.

[12] Chou, H.-P., M.A. Unger, and S.R. Quake, A microfabricated rotary pump. Biomedical Microdevices, 2001. **3**(4): p. 323-330.

[13] Uluşan, A.B., et al., On the conduction mechanisms of Au/(Cu 2 O–CuO–PVA)/n-Si (MPS) Schottky barrier diodes (SBDs) using current–voltage–temperature (I–V–T) characteristics. Journal of Materials Science: Materials in Electronics, 2018. **29**(1): p. 159-170.

[14] Lehmann, V. and U. Gösele, Porous silicon formation: A quantum wire effect. Applied Physics Letters, 1991. **58**(8): p. 856-858.

[15] Farazin, J., G. Pirgholi-Givi, and Y. Azizian-Kalandaragh, Wettability measurement, optical characteristics, and investigation of the quantum confinement effect of ZnS-scotch tape nanocomposite films prepared by successive ionic layer adsorption and reaction (SILAR) method. Physica B: Condensed Matter, 2019. **564**: p. 94-103.

[16] Tang, X., G. Wen, and Y. Song, Stable silicon/3D porous N-doped graphene composite for lithium-ion battery anodes with self-assembly. Applied Surface Science, 2018. **436**: p. 398-404.

[17] Lyuleeva, A., et al., Charge Transfer Doping in Functionalized Silicon Nanosheets/P3HT Hybrid Material for Applications in Electrolyte-Gated Field-Effect Transistors. Journal of Materials Chemistry C, 2018.

[18] Macco, B., et al., Correlating the silicon surface passivation to the nanostructure of low-temperature a-Si: H after rapid thermal annealing. Journal of Applied Physics, 2017. **122**(3): p. 035302.

[19] Kim, M., et al., Modulating the extent of fast and slow boron-oxygen related degradation in Czochralski silicon by thermal annealing: Evidence of a single defect. Journal of Applied Physics, 2017. **121**(5): p. 053106.

[20] Wiegand, M., M. Reiche, and U. Gösele, Time- Dependent Surface Properties and Wafer Bonding of O 2- Plasma- Treated Silicon (100) Surfaces. Journal of The Electrochemical Society, 2000. **147**(7): p. 2734-2740.

[21] Descoeudres, A., et al., Improved amorphous/crystalline silicon interface passivation by hydrogen plasma treatment. Applied Physics Letters, 2011. **99**(12): p. 123506.

[22] Bisi, O., S. Ossicini, and L. Pavesi, Porous silicon: a quantum sponge structure for silicon based optoelectronics. Surface science reports, 2000. **38**(1-3): p. 1-126.

[23] Zabotnov, S., et al., Formation of nanoparticles on the silicon surface under the effect of femtosecond laser pulses. Semiconductors, 2007. **41**(8): p. 998-1001.

[24] Canham, L.T. Properties of porous silicon. 1997. Institution of Electrical Engineers.

[25] Collins, R., P. Fauchet, and M. Tischler, Phys. Today, 24 (January 1997); LC Kimerling, KD Kolenbrander, J. Michel, and J. Palm. Solid State Phys, 1997. **50**: p. 333.

[26] Oton, C.J., et al., Scattering rings as a tool for birefringence measurements in porous silicon. Journal of applied physics, 2003. **94**(10): p. 6334-6340.

[27] Agarwal, V. and J. Del Río, Tailoring the photonic band gap of a porous silicon dielectric mirror. Applied physics letters, 2003. **82**(10): p. 1512-1514.

[28] Yang, P., R. Yan, and M. Fardy, Semiconductor nanowire: what's next? Nano letters, 2010. **10**(5): p. 1529-1536.

[29] Ferrand, P., R. Romestain, and J. Vial, Photonic band-gap properties of a porous silicon periodic planar waveguide. Physical Review B, 2001. **63**(11): p. 115106.

[30] Mazzoleni, C. and L. Pavesi, Application to optical components of dielectric porous silicon multilayers. Applied Physics Letters, 1995. **67**(20): p. 2983-2985.

[31] Pavesi, L., et al., Controlled photon emission in porous silicon microcavities. Applied physics letters, 1995. **67**(22): p. 3280-3282.

[32] Zhou, Y., P. Snow, and P.S.J. Russell, Strong modification of photoluminescence in erbium-doped porous silicon microcavities. Applied Physics Letters, 2000. **77**(16): p. 2440-2442.

[33] Dubey, R. and D. Gautam, Fabrication and characterization of porous silicon layers for applications in optoelectronics. Optical quantum electronics, 2009. **41**(3): p. 189.

[34] Calcott, P., et al., Identification of radiative transitions in highly porous silicon. Journal of Physics: Condensed Matter, 1993. **5**(7): p. L91.

[35] Barillaro, G., et al., Integrated porous-silicon light-emitting diodes: a fabrication process using graded doping profiles. Applied Physics Letters, 2001. **78**(26): p. 4154-4156.

[36] Dhanekar, S. and S. Jain, Porous silicon biosensor: current status. Biosensors bioelectronics, 2013. **41**: p. 54-64.

[37] Föll, H., et al., Formation and application of porous silicon. Materials Science Engineering: R: Reports, 2002. **39**(4): p. 93-141.

[38] Efimova, A., et al., Enhanced photon lifetime in silicon nanowire arrays and increased efficiency of optical processes in them. Optical and Quantum Electronics, 2016. **48**(4): p. 232.

[39] Sokolov, A., et al., Increase in the lifetime of a photon and in the efficiency of raman scattering and second-harmonic generation processes in porous silicon carbide. JETP letters, 2015. **101**(12): p. 793-797.

[40] Alptekin, S. and Ş. Altındal, A comparative study on current/capacitance: voltage characteristics of Au/n-Si (MS) structures with and without PVP interlayer. Journal of Materials Science: Materials in Electronics, 2019: p. 1-9.

[41] Ersöz, G., et al., Investigation of electrical characteristics in Al/CdS-PVA/p-Si (MPS) structures using impedance spectroscopy method. 2016. **63**(7): p. 2948-2955.

[42] Alptekin, S. and Ş. Altındal, A comparative study on current/capacitance: voltage characteristics of Au/n-Si (MS) structures with and without PVP interlayer. Journal of Materials Science: Materials in Electronics, 2019. **30**(7): p. 6491-6499.

[43] Sevgili, Ö., et al., Examination of dielectric response of Au/HgS-PVA/n-Si (MPS) structure by impedance spectroscopy method. Physica B Condensed Matter, 2019. **566**: p. 125-135.

[44] Bilkan, Ç., et al., On the temperature dependent current transport mechanisms and barrier inhomogeneity in Au/SnO 2–PVA/n-Si Schottky barrier diodes. Applied Physics A, 2017. **123**(8): p. 560.

[45] Sze, S.M., Semiconductor devices: physics and technology. 2008: John Wiley & Sons.

[46] Rhoderick, E. and R. Williams, Metal–Semiconductor Contacts, Clarendon Press, Oxford 1988.

[47] Azizian-Kalandaragh, Y., Preparation of Lead Oxide Nanostructures in Presence of Polyvinyl Alcohol (PVA) as Capping Agent and Investigation of Their Structural and Optical Properties. JOURNAL OF SEMICONDUCTOR TECHNOLOGY AND SCIENCE, 2018. **18**(1): p. 91-99.

[48] Çetinkaya, H.G., Ö. Sevgili, and Ş. Altındal, The fabrication of Al/p-Si (MS) type photodiode with (% 2 ZnO-doped CuO) interfacial layer by sol gel method and their electrical characteristics. Physica B: Condensed Matter, 2019. **560**: p. 91-96.

[49] Farag, A.A., et al., Temperature dependence of J–V and C–V characteristics of n-InAs/p-GaAs heterojunctions prepared by flash evaporation technique and liquid phase epitaxy. Indian Journal of Pure & Applied Physics (IJPAP), 2018. **56**(3): p. 203-209.

[50] Cheung, S. and N. Cheung, Extraction of Schottky diode parameters from forward current- voltage characteristics. Applied Physics Letters, 1986. **49**(2): p. 85-87.

[51] Card, H. and E. Rhoderick, Studies of tunnel MOS diodes I. Interface effects in silicon Schottky diodes. Journal of Physics D: Applied Physics, 1971. **4**(10): p. 1589.

[52] Singh, T.B., et al., High- performance ambipolar pentacene organic field- effect transistors on poly (vinyl alcohol) organic gate dielectric. Advanced Materials, 2005. **17**(19): p. 2315-2320.

ANALYTICAL SOLUTION FOR DOUBLE CONFLUENT FORM OF HEUN EQUATION

H. Hale KARAYER

Department of Physics, Faculty of Arts and Sciences, Kirklareli University,39100 Kirklareli, Turkey

E-mail: hale.karayer@gmail.com

Abstract

Double confluent Heun equation (DHE) is studied analytically by using extended NU method. Heun equation in which Gauss hypergeometric, confluent hypergeometric, Mathieu, Ince, Legendre, Laguerre, Bessel functions are involved, is a general second order linear differential equation. The Heun equation is a Fuchsian type equation with four regular singular points. The DHE which is derived from Heun equation when two regular singular singularities coalesce, has two irregular singularities at zero and infinity and contains four parameters. Since there is no regular singular points, the DHE has not got convergent Frobenius solutions. On the other hand, solutions have the DHE have great importance in some physical problems as in gravitational theory. Therefore, eigenvalue problem of the DHE must be solved analytically.

Keywords: Extended Nikiforov-Uvarov method, Double confluent Heun equation, Eigenvalue problem

1. INTRODUCTION

Heun equation in which Gauss hypergeometric, confluent hypergeometric, Mathieu, Ince, Legendre, Laguerre, Bessel functions are involved, is a general second order linear differential equation:

$$\frac{d^2 w}{dz^2} + \left[\frac{\gamma}{z} + \frac{\delta}{z-1} + \frac{\epsilon}{z-a}\right]\frac{dw}{dz} + \frac{\alpha\beta z - q}{z(z-1)(z-a)} w = 0. \tag{1}$$

where $\gamma, \delta, \epsilon, \alpha$ and β are constant parameters and the complex number q is called accessory parameter [1]. The Heun equation is a Fuchsian equation with four regular singular points. Irregular singularities can be generated by confluences in Heun equation. Confluent, biconfluent, double and triconfluent Heun equation are important confluent forms of Heun equation. Scientists encounter Heun equation and its confluent forms in many branches of Physics [2]. Solutions of Heun type equations are given by using the power series method [1] which involves detailed processes. As an alternative solution method for Heun type differential equations we have introduced extended Nikiforov-Uvarov (NU) method and presented applicability for some physical problems [3, 4, 5, 6]. Extended form of NU method is achieved by changing boundary conditions of the NU method which are related to the degrees of polynomial coefficients in the basic equation of NU method. If any second order differential equation can be reduced to the basic equation, the differential equation can be solved exactly in a systematic way [7, 8]. NU method succeed only differential equations which has at most three singular points. The motivation of derivation of extended NU method is to expand the number of solvable differential equations and it is based on solving extended hypergeometric type equations systematically.

The aim of this work is analytical study of double confluent Heun equation (DHE) by using extended NU method. The DHE which is derived from Heun equation when two regular singular singularities coalesce, has two irregular singularities at zero and infinity and contains four parameters. The DHE is given in the following form;

$$z^2 \frac{d^2 y(z)}{dz^2} + (-z^2 + cz + t)\frac{dy(z)}{dz} + (-az + \lambda)y(z) = 0, \tag{2}$$

where c and a are local parameters which indicate the behavior of the solution at $z = 0$ and $z = \infty$, t is scaling parameter and λ is the accessory parameter [9]. Since there is no regular singular points, the DHE has not got convergent Frobenius solutions. On the other hand, solutions have the DHE have great importance in some physical problems as in gravitational theory [9, 10]. Therefore, eigenvalue problem of the DHE must be solved analytically. The manuscript is organized as follows: In Sec.2 the extended NU method is explained

briefly. Exact eigenvalue solutions of the DHE are achieved by extended NU method in Sec.3. Finally, our results were presented.

2. EXTENDED NIKIFOROV-UVAROV METHOD

If any second order differential equation which can be reduced to the following form;

$$\psi''(z) + \frac{\widetilde{\tau_e}(z)}{\sigma_e(z)}\psi'(z) + \frac{\widetilde{\sigma_e}(z)}{\sigma_e^2(z)}\psi(z) = 0 \tag{3}$$

where $\tilde{\tau}_e(z)$, $\sigma_e(z)$ and $\tilde{\sigma}_e(z)$ are polynomials of at most second, third and fourth-degrees respectively, the equation can be solved analytically. Eq.(3) is the basic equation of the extended NU method. Starting with transformation given as;

$$\psi(z) = \phi_e(z)y(z), \tag{4}$$

where $y(z)$ corresponds to polynomial solution of the equation, Eq.(3) is reduced to a more comprehensible form;

$$\sigma_e(z)y''(z) + \tau_e(z)y'(z) + h(z)y(z) = 0, \tag{5}$$

where

$$\tau_e(z) = \widetilde{\tau_e}(z) + 2\pi_e(z), \tag{6}$$
$$h(z) - \pi_e'(z) = g(z) \tag{7}$$

and

$$\pi_e(z) = \frac{\sigma_e'(z)-\widetilde{\tau_e}(z)}{2} \pm \sqrt{(\frac{\sigma_e'(z)-\widetilde{\tau_e}(z)}{2})^2 - \widetilde{\sigma_e}(z) + g(z)\sigma_e(z)}. \tag{8}$$

Recently defined polynomials $\tau_e(z)$ and $\pi_e(z)$ are polynomials of at most second-degree and $h(z)$ is a polynomial at most first degree. In order to determine all of possible values of the polynomial $\pi_e(z)$, the polynomial $g(z)$ must be known explicitly. According to the condition on $\pi_e(z)$ namely a polynomial of at most second-degree, the expression under the square root sign must be square of a polynomial at most second-degree. Thus the polynomial $g(z)$ must be chosen appropriately.

In order to generalize the solutions of Eq.(5), this equation is differentiated once;

$$\sigma_e(z)y^{(3)}(z) + (\tau_e(z) + \sigma_e'(z))y''(z) + (\tau_e'(z) + h(z))y'(z) + h'(z)y(z) = 0. \tag{9}$$

Eq.(9) is an extended hypergeometric type differential equation and its all derivatives have the same form. Therefore, it can be differentiated n times by using the new representation $y^{(n)}(z) = v_n(z)$ [3, 4]. When the coefficient of $v_n(z)$ is equal to zero, polynomial $h_n(z)$ is defined as

$$h_n(z) = -\frac{n}{2}\tau_e'(z) - \frac{n(n-1)}{6}\sigma_e''(z) + C_n, \tag{10}$$

618

where C_n is an integration constant. Eigenvalue solution of the problem can be found out by taking $h(z)$ equals to $h_n(z)$. Therefore Eq.(5) can be rewritten in the following form;

$$\sigma_e(z)y''(z) + \tau_e(z)y'(z) + h_n(z)y(z) = 0. \tag{11}$$

This equation has a particular solution of the form $y(z) = y_n(z)$ which is a polynomial of degree n. The function $\phi(z)$ in the initial transformation $\psi(z) = \phi(z)y(z)$ is defined as a logarithmic derivative;

$$\frac{\phi'(z)}{\phi(z)} = \frac{\pi(z)}{\sigma(z)}. \tag{12}$$

Determining all of the newly defined polynomials, eigenvalue and eigenfunction spectra can be obtained analytically by the extended NU method.

3. SOLUTION OF DOUBLE CONFLUENT HEUN EQUATION

The DHE provides the boundary conditions of extended NU method. Comparing Eq.(2) with the basic equation of the extended method given by Eq.(3) the polynomial coefficients can be associated as;

$$\tilde{\tau}_e(z) = -z^2 + cz + t$$
$$\sigma_e(z) = z^2$$
$$\tilde{\sigma}_e(z) = -az^3 + \lambda z^2. \tag{13}$$

The polynomial $\pi_e(z)$ can be obtained by substituting these polynomials in Eq.(8);

$$\pi_e(z) = \frac{z^2 + (2-c)z - t}{2} \pm \sqrt{(\frac{z^2 + (2-c)z - t}{2})^2 + az^3 - \lambda z^2 + g(z)z^2}. \tag{14}$$

The polynomial $g(z)$ which provides the condition of $\pi_e(z)$ is a second degree polynomial and corresponding polynomials $\pi_e(z)$ can be listed as follows;

$$\pi_{e1}(z) = z^2 + (2-c)z - t \tag{15}$$
$$\pi_{e2}(z) = 0 \tag{16}$$

for $g_1(z) = -az - \lambda$. Each of the polynomials $\pi_e(z)$ generates a different eigenstate solution for DHE. The solution for $\pi_{e1}(z)$ is given in details; by using Eq.(7), Eq.(6) and Eq.(10) respectively the polynomials $h(z)$, $\tau(z)$ and $h_n(z)$ can be achieved as;

$$h(z) = (2-a)z + 2 - c - \lambda \tag{17}$$
$$\tau(z) = z^2 + (4-c)z - 2t \tag{18}$$
$$h_n(z) = -nz - n(\frac{4-c}{2} + \frac{n-1}{3}) \tag{19}$$

Equating the right hand sides of $h(z)$ and $h_n(z)$ and taking the integration constant $C_{n1} = 0$ one can get the following relations;

$$2 - a = -n \tag{20}$$

$$\lambda = n(\frac{4-c}{2} + \frac{n-1}{3}) + 2 - c \tag{21}$$

Eq.(20) indicates the necessary condition for an eigensolution to be a polynomial where $n = 0,1\ldots$ and Eq.(21) gives eigenvalue solution of the DHE for the polynomial $\pi_{e1}(z)$.

Eigenfunction solution behaves related to the function $\phi_e(z)$ defined by Eq.(12). The function $\phi_e(z)$ becomes in this stage;

$$\phi_{e1}(z) = exp[z + \frac{t}{z}]z^{2-c}. \tag{22}$$

One can achieve to the following results for the polynomial $\pi_{e2}(z)$ by using the above mentioned process;

For Eq. (16);

$$a = -n \tag{23}$$

$$\lambda = n(\frac{c}{2} + \frac{n-1}{3}) \tag{24}$$

$$\phi_{e1}(z) = 1. \tag{25}$$

4. CONCLUSION

The DHE is handled in analytical treatment by using extended NU method. The parameter λ which plays the role of eigenvalue parameter is derived together with the necessary condition for the eigenfunction to be a polynomial in each stage corresponds to the different values of the polynomials π_e (z). To the best of our knowledge, the DHE has been solved analytically by the first time.

ACKNOWLEDGMENTS

REFERENCES

[1] A. Ronveaux, Heun's Differential Equations, Oxford University Press, New York, (1995)

[2] M. Hortaçsu, "Heun Functions and their uses in Physics" arXiv:1101.0471v1 [math-ph] (2011).

[3] H. Karayer, D.Demirhan and F. Büyükkılıç, "Extension of Nikiforov-Uvarov Method for the Solution of Heun Equation", J. Math. Phys., 56, 063504 (2015)

[4] H. Karayer, D.Demirhan and F. Büyükkılıç, "Some Special Solutions of Biconfluent and Triconfluent Heun Equations in elementary functions by Extended Nikiforov–Uvarov Method", Reports on Mathematical Physics, 76(3), 271-281 (2015)

[5] H. Karayer, D. Demirhan and F. Buyukkilic, "Solution of Schrödinger equation for two different potentials using extended Nikiforov-Uvarov method and polynomial solutions of biconfluent Heun equation", J. Math. Phys. 59, 053501 (2018)

[6] H. Karayer, D. Demirhan and F. Buyukkilic, "Analytical Solution of Dirac Equation for Hyperbolic Potential by Extended Nikiforov-Uvarov Method", Eur. Phys. J Plus, (2019)

[7] A. V. Nikiforov, and V. B. Uvarov, Special Functions of Mathematical Physics, Birkhauser, Boston, (1988).

[8] M. R. Pahlavani, Theoretical Concepts of Quantum Mechanics, Rijeka, Croatia, (2012).

[9] W. Lay, K. Bay and S. Y. Slavyanov, "Asymptotic and numeric study of eigenvalues of the double confluent Heun equation", J. Phys. A: Math. Gen. 31, 8521-8531 (1998)

[10] A. Roseau, "On the solutions of double confluent Heun equations", Aequationes Mathematicae, 60, 116–136 (2000)

INVESTIGATION OF ELECTRICAL AND OPTICAL PROPERTIES OF Ag DOPED ZnO THIN FILMS

B. Coşkun[1], A.Dere[2], F. Yakuphanoğlu[3]

[1]Department of Physics, Faculty of Sciences, Kırklareli University, Kırklareli, TURKEY
[2]Firat University, Nanoscience and Nanotechnology Laboratory, Elazig, 23200 TURKEY
[3] Firat University, Department of Physics, Elazig, 23200 TURKEY

E-mail: burhan.coskun@klu.edu.tr

The effect of Ag doping on dielectric behaviors of ZnO nanocrystals was investigated using spectroscopy. The AFM images indicate that the ZnO films are formed from the nanofibers. Moreover, the dispersion parameters such as dispersion energy, oscillator energy, dielectric constants and dissipation factor were determined. From optical constants analysis for ZnO films, the real (ε_1) and imaginary (ε_2) dielectric constants, optical conductivity and dissipation factor were also studied. The dielectric constants was found to decrease with Ag amounts. Low values of dielectric loss with Ag doping suggest that Ag-doped ZnO is suitable way for low frequency devices applications.

Keywords: Ag doped ZnO, Sol-gel Method, Electrical Modulus

1. INTRODUCTION

Zinc oxide (ZnO) is highly transparent conducting oxide in the visible region with a wide and direct band gap of about 3.37 eV at room temperature and a high exciton binding energy of 60 meV [1]. The exciton binding energy of ZnO is up to 60 meV, so devices made from ZnO can operate more efficiently at a high temperature. It possesses good optical, electrical and piezoelectric properties, which has been extensively used in many fields including electronic and photonic application [2-4]. Especially, ZnO is deemed as very promising photonic materials in industry owing to its outstanding optical and electrical properties [5,6]. Due to its wide band gap characteristics, ZnO has attracted a lot of attention for a variety of potential applications in both microelectronic and optoelectronic devices such as solar cell, transparent conducting electrode, UV and blue light emitter and thin film transistor.

ZnO thin films are prepared by variety of techniques, such as pulsed laser deposition, magnetron sputtering, chemical vapor deposition, atomic layer deposition, molecular beam epitaxy, and sol-gel method. However, the sol-gel method offers some advantages over all above mentioned techniques, e.g. it is very simple, cost is low, no requirement of vacuum, composition can be easily controlled, and one can also coat a large substrate area. The sol-gel method for the synthesis of inorganic nanoparticles such as ZnO, TiO2 and SiO2 has become one of the most popular chemical procedures [7,8].

At the same time, various metal and non-metal co-doping can also change electrical conductivity and optical characteristics of ZnO doped system. Doping process has ability to absorb photons of light with a widening range of the solar spectrum. The photocatalytic activity of ZnO nanoparticles was improved using various dopants such as Ag, Ni, Mn, Fe, Co, and Pd [9,10]. In the present study, we have investigated the effect of Ag dopants as well as their concentration on the structural and electrical properties of ZnO thin films.

2. MATERIAL AND METHODS

ZnO and Ag doped ZnO solutions were produced by sol-gel method and p type silicon substrates were coated using spin coating method. For the thin film preparation, 0.5 M zinc acetate was dissolved in 10 ml isopropanol (IPA) and silver acetate was added to the solution with the molar ratios of 0,2 % and 0,5 % and stirred using magnetic stirrer at 500 rpm. When the metallic salts totally dissolved in the liquid ethanolamine was added as a stabilizer to the solution and final solution was stirred for 1 hour at room temperature. Then, p type Si wafers were kept in IPA and water for 5-minute periods, respectively. Si wafers then cleaned with nitrogen gas. Prepared undoped ZnO and Ag doped ZnO solutions were drop cast on Si wafers and the spin

coating process was performed under 3000 rpm for 30 seconds. To evaporate the solvents existing in solutions, thin films were baked at 150 ˚C for 5 minutes. Final products were then annealed at 450 ˚C for 1 hour. Surface properties of the thin films were investigated using PARK SYSTEM XE-100E atomic force microscope (AFM) in non-contact mode at room temperature in ambient conditions. The optical properties of the thin films were assessed at room temperature using SHIMADZU UV–Vis–NIR 3600 spectrophotometer in the wavelength between 200 and 1200nm. Electric and optoelectronic properties of photodiodes were investigated using FYTRONIX FY-7000 Solar Simulator I-V Characterization System.

In this way, the photodiodes were ready for determining their characterizations. Thus, photodiodes were called Z01 (Undoped ZnO), Z02 (% 0.5 Ag doped ZnO) and Z03 (% 2 Ag doped ZnO).

3. RESULTS AND DISCUSSION

The structural properties of the samples were characterized by using non-contact mode AFM which is used an appropriate special tip. The $5\,\mu m \times 5\,\mu m$ AFM images were taken from the prepared thin film samples. AFM images of the surfaces were presented in Fig. 1. AFM images were obtained in non-contact mode at room temperature in ambient conditions. When the images were assessed, it was seen that undoped ZnO films consist of flake like structures. AFM images revealed that flake like structures covered the substrate homogeneously and form cascaded arrangement.
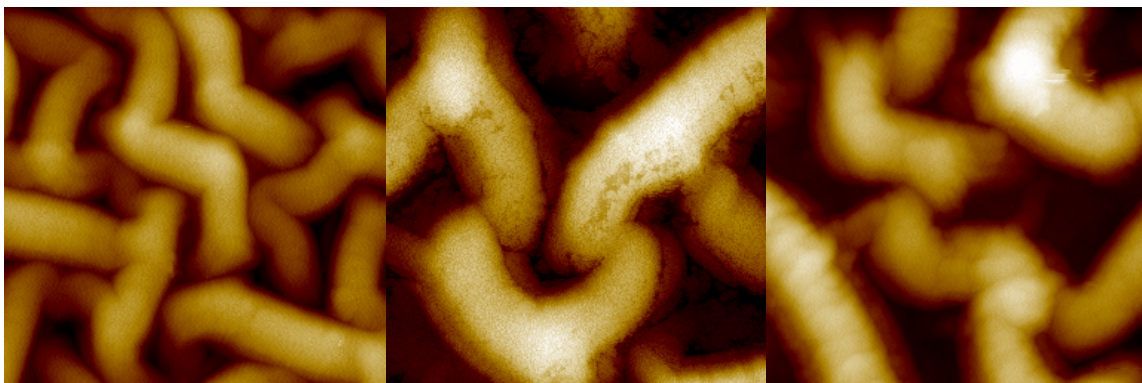

Figure 1: AFM images belonging Z01, Z02 and Z03 thin films

The electrical characteristics of *Z01*, *Z02* and *Z03 Ag* doped ZnO based photodiodes which are were investigated at room temperature. The semi-logarithmic *I-V* graph given in Fig. 2 was drawn with obtained *I-V* data of *Z01*, *Z02* and *Z03* photodiodes.
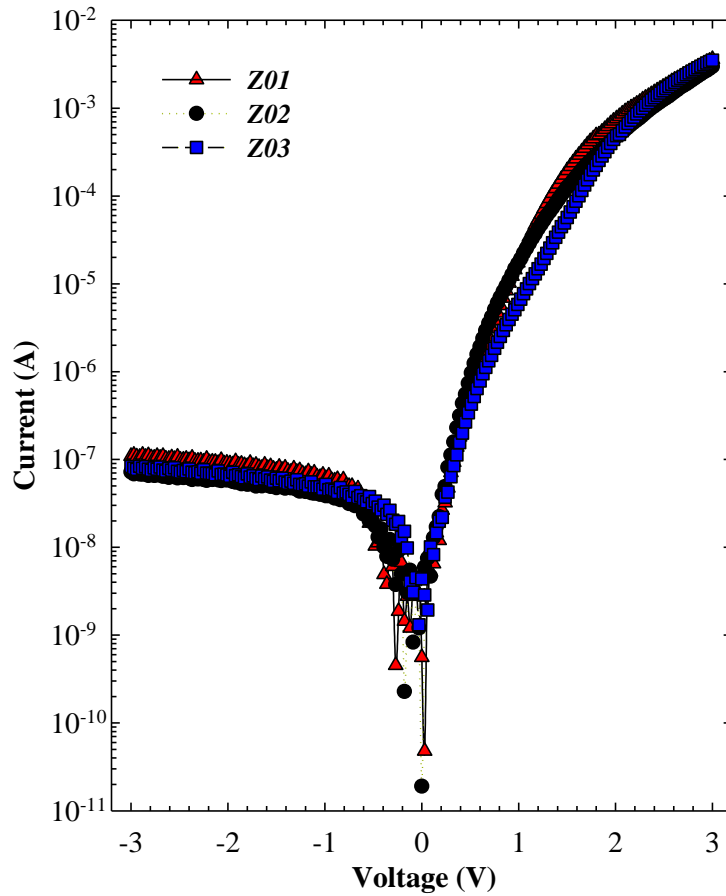
Figure 2. The *lnI-V* characteristics of the photodiodes.

The photodiodes were quantitatively analyzed by using the standard thermionic emission (TE) theory [11].

$$I = I_o \exp\left(\frac{q(V - IR_s)}{nkT}\right) \tag{1}$$

where k is the Boltzmann's constant, I_o is reverse saturation current, IR_s is the voltage drop across the series resistance, q is the electronic charge, n is the ideality factor and T is the absolute temperature in Kelvin.

The fundamental electron excitation spectrum of the films was described by means of the frequency dependence of the complex electronic dielectric constant. The complex refractive index $(\hat{n} = n + ik)$ and the dielectric function $\hat{\varepsilon} = \varepsilon_1 + i\varepsilon_2$ characterize the optical properties of any solid material.

The real and imaginary parts of the complex dielectric constants are expressed as [12, 13]

$$\varepsilon(\omega) = \varepsilon_1(\omega) + i\varepsilon_2(\omega) \tag{8}$$

where e1 and e2 are the real and imaginary parts of the dielectric constant, respectively.

$$\varepsilon_1(\omega) = n^2(\omega) - k^2(\omega) \tag{9}$$

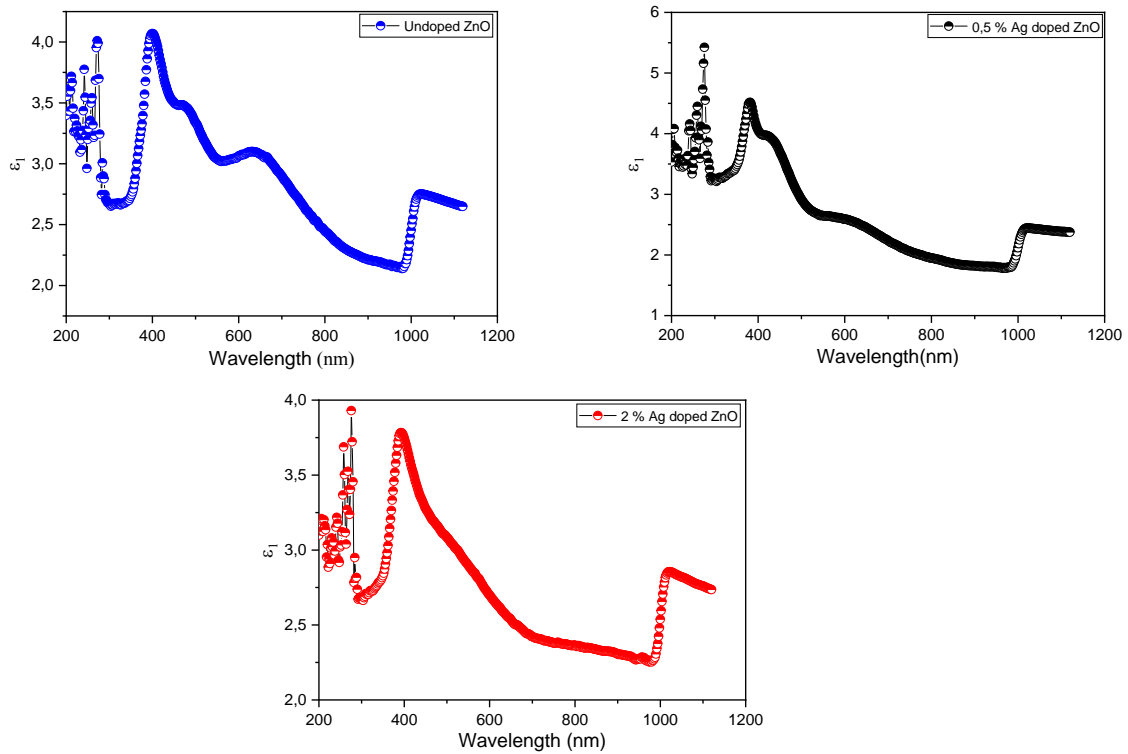$$\varepsilon_2(\omega) = 2n(\omega)k(\omega) \tag{10}$$

Some other optical properties such as refractive index and extinction coefficients of the samples were studied. The refractive index is an important optical parameter. The refractive index of the films was calculated using reflectance and absorption data. The refractive index (n) of the films was determined by the following relations [14];
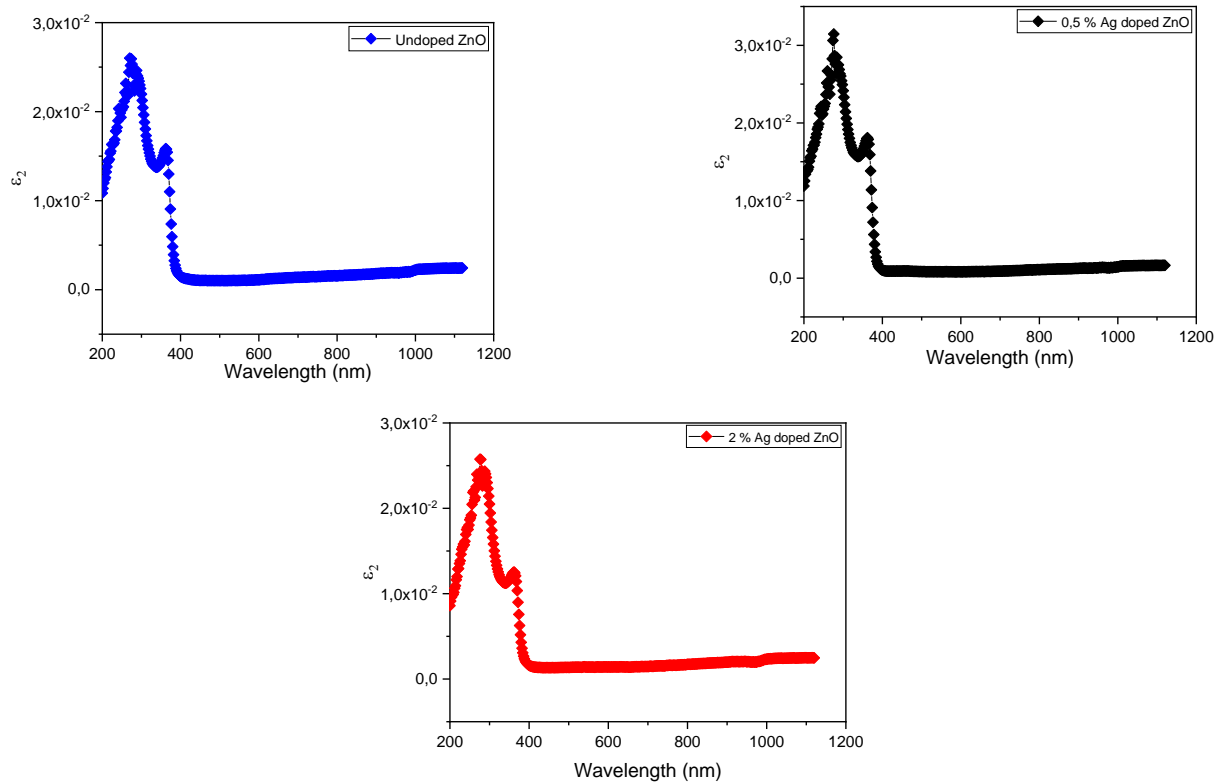
$$R = \frac{(n-1)^2 + k^2}{(n+1)^2 + k^2} \tag{11}$$

$$n = \left(\frac{1+R}{1-R}\right) + \sqrt{\frac{4R}{(1-R)^2} - k^2} \tag{12}$$

k (k=$\alpha\lambda/4\pi$) where k is the extinction coefficient.

The dependence of ε1 and ε2 on the wavelength for undoped ZnO and Ag doped ZnO, films are shown in Fig. 3. It is seen that the real and imaginary part of dielectric constant changes with the wavelength, which suggest that some interactions between the photons and electrons in the films are taking place. The real part of the complex dielectric constant is higher than the imaginary part of the dielectric constant.
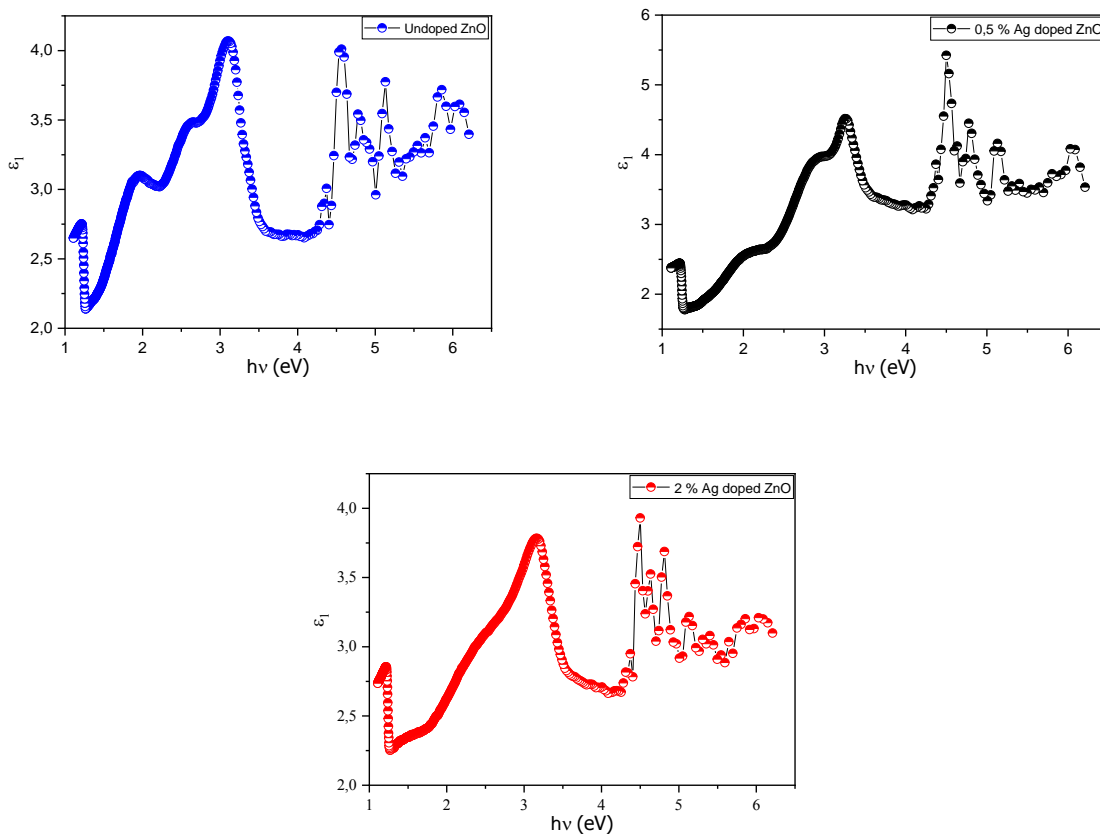
Figure 3: The plot of wavelength dependent real part of dielectric constant of the undoped ZnO and Ag doped ZnO thin films.
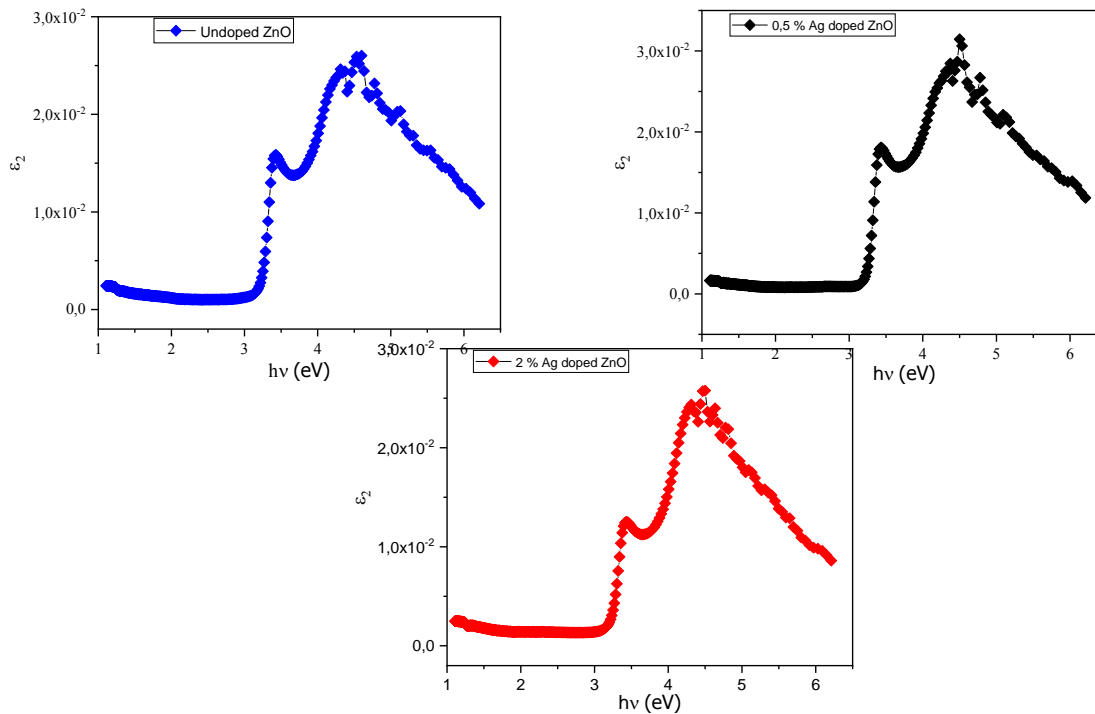

Figure 4: The plot of wavelength dependent imaginary part of dielectric constant of the undoped and Ag doped ZnO thin films.

Photon energy dependence of both ε_1 and ε_2 are depicted in Fig. 3. Values of ε_1 exhibits are higher than those for the ε_2 in the studied photon energy range. There are different behaviors for the two parts of the dielectric constant. The variation of the dielectric constant with photon energy indicates different interactions between photons and electrons in the films are produced in this energy range. These interactions are observed on the shapes of the real and imaginary parts of the dielectric constant and they cause formation of peaks in the dielectric spectra which depends on the material type different behaviours were observed for both ε_1 and ε_2 and the spectral dependence indicates different interactions between photons and charge carriers in the semi-conductor are achieved in this energy range [15, 16] which causes characteristic peaks in the dielectric spectra. An intense peak, shown in the spectral dependence of ε_2 is observed at ≈3 eV fool-lowed by a minimum intensity in ε_1 at the same energy.

Figure 5: The plot of photon energy dependent real part of dielectric constant of the undoped and Ag doped ZnO thin films.

Figure 5: The plot of photon energy dependent imaginary part of dielectric constant of the undoped and Ag doped ZnO thin films.

4. CONCLUSION

In this work, ZnO thin films were doped with 0,5 % and 2 % Ag for photodiode applications. Surface characteristics of the photodiodes were characterized using AFM. AFM images revealed that flake like structures covered the substrate homogeneously and form cascaded arrangement.

The optical analysis of the films indicates that the optical constants such as, dielectric constants depend on the composition of the film. The real part of the complex dielectric constant is higher than the imaginary part of the dielectric constant

ACKNOWLEDGMENTS

REFERENCES

[22] M. Caglar, S. Ruzgar J. Alloy. Compd., 644 (2015), pp. 101-105

[23] C.E. Benouisa, M. Benhalilibaa, A. Sanchez Juarezb, M.S. Aidac, F. Chamid, F. Yakuphanoglu
J. Alloy. Compd., 490 (2010), pp. 62-67

[24] S. Dutta, S. Chattopadhyay, A. Sarkar, M. Chakrabarti, D. Sanyal, D. Jana Role of defects in tailoring structural, electrical and optical properties of ZnO Prog. Mater. Sci., 54 (2009), pp. 89-136

[25] K.G. Girija, K. Somasundaram, A. Topkar, R.K. Vatsa, Highly selective H2S gas sensor based on Cu-doped ZnO

nanocrystalline films deposited by RF magnetron sputtering of powder target, J. Alloy. Comp. 684 (684) 15-20.

[26] Z.K. Tang, G.K.L. Wong, P. Yu Room-temperature ultraviolet laser emission from self-assembled ZnO microcrystallite thin films Appl. Phys. Lett., 72 (1998), pp. 3270-3272

[27] M.H. Huang, S. Mao, H. Feick, H. Yan, Y.Y. Wu, H. Kind, E. Weber, R. Russo, P. Yang Science, 292 (2001), p. 1897

[28] S. Okur, F. Yakuphanoglu, E. Stathatos Microelectronic Eng., 87 (2010), p. 635

[29] Q. Xiao, J. Zhang, C. Xiao, X. Tan, 2007, Photocatalytic decolorization of methylene blue over Zn1−xCoxO under visible light irradiation, Materials Science and Engineering B, 142,121-125

[30] Jun bo Zhong, Jian zhang Li, Xi yang He, Jun Zeng, Yan Lu, Wei Hu and Kun Lin, Improved photocatalytic performance of Pd-doped ZnO, Current Applied Physics 12 (2012) 998e1001.

[31] Şenay Şen Türkyılmaz, Nuray Güy and Mahmut Özacar, Photocatalytic efficiencies of Ni, Mn, Fe and Ag doped ZnO nanostructures synthesized by hydrothermal method: The synergistic/antagonistic effect between ZnO and metals, Journal of Photochemistry and Photobiology A: Chemistry, 341 (2017), pp. 39-50

[32] T. Asar, B. Korkmaz, S. Özçelİk, Effect of Platinum Doping on the Structural and Electrical Properties of SnO2 Thin Films, J. Exp. Nanosci. 11 (2016). doi:10.1080/17458080.2016.1212408.

[12] El-Korashy, A., El-Zahed, H., Radwan, M., 2003. Optical studies of [N(CH3)4]2 CoCl4, [N(CH3)4]2 MnCl4 single crystals in the normal paraelectric phase, Physica B 334, 75.

[13] Maeda, Y., Andoh, H., Ikuta, I., Minemura, H., 1988. Appl. Opt. 64, 1715.

[14] Abeles, F., 1972. Optical Properties of Solids, North-Holland, Publishing Company, London, UK.

[15] Fadel, M., Fayek, S. A., Abou-Helal, M. O., İbrahim, M. M., Shakra, A. M. L., 2009. Structural and optical properties of SeGe and SeGeX (X= In, Sb and Bi) amorphous films, Alloys Compd. 485, 604-609.

[16] Khan, S. A., Hazmi, F. S., Al-Heniti, S. A., Faidah, S. A. Al-Gamdi, A., 2010. Effect of cadmium addition on the optical constants of termally evaporated amorphous Se-S-Cd thin films, Curr. Appl. Phys. 10, 145-152

ON THE FREQUENCY AND VOLTAGE DEPENDENCE OF COMPLEX DIELECTRIC, COMPLEX ELECTRIC MODULUS, AN AC ELECTRICAL CONDUCTIVITY IN AU/(ZNO₂FE₄-PVP)/N-SI (MPS) CAPACITORS

Şemsettin Altındal

Department of Physics, Faculty of Sciences, Gazi University, Ankara-Turkey

E-mail: altundal@gazi.edu.tr

Abstract

Frequency and voltage dependence of complex-dielectric, complex-electric modulus, and dielectric loss tangent (tanδ) of the Au-(ZnO₂Fe₄-PVP)-nSi (MPS) capacitors were investigated in wide range of frequency (10kHz-5MHz) and voltage (-2V/+5V) by using capacitance/conductance-voltage (C/G-V) measurements to get accuracy and reliable results on the dielectric properties. The decreases of ε' and dielectric loss (ε'') with increasing frequency was attributed to the polarization and surface states (N_{ss}). Both the tanδ and M'' was changed with bias voltage and dhow a peak behavior and changes their magnitudes and positions with frequency were attributed a special distribution of Nss, their lifetime, and polarization. Thes results show that the -(ZnO₂Fe₄-PVP) organic interlayer can be successfully used instead of traditional insulator materials in respect of low cost, low weight, flexibility, required low energy consumption, and easy grown processes.

Keywords: Interfacial (ZnO₂Fe₄-PVP) interlayer; Surface states and polarization effects; Series resistance

1. INTRODUCTION

In recently, many studies were performed on the electrical and dielectric properties of the MS type electronic devices by using various interlayer materials such as insulator (TiO_2) [1]), ferroelectric ($Bi_4Ti_3O_{12}$ [2], polymer (graphene-PVA) [3]. Among them, polymer has grasped more attention due to its low-cost production, flexibility, and large area of production compared to traditional insulator materials. Especially PVA and PVP have unique features such as high-water solubility and a large crystallinity range. At low and moderate frequencies C and G values become strong function of frequency and voltage due surface states (N_{ss}) and dislocations and their lifetimes (τ) [10,11]. Additionally, the value of series resistance (R_s) becomes more effective on the C/G-V plots at accumulation region [6]. Therefore, the investigation of the electric and dielectric properties of semiconductor devices in wide range of frequency and bias voltage is more important because of a detail physical mechanism of them are not well understood yet.

The aim of this study is to fabricate Au/nSi capacitor with (ZnO_2Fe_4-PVP) polymer interlayer utilizing electrospinning method and their dielectric properties, ac electrical conductivity (σ_{ac}), and complex electric modulus of them in wide range of frequency and voltage at room temperature by using by using impedance spectroscopy method to get more accuracy and reliable results.

2. EXPERIMENTAL DETAILS

Au/(ZnO_2Fe_4-doped PVP/n-Si capacitors were performed on the P-doped Si wafer with (100) float zone, 300 μm thickness, and $\sim 10^{15} cm^{-3}$ doping donor atoms. Before the formation of ohmic and rectifier contacts, n-Si wafer was cleaned in various acid solutions and dried with high-pure nitrogen gas. After that 150 nm thickness of high-pure Au (99.999%) was thermally evaporated onto the backside of wafer at 10^{-6} and then it was sintered at 550 °C for 5 min in a N_2 atmosphere to perform a good ohmic contact. Immediately, the prepared (ZnO_2O_4-PVP) organic solution utilizing electrospinning method was grown on the front of wafer with 22 nm from the interlayer-capacitance (C_i). Finally, Au circular dots with 150 nm thickness and 7.85×10^{-3} cm^{-2} were evaporated on the (ZnO_2O_4-PVP) in the same system.

3. RESULTS AND DISCUSSIONS

Fig. 1 and 2 show the (ε'-V-f) and (ε''-V-f) plots of the Au/(ZnO_2Fe_4-PVP)/n-Si (MPS) capacitor were obtained from the measured C_m and G_m data by using following relations [7].

$$\varepsilon' = \frac{C}{C_0} = \frac{Cd_i}{\varepsilon_0 A} \tag{1}$$

$$\varepsilon'' = \frac{G}{\omega C_0} = \frac{G d_i}{\varepsilon_0 \omega A} \qquad (2)$$

The loss tangent ($\tan\delta = \varepsilon''/\varepsilon'$) which is a ratio of ε'' to ε' and the investigation of it is depend on both frequency and voltage. As shown in Figs 1 and 2, the changes in ε' and ε'' in the depletion region is result of N_{ss} and their restructure and reordering under an external electric field but the changes at accumulation region usually is result of R_s and organic layer. According to Maxwell-Wagner-Sillars effect, current follows from the interface of the composites, space charges can be accumulated and so leads to polarization [8].
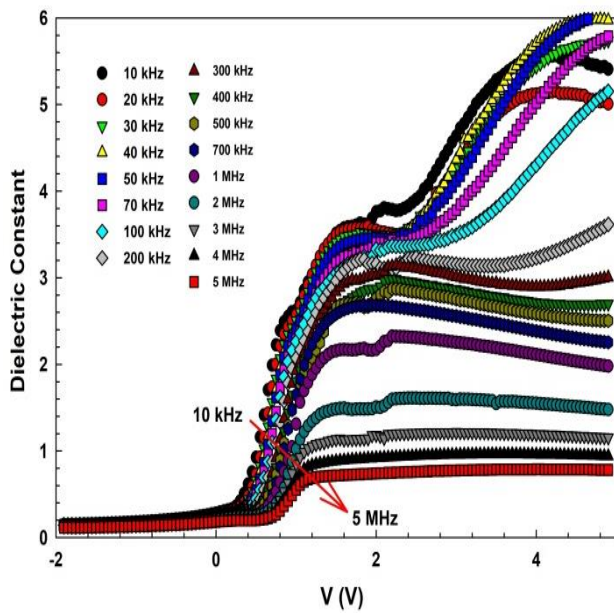

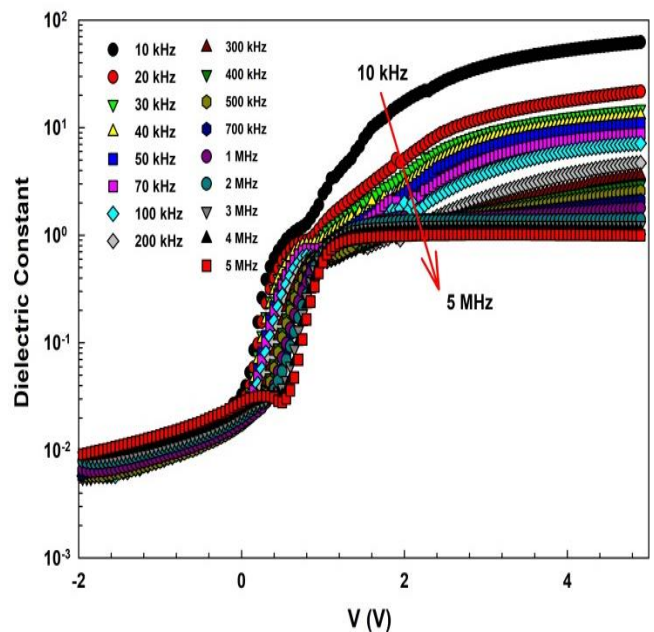Fig 1. The frequency dependent (ε'-V) plots of Au/(ZnO$_2$Fe$_4$-PVP)/n-Si (MPS) capacitor.

Fig 2. The frequency dependent (ε''-V) plots of Au/(ZnO$_2$Fe$_4$-PVP)/n-Si (MPS) capacitor.

The complex electric modulus (M^*) is defined in terms of the complex ε^* as given following form [7]:

$$M^* = \frac{1}{\varepsilon^*} = M' + jM'' = \frac{\varepsilon'}{\varepsilon'^2 + \varepsilon''^2} + j\frac{\varepsilon''}{\varepsilon'^2 + \varepsilon''^2} \qquad (3)$$

Thus, the real (M') and imaginary (M") parts of M* were calculated from the Eq. 3 using ε' and ε'' values. The value of M' decreases with increasing bias voltage but increases rapidly with increasing frequency due to the shortrange mobility of electrons. The observed in M'' vs V which is corresponding to the dielectric relaxation processes and peak position shift towards to higher voltage with increasing frequency due to N_{ss} and Maxwell-Wenger type polarization [7,8]. The σ_{ac}-ln(f) and ln(σ_{ac})-ln(f) plots of the capacitor for various voltages at accumulation region were obtained by using the following equation.

$$\sigma_{ac} = \left(\frac{d_i}{A}\right)\omega C \tan\delta = \varepsilon'' \omega \varepsilon_0$$

(4)

The σ_{ac} value remains almost constant at low frequencies which is corresponding to the dc conductivity (σ_{dc}) and then starts increase almost as exponentially at high frequencies due to Josher's power law [9].

4. CONCLUSION

The calculated value of ε' (~ 6) even at 10 kHz for the fabricated Au/(ZnO$_2$Fe$_4$-PVP)/n-Si (MPS) capacitor is considerably high when compared the SiO$_2$ insulator. The surface morphology of the zinc ferrite nanostructures was investigated by FE-SEM and the image show that the surface analysis shows the formation of clusters. The values of tanδ and M'' were found changed with bias voltage and show a peak behavior and changes their magnitudes and positions with frequency were attributed a special distribution of Nss, their lifetime, and polarizationThe tanδ and M'' show a peak behavior and changes their magnitudes and positions with frequency were attributed a special distribution of Nss, their lifetime, and polarization. These results are confirmed that the value of C one has to increase of the ε' and the decrease of interlayer thickness, but it is largely determined by the working voltage and cannot be tempered. As a result, the grown organic interlayer at M/S interface is more important due to its low cost and low molecular weight, flexibility, and large area of production compared to insulators.

REFERENCES

[1] Y. Şafak-Asar, T. Asar, Ş. Altındal, S. Özçelik, Investigation of dielectric relaxation and ac electrical conductivity using impedance spectroscopy method in (AuZn)/TiO$_2$/p-GaAs(110) Schottky barrier diodes, J. Alloys Compd. 628 (2017) 442–9

[2] H.G. Çetinkaya, M. Yıldırım, P. Durmus, Ş. Altındal, Diode-to-diode variation in dielectric parameters of identically prepared metal-ferroelectric-semiconductor structures, J. Alloys Compd., 728 (2017) 896-901.

[3] S. Altındal Yerişkin, M. Balbaşı, İ. Orak, The effects of (graphene doped-PVA) interlayer on the determinative electrical parameters of the Au/n-Si (MS) structures at room temperature. J Mater Sci Mater Electron 28 (2017)14040-8.

[4] S. M. Sze, Physics of Semiconductor Devices, 2nd ed. New York: Willey, 1981.

[5] H.C. Card, E.H. Rhoderick, Studies of tunnel MOS diodes I. Interface effects in silicon Schottky diodes. J. Phys. D Appl. Phys. 4, 1589–1601 (1971)

[6] E.H. Nicollian, J.R. Brews, Metal oxide semiconductor (MOS) physics and technology, New York, John Willey & Sons;1982.

[7] C.P. Symth, Dielectric Behaviour and Structure, McGraw-Hill, New York, 1995.

[8] Z. Wang, W. Zhou, L. Dong, X. Sui, H. Cai, J. Zuo, Q. Chen, Dielectric spectroscopy characterization of relaxation process in Ni/epoxy composites, 682 (2016) 738-745.

[9] S. Hlali, N. Hizem, L. Militaru, A. Kalboussi, A Souifi, Effect of interface traps for ultra-thin high-k gate dielectric based MIS devices on the capacitance-voltage characteristics, Microelectronics Reliability, 75 (2017) 154-161.

SYNTHESIS OF NANOMATERIALS FOR QUANTUM ELECTRONIC APPLICATIONS

A.Dere[1], B. Coşkun[2], F. Yakuphanoğlu[3]

[1]Firat University, Nanoscience and Nanotechnology Laboratory, Elazig, 23200 TURKEY
[2]Department of Physics, Faculty of Arts and Sciences, Kırklareli University, Kırklareli, TURKEY
[3] Firat University, Department of Physics, Elazig, 23200 TURKEY

E-mail:fyhan@hotmail.com

Abstract

Hydrothermal method is the method of producing nanomaterial with the help of high pressure and temperature. In this way, nanomaterials with different morphologies are produced by changing the pressure and temperature values depending on the main material. In hydrothermal system produce all materials from the solutions such organic materials and metal oxides and all-in solutions for various applications. FYHD-8000 produce materials from the solution as powder and thin films on any substrate. Hydrothermal method is the most suitable and inexpensive method for these applications. High efficiency materials can be produced with minimum loss of material under high vapor pressure
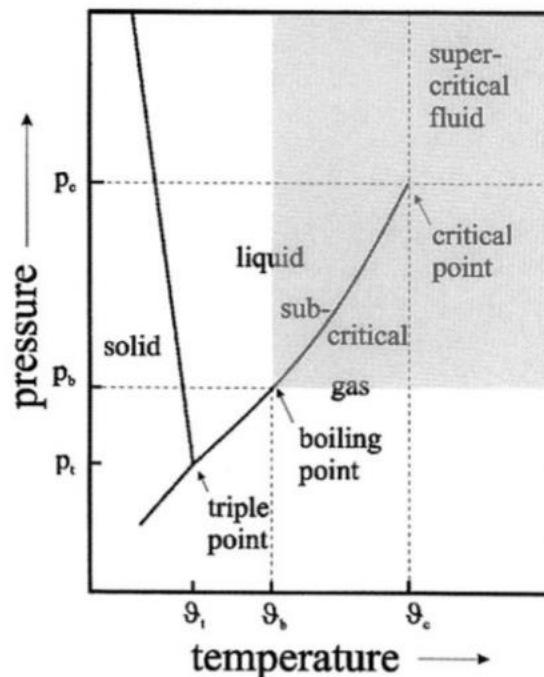
Keywords: Nanomaterial, hydrothermal synthesis, fytronix.

1. INTRODUCTION

Hydrothermal synthesis is the synthesis of single crystalline materials due to the solubility of materials under high temperature and pressure in a closed ambient [1]. Hydrothermal synthesis in aqueous ambient corresponds to reactions above 100 ° C and 1 bar. Natural phenomena are the best examples of hydrothermal reaction. This method is also used in the separation of various chemicals especially in the industrial field [1]. In order to control the morphology of the materials to be prepared by hydrothermal method, low pressure or high pressure conditions can be used depending on the vapor pressure of the main material in the reaction. Also materials having different morphologies can be obtained by changing the reaction time. Many nanomaterials can be synthesized easily and successfully by hydrothermal method. this method has significant advantages over other nanomaterials production methods. It can produce nanomaterials at variable high temperatures. For this during the hydrothermal reaction process the conditions of the reaction are very important.

Physical and chemical properties of water under hydrothermal conditions investigated by Franck (1978). The Physical properties of the water with PVT data 1000 ºC and 10 kb under can be better detected [2].

Fig.1. Schematic phase diagram of water showing specific areas during hydrothermal process
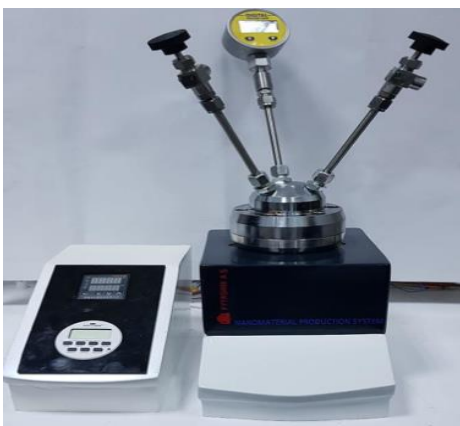
As seen Fig.1 Pt,Vt and PbVb indicate the triple point and boiling point respectively, while PcVc are the pressure and temperature of the critical point (374°C and 221 bar). In addition, the Pc curve is automatically generated in all temperature ranges [3].

2. MATERIAL AND METHODS

In seen Fig.2. System includes a high pressure reactor and temperature controller. This system Reaction temperature: 50-300 ^{o}C 100 ml PTFE or black carbon:TFE sample holder as seen in Fig.3. PID Temperature controller System automatically adjusts internal-pressure from low to high pressure by temperature or solution volume or external gas. The solution prepared in aqueous ambient is placed into the teflon holder, then placed into the system and the screws are closed. External gas valve is also closed after the screws are closed. After a completely airless indoor ambient, pressure-temperature and heating steps are determined according to the properties of the main material and the system is operated. The system automatically turns off after the set time has elapsed. In order to remove the nanomaterials from the closed system, first the external valve is opened and then the nanomaterials are obtained by applying centrifugation or filtration to the aqueous nanomaterials.

3. RESULTS AND DISCUSSION

FYTRONIX FYHD-8000 System includes a high pressure reactor and temperature controller. Synthesize powder nanomaterials, nanostructure thin films with FYHD-8000 hydrothermal device. Also controlling of nanosize with reaction time, nanosize and nanostructure with reaction temperature and controlling of nanosize and nanostructure with pressure.

Fig.2. Nanomaterial production system FYTRONIX F 8000

Fig.3. Teflon Holder

Systems produces the following materials or more; All ceramic materials, Bioceramics, Polymer nanocomposites, Polymers, Metal complexs, Organometallic complex, Metal complex nanocomposites, Bioglass ceramic materials, Carbon based materials, Graphene , Graphene Oxide, Boron based materials, Coating metal oxide films on substrate, Coating bioceramic films on substrate

, Graphene-nanocomposite materials, Nanocomposite metal oxide materials, Metal oxide semiconductors, Boron nitride, boron carbide, Film growth on any substrate, Battery materials, Solar cell materials, Ferroelectric materials, Piezzo materials, PL materials, Chalcogenide materials, Biomaterials, Hybrid materials and more.

4. CONCLUSION

As a result, the hydrothermal method is one of the easiest and most successful methods for the production of single crystal nanomaterials. Hydrothermal method, which is commonly used in chemistry and materials field, is also used in quantum dot and drug delivery systems in medicine [4].

REFERENCES

[1] Voltage and frequency dependence of negative capacitance behavior in a Graphene-TiO2 nanocomposite photoanode based on quantum dot sensitized solar cells, MesutYalcin, FahrettinYakuphanoglu, Optik Volume 183, April 2019, Pages 1099-1105.

[2] Hydrothermal Synthesis, Encyclopedia of Materials: Science and Technology (Second Edition), 2001, Pages 3989-3992

[3] Hydrothermal synthesis of nanomaterials, O. Schäf, H. Ghobarkar* and P. Knauth, Nanostructured Materials pp 23-41.

[4] Graphene Quantum Dots: Syntheses, Properties, and Biological Applications, T.A.Tabish, S Zhang, Comprehensive Nanoscience and Nanotechnology (Second Edition), Volume 3, 2016, Pages 171-192.

FULL AUTOMATIC SOLAR SIMULATOR SYSTEMS FOR PHOTOVOLTAIC APPLICATIONS

A.Dere[1], B. Coşkun[2], F. Yakuphanoğlu[3]

[1]Firat University, Nanoscience and Nanotechnology Laboratory, Elazig, 23200 TURKEY
[2]Department of Physics, Faculty of Arts and Sciences, Kırklareli University, Kırklareli, TURKEY
[3] Firat University, Department of Physics, Elazig, 23200 TURKEY

E-mail: a.dere@firat.edu.tr

Abstract

This system analyze all photovoltaic and photoconducting characteristics of all solar cells such Dye sensitized solar cell, quantum dots solar cells, Organic solar Cells, Silicon Solar cells, Thin films solar Cells under various solar light intensities from 0.1 W/cm2 to 1500 W/m2. This system is a complete current-voltage (I-V), current-time (I-t) and power-voltage (P- V) measurement environment. Voltage range: -45 V to +45 V Current range: 100 pA to 200 mA. 19 independently controlled LED wavelengths from 400 nm – 1100 nm. FY-8000 solar simulator should have sample holder and it is comprised of two probes. Holder size should have 132.5mmx132.5mm. This solar simulator should have software to control measurements and analysis of data. Device should automatically measure open circuit voltage Voc and short circuit current, I_{SC} , Shunt resistance (Rsh) • Conversion efficiency (n), Maximum power output (Pmax), Voltage at Pmax (Vmax), characteristic resistance, Rch , Fill factor (FF) • Series resistance (Rs).

Keywords: Solar simulator, electrical properties, diode, solar cell.

1. INTRODUCTION

Semiconductor compounds are of great interest in electronic technology because they have important electronic, structural and optical properties in various phase structures [1].

Accurate measurement of the electrical properties of semiconductors is very important for the correct and safe operation of any electronic device produced [2]. The performance of electronic devices depends on how the charge carriers move in the conduction and valence band. Electrical behavior of materials is explained by band structures. electrical conduction is the physical properties of materials that vary according to the distance and electron density between these bands.Conductivity equation of materials;

$$\sigma = ne\mu \tag{1}$$

σ, $(\Omega^{-1}cm^{-1}$ or Scm) expressed as a function of the charge carrier density, n, (cm^{-3}) the electron charge, e, (C) the μ (cm^2/Vs) is the so called drift mobility. The mobility expresses the average velocity gained by a charge carrier in an applied electric field of 1 V/cm.

According to quantum theory, an electric current can flow through a material if it has a partially filled electron band (the so called conduction band). In this way, electrons can be brought slightly above the fermi energy. Thus, current is generated by the electric field. but only those close to the fermi energy allow the transmission of electric current. conductivity equation according to quantum mechanics is given as follows;

$$\sigma = 1/3\ e^2\ v_F\ \tau\ N(E_F) \tag{2}$$

where v_F is the velocity of the electrons at the Fermi energy and $\tau N (E_F)$ is the density of filled electron states at the Fermi energy.

Figure 1: Schematic of a band diagram showing the energy levels filing for a semiconductor, near 0 K, and for an insulator. Eg represents the amplitude of the energy gap of the material.

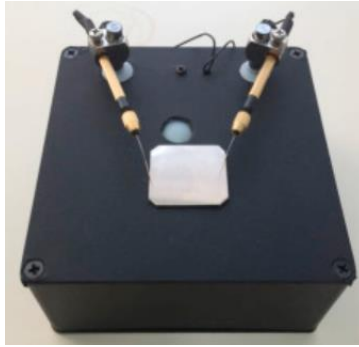At 0 K, the VB, entirely filled with valence electrons is separated by a gap, Eg from the entirely free conduction band. Band gap (Eg) of semiconductors is in the range of about 0.1-4 eV.

The electronic properties of the devices produced from semiconductors can be determined by optical, electrical and dielectric analysis. performance of solar cells made of semiconductor materials can be measured by several electrical characterization techniques. Tests in PV cells include current or capacitance measurements by applying external DC voltage. Tests in PV systems include various parameters; wavelength of monochrome light, intensity of illumination, illumination position and device temperature etc. Device parameters such as output current and voltage; energy conversion efficiency; maximum power output; doping intensity; Resistance, etc. data are obtained from current voltage (I-V) or capacitance voltage (C-V) measurements performed in DC or pulsed mode. One of the main conditions of characterization is the measurement of current - voltage (I - V) curves under standard conditions, ie at 25 ° C and under illumination using an AM1.5G spectrum. Solar Simulator system is controlled automatically by computer. System adjusts automatically the intensity of light 0.1 W/m2-1000 W /m2 by any step, for example from 1 W/m2 to 1000 W/m2 with 1 W/m2. System automatically measures current-voltage (I-V) under various light intensities and automatically measures power-voltage (P-V) under various light intensities, automatically analyses photovoltaic mechanism (I-V) under various light intensities also this system system automatically measures photo transient current-time (I-t) under various light intensities however system measures automatically open circuit voltage-time (Voc-t) under various light intensities Solar Simulator system measures automatically short current-time (Isc-t) under various light intensities

2. MATERIAL AND METHODS

The sample to be analyzed is characterized on the electronic parameters by means of computer control by touching the metal part of the probe to the contact point of the probe at one end of the probe by placing it on the probe of Figure 2. The intensity of solar simulator should automatically adjust by system. seen in Figure 3 solar simulator system should simultaneously measure I-V characteristics curve of the device, Solar Cell I-V characteristic curve, Power-voltage curve, lsc-Solar light intensity curve and photovoltaic mechanism curve and should analyse photovoltaic mechanism and write type of the mechanism on computer screen.

Fig. 2. Probe holder for electrical measurements

3. RESULTS AND DISCUSSION

The FYTRONIX FY 8000 fully automatic solar simulator system used to characterize the electronic properties of the various circuit elements is shown in Figure 3. Then, the current voltage I-V, power-voltage (P-V) and solar irradiation graphs analyzed by this device are shown. The current voltage (I-V) characteristics of any PV cell characterized by the FYTRONIX FY-8000 Solar simulator system are shown in Figure 4. As shown in Figure 4, the current of the PV cell increases as the photo current increased. This explains that the device exhibits rectifying behavior. This result can be explained by the thermionic emission theory (TE). TE theory, the correlation between current (I) and voltage (V) for forward biases of $V > 3kT/q$ is given as;

$$I = I_o[\exp(q(V - IR_s)/nkT) - 1]$$

where I_0 is the reverse saturation current, V is the applied bias voltage, Rs is the series resistance, n is the ideality factor, k is the Boltzman's constant, and T is the absolute temperature.

Fig.3. FYTRONIX FY 8000 Solar Simulator

Fig.4. Solar Simulator system automatically measures current-voltage (I-V) under various light intensities

Fig.5. Solar Simulator system automatically measures power-voltage (P-V) under various light intensities

Fig.6. Technical data and calibration results photovoltaic I-V test results

The power voltage (P-V) characteristics of any PV cell characterized by the FYTRONIX FY-8000 Solar simulator system are shown in Figure 5. As shown in Figure 5, the power-voltage curve is obtained by increasing the light intensity from 10 mW/cm^2 to 100 mW/cm^2 with 1 mW/cm^2 steps.

4. CONCLUSION

FYTRONIX FY-8000 solar simulator system determine all photovoltaic parameters. Software of Solar Simulator system determine the following photovoltaic parameters such as short circuit current Isc, open circuit voltage Voc, maximum power Pmax, maximum current Imax, maximum voltage Vmax,

efficiency η, shunt resistance Rsh and series resistance Rs.Also ,system analyze the automatically the photovoltaic mechanism analysis.

REFERENCES

[1] Frequency and electric field controllable photodevice: FYTRONIX device, A.Tataroğlu, Abdullah G.Al-Sehemi, Mehmet Özdemir, Resul Özdemir, Hakan Usta, Ahmed A.Al-Ghamdi, W.A.Farooq, F.Yakuphanoglu, Physica B: Condensed Matter,Volume 519, 15 August 2017, Pages 53-58.
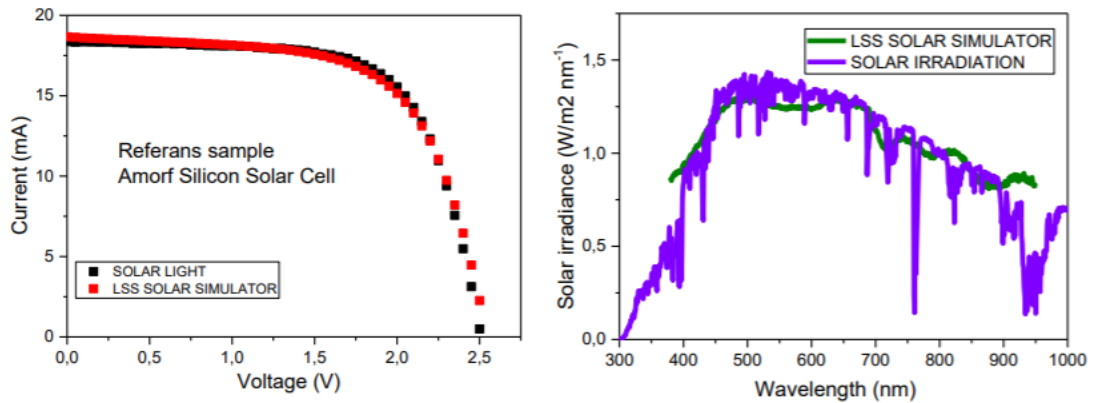
[2] Electrical Properties of Semiconductors, Nicola Pinto*, Marco Ficcadenti and Lorenzo Morresi, Silicon Based Thin Film Solar Cells, 2013, 243-276.

[3] Pinto N, Murri R, Nowak M. Magnetotransport effects in semiconductors. In: Nalwa HS, Eds Handbook of Thin Films, Vol 5, Chap 9. New York: Academic Press 2002; pp. 439 – 494.

[4] Ashcroft NW, Mermin ND, Eds. Solid State Physics. USA: John Wiley & Sons 2005.

[5] Kirchartz T, Ding K, Rau U. Fundamental electrical characterization of thin-film solar cells. In: Abou-Ras D, Kirchartz T, Rau U, Eds. Advanced Characterization Techniques for Thin Film Solar Cells. Weinheim Germany: Wiley-VCH Verlag GmbH & Co KGaA 2011; pp. 36 – 44.

DAMAGES THROUGH AESTHETIC PROBLEMS IN BUILDING FACADE: DUZCE KALICI KONUTLAR (YENIKENT) SAMPLE

A. Özata[1], A. Dilaver[1], A. Bideci[2], Ö. Sallı Bideci[2]

[1]Department of Architecture, Institute of Science, Düzce University, Düzce, TURKEY

[2]Department of Architecture, Faculty of Art, Design and Architecture, Düzce University, Düzce, TURKEY

E-mail: aygun.dilaver0@gmail.com

ABSTRACT

In this study, the damages of the buildings in the Düzce Kalıcı Konutlar (Yenikent) area built for earthquake victims in Düzce province after the 17 August 1999 and 12 November 1999 earthquakes were investigated. The aim of the study is examination of the facade damages, analyze the causes and suggest solutions. Four different buildings of two different types, two buildings with two apartments on the floor and two buildings with four apartments on the floor, were selected from four different islands in the region. Elevations and orientations diffrence of the selected buildings were considered. A field study was carried out in order to identify the damages causing aesthetic problems and photographs of the damaged areas on the facades were taken. Damages that cause damage to building facade materials and aesthetic problems were identified; efflorence, surface deterioration, color changes, atmospheric contamination, atmospheric corrosion, obsolete appearance, deterioration due to usage errors and surface corrosion of metals.

When the errors made during the design, application and usage process were examined, it was found that the most damaging factor was caused by the errors in the application phase.

Keywords: Duzce Kalıcı Konutlar, Facade Damages, Physical Building Problems.

INTRODUCTION

Depending on the functions of the building facades, it is necessary to meet the needs of its users such as aesthetics, comfort and protection from environmental influences. Facade materials cover the surfaces of building materials, and they appear to be smooth and designed, while at the same time protecting the structure from atmospheric effects and rainfall[1]. Regulations, specifications, standards have been prepared in order to provide a quality use of the structures. However, errors occur in the buildings due to reasons such as controls and inspections being carried out randomly, lack of employees who will perform the application meticulously on the construction sites, and lack of materials in compliance with the relevant standards. Due to these errors, especially building facades are damaged and worn out and these errors lead to damages that cause aesthetic problems. Failure to perform the applications properly in the first stage will result in maintenance and repair costs after damage occurs. Considering that construction materials are expensive and limited, the costs incur damage to the building owners and the national economy[2].

METHODOLOGY

In this study, Banu Erturan, Özlem Eren 's ,evaluation of building facades can be used to decide on the renovation model [3] in the work of the list of damage prepared for the facade of the example of the aesthetic problems based on the title of damage; effloresence, surface deterioration, atmospheric corrosion, deterioration due to usage errors, surface corrosion in metals, were investigated in the context of substances.

1.Effloresence

The definition of effloresence can be expressed as water entering the building element to dissolve the salts in the environment and evaporating after the heat changes, and observing the salts in the form of white spots and feathery formations on the inner surfaces. Effloresence on the facades is observed depending on the properties of the building material and the conditions of the environment. Used in the structure; bricks, mortar containing sea sand, some cement and additives are effective in the formation of effloresence [4]. In addition, the forms of storage of building materials trigger the formation of effloresence, materials should be prevented from the interaction with the soil when stored, stored in appropriate conditions. Blossoms seen at the basement level are caused by moisture, surface waters and splash rising from the ground by capillary; the causes of effloresence seen above the basin level can be shown as soil moisture and rainfall [5].

2.Surface Deterioration

These are surface deformations that occur in various factors in building materials. Material losses occur due to changes in the integrity of the material with a physical effect or fracture. Due to climatic factors such as temperature changes and frost-thawing events and physical effects, cracks and crevices may occur in the material. When the necessary precautions are not taken, these cracks grow in time and cause part losses. Another surface deterioration is contamination. Contamination Superficial contamination occurs when pollutants such as dust and soil accumulate on the surface of the material. Black colored contamination occurs due to atmospheric reasons. Depending on the usage, paint residues on the facades also cause contamination [6].

3.Atmospheric Corrosion

It is the abrasion and melting of the surfaces of materials due to the effects of rain, snow and wind. One of the damages on the surface of the structure is erosion. Climatic factors such as rain, snow and wind cause abrasion and wear on the surface of the material [6].

4.Deterioration Due to Use Errors

Human-induced defects are effective in causing physical damage to building materials. As a result of the wrong practices, damages occur on the exterior of the building due to natural events and living things. Problems caused by human effects are caused by incorrect or incomplete information and also by careless practices. Human factor in the process of damage and defect formation; incorrect detail design, misapplication, misuse and maintenance of the building [7].

Damages occur in the buildings due to the intervention and changes made by the building owners at their own will. During the usage phase, the building owners can open the windows to their facades as they wish and cause the balconies to be closed and to look different from the facades drawn in the architectural project[2] .

5. Surface Corrosion in Metals

The corrosion of metal or metal alloys by chemical effects is called corrosion. Corrosion causes staining of surfaces and cracking and separation of metal-containing composite material from other material. [8]. The main important effect of corrosion is the damage of structures to the carrier system. When the metal inside the building elements expands due to corrosion, the volume increases and starts to press around it; color

deformation on the facade can cause damage such as cracks and fragment breaks[9]. In addition, the main reason for demolition of buildings in earthquakes is the corrosion occurring in the reinforcement, the reason is not water insulation or insufficient.

AREA STUDY

Duzce-Permanent Houses (Yenikent) region, which was selected as the study area, was opened to settlement in 2003, consists of 14 regions and these regions are divided into 6 neighborhoods and there are approximately 7000 houses. In this study, four buildings of two different plan types were selected from four different islands in Bahçelievler Neighborhood.

The climate here is mild, and generally warm and temperate. The average annual temperature is 11.8 c in Düzce with significant rainfall and the average annual rainfall is 660 mm. During the year, the average temperatures vary by 17.9 ° C. Northern winds are dominant [10].

Fig.1. Bahçelievler neighborhood satellite view	*Fig.2. Working area satellite view*

Fig. 3. Selected buildings

Type-1 floor two-room buildings, Type-2 floor four-room buildings were identified as.
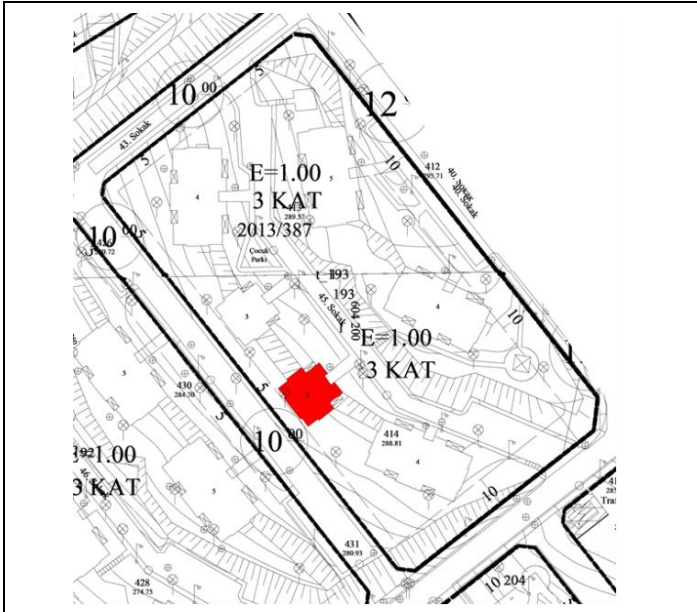
Fig 4-Type-1.1 The building was placed on the 193th island at 288 m elevation in northeast-southwest direction. The residence area is approximately 210 m2 with three floors and a total of 6 apartments.
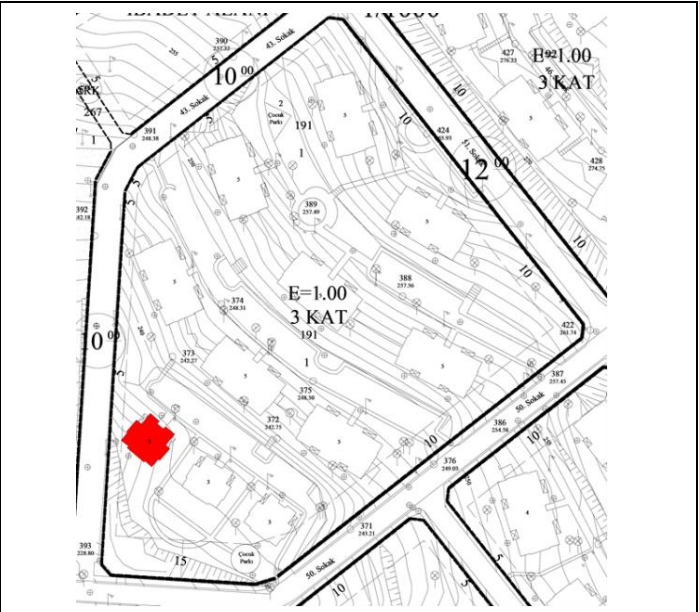

Fig 5-Type-1.2The building was placed on the 191th island at 238 m elevation in the northeast-southwest direction. The residence area is approximately 210 m2 with three floors and a total of 6 apartments.

Fig 6-Type-2.1 The building was placed on the 137th island at 280 m elevation in northwest-southeast direction. The residence area is approximately 465 m2. It has five floors and consists of 18 apartments in total.
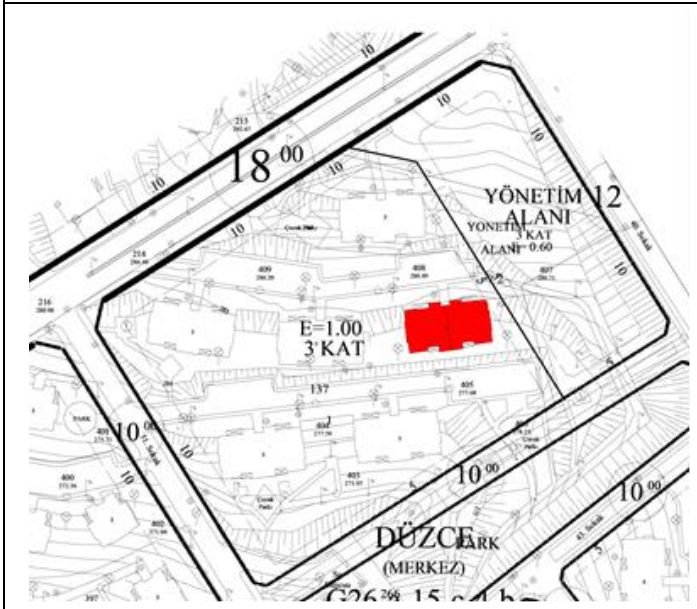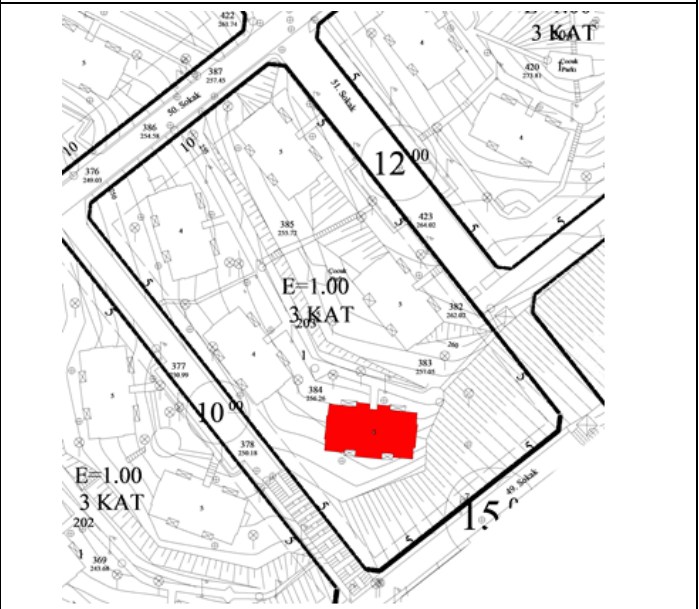

Fig 7-Type-2.2 The building was placed on the 203th island at 254 m elevation in northwest-southeast direction. The residence area is approximately 465 m2. It consists of four floors and 14 apartments in total.

Fındıngs And Evaluatıon

Effloresence

Fig.8 Type-1.1 effloresence(northeast)	*Fig.9Type-1.1 efflorence (northwest)*

The waterlogging level of the structure and the effloresence at the junction of the ground are the formation of the water rising from the ground by capillary on the surface of the facade by evaporation by combining with the chemicals in the wetted material. With the arrangements around the building, the water coming to the ground should be removed from the building.
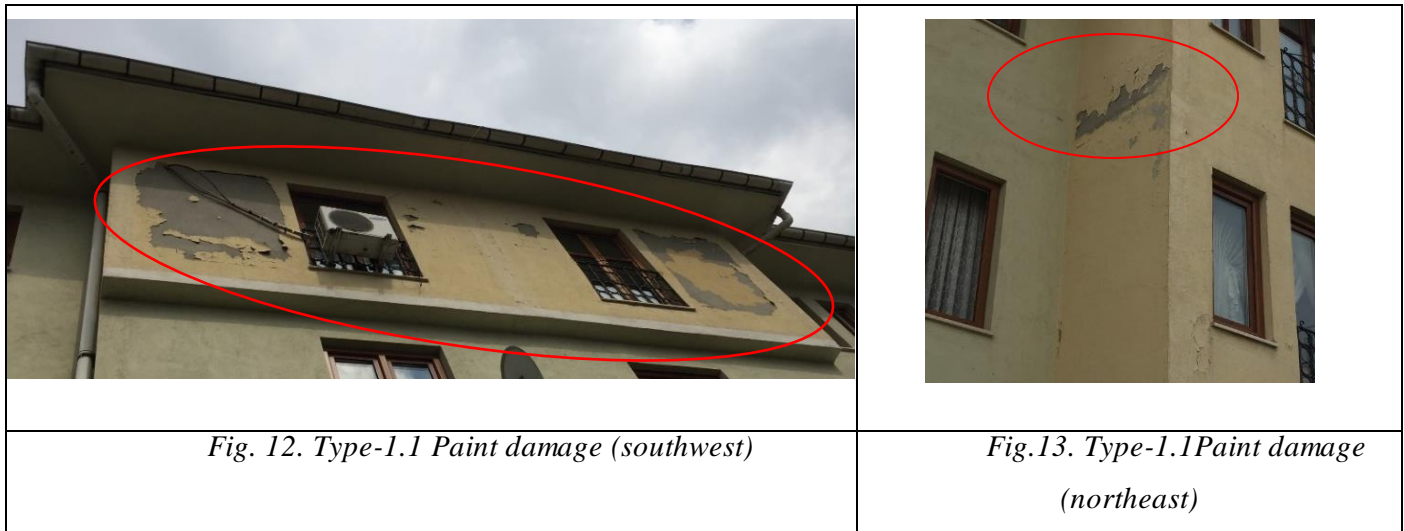

Fig.10 Type-1.2 Effloresence (southeast)	*Fig.11 Type-2.3 effloresence(northwest)*

Surface Deterioration

When rainwater enters the facade cladding materials or the water vapor coming from the interior is under the impermeable layer due to the impermeable material, the water condenses and the swelling cracks occur due to the difference in the thermal expansion coefficients of the two materials.

Fig. 12. Type-1.1 Paint damage (southwest)	*Fig.13. Type-1.1Paint damage (northeast)*

Changes in temperature cause effects such as expansion-shrinkage of materials. The application of materials with different properties interactively causes separation from the joints and damage to the coating surfaces and paint coatings.

Fig.14 Type-2.2 Paint damage (southwest)	*Fig. 15. Type-1.2 Paint damage (southwest)*

In reinforced concrete surfaces without using primer materials or coatings with insufficient quality materials, temperature changes, rainfall, sun and wind combined with the effects of breakage and spills caused.

Atmospheric Corrosion

Coating materials get wet when in contact with water and damage the internal structure of the material. Due to the effects of climatic factors, these damages are seen as cracks and breaks in facade materials in time.

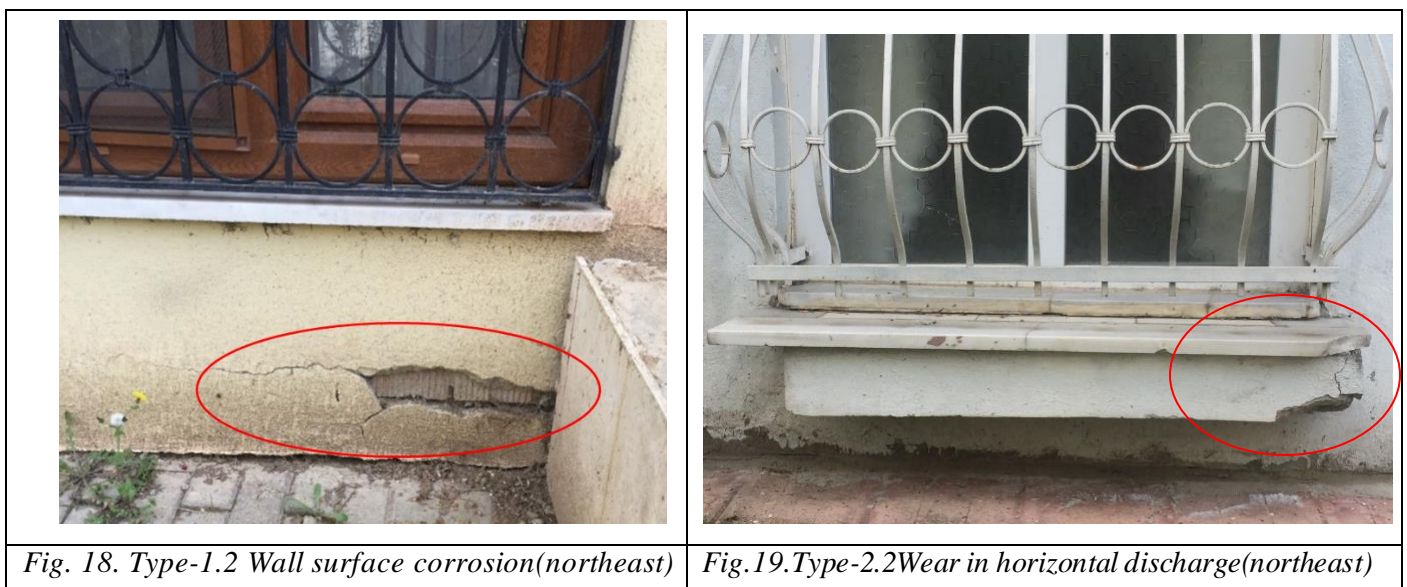|	
Fig. 16. Type 1.1 Corrosion on the roof (southwest)	*Fig. 17. Type-1.2 Corrosion on the roof (southwest)*

Damage of rain gutters, insufficient water carrying capacity, etc. due to various reasons such as water coming down from the roof to come into contact with the building surfaces, water adheres to the surfaces and penetrates into the material with the effects of wind. These damages on the roof pavement continued as the water caused swelling, cracking and subsequent rupture.

Fig. 18. Type-1.2 Wall surface corrosion(northeast)	*Fig.19.Type-2.2Wear in horizontal discharge(northeast)*

Elevated water that is not removed from the ground by appropriate methods and the material used in subsequent additions to the structure with different characteristics of the facade cladding material caused cracking, breakage and abrasion by atmospheric factors. With the lack of proper detailing in the horizontal protrusions, the water could not be removed from the structure of the material and cracking from weak points and abrasion occurred over time [11].

Deterioration Due to Use Errors

Fig.20.Type-1.2 surface contamination (southwest)	*Fig.21.Type-1.2 Damages under dropper unregulated windowsill (southeast)*

In the windowsills without dropper details, the pollutants (exhaust smoke, dust, etc.) accumulated on the facade surface started to flow from the corners of the windowsills and unwanted images were formed on the coating material. deterioration and swelling of the paint, followed by cracking and various deformations.

Fig. 22. Type-2.2 facade view (southeast)	*Fig.23.Type-1.2 anchor materials and drilled holes*

Appliances such as antennas, air conditioners added to the building facades, and also the devices added by the building users for hanging clothes, cause visual negative effects on the building facades. The difference between the properties of the materials used during the installation of the devices will be combined with the effect of heat and water, causing damage to the facades over time. Failure to plan these additions to the facades and the subsequent displacements results in both aesthetic and physical damage to the facade.

Fig.24. Type-2.2Eaves attached to the facade(southeast)	*Fig. 25. Type-2.2 Closed balcony*

Building users can make changes in the building facades in line with their wishes and damage the facades. In use, as shown in the figures, unlike the architectural project, balconies have been closed, garden floor users have entered the apartments from the balcony and covered the garden entrances with sheet metal porch. Due to the material properties, structural and aesthetic damage has occurred. Failure to apply sanctions to prevent the building owners from acting in accordance with their wishes, lack of controls has led to the appearance of images in the figures.

Fig. 26. Type-1.1 Rain downpipe (northeast)	*Fig. 27. Type-2.2 rain downpipe (northwest)*

The building material gets wet and damages the internal structure of the water as the rain down pipes are not lowered to the ground or the water coming from the pipes is not removed from the ground. Various microorganisms, algae and so on. It is formed. These formations damage the structure both aesthetically and because of the smell they emit.

Fig.28.Type-2.2 Rain downpipe and bird droppings	*Fig.29. Type-2.1 rain downspout (northeast)*

The feces of the birds perching on the rain downpipes cause a dirty appearance in the facade covering material. Combines with precipitation waters and damages the material as abrasive on the surface.

Fig. 30.. Type-2.1 facade deterioration	*Fig. 31.. Type-2.1 facade deterioration*

In the structure seen in the figures, it was decided to renew the facade cladding but due to the characteristics of the material used, the insufficiencies in application, and the lack of binding primer on the surface to be applied, the new material could not provide adherence with the existing surface, and breaks were observed in all parts of the facade.

Fig.32. Type-2.1 Facade deterioration (southeast)	*Fig 33. Type-2.1 Facade deterioration (southeast)*

The main reason for the formation of ruptures can be shown as the lack of adherence of the material with the existing surface, while atmospheric factors have triggered the formation of ruptures.

Surface Corrosion in Metals

The physical properties of the ceramic and the plastered surface were not the same, the expansion coefficients in the temperature changes were different, causing cracks from the joints and water leakage from these cracks for various reasons. chemical reactions on metal surfaces and the increase in the volume of metal as a result of these reactions caused fractures with various stresses in the coating to break the parts.

Fig. 34. Type-1.1 corrosion (northeast)

RESULTS AND RECOMMENDATIONS

As a result of the study, after the 17 August 1999 and 12 November 1999 earthquakes in the Permanent Houses (Yenikent) built for earthquake victims in the province of Düzce, causing damage to the front of the buildings and causing damage to the aesthetic problems, the most damage when examined through the design, application and use of the damage It was determined that the causative factor was caused by errors in the application phase.

Results

• Fragmentation and ruptures occurred due to frost and corrosion effects in the facade cladding materials and the damaged parts should be repaired with suitable materials in order to prevent these ruptures and breaks.

• It has been observed that the water leaking into the ground is not solved by appropriate drainage systems and the presence of rising water sucked from the ground due to pressurized ground water. Due to the lack of proper waterproofing on the surfaces that come into contact with the soil, the water has risen through the capillary and the water, which is combined with the effect of temperature differences, frost and thawing

during the day and night, has caused breaks. In order to prevent this, waterproofing should be repeated on surfaces where the material interacts with the soil.

• It should be solved and applied with correct details at the connection points of the buildings with the ground. The detachment should be made prone from the ground junctions, and water should be prevented from accumulation and removed from the structure. Rain downpipes should be lowered to the ground, hidden channels should be arranged and water should be removed from the structure.

• In the presence of oxygen and water, metals such as iron and steel are corroded by chemical reactions. As it is seen in the buildings, corrosion occurs with the effect of atmosphere and water. Corrosion-induced rust takes up more space than metal, resulting in internal stresses and cracking caused by structural damage.

• It is seen that bird nests and wastes damage the facade and floor coverings. Precautions should be taken to prevent birds from roosting and away from the structure.

• The appropriate installation details of the satellite antennas and air conditioners added to the building facades must be arranged. Damages were observed at the mounting points, anchoring elements remaining on the facade after unnecessary assemblies damage the facade aesthetically. Mounting materials should be chosen appropriately and labor errors should be prevented.

• When the structures after the earthquake were examined, it was observed that structural damages were caused by corrosion of reinforced concrete reinforcement with water moisture. For this reason, necessary precautions should be taken in the buildings before they reach the extent of structural damage.

• Since the dropper detail was not made, the water was held on the surface and caused damage. The dripping of the coating materials and water should be detailed and applied.

Suggestions

• In order to prevent effloresence on the facades of buildings, it is possible to prevent effloresence and staining with chemical additives as well as preventing contact with soil when storing building materials.

• In order to prevent corrosion from physico-chemical problems in the structures, cathodization can be done on the materials or protection can be realized by covering or covering the surface of the metals. Metal surfaces to be protected in this method; oxide, silicate, metallic or organic based (oil, bitumen, plastic and oil paint) coatings. In order to protect against corrosion, it is necessary not to put together two different metals without insulation and to apply protection methods and to maintain them continuously.

REFERENCES

[1]Güler,H. 2010, Binalarda Yapı Fiziği Problemleri: Bursa'da Bir Kamu Kurumu Örneği,Uludağ Üniversitesi Mühendislik-Mimarlık Fakültesi Dergisi, Cilt 15, Sayı 2,Bursa. (In Turkish)

[2] Koçu, N. 2008, 4. Ulusal Çatı & Cephe Kaplamalarında Çağdaş Malzeme ve Teknolojiler"Sempozyumu, İTÜ Mimarlık Fakültesi, Yapı Cephelerinde Görsel Yönden Olumsuz Olarak Etkileyen Sorunlar ve Nedenlerin Analizi , İstanbul. (In Turkish)

[3] Erturan, B. Eren, Ö. 2017, Bina Cephelerinin Yenilemesine Karar Vermek İçin Kullanılabilecek Bir Değerlendirme Modeli, Aralık, İstanbul, Görsel Yönden Olumsuz Olarak Etkileyen Sorunlar ve Nedenlerin Analizi , İstanbul. (In Turkish)

[4] Tuncel, S. (1998), Cephe Kaplama Malzemesi Olarak Tuğlanın Betonarme Karkas Yapı Dış Duvarlarına Uygulanması ve Yağmur Suyu Etkilerinin Araştırılması, Yüksek Lisans Tezi, YTÜ Fen Bilimleri Enstitüsü(In Turkish)

[5] Güzelçoban, S. 2007, Yapılarda Su ve Isı Etkenleri, Oluşturduğu Sorunlar, Nedenleri ve Çözüm Önerileri, Yüksek Lisans Tezi, Ytü Fen Bilimleri Enstitüsü, İstanbul. (In Turkish)

[6] Eskici, B. 2006, Erzurum Yakutiye Medresesi Yapı Malzemeleri, Bozulmalar ve Koruma Problemleri, Ankara Üniversitesi Dil ve Tarih-Coğrafya Fakültesi Dergisi 46,165-188, Ankara. (In Turkish)

[7] Koç, İ. 2000, Konut Kooperatif Yapılarında Görülen Hasar ve Kusurların, Kooperatifin Yapısal Özellikleri Bakımından İrdelenmesine İlişkin Bir Model Önerisi; 1980 Sonrası Konya Örneği, Doktora Tezi, İTÜ Fen Bilimleri Enstitüsü, Yayınlanmamış, İstanbul. (In Turkish)

[8] Doruk, M. (1982) Korozyon ve Önlenmesi, Ankara, Ortadoğu Teknik Üniversitesi Yayını, Ankara, 239s. (In Turkish)

[9] Ergi, E., Bilgin, G. S., Zeybek, M. S., Asan, A. (2007), Endüstriyel Atık Katkılı Çimentoların Beton Dayanımı ve Donatı Korozyonuna Etkileri, 2.Yapılarda Kimyasal Katkılar Sempozyumu, Ankara-Türkiye. (In Turkish)

[10] URL.(2019).https://tr.climate-data.org/asya/tuerkiye/duezce/duezce-187/

[11]Dereli, M. 2018,Yapıların Cephe Kaplama Malzemelerinde Hasar Oluşturan Etkilerin Tespiti ve Çözüm Önerileri – Konya Ptt Hizmet Binası Örneği*, Konya. (In Turkish)